THE ROLE OF MEDIATOR COMPLEX IN TAMOXIFEN RESISTANCE OF ER-POSITIVE BREAST CANCER

A DISSERTATION SUBMITTED TO

THE GRADUATE SCHOOL OF ENGINEERING AND SCIENCE

OF BILKENT UNIVERSITY

IN PARTIAL FULFILLMENT OF THE REQUIREMENTS FOR

THE DEGREE OF

DOCTOR OF PHILOSOPHY

IN

MOLECULAR BIOLOGY AND GENETICS

By

Pelin Gülizar Ersan

January, 2022

The Role of Mediator Complex in Tamoxifen Resistance of ER-positive Breast Cancer

By Pelin Gülizar Ersan

January 2022

We certify that we have read this dissertation and that in our opinion it is fully adequate in scope and in quality, as a dissertation for the degree of Doctor of Philosophy.

_____

Onur Çizmecioğlu

(Advisor)

_____

Özgür Şahin

(Co-Advisor)

_____

Öznur Taştan Okan

_____

Serkan İsmail Göktuna

_____

Tolga Can

_____

Murat Alper Cevher

Approved for Graduate School of Engineering and Science

_____

Ezhan Karaşan

Director of the Graduate School of Engineering and Science

ABSTRACT

THE ROLE OF MEDIATOR COMPLEX IN TAMOXIFEN RESISTANCE OF ER-POSITIVE BREAST CANCER

Pelin Gülizar Ersan
Ph.D. in Molecular Biology and Genetics
Advisor: Onur Çizmecioğlu
Co-Advisor: Özgür Şahin
January, 2022

Breast cancer is the most prevalent cancer type and the leading cause of cancer mortality among women worldwide. Estrogen receptor-positive (ER+) breast cancer is the most common clinical subtype with an incidence rate of approximately 80% of all breast cancers. Tamoxifen is a highly effective hormonal therapy for ER-positive breast cancer patients. However, its remarkable success is hampered by *de novo* or acquired resistance. Despite several advances in therapy options for relapsing patients, tamoxifen resistance is still an urgent clinical problem that needs to be addressed. Therefore, there is a dire need for novel targeted therapies to confer tamoxifen resistance in ER-positive breast cancer. The architecture of Mediator complex links DNA-bound transcription factors to the general transcription machinery RNA polymerase II. Mediator kinase module is dissociable part of the Mediator complex and broadly involved in human cancers. However, the role of kinase module in tamoxifen resistance has not been investigated.

In this dissertation, I deciphered the association of Mediator kinase module in tamoxifen resistance both *in vitro* and *in vivo* settings. Initially, our gene expression

profiling and survival analyses revealed that Mediator subunit 13 (MED13) and cyclin-dependent kinase 8 (CDK8) were significantly higher in tamoxifen-treated patients, and this outcome strongly correlated with worsened patient survival. *In vitro* inhibition of either MED13 *via* genetic modulation or CDK8 by highly selective inhibitor, SNX631, significantly reversed tamoxifen resistance. Notably, targeting MED13 or CDK8 resulted in inhibition of HER2/mTOR signaling and triggered apoptosis. Mechanistically, we identified that inhibition of either MED13 or CDK8 combined with tamoxifen treatment reduced ErbB2 mRNA level. We further demonstrated that CDK8 post-transcriptionally controls ErbB2 level *via* regulating mRNA stability. Moreover, inducible silencing of MED13 in combination with tamoxifen impaired the tumor growth. Similarly, *in vivo* treatment of SNX631 together with tamoxifen reduced tumor growth in xenografts and prolonged the life-span in an aggressive transgenic mouse model. These results provided insight into how transcriptional programmers MED13 and CDK8, could contribute to mediating tamoxifen resistance and added new dimension to treatment strategies for ER-positive breast cancer.

***Keywords*:** ER-positive breast cancer, tamoxifen resistance, Mediator complex, MED13, CDK8

ÖZET

MEDİATÖR KOMPLEKSİNİN ÖSTROJEN RESEPTÖRÜ-POZİTİF MEME KANSERİNİN TAMOKSİFEN DİRENCİNDEKİ ROLÜ

Pelin Gülizar Ersan
Moleküler Biyoloji ve Genetik, Doktora
Tez Danışmanı: Onur Çizmecioğlu
Tez Eş Danışmanı: Özgür Şahin
Ocak 2022

Meme kanseri kadınlarda görülen en yaygın kanser türü olup kanser kaynaklı ölümlerin önde gelen nedenidir. Östrojen reseptörü-pozitif meme kanseri yaklaşık %80 vaka oranı ile tüm meme kanserleri içinde en yaygın görülen klinik alt türüdür. Tamoksifen, Östrojen reseptörü-pozitif meme kanseri hastalarında kullanılan son derece etkili hormonal tedavi türüdür. Fakat tamoksifenin klinikteki büyük başarısı spontan ya da sonradan kazanılan ilaç direnci nedeniyle engellenmektedir. Nükse uğrayan hastalar için birçok tedavi olanağı geliştirilse de tamoksifen direnci, üzerinde durulması gereken önemli bir klinik problemdir. Bu nedenle, östrojen reseptörü-pozitif meme kanseri hastalarında tamoksifen direncini düzenleyen yeni hedeflenebilir tedavilerin bulunması büyük önem arz etmektedir. Mediatör kompleksi, DNA'ya bağlı transkripsiyon faktörleri ile genel transkripsiyon makinesi RNA polimeraz arasında bağlantı kurar. Mediatör kinaz modülü, Mediatör kompleksinin ayrılabilir parçasıdır ve birçok kanser türü ile ilişkilendirilmiştir. Fakat kinaz modülünün tamoksifen direncindeki rolü bilinmemektedir.

Bu tezde hem *in vitro* hem *in vivo* deney koşullarında Mediatör kompleksinin tamoksifen direnci ile olan ilişkisini aydınlatmaya çalıştım. Öncelikle, gen ekspresyonu profillemesi ve hasta hayatta kalım analizleri ile Mediatör alt-birim 13 (MED13) ve siklin-bağımlı kinaz 8 (CDK8)'in tamoksifen ile tedavi edilmiş hastalarda daha yüksek seviyede olduğu görülmüş ve bunun kötü seyreden hayatta kalım ile ilişkisi gösterilmiştir. Genetik modülasyon ile MED13'ün baskılanması ya da yüksek ölçüde seçicilik gösteren bir inhibitör olan SNX631 ile CDK8'in baskılanması tamoksifen direncini geri çevirmiştir. Önemli olarak, MED13 ya da CDK8'in hedeflenmesi HER2/mTOR sinyal yolağında baskılanmaya yol açarak, apoptoza neden olmuştur. Mekaniksel olarak, MED13 ya da CDK8'in baskılanmasının tamoksifen tedavisi ile birlikte ErbB2 mRNA seviyesinde azalmaya neden olduğu belirlenmiştir. Daha sonra CDK8'in ErbB2 seviyesini mRNA stabilitesini düzenleyerek post-transkripsiyonel olarak kontrol ettiği gösterilmiştir. Ayrıca, indüklenebilir susturulma yöntemi ile MED13 ifadesi baskılanıp tamoksifen tedavisi uygulandığında tümör gelişimi yavaşlamıştır. Buna benzer olarak, SNX631 ilacının tamoksifen ile birlikte kullanılması zenograftlarda tümör hacmini küçültürken, agresif bir transgenik fare modelinde hayatta kalım süresini uzatmıştır. Bu sonuçlar transkripsiyonel programlayıcı olan MED13 ve CDK8'in tamoksifen direncine nasıl katkıda bulunduğuna dair yeni bakış açıları kazandırmış, östrojen reseptörü-pozitif meme kanseri tedavisinde kullanılmak üzere yeni bir strateji olarak sunulmuştur.

Anahtar kelimeler: ER-pozitif meme kanseri, tamoksifen direnci, Mediatör kompleksi, MED13, CDK8

I dedicate this work

To my endless power and inspiration- **my mother**

To my honesty- **my father**

To my motivation and best friend ever- **Selin**

To my humor- **Taner**

ACKNOWLEDGEMENTS

First and foremost, I would like to express my sincere gratitude and appreciation to my advisor Assoc. Prof. Özgür Şahin for offering me the opportunity to work in his lab, for introducing cancer research field to me, and for shaping my scientific career with his wide knowledge and inspiring suggestions.

I also would like to thank Assist. Prof. Onur Çizmecioğlu for being my advisor at the last two years of my Ph.D. study. His attitude to young scientists, constructive comments, invaluable advice and scientific guidance are really influential and make an example of perfect mentor. My special appreciations to Assist. Prof. Öznur Taştan Okan and Assist. Prof. Serkan İsmail Göktuna for being a member of my thesis committee and constructive comments directing my study over the years. I also would like to acknowledge Prof. Dr. Tolga Can for being a member of my Ph.D. defense committee.

I sincerely thank to Prof. Dr. Igor Roninson, Assoc. Prof Eugenia Broude for providing SNX631 compound and for sharing their experience and knowledge about CDK8 field, to Assist. Prof. Mengqian Chen for his guidance on the use of SNX631 compound.

My special thanks to Assist. Prof. Murat Alper Cevher for sharing his expertise on Mediator complex and to his lab members Melike Dinçelik Aslan and Volkan Aslan for their help and great friendship.

My sincere thanks to Ünal Metin Tokat for his life-saving efforts and being perfect partner in all scientific meetings and travels, to Özge Akbulut Çalışkan for her

valuable friendship and endless support, to İbrahim Oğuzhan Tarman for his perfect guidance in almost all technical problems and great friendship.

I owe my deepest appreciation to the ‘tamoxifen resistance crew’- Suhail Akhtar Ansari, Rasmi Rekha Mishra, Nevin Belder, and Hilal Bal for their accumulated data, practical knowledge and scientific guidance which help me in every step of my study.

As one of the frequent users of the animal facility, I would like to thank Gamze Aykut for teaching me different techniques with full of kindness and patience and Ulaş Saçıntı for all the efforts and time he had generously given to make the facility appropriate for animal research.

I also want to thank all the present and former members of Şahin Lab; Özge Saatci, Ridho Assidicky, Özlem Şener Şahin, Erol Eyüpoğlu, Umar Raza, Merve Mutlu, Selvi Durmuş, Ayşegül Kaymak, Mertkaya Aras and Emre Yurdusev for their help and support.

I am sincerely thankful to İrem Evcili for her patience during my thesis writing period, and very grateful to Barış Küçükkaraduman, Seniye Targen, Tuğçe Kadriye Bildik, Aslı Gülce Bartan, Berfu Saraydar, Yasemin Ceylan, İrem Abraş, Ege Dedeoğlu, Özlem Aybüke Işık, Taha Buğra Güngül and Irmak Kaysudu for all beautiful memories we shared together.

My sincere appreciations to Nigar Pelin Makas, Seda Şengül Birkan, Okan Erşahan, Yavuz Ceylan, and Sultan Turan for their warmest attitude made me feel at home.

I would like to acknowledge European Molecular Biology Organization Installation Grant 2791, Bilkent University, Department of Molecular Biology and Genetics and

University of South Carolina, Department of Drug Discovery and Biomedical Sciences for their support throughout my Ph.D. study.

Last but not least, I would like to thank my parents- the reason what I have become today- for their wholehearted support and faith on me, to my sister and brother not only for sharing my happiness but also for listening my troubles. They always provided moral and encouraged me to go on every adventure, in particular this one.

TABLE OF CONTENTS

ABSTRACT ii
ÖZET iv
ACKNOWLEDGEMENTS vii
TABLE OF CONTENTS x
LIST OF FIGURES xii
LIST OF TABLES xiv
ABBREVIATIONS xv

CHAPTER 1 1

INTRODUCTION 1

1.1. Breast Cancer 1
1.2. ER-positive breast cancer 2

1.2.1. Treatment strategies for ER-positive breast cancer 3
1.2.2. Mechanisms of Endocrine Resistance in Breast Cancer 6

1.3. Mediator 10

1.3.1. Kinase module 11
1.3.2. The role of kinase module in human disease 12

1.4. The rationale and the aims of the dissertation 14

CHAPTER 2 15

MATERIALS 15

2.1. Buffers 15
2.2. Chemicals and reagents 15
2.3. Media and Supplements 18
2.4. Kits 19
2.5. Equipment 19
2.6. Consumables 20

CHAPTER 3 22

METHODS 22

3.1. *In vitro* experiments 22

3.1.1. Culturing cell lines 22
3.1.2. siRNA Transfections 22
3.1.3. Cell viability assays 23
3.1.4. Colony Formation Assay 23
3.1.5. Lentiviral vector-based transfections 24

3.2. Quantitative Real-Time Polymerase Chain Reaction (qRT-PCR) 25

3.2.1. Total RNA isolation 25
3.2.2. cDNA synthesis 25
3.2.3. qRT-PCR 26

3.3. Protein Biochemistry 28

3.3.1. Protein isolation 28
3.3.2. Protein quantification 29
3.3.3. Sodium dodecyl sulfate polyacrylamide gel electrophoresis (SDS-PAGE) 30
3.3.4. Western blotting 31
3.4. *In vivo* experiments 33
3.4.1. Primary tumor growths 33
3.4.2. *In vivo* imaging system (IVIS) 34
3.4.3. Transgenic animal model and syngeneic tumor transplantation 34
3.4.4. Immunohistochemistry 37
3.5. Bioinformatics and statistical analysis 37
3.5.1. Patient dataset analysis and Gene Set Enrichment Analysis (GSEA) 37
3.5.2. Statistical analysis 37
CHAPTER 4 39
RESULTS 39
4.1. MED13 and CDK8 are overexpressed in tamoxifen resistant breast cancer 39
4.2. Inhibition of either MED13 or CDK8 re-sensitizes the tamoxifen resistant cells 45
4.3. MED13 and CDK8 dependent tamoxifen resistance is mediated via HER2/mTOR axis 48
4.4. Inhibition of either MED13 or CDK8 reduced the mRNA expression of ErbB2 53
4.5. MED13 inhibition overcomes tamoxifen resistance *in vivo* 57
4.6. CDK8 inhibition overcomes tamoxifen resistance *in vivo* 59
4.7. Targeting CDK8 overcomes tamoxifen resistance in an aggressive transgenic mouse model 61
4.8. Selected projects/collaboration studies 65
CHAPTER 5 78
DISCUSSION 78
5.1. MED13 and CDK8 in tamoxifen resistance 78
5.2. MED13/CDK8/HER2/mTOR axis: Biomarker of tamoxifen response 81
5.3. A more potent CDK8 inhibitor, SNX631 83
CHAPTER 6 87
CONCLUSIONS AND FUTURE PERSPECTIVES 87
MED13/CDK8/HER2/mTOR axis confers tamoxifen resistance in ER-positive breast cancer 87
BIBLIOGRAPHY 90
APPENDIX 109

LIST OF FIGURES

Figure 1.1. A dendrogram showing molecular subtype classification.....2
Figure 1.2. Simplified diagram of estrogen signaling pathways 3
Figure 1.3. Mechanism of action of the different endocrine therapy 6
Figure 1.4. Signaling pathways leading to endocrine resistance and current therapies 9
Figure 1.5. Mediator complex subunits 11
Figure 4.1. Characterization of tamoxifen resistance in MCF-7 and T47D cells.....40
Figure 4.2. Graphical depiction of CDK8 kinase module (CKM) 41
Figure 4.3. CDK8 and MED13 are overexpressed in tamoxifen-treated ER positive patients. 41
Figure 4.4. Expression levels of MED12 and CCNC in tamoxifen-treated ER-positive breast cancer patients. 42
Figure 4.5. Overexpression of CDK8 and MED13 is correlated with higher tumor grade. 43
Figure 4.6. CDK8 and MED13 overexpression predicts poor relapse-free survival in tamoxifen- or endocrine-treated ER-positive patients. 43
Figure 4.7. Kaplan Meier plots showing the effects of MED12 and CCNC on patient survivals. 44
Figure 4.8. CDK8 and MED13 are overexpressed in well-established tamoxifen resistant cell line models unlike other components of kinase module.....45
Figure 4.9. MED13 inhibition re-sensitizes the tamoxifen resistant cells 46
Figure 4.10. CDK8 inhibitor, SNX631, suppressed phosphorylation of STAT1.....47
Figure 4.11. CDK8 inhibition re-sensitizes the tamoxifen resistant cells. 48
Figure 4.12. SNX631 treatment combined with tamoxifen reduces colony forming capabilities of TamR cells 48
Figure 4.13. MTOR signaling is associated with tamoxifen resistance. 49
Figure 4.14. HER2/mTOR signaling markers are upregulated in TamR cell line models. 50
Figure 4.15. MED13 dependent tamoxifen resistance is mediated *via* HER2/mTOR axis. 50
Figure 4.16. Combination of MED13 knockdown and tamoxifen treatment triggered apoptosis. 51
Figure 4.17. Gene set enrichment analysis identified CDK8 associated MTORC signaling.....51
Figure 4.18. CDK8 dependent tamoxifen resistance is mediated *via* HER2/mTOR axis 52
Figure 4.19. Combination of SNX631 and tamoxifen treatment induced apoptosis. 52

Figure 4.20. MED13 positively correlates with ErbB2 expression in tamoxifen treated ER-positive breast cancer patients. 53

Figure 4.21. Combining MED13 knockdown with tamoxifen treatment reduced ErbB2 mRNA level. 54

Figure 4.22. Gene set enrichment analysis identified CDK8 associated ERBB2 signaling 54

Figure 4.23. CDK8 positively correlates with ErbB2 expression in tamoxifen treated ER-positive breast cancer patients. 55

Figure 4.24. Combination treatment of tamoxifen and SNX631 downregulated mRNA expression of ErbB2. 55

Figure 4.25. Combined therapy of tamoxifen and SNX631 significantly reduced ErbB2 mRNA stability. 56

Figure 4.26. Validation of inducible MED13 knockdown in MCF-7 TamR cells 57

Figure 4.27. MED13 inhibition combined with tamoxifen treatment reduces colony forming capabilities of TamR cells 58

Figure 4.28. MED13 inhibition overcomes tamoxifen resistance *in vivo.* 59

Figure 4.29. CDK8 inhibition overcomes tamoxifen resistance *in vivo.* 61

Figure 4.30. Summary of tumor progression and biomarker expression in the MMTV-PyMT mouse model. 62

Figure 4.31. GSEA shows significant enrichment of gene sets involved in endocrine therapy resistance and ErbB2 signaling in late-stage tumors. 63

Figure 4.32. Enrichment of CDK8 and HER2, but loss of ER expression at later stages of tumor progression in MMTV-PyMT mouse model. 63

Figure 4.33. Targeting CDK8 overcomes tamoxifen resistance in an aggressive transgenic mouse model 64

Figure 4.34. Schematic representation of the study plan and methodology. 66

Figure 4.35. Schematic summary of the findings. 67

Figure 4.36. PDE4D inhibition overcomes tamoxifen resistance *in vivo.* 68

Figure 4.37. Constructing miRNA-mRNA interaction network of TNBC chemoresistance. 70

Figure 4.38. Schematic representation of the mechanistic summary 71

Figure 4.39. miR-326 potentiates doxorubicin response *in vivo.* 72

Figure 4.40. Inhibiting ITGA5 potentiates chemo-response *in vivo.* 73

Figure 4.41. Graphical abstract summarizing the findings. 74

Figure 4.42. Inhibition of CD81 and DNAJB4 reduced primary tumor growth, blocks spontaneous metastasis and extravasation/colonization. 76

Figure 5.1. Schematic representation of MED13/CDK8/HER2/mTOR axis mediated tamoxifen resistance 82

LIST OF TABLES

Table 3.1. List of siRNAs used in transfections 23
Table 3.2. List of shRNAs used in transfections 24
Table 3.3. Components of reverse transcription reaction 25
Table 3.4. Thermocycler program for cDNA synthesis 26
Table 3.5. Master mix for qRT-PCR reaction 26
Table 3.6. List of primers used for qRT-PCR 27
Table 3.7. Program for qRT-PCR 27
Table 3.8. Contents of the RIPA buffer 29
Table 3.9. Components of the 4X loading dye 30
Table 3.10. Components of resolving and stacking gels at different concentrations 31
Table 3.11. List of primary and secondary antibodies used in the study 32
Table 3.12. Components of lysis buffer 35
Table 3.13. Protocol primer sequences 35
Table 3.14. PCR Components 35
Table 3.15. PCR program 36

ABBREVIATIONS

4-OHT	4-Hydroxytamoxifen
AI	Aromatase inhibitor
AKT	Serine/Threonine Kinase
ANOVA	Analysis of variance
APS	Ammonium peroxodisulfate
BCA	Bicinchoninic acid
BSA	Bovine Serum Albumin
cAMP	Cyclic adenosine monophosphate
CCNC	Cyclin C
CD81	Cluster of differentiation 81
CDK8	Cyclin-dependent kinase 8
cDNA	Complementary DNA
CKM	CDK8 kinase module
DMEM	Dulbecco's modified eagle medium
DNA	Deoxyribonucleic acid
DNAJB4	DnaJ Heat Shock Protein Family (Hsp40) Member B4
dNTP	Deoxynucleotide triphosphate
E1	Estrone

E2	17β-estradiol or estradiol
E3	Estriol
ECL	Enhanced chemiluminescence
EGFR	Epidermal Growth Factor Receptor
eIF2α	Eukaryotic translation initiation factor 2α
ER	Estrogen receptor
EnR	Endoplasmic reticulum
ERE	Estrogen response element
FBS	Fetal bovine serum
FDA	Food and Drug Administration
FDR	False Discovery Rate
GAPDH	Glyceraldehyde-3-Phosphate Dehydrogenase
GEMM	Genetically engineered mouse model
GEO	Gene expression omnibus
GSEA	Gene set enrichment analysis
GTF	General transcription factors
H&E	Haematoxylin & Eosin
HER2	Human epidermal growth factor receptor 2
HRP	Horseradish peroxidase
IPA	Ingenuity Pathway Analysis

ITGA5	Integrin subunit alpha 5
IVIS	*In vivo* imaging system
JNK	c-Jun N-terminal kinase
KM	Kaplan Meier
MAPK	Mitogen-activated protein kinase
MED12	Mediator subunit 12
MED13	Mediator subunit 13
MMTV	Mouse mammary tumor virus
mRNA	Messenger RNA
mTOR	Mammalian target of rapamycin
NEAA	Non-essential amino acid
NES	Normalized Enrichment Score
NP	Nominal p-value
PBS	Phosphate buffered saline
PCR	Polymerase chain reaction
PDE4D	Phosphodiesterase 4D
PDX	Patient derived xenograft
PIC	Pre-initiation complex
Pol II	Polymerase II
P/S	Penicillin/Streptomycin

PVDF	Polyvinylidene difluoride
PyMT	Polyoma middle tumor-antigen
qRT-PCR	Quantitative real time polymerase chain reaction
RNA	Ribonucleic acid
RFP	Red fluorescence protein
RFS	Relapse free survival
RIPA	Radioimmunoprecipitation assay
RPM	Revolutions per minute
SD	Standard deviation
SDS-PAGE	Sodium dodecyl sulfate polyacrylamide gel electrophoresis
SERD	Selective estrogen receptor degrader
SERM	Selective estrogen receptor modulator
shRNA	Short/small hairpin ribonucleic acid
siRNA	Small interfering ribonucleic acid
SNX631	Senexin 631
SRB	Sulforhodamine B
STAT1	Signal transducer and activator of transcription 1
STE	Sodium Tris EDTA
TamR	Tamoxifen resistant
TBS-T	Tris buffer saline Tween20

TEMED	N,N,N',N'-Tetramethyl ethylenediamine
TNBC	Triple negative breast cancer
v/v	volume/volume

CHAPTER 1

INTRODUCTION

1.1. Breast Cancer

Although new treatment concepts have emerged and many novel preventives have been developed, breast cancer (BC) is still the most prevalent cancer type and the leading cause of cancer mortality among women worldwide (1). In 2020, there were 2.3 million women diagnosed with breast cancer globally, contributing 24.5% of all cancer cases in females, and 685,000 deaths occurred (1). In 2021, estimated 281,550 new cases of invasive breast cancer and 49,290 new cases of non-invasive (*in situ*) breast cancer are expected to be diagnosed in women from the United States. Unfortunately, nearly 43,600 women in the U.S. will die from breast cancer in 2021 (2).

Breast cancer is a heterogeneous disease both from a clinical and molecular perspective. Accurate classification of the disease is pivotal for diagnosis, and largely influences the treatment strategies. Estrogen receptor (ER), progesterone receptor (PR), and human epidermal growth factor receptor 2 (HER2) are key histopathological markers used for the classification of breast cancer tumors (3, 4). Based on the expression status of these markers, breast cancer is categorized into 3 groups in the clinics: HER2-amplified, hormone receptor-positive (HR+) expressing higher levels of ER and PR, and triple-negative breast cancer (TNBC) characterized by loss of all three receptors (5). Global gene expression profiling added new groups of breast cancer patients and stratified breast cancer into 5 major subtypes at the molecular

level: Luminal A, Luminal B, HER-2 enriched, basal-like, and normal breast-like **(Figure 1.1)** (6).

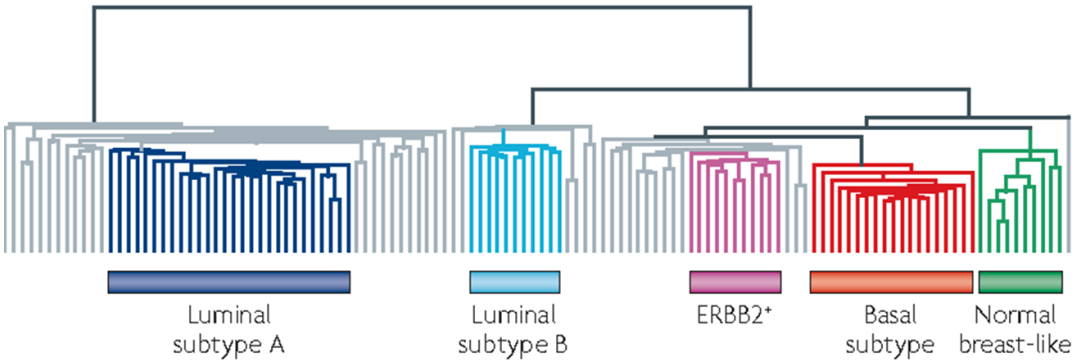


Figure 1.1. A dendrogram showing molecular subtype classification Modified from (7) See Appendix for the copyright permission.

1.2. ER-positive breast cancer

Breast tumors showing at least 1% positivity for ER are considered as luminal subtype (3) and approximately 80% of breast cancer cases are ER-positive (8). Estrogen is a steroid hormone and can be present as three different endogenous forms in females: estrone (E1), estradiol (E2, or 17β-estradiol), and estriol (E3) (9). Estradiol, the most potent form of estrogen, exerts its function once it binds to the estrogen receptor (ER). There are two distinct forms of ER: ERα and ERβ which are encoded by *ESR1* and *ESR2* genes, respectively (10). They both may function through genomic (canonical) or non-genomic (non-canonical) pathways (11) **(Figure 1.2)**. In the genomic pathway, the action of ER requires estrogen binding followed by dimerization of ER with another monomer and nuclear localization. Activated ERs can either directly bind to estrogen response elements (ERE) in the promoter of target genes (12) or interact with other transcription factors (ERE-independent genomic action) (13). A number of studies demonstrated that the E2-ER complex may localize to the plasma membrane

and can regulate transcription without binding to DNA (14, 15). This non-genomic function of ER rapidly activates various signaling molecules such as Src kinase (16) and IGF-I receptor (17), further resulting in the activation of signaling cascades including the MAPK pathway.

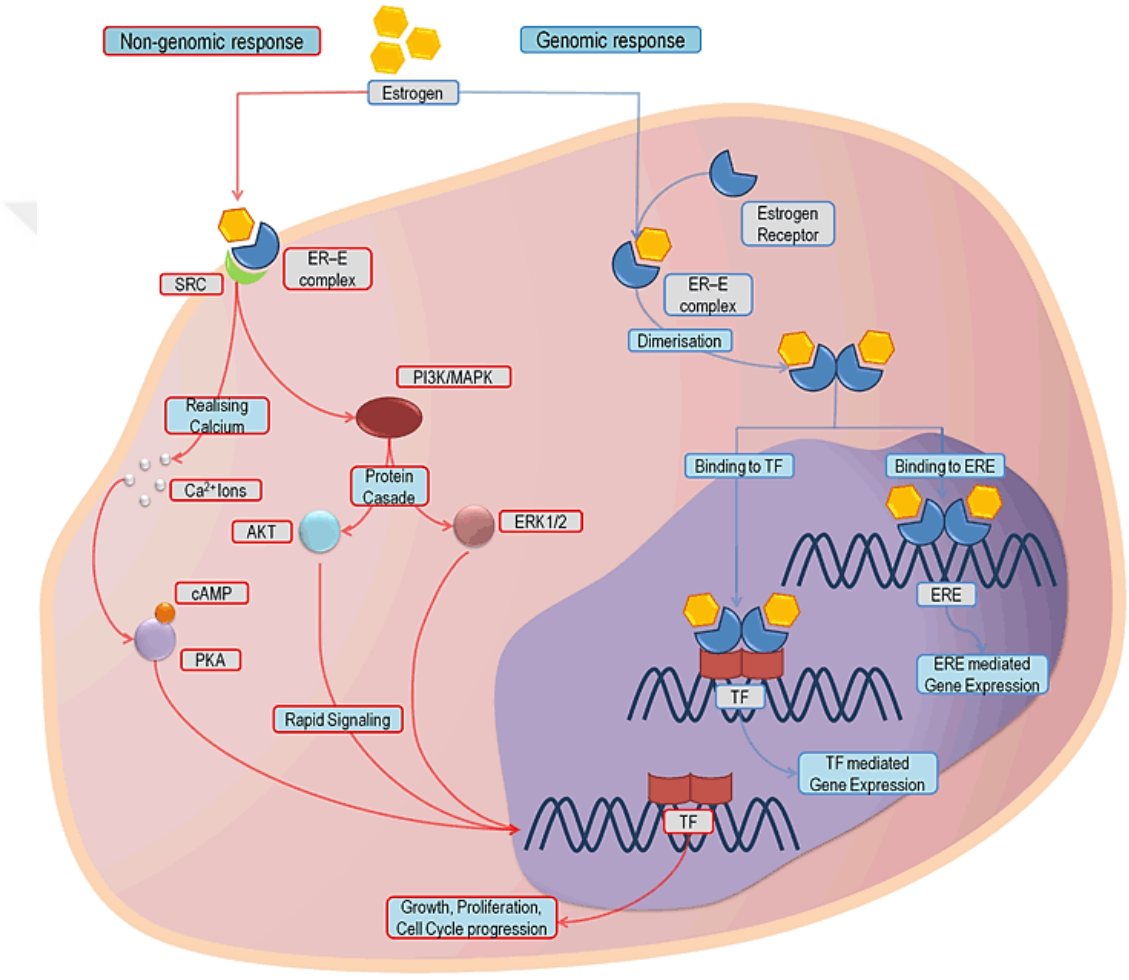


Figure 1.2. Simplified diagram of estrogen signaling pathways (18) See Appendix for the copyright permission.

1.2.1. Treatment strategies for ER-positive breast cancer

Understanding how ER (here mainly ERα) functions and leads to breast tumorigenesis is crucial to designing and developing new agents with impactful clinical outcomes.

ER-targeted therapies are the cornerstone for the treatment of ER-positive tumors and provide a better prognosis to patients. Many antiestrogenic agents are used for the treatment of all stages of ER-positive tumors. Endocrine therapy can be classified into three groups according to their mechanism of action **(Figure 1.3)**:

i.) ***Ligand deprivation via aromatase inhibitors (AIs)***: The study published in 1896 revealed the regression of breast tumors upon oophorectomy (surgical removal of ovaries) (19). This finding set the stage for studying estrogen deprivation to prevent relapse in breast cancer patients. Estrogen production occurs mainly in ovaries, where aromatase catalyzes the conversion of androgens to estrogens. Widely-used aromatase inhibitors letrozole (20), exemestane (21), and anastrozole (22) function by blocking aromatases. Since estrogen is the main fertility hormone, aromatase inhibitors are preferred to be used in postmenopausal women or advanced breast cancer patients (23).

ii.) ***ER downregulation using selective estrogen receptor downregulators/degraders (SERDs):*** The drugs of this class are known as pure ER antagonists. As they have the capability to bind ER with high affinity (24), they can block ER dimerization and further prevent translocation to the nucleus (25). Food and Drug Administration (FDA) approved intramuscular injection of fulvestrant (250 mg) for advanced ER-positive breast cancer profiles. However, increasing the dose to 500 mg showed higher efficacy and bioavailability (26). Due to limitations in the route of administration and high dosage for bioavailability of fulvestrant, novel strategies are being developed for orally available SERD drugs with more favorable bioavailability profiles (27).

iii.) ER modulation with selective estrogen receptor modulators (SERMs): Tamoxifen is the first SERM and unlike SERDs, contributes to breast cancer therapy by exhibiting both agonist and antagonist effects towards estrogen (28). Besides, tamoxifen exerts tissue-specific activities. In the breast tissue, it acts as an antagonist and shows antitumor effects. This function of tamoxifen leads to a slowdown in the cell cycle and thus it is categorized as a cytostatic drug. On the other hand, tamoxifen can gain an estrogenic agonist effect as it happens in bone and blocks osteoporosis in postmenopausal women (29). Moreover, tamoxifen has been shown as preventive in invasive breast cancer. A follow-up study for 54.6 months showed a 49% reduction in the risk of invasive breast cancer in patients who received tamoxifen therapy (30). Similarly, an Italian case trial revealed that tamoxifen treatment decreases the risk of invasive breast cancer according to 11 years follow-up results (31). Both selective function and successful clinical outcome refer tamoxifen as a standard of care agent with established benefit in the adjuvant treatment of all stages (both pre-menopause and post-menopause) of ER-positive breast cancer.

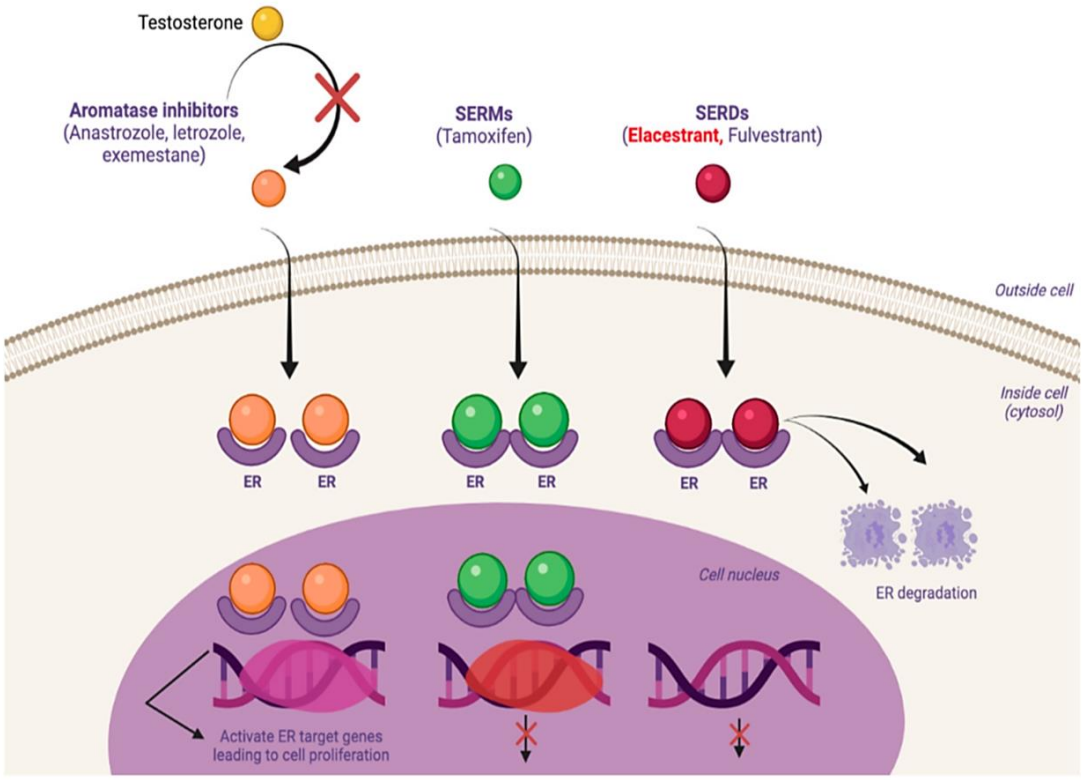


Figure 1.3. Mechanism of action of the different endocrine therapy (32) See Appendix for the copyright permission.

1.2.2. Mechanisms of Endocrine Resistance in Breast Cancer

Despite numerous successes in ER-targeted therapies, cancer cells do not achieve to respond to treatment agents. This phenomenon is designated as drug resistance which in turn could be classified as d*e novo* (intrinsic or primary) endocrine resistance or as acquired (secondary) resistance (33). In *de novo* resistance, there is no benefit at the initial steps of the endocrine treatment while acquired resistance occurs over time following first exposure to treatment. Distinct mechanisms underscoring endocrine resistance have been postulated:

i.) ***Alterations in ER signaling***

As abovementioned ER expression, itself, mainly define the clinical fate of breast cancer patients. In fact, loss of ER had been shown as the

principal mechanism of the *de novo* resistance (34). One cause of ER loss was shown to be through epigenetic changes such as aberrant methylation of CpG islands of the ER promoter or deacetylation of histones, which blocks transcription due to compact nucleosome structure (35, 36). In other case, single amino acid mutations in the ligand-binding domain of *ESR1* had caused constitutively activation of ER. Cells harboring these mutations acquire higher amounts of drug to inhibit ER signaling, therefore promoting ER transcriptional activity and eventually leading to endocrine resistance (37). Lastly, *ESR1* amplifications are also associated with tamoxifen resistance (38). However, the roles of *ESR*1 amplifications in the clinics need to be further investigated as increased sensitivity to tamoxifen treatment and improved disease-free survival through *ESR1* amplifications are also pointed out by other researchers (39, 40).

ii.) Overexpression of growth factor receptors and kinase signaling pathways

Endocrine resistance is also governed by the activation of growth factor receptors. For instance, overexpression of ErbB2 (HER2) is one of the well-characterized mechanisms of tamoxifen resistance (41). Overexpression and/or activation of growth factor receptors, such as EGFR, HER2, and IGF1R, prompt the MAPK and PI3K/AKT signaling pathways impinging on cell proliferation and survival (42). Moreover, preclinical studies elucidated that aberrant activation of the PI3K/AKT/mTOR pathway plays role in resistance to hormone-targeted therapies (43, 44) **(Figure 1.4).** To tackle the resistance problem, drug combination strategies are generally preferred. A phase II study

demonstrated that advanced ER+ breast cancer patients resistant to aromatase inhibitors showed improved overall survival upon combination treatment of tamoxifen with mTOR inhibitor, Everolimus compared with a single treatment of tamoxifen (45).

iii.) Dysregulated cell cycle progression

Deregulation of the cell cycle also contributes to the loss of endocrine responsiveness. Cyclin D1 is one of the established transcriptional targets of ER (46) and its overexpression is involved in tamoxifen resistance (47). Cyclin D1 binding activates its partner CDK4/6. The CDK4/6-cyclin D complex phosphorylates retinoblastoma (Rb) protein and triggers the release of E2F transcription factors, which is critical for entry into the S phase. Once cells enter into the S phase, DNA replication occurs and eventually promotes cancer progression (48). Thus, a rational design for targeting CDK4/6 is urgent to restore cell cycle control. There are currently three highly selective CDK4/6 inhibitors available and they show potent anti-proliferative properties: palbociclib (Ibrance, Pfizer), ribociclib (Kisqali, Novartis), and abemaciclib (Verzenio, Eli Lily). These inhibitors are approved by FDA to be used for the treatment of ER+/HER- breast cancer patients in combination with other endocrine therapies. For example, a combination regimen of palbociclib and fulvestrant has been utilized at the second-line setting in advanced metastatic ER+ breast cancer patients (49).

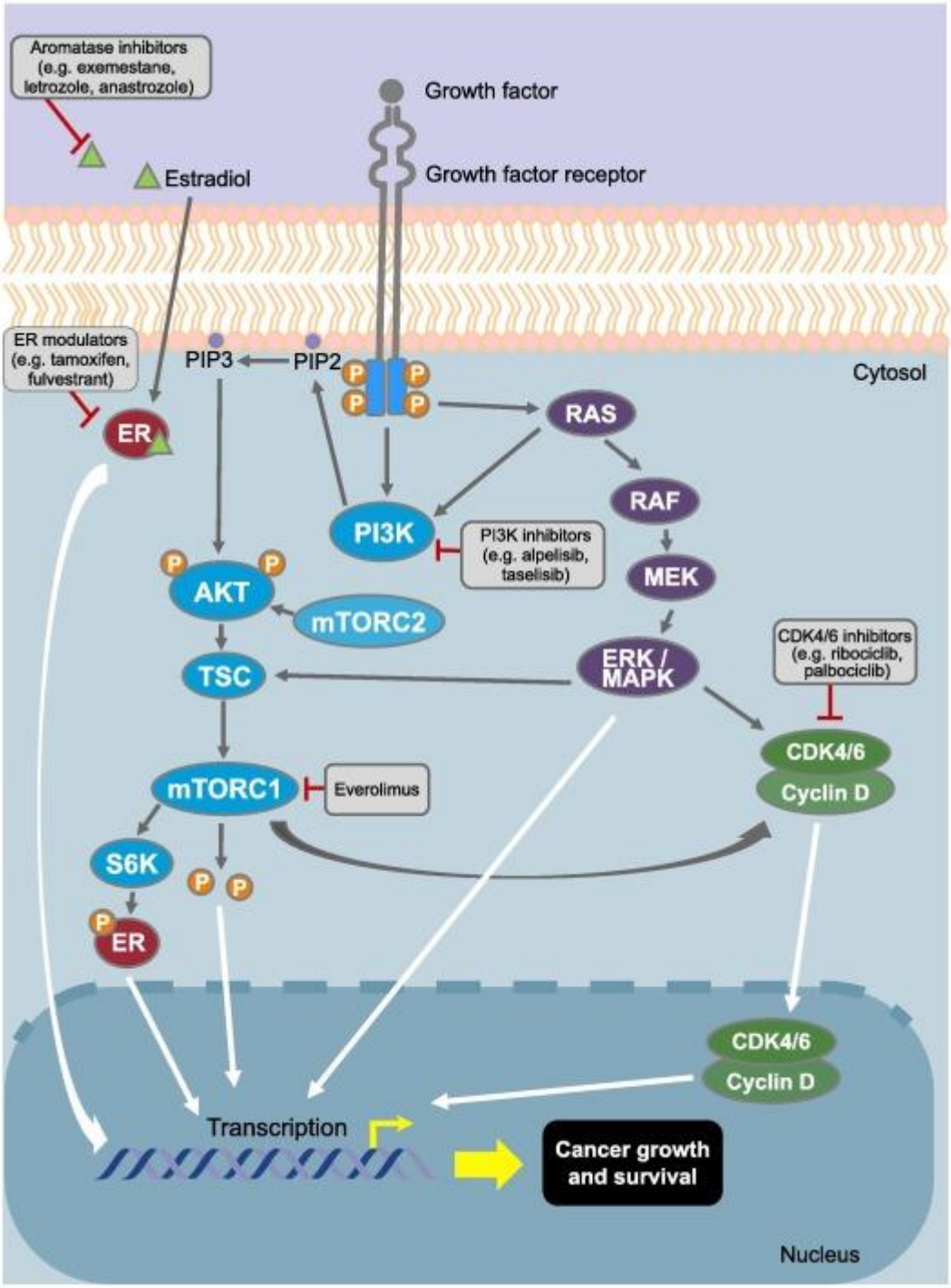


Figure 1.4. Signaling pathways leading to endocrine resistance and current therapies (50) See Appendix for the copyright permission.

1.3. Mediator

The unique transcription program is governed by RNA polymerase II (pol II); however, pol II is not capable of starting transcription on its own. Eukaryotic transcription starts with the macromolecular assembly of the pre-initiation complex (PIC), which is composed of evolutionarily conserved general transcription factors (GTFs), RNA polymerase II (pol II), and Mediator (51, 52). Using elegant biochemical and genetics studies in yeast, the Young and Kornberg labs characterized the Mediator (also named as Mediator complex) as a co-regulator of the transcription (53, 54). This discovery more than 20 years ago broadened our vision to understand the impact of Mediator on transcriptional regulation.

Mediator is an evolutionarily conserved protein complex with 25 subunits in budding yeast and 30 subunits in human. Over the past years, several studies have been performed to determine the structure and architecture of the Mediator Complex. Electron microscopy (EM) studies revealed that the subunits of the Mediator Complex are organized into four distinct modules namely head, middle, tail, and the kinase module both in yeast and human (Figure 1.5) (55).

The basic function of Mediator is linking DNA-bound transcription factors directly to the RNA polymerase II enzyme (56). Mediator is also involved in chromatin architecture, formation of phase-separated condensates on super-enhancers, and DNA repair (57).

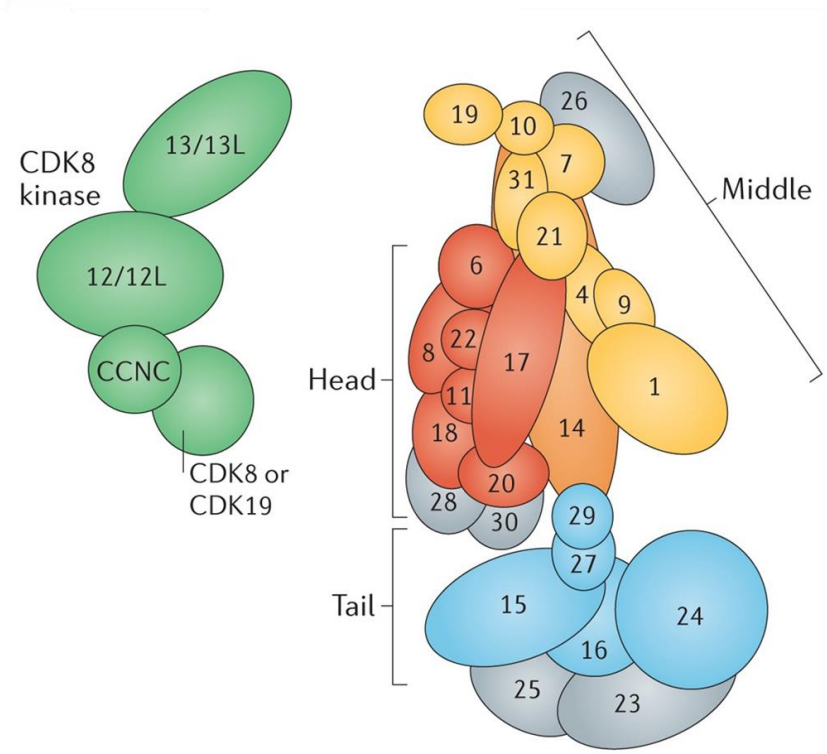


Figure 1.5. Mediator complex subunits The Mediator complex is organized within 3 core modules: head, middle and tail modules joined by a dissociable CDK8 kinase module (CKM). Modified from (58). See Appendix for the copyright permission.

1.3.1. Kinase module

The kinase module consists of Mediator subunit 13 (MED13), MED12, cyclin C (CCNC), and cyclin-dependent kinase 8 (CDK8) (59). Moreover, the kinase module can also include the paralogs CDK19, MED12L, and MED13L in mammalian cells (60). CDK19, MED12L, and MED13L can associate with kinase module in a mutually exclusive manner.

The kinase module reversibly dissociates from Mediator, which is important for the PIC assembly (61). Indeed, electron microscopy studies in human HeLa cells showed that kinase module act as transcriptional repressor by blocking the binding of RNA

pol II to Mediator (62). On the other hand, ChIP analysis and genome occupancy profiles of elongation factors in human cells demonstrated how kinase module can also promote gene expression, thereby regulates transcription. CDK8 phosphorylates the C-terminal domain of RNA pol II, which is key event for RNA pol II-dependent elongation (63).

1.3.2. The role of kinase module in human disease

MED13 is the largest subunit of the complex and essential for bridging the kinase module to the Mediator complex (64). CKM-Mediator association is controlled by MED13 phosphorylation, ubiquitylation, and turnover (60). Accordingly, MED13 dysregulation has been implicated in several diseases and disorders. *De novo* or frameshift mutations in *MED13* has been linked to neurodevelopmental disorder or gastric and colorectal cancers, respectively (65, 66). Similarly, MED13 amplification and/or overexpression has been observed in many cancer types including breast (67). In another study, loss of MED13 has been reported to promote resistance to alkylating agents in CML or glioma models (68).

Unlike other cyclin-dependent kinases which are involved in cell cycle regulation, CDK8 functions as a transcriptional regulator. The role of CDK8 is highly divergent and controversial. While it is essential during embryonic development (69), its conditional deletion in adult mice do not cause any abnormality (70). On the other hand, *CDK8* was found to be frequently dysregulated in a myriad of diseases including cancer. For example, missense mutations in *CDK8* leads to a syndromic developmental disorder (71) whereas knockdown or targeted inactivation of CDK8 was associated with congenital heart disease (72). In another study, it has been found

that inhibition of CDK8 suppresses estrogen-dependent transcription and the growth of ER-positive breast cancer (73). CDK8 was also shown to directly or indirectly regulate trastuzumab and cisplatin sensitivity in breast and lung cancer, respectively (74, 75).

1.4. The rationale and the aims of the dissertation

Tamoxifen resistance is the major challenge which prevents to get impactful clinical outcomes in the treatment of ER-positive breast cancer patients. Although many therapeutic strategies are evolved to hinder tamoxifen resistance, the vast majority of breast cancer patients do not significantly benefit from these interventions. Thus, it is pivotal to elucidate new molecular mechanisms of tamoxifen resistance and to determine new drivers which can be therapeutically targeted.

In this dissertation, the aims are as following:

- to shed light on the roles of MED13 and CDK8 in tamoxifen resistance
- to identify the tamoxifen sensitizer role of newly characterized and more potent CDK8 inhibitor both in *in vivo* and *in vitro* settings

CHAPTER 2

MATERIALS

2.1. Buffers

1X Anode Buffer I	300 mM Tris, 20% (v/v) methanol
1X Anode Buffer II	25 mM Tris, 20% (v/v) methanol
1X Cathode Buffer	40 mM 6-aminocaparoic acid, 20% (v/v) methanol
1X PBS	137 mM NaCl, 2.7 mM KCl, 10 mM Na_2HPO_4, 2 mM KH_2PO_4 (pH: 7.4)
1X SDS-PAGE Running Buffer	25 mM Tris, 14.41 g/L glycine, 1% (v/v) SDS
1X TAE	40 mM Tris, 20 mM acetic acid, 1 mM EDTA
1X TBS-T	20 mM Tris, 8 g/L NaCl 0.2% (v/v) Tween20
RIPA Lysis Buffer	150 mM NaCl, 1% (v/v) NP-40, 0.5% (v/v) Sodium DOC, 50 mM Tris-HCl (pH 8.0), 50 mM NAF, 1 mM Na_3VO_4, 4% (v/v) Protease inhibitor, 4% (v/v) Phosphatase inhibitor

2.2. Chemicals and reagents

4-Hydroxytamoxifen	Sigma Aldrich, St Louis, MO, USA
4X protein loading dye	250 mM Tris HCl (pH:6.8), 10% (w/v) SDS, 0.1% (w/v) Bromophenol blue, 50% Glycerol (v/v), 25% (v/v) β-mercaptoethanol
6-aminocaparoic acid	Sigma Aldrich, St Louis, MO, USA

Acetic acid (glacial)	Isolab, Wertheim, Germany
Acrylamide/bisacrylamide	Applichem, Darmstadt, Germany
Agar	Sigma Aldrich, St Louis, MO, USA
Agarose	Promega, Madison, WI, USA
Ammonium persulfate	Carlo Erba, Cornaredu, Italy
Ampicillin	Sigma Aldrich, St Louis, MO, USA
Blasticidin	Thermo Fisher Scientific, Waltham, MA, USA
Bovine serum albumin	Santa Cruz, Dallas, TX, USA
Chloroform	Sigma Aldrich, St Louis, MO, USA
Crystal Violet	Merck, Darmstadt, Germany
dNTPs	Thermo Fisher Scientific, Waltham, MA, USA
Doxycycline	Thermo Fisher Scientific, Waltham, MA, USA
ECL	Amersham Pharmacia Biotech, Amersham, UK Thermo Fisher Scientific, Waltham, MA, USA
Ethylenediaminetetraacetic acid (EDTA)	Sigma Aldrich, St Louis, MO, USA
Ethanol	Sigma Aldrich, St Louis, MO, USA
Ethidium bromide	Thermo Fisher Scientific, Waltham, MA, USA
Gebr-7b	Merck, Darmstadt, Germany
Formalin	Merck, Darmstadt, Germany
Gene Ruler 100bp DNA Ladder	New England Biolabs, Ipswich, MA, USA
Gene Ruler 1kb DNA Ladder	New England Biolabs, Ipswich, MA, USA
Glycine	Santa Cruz, Dallas, TX, USA
Isoflurane	Piramal Critical Care, Bethlehem, PA, USA
Isopropanol	Sigma Aldrich, St Louis, MO, USA

Ketasol	Richter Pharma, Wels, Austria
LightCycler 480 SYBR Green I Master	Roche Applied Science, Mannheim, Germany
Lipofectamine™ 2000	Invitrogen, Carlsbad, CA, USA
Matrigel	BD, Flanklin Lakes, NJ, USA
Methanol	Sigma Aldrich, St Louis, MO, USA
Methyl 2-hydroxyethyl cellulose	Sigma Aldrich, St Louis, MO, USA
Nuclease free water	ChemCruz, Dallas, TX, USA
Page Ruler protein ladder	Thermo Fisher Scientific, Waltham, MA, USA
Paraformaldehyde	Sigma Aldrich, St Louis, MO, USA
Phenol: Chloroform: Isoamyl Alcohol (25:24:1)	Acros Organics, New Jersey, USA
Phosstop	Roche Applied Science, Mannheim, Germany
Polybrene	Santa Cruz, Dallas, TX, USA
Polyethylene glycol (PEG) 400	Merck, Darmstadt, Germany
Ponceau S	Sigma Aldrich, St Louis, MO, USA
Propylene glycol (PG)	Sigma Aldrich, St Louis, MO, USA
Protease inhibitor cocktail	Roche Applied Science, Mannheim, Germany
Proteinase K	Thermo Fisher Scientific, Waltham, MA, USA
Puromycin	Thermo Fisher Scientific, Waltham, MA, USA
Rompun 2% (Xylazin)	Bayer, Leverkusen, Germany
SNX631	developed in-house, University of South Carolina
Sodium chloride	Merck, Darmstadt, Germany
Sodium dodecyl sulfate	Merck, Darmstadt, Germany
Sulforhodamine B sodium salt	Sigma Aldrich, St Louis, MO, USA

TEMED	Serva, Heidelberg, Germany
Trichloroacetic acid	Sigma Aldrich, St Louis, MO, USA
TRIsure	Bioline, Luckenwalde, Germany
Triton X-100	Sigma Aldrich, St Louis, MO, USA
Trizma base	Sigma Aldrich, St Louis, MO, USA
Tryptone	Sigma Aldrich, St Louis, MO, USA
Tween-20	VWR, Radnor, PA, USA
Yeast extract	Merck, Darmstadt, Germany

2.3. Media and Supplements

Dulbecco's modified Eagle's Medium (DMEM) (without L-glutamine, phenol red; with 1 g/L D-glucose, pyruvate	Thermo Fisher Scientific, Waltham, MA, USA
Fetal bovine serum	Biowest, Nuaille, France
Insulin	Sigma Aldrich, St Louis, MO, USA
Lysogeny Broth (LB) Agar	1.5% (w/v) agar, 10 g/l 18hosphor, 5 g/l yeast extract, 10 g/l NaCl
LB Broth	10 g/l 18hosphor, 5 g/l yeast extract, 10 g/l NaCl
Non-essential aminoacids	Lonza, Basel, Switzerland
optiMEM	Invitrogen, Carlsbad, CA, USA
Penicillin/Streptomycin	Lonza, Basel, Switzerland
Trypsin (10X)	Biowest, Nuaille, France

2.4. Kits

ApopTag® Fluorescein *In Situ* Apoptosis Detection Kit	Merck KgaA, Darmstadt, Germany
Cell Titer-Glo Luminescent Cell Viability Assay kit	Promega, Madison, WI, USA
First strand cDNA synthesis kit	Fermantas, St. Leon-Roth, Germany
LookOut® Mycoplasma Detection Kit	Sigma Aldrich, St Louis, MO, USA
Pierce™ Protein Assay Kit	Pierce, Rockford, IL, USA
Plasmid isolation kit	MN, Duren, Germany
Plasmid Maxi kit	Qiagen, Hilden, Germany
Q5® High-Fidelity DNA Polymerase	NEB, Ipswich, MA, USA
Trans-lentiviral Packaging kit	Dharmacon, Lafayette, Colorado, United States

2.5. Equipment

Amersham™ Imager 600	GE Healthcare, Chicago, Illinois, USA
Axiovision 4.3 microscopy	Carl Zeiss, Munich, Germany
Cell counting chamber	Marienfeld, Könighofen, Germany
Centrifuges	Thermo Fisher Scientific, Waltham, MA, USA Beckman, Pasadena, CA, USA
Freezer (-20^{o}C)	Bosch, Stuttgart, Germany
Freezer (-80^{o}C)	Hettich, Geldermansen, Germany Thermo Fisher Scientific, Waltham, MA, USA

Fridge (+4^{o}C)	Bosch, Stuttgart, Germany
Horizontal shakers	FinePCR, Seoul, South Korea Bellco, Vineland, NJ, USA
Laminar flow hood	Nüve, Ankara, Turkey
Leica Dmi8 Inverted Microscope	Leica Microsystems, Wetzlar, Germany
LightCycler 96	Roche Applied Science, Mannheim, Germany
Lumina III In Vivo Imaging System	Perkin Elmer, MA, USA
Mini-PROTEAN® gel casting module	Bio-Rad, Hercules, CA, USA
Mini-PROTEAN® Tetra Cell	Bio-Rad, Hercules, CA, USA
Multichannel pipette	Thermo Fisher Scientific, Waltham, MA, USA
NanoDrop 1000	Thermo Fisher Scientific, Waltham, MA, USA
Nikon TS300 Inverted Microscope	Nikon, Tokyo, Japan
Power supplies	Bio-Rad, Hercules, CA, USA
Synergy HT™ Multi-Mode Microplate Reader	Biotek, Winooski, VT, USA
Trans-Blot® Turbo™ Transfer System	Bio-Rad, Hercules, CA, USA
Thermal cycler	Applied Biosciences, Foster City, CA, USA
Vortex	Isolab, Wertheim, Germany
Water bath	Nüve, Ankara, Turkey

2.6. Consumables

100 mm cell culture dishes	TPP, Trasadingen, Switzerland

145 mm cell culture dishes	TPP, Trasadingen, Switzerland
6-well plates	Greiner bio-one, Frickenhausen, Germany
96-well plates	Greiner bio-one, Frickenhausen, Germany
Cell scrapers	Greiner bio-one, Frickenhausen, Germany
Coverslips	Marienfeld, Königshofen, Germany
Cryovials	Greiner bio-one, Frickenhausen, Germany
Cuvettes	VWR, Radnor,PA, USA
Filtered pipette tips (10, 20, 200, 1000 µL)	Greiner bio-one, Frickenhausen, Germany
LightCycler® 480 Multiwell Plate 96, white	Roche Applied Science, Mannheim, Germany
Micropipettes (Pipetman)	Gilson, Middleton, WI, USA
Microscope slides	Marienfeld, Königshofen, Germany
Parafilms	VWR, Radnor, PA, USA
PCR tubes	Greiner bio-one, Frickenhausen, Germany
Plastic pipettes (5 mL)	Isolab, Wertheim, Germany
Plastic pipettes (10, 25 mL)	Greiner bio-one, Frickenhausen, Germany
PVDF membrane	Bio-Rad, Hercules, CA, USA
Reaction tubes (0.5, 1.5, 2 mL)	Greiner bio-one, Frickenhausen, Germany
Storage bottles	Corning Incorporated, Corning, NY, USA
Sutures	Boz Medical Equipment, Ankara, Turkey
Unfiltered tips (1000 µL)	LP Italiana, Milano, Italy
Unfiltered tips (10, 200 µL)	Corning Incorporated, Corning, NY, USA
Whatman paper	GE Healthcare, Little Chalfont, UK

CHAPTER 3

METHODS

3.1. *In vitro* experiments

3.1.1. Culturing cell lines

MCF-7 and T47D cell lines were purchased from ATCC (Manassas, VA, USA) and were cultured in Dulbecco's modified Eagle's Medium (DMEM) (without L-glutamine, phenol red; with 1 g/L D-glucose, pyruvate) supplemented with 10% heat inactivated fetal bovine serum (FBS), 50 U/mL penicillin/streptomycin (P/S), 1% nonessential amino acids (NEAA) and 0.1% insulin. Tamoxifen-resistant cells (MCF-7 TamR and T47D TamR) were established by exposure of cells to 5 μM 4-Hydroxytamoxifen (Sigma Aldrich, St Louis, MO, USA) for more than 6 months. All cells were maintained at 37°C incubator with 5% CO_2 for optimal growth and periodically tested for mycoplasma contamination using LookOut® Mycoplasma Detection Kit (Sigma Aldrich, St Louis, MO, USA). The cumulative culture length of the cells between thawing and use in the experiments was less than 20 passages.

3.1.2. siRNA Transfections

All siRNA transfections were achieved by using Lipofectamine 2000 (Invitrogen, Carlsbad, CA). Briefly, MCF-7 TamR and T47D TamR cells were seeded one day before assay. At the day of transfection, both siRNAs (40 nM) and transfection reagent were separately diluted in OptiMEM, vortexed at the highest speed and incubated for 5 minutes at room temperature. Following the incubation, two solutions were mixed

and further incubated for 20 minutes at room temperature. Meantime, media were replaced to antibiotic free medium (transfection medium). The siRNA-Lipofectamine mixture was then added to the cells and the dishes were shaken gently.

Table 3.1. List of siRNAs used in transfections

siRNA	Catalog number	Manufacturer
MED13 #1 siRNA	D-019908-03	Dharmacon
MED13 #2 siRNA	D-019908-018	Dharmacon

3.1.3. Cell viability assays

MCF-7 TamR and T47D TamR cells were seeded at a density of 8,000 and 5,000 cells/well in 96-well plates, respectively. Cells were treated with tamoxifen (7.5 μM and 5.0 μM for MCF-7 TamR and T47D TamR, respectively) one day after the transfection with siRNAs. Following 72 hours post-treatment with tamoxifen, relative cell numbers were quantified. To assess the role of CDK8 on sensitization, cells were treated with tamoxifen and different doses of SNX631 at the same time. One week following the treatment, cell viability was measured with Sulforhodamine B (SRB) (Sigma Aldrich).

3.1.4. Colony Formation Assay

About 2000-3000 cells were seeded in 12 well plates and incubated for 14-21 days. For the induction of MED13, shMED13 MCF-7 TamR cells were treated with doxycycline (1 ug/ml). After 3 days of doxycycline induction, cells were treated with tamoxifen and incubated for next two weeks days before colony formation assay.

During the incubation period, the doxycycline and tamoxifen were replaced every 3 days. SNX631 and tamoxifen treatments were performed at the same time and the media containing drugs were replenished every 5 days. The staining of the colonies was performed in 0.5% crystal violet with 50% methanol.

3.1.5. Lentiviral vector-based transfections

SMARTvector Human Inducible MED13 shRNAs and TRIPZ non-silencing lentiviral shRNA were purchased from Dharmacon. In order to generate the viral particles, 6 µg each of the vector was co-transfected using the trans-lentiviral packaging mix (Dharmacon) into HEK293-FT cells. 48 hours post-transfection, virus particles were collected and transduced to MCF-7 TamR cells. 36 hrs post transduction, puromycin (1 µg/ml) selection was initiated.

Table 3.2. List of shRNAs used in transfections

shRNA	**Catalog number**	**Manufacturer**
Inducible TurboRFP shRNA vector MED13#3	V3IHSPGR_7693165	Dharmacon
Inducible TurboRFP shRNA vector MED13#4	V3IHSPGR_5504011	Dharmacon

3.2. Quantitative Real-Time Polymerase Chain Reaction (qRT-PCR)

3.2.1. Total RNA isolation

Cells were seeded in 6-well plates followed by siRNA transfections and/or drug treatments as described in **3.1.2.** After indicated times, medium was removed, cells were washed with 1X PBS and cell pellets were collected through trypsinization. Total RNA isolation was performed according to manufacturer's instructions.

3.2.2. cDNA synthesis

RevertAid RT Reverse Transcription kit was used to synthesize cDNAs from desired amount of RNA (generally 2 µg) according to manufacturer's protocol. Total RNA was mixed with the reaction components given in the **Table 3.3** and the reaction were carried out in thermocyler using the program given in the **Table 3.4**. After the reaction was completed, cDNA samples were diluted to the concentration of 10 ng/µl cDNA with nuclease-free water.

Table 3.3. Components of reverse transcription reaction

Reagent	**Concentration/Volume**
RNA	2 µg (X µL)
Randem primer	1 µL
5x Revert Aid reaction buffer	4 µL
Ribolock Ribonuclease Inhibitor	1 µL
dNTPs (10mM)	2 µL
Revert Aid H Minus M-MuLV RT	1 µL

Nuclease-free water	(20-X) µL

Table 3.4. Thermocycler program for cDNA synthesis

Temperature	**Time (minutes)**
37°C	5
42°C	60
70°C	10
4°C	∞

3.2.3. qRT-PCR

SYBR Green Master mix was prepared for each primer pair and each component were used according to given amount in **Table 3.5**.

Table 3.5. Master mix for qRT-PCR reaction

Reagent	**Volume**
SYBR Green	5 ul
Forward primer (20 uM)	0.25 ul
Reverse primer (20 uM)	0.25 ul
H_2O	2.5 ul

All master mix components were completed to total 10 ul reaction together with 2 ul cDNA and reaction were carried out in 96-well plate. The plate was slightly sealed to and centrifuged at 1200 rpm for 4 minutes. qRT-PCR program given at Table 3.7 was

ran on LightCycler 96 qRT-PCR Thermocycler (Roche Applied Science, Mannheim, Germany). Sequences of primers used in the experiment were listed in **Table 3.6**.

Table 3.6. List of primers used for qRT-PCR

Gene	**Primer sequences**
ACTB	Forward: 5'- CCAACCGCGAGAAGATGA –'3
	Reverse: 5'- CCAGAGGCGTACAGGGATAG –'3
GAPDH	Forward: 5'- GCCCAATACGACCAAATCC –'3
	Reverse: 5'- AGCCACATCGCTCAGACAC –'3
ERBB2	Forward: 5'- GGGAAACCTGGAACTCACCT –'3
	Reverse: 5'- CCCTGCACCTCCTGGATA –'3

Table 3.7. Program for qRT-PCR

Pre-incubation

Target (°C)	Acquisition Mode	Hold (hh:mm:ss)	Ramp Rate (°C/s)	Acquisitions (per °C)	Sec Target (°C)	Step size (°C)	Step Delay (cycles)
95	None	0:05:00	4.4	5	0	0	0

Amplification

Target (°C)	Acquisition Mode	Hold (hh:mm:ss)	Ramp Rate (°C/s)	Acquisitions (per °C)	Sec Target (°C)	Step size (°C)	Step Delay (cycles)
95	None	0:00:10	4.4	5	0	0	0
58	Single	0:00:20	2.2	5	0	0	0
72	None	0:00:20	4.4	5	0	0	0

Melting curve

Target (°C)	Acquisition Mode	Hold (hh:mm:ss)	Ramp Rate (°C/s)	Acquisitions (per °C)	Sec Target (°C)	Step size (°C)	Step Delay (cycles)
95	None	0:00:05	4.4	5	0	0	0
55	None	0:01:00	2.2	5	0	0	0
95	Continuous	0:00:00	0.11	5	0	0	0

Cooling

Target (°C)	Acquisition Mode	Hold (hh:mm:ss)	Ramp Rate (°C/s)	Acquisitions (per °C)	Sec Target (°C)	Step size (°C)	Step Delay (cycles)
40	None	0:00:30	2.2	5	0	0	0

3.3. Protein Biochemistry

3.3.1. Protein isolation

Prior to protein extraction, media containing the apoptotic bodies were collected and then centrifuged at 5000 RPM for 5 minutes. Following the trypsinization, cell pellets were obtained by centrifugation. Depending on cell pellet size, 40-100 µl RIPA lysis buffer (**Table 3.8**) was added and vortexed for 5-10 seconds every 5 minutes for a total of 30 minutes. Proteins were separated by centrifuging the cell suspensions at 13000 rpm for at least 30 minutes. Protein lysates were stored at -80°C for future experiments.

For protein isolation from tumors, 2-3 mm tissue pieces were first minced by scalpels and washed with PBS to remove blood cells. Then, tumors were homogenized in RIPA buffer using a tissue grinder.

Table 3.8. Contents of the RIPA buffer

Ingredient	Stock Concentration	Final Concentration	For 1 mL
NaCl	2 M	150 mM	75 µL
NP-40	10%	1%	100 µL
Sodium DOC	10%	0.5%	50 µL
SDS	10%	0.1%	10 µL
Tris HCl (pH 8.0)	2 M	50 mM	25 µL
NAF	1 M	50 mM	50 µL
Na_3VO_4	100 mM	1 mM	10 µL
Protease inhibitor	25X	4%	40 µL
Phosphatase inhibitor	20X	4%	40 µL
ddH_2O			600 µL

3.3.2. Protein quantification

Total protein amounts were quantified by using Pierce™ BCA Protein Assay Kit. As manufacturer's protocol suggested, standard solutions containing bovine serum albumin (BSA) were prepared at 9 different concentrations ranging from 0 to 2 µg/µl. 24 µl protein samples and 3 µl standard sample were placed in 96 well plates and dilution factor was taken as 8 for further analysis. Working solution was prepared freshly in ratio 50:1 by mixing reagent A and reagent B and added onto wells with 200 µl volume per well. Both samples and standards were incubated in working solution at 37°C for 30 minutes. Absorbance was measured on SynergyHT microplate

reader at 562 nm. Protein sample concentrations were estimated by reference to a standard calibration curve based on readings from BSA standards.

3.3.3. Sodium dodecyl sulfate polyacrylamide gel electrophoresis (SDS-PAGE)

Following the protein quantification, equal amounts of protein from each sample were mixed with 4X protein loading dye **(Table 3.9)** and heated at 95°C for 5 minutes. Polyacrylamide stacking and resolving gels were prepared using the ingredients listed in **Table 3.10**.

Table 3.9. Components of the 4X loading dye

Reagent	**Stock Concentration**	**Final Concentration**	**For 10 ml**
Glycerol	100%	40%	4 ml
Tris HCl (pH 6.8)	1M	240 mM	2.4 ml
SDS	-	8%	0.8 g
Bromophenol blue	-	0.04%	0.004 g
β-mercaptoethanol	100%	5%	0.5 ml
ddH_2O			Up to 10 ml

Using Mini-PROTEAN Gel casting module, first resolving gel solution was poured between the thin and thick glasses. The top of the gel was overlaid with isopropanol until gel polymerized. Following the polymerization, isopropanol was removed from gel casting system, stacking gel solution was casted on top of the resolving gel, and 10 or 15 well comb was placed inside the stacking gel. The first well was filled with

protein ladder and other wells were loaded with 15-20 µg of protein samples. Electrophoresis was performed at 120V for 60 minutes.

Table 3.10. Components of resolving and stacking gels at different concentrations

Reagent	Resolving gel (8%)	Resolving gel (10%)	Resolving gel (12%)	Stacking gel (5%)
dH_2O	2.3 ml	1.9 ml	1.6 ml	1.36 ml
30% acrylamide mix	1.3 ml	1.7 ml	2 ml	340 µl
1M Tris	1.3 ml (pH 8.8)	1.3 ml (pH 8.8)	1.3 ml (pH 8.8)	260 µl (pH 6.8)
10% SDS	50 µl	50 µl	50 µl	20 µl
10% APS	50 µl	50 µl	50 µl	20 µl
TEMED	5 µl	5 µl	5 µl	2 µl
Total volume	**5 ml**	**5 ml**	**5 ml**	**2 ml**

3.3.4. Western blotting

Following protein separation, the semi-dry transfer method was assessed to transfer proteins from gel onto the PVDF membrane. Briefly, 3-mm thick Whatmann papers were cut in the dimensions of 7 to 9 cm while the dimensions of PVDF membrane were 6.5 to 8.5 cm. The Whatmann papers were rinsed as follows: 3 pieces of Whatmann paper in Anode I buffer, 2 pieces in Anode II buffer and 5 pieces in Cathode buffer. The membrane was activated in 100 % methanol for 3-5 minutes and then placed in Anode II buffer. The sandwich was assembled with the following order (from bottom to top): 3 Anode I buffer, 2 Anode II buffer, membrane, gel and 5

Cathode papers. Transfer was completed in Bio-Rad Trans-Blot® Turbo™ Transfer System for 30 minutes at 25V.

Table 3.11. List of primary and secondary antibodies used in the study

Antibody	**Company**	**Catalog Number**	**Dilution**
β-actin	Sigma-Aldrich	A5441	1:10000
HER2	Cell Signaling Technology	CST2165	1:1000
MED13	developed in-house	-	1:1000
MED12	developed in-house	-	1:1000
CDK8	Santa Cruz Biotechnology	sc-13155	1:1000
CCNC	Abcam	Ab85927	1:1000
p-STAT1 (Ser727)	Cell Signaling Technology	CST9177	1:1000
p-4EBP1	Cell Signaling Technology	CST9451	1:1000
4EBP1	Cell Signaling Technology	CST9452	1:1000
AKT	Cell Signaling Technology	CST9272	1:1000
p-AKT (Thr308)	Cell Signaling Technology	CST4056	1:1000
p-AKT (Ser473)	Cell Signaling Technology	CST9018	1:1000
cleaved caspase 7 (Asp198)	Cell Signaling Technology	CST8438	1:1000
ERα-F10	Santa Cruz Biotechnology	sc-8002	1:1000
p-mTOR	Cell Signaling Technology	CST5536	1:1000
mTOR (Ser2448)	Cell Signaling Technology	CST5536	1:1000
S6	Cell Signaling Technology	CST2217	1:1000
p-S6 (Ser235/236)	Cell Signaling Technology	CST2211	1:1000
p-S6 (Ser240/244)	Cell Signaling Technology	CST5364	1:1000
PDE4D	Santa Cruz Biotechnology	sc-25814	1:1000
EGFR	Cell Signaling Technology	CST2646	1:1000
PGR	Santa Cruz Biotechnology	sc-7208	1:1000
HRP-coupled anti-rabbit IgG	Cell Signaling Technology	CST7074	1:10000

HRP-coupled anti-mouse IgG	Cell Signaling Technology	CST7076	1:10000

3.4. *In vivo* experiments

All animal work was approved by the Institutional Animal Care and Use Committee of Bilkent University and carried out according to the institution's guidelines and animal research principles. Six-to-eight-week-old female athymic nude and FVB/N mice were housed under a temperature-controlled and 12-hour light/12-hour dark cycle environment.

3.4.1. Primary tumor growths

For xenograft studies, $1x10^7$ MCF-7 TamR cells were prepared in 150 μl of 1:1 PBS and Matrigel (Corning, NY, USA) (v/v) and injected into mammary fat pads (MFP) of 6-8 weeks old female nude mice. Estradiol pellets (60-day slow release) (Innovative Research of America) were implanted subcutaneously (s.c) at the nape of the neck one day before injection. Once tumors reached to around 100 mm^3, SNX631 (25 mg/kg, daily, oral gavage), Gebr-7b (3 μg/kg, daily, intraperitoneal injection) and tamoxifen (2 mg/kg, daily, oral gavage) treatments were initiated. 30% PG + 70% PEG 400 and corn oil was used as vehicle for SNX631 and tamoxifen, respectively. Similarly, shMED13 transduced MCF-7 TamR cells were injected and mice were first given the doxycycline (100 ug/ml) in drinking water to induce the shRNA expression. Tumor growth was regularly monitored, and both tumor size and body weight measurements were recorded every 2 days. Tumor volume is calculated by measuring the length (L) and width (W) of the tumors using the formula $(L \times W^2)/2$. Mice were sacrificed 28

days after initiation of the treatment, and the tumors were collected and stored for subsequent analyses.

3.4.2. *In vivo* imaging system (IVIS)

Biofluorescent images of MCF-7 TamR shMED13 xenograft tumors were acquired with Lumina III In Vivo Imaging System (Perkin Elmer, Waltham, MA, USA). Turbo RFP was chosen as fluorophore, spectral unmixing method was applied to avoid auto fluorescence and to minimize the background noise level. RFP signal was evaluated with live imaging software.

3.4.3. Transgenic animal model and syngeneic tumor transplantation

MMTV-PyMT transgenic mouse model [full name given as FVB/N-Tg (MMTV-PyVT) 634Mul/J] were obtained from The Jackson Laboratory. In order to maintain live colony, hemizygous male mice were bred with FVB/NJ (non-carrier) inbred female mice.

Genotyping of newborn mice was assessed by phenol:chloroform DNA extraction method followed by polymerase chain reaction (PCR). Briefly, approximately 5 mm tail biopsies were obtained from 21-days-old pups. Samples were incubated in lysis buffer given in the **Table 3.12** overnight at 56°C. After incubation, lysed samples were centrifuged to pellet undigested hair and the supernatants were transferred to new 34hosphor34. One volume of phenol:chloroform:isoamyl alcohol (25:24:1) were added to sample and shaken vigorously. Top aqueous solution was transferred to new tube followed by centrifugation at 13000 rpm at 4°C. DNA precipitation was achieved by the addition of ethanol series. Pelleted DNA was dissolved in nuclease free water.

Table 3.12. Components of lysis buffer

Reagent	**Volume (µl)**
Sodium Tris EDTA (STE) (0.1 M NaCl, 10 mM Tris HCl pH: 8.0, 1 mM EDTA pH: 8.0)	500
10% SDS	30
Proteinase K (20 mg/ml)	20

PCR primers in **Table 3.13** were used to specifically amplify transgene and internal positive control.

Table 3.13. Protocol primer sequences

Primer type	**Sequence 5`→3`**
Transgene forward	GGA AGC AAG TAC TTC ACA AGG G
Transgene reverse	GGA AAG TCA CTA GGA GCA GGG
Internal positive control forward	CAA ATG TTG CTT GTC TGG TG
Internal positive control reverse	GTC AGT CGA GTG CAC AGT TT

PCR reaction containing components in **Table 3.14** was run according to program given in **Table 3.15**.

Table 3.14. PCR Components

Reagent	**Volume (µl)**
5X Q5 reaction buffer	5
5X Q5 high GC enhancer	5
dNTPs	0.5

10 μM internal positive control forward primer	1.25
10 μM internal positive control reverse primer	1.25
10 μM transgene forward primer	1.25
10 μM transgene forward primer	1.25
Q5 high fidelity DNA polymerase	0.25
50 ng/μl DNA	2
Nuclease free water	7.25

Table 3.15. PCR program

Step	**Temperature**	**Duration**
Initial denaturation	98°C	1 min
35 cycles	98°C	10 secs
	60°C	30 secs
	72°C	30 secs
Final extension	72°C	2 minutes
Final hold	4°C	∞

Ten ul of PCR product was mixed with 6X DNA loading dye and loaded into 2% agarose gel. Expected bands (transgene band= 556 bp, internal band= 200 bp) were visualized under ultraviolet light.

For mammary tumor transplantation, tumor fragments (2-3 mm^3) were prepared from a 12-weeks-old hemizygous MMTV-PyMT female mouse, and transplanted bilaterally into the #4 fat pads of wild type FVB/N females. SNX631, and tamoxifen

were administered as we performed in xenograft studies. Survival was calculated using a predefined tumor volume cut-off of 1500 mm^3.

3.4.4. Immunohistochemistry

Tumor samples isolated from the MCF-7 TamR xenografts were fixed in 10% formalin and processed into paraffin blocks. Histologic sections were taken with 5-mm thickness and deparaffinized. All sections were prepared for Haematoxylin & Eosin, Ki-67 (Dako, catalog no: 7240) and ApopTag Fluorescein *In Situ* Apoptosis Detection Kit (Merck KgaA, Darmstadt, Germany), staining according to the standard procedures.

3.5. Bioinformatics and statistical analysis

3.5.1. Patient dataset analysis and Gene Set Enrichment Analysis (GSEA)

Patient data were retrieved from the NCBI GEO database (GSE82173 (76), GSE58644 (77), GSE1378 (78), GSE76772 (79), GSE38061 (80) and GSE6532 (81)) and from online survival analysis tool, KM-plotter. GSEA was performed using gene sets related to tamoxifen resistance, mTOR and ErbB2 signaling downloaded from the GSEA website: http://software.broadinstitute.org/gsea/index.jsp.

3.5.2. Statistical analysis

All data were analyzed using GraphPad Prism software (GraphPad Software, Inc) and all results were represented as mean ± standard deviation (SD). Student's t-test was used to calculate statistical difference between two groups. One-way ANOVA test was performed to determine statistical significance between combination-treated

groups and single agent treatment groups. Two-way ANOVA test was used for the comparison of tumor growth over time among different treatment groups. Significance for survival curve analyses was calculated by log-rank (Mantel-Cox) test.

CHAPTER 4

RESULTS

PART I

4.1. MED13 and CDK8 are overexpressed in tamoxifen resistant breast cancer

To investigate the new mechanisms underpinning tamoxifen resistance and elucidate novel modulators of tamoxifen resistance, we first aimed to develop tamoxifen-resistant cell line models using two different ER-positive (ER+) cell lines- MCF-7 and T47D. We confirmed the acquired tamoxifen-resistant profile, obtained by exposure to tamoxifen for more than six months, by cell viability assay **(Figure 4.1 A** and **B)**. Several studies have demonstrated that decreased ER and PR phenotype occurs through the acquisition of tamoxifen resistance (82) while upregulated HER2 and EGFR levels are adopted (83-85). In line with this, we have shown enhanced HER2 and EGFR protein levels in response to tamoxifen, whereas ER and PR expressions were lower in tamoxifen resistant (TamR) cells compared to parental counterparts **(Figure 4.1 C** and **D)**.

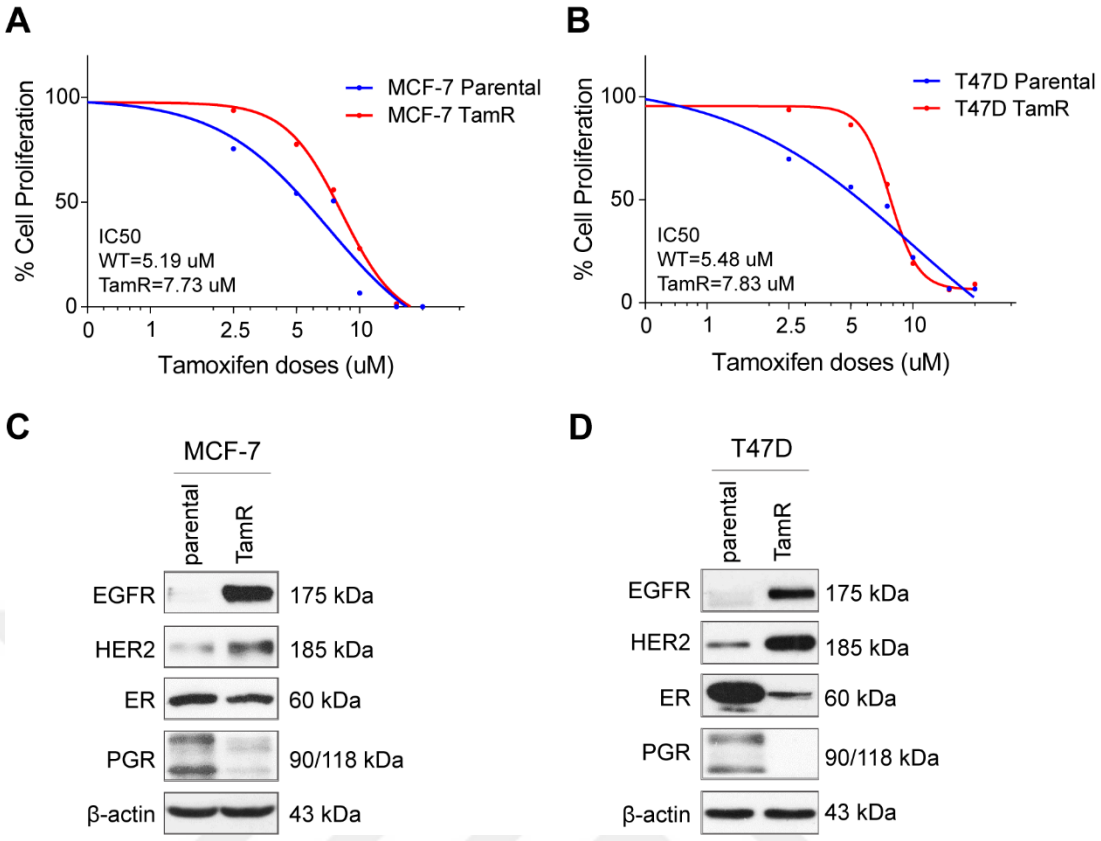


Figure 4.1. Characterization of tamoxifen resistance in MCF-7 and T47D cells A. Dose response curves of tamoxifen in MCF-7 (A) and T47D (B) cells. Cells were treated with increasing doses of tamoxifen for one week and three days in MCF-7 and T47D cell lines, respectively. Western blot analysis of molecular markers of tamoxifen resistance (EGFR, HER2, ER and PGR) in MCF-7 (C) and T47D (D) cells. β-actin was used as a loading control.

Next, to systematically characterize the components of the Mediator kinase module in tamoxifen resistance **(Figure 4.2)** and to show whether targeting MED13 and CDK8 is clinically relevant in this context, we first examined the mRNA expression of *MED13* and *CDK8* in tamoxifen-treated ER-positive patients. Our results depicted that ER-positive patients who failed to respond to tamoxifen have significantly higher levels of *MED13* and *CDK8* **(Figure 4.3 A-D)**.

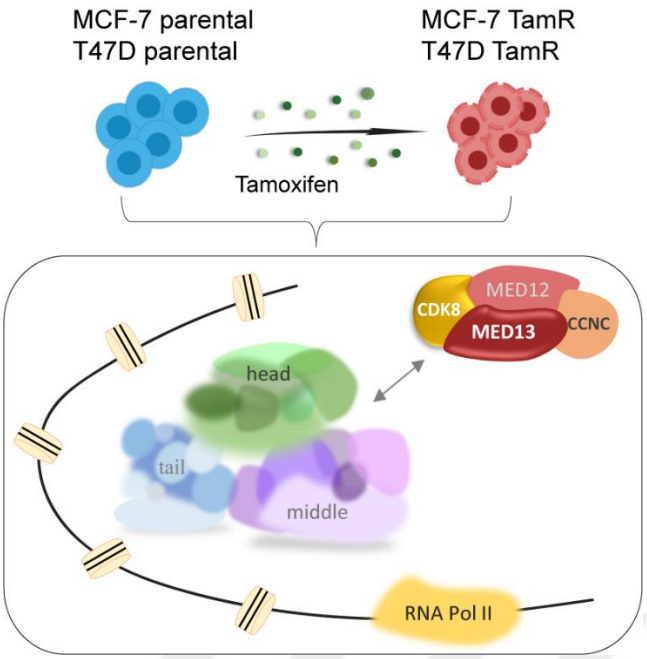


Figure 4.2. Graphical depiction of CDK8 kinase module (CKM)

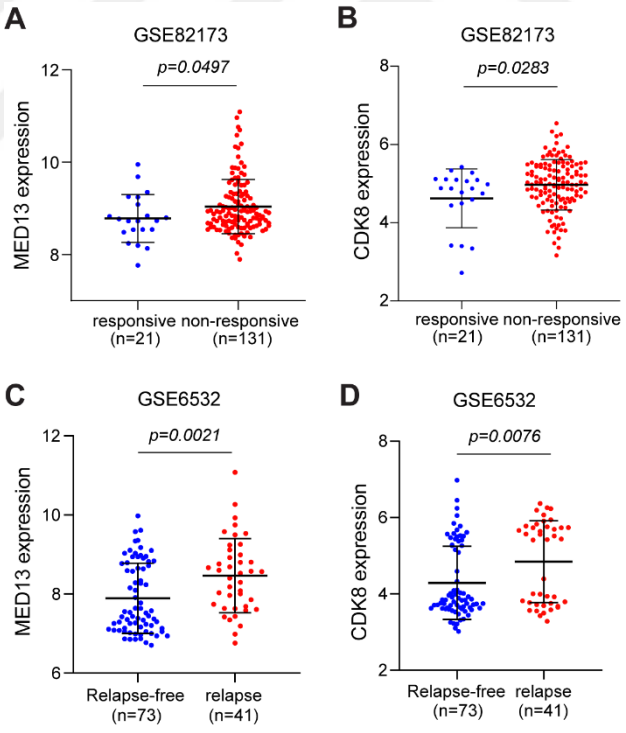


Figure 4.3. CDK8 and MED13 are overexpressed in tamoxifen-treated ER positive patients. (A) Association between MED13 expression and tamoxifen responsiveness in GSE82173. (B) Changes in CDK8 expression according to tamoxifen responsiveness. MED13 (C) and CDK8 (D) expression levels according to

relapse status of patients from GSE6532. Student's t-test was used to calculate statistical difference between groups.

However, we could not observe significantly differential expression of MED12 or CCNC between groups in the direction we expected **(Figure 4.4 A** and **B)**. Patients who are not responsive to tamoxifen treatment showed lower level of MED12 while CCNC level was similar between groups.

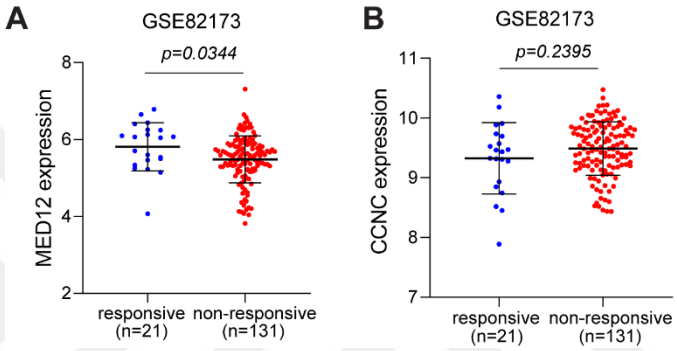


Figure 4.4. Expression levels of MED12 and CCNC in tamoxifen-treated ER-positive breast cancer patients.(A) MED12 and (B) CCNC levels in tamoxifen responsive vs non-responsive patients from GSE82173. Student's t-test was used to calculate statistical difference between groups.

Clinical relevance of CDK8 and MED13 in tamoxifen resistance has been further investigated by analyzing GSE58644 dataset where *MED13* and *CDK8* levels were higher in tumors with a more aggressive disease state characterized by higher tumor grade **(Figure 4.5).** Moreover, we performed survival analyses by using different patient datasets. Patients from GSE6532 with elevated levels of either MED13 or CDK8 showed poorer relapse-free survival **(Figure 4.6 A** and **B)**. Similarly, we observed a lower survival rate in patients with higher MED13 and CDK8 expression compared to patients with lower expression **(Figure 4.6 C** and **D)**.

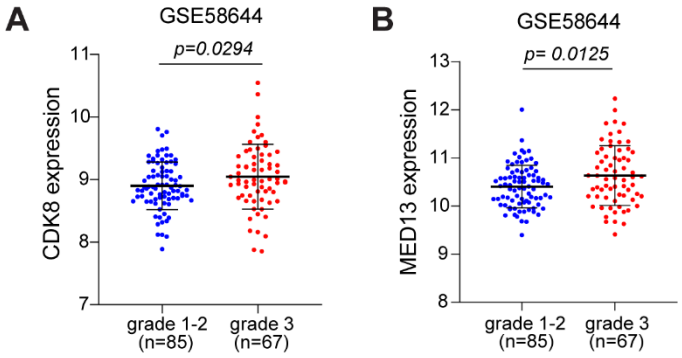


Figure 4.5. Overexpression of CDK8 and MED13 is correlated with higher tumor grade. Expression level of CDK8 (A) and MED13 (B) according to tumor grade in tamoxifen treated ER positive patients from GSE58644. Student's t-test was used for statistical analysis.

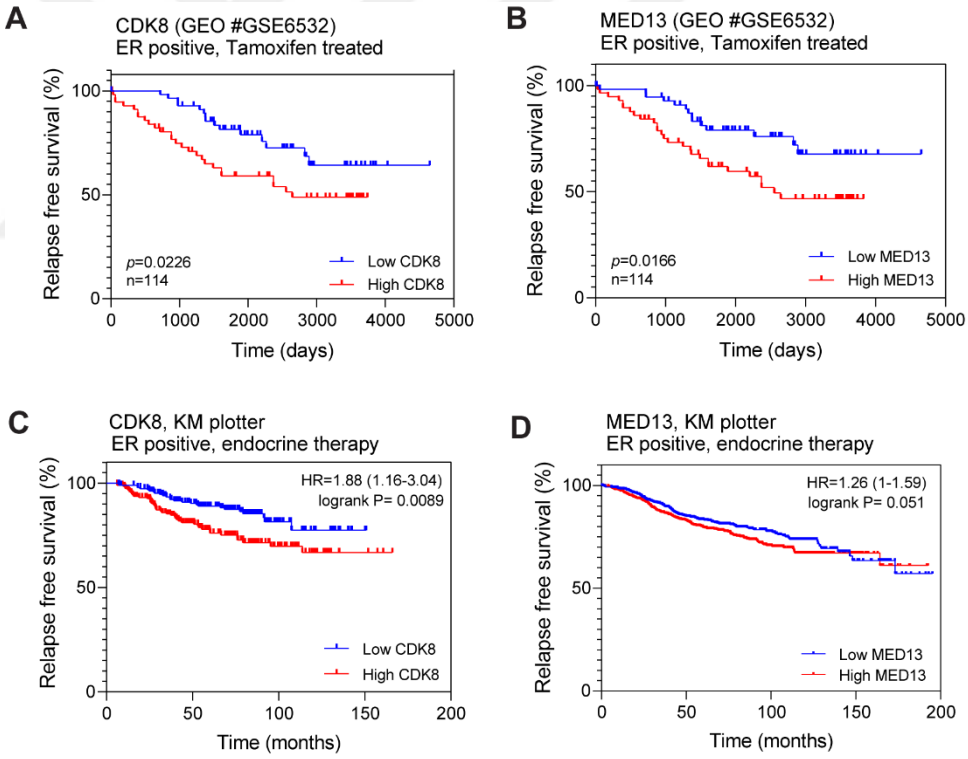


Figure 4.6. CDK8 and MED13 overexpression predicts poor relapse-free survival in tamoxifen- or endocrine-treated ER-positive patients. Effect of CDK8 (A) and MED13 (B) on relapse-free survival of tamoxifen treated ER-positive breast cancer patients from GSE6532. KM plotter results showing the percent relapse-free survival

in endocrine-therapy treated ER-positive breast cancer patients based on CDK8 (C) and MED13 (D) expression. Log-rank test was used for statistical analyses.

In order to investigate the effects of other kinase module components (MED12 and CCNC) on patient survival outcome, we analyzed same datasets (GSE6532 and KM plotter). However, we could not observe the pattern we expected **(Figure 4.7 A-D)**. Both CCNC and MED12 expression was failed to differentiate relapse free survival of the patients.

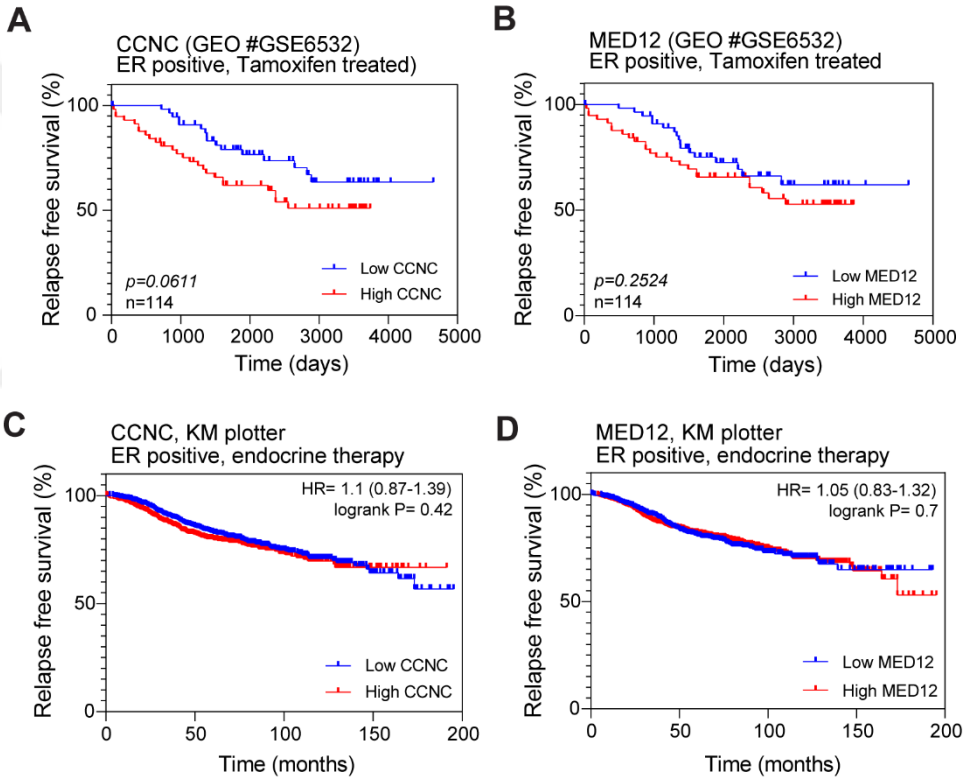


Figure 4.7. Kaplan Meier plots showing the effects of MED12 and CCNC on patient survivals. Effect of CCNC (A) and MED12 (B) on relapse-free survival of tamoxifen treated ER positive breast cancer patients from GSE6532 (n=114). Relapse free survival of ER positive patients from KM plotter who underwent endocrine therapy with respect to CCNC (C) and MED12 expression (D). Log-rank test was used for statistical analyses.

Demonstrating the clinical relevance of *MED13* and *CDK8*, we next validated the substantial upregulation of MED13 and CDK8 in our well-established tamoxifen-resistant cell line models (MCF-7 TamR and T47D TamR) compared with their parental counterparts (84, 86, 87). In line with this, CDK8 kinase activity in the TamR cells is augmented as shown by higher level of STAT1, a substrate of CDK8, phosphorylation **(Figure 4.8)**. Overall, these results suggested that MED13 and CDK8, thus the CKM, might be involved in tamoxifen resistance in breast cancer.

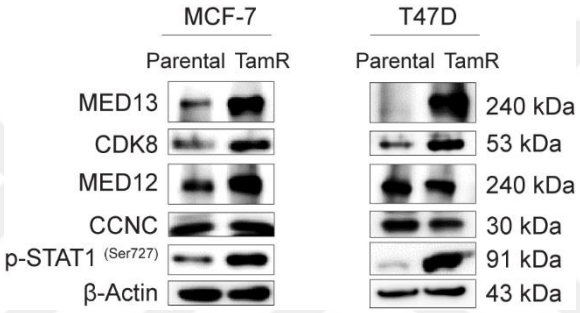


Figure 4.8. CDK8 and MED13 are overexpressed in well-established tamoxifen resistant cell line models unlike other components of kinase module. Western blot analysis of kinase module components in TamR cells compared with their parental counterparts. β-Actin was used as a loading control.

4.2. Inhibition of either MED13 or CDK8 re-sensitizes the tamoxifen resistant cells

Next, to test whether modulating *MED13* expression can restore sensitivity to tamoxifen, we performed siRNA-mediated knockdown in both TamR cell lines. Combination of tamoxifen with siMED13 resulted in a strong growth inhibition in both models **(Figure 4.9 A** and **B)**, implying its potential role in resistance development.

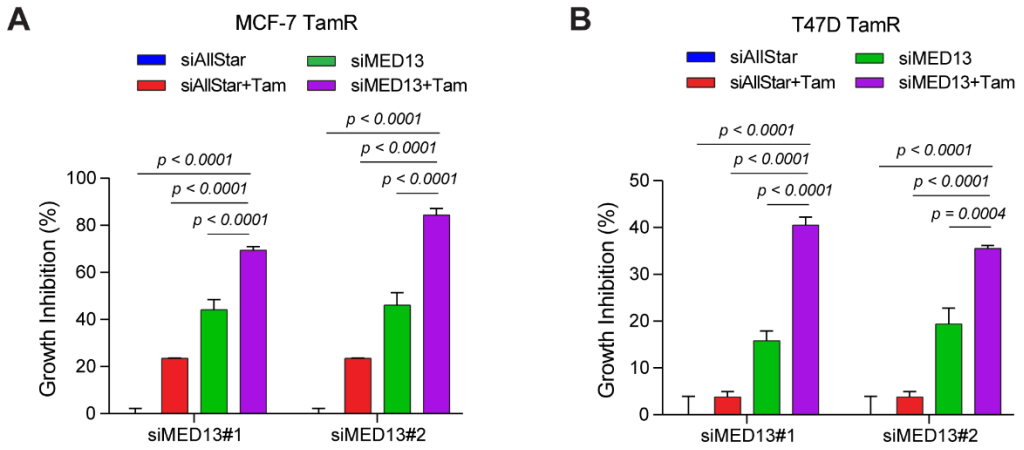


Figure 4.9. MED13 inhibition re-sensitizes the tamoxifen resistant cells Percent growth inhibition of MCF-7 TamR (A) and T47D TamR (B) cells transfected with MED13 specific siRNAs in the absence and presence of tamoxifen. Cells viability was assessed at 72 hours of tamoxifen treatment (7.5 μM in MCF-7 TamR cells, 5 μM in T47D TamR cells).

Dynamic structure and ubiquity of Mediator complex are daunting tasks to pharmacologically target and design specific inhibitors for MED13. Thus, we aimed to repeat the same set of experiments through modulation of CDK8 as it is a druggable kinase with a specific inhibitor, SNX631 (88). It is noteworthy to mention that STAT1 phosphorylation has been denoted as a robust marker to assess CDK8 activity (89). To this end, we first evaluated the ability of SNX631 to modulate the phospho-STAT1 level. Treatment with increasing doses of SNX631 dramatically inhibited STAT1 phosphorylation both in parental and TamR cell lines **(Figure 4.10 A** and **B)**, showing the potency of our inhibitor to suppress CDK8 activity.

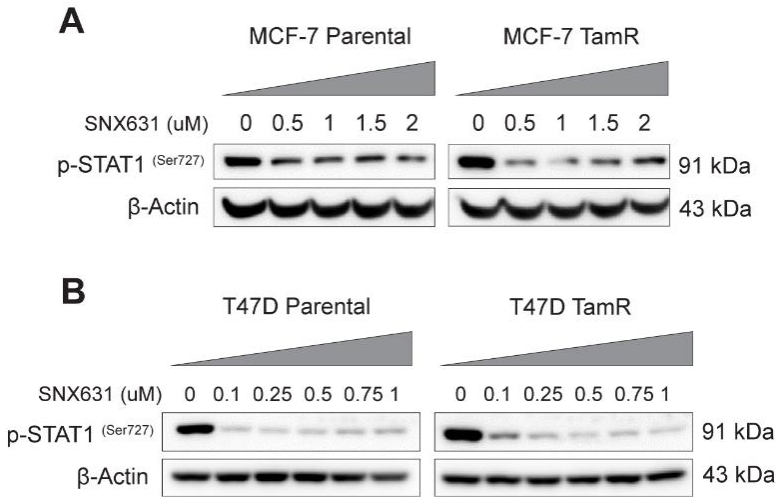


Figure 4.10. CDK8 inhibitor, SNX631, suppressed phosphorylation of STAT1 Pharmacological CDK8 inhibition with increasing doses of specific CDK8 inhibitor, SNX631, in MCF-7 (A) and T47D (B) cells. Both parental and TamR cells were treated with SNX631 for 24 hours. β-Actin was used as a loading control.

To determine whether pharmacological inhibition of CDK8 can confer tamoxifen resistance, we carried out individual and combinatorial treatment of tamoxifen and SNX631. Combined treatment inhibited cell growth in a dose-dependent manner in both TamR cell lines **(Figure 4.11 A** and **B)**.

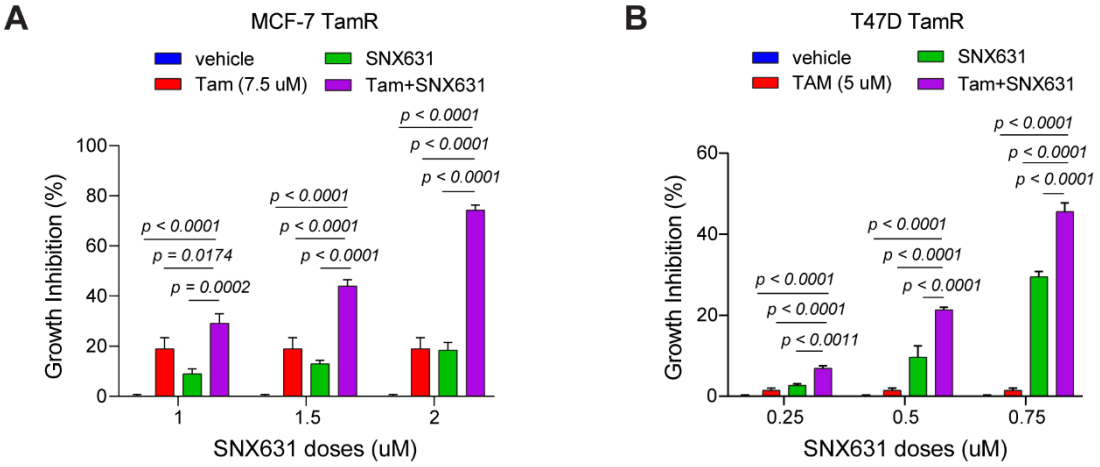


Figure 4.11. CDK8 inhibition re-sensitizes the tamoxifen resistant cells. Tamoxifen sensitization with different doses of SNX631 in MCF-7 TamR (A) and T47D TamR (B) cells. Cells were treated with tamoxifen and SNX631 alone or in combination for one week. Cell viability was measured by SRB assay as triplicates.

Moreover, modulator role of CDK8 in tamoxifen resistance has been validated with colony formation assay. Inhibiting CDK8 in combination with tamoxifen treatment decreased colony formation capacity of the TamR cells **(Figure 4.12)**. Overall, these results revealed the potential of the kinase module to overcome tamoxifen resistance.

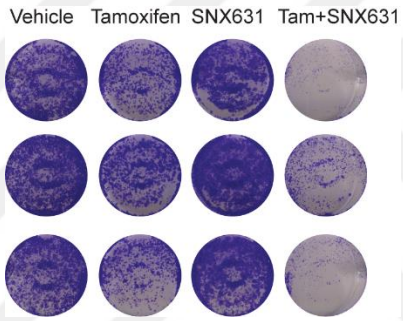


Figure 4.12. SNX631 treatment combined with tamoxifen reduces colony forming capabilities of TamR cells Colony formation assay of TamR cells following CDK8 inhibition and tamoxifen treatment for 2 weeks. Colonies were stained with crystal violet.

4.3. MED13 and CDK8 dependent tamoxifen resistance is mediated via HER2/mTOR axis

Preclinical studies elucidated that aberrant activation of PI3K/Akt/mTOR pathway plays role in resistance to hormone-targeted therapies. We further validated this observation by GSEA analysis and demonstrated that genes involved in MTORC1 signaling were significantly enriched in tamoxifen-treated patients with recurrence in GSE1378 dataset **(Figure 4.13)**.

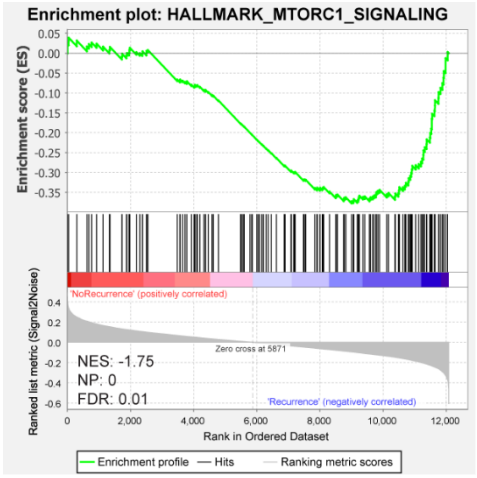


Figure 4.13. MTOR signaling is associated with tamoxifen resistance. Gene set enrichment analysis (GSEA) of recurred patients compared with non-recurred patients from GSE1378. Data significance is presented as Normalized Enrichment Score (NES), Nominal p-value (NP) and False Discovery Rate (FDR) value.

Previous studies have also revealed that elevated levels of EGFR, HER2 and phosphorylated Akt are involved in tamoxifen resistance (85). To confirm these findings in our models, we examined the activation of HER2 and mTOR signaling in TamR cells compared to their sensitive counterparts and observed markedly higher level of HER2 together with phosphorylation of mTOR, S6, Akt, and 4EBP1 **(Figure 4.14)**.

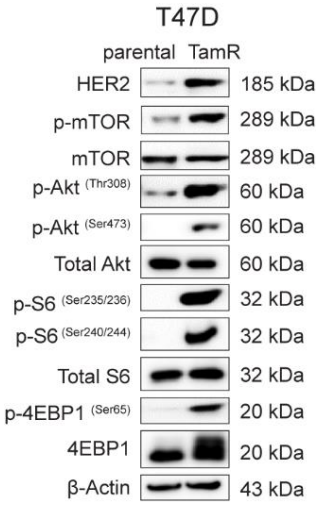


Figure 4.14. HER2/mTOR signaling markers are upregulated in TamR cell line models. Western blot results depicting enhanced levels of HER2, mTOR and AKT signaling proteins in TamR cells compared with parental cells. β-actin was used as a loading control.

To test whether MED13 knockdown lead to changes in HER2 signaling, TamR cells were transfected with siRNAs targeting MED13 (referred as siMED13) followed by tamoxifen treatment for 48 hours. Inhibition of MED13 combined with tamoxifen treatment downregulated HER2 protein level and decreased phosphorylated S6 and 4EBP1 levels **(Figure 4.15 A** and **B)**. In addition, tamoxifen treatment of cells after transfection with siMED13 activated cleavage of caspase 7, inducing apoptosis **(Figure 4.16 A** and **B).**

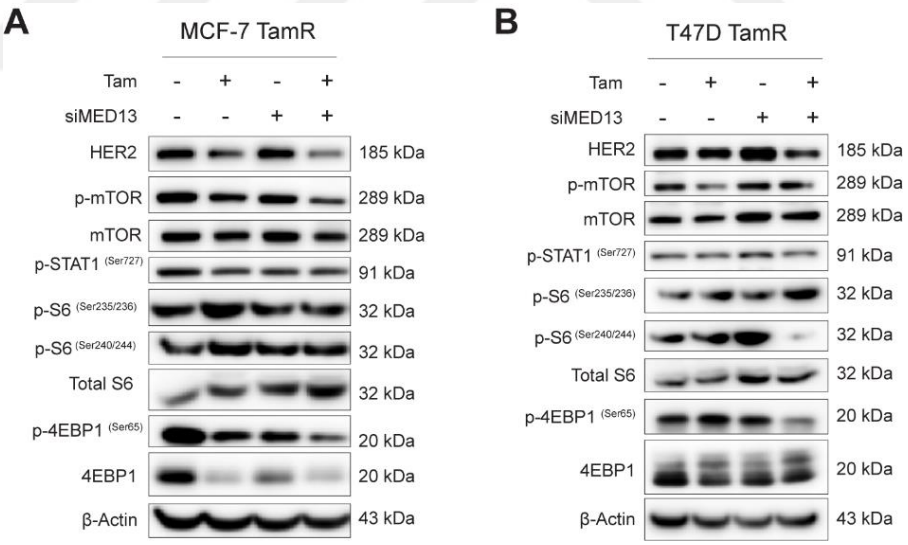


Figure 4.15. MED13 dependent tamoxifen resistance is mediated *via* HER2/mTOR axis. Western blot analysis of HER2/mTOR signaling markers upon MED13 knockdown followed by tamoxifen treatment in (A) MCF-7 TamR and (B) T47D TamR cells. After 24 hours of 40 nM siRNA transfection, cells were treated with 5.0 μM tamoxifen for 48 hours. β-Actin was used as a loading control.

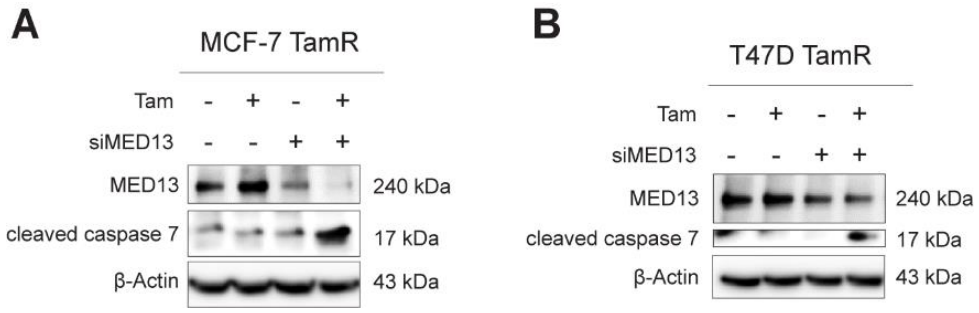


Figure 4.16. Combination of MED13 knockdown and tamoxifen treatment triggered apoptosis. Western Blot analysis showing the levels of cleaved caspase-7 in (A) MCF-7 TamR and (B) T47D TamR cells upon MED13 inhibition followed by tamoxifen treatment for 72 hours. β-Actin was used as a loading control.

To elucidate how HER2-mediated CDK8 regulation may lead to tamoxifen resistance, we first performed GSEA analysis and found that MTORC1 signaling was enriched in cells expressing CDK8 compared to those with CDK8 knockdown in GSE38061 (80) **(Figure 4.17)**. Moreover, SNX631 and tamoxifen combination significantly downregulated the downstream HER2/mTOR signaling **(Figure 4.18)**.

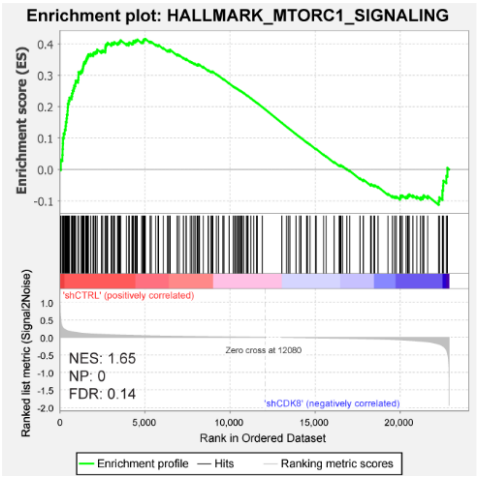


Figure 4.17. Gene set enrichment analysis identified CDK8 associated MTORC signaling Enrichment of MTORC1 signaling in shCtrl cells compared with shCDK8 cells from GSE38061. Data significance is presented as Normalized Enrichment Score (NES), Nominal p-value (NP) and False Discovery Rate (FDR) value.

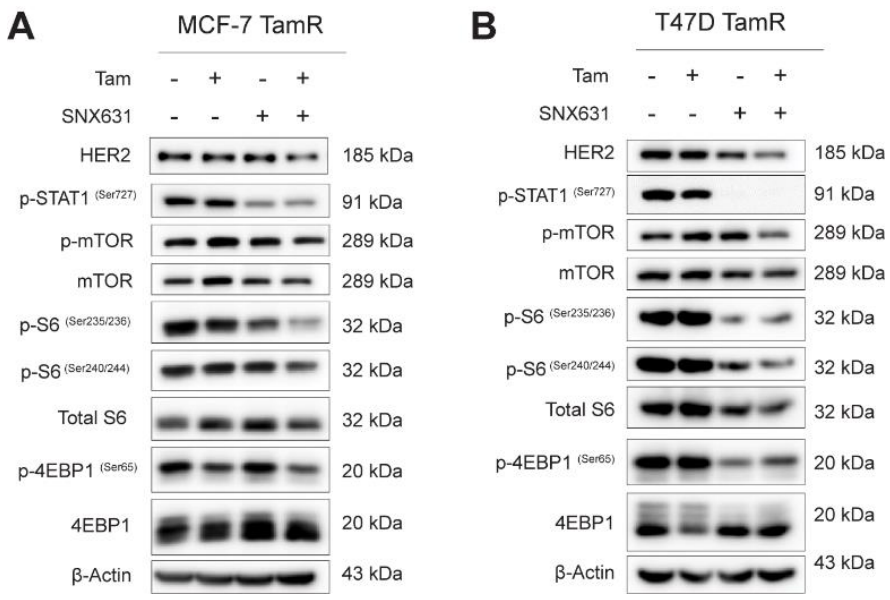


Figure 4.18. CDK8 dependent tamoxifen resistance is mediated *via* HER2/mTOR axis (A)Western blot analysis of HER2/mTOR signaling markers upon treatment with 2.0 μM SNX631 combined with 5.0 μM tamoxifen in MCF-7 TamR cells (B) Western blot analysis of HER2/mTOR signaling markers upon treatment with 0.5 μM SNX631 combined with 5.0 μM tamoxifen in T47D TamR cells. All treatments were performed for 48 hours. β-Actin was used as a loading control.

Similar to results obtained upon MED13 knockdown, SNX631 treatment combined with tamoxifen induced apoptosis as shown by an increase in cleaved caspase-7 level **(Figure 4.19)**.

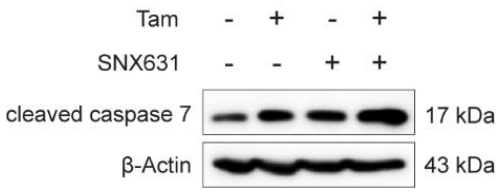


Figure 4.19. Combination of SNX631 and tamoxifen treatment induced apoptosis. Western Blot analysis showing the levels of cleaved caspase-7 in MCF-7 TamR cells upon SNX631 (2 μM) plus tamoxifen (5 μM) treatment for one week. β-Actin was used as a loading control.

4.4. Inhibition of either MED13 or CDK8 reduced the mRNA expression of ErbB2

Cui et al previously showed that MED1 is recruited to the ErbB2 gene and required for its optimal transcription (90). To determine whether MED13 also has potential to regulate ErbB2 expression, we first analyzed correlation between mRNA levels of ErbB2 and MED13 by using two different GEO datasets, GSE17705 (91) and GSE6532 (81). Our analyses demonstrated that expression of ErbB2 is positively correlated with the expression of MED13 in the ER-positive tamoxifen-treated patients **(Figure 4.20 A** and **B)**. Furthermore, MED13 silencing combined with tamoxifen treatment reduced ErbB2 mRNA level **(Figure 4.21)**.

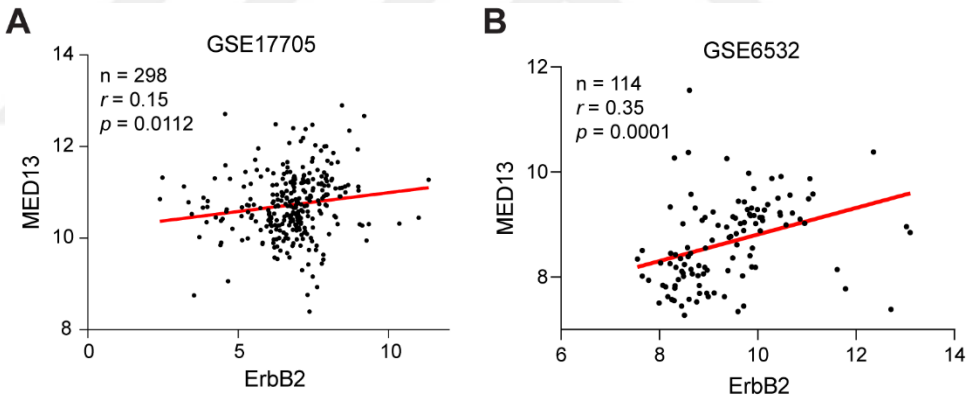


Figure 4.20. MED13 positively correlates with ErbB2 expression in tamoxifen treated ER-positive breast cancer patients. Pearson's correlation analyses showing gene expression levels of ErbB2 and MED13 in (A) GSE17705 and (B) GSE6532 datasets. *r*: Pearson's correlation coefficient value, n: patient number.

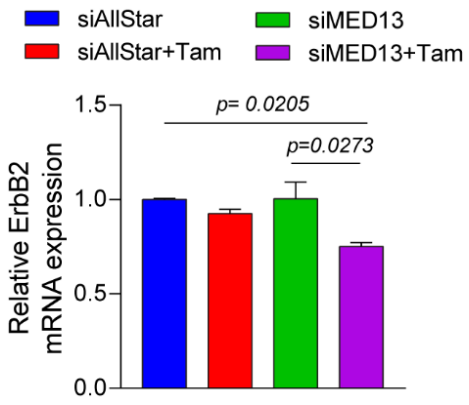


Figure 4.21. Combining MED13 knockdown with tamoxifen treatment reduced ErbB2 mRNA level. qRT-PCR analysis showing changes in the mRNA expression of ErbB2 upon transfection with siAllStar or siMED13 followed by 48 hours of tamoxifen treatment.

To gain insight whether ErbB2 signaling can be controlled by CDK8 in tamoxifen resistance, we further analyzed dataset used in Figure 4.17 and confirmed that ErbB2 signaling was enriched in the cells expressing CDK8 compared to the ones with CDK8 knockdown **(Figure 4.22)**. Supporting this, expression of CDK8 positively correlates with ErbB2 in the same datasets **(Figure 4.23 A** and **B)**. Moreover, we observed decreased ErbB2 mRNA level in response to SNX631 alone and combination treatment **(Figure 4.24)**.

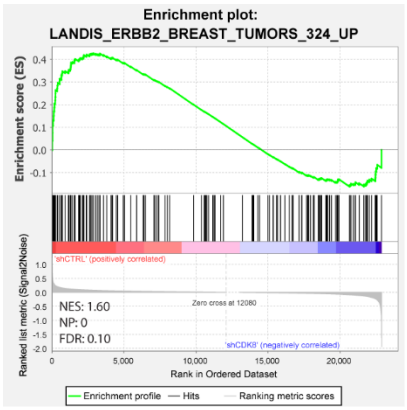


Figure 4.22. Gene set enrichment analysis identified CDK8 associated ERBB2 signaling Enrichment of upregulated genes upon ErbB2 expression in shCtrl cells

compared with shCDK8 cells from GSE38061. Data significance is presented as Normalized Enrichment Score (NES), Nominal p-value (NP) and False Discovery Rate (FDR) value.

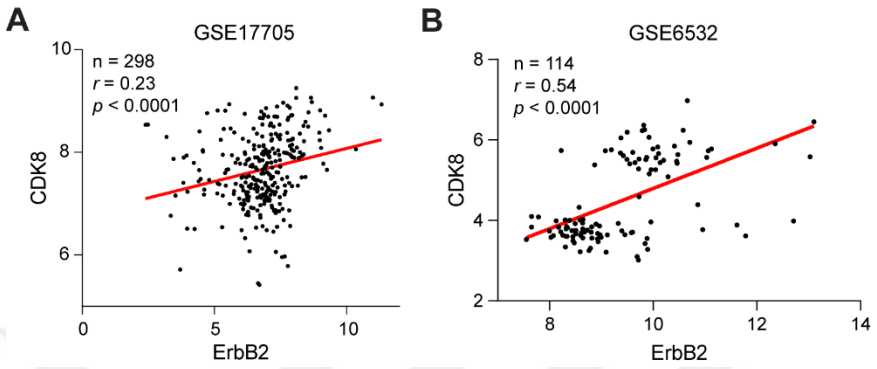


Figure 4.23. CDK8 positively correlates with ErbB2 expression in tamoxifen treated ER-positive breast cancer patients. Pearson's correlation analyses showing gene expression levels of ErbB2 and CDK8 in (A) GSE17705 and (B) GSE6532 datasets. *r*: Pearson's correlation coefficient value, n: patient number.

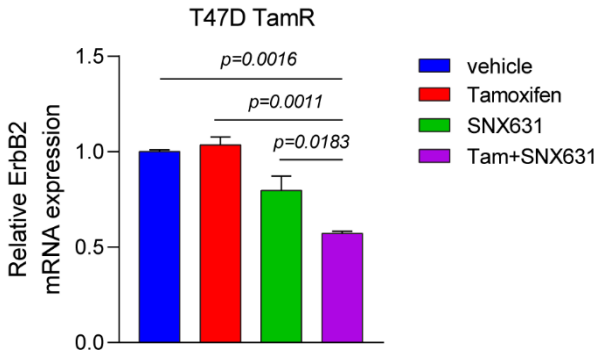


Figure 4.24. Combination treatment of tamoxifen and SNX631 downregulated mRNA expression of ErbB2. qRT-PCR analysis showing changes in the mRNA expression of ErbB2 48 hours after SNX631 treatment combined with tamoxifen.

Several oncogenes and growth factors are regulated post-transcriptionally (92, 93). A recent study revealed the function of a group of amplified oncogenes in the post-transcriptional regulation of ErbB2 (94). Moreover, tolfenamic acid -nonsteroidal anti-inflammatory drug- showed antitumorigenic effects in breast cancer *via* induction of ErbB2 mRNA decay. In the light of these findings, we conducted a time series treatment of Actinomycin D, which is a transcription inhibitor intercalating into DNA (95). Combination treatment resulted in significantly increased ErbB2 mRNA decay following transcription blockade **(Figure 4.25)**, confirming the post-transcriptional regulation of ErbB2.

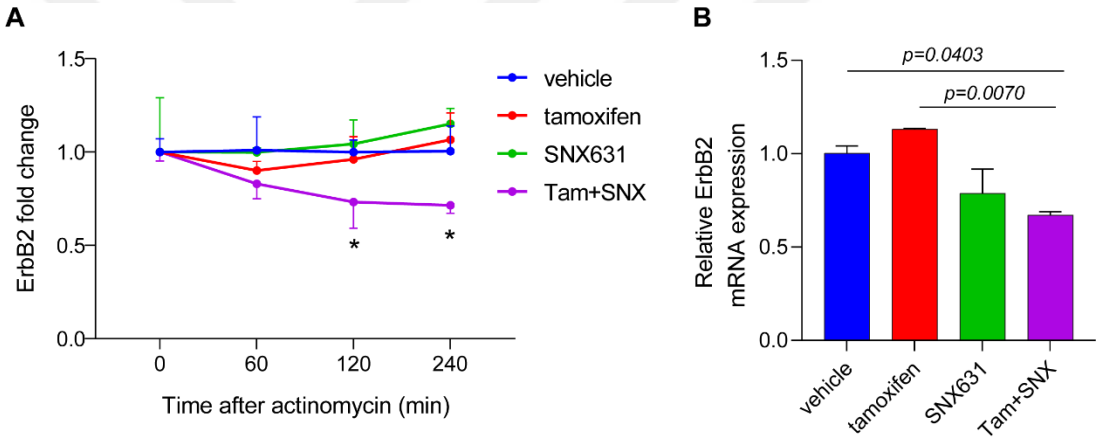


Figure 4.25. Combined therapy of tamoxifen and SNX631 significantly reduced ErbB2 mRNA stability.(A) qRT-PCR analysis showing changes in the ErbB2 mRNA level. T47D TamR cells were treated with 5 μg/ml of actinomycin D at the indicated time points following the 48 hours of treatment of SNX631 (0.5 uM) in the absence and presence of tamoxifen (5 uM). * $p < 0.05$; ** $p < 0.01$; *** $p < 0.001$. Statistical significance was evaluated by two-way Anova test. (B) ErbB2 knockdown upon combination treatment has been confirmed prior to actinomycin treatment. Statistical significance was evaluated by one-way Anova test.

4.5. MED13 inhibition overcomes tamoxifen resistance *in vivo*

Next, in order to test tamoxifen sensitizer role of MED13 in *in vivo* settings, we first engineered MCF-7 TamR cells to inducibly express an shRNA targeting MED13 (referred as MCF-7 TamR shMED13 #3 and MCF-7 TamR shMED13 #4). Upon doxycycline induction, we observed downregulation of MED13 protein level **(Figure 4.26)**. Since MCF-7 TamR shMED13 #4 cells showed robust reduction, we used them for further experiments.

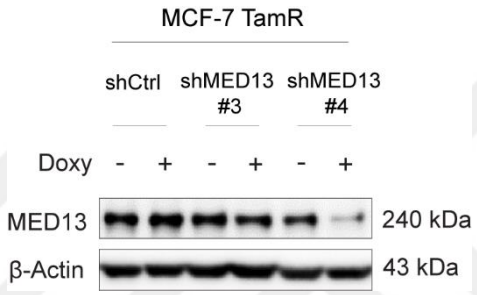


Figure 4.26. Validation of inducible MED13 knockdown in MCF-7 TamR cells Western blot analysis showing the reduction of MED13 protein level in shRNA transduced MCF-7 TamR cells upon doxycycline (1 μg/ml) exposure. β-Actin was used as a loading control.

Later, to observe tumor-initiating capabilities of cells under combinatorial treatment, we assessed colony formation assay. Inhibiting MED13 in combination with tamoxifen treatment significantly decreased the colony numbers **(Figure 4.27)**.

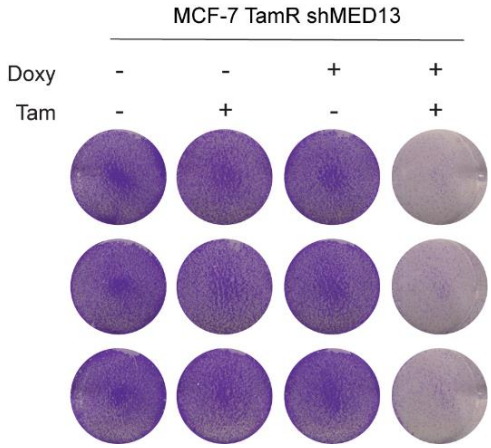


Figure 4.27. MED13 inhibition combined with tamoxifen treatment reduces colony forming capabilities of TamR cells Colony formation assay of MCF-7 TamR cells following MED13 inhibition *via* gene specific shRNA and tamoxifen treatment for 2 weeks. Colonies were stained with crystal violet.

Notably, similar to the phenotypes obtained *in vitro*, the combination of MED13 inhibition and tamoxifen treatment possessed a strong inhibitory effect on the tumor growth compared to individual treatment groups **(Figure 4.28 A** and **B)**. In addition, the tumor weight in shMED13 group with tamoxifen treatment was lower than the control and single treatment groups **(Figure 4.28 C)**. We further observed inhibition of HER2/mTOR signaling in shMED13 tumors upon tamoxifen treatment **(Figure 4.28 D)**. Taken together, these results clearly demonstrate that MED13 inhibition results in tamoxifen sensitization *in vivo.*

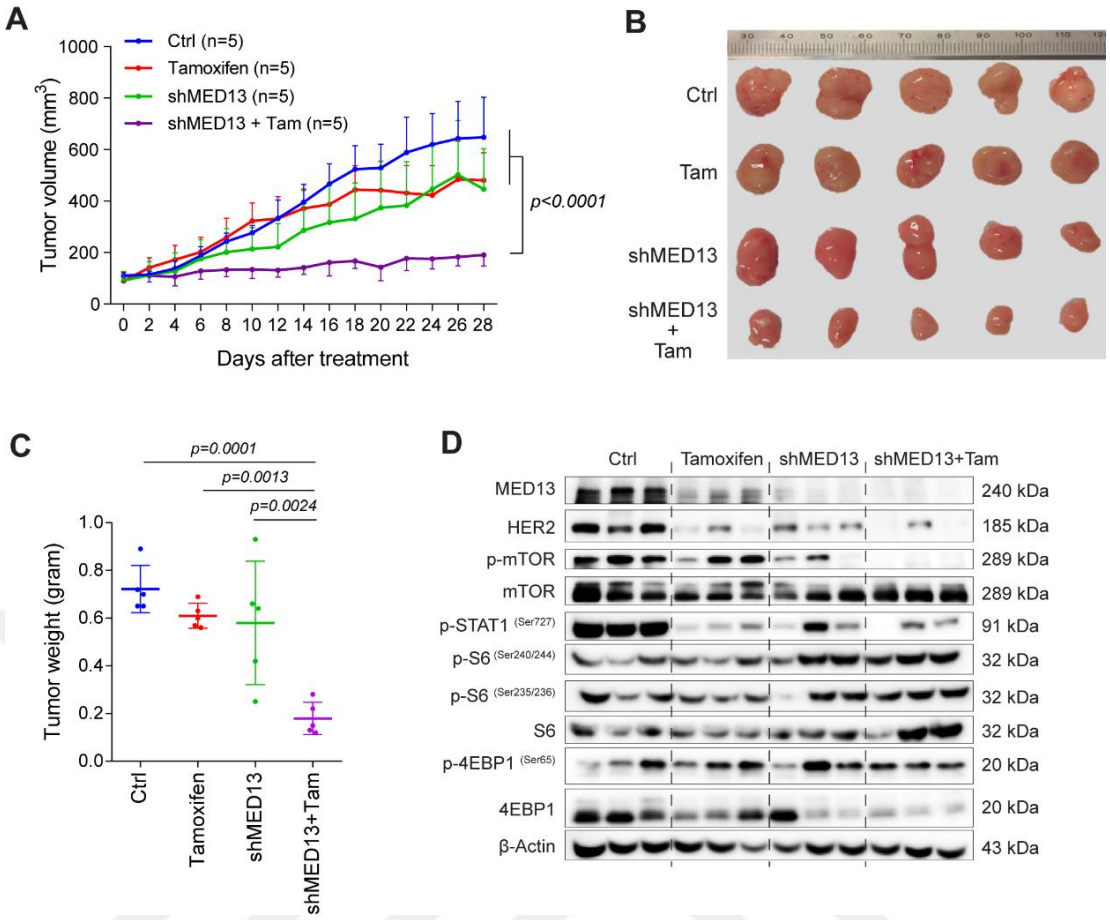


Figure 4.28. MED13 inhibition overcomes tamoxifen resistance *in vivo*. (A) Tumor volume changes of MCF-7 TamR xenografts upon shMED13 induction for 28 days after treatment. Both doxycycline and tamoxifen treatments were initiated once tumors reached to around 100 mm3. (B) Tumor pictures obtained from mice in A. (C) Tumor weights of the treatment groups. (D) Western blot analyses of HER2/mTOR signaling axis upon individual or combined treatment. β-Actin was used as a loading control.

4.6. CDK8 inhibition overcomes tamoxifen resistance *in vivo*

Upon showing the tamoxifen sensitizer role of MED13 *in vivo*, we next examined whether CDK8 inhibition overcomes tamoxifen resistance in the same setting. To this end, we used the xenografts of MCF-7 TamR cells and treated mice with either SNX631 or tamoxifen or both. Combination therapy significantly suppressed the

tumor growth compared to the single agent treatments **(Fig. 4.29 A** and **B**). Tumor weights were also lower in the combination group as compared to single agent-treated groups **(Fig. 4.29 C)**. Importantly, we did not observe significant body weight loss in any of the treatment groups, suggesting well toleration of the drugs and negligible toxicity **(Fig. 4.29 D)**. Moreover, phosphorylation of STAT1, mTOR, S6 and 4EBP1 was diminished following combination treatment **(Fig. 4.29 E)**. Overall, these data revealed the tamoxifen sensitizer role of CDK8 *in vivo*.

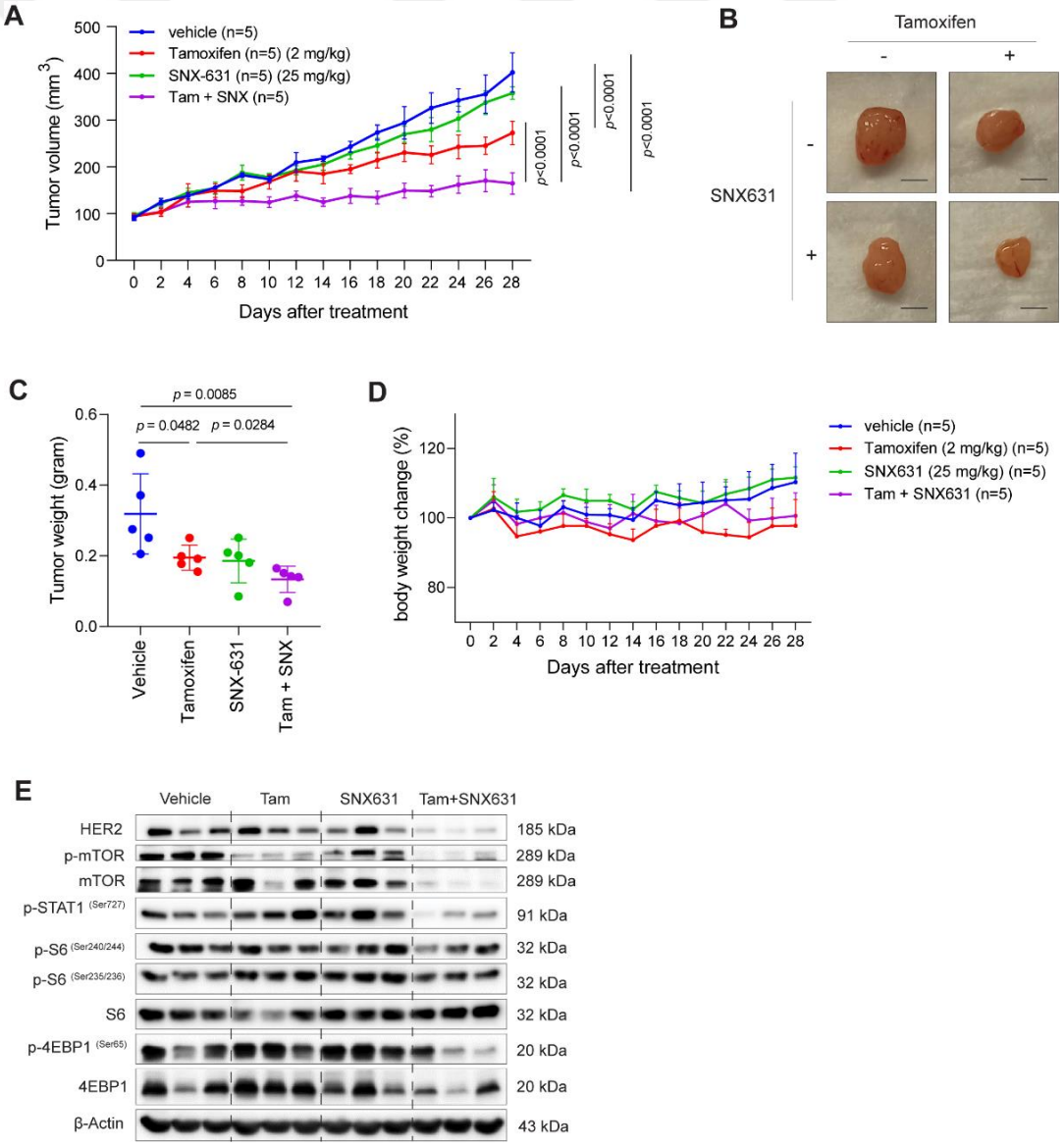


Figure 4.29. CDK8 inhibition overcomes tamoxifen resistance *in vivo.* (A) Tumor volume changes of MCF-7 TamR xenografts for 28 days after treatment with tamoxifen and SNX631 individually or in combination. Drugs were administered once tumors reached to around 100 mm3. n indicates mice number. (B) Representative tumor pictures from A. (C) Tumor weights of the treatment groups. (D) Percentage change in the body weights of mice treated with tamoxifen and SNX631 alone or in combination. (E) Western blot analyses of HER2/mTOR signaling axis upon individual or combined treatment. β-Actin was used as a loading control.

4.7. Targeting CDK8 overcomes tamoxifen resistance in an aggressive transgenic mouse model

Demonstrating the pivotal role of SNX631 on tumor growth inhibition in xenografts encouraged us to test tamoxifen sensitizer potential of CDK8 in an aggressive transgenic mouse model. To this end, we utilized FVB/N-Tg (MMTV-PyMT)634 Mul/J (also known as MMTV-PyMT) which is very well established and commonly used genetically engineered mouse model (GEMM) in the cancer field (96). This model is first reported in 1992 with the use of the murine mammary tumor virus long terminal repeat promoter (MMTV-LTR) to control the expression of Polyomavirus Middle T antigen (PyMT) (97). Mammary tumor formation is divided into 3 stages with respect to tumor burden and rate of tumor occurrence. Pre-stage of tumor progression starts with hyperplasia at 4-5 weeks of age which evolves through appearance of mammary tumor tissue on normal gross termed mammary intraepithelial neoplasia (MIN). While the Early stage is defined with 1-2 solid tumors at 6-8 weeks of age, the late stage is based on the presence of all 10 primary mammary tumors capable to metastasize to the lungs, forming adenocarcinomas in the lung parenchyma after 10 weeks of age (98).

Transcriptomic profiling clustered PyMT tumors with the luminal B subtype of human breast cancers (99). Moreover, loss of ER and PR expression, and augmentation of cyclin D1 and ErbB2 through progression the malignancy **(Figure 4.30)** are the main characteristics resembling the poor prognosis of human breast cancer (100, 101). Importantly, lose ER positivity of end-stage tumors of this model towards disease progression recapitulates the clinical characteristics of tamoxifen resistant patients (102).

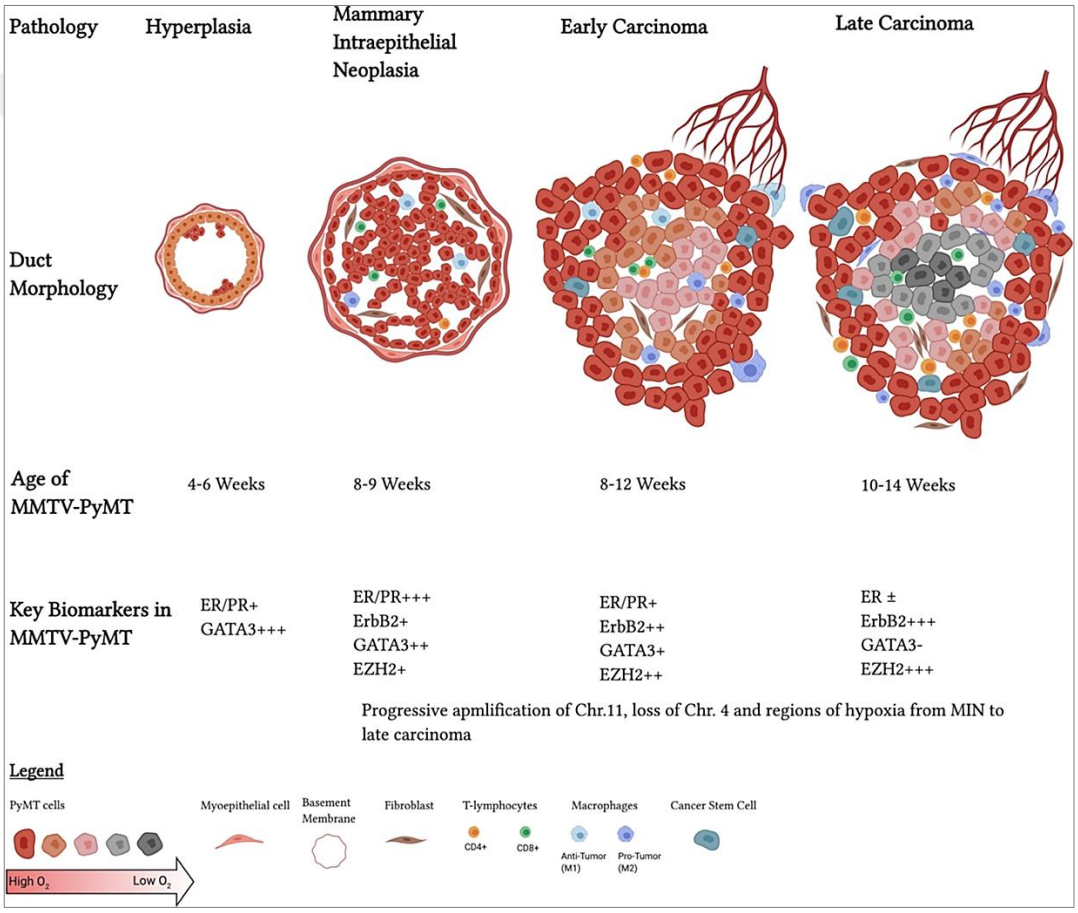


Figure 4.30. Summary of tumor progression and biomarker expression in the MMTV-PyMT mouse model. Modified from (100) See Appendix for the copyright permission.

To characterize this model in tamoxifen resistance context, we first analyzed RNA-seq results comparing transcriptomes of late-stage tumors to early-stage tumors from GSE76772 (79). We found that genes involved in endocrine resistance **(Fig 4.31 A)** and ErbB2 signaling **(Fig 4.31 B)** were significantly enriched in the late-stage tumors.

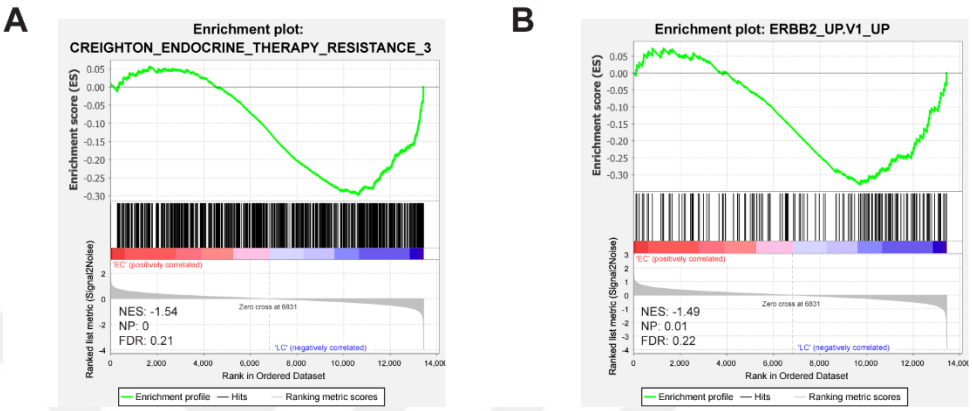


Figure 4.31. GSEA shows significant enrichment of gene sets involved in endocrine therapy resistance and ErbB2 signaling in late-stage tumors. Enrichment plots of early-stage and late-stage tumors from MMTV-PyMT mice from GSE76772.

Moreover, our Western blotting in tumors representing different steps of human breast cancer pathogenesis demonstrated decreased ER but increased HER2 and CDK8 expression at the later stages of tumor progression **(Fig 4.32).**

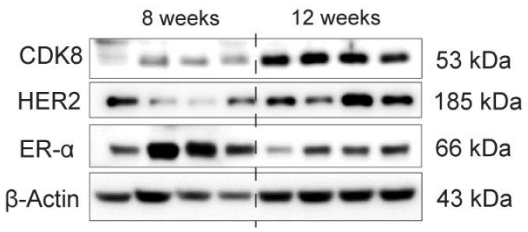


Figure 4.32. Enrichment of CDK8 and HER2, but loss of ER expression at later stages of tumor progression in MMTV-PyMT mouse model. Western blot results showing protein levels of CDK8, ER and HER2 towards tumor progression in

MMTV-PyMT mouse tumors. Mice were sacrificed and tumors were harvested on indicated time periods. β-Actin was used as a loading control.

Finally, in order to test the effect of CDK8 inhibition in this model, tumor pieces around 2-3 mm from 12 weeks old MMTV-PyMT mouse were transplanted into MFPs of FVB/N mice. The same treatment regimen used in xenograft experiments was administered and mice were treated with SNX631 and tamoxifen in single or in combination. Tumor growth was significantly delayed in the combination treatment group **(Fig 4.33 A)** without major toxicity **(Fig 4.33 B)**. Remarkably, these mice had higher life-span compared to other groups **(Fig 4.33 C).**

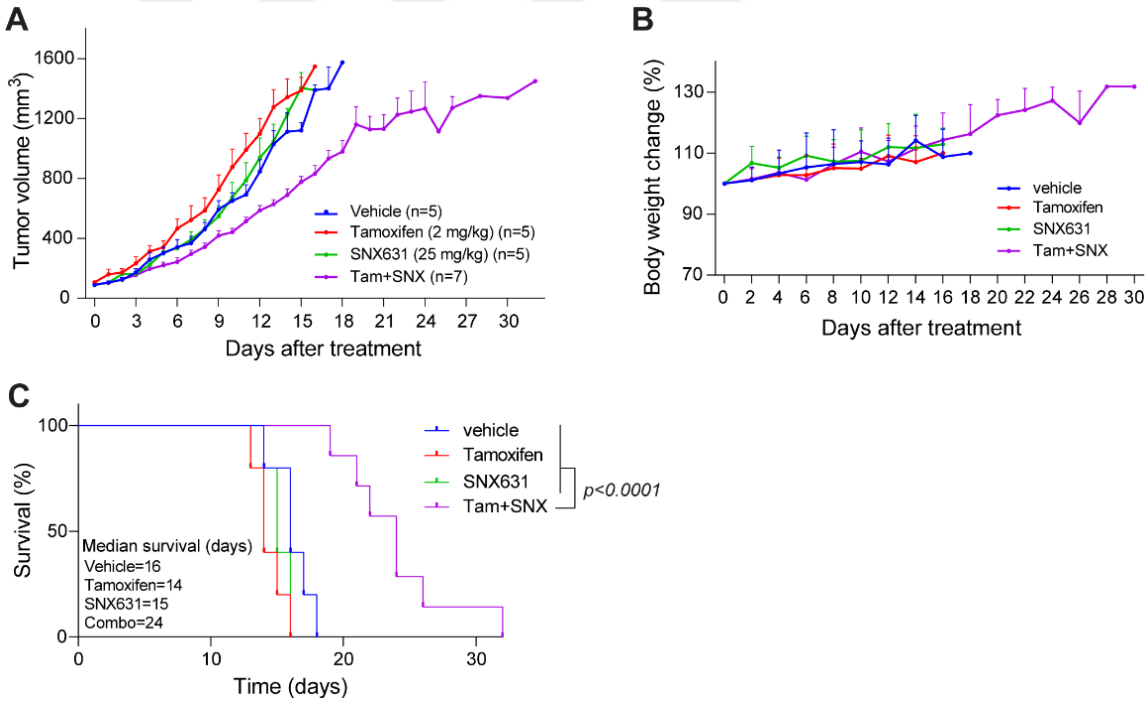


Figure 4.33. Targeting CDK8 overcomes tamoxifen resistance in an aggressive transgenic mouse model (A) Tumor volume change of SNX631 and tamoxifen-treated FVB transplants. Drugs were administered once tumors reached to around 100 mm3. n indicates mice number. (B) Percentage change in the body weight of treated

mice. (C) Kaplan-Meier survival curves of FVB transplants treated with vehicle (median survival=16), tamoxifen (median survival=14), SNX631 (median survival=15) or in combination (median survival=24). *P* value was calculated using the log rank test.

PART II

4.8. Selected projects/collaboration studies

I will dedicate the second part of my dissertation to the additional projects and collaboration studies, of which I was a part of and performed various experiments. I will use the following approach:

i.) I will summarize the context and important findings of the study to facilitate the reading and understanding

ii.) I will present study plan/methodology and/or schematic summary of the findings

iii.) I will explain the experiments that I carried out and generated the data

1. In our study entitled "Reactivation of cAMP Pathway by PDE4D Inhibition Represents a Novel Druggable Axis for Overcoming Tamoxifen Resistance in ER-positive Breast Cancer", Mishra et al., deciphered the molecular mechanisms of tamoxifen resistance by combining whole-transcriptome sequencing, pathway enrichment, patient survival analyses, *in vitro* and *in vivo* experiments. Consequently, PDE4D has been identified as a novel druggable candidate for overcoming resistance to tamoxifen **(Figure 4.34).** Mechanistically, PDE4D inhibition *via* specific siRNAs

or pharmacologic inhibitor (Gebr-7b) resulted in an increase in cAMP levels, induction of endoplasmic reticulum (EnR) stress and increased JNK/p38 phosphorylation followed by apoptosis, eventually overcoming resistance **(Figure 4.35).**

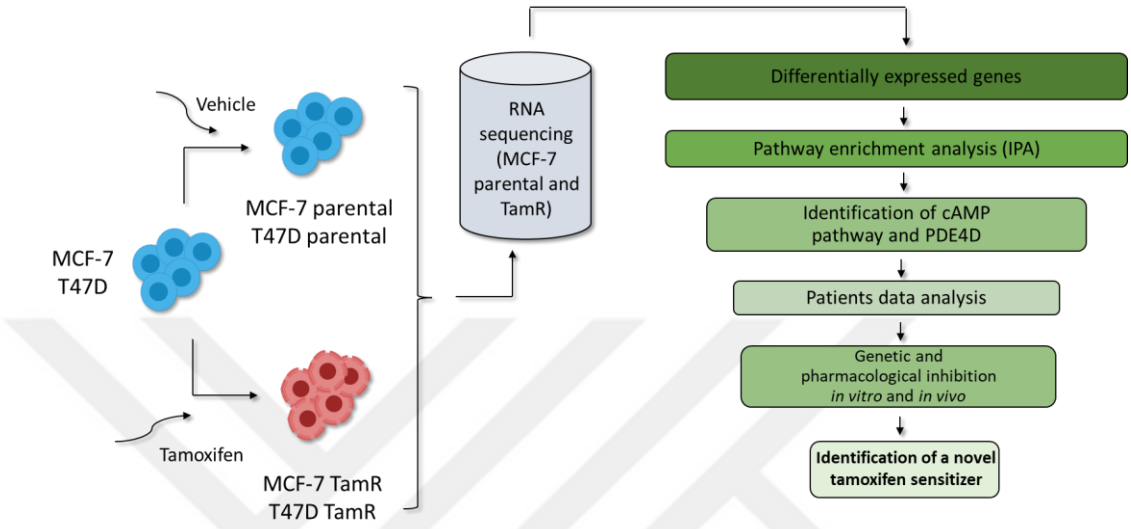


Figure 4.34. Schematic representation of the study plan and methodology. RNA-sequencing analysis of MCF-7 parental and MCF-7 tamoxifen resistant (MCF-7 TamR) cells followed by pathway enrichment, *in vitro*, and *in vivo* assays and analyses of patient data identify cAMP pathway and its component PDE4D as novel regulator of tamoxifen resistance. Modified from (86). See Appendix for the copyright permission.

The PDE4 family is the largest PDE family transcribed by 4 genes (*PDE4A*, *PDE4B*, *PDE4C*, and *PDE4D*) and at least 25 PDE4 proteins are encoded by various alternative mRNA splicing (103). PDE4 is an attractive pharmaceutical target due to its significant involvement in the regulation of the neural, cardiovascular, immune, and inflammatory systems (104-107). Several PDE4 inhibitors are used clinically for the treatment of asthma, chronic obstructive pulmonary disease (COPD), rheumatoid arthritis, and multiple sclerosis (108-110). Gebr-7b is the most active and selective

PDE4D inhibitor and shows more isoform-specific activity compared to FDA-approved general PDE inhibitor, rolipram (111).

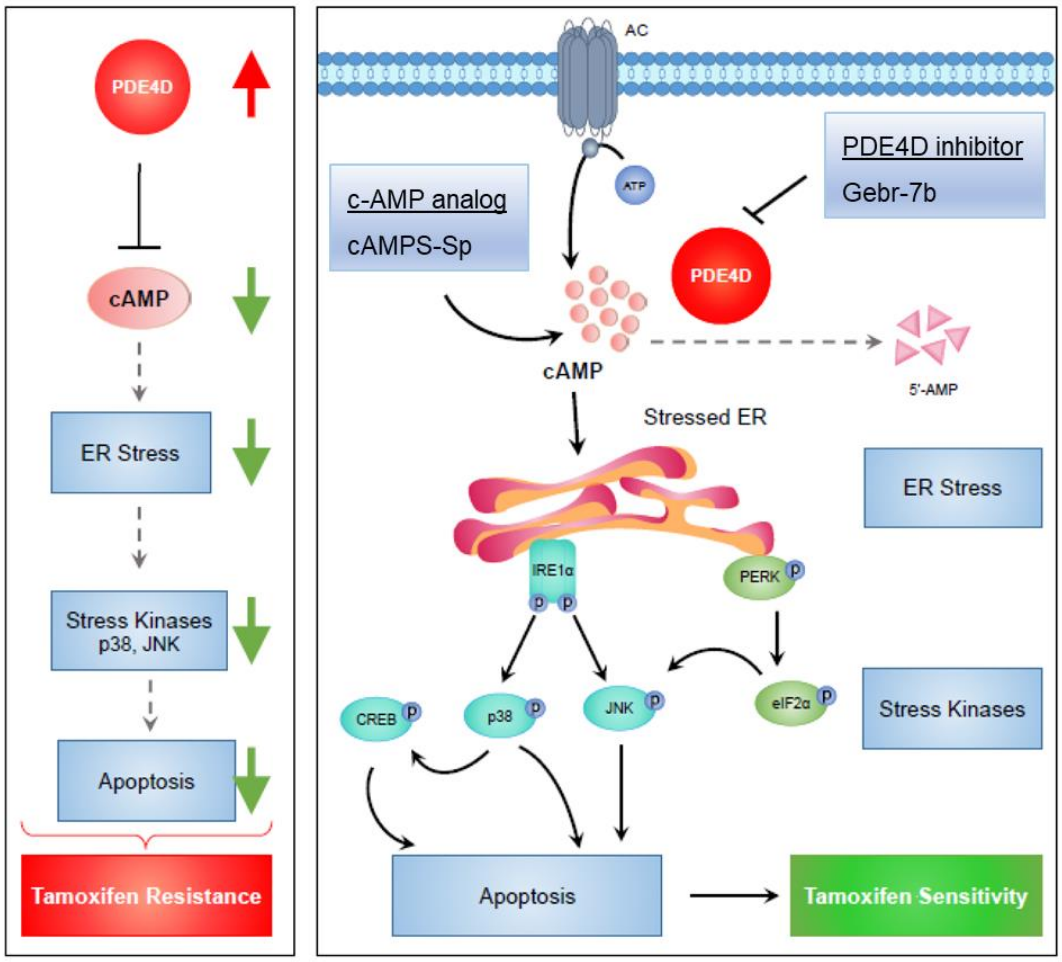


Figure 4.35. Schematic summary of the findings. ***Left,*** Elevated PDE4D levels in TamR cells leads to a decreased cAMP level, subsequently giving rise to a decrease in EnR stress, activation of stress kinases and apoptosis conferring tamoxifen resistance. ***Right,*** Inhibition of PDE4D (with Gebr-7b) or inducing cAMP directly (with cAMPS-Sp) together with tamoxifen leads to elevated cAMP levels, induction of EnR stress and increased JNK/p38 phosphorylation leading to activation and phosphorylation of CREB followed by apoptosis and tamoxifen sensitization. Modified from (86). See Appendix for the copyright permission.

To test whether targeting PDE4D overcomes tamoxifen resistance *in vivo*, I performed *in vivo* experiment where I tested the effects of Gebr-7b on tumor growth. I first generated MCF-7 TamR xenografts and conducted a treatment regimen with tamoxifen or Gebr-7b or in combination. Combination therapy inhibited the growth of the MCF-7 TamR tumors in nude mice compared to the vehicle or single-agent treatments **(Figure 4.36 A and B)**. Tumor weights in the combination-treated group were lower than the control and single treatment groups **(Figure 4.36 C).** The expression level of Ki67, a marker of cell proliferation, was markedly reduced in combination treatment. Moreover, the visualization of tumors with fluorescence-based TUNEL (**T**erminal deoxynucleotidyl transferase d**U**TP **n**ick **e**nd **l**abeling) assay resulted in increased apoptosis upon combined therapy **(Figure 4.36 D)**.

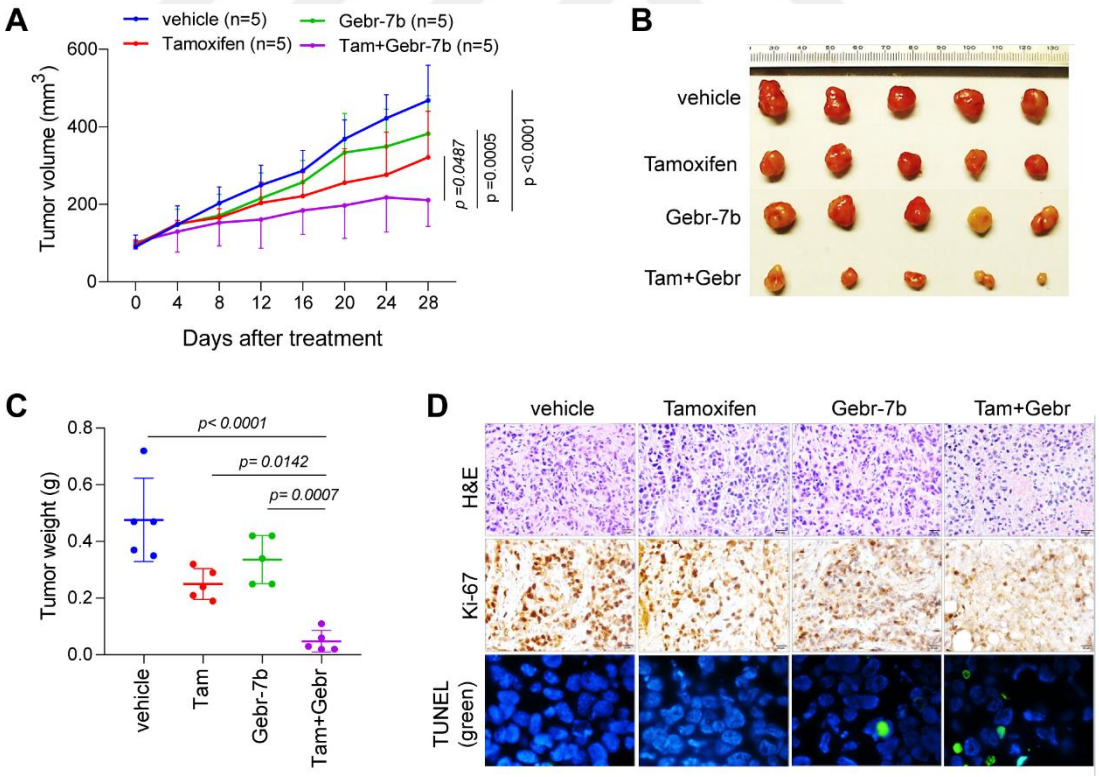


Figure 4.36. PDE4D inhibition overcomes tamoxifen resistance *in vivo*. (A) Tumor volume changes of MCF-7 TamR xenografts for 28 days after treatment with

tamoxifen and Gebr-7b individually or in combination. Drugs were administered once tumors reached to around 100 mm3. n indicates mice number. (B) Tumor pictures from A. (C) Tumor weights of the treatment groups. (D) H&E, Ki-67, and fluorescence-based TUNEL stainings of the tumors. Pictures of H&E and Ki-67 stainings were taken at 40X while TUNEL was taken at 100X magnification.

2. In our study entitled "Targeting HIF1/miR-326/ITGA5 axis potentiates chemotherapy response in triple negative breast cancer" (submitted to a journal), the first miRNA-mRNA network of chemoresistance in TNBCs has been constructed by combining mRNA- and miRNA-sequencing from an *in vivo* doxorubicin resistance model, network simulations and patient data analyses. This systematical approach identified Fibronectin (FN1) as the central hub of the chemoresistance network **(Figure 4.37)**. FN1-driven chemoresistance is mediated *via* enhanced cell surface receptor Integrin Subunit Alpha 5 (ITGA5). The activity of integrin signaling was controlled by hypoxia-regulated miR-326, whose overexpression reverses chemoresistance by transcriptionally suppressing ITGA5 and deactivating FAK/Src downstream signaling **(Figure 4.38).**

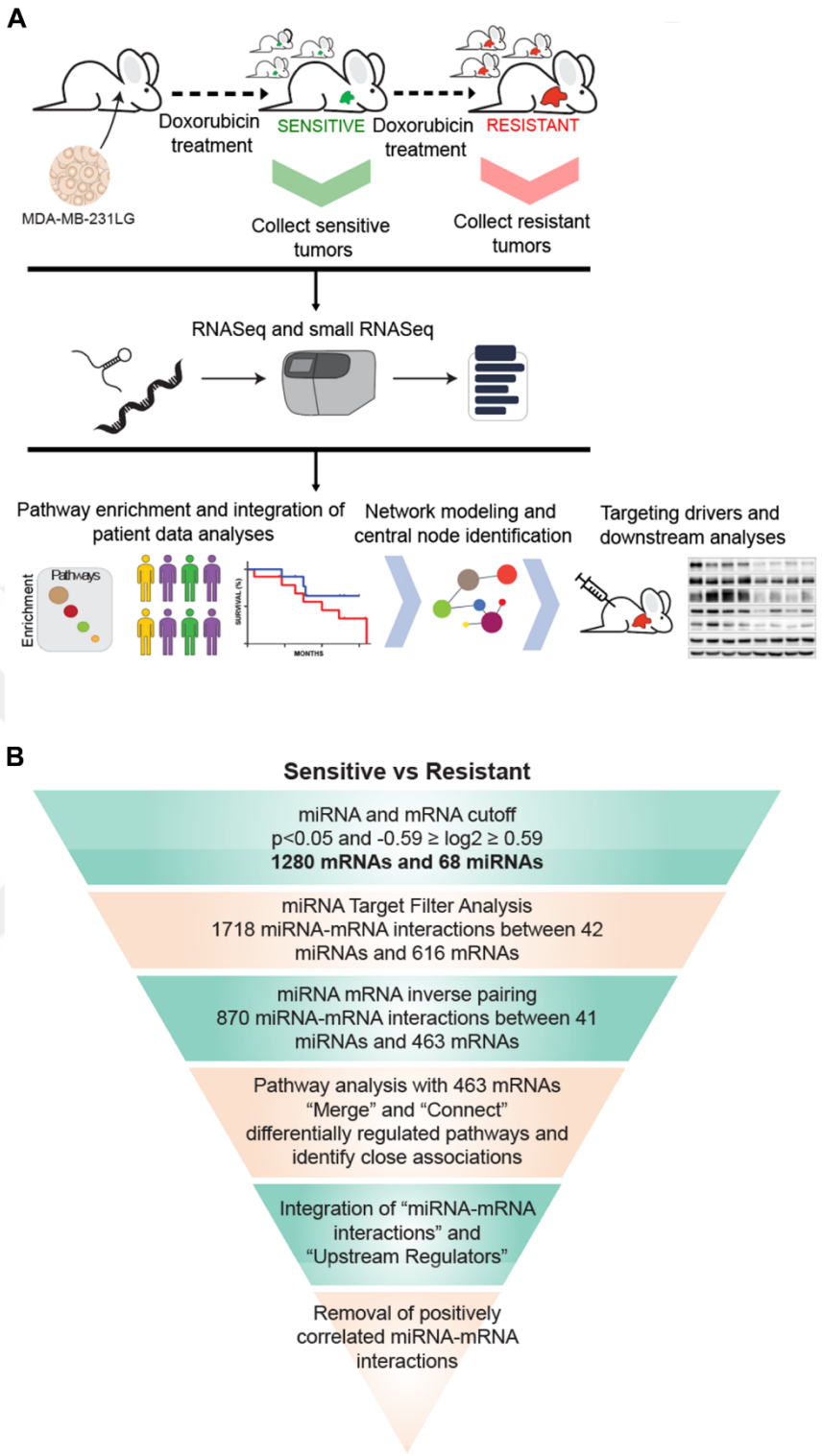


Figure 4.37. Constructing miRNA-mRNA interaction network of TNBC chemoresistance. (A) Schematic representation of the study plan and methodology. (B) Workflow describing the step-by-step selection process of the candidate miRNAs and mRNAs *via* IPA to generate doxorubicin resistance miRNA-mRNA interaction network.

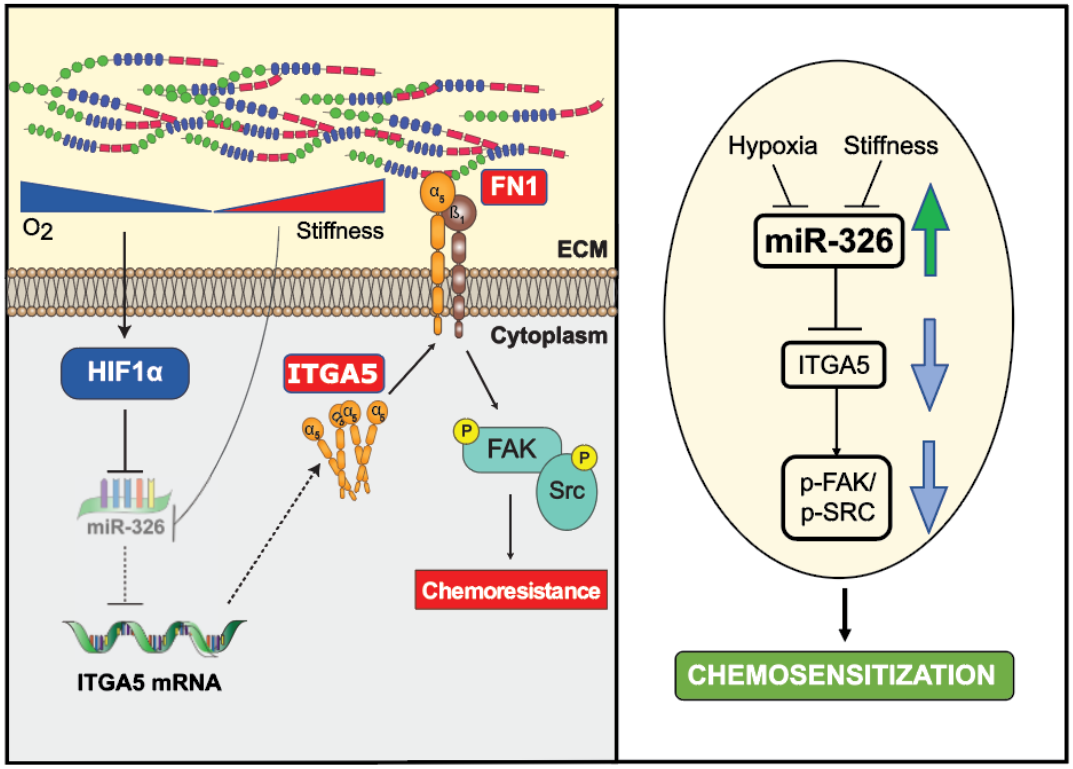


Figure 4.38. Schematic representation of the mechanistic summary

In order to test whether miR-326 could potentiate doxorubicin response *in vivo*, we first generated derivatives of the luciferase expressing MDA-MB-231-Luc2-GFP cells ("231.Luc2.GFP") that stably express doxycycline-inducible miR-326 ("231.miR-326"). Next, we orthotopically injected the control and inducible miR-326 expressing cells into mammary fat pads (MFPs) of nude mice. A combination treatment of doxorubicin upon induction of miR-326 expression led to a prominent decrease in tumor burden as compared to single agent treated groups **(Figure 4.39 A)**, which is further confirmed by IVIS imaging **(Figure 4.39 B** and **C)**. Moreover, tumors obtained from the combination group were considerably smaller than single agent treated groups **(Figure 4.39 D** and **E)**.

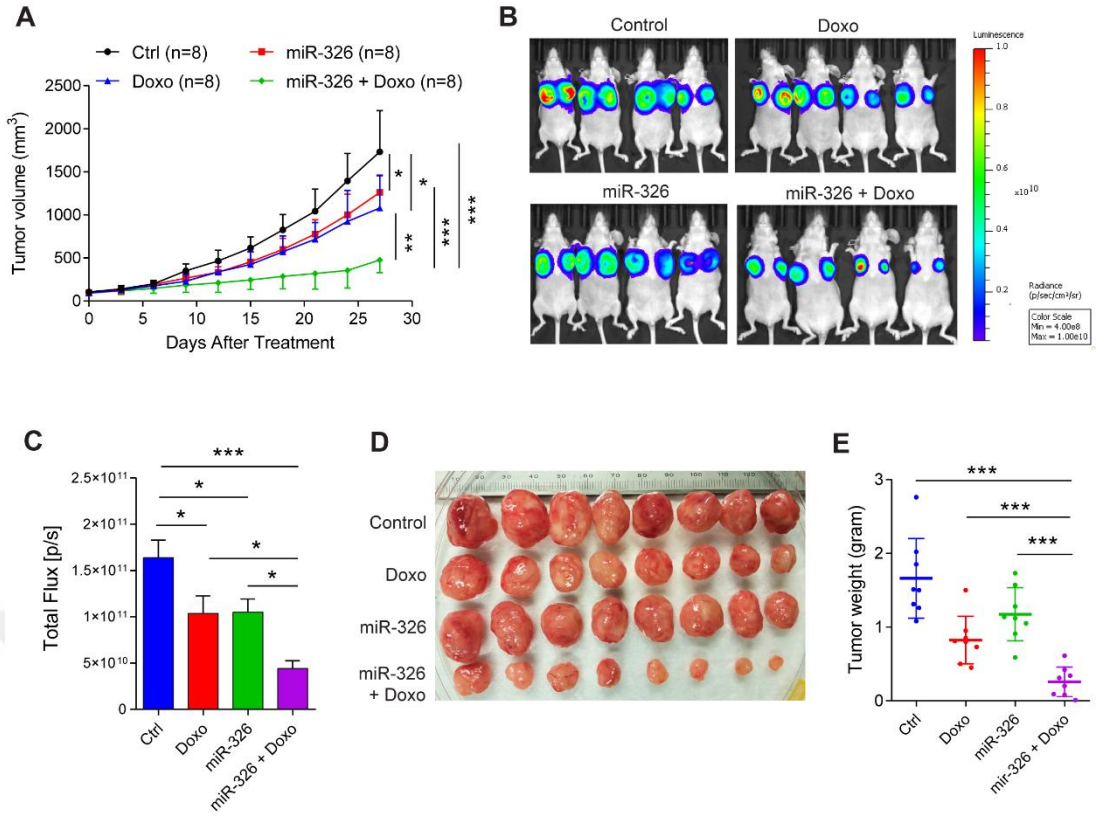


Figure 4.39. miR-326 potentiates doxorubicin response *in vivo*. (A) Tumor volume changes in MDA-MB-231 xenografts upon vehicle treatment or miR-326 induction in the presence or absence of doxorubicin treatment. Both doxorubicin treatment and miR-326 induction were initiated once tumors reached to 100 mm^3. n indicates tumor number. (B) IVIS images of mice (n=4) from A, visualized on the last day of the experiment. (C) Quantifications of luciferase signals detected from tumors from B. (D) Images showing isolated tumors from A. (E) Tumor weights of the treatment groups shown in A. *$p < 0.05$; **$p < 0.01$; ***$p < 0.001$. Statistical significance was evaluated by unpaired t-test.

Next, we examined the combinatorial effect of ITGA5 knockdown and doxorubicin treatment by developing primary tumor xenografts of the 231.shITGA5 cells. Combined therapy induced a significant delay in tumor growth compared to control or single-agent treatments **(Figure 4.40 A)**. Bioluminescence signal obtained from combination treatment group was also significantly lower than other groups **(Figure**

4.40 B and C). Moreover, tumor weights were also lower in the combination group as compared to single agent-treated groups **(Figure 4.40 E)**.

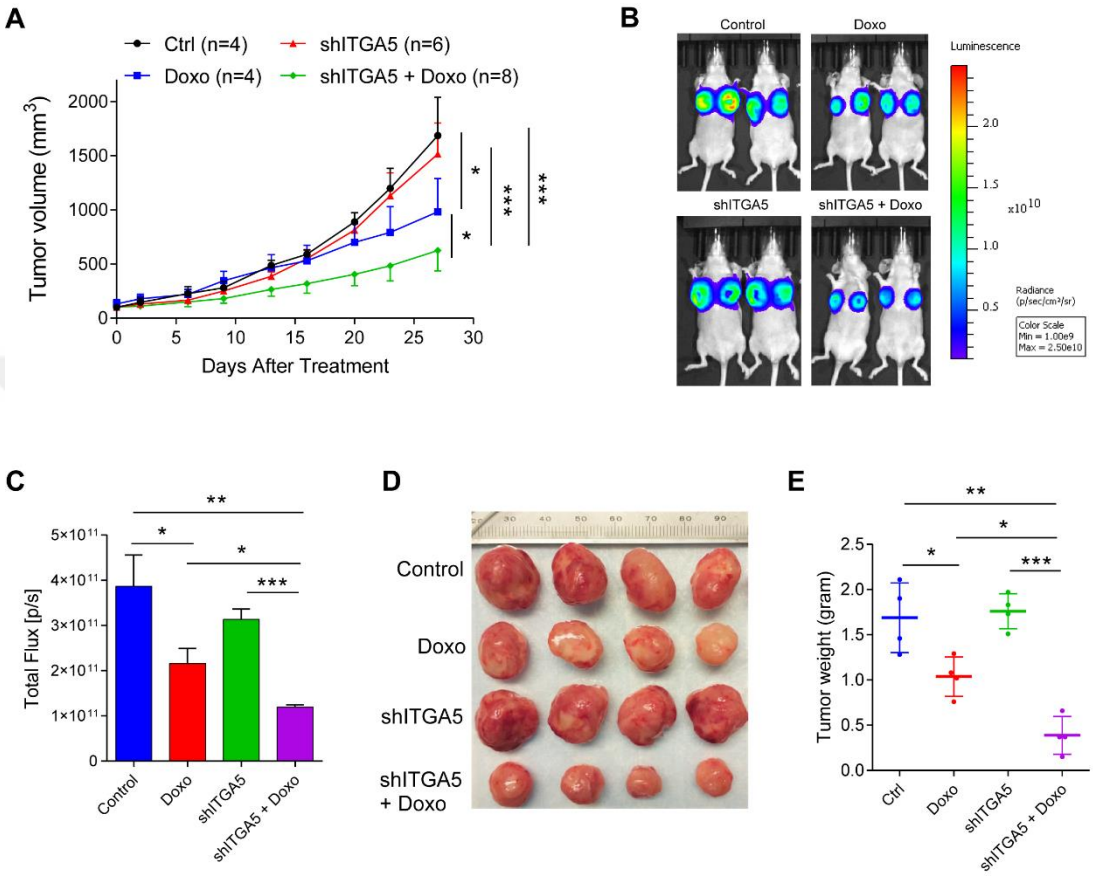


Figure 4.40. Inhibiting ITGA5 potentiates chemo-response *in vivo*. (A) Tumor volume changes in MDA-MB-231 xenografts upon vehicle treatment or shITGA5 induction in the presence or absence of doxorubicin treatment. Both doxorubicin treatment and shITGA5 induction were initiated once tumors reached to 100 mm^3. n indicates tumor number. (B) IVIS images of mice from A, taken on the last day of the experiment. (C) Quantifications of luciferase signal in tumors from B. (D) Images showing isolated tumors from A. (E) Tumor weights of the treatment groups shown in A. * $p < 0.05$; ** $p < 0.01$; *** $p < 0.001$. Statistical significance was evaluated by unpaired t-test.

3. In our collaboration study entitled "Systems-level Analysis Reveals Multiple Modulators of Epithelial-mesenchymal Transition and Identifies DNAJB4 and CD81 as Novel Metastasis Inducers in Breast Cancer", Uretmen et al., utilized mass spectrometry based quantitative proteomics approach to systematically analyze the post-translational biochemical changes during epithelial-to-mesenchymal transition (EMT). The proteome level analysis and potential modeling of kinase-substrate groups discovered key signaling pathways such as Hippo, TGF-β and sphingolipid signaling. Consequently, they highlighted DnaJ heat shock protein family (Hsp40) member B4 (DNAJB4) and cluster of differentiation 81 (CD81) as novel metastasis inducers in breast cancer **(Figure 4.41).**

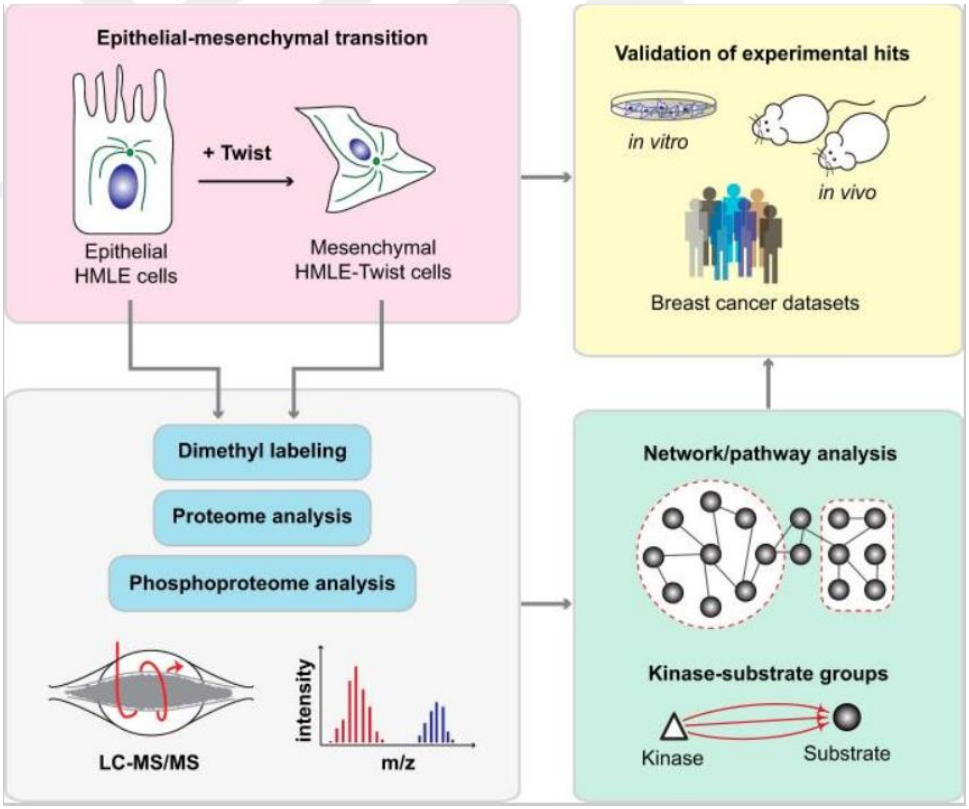


Figure 4.41. Graphical abstract summarizing the findings. Obtained from (112) See Appendix for the copyright permission.

In this study in order to check effects of DNAJB4 and CD81 on primary tumor growth, MDA-MB-231-Luc2-GFP cells were first engineered to stably express shRNA targeting DNAJB4 and CD81 (referred as shDNAJB4 and shCD81). Knockdown of CD81 and DNAJB4 possessed a strong inhibitory effect on the tumor growth **(Figure 4.42 A-C)**. To test whether targeting CD81 and DNAJB4 prevents spontaneous metastasis, tumor growth has been measured until tumors in each group reached to 1000 mm^3. At this point primary tumors were removed surgically and mice were monitored for one month. At the end of the period, mice were sacrificed and lungs and livers were collected to quantify luciferase density. Ex vivo luciferase assay showed that knockdown of CD81 and DNAJB4 significantly blocked both lung and liver metastases **(Figure 4.42 D)**.

Next, to check whether DNAJB4 and CD81 play a role in extravasation/colonization, tail-vein experimental metastasis assay was performed by using MDA-MB-231-Luc2-GFP shCtrl, shDNAJB4 and shCD81 cells. Following the 6 weeks of intravenous injection of DNAJB4 and CD81 depleted cells into nude mice, lung metastases between groups were compared by checking luciferase signal from lungs. Mice injected with either CD81 or DNAJB4 knockdown cells showed a low level of lung metastasis compared with control **(Figure 4.42 E)**. Similarly, knockdown groups have less nodules in lungs in compared with control mice as indicated with Bouin's solution fixation **(Figure 4.42 F)**. Moreover, hematoxylin and eosin (H&E) staining confirmed the reduction of metastatic cells on lung surface of both DNAJB4 and CD81 knockdown groups **(Figure 4.42 G)**.

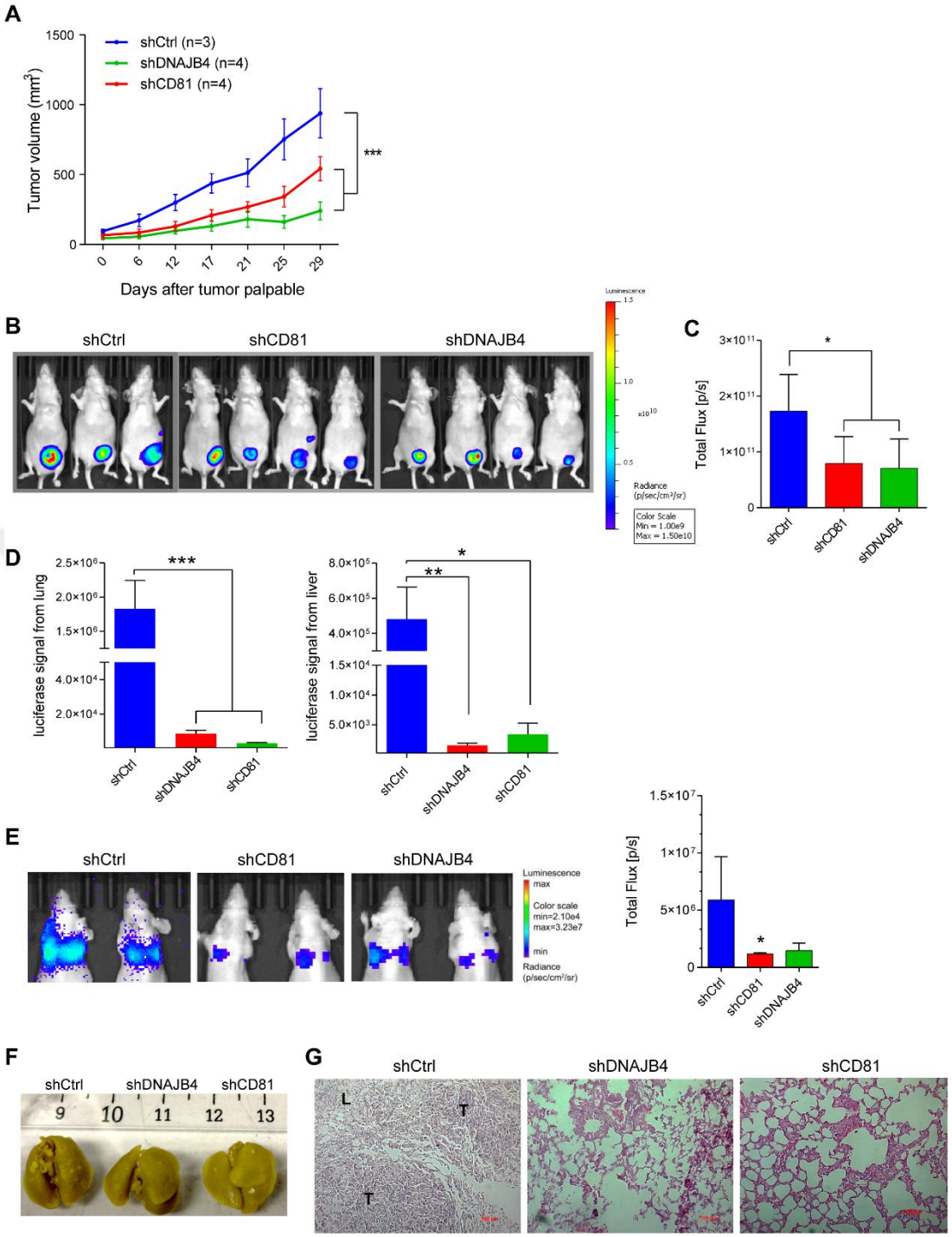


Figure 4.42. Inhibition of CD81 and DNAJB4 reduced primary tumor growth, blocks spontaneous metastasis and extravasation/colonization. (A) Tumor volume changes in xenografts generated using MDA-MB-231 shCtrl, shCD81 and shDNAJB4 cells. n represents mice number. (B) Bioluminescence images of nude mice from A. (C) Quantifications of luciferase signals detected in tumors from B. (D) Luciferase signal coming from lungs and livers of mice in B as quantified by ex vivo luciferase assay (E) Representative bioluminescence images of nude mice intravenously injected

with MDA-MB-231-Luc2-GFP shControl, shDNAJB4 and shCD81 cells obtained by IVIS. Bioluminescence signal was quantified as total flux on the right. (F) Representative images of lungs collected from the groups given in Figure A. Mice were sacrificed at week 6 and lungs were fixed in Bouin's Solution. (G) Representative images of lungs stained with hematoxylin and eosin. T stands for tumor, L stands for lung.

I have contributed to several other articles from our lab or through our collaboration projects, where I have been as a co-author. These articles are provided in the Appendix section of this dissertation.

CHAPTER 5

DISCUSSION

PART I

Tamoxifen is a blockbuster drug and prescribed for the treatment of all stages of ER-positive breast cancer. Adjuvant treatment of tamoxifen not only decreases the risk of breast cancer recurrence but also reduces the breast cancer mortality rate in the first 15 years after therapy. However, its clinical benefit is impeded by intrinsic and acquired resistance, constituting a major obstacle for clinical management. Therefore, there is an urgent need for novel targeted therapies to confer tamoxifen resistance.

5.1. MED13 and CDK8 in tamoxifen resistance

The Mediator kinase, CDK8, is an evolutionarily conserved serine/threonine kinase and represents a major ingress of signal transduction (113). However, CDK8 does not function independently. Once CDK8 interacts with its regulatory partner cyclin C, it becomes active. Moreover, CDK8 is essential for the maturation of embryos at the preimplantation stage but does not cause any abnormalities in adult mice (69). It has also been reported that CDK8 knockdown does not affect cell viability (114).

Although CDK8 deletion or downregulation has been observed in esophageal squamous cell carcinoma (115) and bladder cancers (116), CDK8 widely exerts oncogenic properties in a broad spectrum of cancers including colorectal cancer (117, 118), gastric cancer (119), breast (73) and melanoma (120). Additionally, CDK8 facilitates several important cellular signaling pathways including NOTCH signaling (121), WNT/β-catenin signaling (122), and BMP/TGF-β pathway (123).

The reversible interaction between the four-subunit kinase module and the core modules occurs through the MED13 interface (124). MED13 accounts for numerous developmental processes such as inhibition of mitochondrial fission and programmed cell death (125). Besides, mutations in *MED13* gene result in neurodevelopmental disorders (65) and abnormal heart development (126). Not surprisingly, MED13 also, like CDK8, has been implicated in cancer. It has been shown that depletion of MED13 together with MED13L in colon cancer suppresses the expression of cancer-acquired super-enhancer genes such as *MYC* (127).

Although both MED13 and CDK8 have been shown as indispensable player in the modulation of key oncogenic pathways, there was no functional study elucidating their potential in tamoxifen resistance. To best of our knowledge, for the first time, we demonstrated tamoxifen sensitizer roles of both MED13 and CDK8 in ER-positive breast cancer. Our patient data analyses revealed that both *MED13* and *CDK8* were upregulated in ER-positive patients non-responsive to tamoxifen and patients with relapse following tamoxifen treatment. Here, the former group can be considered *de novo* resistant as non-responsive patients exhibit either stable or progressive disease, and the latter group can be denoted as acquired resistance. Notably, patients with high *MED13* or *CDK8* expression, but not *MED12* or *CCNC*, experience worse relapse-free survival. These data imply that two genes are potentially involved in both types of tamoxifen resistance. To verify that these genes did not merely increase as an accompanying event but were driving factors and have a better representation of patient heterogeneity, we utilized two established tamoxifen-resistant cell line models. In these models, MED13 and CDK8 were markedly and consistently increased

compared with their parental counterparts unlike other subunits of the CKM, confirming their clinical relevance.

Moreover, we found that the knockdown of *MED13* and pharmacologic inhibition of CDK8 with a specific inhibitor, SNX631, significantly sensitized the cells to tamoxifen. Several inhibitor molecules targeting CDK8/19 kinase activity have been designed including Cortistatin A (128), Senexin A (129), Senexin B (a more potent derivative of Senexin A) (130), CCT251921 (Cmpd3) (131), MSC2530818 (Cmpd4) (132), 15w (133), and BRD6989 (134). Despite the encouraging results achieved by oncological applications, some CDK8/19 inhibitors pose several novel challenges prior to preclinical and clinical trials. Chen and colleagues (135) established a panel of CDK8/19 inhibitors with different chemical structures and compared these inhibitors using different strategies. Their KINOMEscan profiling (DiscoverX/Eurofins) identified several off-target kinases for both Cmpd3 and Cmpd4, which might give rise to adverse effects, while Senexin B (premature/less potent form of our inhibitor) did not reveal any off-target activity. Senexin B is the first selective CDK8/19 inhibitor to enter clinical trials (ClinicalTrials.gov Identifier: NCT03065010), and inhibited STAT1 phosphorylation [robust marker/substrate to assess CDK8 kinase activity (89)] in all tested tumor cell lines (135), supporting our findings. Moreover, we observed a synergistic outcome when we combined SNX631 with tamoxifen. Accordingly, combination treatment dramatically reduced clonogenic activity as shown by colony formation assay. Similar to Senexin B, SNX631 functions through regulation of CDK8 kinase activity and its effect can be deducted from phosphorylation level of STAT1. Although MED13 and CDK8 regulate several biological events in the same manner as they are part of the same Mediator module,

MED13 inhibition itself or its combination with tamoxifen did not cause any changes in p-STAT1 levels.

5.2. MED13/CDK8/HER2/mTOR axis: Biomarker of tamoxifen response

Overactivation of Akt/mTOR signaling pathway has been reported in various cancer types, including liver (136), colon (137, 138), and leukemia (139). Moreover, several preclinical studies suggested that aberrant activation of Akt/mTOR may be involved in resistance to hormone-targeted therapies. In this line, numerous approaches are attempting to increase the responses to therapy. A study in breast cancer demonstrated that targeting mTOR in cancer cells with high Akt activity restores tamoxifen response (140). Furthermore, in a previous study, CDK8 has been proposed to regulate mTOR pathway in leukemia (141). Given the functional contribution of CDK8 on mTOR signaling, here we examined whether this is also the case in breast cancer. Unlike their differential effect on p-STAT1 levels inhibition of both MED13 and CDK8 works in tandem for the deregulation of mTOR/HER2 signaling. Combining CDK8 inhibition with tamoxifen treatment decreased HER2 level and reduced phosphorylation of mTOR, S6 and 4EBP1, leading to apoptosis. Similarly, MED13 knockdown also inhibited HER2/mTOR signaling in tamoxifen-resistant cells and triggered apoptosis.

Post-transcriptional regulation is crucial for controlling gene expression at RNA level. 5′ capping, 3′ polyadenylation, RNA splicing, nuclear export of mRNAs, and mRNA stability are the major mechanisms contributing to post-transcriptional regulation (142), together with miRNAs and long noncoding RNAs (143). Regulation of mRNA stability is observed for the control of RNA levels in many disease related genes and represents rapid and local mechanism (144). Deregulation of ErbB2 occurs in a wide

range of cancer types and its upregulation is one of the well-established markers in tamoxifen resistance. Here, we demonstrated that combination of SNX631 and tamoxifen remarkably decreased the ErbB2 mRNA level at least in part by reducing the mRNA stability, suggesting a therapeutic approach for reversing the effects of ErbB2 in tamoxifen resistance.

Overall, both RNA and protein level studies in this dissertation have discovered the MED13/CDK8/HER2/mTOR signaling axis as a biomarker of tamoxifen resistance **(Figure 5.1)**.

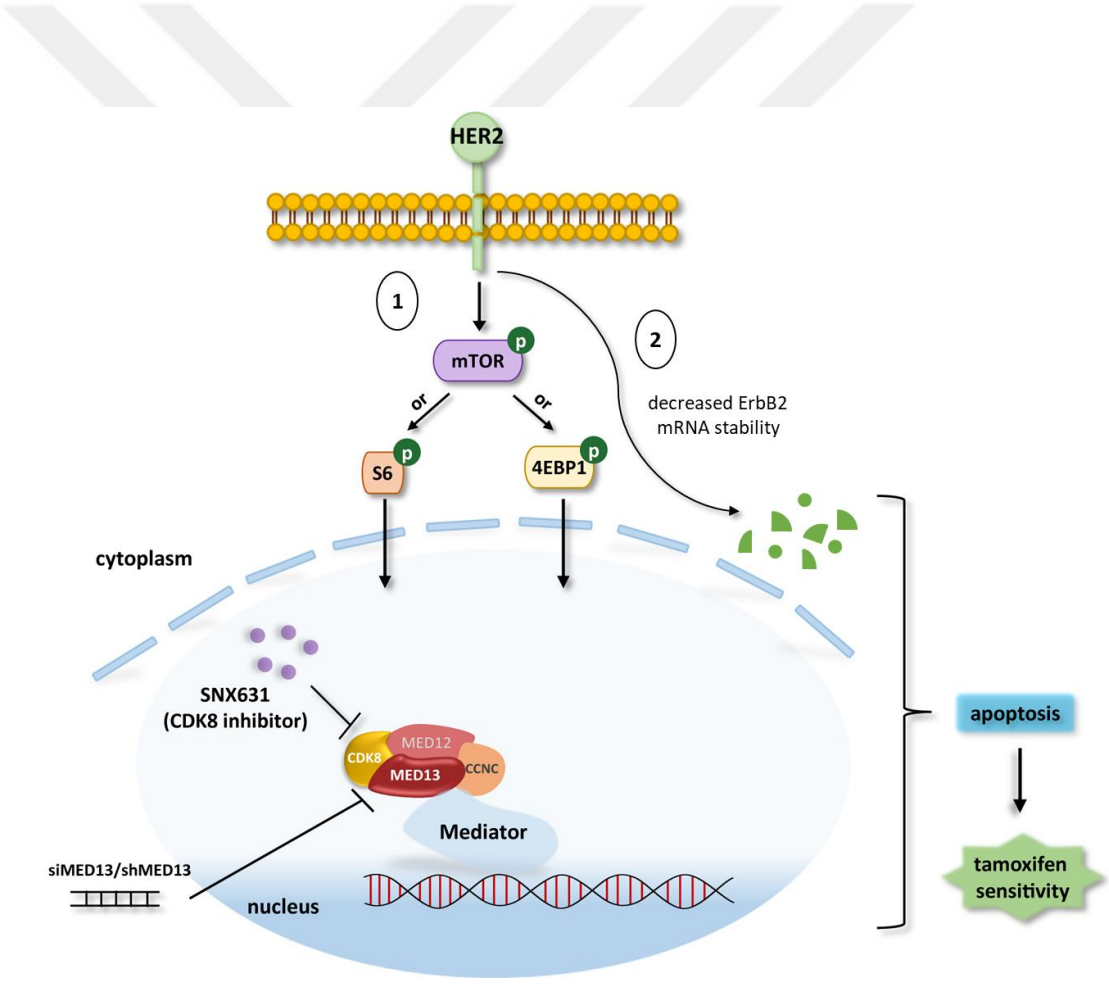


Figure 5.1. Schematic representation of MED13/CDK8/HER2/mTOR axis mediated tamoxifen resistance

5.3. A more potent CDK8 inhibitor, SNX631

Little is known about the structure of the MED13 subunit (124) and the domain annotation is also incomplete (65). As a result, there are no preclinical or clinical inhibitors available for MED13, hampering its translation to the clinic. However, crystal structures of the human CDK8-CCNC dimer have been obtained (124, 145). Besides, it is only natural to target ATP binding site in the active or inactive conformation with the most crucial parameter being kinase selectivity. Up to date, several CDK8/19 kinase inhibitors (as mentioned in 5.1) emerged and they showed *in vivo* therapeutic effects in different types of cancer disease. These inhibitors were tested for systemic toxicity to provide strong preclinical support for future clinical use. Notably, zebrafish assays performed in a panel of CDK8/19 inhibitors revealed severe toxicity of Cmpd4 after 72 hours of treatment while other inhibitors (dCA, Cmpd3, 15w and Senexin B) did not show any *in vivo* toxicity (135). It is also noteworthy that in our xenografts, SNX631 (potent form of Senexin B) perfectly tolerated alone or with tamoxifen as inferred from the body weight change graphs, implying minimal toxicity. Moreover, SNX631 treatment together with tamoxifen improved survival in MMTV-PyMT transgenic mouse model, without toxicity. Among murine cancer models, genetically engineered mouse models with their natural microenvironment context exhibit the most complete representation of cancer development (146). Besides, genetically engineered mouse models provide the preclinical platform to evaluate and optimize immunomodulatory therapies (147). All these findings suggests that our inhibitor has a translational potential to be used as a HER2/mTOR signaling inhibitor in clinical studies.

PART II

1. Phosphodiesterases (also named as cyclic phosphodiesterases, PDE) (at least 11 family and 25 genes) hydrolyze cyclic nucleotides such as cAMP and cGMP, and suppress the signaling of these important intracellular secondary messengers, thereby controlling myriad biological responses in health and disease (103, 148). The PDE4 family is the most divergent family among PDEs encoded by four genes (*PDE4A-D)*. PDE4D is the most studied subtype in a wide range of malignancies (149-152).

PDE4 is majorly expressed in brain, cardiovascular tissues and muscles (153). Overexpression of PDE4 facilitates the progression of neurological disorders such as Alzheimer's disease, schizophrenia, and depression (154). Furthermore, dysregulation of cAMP/CREB signaling is associated with disruption of neuroplasticity (organization of neural cells) (155). Thus, PDE4 inhibition is considered to be an ideal strategy for recovering deficits in neuroplasticity (156, 157). Over the 20 years, several oral and topical compounds targeting PDE4 are marketed for clinical proof-of-concept studies in cancer. Apremilast, rolipram, and roflumilast are known first generation PDE4 inhibitors displaying prominent therapeutic effect in pre-clinical trials (158-160). For example, roflumilast has been tested in patients with advanced B-Cell hematologic malignancies for its pharmacodynamic properties under clinical Phase 0/1 trial (NCT01888952) (161). Additionally, rolipram potentiates the antitumor efficacy of bevacizumab -VEGF inhibitor- in glioblastoma by blocking ERK/AKT signaling (162).

Despite worthwhile therapeutic option of PDE4 inhibitors, they have a narrow therapeutic window and importantly, their poor gastrointestinal tolerability due to emesis, nausea, dyspepsia, abdominal pain and diarrhea is major obstacle pertaining

to clinical applications (163). Non-selective competitive PDE4 inhibitors might give rise to adverse effects. Alternatively, it has been suggested that designing PDE4 inhibitors based on subtype selectivity may result in better tolerability (164). Gebr-7b is a newly developed cell-permeable and the most specific PDE4D inhibitor and experiments performed on different species have been shown that Gebr-7b is 100-3,000 times less emetic than other PDE4D inhibitors (165). In our hands, both *in vitro* and *in vivo* settings, Gebr-7b did not cause any toxicity at the optimal doses. Based on observations by naked eye on the structure of organs, Gebr-7b is well tolerated in xenografts. Besides, we observed regular movement without any hypo/hyperactivity and usual nutritional habit in animals, showing favorable effects of Gebr-7b on neurological parameters. Importantly, administration of Gebr-7b with tamoxifen decreased the tumor burden significantly in nude mice.

2. MicroRNAs are indispensable for animal development, differentiation and homeostasis, and are also involved in cancer initiation, progression and drug resistance as tumor suppressors or oncogenes (166, 167). Accordingly, miR-326 has been reported to function as a tumor suppressor in different cancer types including breast cancer, cervical cancer, lung cancer, and glioblastoma (168-171). Moreover, miR-326 has been shown to regulate multidrug resistance-associated protein (MDR) and its elevated levels sensitized ER-positive breast cancer cells to doxorubicin and VP-16 (172).

To date, therapeutic miRNAs or delivery system for miRNA-based drugs become attractive and reported as biopharmaceuticals resources in the clinics. Here, we deciphered tumor suppressor role of miR-326 in chemotherapy response. Moreover, ectopic expression of miR-326 decreases ITGA5 expression and impairs downstream

signaling, thus resulting in chemotherapy sensitization. Importantly, either overexpression of miR-326 or inhibition of ITGA5 resulted in tumor growth inhibition. Overall, these findings provide a pre-clinical support for the potential use of miR-326 or inhibitors against miR-326 targets, namely ITGA5, to overcome chemotherapy resistance in TNBC.

3. In our collaboration study, quantitative proteomic and phospho-proteomic analysis identified two important regulators of EMT, DNAJB4 and CD81. DNAJB4 has controversial role in cancer progression. Here, it has been described as a metastasis inducer in breast cancer cells whereas several studies have been shown its tumor-suppressor roles (173). Moreover, CD81 has been reported as mesenchymal marker (174) and surprisingly, its mRNA level does not markedly alter during EMT (175). However, Western blot results performed in this study showed increased CD81 protein expression in mesenchymal state.

Our *in vivo* studies demonstrated that knockdown of DNAJB4 in MDA-MB-231 cells showed growth-inhibitory effect on primary tumors, and impairs lung metastasis of invasive breast cancer cells. Similarly, inhibition of CD81 decreased the primary tumor growth rate of MDA-MB-231 xenografts and diminished the metastasis. These data confirmed that depletion of DNAJB4 and CD81 not only shrink primary tumors but also prevent metastasis of disseminated tumor cells.

CHAPTER 6

CONCLUSIONS AND FUTURE PERSPECTIVES

MED13/CDK8/HER2/mTOR axis confers tamoxifen resistance in ER-positive breast cancer

In this dissertation, I have characterized MED13/CDK8/HER2/mTOR signaling axis facilitating tamoxifen resistance. The systematical analyses of the kinase module in ER-positive tamoxifen-treated patients identified MED13 and CDK8 as novel tamoxifen sensitizers. Inhibiting either MED13 *via* genetic modulation or CDK8 by highly selective inhibitor, SNX631, significantly reversed tamoxifen resistance and induced apoptosis. Moreover, I have demonstrated that the activity of HER2/mTOR signaling was modulated by MED13 and CDK8. Finally, using xenograft models targeting either MED13 or CDK8 led to a significant decrease in tumor growth and combinatorial application of tamoxifen and SNX631 improved survival in transgenic mouse model.

Upregulation of ErbB2 contributes to tamoxifen resistance, however; several mechanistical studies revealed key genes acting as transcriptional repressor of *ERBB2* gene, thereby determining tamoxifen efficacy (176). In our resistant cell line models, tamoxifen treatment together with either MED13 knockdown or CDK8 inhibition repressed ErbB2 mRNA levels. Although we showed that combined treatment of tamoxifen and SNX631 reduces ErbB2 levels at post-transcriptional level *via* increased mRNA decay, much work has to be done to investigate if it is regulated

at transcription level. For this purpose, chromatin immunoprecipitation (ChIP) assay can be utilized.

CDK8 is an oncogene and its higher expression correlates with poor prognosis of several cancer types including colon, breast, and ovarian (122, 129, 177). Importantly, CDK8 functions as transcriptional re-programmer and increases the activity of several tumor-promoting transcriptional pathways such as HIF1A, β-catenin, and TGFβ (80, 117). Here, we reported that CDK8 is highly overexpressed in tamoxifen resistance. Upregulation of CDK8 or its activator effect on many oncogenic pathways encouraged us to test outcomes of CDK8 inhibition in tamoxifen resistance. However, it could be interesting to check whether overexpression of CDK8 could further drives tamoxifen resistance and increases cell proliferation.

Even though SNX631 was sufficient to hinder STAT1 phosphorylation *in vitro*, the same effect was only obvious *in vivo* when SNX631 and tamoxifen were combined. This discrepancy could be due to the availability of other kinases in the tumor microenvironment or factors promoting the expression of these kinases in tumor, which in turn phosphorylates STAT1. For example, p38 kinase was shown to phosphorylate STAT1 *via in vitro* kinase assays (178) and was frequently expressed in stromal cells surrounding tumor (179). Similarly, ERK1/2 is able to act on STAT1 (178) and is highly expressed in cancer-associated stellate cells (180). Tumor microenvironment (TME) is a dynamic tissue structure and several kinases modulate dysregulation of TME components. Kinase inhibition in TME and/or cancer cells by src kinase inhibitors or tyrosine kinase inhibitors provides benefit to cancer patients (181, 182). Adding SNX631 regimen to kinase targeted therapies might increase response to treatment when targeting STAT1 is struggling.

CDK8 inhibition has been known to promote the differentiation of Treg cells and the expression of Treg signature genes, such as *CTLA4*, *Foxp3*, *PD-1*, and *GITR* (183). In another study, targeting CDK8 enhanced the NK-cell responses against tumor cells (184). Having the *in vivo* results in an immunocompetent transgenic mouse model, investigation of possible immunological responses upon CDK8 inhibition might be useful and can provide more insights into breast cancer immunotherapy. Moreover, xenograft studies in this dissertation performed using ER-positive cell lines do not reflect the tumor heterogeneity in the clinics. Therefore, a combination treatment in patient derived xenograft (PDX) models from ER positive patients with different molecular, genetic, histopathological background could provide preclinical data and offer new insights for personalized medicine.

To sum up, targeting CDK8 represents an attractive therapeutic strategy. Our animal studies using xenografts derived from tamoxifen-resistant cell lines and aggressive transgenic mouse models culminated in a remarkable reduction in tumor growth upon CDK8 inhibition plus tamoxifen, consecutively reflected by deterioration of the HER2/mTOR signaling. Adding SNX631 to endocrine therapy regimens rather than using alone could be a better strategy to address treatment-related hurdles. Fortunately, though, it may offer hope not only for tamoxifen-resistant breast cancer but also any disease driven by HER2 overexpression and/or HER2/mTOR pathway activation.

BIBLIOGRAPHY

1. Sung H, Ferlay J, Siegel RL, Laversanne M, Soerjomataram I, Jemal A, et al. Global Cancer Statistics 2020: GLOBOCAN Estimates of Incidence and Mortality Worldwide for 36 Cancers in 185 Countries. CA Cancer J Clin. 2021;71(3):209-49.

2. Siegel RL, Miller KD, Fuchs HE, Jemal A. Cancer Statistics, 2021. CA Cancer J Clin. 2021;71(1):7-33.

3. Hammond ME, Hayes DF, Dowsett M, Allred DC, Hagerty KL, Badve S, et al. American Society of Clinical Oncology/College Of American Pathologists guideline recommendations for immunohistochemical testing of estrogen and progesterone receptors in breast cancer. J Clin Oncol. 2010;28(16):2784-95.

4. Wolff AC, Hammond ME, Hicks DG, Dowsett M, McShane LM, Allison KH, et al. Recommendations for human epidermal growth factor receptor 2 testing in breast cancer: American Society of Clinical Oncology/College of American Pathologists clinical practice guideline update. J Clin Oncol. 2013;31(31):3997-4013.

5. Santagata S, Thakkar A, Ergonul A, Wang B, Woo T, Hu R, et al. Taxonomy of breast cancer based on normal cell phenotype predicts outcome. J Clin Invest. 2014;124(2):859-70.

6. Sorlie T, Tibshirani R, Parker J, Hastie T, Marron JS, Nobel A, et al. Repeated observation of breast tumor subtypes in independent gene expression data sets. Proc Natl Acad Sci U S A. 2003;100(14):8418-23.

7. Vargo-Gogola T, Rosen JM. Modelling breast cancer: one size does not fit all. Nat Rev Cancer. 2007;7(9):659-72.

8. DeSantis CE, Ma J, Gaudet MM, Newman LA, Miller KD, Goding Sauer A, et al. Breast cancer statistics, 2019. CA Cancer J Clin. 2019;69(6):438-51.

9. Szostakowska M, Trebinska-Stryjewska A, Grzybowska EA, Fabisiewicz A. Resistance to endocrine therapy in breast cancer: molecular mechanisms and future goals. Breast Cancer Res Treat. 2019;173(3):489-97.

10. Paterni I, Granchi C, Katzenellenbogen JA, Minutolo F. Estrogen receptors alpha (ERalpha) and beta (ERbeta): subtype-selective ligands and clinical potential. Steroids. 2014;90:13-29.

11. Heldring N, Pike A, Andersson S, Matthews J, Cheng G, Hartman J, et al. Estrogen receptors: how do they signal and what are their targets. Physiol Rev. 2007;87(3):905-31.

12. Kushner PJ, Agard DA, Greene GL, Scanlan TS, Shiau AK, Uht RM, et al. Estrogen receptor pathways to AP-1. J Steroid Biochem Mol Biol. 2000;74(5):311-7.

13. Safe S, Kim K. Non-classical genomic estrogen receptor (ER)/specificity protein and ER/activating protein-1 signaling pathways. J Mol Endocrinol. 2008;41(5):263-75.

14. Li Y, Lambert MH, Xu HE. Activation of nuclear receptors: a perspective from structural genomics. Structure. 2003;11(7):741-6.

15. Bjornstrom L, Sjoberg M. Mechanisms of estrogen receptor signaling: convergence of genomic and nongenomic actions on target genes. Mol Endocrinol. 2005;19(4):833-42.

16. Wong CW, McNally C, Nickbarg E, Komm BS, Cheskis BJ. Estrogen receptor-interacting protein that modulates its nongenomic activity-crosstalk with Src/Erk phosphorylation cascade. Proc Natl Acad Sci U S A. 2002;99(23):14783-8.

17. Kahlert S, Nuedling S, van Eickels M, Vetter H, Meyer R, Grohe C. Estrogen receptor alpha rapidly activates the IGF-1 receptor pathway. J Biol Chem. 2000;275(24):18447-53.

18. Slowikowski BK, Lianeri M, Jagodzinski PP. Exploring estrogenic activity in lung cancer. Mol Biol Rep. 2017;44(1):35-50.

19. Beatson GT. On the Treatment of Inoperable Cases of Carcinoma of the Mamma: Suggestions for a New Method of Treatment, with Illustrative Cases. Trans Med Chir Soc Edinb. 1896;15:153-79.

20. Smith IE, Dowsett M. Aromatase inhibitors in breast cancer. N Engl J Med. 2003;348(24):2431-42.

21. Lonning PE. Exemestane: a review of its clinical efficacy and safety. Breast. 2001;10(3):198-208.

22. Cuzick J, Sestak I, Forbes JF, Dowsett M, Cawthorn S, Mansel RE, et al. Use of anastrozole for breast cancer prevention (IBIS-II): long-term results of a randomised controlled trial. Lancet. 2020;395(10218):117-22.

23. Goss PE, Powles TJ, Dowsett M, Hutchison G, Brodie AM, Gazet JC, et al. Treatment of advanced postmenopausal breast cancer with an aromatase inhibitor, 4-hydroxyandrostenedione: phase II report. Cancer Res. 1986;46(9):4823-6.

24. Wakeling AE, Dukes M, Bowler J. A potent specific pure antiestrogen with clinical potential. Cancer Res. 1991;51(15):3867-73.

25. McDonnell DP, Wardell SE. The molecular mechanisms underlying the pharmacological actions of ER modulators: implications for new drug discovery in breast cancer. Curr Opin Pharmacol. 2010;10(6):620-8.

26. Di Leo A, Jerusalem G, Petruzelka L, Torres R, Bondarenko IN, Khasanov R, et al. Results of the CONFIRM phase III trial comparing fulvestrant 250 mg with fulvestrant 500 mg in postmenopausal women with estrogen receptor-positive advanced breast cancer. J Clin Oncol. 2010;28(30):4594-600.

27. Weir HM, Bradbury RH, Lawson M, Rabow AA, Buttar D, Callis RJ, et al. AZD9496: An Oral Estrogen Receptor Inhibitor That Blocks the Growth of ER-Positive and ESR1-Mutant Breast Tumors in Preclinical Models. Cancer Res. 2016;76(11):3307-18.

28. Martinkovich S, Shah D, Planey SL, Arnott JA. Selective estrogen receptor modulators: tissue specificity and clinical utility. Clin Interv Aging. 2014;9:1437-52.

29. Farrar MC, Jacobs TF. Tamoxifen. StatPearls. Treasure Island (FL)2021.

30. Fisher B, Costantino JP, Wickerham DL, Redmond CK, Kavanah M, Cronin WM, et al. Tamoxifen for prevention of breast cancer: report of the National Surgical Adjuvant Breast and Bowel Project P-1 Study. J Natl Cancer Inst. 1998;90(18):1371-88.

31. Veronesi U, Maisonneuve P, Rotmensz N, Bonanni B, Boyle P, Viale G, et al. Tamoxifen for the prevention of breast cancer: late results of the Italian Randomized Tamoxifen Prevention Trial among women with hysterectomy. J Natl Cancer Inst. 2007;99(9):727-37.

32. Hernando C, Ortega-Morillo B, Tapia M, Moragon S, Martinez MT, Eroles P, et al. Oral Selective Estrogen Receptor Degraders (SERDs) as a Novel Breast Cancer Therapy: Present and Future from a Clinical Perspective. Int J Mol Sci. 2021;22(15).

33. Aggelis V, Johnston SRD. Advances in Endocrine-Based Therapies for Estrogen Receptor-Positive Metastatic Breast Cancer. Drugs. 2019;79(17):1849-66.

34. Garcia-Becerra R, Santos N, Diaz L, Camacho J. Mechanisms of resistance to endocrine therapy in breast cancer: focus on signaling pathways, miRNAs and genetically based resistance. Int J Mol Sci. 2012;14(1):108-45.

35. Yang X, Phillips DL, Ferguson AT, Nelson WG, Herman JG, Davidson NE. Synergistic activation of functional estrogen receptor (ER)-alpha by DNA methyltransferase and histone deacetylase inhibition in human ER-alpha-negative breast cancer cells. Cancer Res. 2001;61(19):7025-9.

36. Fan M, Yan PS, Hartman-Frey C, Chen L, Paik H, Oyer SL, et al. Diverse gene expression and DNA methylation profiles correlate with differential adaptation of breast cancer cells to the antiestrogens tamoxifen and fulvestrant. Cancer Res. 2006;66(24):11954-66.

37. Toy W, Weir H, Razavi P, Lawson M, Goeppert AU, Mazzola AM, et al. Activating ESR1 Mutations Differentially Affect the Efficacy of ER Antagonists. Cancer Discov. 2017;7(3):277-87.

38. Nielsen KV, Ejlertsen B, Muller S, Moller S, Rasmussen BB, Balslev E, et al. Amplification of ESR1 may predict resistance to adjuvant tamoxifen in postmenopausal patients with hormone receptor positive breast cancer. Breast Cancer Res Treat. 2011;127(2):345-55.

39. Tomita S, Zhang Z, Nakano M, Ibusuki M, Kawazoe T, Yamamoto Y, et al. Estrogen receptor alpha gene ESR1 amplification may predict endocrine therapy responsiveness in breast cancer patients. Cancer Sci. 2009;100(6):1012-7.

40. Holst F, Singer CF. ESR1-Amplification-Associated Estrogen Receptor alpha Activity in Breast Cancer. Trends Endocrinol Metab. 2016;27(11):751-2.

41. Benz CC, Scott GK, Sarup JC, Johnson RM, Tripathy D, Coronado E, et al. Estrogen-dependent, tamoxifen-resistant tumorigenic growth of MCF-7 cells transfected with HER2/neu. Breast Cancer Res Treat. 1992;24(2):85-95.

42. Nicholson RI, Hutcheson IR, Jones HE, Hiscox SE, Giles M, Taylor KM, et al. Growth factor signalling in endocrine and anti-growth factor resistant breast cancer. Rev Endocr Metab Disord. 2007;8(3):241-53.

43. Bostner J, Karlsson E, Pandiyan MJ, Westman H, Skoog L, Fornander T, et al. Activation of Akt, mTOR, and the estrogen receptor as a signature to predict tamoxifen treatment benefit. Breast Cancer Res Treat. 2013;137(2):397-406.

44. Miller TW, Hennessy BT, Gonzalez-Angulo AM, Fox EM, Mills GB, Chen H, et al. Hyperactivation of phosphatidylinositol-3 kinase promotes escape from hormone dependence in estrogen receptor-positive human breast cancer. J Clin Invest. 2010;120(7):2406-13.

45. Bachelot T, Bourgier C, Cropet C, Ray-Coquard I, Ferrero JM, Freyer G, et al. Randomized phase II trial of everolimus in combination with tamoxifen in patients with hormone receptor-positive, human epidermal growth factor receptor 2-negative metastatic breast cancer with prior exposure to aromatase inhibitors: a GINECO study. J Clin Oncol. 2012;30(22):2718-24.

46. Sabbah M, Courilleau D, Mester J, Redeuilh G. Estrogen induction of the cyclin D1 promoter: involvement of a cAMP response-like element. Proc Natl Acad Sci U S A. 1999;96(20):11217-22.

47. Lundgren K, Brown M, Pineda S, Cuzick J, Salter J, Zabaglo L, et al. Effects of cyclin D1 gene amplification and protein expression on time to recurrence in postmenopausal breast cancer patients treated with anastrozole or tamoxifen: a TransATAC study. Breast Cancer Res. 2012;14(2):R57.

48. Johnson J, Thijssen B, McDermott U, Garnett M, Wessels LF, Bernards R. Targeting the RB-E2F pathway in breast cancer. Oncogene. 2016;35(37):4829-35.

49. Walker AJ, Wedam S, Amiri-Kordestani L, Bloomquist E, Tang S, Sridhara R, et al. FDA Approval of Palbociclib in Combination with Fulvestrant for the Treatment of Hormone Receptor-Positive, HER2-Negative Metastatic Breast Cancer. Clin Cancer Res. 2016;22(20):4968-72.

50. O'Shaughnessy J, Thaddeus Beck J, Royce M. Everolimus-based combination therapies for HR+, HER2- metastatic breast cancer. Cancer Treat Rev. 2018;69:204-14.

51. Thomas MC, Chiang CM. The general transcription machinery and general cofactors. Crit Rev Biochem Mol Biol. 2006;41(3):105-78.

52. Hahn S. Structure and mechanism of the RNA polymerase II transcription machinery. Nat Struct Mol Biol. 2004;11(5):394-403.

53. Myers LC, Kornberg RD. Mediator of transcriptional regulation. Annu Rev Biochem. 2000;69:729-49.

54. Lee TI, Young RA. Transcription of eukaryotic protein-coding genes. Annu Rev Genet. 2000;34:77-137.

55. Malik S, Roeder RG. The metazoan Mediator co-activator complex as an integrative hub for transcriptional regulation. Nat Rev Genet. 2010;11(11):761-72.

56. Allen BL, Taatjes DJ. The Mediator complex: a central integrator of transcription. Nat Rev Mol Cell Biol. 2015;16(3):155-66.

57. Andre KM, Sipos EH, Soutourina J. Mediator Roles Going Beyond Transcription. Trends Genet. 2021;37(3):224-34.

58. Soutourina J. Transcription regulation by the Mediator complex. Nat Rev Mol Cell Biol. 2018;19(4):262-74.

59. Taatjes DJ. The human Mediator complex: a versatile, genome-wide regulator of transcription. Trends Biochem Sci. 2010;35(6):315-22.

60. Friedson B, Cooper KF. Cdk8 Kinase Module: A Mediator of Life and Death Decisions in Times of Stress. Microorganisms. 2021;9(10).

61. Jeronimo C, Robert F. The Mediator Complex: At the Nexus of RNA Polymerase II Transcription. Trends Cell Biol. 2017;27(10):765-83.

62. Straub J, Venigalla S, Newman JJ. Mediator's Kinase Module: A Modular Regulator of Cell Fate. Stem Cells Dev. 2020;29(24):1535-51.

63. Donner AJ, Ebmeier CC, Taatjes DJ, Espinosa JM. CDK8 is a positive regulator of transcriptional elongation within the serum response network. Nat Struct Mol Biol. 2010;17(2):194-201.

64. Knuesel MT, Meyer KD, Bernecky C, Taatjes DJ. The human CDK8 subcomplex is a molecular switch that controls Mediator coactivator function. Genes Dev. 2009;23(4):439-51.

65. Snijders Blok L, Hiatt SM, Bowling KM, Prokop JW, Engel KL, Cochran JN, et al. De novo mutations in MED13, a component of the Mediator complex, are associated with a novel neurodevelopmental disorder. Hum Genet. 2018;137(5):375-88.

66. Jo YS, Choi MR, Song SY, Kim MS, Yoo NJ, Lee SH. Frameshift Mutations of HSPA4 and MED13 in Gastric and Colorectal Cancers. Pathol Oncol Res. 2016;22(4):769-72.

67. Monni O, Barlund M, Mousses S, Kononen J, Sauter G, Heiskanen M, et al. Comprehensive copy number and gene expression profiling of the 17q23 amplicon in human breast cancer. Proc Natl Acad Sci U S A. 2001;98(10):5711-6.

68. Rolinski M, Montaldo NP, Aksu ME, Fordyce Martin SL, Brambilla A, Kunath N, et al. Loss of Mediator complex subunit 13 (MED13) promotes resistance to alkylation through cyclin D1 upregulation. Nucleic Acids Res. 2021;49(3):1470-84.

69. Westerling T, Kuuluvainen E, Makela TP. Cdk8 is essential for preimplantation mouse development. Mol Cell Biol. 2007;27(17):6177-82.

70. McCleland ML, Soukup TM, Liu SD, Esensten JH, de Sousa e Melo F, Yaylaoglu M, et al. Cdk8 deletion in the Apc(Min) murine tumour model represses EZH2 activity and accelerates tumourigenesis. J Pathol. 2015;237(4):508-19.

71. Calpena E, Hervieu A, Kaserer T, Swagemakers SMA, Goos JAC, Popoola O, et al. De Novo Missense Substitutions in the Gene Encoding CDK8, a Regulator of the Mediator Complex, Cause a Syndromic Developmental Disorder. Am J Hum Genet. 2019;104(4):709-20.

72. Yin JW, Wang G. The Mediator complex: a master coordinator of transcription and cell lineage development. Development. 2014;141(5):977-87.

73. McDermott MS, Chumanevich AA, Lim CU, Liang J, Chen M, Altilia S, et al. Inhibition of CDK8 mediator kinase suppresses estrogen dependent transcription and the growth of estrogen receptor positive breast cancer. Oncotarget. 2017;8(8):12558-75.

74. Song W, Wu S, Wu Q, Zhou L, Yu L, Zhu B, et al. The microRNA-141-3p/CDK8 pathway regulates the chemosensitivity of breast cancer cells to trastuzumab. J Cell Biochem. 2019;120(8):14095-106.

75. Zhang Z, Zhang L, Yin ZY, Fan XL, Hu B, Wang LQ, et al. miR-107 regulates cisplatin chemosensitivity of A549 non small cell lung cancer cell line by targeting cyclin dependent kinase 8. Int J Clin Exp Pathol. 2014;7(10):7236-41.

76. De Marchi T, Timmermans MA, Sieuwerts AM, Smid M, Look MP, Grebenchtchikov N, et al. Phosphoserine aminotransferase 1 is associated to poor outcome on tamoxifen therapy in recurrent breast cancer. Sci Rep. 2017;7(1):2099.

77. Tofigh A, Suderman M, Paquet ER, Livingstone J, Bertos N, Saleh SM, et al. The prognostic ease and difficulty of invasive breast carcinoma. Cell Rep. 2014;9(1):129-42.

78. Ma XJ, Wang Z, Ryan PD, Isakoff SJ, Barmettler A, Fuller A, et al. A two-gene expression ratio predicts clinical outcome in breast cancer patients treated with tamoxifen. Cancer Cell. 2004;5(6):607-16.

79. Cai Y, Nogales-Cadenas R, Zhang Q, Lin JR, Zhang W, O'Brien K, et al. Transcriptomic dynamics of breast cancer progression in the MMTV-PyMT mouse model. BMC Genomics. 2017;18(1):185.

80. Galbraith MD, Allen MA, Bensard CL, Wang X, Schwinn MK, Qin B, et al. HIF1A employs CDK8-mediator to stimulate RNAPII elongation in response to hypoxia. Cell. 2013;153(6):1327-39.

81. Loi S, Haibe-Kains B, Desmedt C, Lallemand F, Tutt AM, Gillet C, et al. Definition of clinically distinct molecular subtypes in estrogen receptor-positive breast carcinomas through genomic grade. J Clin Oncol. 2007;25(10):1239-46.

82. Johnston SR, Saccani-Jotti G, Smith IE, Salter J, Newby J, Coppen M, et al. Changes in estrogen receptor, progesterone receptor, and pS2 expression in tamoxifen-resistant human breast cancer. Cancer Res. 1995;55(15):3331-8.

83. Knowlden JM, Hutcheson IR, Jones HE, Madden T, Gee JM, Harper ME, et al. Elevated levels of epidermal growth factor receptor/c-erbB2 heterodimers mediate an autocrine growth regulatory pathway in tamoxifen-resistant MCF-7 cells. Endocrinology. 2003;144(3):1032-44.

84. Ward A, Balwierz A, Zhang JD, Kublbeck M, Pawitan Y, Hielscher T, et al. Re-expression of microRNA-375 reverses both tamoxifen resistance and accompanying EMT-like properties in breast cancer. Oncogene. 2013;32(9):1173-82.

85. Arpino G, Wiechmann L, Osborne CK, Schiff R. Crosstalk between the estrogen receptor and the HER tyrosine kinase receptor family: molecular mechanism and clinical implications for endocrine therapy resistance. Endocr Rev. 2008;29(2):217-33.

86. Mishra RR, Belder N, Ansari SA, Kayhan M, Bal H, Raza U, et al. Reactivation of cAMP Pathway by PDE4D Inhibition Represents a Novel Druggable Axis for Overcoming Tamoxifen Resistance in ER-positive Breast Cancer. Clin Cancer Res. 2018;24(8):1987-2001.

87. Ward A, Shukla K, Balwierz A, Soons Z, Konig R, Sahin O, et al. MicroRNA-519a is a novel oncomir conferring tamoxifen resistance by targeting a network of tumour-suppressor genes in ER+ breast cancer. J Pathol. 2014;233(4):368-79.

88. Ding X, Sharko AC, McDermott MS-J, Ji H, Chumanevich A, Schools GP, et al. Abstract LB132: CDK8/19 inhibition overcomes in vitro and in vivo resistance to lapatinib in HER2+ breast cancer via STAT1 and STAT3. Cancer Research. 2021;81(13 Supplement):LB132-LB.

89. Bancerek J, Poss ZC, Steinparzer I, Sedlyarov V, Pfaffenwimmer T, Mikulic I, et al. CDK8 kinase phosphorylates transcription factor STAT1 to selectively regulate the interferon response. Immunity. 2013;38(2):250-62.

90. Cui J, Germer K, Wu T, Wang J, Luo J, Wang SC, et al. Cross-talk between HER2 and MED1 regulates tamoxifen resistance of human breast cancer cells. Cancer Res. 2012;72(21):5625-34.

91. Symmans WF, Hatzis C, Sotiriou C, Andre F, Peintinger F, Regitnig P, et al. Genomic index of sensitivity to endocrine therapy for breast cancer. J Clin Oncol. 2010;28(27):4111-9.

92. Wang XQ, Rothnagel JA. Post-transcriptional regulation of the gli1 oncogene by the expression of alternative 5' untranslated regions. J Biol Chem. 2001;276(2):1311-6.

93. Maroder M, Martinotti S, Vacca A, Screpanti I, Petrangeli E, Frati L, et al. Post-transcriptional control of c-myc proto-oncogene expression by glucocorticoid hormones in human T lymphoblastic leukemic cells. Nucleic Acids Res. 1990;18(5):1153-7.

94. Al-Matouq J, Al-Haj L, Al-Saif M, Khabar KSA. Post-transcriptional screen of cancer amplified genes identifies ERBB2/Her2 signaling as AU-rich mRNA stability-promoting pathway. Oncogenesis. 2021;10(9):61.

95. Ratnadiwakara M, Anko ML. mRNA Stability Assay Using transcription inhibition by Actinomycin D in Mouse Pluripotent Stem Cells. Bio Protoc. 2018;8(21):e3072.

96. Fluck MM, Schaffhausen BS. Lessons in signaling and tumorigenesis from polyomavirus middle T antigen. Microbiol Mol Biol Rev. 2009;73(3):542-63, Table of Contents.

97. Guy CT, Cardiff RD, Muller WJ. Induction of mammary tumors by expression of polyomavirus middle T oncogene: a transgenic mouse model for metastatic disease. Mol Cell Biol. 1992;12(3):954-61.

98. Shishido S, Delahaye A, Beck A, Nguyen TA. The MMTV-PyVT Transgenic Mouse as a Multistage Model for Mammary Carcinoma and the Efficacy of Antineoplastic Treatment. Journal of Cancer Therapy. 2013;4(7).

99. Pfefferle AD, Herschkowitz JI, Usary J, Harrell JC, Spike BT, Adams JR, et al. Transcriptomic classification of genetically engineered mouse models of breast cancer identifies human subtype counterparts. Genome Biol. 2013;14(11):R125.

100. Attalla S, Taifour T, Bui T, Muller W. Insights from transgenic mouse models of PyMT-induced breast cancer: recapitulating human breast cancer progression in vivo. Oncogene. 2021;40(3):475-91.

101. Lin EY, Jones JG, Li P, Zhu L, Whitney KD, Muller WJ, et al. Progression to malignancy in the polyoma middle T oncoprotein mouse breast cancer model provides a reliable model for human diseases. Am J Pathol. 2003;163(5):2113-26.

102. Lopez-Tarruella S, Schiff R. The dynamics of estrogen receptor status in breast cancer: re-shaping the paradigm. Clin Cancer Res. 2007;13(23):6921-5.

103. Maurice DH, Ke H, Ahmad F, Wang Y, Chung J, Manganiello VC. Advances in targeting cyclic nucleotide phosphodiesterases. Nat Rev Drug Discov. 2014;13(4):290-314.

104. Francis SH, Blount MA, Corbin JD. Mammalian cyclic nucleotide phosphodiesterases: molecular mechanisms and physiological functions. Physiol Rev. 2011;91(2):651-90.

105. Conti M, Beavo J. Biochemistry and physiology of cyclic nucleotide phosphodiesterases: essential components in cyclic nucleotide signaling. Annu Rev Biochem. 2007;76:481-511.

106. Keravis T, Lugnier C. Cyclic nucleotide phosphodiesterase (PDE) isozymes as targets of the intracellular signalling network: benefits of PDE inhibitors in various diseases and perspectives for future therapeutic developments. Br J Pharmacol. 2012;165(5):1288-305.

107. Bender AT, Beavo JA. Cyclic nucleotide phosphodiesterases: molecular regulation to clinical use. Pharmacol Rev. 2006;58(3):488-520.

108. Fabbri LM, Calverley PM, Izquierdo-Alonso JL, Bundschuh DS, Brose M, Martinez FJ, et al. Roflumilast in moderate-to-severe chronic obstructive pulmonary disease treated with longacting bronchodilators: two randomised clinical trials. Lancet. 2009;374(9691):695-703.

109. Page CP, Spina D. Selective PDE inhibitors as novel treatments for respiratory diseases. Curr Opin Pharmacol. 2012;12(3):275-86.

110. Schafer PH, Parton A, Capone L, Cedzik D, Brady H, Evans JF, et al. Apremilast is a selective PDE4 inhibitor with regulatory effects on innate immunity. Cell Signal. 2014;26(9):2016-29.

111. Prosdocimi T, Mollica L, Donini S, Semrau MS, Lucarelli AP, Aiolfi E, et al. Molecular Bases of PDE4D Inhibition by Memory-Enhancing GEBR Library Compounds. Biochemistry. 2018;57(19):2876-88.

112. Uretmen Kagiali ZC, Sanal E, Karayel O, Polat AN, Saatci O, Ersan PG, et al. Systems-level Analysis Reveals Multiple Modulators of Epithelial-mesenchymal Transition and Identifies DNAJB4 and CD81 as Novel Metastasis Inducers in Breast Cancer. Mol Cell Proteomics. 2019;18(9):1756-71.

113. Clark AD, Oldenbroek M, Boyer TG. Mediator kinase module and human tumorigenesis. Crit Rev Biochem Mol Biol. 2015;50(5):393-426.

114. Loncle N, Boube M, Joulia L, Boschiero C, Werner M, Cribbs DL, et al. Distinct roles for Mediator Cdk8 module subunits in Drosophila development. EMBO J. 2007;26(4):1045-54.

115. Chattopadhyay I, Singh A, Phukan R, Purkayastha J, Kataki A, Mahanta J, et al. Genome-wide analysis of chromosomal alterations in patients with esophageal squamous cell carcinoma exposed to tobacco and betel quid from high-risk area in India. Mutat Res. 2010;696(2):130-8.

116. Mitra AP, Almal AA, George B, Fry DW, Lenehan PF, Pagliarulo V, et al. The use of genetic programming in the analysis of quantitative gene expression profiles for identification of nodal status in bladder cancer. BMC Cancer. 2006;6:159.

117. Firestein R, Bass AJ, Kim SY, Dunn IF, Silver SJ, Guney I, et al. CDK8 is a colorectal cancer oncogene that regulates beta-catenin activity. Nature. 2008;455(7212):547-51.

118. Oliveira DM, Santamaria G, Laudanna C, Migliozzi S, Zoppoli P, Quist M, et al. Identification of copy number alterations in colon cancer from analysis of amplicon-based next generation sequencing data. Oncotarget. 2018;9(29):20409-25.

119. Kim MY, Han SI, Lim SC. Roles of cyclin-dependent kinase 8 and beta-catenin in the oncogenesis and progression of gastric adenocarcinoma. Int J Oncol. 2011;38(5):1375-83.

120. Kapoor A, Goldberg MS, Cumberland LK, Ratnakumar K, Segura MF, Emanuel PO, et al. The histone variant macroH2A suppresses melanoma progression through regulation of CDK8. Nature. 2010;468(7327):1105-9.

121. Fryer CJ, White JB, Jones KA. Mastermind recruits CycC:CDK8 to phosphorylate the Notch ICD and coordinate activation with turnover. Mol Cell. 2004;16(4):509-20.

122. Seo JO, Han SI, Lim SC. Role of CDK8 and beta-catenin in colorectal adenocarcinoma. Oncol Rep. 2010;24(1):285-91.

123. Alarcon C, Zaromytidou AI, Xi Q, Gao S, Yu J, Fujisawa S, et al. Nuclear CDKs drive Smad transcriptional activation and turnover in BMP and TGF-beta pathways. Cell. 2009;139(4):757-69.

124. Harper TM, Taatjes DJ. The complex structure and function of Mediator. J Biol Chem. 2018;293(36):13778-85.

125. Khakhina S, Cooper KF, Strich R. Med13p prevents mitochondrial fission and programmed cell death in yeast through nuclear retention of cyclin C. Mol Biol Cell. 2014;25(18):2807-16.

126. Borik S, Simon AJ, Nevo-Caspi Y, Mishali D, Amariglio N, Rechavi G, et al. Increased RNA editing in children with cyanotic congenital heart disease. Intensive Care Med. 2011;37(10):1664-71.

127. Kuuluvainen E, Domenech-Moreno E, Niemela EH, Makela TP. Depletion of Mediator Kinase Module Subunits Represses Superenhancer-Associated Genes in Colon Cancer Cells. Mol Cell Biol. 2018;38(11).

128. Cee VJ, Chen DY, Lee MR, Nicolaou KC. Cortistatin A is a high-affinity ligand of protein kinases ROCK, CDK8, and CDK11. Angew Chem Int Ed Engl. 2009;48(47):8952-7.

129. Porter DC, Farmaki E, Altilia S, Schools GP, West DK, Chen M, et al. Cyclin-dependent kinase 8 mediates chemotherapy-induced tumor-promoting paracrine activities. Proc Natl Acad Sci U S A. 2012;109(34):13799-804.

130. Chen M, Liang J, Ji H, Yang Z, Altilia S, Hu B, et al. CDK8/19 Mediator kinases potentiate induction of transcription by NFkappaB. Proc Natl Acad Sci U S A. 2017;114(38):10208-13.

131. Mallinger A, Schiemann K, Rink C, Stieber F, Calderini M, Crumpler S, et al. Discovery of Potent, Selective, and Orally Bioavailable Small-Molecule Modulators of the Mediator Complex-Associated Kinases CDK8 and CDK19. J Med Chem. 2016;59(3):1078-101.

132. Czodrowski P, Mallinger A, Wienke D, Esdar C, Poschke O, Busch M, et al. Structure-Based Optimization of Potent, Selective, and Orally Bioavailable CDK8 Inhibitors Discovered by High-Throughput Screening. J Med Chem. 2016;59(20):9337-49.

133. Amirhosseini M, Bernhardsson M, Lang P, Andersson G, Flygare J, Fahlgren A. Cyclin-dependent kinase 8/19 inhibition suppresses osteoclastogenesis by downregulating RANK and promotes osteoblast mineralization and cancellous bone healing. J Cell Physiol. 2019.

134. Johannessen L, Sundberg TB, O'Connell DJ, Kolde R, Berstler J, Billings KJ, et al. Small-molecule studies identify CDK8 as a regulator of IL-10 in myeloid cells. Nat Chem Biol. 2017;13(10):1102-8.

135. Chen M, Li J, Liang J, Thompson ZS, Kathrein K, Broude EV, et al. Systemic Toxicity Reported for CDK8/19 Inhibitors CCT251921 and MSC2530818 Is Not Due to Target Inhibition. Cells. 2019;8(11).

136. Li Y, Tsang CK, Wang S, Li XX, Yang Y, Fu L, et al. MAF1 suppresses AKT-mTOR signaling and liver cancer through activation of PTEN transcription. Hepatology. 2016;63(6):1928-42.

137. Johnson SM, Gulhati P, Rampy BA, Han Y, Rychahou PG, Doan HQ, et al. Novel expression patterns of PI3K/Akt/mTOR signaling pathway components in colorectal cancer. J Am Coll Surg. 2010;210(5):767-76, 76-8.

138. Wang H, Duan L, Zou Z, Li H, Yuan S, Chen X, et al. Activation of the PI3K/Akt/mTOR/p70S6K pathway is involved in S100A4-induced viability and migration in colorectal cancer cells. Int J Med Sci. 2014;11(8):841-9.

139. Nepstad I, Hatfield KJ, Gronningsaeter IS, Reikvam H. The PI3K-Akt-mTOR Signaling Pathway in Human Acute Myeloid Leukemia (AML) Cells. Int J Mol Sci. 2020;21(8).

140. deGraffenried LA, Friedrichs WE, Russell DH, Donzis EJ, Middleton AK, Silva JM, et al. Inhibition of mTOR activity restores tamoxifen response in breast cancer cells with aberrant Akt Activity. Clin Cancer Res. 2004;10(23):8059-67.

141. Menzl I, Zhang T, Berger-Becvar A, Grausenburger R, Heller G, Prchal-Murphy M, et al. A kinase-independent role for CDK8 in BCR-ABL1(+) leukemia. Nat Commun. 2019;10(1):4741.

142. Zhao BS, Roundtree IA, He C. Post-transcriptional gene regulation by mRNA modifications. Nat Rev Mol Cell Biol. 2017;18(1):31-42.

143. Filipowicz W, Bhattacharyya SN, Sonenberg N. Mechanisms of post-transcriptional regulation by microRNAs: are the answers in sight? Nat Rev Genet. 2008;9(2):102-14.

144. Feigerlova E, Battaglia-Hsu SF. Role of post-transcriptional regulation of mRNA stability in renal pathophysiology: focus on chronic kidney disease. FASEB J. 2017;31(2):457-68.

145. Li YC, Chao TC, Kim HJ, Cholko T, Chen SF, Li G, et al. Structure and noncanonical Cdk8 activation mechanism within an Argonaute-containing Mediator kinase module. Sci Adv. 2021;7(3).

146. Day CP, Merlino G, Van Dyke T. Preclinical mouse cancer models: a maze of opportunities and challenges. Cell. 2015;163(1):39-53.

147. Scheer N, Snaith M, Wolf CR, Seibler J. Generation and utility of genetically humanized mouse models. Drug Discov Today. 2013;18(23-24):1200-11.

148. Hsien Lai S, Zervoudakis G, Chou J, Gurney ME, Quesnelle KM. PDE4 subtypes in cancer. Oncogene. 2020;39(19):3791-802.

149. Pullamsetti SS, Banat GA, Schmall A, Szibor M, Pomagruk D, Hanze J, et al. Phosphodiesterase-4 promotes proliferation and angiogenesis of lung cancer by crosstalk with HIF. Oncogene. 2013;32(9):1121-34.

150. Rahrmann EP, Collier LS, Knutson TP, Doyal ME, Kuslak SL, Green LE, et al. Identification of PDE4D as a proliferation promoting factor in prostate cancer using a Sleeping Beauty transposon-based somatic mutagenesis screen. Cancer Res. 2009;69(10):4388-97.

151. Delyon J, Servy A, Laugier F, Andre J, Ortonne N, Battistella M, et al. PDE4D promotes FAK-mediated cell invasion in BRAF-mutated melanoma. Oncogene. 2017;36(23):3252-62.

152. Xu T, Wu S, Yuan Y, Yan G, Xiao D. Knockdown of phosphodiesterase 4D inhibits nasopharyngeal carcinoma proliferation via the epidermal growth factor receptor signaling pathway. Oncol Lett. 2014;8(5):2110-6.

153. Azevedo MF, Faucz FR, Bimpaki E, Horvath A, Levy I, de Alexandre RB, et al. Clinical and molecular genetics of the phosphodiesterases (PDEs). Endocr Rev. 2014;35(2):195-233.

154. Bhat A, Ray B, Mahalakshmi AM, Tuladhar S, Nandakumar DN, Srinivasan M, et al. Phosphodiesterase-4 enzyme as a therapeutic target in neurological disorders. Pharmacol Res. 2020;160:105078.

155. Pittenger C, Duman RS. Stress, depression, and neuroplasticity: a convergence of mechanisms. Neuropsychopharmacology. 2008;33(1):88-109.

156. Jorgensen C, Yasmeen S, Iversen HK, Kruuse C. Phosphodiesterase4D (PDE4D)--A risk factor for atrial fibrillation and stroke? J Neurol Sci. 2015;359(1-2):266-74.

157. Wang H, Gaur U, Xiao J, Xu B, Xu J, Zheng W. Targeting phosphodiesterase 4 as a potential therapeutic strategy for enhancing neuroplasticity following ischemic stroke. Int J Biol Sci. 2018;14(12):1745-54.

158. Van Duinen MA, Sambeth A, Heckman PRA, Smit S, Tsai M, Lahu G, et al. Acute administration of roflumilast enhances immediate recall of verbal word memory in healthy young adults. Neuropharmacology. 2018;131:31-8.

159. Fleischhacker WW, Hinterhuber H, Bauer H, Pflug B, Berner P, Simhandl C, et al. A multicenter double-blind study of three different doses of the new cAMP-phosphodiesterase inhibitor rolipram in patients with major depressive disorder. Neuropsychobiology. 1992;26(1-2):59-64.

160. Papp K, Reich K, Leonardi CL, Kircik L, Chimenti S, Langley RG, et al. Apremilast, an oral phosphodiesterase 4 (PDE4) inhibitor, in patients with moderate to severe plaque psoriasis: Results of a phase III, randomized, controlled trial (Efficacy and Safety Trial Evaluating the Effects of Apremilast in Psoriasis [ESTEEM] 1). J Am Acad Dermatol. 2015;73(1):37-49.

161. Kelly K, Mejia A, Suhasini AN, Lin AP, Kuhn J, Karnad AB, et al. Safety and Pharmacodynamics of the PDE4 Inhibitor Roflumilast in Advanced B-cell Malignancies. Clin Cancer Res. 2017;23(5):1186-92.

162. Ramezani S, Vousooghi N, Kapourchali FR, Hadjighasem M, Hayat P, Amini N, et al. Rolipram potentiates bevacizumab-induced cell death in human glioblastoma stem-like cells. Life Sci. 2017;173:11-9.

163. Zebda R, Paller AS. Phosphodiesterase 4 inhibitors. J Am Acad Dermatol. 2018;78(3 Suppl 1):S43-S52.

164. Burgin AB, Magnusson OT, Singh J, Witte P, Staker BL, Bjornsson JM, et al. Design of phosphodiesterase 4D (PDE4D) allosteric modulators for enhancing cognition with improved safety. Nat Biotechnol. 2010;28(1):63-70.

165. Bruno O, Fedele E, Prickaerts J, Parker LA, Canepa E, Brullo C, et al. GEBR-7b, a novel PDE4D selective inhibitor that improves memory in rodents at non-emetic doses. Br J Pharmacol. 2011;164(8):2054-63.

166. Hong BS, Ryu HS, Kim N, Kim J, Lee E, Moon H, et al. Tumor Suppressor miRNA-204-5p Regulates Growth, Metastasis, and Immune Microenvironment Remodeling in Breast Cancer. Cancer Res. 2019;79(7):1520-34.

167. Rupaimoole R, Calin GA, Lopez-Berestein G, Sood AK. miRNA Deregulation in Cancer Cells and the Tumor Microenvironment. Cancer Discov. 2016;6(3):235-46.

168. Ghaemi Z, Soltani BM, Mowla SJ. MicroRNA-326 Functions as a Tumor Suppressor in Breast Cancer by Targeting ErbB/PI3K Signaling Pathway. Front Oncol. 2019;9:653.

169. Zhang P, Kong F, Deng X, Yu Y, Hou C, Liang T, et al. MicroRNA-326 suppresses the proliferation, migration and invasion of cervical cancer cells by targeting ELK1. Oncol Lett. 2017;13(5):2949-56.

170. Sun C, Huang C, Li S, Yang C, Xi Y, Wang L, et al. Hsa-miR-326 targets CCND1 and inhibits non-small cell lung cancer development. Oncotarget. 2016;7(7):8341-59.

171. Nawaz Z, Patil V, Paul Y, Hegde AS, Arivazhagan A, Santosh V, et al. PI3 kinase pathway regulated miRNome in glioblastoma: identification of miR-326 as a tumour suppressor miRNA. Mol Cancer. 2016;15(1):74.

172. Liang Z, Wu H, Xia J, Li Y, Zhang Y, Huang K, et al. Involvement of miR-326 in chemotherapy resistance of breast cancer through modulating expression of multidrug resistance-associated protein 1. Biochem Pharmacol. 2010;79(6):817-24.

173. Chen HW, Lee JY, Huang JY, Wang CC, Chen WJ, Su SF, et al. Curcumin inhibits lung cancer cell invasion and metastasis through the tumor suppressor HLJ1. Cancer Res. 2008;68(18):7428-38.

174. Battula VL, Evans KW, Hollier BG, Shi Y, Marini FC, Ayyanan A, et al. Epithelial-mesenchymal transition-derived cells exhibit multilineage differentiation potential similar to mesenchymal stem cells. Stem Cells. 2010;28(8):1435-45.

175. Taube JH, Herschkowitz JI, Komurov K, Zhou AY, Gupta S, Yang J, et al. Core epithelial-to-mesenchymal transition interactome gene-expression signature is associated with claudin-low and metaplastic breast cancer subtypes. Proc Natl Acad Sci U S A. 2010;107(35):15449-54.

176. Hurtado A, Holmes KA, Geistlinger TR, Hutcheson IR, Nicholson RI, Brown M, et al. Regulation of ERBB2 by oestrogen receptor-PAX2 determines response to tamoxifen. Nature. 2008;456(7222):663-6.

177. Firestein R, Shima K, Nosho K, Irahara N, Baba Y, Bojarski E, et al. CDK8 expression in 470 colorectal cancers in relation to beta-catenin activation, other molecular alterations and patient survival. Int J Cancer. 2010;126(12):2863-73.

178. Zhang Y, Cho YY, Petersen BL, Zhu F, Dong Z. Evidence of STAT1 phosphorylation modulated by MAPKs, MEK1 and MSK1. Carcinogenesis. 2004;25(7):1165-75.

179. Murali B, Ren Q, Luo X, Faget DV, Wang C, Johnson RM, et al. Inhibition of the Stromal p38MAPK/MK2 Pathway Limits Breast Cancer Metastases and Chemotherapy-Induced Bone Loss. Cancer Res. 2018;78(19):5618-30.

180. Yan Z, Ohuchida K, Fei S, Zheng B, Guan W, Feng H, et al. Inhibition of ERK1/2 in cancer-associated pancreatic stellate cells suppresses cancer-stromal interaction and metastasis. J Exp Clin Cancer Res. 2019;38(1):221.

181. Tan HY, Wang N, Lam W, Guo W, Feng Y, Cheng YC. Targeting tumour microenvironment by tyrosine kinase inhibitor. Mol Cancer. 2018;17(1):43.

182. Chung AS, Ferrara N. Targeting the tumor microenvironment with SRC kinase inhibition. Clin Cancer Res. 2010;16(3):775-7.

183. Guo Z, Wang G, Lv Y, Wan YY, Zheng J. Inhibition of Cdk8/Cdk19 Activity Promotes Treg Cell Differentiation and Suppresses Autoimmune Diseases. Front Immunol. 2019;10:1988.

184. Witalisz-Siepracka A, Gotthardt D, Prchal-Murphy M, Didara Z, Menzl I, Prinz D, et al. NK Cell-Specific CDK8 Deletion Enhances Antitumor Responses. Cancer Immunol Res. 2018;6(4):458-66.

APPENDIX

COPYRIGHT PERMISSIONS

For Figure 1.1

SPRINGER NATURE LICENSE
TERMS AND CONDITIONS

Jan 20, 2022

This Agreement between Bilkent University -- Pelin Ersan ("You") and Springer Nature ("Springer Nature") consists of your license details and the terms and conditions provided by Springer Nature and Copyright Clearance Center.

License Number	5233180243421
License date	Jan 20, 2022
Licensed Content Publisher	Springer Nature
Licensed Content Publication	Nature Reviews Cancer
Licensed Content Title	Modelling breast cancer: one size does not fit all
Licensed Content Author	Tracy Vargo-Gogola et al
Licensed Content Date	Dec 31, 1969
Type of Use	Thesis/Dissertation
Requestor type	academic/university or research institute
Format	print and electronic
Portion	figures/tables/illustrations
Number of figures/tables/illustrations	1

Will you be translating?	no
Circulation/distribution	1 - 29
Author of this Springer Nature content	no
Title	The Role of Mediator Complex in Tamoxifen Resistance of ER-positive Breast Cancer
Institution name	Bilkent University
Expected presentation date	Jan 2022
Portions	Figure 2
Requestor Location	Bilkent University Dept. of Mol. Bio. and Genetics SB Building, 2nd Floor Ankara, 06800 Turkey Attn: Bilkent University
Total	0.00 USD

Terms and Conditions

Springer Nature Customer Service Centre GmbH
Terms and Conditions

This agreement sets out the terms and conditions of the licence (the **Licence**) between you and **Springer Nature Customer Service Centre GmbH** (the **Licensor**). By clicking 'accept' and completing the transaction for the material (**Licensed Material**), you also confirm your acceptance of these terms and conditions.

1. Grant of License

1. 1. The Licensor grants you a personal, non-exclusive, non-transferable, world-wide licence to reproduce the Licensed Material for the purpose specified in your order only. Licences are granted for the specific use requested in the order and for no other use, subject to the conditions below.

1. 2. The Licensor warrants that it has, to the best of its knowledge, the rights to license reuse of the Licensed Material. However, you should ensure that the material you are requesting is original to the Licensor and does not carry the copyright of another entity (as credited in the published version).

1. 3. If the credit line on any part of the material you have requested indicates that it was reprinted or adapted with permission from another source, then you should also seek permission from that source to reuse the material.

2. Scope of Licence

2. 1. You may only use the Licensed Content in the manner and to the extent permitted by these Ts&Cs and any applicable laws.

2. 2. A separate licence may be required for any additional use of the Licensed Material, e.g. where a licence has been purchased for print only use, separate permission must be obtained for electronic re-use. Similarly, a licence is only valid in the language selected and does not apply for editions in other languages unless additional translation rights have been granted separately in the licence. Any content owned by third parties are expressly excluded from the licence.

2. 3. Similarly, rights for additional components such as custom editions and derivatives require additional permission and may be subject to an additional fee. Please apply to Journalpermissions@springernature.com/bookpermissions@springernature.com for these rights.

2. 4. Where permission has been granted **free of charge** for material in print, permission may also be granted for any electronic version of that work, provided that the material is incidental to your work as a whole and that the electronic version is essentially equivalent to, or substitutes for, the print version.

2. 5. An alternative scope of licence may apply to signatories of the STM Permissions Guidelines, as amended from time to time.

3. Duration of Licence

3. 1. A licence for is valid from the date of purchase ('Licence Date') at the end of the relevant period in the below table:

Scope of Licence	Duration of Licence
Post on a website	12 months
Presentations	12 months
Books and journals	Lifetime of the edition in the language purchased

4. Acknowledgement

4. 1. The Licensor's permission must be acknowledged next to the Licenced Material in print. In electronic form, this acknowledgement must be visible at the same time as the figures/tables/illustrations or abstract, and must be hyperlinked to the journal/book's

homepage. Our required acknowledgement format is in the Appendix below.

5. Restrictions on use

5. 1. Use of the Licensed Material may be permitted for incidental promotional use and minor editing privileges e.g. minor adaptations of single figures, changes of format, colour and/or style where the adaptation is credited as set out in Appendix 1 below. Any other changes including but not limited to, cropping, adapting, omitting material that affect the meaning, intention or moral rights of the author are strictly prohibited.

5. 2. You must not use any Licensed Material as part of any design or trademark.

5. 3. Licensed Material may be used in Open Access Publications (OAP) before publication by Springer Nature, but any Licensed Material must be removed from OAP sites prior to final publication.

6. Ownership of Rights

6. 1. Licensed Material remains the property of either Licensor or the relevant third party and any rights not explicitly granted herein are expressly reserved.

7. Warranty

IN NO EVENT SHALL LICENSOR BE LIABLE TO YOU OR ANY OTHER PARTY OR ANY OTHER PERSON OR FOR ANY SPECIAL, CONSEQUENTIAL, INCIDENTAL OR INDIRECT DAMAGES, HOWEVER CAUSED, ARISING OUT OF OR IN CONNECTION WITH THE DOWNLOADING, VIEWING OR USE OF THE MATERIALS REGARDLESS OF THE FORM OF ACTION, WHETHER FOR BREACH OF CONTRACT, BREACH OF WARRANTY, TORT, NEGLIGENCE, INFRINGEMENT OR OTHERWISE (INCLUDING, WITHOUT LIMITATION, DAMAGES BASED ON LOSS OF PROFITS, DATA, FILES, USE, BUSINESS OPPORTUNITY OR CLAIMS OF THIRD PARTIES), AND
WHETHER OR NOT THE PARTY HAS BEEN ADVISED OF THE POSSIBILITY OF SUCH DAMAGES. THIS LIMITATION SHALL APPLY NOTWITHSTANDING ANY FAILURE OF ESSENTIAL PURPOSE OF ANY LIMITED REMEDY PROVIDED HEREIN.

8. Limitations

8. 1. ***BOOKS ONLY:*** Where **'reuse in a dissertation/thesis'** has been selected the following terms apply: Print rights of the final author's accepted manuscript (for clarity, NOT the published version) for up to 100 copies, electronic rights for use only on a personal website or institutional repository as defined by the Sherpa guideline (www.sherpa.ac.uk/romeo/).

8. 2. For content reuse requests that qualify for permission under the STM Permissions Guidelines, which may be updated from time to time, the STM Permissions Guidelines

supersede the terms and conditions contained in this licence.

9. Termination and Cancellation

9. 1. Licences will expire after the period shown in Clause 3 (above).

9. 2. Licensee reserves the right to terminate the Licence in the event that payment is not received in full or if there has been a breach of this agreement by you.

Appendix 1 — Acknowledgements:

For Journal Content:
Reprinted by permission from [**the Licensor**]: [**Journal Publisher** (e.g. Nature/Springer/Palgrave)] [**JOURNAL NAME**] [**REFERENCE CITATION** (Article name, Author(s) Name), [**COPYRIGHT**] (year of publication)

For **Advance Online Publication papers:**
Reprinted by permission from [**the Licensor**]: [**Journal Publisher** (e.g. Nature/Springer/Palgrave)] [**JOURNAL NAME**] [**REFERENCE CITATION** (Article name, Author(s) Name), [**COPYRIGHT**] (year of publication), advance online publication, day month year (doi: 10.1038/sj.[JOURNAL ACRONYM].)

For Adaptations/Translations:
Adapted/Translated by permission from [**the Licensor**]: [**Journal Publisher** (e.g. Nature/Springer/Palgrave)] [**JOURNAL NAME**] [**REFERENCE CITATION** (Article name, Author(s) Name), [**COPYRIGHT**] (year of publication)

Note: For any republication from the British Journal of Cancer, the following credit line style applies:

Reprinted/adapted/translated by permission from [**the Licensor**]: on behalf of Cancer Research UK: : [**Journal Publisher** (e.g. Nature/Springer/Palgrave)] [**JOURNAL NAME**] [**REFERENCE CITATION** (Article name, Author(s) Name), [**COPYRIGHT]** (year of publication)

For **Advance Online Publication** papers:
Reprinted by permission from The [**the Licensor**]: on behalf of Cancer Research UK: [**Journal Publisher** (e.g. Nature/Springer/Palgrave)] [**JOURNAL NAME**] [**REFERENCE CITATION** (Article name, Author(s) Name), [**COPYRIGHT**] (year of publication), advance online publication, day month year (doi: 10.1038/sj.[JOURNAL ACRONYM])

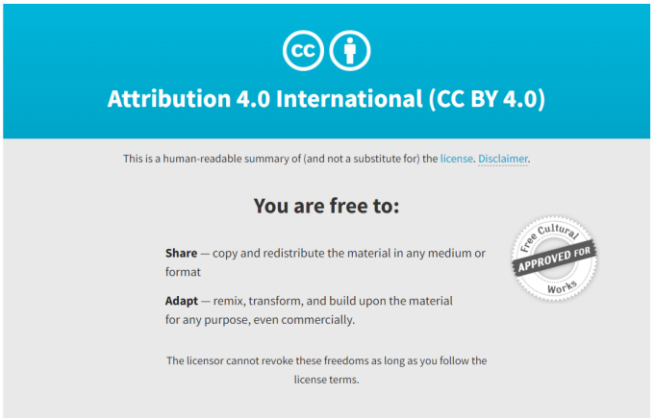
For Book content:
Reprinted/adapted by permission from [**the Licensor**]: [**Book Publisher** (e.g. Palgrave Macmillan, Springer etc) [**Book Title**] by [**Book author**(s)] [**COPYRIGHT**] (year of publication)

Other Conditions:

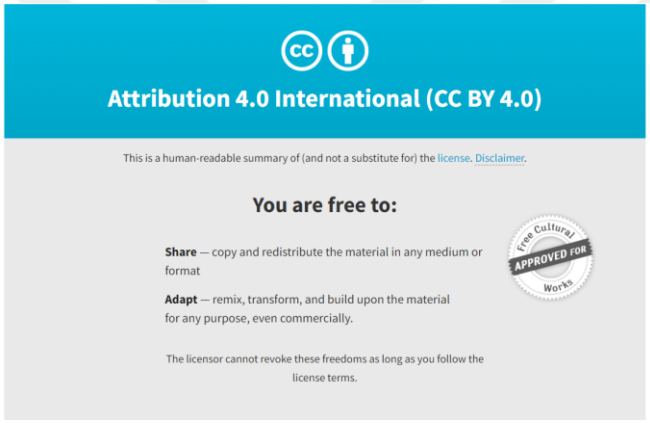
Version 1.3

Questions? customercare@copyright.com or +1-855-239-3415 (toll free in the US) or +1-978-646-2777.

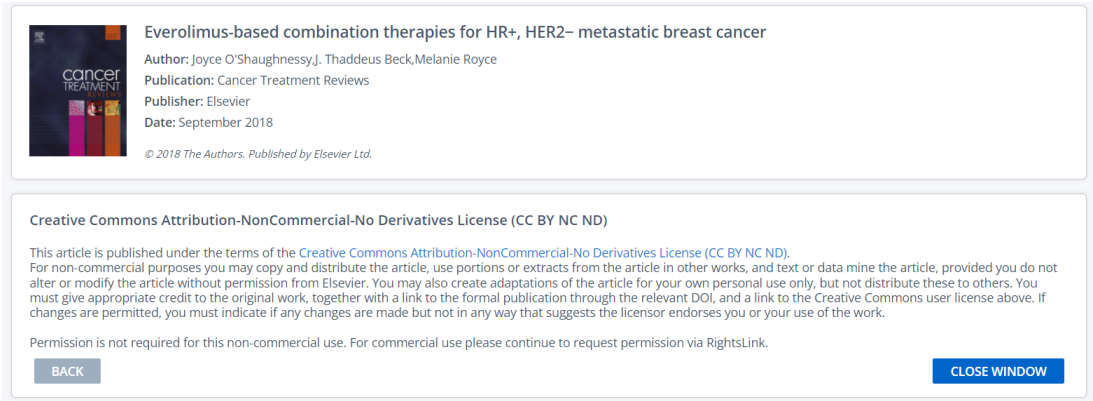
For Figure 1.2



For Figure 1.3



For Figure 1.4



For Figure 1.5

SPRINGER NATURE LICENSE
TERMS AND CONDITIONS

Jan 20, 2022

This Agreement between Bilkent University -- Pelin Ersan ("You") and Springer Nature ("Springer Nature") consists of your license details and the terms and conditions provided by Springer Nature and Copyright Clearance Center.

License Number	5233170096761
License date	Jan 20, 2022
Licensed Content Publisher	Springer Nature
Licensed Content Publication	Nature Reviews Molecular Cell Biology
Licensed Content Title	Transcription regulation by the Mediator complex
Licensed Content Author	Julie Soutourina
Licensed Content Date	Dec 6, 2017
Type of Use	Thesis/Dissertation
Requestor type	academic/university or research institute
Format	print and electronic
Portion	figures/tables/illustrations
Number of figures/tables/illustrations	1

High-res required	no
Will you be translating?	no
Circulation/distribution	1 - 29
Author of this Springer Nature content	no
Title	The Role of Mediator Complex in Tamoxifen Resistance of ER-positive Breast Cancer
Institution name	Bilkent University
Expected presentation date	Jan 2022
Portions	Figure 2
Requestor Location	Bilkent University Dept. of Mol. Bio. and Genetics SB Building, 2nd Floor Ankara, 06800 Turkey Attn: Bilkent University
Total	0.00 USD

Terms and Conditions

Springer Nature Customer Service Centre GmbH
Terms and Conditions

This agreement sets out the terms and conditions of the licence (the **Licence**) between you and **Springer Nature Customer Service Centre GmbH** (the **Licensor**). By clicking 'accept' and completing the transaction for the material (**Licensed Material**), you also confirm your acceptance of these terms and conditions.

1. Grant of License

1. 1. The Licensor grants you a personal, non-exclusive, non-transferable, world-wide licence to reproduce the Licensed Material for the purpose specified in your order only. Licences are granted for the specific use requested in the order and for no other

use, subject to the conditions below.

1. 2. The Licensor warrants that it has, to the best of its knowledge, the rights to license reuse of the Licensed Material. However, you should ensure that the material you are requesting is original to the Licensor and does not carry the copyright of another entity (as credited in the published version).

1. 3. If the credit line on any part of the material you have requested indicates that it was reprinted or adapted with permission from another source, then you should also seek permission from that source to reuse the material.

2. Scope of Licence

2. 1. You may only use the Licensed Content in the manner and to the extent permitted by these Ts&Cs and any applicable laws.

2. 2. A separate licence may be required for any additional use of the Licensed Material, e.g. where a licence has been purchased for print only use, separate permission must be obtained for electronic re-use. Similarly, a licence is only valid in the language selected and does not apply for editions in other languages unless additional translation rights have been granted separately in the licence. Any content owned by third parties are expressly excluded from the licence.

2. 3. Similarly, rights for additional components such as custom editions and derivatives require additional permission and may be subject to an additional fee. Please apply to Journalpermissions@springernature.com/bookpermissions@springernature.com for these rights.

2. 4. Where permission has been granted **free of charge** for material in print, permission may also be granted for any electronic version of that work, provided that the material is incidental to your work as a whole and that the electronic version is essentially equivalent to, or substitutes for, the print version.

2. 5. An alternative scope of licence may apply to signatories of the STM Permissions Guidelines, as amended from time to time.

3. Duration of Licence

3. 1. A licence for is valid from the date of purchase ('Licence Date') at the end of the relevant period in the below table:

Scope of Licence	Duration of Licence
Post on a website	12 months
Presentations	12 months
Books and journals	Lifetime of the edition in the language purchased

4. Acknowledgement

4. 1. The Licensor's permission must be acknowledged next to the Licenced Material in print. In electronic form, this acknowledgement must be visible at the same time as the figures/tables/illustrations or abstract, and must be hyperlinked to the journal/book's homepage. Our required acknowledgement format is in the Appendix below.

5. Restrictions on use

5. 1. Use of the Licensed Material may be permitted for incidental promotional use and minor editing privileges e.g. minor adaptations of single figures, changes of format, colour and/or style where the adaptation is credited as set out in Appendix 1 below. Any other changes including but not limited to, cropping, adapting, omitting material that affect the meaning, intention or moral rights of the author are strictly prohibited.

5. 2. You must not use any Licensed Material as part of any design or trademark.

5. 3. Licensed Material may be used in Open Access Publications (OAP) before publication by Springer Nature, but any Licensed Material must be removed from OAP sites prior to final publication.

6. Ownership of Rights

6. 1. Licensed Material remains the property of either Licensor or the relevant third party and any rights not explicitly granted herein are expressly reserved.

7. Warranty

IN NO EVENT SHALL LICENSOR BE LIABLE TO YOU OR ANY OTHER PARTY OR ANY OTHER PERSON OR FOR ANY SPECIAL, CONSEQUENTIAL, INCIDENTAL OR INDIRECT DAMAGES, HOWEVER CAUSED, ARISING OUT OF OR IN CONNECTION WITH THE DOWNLOADING, VIEWING OR USE OF THE MATERIALS REGARDLESS OF THE FORM OF ACTION, WHETHER FOR BREACH OF CONTRACT, BREACH OF WARRANTY, TORT, NEGLIGENCE, INFRINGEMENT OR OTHERWISE (INCLUDING, WITHOUT LIMITATION, DAMAGES BASED ON LOSS OF PROFITS, DATA, FILES, USE, BUSINESS OPPORTUNITY OR CLAIMS OF THIRD PARTIES), AND
WHETHER OR NOT THE PARTY HAS BEEN ADVISED OF THE POSSIBILITY OF SUCH DAMAGES. THIS LIMITATION SHALL APPLY NOTWITHSTANDING ANY FAILURE OF ESSENTIAL PURPOSE OF ANY LIMITED REMEDY PROVIDED HEREIN.

8. Limitations

8. 1. ***BOOKS ONLY:*** Where **'reuse in a dissertation/thesis'** has been selected the following terms apply: Print rights of the final author's accepted manuscript (for clarity, NOT the published version) for up to 100 copies, electronic rights for use only on a personal website or institutional repository as defined by the Sherpa guideline

(www.sherpa.ac.uk/romeo/).

8. 2. For content reuse requests that qualify for permission under the STM Permissions Guidelines, which may be updated from time to time, the STM Permissions Guidelines supersede the terms and conditions contained in this licence.

9. Termination and Cancellation

9. 1. Licences will expire after the period shown in Clause 3 (above).

9. 2. Licensee reserves the right to terminate the Licence in the event that payment is not received in full or if there has been a breach of this agreement by you.

Appendix 1 — Acknowledgements:

For Journal Content:
Reprinted by permission from [**the Licensor**]: [**Journal Publisher** (e.g. Nature/Springer/Palgrave)] [**JOURNAL NAME**] [**REFERENCE CITATION** (Article name, Author(s) Name), [**COPYRIGHT**] (year of publication)

For **Advance Online Publication papers:**
Reprinted by permission from [**the Licensor**]: [**Journal Publisher** (e.g. Nature/Springer/Palgrave)] [**JOURNAL NAME**] [**REFERENCE CITATION** (Article name, Author(s) Name), [**COPYRIGHT**] (year of publication), advance online publication, day month year (doi: 10.1038/sj.[JOURNAL ACRONYM].)

For Adaptations/Translations:
Adapted/Translated by permission from [**the Licensor**]: [**Journal Publisher** (e.g. Nature/Springer/Palgrave)] [**JOURNAL NAME**] [**REFERENCE CITATION** (Article name, Author(s) Name), [**COPYRIGHT**] (year of publication)

Note: For any republication from the British Journal of Cancer, the following credit line style applies:

Reprinted/adapted/translated by permission from [**the Licensor**]: on behalf of Cancer Research UK: : [**Journal Publisher** (e.g. Nature/Springer/Palgrave)] [**JOURNAL NAME**] [**REFERENCE CITATION** (Article name, Author(s) Name), [**COPYRIGHT**] (year of publication)

For **Advance Online Publication** papers:
Reprinted by permission from The [**the Licensor**]: on behalf of Cancer Research UK: [**Journal Publisher** (e.g. Nature/Springer/Palgrave)] [**JOURNAL NAME**] [**REFERENCE CITATION** (Article name, Author(s) Name), [**COPYRIGHT**] (year of publication), advance online publication, day month year (doi: 10.1038/sj.[JOURNAL ACRONYM])

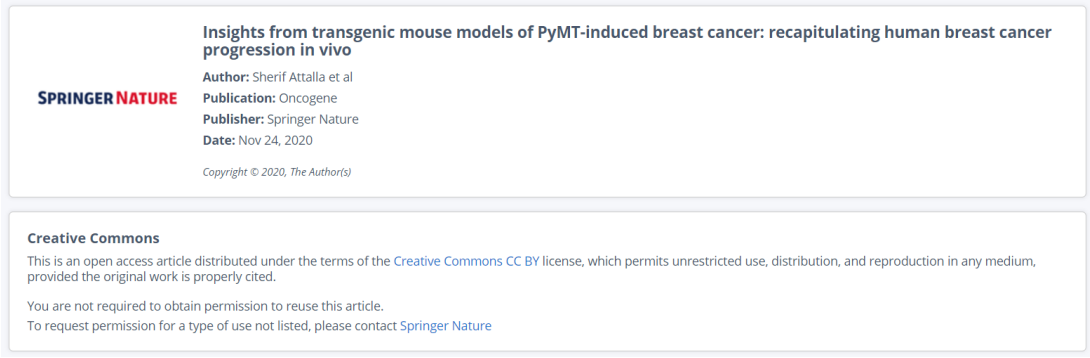
For Book content:
Reprinted/adapted by permission from [**the Licensor**]: [**Book Publisher** (e.g. Palgrave Macmillan, Springer etc) [**Book Title**] by [**Book author**(s)] [**COPYRIGHT**] (year of publication)

Other Conditions:

Version 1.3

Questions? customercare@copyright.com or +1-855-239-3415 (toll free in the US) or +1-978-646-2777.

For Figure 4.30



Insights from transgenic mouse models of PyMT-induced breast cancer: recapitulating human breast cancer progression in vivo

Author: Sherif Attalla et al
Publication: Oncogene
Publisher: Springer Nature
Date: Nov 24, 2020

Copyright © 2020, The Author(s)

Creative Commons

This is an open access article distributed under the terms of the Creative Commons CC BY license, which permits unrestricted use, distribution, and reproduction in any medium, provided the original work is properly cited.

You are not required to obtain permission to reuse this article.
To request permission for a type of use not listed, please contact Springer Nature

PUBLICATIONS

1. Clinical Cancer Research

"Reactivation of cAMP Pathway by PDE4D Inhibition Represents a Novel Druggable Axis for Overcoming Tamoxifen Resistance in ER-positive Breast Cancer"



Reactivation of cAMP Pathway by PDE4D Inhibition Represents a Novel Druggable Axis for Overcoming Tamoxifen Resistance in ER-positive Breast Cancer

Author:
Rasmi R. Mishra,Nevin Belder,Suhail A. Ansari,Merve Kayhan,Hilal Bal,Umar Raza,Pelin G. Ersan,Ünal M. Tokat,Erol Eyüpoğlu,Özge Saatci,Pouria Jandaghi,Stefan Wiemann,Ayşegül Üner,Caglar Cekic,Yasser Riazalhosseini,Özgür Şahin

Publication: Clinical Cancer Research
Publisher: American Association for Cancer Research
Date: 2018-04-15

Copyright © 2018, American Association for Cancer Research

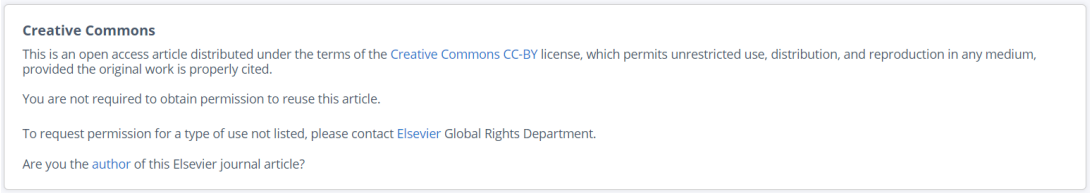
Permission Request

This reuse request is free of charge and you are not required to obtain a license.

BACK CLOSE WINDOW

2. Molecular & Cellular Proteomics (MCP)

"Systems-level Analysis Reveals Multiple Modulators of Epithelial-mesenchymal Transition and Identifies DNAJB4 and CD81 as Novel Metastasis Inducers in Breast Cancer"



Creative Commons

This is an open access article distributed under the terms of the Creative Commons CC-BY license, which permits unrestricted use, distribution, and reproduction in any medium, provided the original work is properly cited.

You are not required to obtain permission to reuse this article.

To request permission for a type of use not listed, please contact Elsevier Global Rights Department.

Are you the author of this Elsevier journal article?

3. Nature Communications

“Targeting lysyl oxidase (LOX) overcomes chemotherapy resistance in triple negative breast cancer”



SPRINGER NATURE

Targeting lysyl oxidase (LOX) overcomes chemotherapy resistance in triple negative breast cancer

Author: Ozge Saatci et al
Publication: Nature Communications
Publisher: Springer Nature
Date: May 15, 2020

Copyright © 2020, The Author(s)

Creative Commons

This is an open access article distributed under the terms of the Creative Commons CC BY license, which permits unrestricted use, distribution, and reproduction in any medium, provided the original work is properly cited.

You are not required to obtain permission to reuse this article.
To request permission for a type of use not listed, please contact Springer Nature

4. Cell Death & Differentiation

Thymidylate synthase maintains the de-differentiated state of triple negative breast cancers



SPRINGER NATURE

Thymidylate synthase maintains the de-differentiated state of triple negative breast cancers

Author: Aarif Siddiqui et al
Publication: Cell Death & Differentiation
Publisher: Springer Nature
Date: Feb 8, 2019

Copyright © 2019, The Author(s)

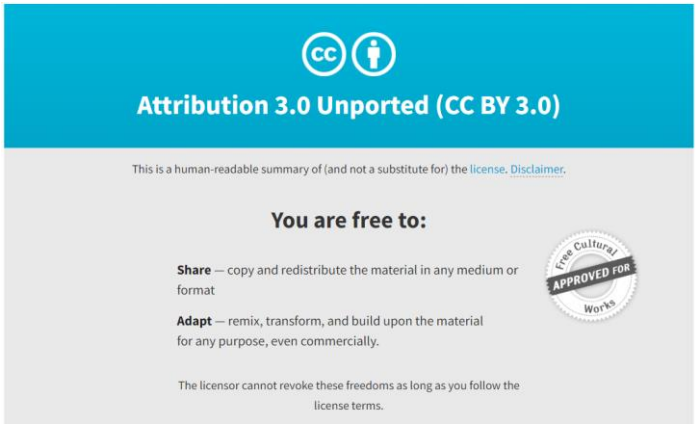
Creative Commons

This is an open access article distributed under the terms of the Creative Commons CC BY license, which permits unrestricted use, distribution, and reproduction in any medium, provided the original work is properly cited.

You are not required to obtain permission to reuse this article.
To request permission for a type of use not listed, please contact Springer Nature

5. Oncotarget

The miR-644a/CTBP1/p53 axis suppresses drug resistance by simultaneous inhibition of cell survival and epithelial-mesenchymal transition in breast cancer



6. Immunology Letters

"TLR ligand loaded exosome mediated immunotherapy of established mammary Tumor in mice"



7. Clinical & Experimental Metastasis

EACR-MRS conference on Seed and Soil: In Vivo Models of Metastasis

SPRINGER NATURE LICENSE
TERMS AND CONDITIONS

Jan 20, 2022

This Agreement between Bilkent University -- Pelin Ersan ("You") and Springer Nature ("Springer Nature") consists of your license details and the terms and conditions provided by Springer Nature and Copyright Clearance Center.

License Number	5233181123123
License date	Jan 20, 2022
Licensed Content Publisher	Springer Nature
Licensed Content Publication	Clinical & Experimental Metastasis
Licensed Content Title	EACR-MRS conference on Seed and Soil: In Vivo Models of Metastasis
Licensed Content Author	I. Teles Alves et al
Licensed Content Date	Mar 27, 2018
Type of Use	Thesis/Dissertation
Requestor type	academic/university or research institute
Format	print and electronic
Portion	full article/chapter
Will you be translating?	no

Circulation/distribution	1 - 29
Author of this Springer Nature content	yes
Title	The Role of Mediator Complex in Tamoxifen Resistance of ER-positive Breast Cancer
Institution name	Bilkent University
Expected presentation date	Jan 2022
Requestor Location	Bilkent University Dept. of Mol. Bio. and Genetics SB Building, 2nd Floor Ankara, 06800 Turkey Attn: Bilkent University
Total	0.00 USD

Terms and Conditions

Springer Nature Customer Service Centre GmbH
Terms and Conditions

This agreement sets out the terms and conditions of the licence (the **Licence**) between you and **Springer Nature Customer Service Centre GmbH** (the **Licensor**). By clicking 'accept' and completing the transaction for the material (**Licensed Material**), you also confirm your acceptance of these terms and conditions.

1. Grant of License

1. 1. The Licensor grants you a personal, non-exclusive, non-transferable, world-wide licence to reproduce the Licensed Material for the purpose specified in your order only. Licences are granted for the specific use requested in the order and for no other use, subject to the conditions below.

1. 2. The Licensor warrants that it has, to the best of its knowledge, the rights to license reuse of the Licensed Material. However, you should ensure that the material you are requesting is original to the Licensor and does not carry the copyright of another entity (as credited in the published version).

1. 3. If the credit line on any part of the material you have requested indicates that it was reprinted or adapted with permission from another source, then you should also

seek permission from that source to reuse the material.

2. Scope of Licence

2. 1. You may only use the Licensed Content in the manner and to the extent permitted by these Ts&Cs and any applicable laws.

2. 2. A separate licence may be required for any additional use of the Licensed Material, e.g. where a licence has been purchased for print only use, separate permission must be obtained for electronic re-use. Similarly, a licence is only valid in the language selected and does not apply for editions in other languages unless additional translation rights have been granted separately in the licence. Any content owned by third parties are expressly excluded from the licence.

2. 3. Similarly, rights for additional components such as custom editions and derivatives require additional permission and may be subject to an additional fee. Please apply to Journalpermissions@springernature.com/bookpermissions@springernature.com for these rights.

2. 4. Where permission has been granted **free of charge** for material in print, permission may also be granted for any electronic version of that work, provided that the material is incidental to your work as a whole and that the electronic version is essentially equivalent to, or substitutes for, the print version.

2. 5. An alternative scope of licence may apply to signatories of the STM Permissions Guidelines, as amended from time to time.

3. Duration of Licence

3. 1. A licence for is valid from the date of purchase ('Licence Date') at the end of the relevant period in the below table:

Scope of Licence	Duration of Licence
Post on a website	12 months
Presentations	12 months
Books and journals	Lifetime of the edition in the language purchased

4. Acknowledgement

4. 1. The Licensor's permission must be acknowledged next to the Licenced Material in print. In electronic form, this acknowledgement must be visible at the same time as the figures/tables/illustrations or abstract, and must be hyperlinked to the journal/book's homepage. Our required acknowledgement format is in the Appendix below.

5. Restrictions on use

5. 1. Use of the Licensed Material may be permitted for incidental promotional use and minor editing privileges e.g. minor adaptations of single figures, changes of format, colour and/or style where the adaptation is credited as set out in Appendix 1 below. Any other changes including but not limited to, cropping, adapting, omitting material that affect the meaning, intention or moral rights of the author are strictly prohibited.

5. 2. You must not use any Licensed Material as part of any design or trademark.

5. 3. Licensed Material may be used in Open Access Publications (OAP) before publication by Springer Nature, but any Licensed Material must be removed from OAP sites prior to final publication.

6. Ownership of Rights

6. 1. Licensed Material remains the property of either Licensor or the relevant third party and any rights not explicitly granted herein are expressly reserved.

7. Warranty

IN NO EVENT SHALL LICENSOR BE LIABLE TO YOU OR ANY OTHER PARTY OR ANY OTHER PERSON OR FOR ANY SPECIAL, CONSEQUENTIAL, INCIDENTAL OR INDIRECT DAMAGES, HOWEVER CAUSED, ARISING OUT OF OR IN CONNECTION WITH THE DOWNLOADING, VIEWING OR USE OF THE MATERIALS REGARDLESS OF THE FORM OF ACTION, WHETHER FOR BREACH OF CONTRACT, BREACH OF WARRANTY, TORT, NEGLIGENCE, INFRINGEMENT OR OTHERWISE (INCLUDING, WITHOUT LIMITATION, DAMAGES BASED ON LOSS OF PROFITS, DATA, FILES, USE, BUSINESS OPPORTUNITY OR CLAIMS OF THIRD PARTIES), AND
WHETHER OR NOT THE PARTY HAS BEEN ADVISED OF THE POSSIBILITY OF SUCH DAMAGES. THIS LIMITATION SHALL APPLY NOTWITHSTANDING ANY FAILURE OF ESSENTIAL PURPOSE OF ANY LIMITED REMEDY PROVIDED HEREIN.

8. Limitations

8. 1. ***BOOKS ONLY:*** Where **'reuse in a dissertation/thesis'** has been selected the following terms apply: Print rights of the final author's accepted manuscript (for clarity, NOT the published version) for up to 100 copies, electronic rights for use only on a personal website or institutional repository as defined by the Sherpa guideline (www.sherpa.ac.uk/romeo/).

8. 2. For content reuse requests that qualify for permission under the STM Permissions Guidelines, which may be updated from time to time, the STM Permissions Guidelines supersede the terms and conditions contained in this licence.

9. Termination and Cancellation

9. 1. Licences will expire after the period shown in Clause 3 (above).

9. 2. Licensee reserves the right to terminate the Licence in the event that payment is not received in full or if there has been a breach of this agreement by you.

Appendix 1 — Acknowledgements:

For Journal Content:
Reprinted by permission from [**the Licensor**]: [**Journal Publisher** (e.g. Nature/Springer/Palgrave)] [**JOURNAL NAME**] [**REFERENCE CITATION** (Article name, Author(s) Name), [**COPYRIGHT**] (year of publication)

For **Advance Online Publication papers:**
Reprinted by permission from [**the Licensor**]: [**Journal Publisher** (e.g. Nature/Springer/Palgrave)] [**JOURNAL NAME**] [**REFERENCE CITATION** (Article name, Author(s) Name), [**COPYRIGHT**] (year of publication), advance online publication, day month year (doi: 10.1038/sj.[JOURNAL ACRONYM].)

For Adaptations/Translations:
Adapted/Translated by permission from [**the Licensor**]: [**Journal Publisher** (e.g. Nature/Springer/Palgrave)] [**JOURNAL NAME**] [**REFERENCE CITATION** (Article name, Author(s) Name), [**COPYRIGHT**] (year of publication)

Note: For any republication from the British Journal of Cancer, the following credit line style applies:

Reprinted/adapted/translated by permission from [**the Licensor**]: on behalf of Cancer Research UK: : [**Journal Publisher** (e.g. Nature/Springer/Palgrave)] [**JOURNAL NAME**] [**REFERENCE CITATION** (Article name, Author(s) Name), [**COPYRIGHT**] (year of publication)

For **Advance Online Publication** papers:
Reprinted by permission from The [**the Licensor**]: on behalf of Cancer Research UK: [**Journal Publisher** (e.g. Nature/Springer/Palgrave)] [**JOURNAL NAME**] [**REFERENCE CITATION** (Article name, Author(s) Name), [**COPYRIGHT**] (year of publication), advance online publication, day month year (doi: 10.1038/sj.[JOURNAL ACRONYM])

For Book content:
Reprinted/adapted by permission from [**the Licensor**]: [**Book Publisher** (e.g. Palgrave Macmillan, Springer etc) [**Book Title**] by [**Book author**(s)] [**COPYRIGHT**] (year of publication)

Other Conditions:

Version 1.3

Questions? customercare@copyright.com or +1-855-239-3415 (toll free in the US) or +1-978-646-2777.

8. Cancer Research

“Targeting adenosine with adenosine deaminase 2 to inhibit growth of solid tumors”



Published OnlineFirst January 31, 2018; DOI: 10.1158/1078-0432.CCR-17-2776

Biology of Human Tumors

Clinical Cancer Research

Reactivation of cAMP Pathway by PDE4D Inhibition Represents a Novel Druggable Axis for Overcoming Tamoxifen Resistance in ER-positive Breast Cancer

Rasmi R. Mishra[1], Nevin Belder[1], Suhail A. Ansari[1], Merve Kayhan[1], Hilal Bal[1], Umar Raza[1], Pelin G. Ersan[1], Ünal M. Tokat[1], Erol Eyüpoğlu[1], Özge Saatci[1], Pouria Jandaghi[2,3], Stefan Wiemann[4], Ayşegül Üner[5], Caglar Cekic[1], Yasser Riazalhosseini[2,3], and Özgür Şahin[1,6]

Abstract

Purpose: Tamoxifen remains an important hormonal therapy for ER-positive breast cancer; however, development of resistance is a major obstacle in clinics. Here, we aimed to identify novel mechanisms of tamoxifen resistance and provide actionable drug targets overcoming resistance.

Experimental Design: Whole-transcriptome sequencing, downstream pathway analysis, and drug repositioning approaches were used to identify novel modulators [here: phosphodiesterase 4D (PDE4D)] of tamoxifen resistance. Clinical data involving tamoxifen-treated patients with ER-positive breast cancer were used to assess the impact of PDE4D in tamoxifen resistance. Tamoxifen sensitization role of PDE4D was tested *in vitro* and *in vivo*. Cytobiology, biochemistry, and functional genomics tools were used to elucidate the mechanisms of PDE4D-mediated tamoxifen resistance.

Results: PDE4D, which hydrolyzes cyclic AMP (cAMP), was significantly overexpressed in both MCF-7 and T47D tamoxifen-resistant (TamR) cells. Higher PDE4D expression predicted worse survival in tamoxifen-treated patients with breast cancer ($n = 469$, $P = 0.0036$ for DMFS; $n = 561$, $P = 0.0229$ for RFS) and remained an independent prognostic factor for RFS in multivariate analysis ($n = 132$, $P = 0.049$). Inhibition of PDE4D by either siRNAs or pharmacologic inhibitors (dipyridamole and Gebr-7b) restored tamoxifen sensitivity. Sensitization to tamoxifen is achieved via cAMP-mediated induction of unfolded protein response/ER stress pathway leading to activation of p38/JNK signaling and apoptosis. Remarkably, acetylsalicylic acid (aspirin) was predicted to be a tamoxifen sensitizer using a drug repositioning approach and was shown to reverse resistance by targeting PDE4D/cAMP/ER stress axis. Finally, combining PDE4D inhibitors and tamoxifen suppressed tumor growth better than individual groups *in vivo*.

Conclusions: PDE4D plays a pivotal role in acquired tamoxifen resistance via blocking cAMP/ER stress/p38-JNK signaling and apoptosis. *Clin Cancer Res; 24(8); 1987–2001. ©2018 AACR.*

Introduction

More than 70% of breast tumors express estrogen receptor alpha (ERα) and consequently receive various endocrine therapies modulating ERα (1, 2). ER-targeted therapies include (i) selective ER modulators (SERMs) like tamoxifen and raloxifene, (ii) aromatase inhibitors (AI) such as letrozole, anastrozole, and exemestane, and (iii) selective ER downregulators (SERDs) like fulvestrant. Tamoxifen is widely used as the standard first-line adjuvant therapy since its discovery in 1970 for treatment of patients with ER-positive breast cancer, particularly in premenopausal women (3, 4). Several clinical trials have showed that treatment with adjuvant tamoxifen for at least 5 years reduces the breast cancer recurrence and mortality rates by around half and one-third, respectively, throughout the first 15 years (3–5). However, approximately 20%–30% cases of high risk, advanced ER-positive breast cancer develop *de novo* or acquired resistance to tamoxifen, despite its clinical success (6).

The mechanism of tamoxifen resistance is partially understood and involves multiple factors. Most common mechanisms include the activation of several receptor tyrosine kinases (RTKs), for example, EGFR, HER2, fibroblast growth factor receptor 1 (FGFR1), and insulin-like growth factor-1 receptor (IGF-1R). This leads to enhanced activity of kinases downstream of these receptors such as extracellular-regulated kinase (ERK) 1/2, AKT, and p21-activated kinase-1 (PAK1), and promotes tumor growth and metastasis (7, 8). Furthermore, altered expressions of cell survival molecules such as c-Myc, Bad, and Bcl-2 are correlated with poor

[1]Department of Molecular Biology and Genetics, Faculty of Science, Bilkent University, Ankara, Turkey. [2]Department of Human Genetics, McGill University, Montreal, Quebec, Canada. [3]McGill University and Genome Quebec Innovation Centre, Montreal, Quebec, Canada. [4]Division of Molecular Genome Analysis, German Cancer Research Center (DKFZ), Heidelberg, Germany. [5]Department of Pathology, Faculty of Medicine, Hacettepe University, Ankara, Turkey. [6]National Nanotechnology Research Center (UNAM), Bilkent University, Ankara, Turkey.

Note: Supplementary data for this article are available at Clinical Cancer Research Online (http://clincancerres.aacrjournals.org/).

Corresponding Author: Özgür Şahin, Bilkent University, Department of Molecular Biology and Genetics, Faculty of Science, B Building SB-247, Ankara 06800, Turkey. Phone: 90-312-290-2402; Fax: 90-312-266-5097; E-mail: sahinozgur@gmail.com

doi: 10.1158/1078-0432.CCR-17-2776

©2018 American Association for Cancer Research.

Downloaded from clincancerres.aacrjournals.org on January 20, 2022. © 2018 American Association for Cancer Research.

Published OnlineFirst January 31, 2018; DOI: 10.1158/1078-0432.CCR-17-2776

Translational Relevance

Tamoxifen remains an important hormonal therapy for patients with ER-positive breast cancer; however, development of resistance is a major obstacle for therapeutic success. Therefore, there is an urgent need for identification of novel druggable targets overcoming resistance. In this study, we identified phosphodiesterase 4D (PDE4D)/cAMP/ER stress axis as a novel tamoxifen resistance mediator in ER-positive breast cancer. Tamoxifen-treated patients with breast cancer with higher PDE4D expression showed poorer distant metastasis and relapse-free survival, and higher PDE4D expression remained an independent prognostic factor in multivariate analysis. Moreover, inhibition of PDE4D by either siRNAs or pharmacologic inhibitors restored tamoxifen sensitivity both *in vitro* and *in vivo*. Overall, our study uncovered a cAMP pathway, specifically PDE4D, as a critical modulator of tamoxifen resistance, and thus paves the way for testing cAMP inducers, some of which are already FDA approved such as dipyridamole and the over-the-counter drug acetylsalicylic acid (aspirin), in tamoxifen-refractory patients with ER-positive breast cancer.

survival of patients under endocrine therapy (9, 10). In addition, involvement of noncoding RNAs, such as microRNAs (miRNAs) and long noncoding RNAs (lncRNA), in tamoxifen resistance has been described. For example, several oncogenic miRNAs, for example, miR-519 and miR-221/222 confer tamoxifen resistance (11, 12), while reexpression of miR-375, let-7, or miR-342 induce tamoxifen sensitivity via their respective mRNA target genes (11, 12). Recently, upregulation of a few lncRNAs, for example, HOTAIR and BCAR4, has also been shown to confer tamoxifen resistance (11).

With nearly 1.2 million new ER-positive breast cancer cases diagnosed in 2012 worldwide (http://www.wcrf.org/) and significant number of cases developing inevitable drug resistance, there is an immediate need for identification of novel druggable targets to overcome tamoxifen resistance. Here, we aim to identify novel mechanisms of tamoxifen resistance and thus pave the way for testing new combinations to improve survival in tamoxifen refractory, ER-positive breast cancer.

Materials and Methods

Cell culture

Human breast cancer cell lines MCF-7 and T47D were purchased from ATCC and cultured in phenol red–free DMEM (Gibco) with 10% FBS, 0.1% insulin, 50 U/mL penicillin/streptomycin, 1% nonessential amino acids (Gibco). Tamoxifen-resistant MCF-7 cells (MCF-7 TamR) were generated as described previously (12). In brief, MCF-7 and T47D TamR cells were grown in the presence of 5 μmol/L of 4-hydroxytamoxifen (Sigma-Aldrich) for 1 year. In parallel, parental MCF-7 and T47D cells were maintained under identical conditions without tamoxifen. Cells were routinely tested for mycoplasma contamination using MycoAlert detection kit (Lonza), and were authenticated by STR sequencing (Promega) at German Cancer Research Center (DKFZ). The cumulative culture length of the cells between thawing and use in the study was less than 20 passages.

Reagents and chemicals

Reagents and other chemicals including their catalog numbers are as following: tamoxifen (Sigma, T176), acetylsalicylic acid (Sigma, A5376), dipyridamole (Tocris, 691), Gebr-7b (Millipore/Calbiochem, 524748), 6-Bnz-cAMP sodium salt (Tocris, 5255), 8-pCPT-2-O-Me-cAMP-AM (Tocris, 4853), cAMPS-Sp triethylammonium salt (Tocris, 1333) and thapsigargin (Sigma, T9033), and SQ22536 (Sigma, AB120642).

Whole-transcriptome sequencing (RNA-Seq) and data analysis

Ribosomal RNA (rRNA)-depleted libraries were generated for each sample, and these sequences were multiplexed. RNA sequencing was performed for each condition (MCF-7 parental and MCF-7 TamR) in triplicates using the Illumina HiSeq 2000 platform at McGill University and Genome Quebec Innovation Centre. Details are provided in Supplementary Data.

Generation of TamR gene signature and bioinformatics analysis

Tamoxifen resistance gene signature (TamR-GS) was generated comprising of the top 417 differentially expressed mRNAs ($\log_2$ FC $\pm$ 2 and $P \leq 0.05$) between MCF-7 TamR cells and their parental counterparts. For the calculation of the TamR-GS score, the sum of z-scores of the downregulated genes in the TamR-GS was subtracted from the sum of z-scores of the upregulated genes for each patient. This method of calculating a gene signature score by using the mRNA expression data has been reported previously (13). In survival analysis and GSEA, patients were separated either from the median or from 25th percentile, as low and high PDE4D or TamR-GS scorers based on their PDE4D expression or the TamR-GS score, respectively. Details of the bioinformatic analysis are provided in Supplementary Data.

qRT-PCR analysis

Total RNA was extracted from cultured cells using TRIsure (Bioline), and cDNAs were generated using RevertAid RT Reverse Transcription Kit (Life Technologies). qRT-PCR analysis was performed with gene-specific primers using LightCycler 480 SYBR Green I Master kit (Roche). *HPRT1*, *GAPDH*, and *ACTB* were used as housekeeping genes. The average C_t value was calculated from triplicates of each sample, and the relative mRNA expression was determined. Sequences of the qRT-PCR primers are listed in Supplementary Table S1.

Transient transfection with siRNAs and overexpression vectors

PDE4D-specific siRNAs were purchased from Dharmacon (Supplementary Table S2). Transfections were done with 20 nmol/L siRNA using Lipofectamine 2000 (Invitrogen) according to manufacturer's instructions. PDE4D cDNA (NM_006203.4) present in pcDNA3.1+/C-(K) DYK mammalian expression vector (GenScript) was used for overexpression experiments. Briefly, 50 ng (for 96-well plate) or 500 ng (for 6-well plate) of PDE4D plasmid DNA was transiently transfected using Effectene transfection reagent (Qiagen).

Inhibitor treatments, cell proliferation and apoptosis assays

Details of the inhibitor treatments, cell proliferation, and apoptosis assays are provided in Supplementary Materials and Methods section in Supplementary Data.

Downloaded from clincancerres.aacrjournals.org on January 20, 2022. © 2018 American Association for Cancer Research.

Published OnlineFirst January 31, 2018; DOI: 10.1158/1078-0432.CCR-17-2776

Western blotting

Total protein was extracted using RIPA buffer (150 mmol/L NaCl, 50 mmol/L Tris base pH 8.0, 1 mmol/L EDTA, 0.5% sodium deoxycholate, 1% NP40, 0.1% SDS, 1 mmol/L DTT, and 1 mmol/L Na_3VO_4) supplemented with Complete Protease Inhibitor (Roche). Protein concentrations were measured using BCA Protein Assay (Thermo Scientific). Equal amounts of protein lysates (15–20 μg) were separated on a 10% SDS-PAGE, transferred onto polyvinylidene difluoride membrane (Bio-Rad) and incubated with primary antibodies (Supplementary Table S3). The blots were developed using enhanced chemiluminescence (ECL) detection kit (Amersham Biosciences) after incubation with horseradish peroxidase–conjugated secondary antibody. β-Actin was used as a loading control.

Intracellular cAMP measurements

To measure intracellular cAMP levels, 10,000 cells were seeded per well in 96-well plates. Following day, cells were treated with PDE4D inhibitors (dipyridamole or Gebr-7b or aspirin) alone or vehicle-only or in combination with tamoxifen (5.0 μmol/L) for 20 minutes. After treatment, cells were washed with PBS and incubated with 100-μL ice-cold 0.6 mol/L perchloric acid followed by 15 μL 2.5 mol/L potassium carbonate for neutralization. Cells were incubated on ice for 30 minutes and then centrifuged at 13,000 rpm to collect the clear lysate. Twenty microliters of the clear lysate was used for measurement of cAMP concentration with the LANCE Ultra cAMP detection reagents (PerkinElmer) according to the manufacturer's protocol.

Mouse xenograft studies

All animal work was approved by the Institutional Animal Care and Use Committee of Bilkent University. In xenograft studies, female athymic nude mice were used. All mice were maintained under a temperature-controlled environment with a 12-hour light/dark cycle and received a standard diet and water *ad libitum*. Primary tumors with MCF-7 TamR cells were developed in 6- to 8-week-old mice. Slow release estradiol pellets (0.36 mg, 60 days; Innovative Research of America) were implanted subcutaneously (s.c) at the nape of the neck one day before injection. A total of 1×10^7 MCF-7 TamR cells were injected subcutaneously into both left and right sides of mammary fat pads. Tumor growth was regularly monitored, and size measurements were performed two times per week. Tumor volume was calculated using the formula (length × width^2)/2. After tumor size reached 100 mm^3, mice were randomly divided into 8 groups, with 5 tumors per group. Animals were treated with vehicle, tamoxifen (2 mg/kg in corn oil, by oral gavage), dipyridamole (15 mg/kg in PBS: PEG 400 (1: 1), daily intraperitoneally), Gebr-7b (3 μg/kg in 0.5 % methyl 2-hydroxyethyl cellulose+0.005% DMSO, daily via intraperitoneally), aspirin [100 mg/kg in PBS: PEG 400 (1: 1), daily intraperitoneally) or combinations. The body weight and tumor size of each mouse were recorded twice a week. Mice were sacrificed 28 days after initiation of the treatment, and the tumors were collected and stored for subsequent analysis.

IHC

Tumor samples isolated from the MCF-7 TamR xenografts were fixed in 10% formalin and processed into paraffin blocks. Histologic sections were taken with 5-μm thickness and deparaffinized. All sections were prepared for Haematoxylin & Eosin, Ki-67 (Dako, catalog no: 7240) and ApopTag Fluorescein *In Situ* Apoptosis Detection Kit (Millipore SiGMa), staining according to the standard procedures.

Statistical analysis

All statistical analyses were performed using either Student *t* test or one-way ANOVA (multiple comparisons) in GraphPad Prism 6 (GraphPad Software, Inc). All results were represented as mean ± standard deviation (SD) and obtained from three independent experiments. The Kaplan–Meier survival plot, HR, and log-rank *P* values were calculated and plotted using GraphPad Prism. The differences were considered statistically significant if $P < 0.05$ and indicated by, *, $P < 0.05$; **, $P < 0.01$.

Results

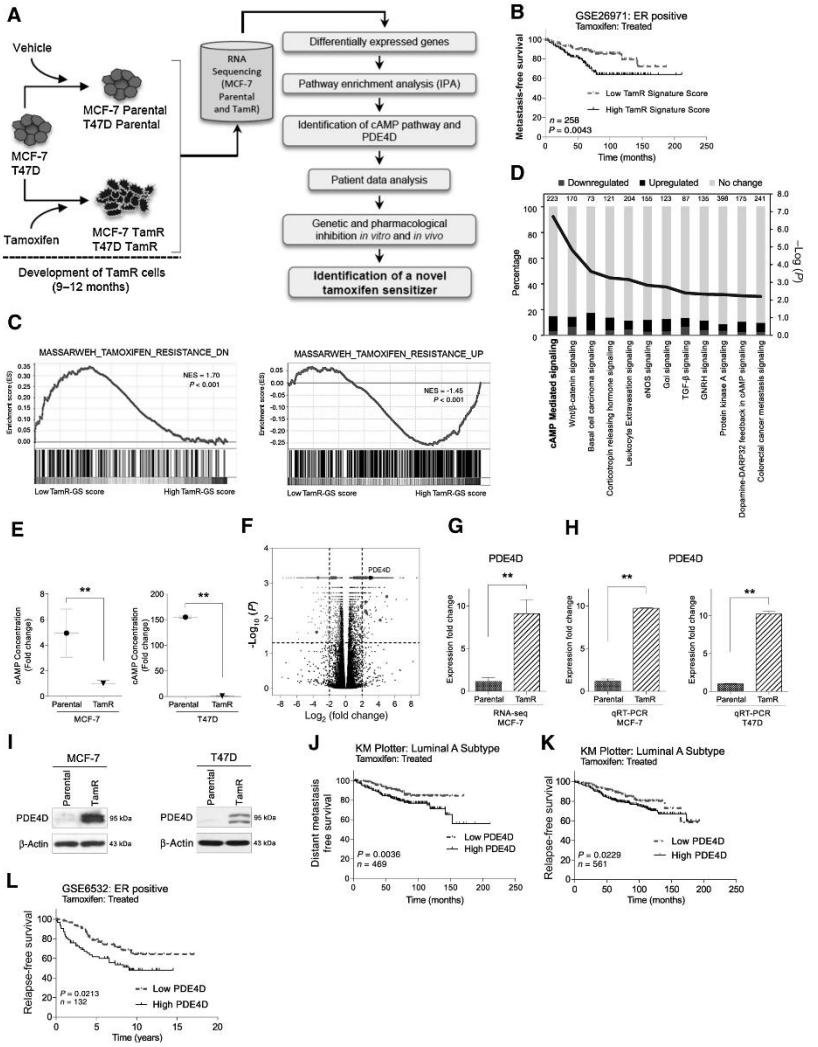
Whole-transcriptome sequencing combined with pathway enrichment and patient data analyses identify PDE4D as a potential mediator of tamoxifen resistance.

We had previously developed, characterized, and reported an acquired tamoxifen-resistant model of MCF-7 cell line (MCF-7 TamR cells and their sensitive counterpart MCF-7 parental) to identify miRNA regulators of tamoxifen resistance (12, 14). To further understand the molecular underpinnings of tamoxifen resistance, and to identify novel druggable targets in ER-positive breast cancer, we performed whole-transcriptome sequencing in these cells, and derived a tamoxifen resistance gene signature (TamR-GS) comprising the most differentially expressed mRNAs ($\log_2$FC ±2 and $P \leq 0.05$; 417 genes; Supplementary Table S4) between sensitive and resistant cells (Fig. 1A). To examine the clinical relevance of our tamoxifen-resistant cell line and the TamR-GS, we applied this signature to a gene expression profiling data of tumors obtained from patients treated with tamoxifen (GEO dataset GSE26971), and assigned each patient a TamR-GS score by subtracting the sum of *z*-scores of the downregulated genes in the TamR-GS from the sum of z-scores of the upregulated genes (see Materials and Methods for details). We observed that the patients with high TamR-GS scores showed poor metastasis-free survival (MFS) as compared with their counterparts with low TamR-GS score (Fig. 1B), confirming the clinical relevance of our cell line. Furthermore, we performed gene-set enrichment analysis (GSEA) after separating tamoxifen-treated, ER-positive patients from GSE22220 as low or high TamR-GS scorers and found that genes downregulated in tamoxifen-resistant xenografts were significantly enriched in patients having low TamR-GS scores while genes upregulated in the same xenografts were significantly enriched in patients having high TamR-GS scores, further supporting the validity of our tamoxifen-resistant cells (Fig. 1C). Ingenuity Pathway Analysis (IPA) indicated that the most significantly enriched canonical pathway in MCF-7 TamR cells compared with their parental cells was cAMP-mediated signaling ($P < 8.77 \times 10^{-8}$; Fig. 1D). Therefore, we measured the cellular cAMP levels in sensitive and resistant derivatives of MCF-7 and of an additional cell line, T47D, which has recently been developed and characterized in our laboratory (Supplementary Fig. S1A–S1D). We observed that the TamR derivatives of both cell lines have markedly lower cellular cAMP levels compared with their sensitive counterparts (Fig. 1E). These observations confirmed our pathway analysis results, and suggest a possible involvement of cAMP pathway in acquired tamoxifen resistance.

Investigating the mechanisms responsible for the observed deregulation of cAMP pathway, we examined the expression of genes associated with this pathway and observed that majority of

Downloaded from clincancerres.aacrjournals.org on January 20, 2022. © 2018 American Association for Cancer Research.

Published OnlineFirst January 31, 2018; DOI: 10.1158/1078-0432.CCR-17-2776



Downloaded from clincancerres.aacrjournals.org on January 20, 2022. © 2018 American Association for Cancer Research.

Published OnlineFirst January 31, 2018; DOI: 10.1158/1078-0432.CCR-17-2776

these genes (25 of 33 with differential expression) are upregulated in TamR cells (big gray circles in Fig. 1F and PDE4D as black circle), and three of them were validated by qRT-PCR (Supplementary Fig. S2A). Two phosphodiesterases; PDE10A (32.4-fold; $P < 0.002$) and PDE4D (9.1-fold; $P < 0.0007$) were among the most significantly upregulated genes in MCF-7 TamR cells (Supplementary Fig. S2A; Fig. 1G), which are amenable for therapeutic intervention. PDE10A can hydrolyze both cAMP and cGMP, whereas PDE4D is a cAMP-specific phosphodiesterase and thus both are important regulators of cAMP signaling (15). However, siRNA-mediated silencing of PDE10A in MCF-7 TamR did not restore tamoxifen sensitivity (Supplementary Fig. S2B). On the other hand, qRT-PCR and Western blotting (WB) validated the substantial upregulation of PDE4D in both MCF-7 TamR and T47D TamR cells compared with their sensitive counterparts (Fig. 1H and I), and siRNA-mediated knockdown resulted in tamoxifen sensitization as described below. Therefore, we focused on the role of PDE4D, but not that of PDE10A, in tamoxifen resistance.

To determine whether expression of PDE4D is associated with tamoxifen resistance in breast cancer, we first examined PDE4D expression in tamoxifen-treated luminal A breast cancer patients ($n = 469$) using KM plotter tool (16). We found a significant association between higher PDE4D expression and poorer distant metastasis-free survival (DMFS; $P = 0.0036$; $n = 469$) in tamoxifen-treated patients with luminal A breast cancer (Fig. 1J). We also found a significant association between higher PDE4D expression and poorer relapse-free survival (RFS; $P = 0.029$; $n = 561$) in tamoxifen-treated patients (Fig. 1K and L). Particularly, prognostic effect of PDE4D expression was specific to tamoxifen treatment, as high or low PDE4D expression alone could not significantly predict survival in systemically untreated (no treatment received) luminal A patients (Supplementary Fig. S3A and S3B) or patients who did not receive endocrine therapy, but may have received chemotherapy (Supplementary Fig. S3C and D). Notably, PDE4D expression remained an independent prognostic factor in the multivariate analysis by using an expression profiling dataset of tamoxifen-treated patients with breast cancer, GSE6532 (Supplementary Table S5). Overall, our results demonstrate that there is an inverse correlation between cellular cAMP and PDE4D levels, and PDE4D expression has an independent prognostic role in tamoxifen-treated patients with luminal A breast cancer. These results suggested that PDE4D might regulate tamoxifen resistance in breast cancer.

Genetic or pharmacologic inhibition of PDE4D resensitizes tamoxifen-resistant breast cancer cells *in vitro*

To test whether modulating PDE4D expression can overcome tamoxifen resistance, siRNA-mediated knockdown of PDE4D was carried out in both MCF-7 TamR and T47D TamR cells using two different siRNA sequences, and cell proliferation was assessed. The efficiency of PDE4D knockdown was validated by qRT-PCR and Western blot analysis (Supplementary Fig. S4A and S4B). Silencing of endogenous PDE4D restored sensitivity to tamoxifen in both TamR cells (Fig. 2A and B). To further test whether PDE4D could drive tamoxifen resistance *in vitro*, a PDE4D overexpression construct was transiently transfected into MCF-7 and T47D parental cells (Fig. 2C), and these cells were subjected to a cell proliferation assay, which showed significantly increased cell proliferation in PDE4D-transfected cells as compared with control cells (empty vector) in the presence of tamoxifen (Fig. 2D). Next, we sought to examine the effects of pharmacologic inhibition of PDE4D via PDE4D inhibitors (PDE4Is) on tamoxifen sensitization by using Gebr-7b, a highly potent and specific PDE4D inhibitor (17), and dipyridamole (Dipy), a nonselective PDE inhibitor predicted to be a PDE4D inhibitor in our Ingenuity Pathway Analysis (IPA). To examine the effects of pharmacologic inhibition of PDE4D on tamoxifen sensitization, MCF-7 TamR, and T47D TamR cells were treated with dipyridamole or Gebr-7b in the absence and presence of tamoxifen. Combinatorial treatment (tamoxifen with either of the examined PDE4Is) inhibited cell growth in a dose-dependent manner for both dipyridamole (Fig. 2E and F) and Gebr-7b (Fig. 2G and H) in both TamR cell lines. Notably, among the two PDE4Is, Gebr-7b was more potent and showed stronger proliferation inhibitory effect together with tamoxifen at doses as low as 10 ng/mL, which is in agreement with the selective inhibitory effect of Gebr-7b on PDE4D. Altogether, our results demonstrate that inhibition of PDE4D activity acts as a tamoxifen sensitizer in tamoxifen-resistant breast cancer cells.

Elevation of cAMP levels overcomes tamoxifen resistance and is necessary for PDE4D inhibition–mediated tamoxifen sensitization

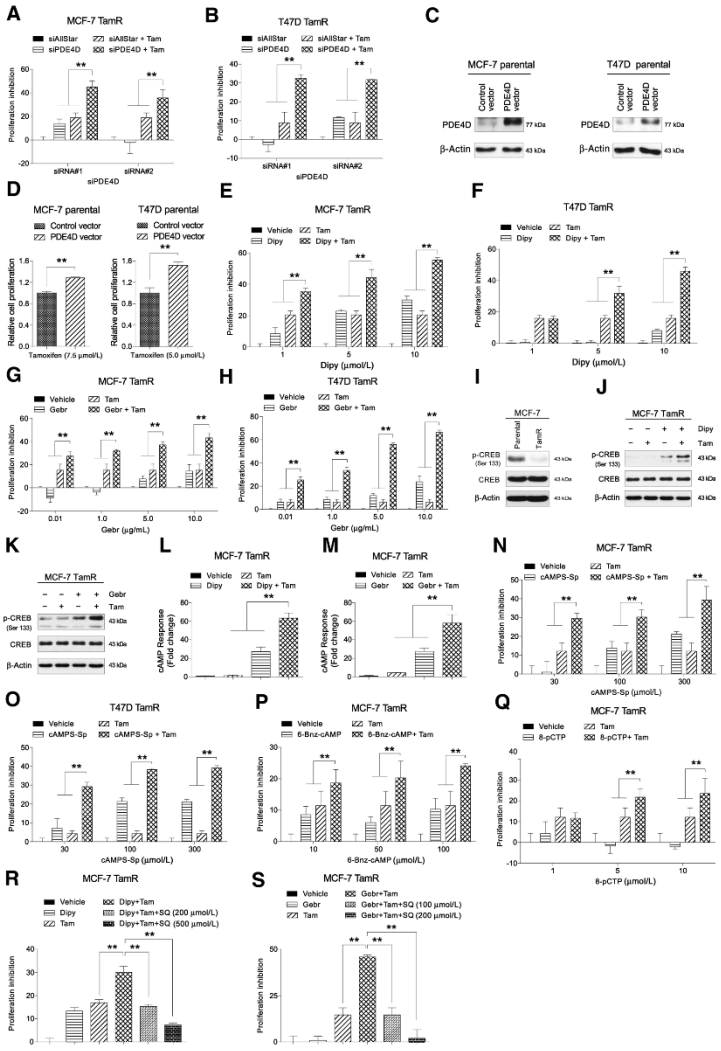
cAMP binds to and activates cAMP-dependent protein kinase A (PKA) and Rap guanine nucleotide-exchange factor 3 (RAPGEF3), more commonly known as EPAC (exchange protein directly activated by cAMP; refs. 18, 19). Furthermore, cAMP induction and thus activated PKA and EPAC induce phosphorylation of the transcription factor cAMP response element-binding protein (CREB) at Ser133 (20). In line with these reports, we observed significantly higher levels of phosphorylated CREB (p-CREB) in parental cells compared with TamR cells (Fig. 2I) corresponding to higher cAMP levels (Fig. 1E). As PDE4D is a cAMP-specific phosphodiesterase, we tested whether pharmacologic inhibition of PDE4D increases cellular cAMP levels and increases the phosphorylation of CREB. We observed an increase

Figure 1.

Whole-transcriptome sequencing combined with pathway enrichment and patient data analyses identify PDE4D as a potential mediator of tamoxifen resistance. **A,** Workflow of the identification and validation of PDE4D as a novel modulator of tamoxifen resistance. Whole-transcriptome analysis followed by pathway enrichment, *in vitro*, and *in vivo* assays and analyses of clinical data identify cAMP pathway and its component PDE4D as novel regulator of tamoxifen resistant in MCF-7 cells. **B,** Association of high and low TamR signature score with metastasis-free survival (MFS) in patients with breast cancer treated with tamoxifen validating the clinical relevance of our TamR cell line. **C,** Enrichment plots of tamoxifen-treated ER-positive patient tumors from GSE22226 with low and high TamR-GS scores. **D,** Ingenuity Pathway Analysis (IPA) of significantly enriched pathways (z-score >±1) in MCF-7 TamR cells compared with the parental MCF-7 cells. **E,** Intracellular levels of cAMP in parental MCF-7 and T47D cells compared with MCF-7 TamR and T47D TamR cells, respectively. **F,** Volcano plot showing significantly differentially expressed genes in MCF-7 TamR cells compared with parental ones. The genes belonging to cAMP signaling are shown as big gray circles and PDE4D is highlighted with a big black circle. **G,** PDE4D expression in MCF-7 TamR cells compared with parental MCF-7 cells in RNA-Seq data. FPKM values were used to calculate expression fold change in RNA-Seq data. **H,** qRT-PCR validations of PDE4D upregulation in TamR cells. **I,** Western blot analysis of PDE4D expression in parental and TamR MCF-7 and T47D cells. β-Actin was used as a loading control. **J–L,** DMFS (**J**), and RFS (**K**), and RFS (**L**; univariate analysis) of patients with luminal A breast cancer who underwent tamoxifen therapy with respect to the PDE4D expression.

Downloaded from clincancerres.aacrjournals.org on January 20, 2022. © 2018 American Association for Cancer Research.

Published OnlineFirst January 31, 2018; DOI: 10.1158/1078-0432.CCR-17-2776



Downloaded from clincancerres.aacrjournals.org on January 20, 2022. © 2018 American Association for Cancer Research.

Published OnlineFirst January 31, 2018; DOI: 10.1158/1078-0432.CCR-17-2776

in the phosphorylated CREB (Fig. 2J and K) and intracellular cAMP levels (Fig. 2L and M; Supplementary Fig. S5A and S5B) in both MCF-7 and T47D TamR cells when treated with dipyridamole or Gebr-7b. Interestingly addition of tamoxifen along with dipyridamole or Gebr-7b led to further increase in p-CREB and cAMP levels (Fig. 2J–M).

Next, we tested whether elevated cAMP levels by PDE4D inhibition will sensitize resistant cells to tamoxifen by using stable cell–permeable cAMP analogues (21). Treatment with general cAMP analogue, cAMPS-Sp, triethylammonium salt (cAMPS-Sp) resulted in sensitization of both MCF-7 TamR and T47D TamR cells to tamoxifen in a dose-dependent manner (Fig. 2N and O). Treatment with PKA-specific analogue (6-Bnz-cAMP sodium salt) or EPAC- specific analogue (8-pCPT-2-O-Me-cAMP-AM) also sensitized cells to tamoxifen in a dose-dependent manner (Fig. 2P and Q). To further prove that the sensitizer role of PDE4D in tamoxifen resistance is due to its ability to increase cAMP levels, MCF-7 TamR cells were pretreated with SQ22536, a specific adenylyl cyclase inhibitor, to prevent cAMP accumulation even in the presence of PDE4D inhibitors and tamoxifen. SQ22536 completely reversed the sensitization of resistant cells by both dipyridamole (Fig. 2R) and Gebr-7b (Fig. 2S) in a dose-dependent manner. Overall, these results suggest that PDE4D reduces intracellular cAMP to cause tamoxifen resistance.

Activation of stress-related kinases downstream of cAMP leads to apoptosis and tamoxifen sensitization

Elevated cAMP levels are known to activate the stress-related kinases (p38 and JNK) and subsequently lead to phosphorylation and activation of CREB (18, 22). Importantly, PI3K pathway crosstalks with cAMP signaling (23), and activated AKT was shown to play a critical role in endocrine resistance (14). Therefore, we initially examined the basal expression and phosphorylation levels of JNK, p38/SAPK and AKT in parental and tamoxifen-resistant cells. Western blot analysis showed that phosphorylation levels of JNK and p38 were significantly reduced while those of AKT were upregulated in TamR cells compared with the parental ones in both MCF-7 and T47D cells (Fig. 3A; Supplementary Fig. S6A). To test the effects of elevated cAMP on the phosphorylation status of JNK and p38 proteins, MCF-7 TamR cells were treated with PDE4D siRNA or cAMP analogue (cAMPS-Sp). Elevated levels of cAMP resulted in activation of JNK and p38 proteins. Interestingly, p-JNK and p-p38 signals were further enhanced in the treatment groups combined with tamoxifen (Fig. 3B and C). Inhibition of PDE4D via treatment with dipyridamole or Gebr-7b also resulted in similar increase in p-JNK and p-p38 as in case of cAMP-Sp or PDE4D siRNA (Fig. 3D and E). Significant decrease in phosphorylated AKT (both Thr-308 and Ser-473) levels was observed upon treatment with PDE4D siRNA, cAMPS-Sp, dipyridamole, and Gebr-7b, especially when combined with tamoxifen (Fig. 3B–E). These results suggest that elevated cAMP levels upon PDE4D inhibition activates JNK and p38 signaling and inhibits AKT activation.

As AKT pathway is a major regulator of cell survival, and PDE4D is a potential oncogenic protein regulating cancer cell proliferation and apoptosis (24), apoptosis levels were evaluated where MCF-7 TamR cells were treated with dipyridamole or Gebr-7b alone or in combination with tamoxifen for 72 hours. Pharmacologic inhibition of PDE4D in combination with tamoxifen activated cleavage of caspase-7 and PARP proteins and induced apoptosis (Fig. 3F–I). Finally, treatment with JNK inhibitor SP600125 or p38 inhibitor SB203580 completely reversed the measurable effects of PDE4Is on proliferation inhibition and sensitization to tamoxifen, confirming the mediatory roles of JNK or p38 pathways in this context (Fig. 3J and K).

PDE4D inhibition–mediated cAMP induction leads to ER stress conferring tamoxifen sensitivity

One of the well-known mediators of p38/JNK–induced apoptosis is activation of unfolded protein response (UPR)/ER stress pathway (25). Therefore, we examined whether elevated PDE4D activity regulates ER stress response to cause tamoxifen resistance. We observed that activated inositol-requiring enzyme 1α (IRE1α), protein kinase RNA-like ER kinase (PERK), and eukaryotic translation initiator factor 2α (eIF2α) levels were significantly reduced in both MCF-7 TamR and T47D TamR cells compared with their parental counterparts (Fig. 3L; Supplementary Fig. S6B). We then examined possible consequences of PDE4D inhibition on ER stress pathway. Notably, treatment with PDE4D siRNAs or with a cell-permeable cAMP analogue (cAMPS-Sp) resulted in activation of IRE1α, PERK and eIF2α proteins, especially when combined with tamoxifen (Fig. 3M and N). Similar results were obtained with pharmacologic inhibition of PDE4D with dipyridamole or Gebr-7b (Fig. 3O and P).

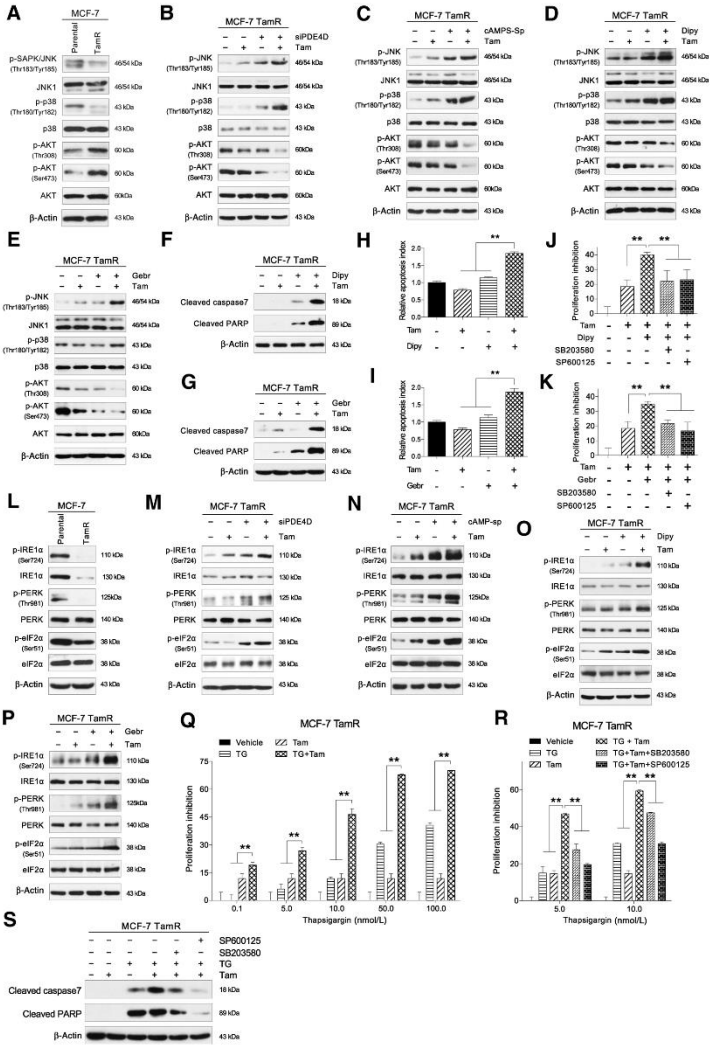
To further prove that induction of ER stress is directly involved in tamoxifen sensitization, we investigated the effects of a well-known ER stress inducer thapsigargin (TG) (26) on tamoxifen sensitization in MCF-7 TamR cells. While a certain level of proliferation inhibition was observed with thapsigargin alone, combination of thapsigargin with tamoxifen further inhibited cell proliferation (Fig. 3Q). Importantly, the blockade of JNK or p38 pathways by SB203580 or SP600125 reversed the combinatorial

Figure 2.

Inhibition of PDE4D overcomes tamoxifen resistance and increasing cAMP levels is necessary for PDE4D inhibition–mediated tamoxifen sensitization. **A** and **B,** Cell proliferation of tamoxifen-resistant cells MCF-7 TamR (**A**) and T47D TamR (**B**) transfected with two different siRNA sequences against PDE4D in the absence and presence of tamoxifen. The concentrations of tamoxifen used were 7.5 μmol/L and 5.0 μmol/L for MCF-7 TamR and T47D TamR cells, respectively. **C,** PDE4D overexpression was detected using DYKDDDDK tagged antibody in parental MCF-7 and T47D cells. Predicted molecular weight of overexpressed protein is 77 KDa (**D**) Cell proliferation after ectopic expression of PDE4D in parental MCF-7 and T47D cells. **E–H,** Tamoxifen sensitization with pharmacologic PDE4D inhibition with different doses of PDE inhibitor (dipyridamole) and PDE4D-specific inhibitor (Gebr-7b) in MCF-7 TamR (**E** and **G**) and T-47D TamR (**F** and **H**) cells. **I,** Western blot analysis showing reduced p-CREB in MCF-7 TamR cells relative to parental cells. β-Actin was used as a loading control. **J** and **K,** Western blot analysis of p-CREB in MCF-7-TamR cells treated with tamoxifen (5.0 μmol/L) in combination with PDE inhibitor (dipyridamole; **J**) and PDE4D inhibitor (Gebr-7b; **K**), respectively. **L–M,** Intracellular cAMP levels in MCF-7 TamR cells upon treatment with tamoxifen (5.0 μmol/L) in combination with PDE inhibitor (dipyridamole) (**L**) and PDE4D inhibitor (Gebr-7b; **M**), respectively. **N–Q,** Tamoxifen sensitization with different doses of general cAMP analogue (cAMP-Sp; **N** and **O**), PKA-specific analogue (6-Benz-cAMP; **P**) and EPAC-specific analogue (8-pCPT-2-O-Me-cAMP; **Q**) in the presence of 7.5 μmol/L tamoxifen. **R** and **S,** Cell proliferation of the resistant MCF-7 cells pretreated with SQ22536, a specific cAMP inhibitor, in combination with tamoxifen and PDE inhibitor (dipyridamole; **R**) and PDE4D inhibitor (Gebr-7b; **S**). Dipy: dipyridamole, Gebr: Gebr-7b, 8-pCPT: 8-pCPT-2-O-Me-cAMP.

Downloaded from clincancerres.aacrjournals.org on January 20, 2022. © 2018 American Association for Cancer Research.

Published OnlineFirst January 31, 2018; DOI: 10.1158/1078-0432.CCR-17-2776



Downloaded from clincancerres.aacrjournals.org on January 20, 2022. © 2018 American Association for Cancer Research.

Published OnlineFirst January 31, 2018; DOI: 10.1158/1078-0432.CCR-17-2776

effect of thapsigargin and tamoxifen on the proliferation inhibition (Fig. 3R) and apoptosis (Fig. 3S), establishing JNK/p38 signaling as the mediator of ER stress-induced tamoxifen sensitization. Taken together, our results demonstrate that pharmacologic blockade of PDE4D elevates cAMP levels, which results in cAMP-dependent activation of ER stress downstream kinases, leading to apoptosis in tamoxifen-resistant cells.

Pharmacologic blockade of PDE4D by dipyridamole or Gebr-7b overcomes tamoxifen resistance *in vivo*

To examine whether targeting PDE4D overcomes tamoxifen resistance *in vivo*, xenografts using tamoxifen resistant MCF-7 TamR cells were generated. The dipyridamole or Gebr-7b combination with tamoxifen inhibited the growth of the MCF-7 TamR tumors in nude mice compared to the vehicle or single-agent treatments (Fig. 4A and B). Tumor weights were also significantly less in combination-treated groups as compared with vehicle or individual treatments (Fig. 4C). While the expression level of Ki-67, a marker of cell proliferation, was markedly reduced, fluorescence-based TUNEL assay showed an increased apoptosis in combination treatments with tamoxifen and PDE4Is (Fig. 4D and E). These results demonstrate that pharmacologic inhibition of PDE4D results in tamoxifen sensitization in resistant tumors *in vivo*.

Aspirin overcomes tamoxifen resistance via increasing cAMP levels and activation of ER stress–mediated p38/JNK signaling leading to apoptosis

Although there are several resistance mechanisms put forward for tamoxifen resistance, one of the major challenges is to identify druggable targets which may help rapid translation into clinic. Our IPA results predicted that acetylsalicylic acid (ASA), commonly known as aspirin, could be a potential PDE4D inhibitor. Analysis of disease-associated and drug-induced phenotypes in terms of their differential gene expression profiles can predict the cytotoxic effect of a drug on the model system being used. Therefore, we analyzed our TamR-GS based on its correlation with the aspirin-responsive genes (provided in Connectivity map analysis; ref. 27). As shown in Fig. 5A, the genes upregulated in our TamR-GS are significantly downregulated and vice versa by aspirin treatment in MCF-7 cells ($P = 0.0004$; details are given in Methods). This suggests that resistance phenotype can be reversed by aspirin treatment, that is, aspirin might be repositioned to treat tamoxifen resistance. Importantly, such a negative correlation was not observed with other COX inhibitors and lapatinib, an EGFR/HER2 inhibitor, ($P = 0.053$, $P = 0.655$, $P = 0.12$ for piroxicam, diclofenac, and lapatinib, respectively), suggesting that the therapeutic effect of aspirin on tamoxifen resistance might not rely on its inhibitory action on COX pathway. Rather, it could be due to COX-independent activities, one of which could be PDE4D inhibition as predicted by IPA. We further tested potential clinical effects of aspirin treatment by evaluating the correlation between TamR-GS and the expression of aspirin-responsive genes generated from GSE76583 (28) in patients treated with tamoxifen. We observed a significant negative correlation between the expression of TamR-GS and aspirin-responsive genes in tamoxifen-treated patients ($r = -0.21$, $P = 0.0004$; Fig. 5B). Our analysis suggests that tamoxifen-resistant patients could potentially be responsive to aspirin treatment by restoring aspirin-responsive genes which are expressed at low levels. All these results prompted us to test whether aspirin can act as tamoxifen sensitizer, as seen with PDE4D inhibition. Therefore, we treated both MCF-7 TamR and T47D TamR cells with increasing concentration of aspirin alone or in combination with tamoxifen for 72 hours. Aspirin significantly resensitized both MCF-7 TamR and T47D TamR cells to tamoxifen (Fig. 5C and D). We also observed that cellular cAMP (Fig. 5E; Supplementary Fig. S7) and p-CREB levels (Fig. 5F) were increased substantially upon treatment with aspirin in combination with tamoxifen in both MCF-7 and T47D TamR cells. Remarkably, treatment with SQ22536 completely abrogated the sensitizer effects of aspirin (Fig. 5G), confirming that tamoxifen sensitization effects of aspirin is mediated by cAMP pathway.

To test whether increased cAMP upon tamoxifen and aspirin combination induces the activation of stress-related kinases, we treated the MCF-7 TamR cells with aspirin alone or in combination with tamoxifen. While aspirin treatment alone significantly increased p-JNK and p-p38 levels, phosphorylation of AKT (Thr-308) was decreased. Importantly, the combination of aspirin and tamoxifen had a stronger effect on the phosphorylation status of all the proteins tested (Fig. 5H), phenocopying the effects of dipyridamole and Gebr-7b in combination with tamoxifen. Specific inhibition of JNK by SP600125 or p38 by SB203580 completely reversed the effects of aspirin and tamoxifen combination on the proliferation inhibition and sensitization in MCF-7 TamR cells (Fig. 5I). Treatment with aspirin also increased the levels of p-IRE1α, p-PERK, and p-eIF2α, and they were further

Figure 3.

Induction of cAMP activates stress-related kinases downstream of ER stress pathway and resensitizes tamoxifen-resistant breast cancer cells. **A,** Western blot analysis of stress-related kinases (JNK and p38) and AKT pathway in parental and tamoxifen-resistant MCF-7 cells. β-Actin was used as a loading control. **B–E,** Western blot analysis of stress-related kinases and AKT pathway in MCF-7 TamR cells upon knockdown of PDE4D with PDE4D specific siRNA (**B**), treatment with cAMP analogue (cAMPS-Sp; **C**), treatment with PDE inhibitor (dipyridamole; **D**), and treatment with PDE4D-specific inhibitor (Gebr-7b; **E**) in combination with tamoxifen (5.0 μmol/L). **F** and **G,** Western blot analysis for apoptosis markers in MCF-7 TamR cells after treatment with dipyridamole (**F**) and Gebr-7b (**G**) in combination with tamoxifen (5.0 μmol/L). **H** and **I,** Luminescence-based caspase-3/7 assay in MCF-7 TamR cells upon treatment with PDE inhibitor (dipyridamole; **H**) and PDE4D-specific inhibitor (Gebr-7b; **I**) in combination with tamoxifen (7.5 μmol/L). **J** and **K,** Cell proliferation of the resistant MCF-7 cells treated with PDE inhibitor (dipyridamole; **J**) and PDE4D-specific inhibitor (Gebr-7b; **K**) together with p38 inhbitor (SB203580) or JNK inhibitor (SP600125) in presence of tamoxifen (7.5 μmol/L). **L,** Western blot analysis of ER stress–related proteins in parental and tamoxifen-resistant MCF-7cells. β-Actin was used as a loading control. **M–P,** Western blot analysis of ER stress–related proteins in MCF-7 TamR cells upon knockdown of PDE4D (**M**), treatment with cAMP analogue (cAMPS-Sp; **N**), treatment with PDE inhibitor (dipyridamole; **O**), and treatment with PDE4D-specific inhibitor (Gebr-7b; **P**) in combination with tamoxifen (5.0 μmol/L). **Q,** Cell proliferation of the resistant MCF-7 cells treated with ER stress inducer (thapsigargin) in the absence and presence of tamoxifen (7.5 μmol/L). **R,** Cell proliferation of the resistant MCF-7 cells treated with thapsigargin in the absence and presence of tamoxifen (7.5 μmol/L) or together with p38 inhibitor (SB203580) or JNK inhibitor (SP600125) in presence of tamoxifen. **S,** Western blot analysis for apoptosis markers for combination therapies in MCF-7 TamR cells after treatment with thapsigargin alone or in combination with tamoxifen (5.0 μmol/L) or together with p38-inhbitor (SB203580) or JNK inhibitor (SP600125) in presence of tamoxifen (5.0 μmol/L). TG, thapsigargin.

Downloaded from clincancerres.aacrjournals.org on January 20, 2022. © 2018 American Association for Cancer Research.

Published OnlineFirst January 31, 2018; DOI: 10.1158/1078-0432.CCR-17-2776

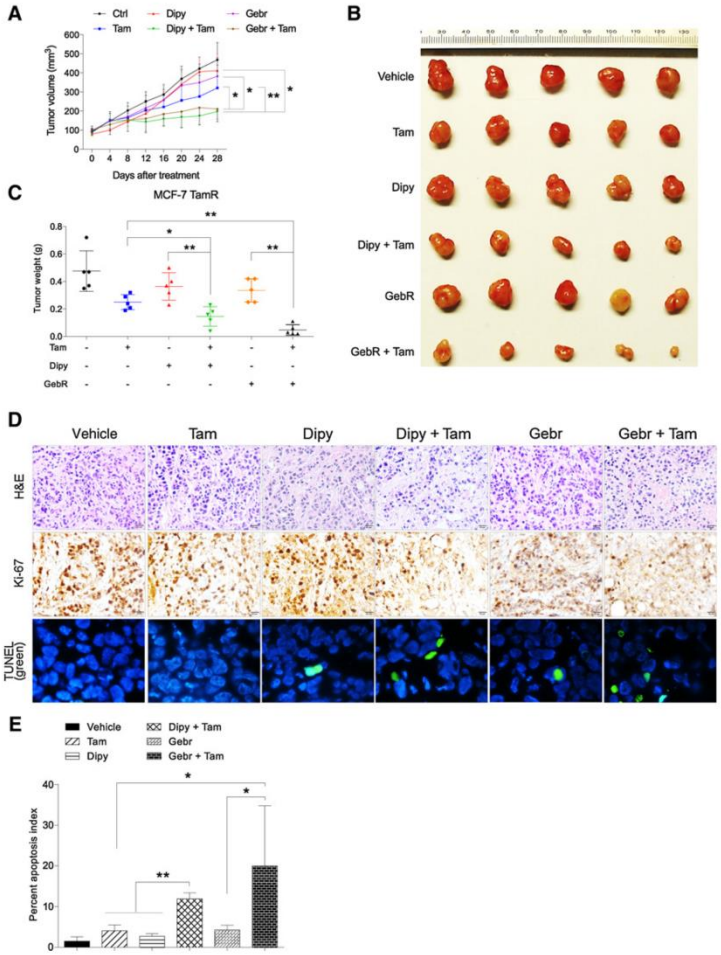


Figure 4.

Dipyridamole or Gebr-7b overcomes tamoxifen resistance *in vivo*. **A,** Tumor growth in MCF-7 TamR xenografts treated with tamoxifen and dipyridamole or Gebr-7b, individually or in combination. Treatments were started when tumor volumes reached around 100 mm^3. Mice were treated daily with tamoxifen (2 mg/kg), dipyridamole (15 mg/kg), Gebr-7b (3 μg/kg), or combinations for 28 days. **B,** Pictures of the tumors from mice treated with vehicle, tamoxifen, dipyridamole, Gebr-7b or the combination from the treatment groups. **C,** Tumor weights of the treatment groups. Statistical significance was determined with an unpaired, two-tailed Student *t* test. **D,** H&E, Ki-67, and fluorescence-based TUNEL stainings of the tumors. Pictures of H&E and Ki-67 stainings were taken at 40× while TUNEL was taken at 100× magnification. **E,** Quantification of the apoptotic cells from TUNEL staining.

Downloaded from clincancerres.aacrjournals.org on January 20, 2022. © 2018 American Association for Cancer Research.

Published OnlineFirst January 31, 2018; DOI: 10.1158/1078-0432.CCR-17-2776

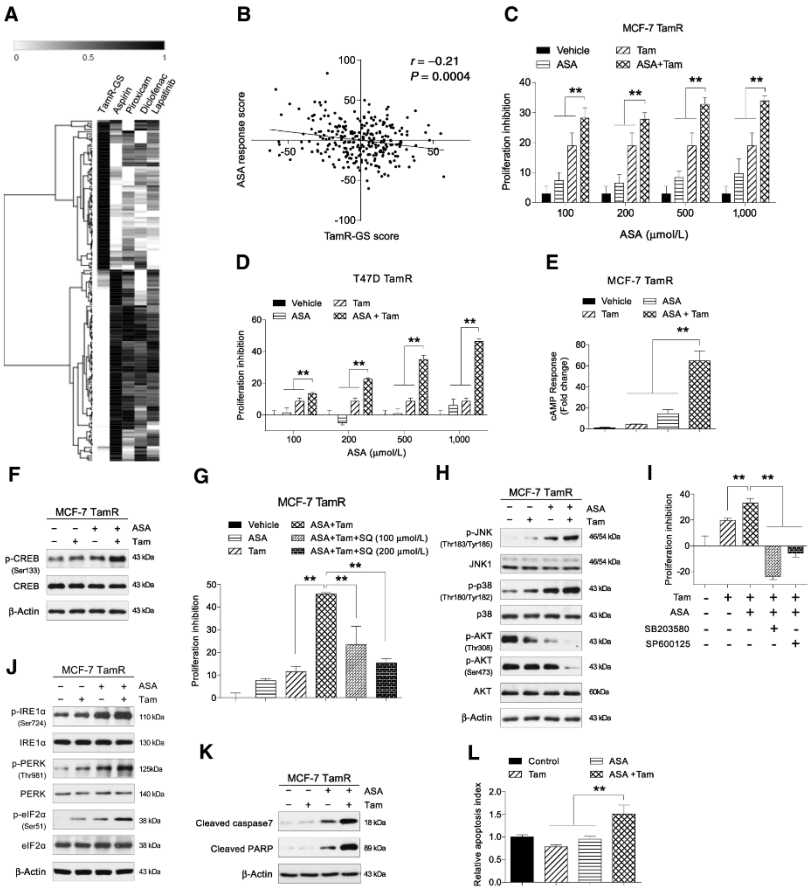


Figure 5.

Aspirin overcomes tamoxifen resistance via modulating cAMP levels and activation of ER stress–mediated p38/JNK signaling leading to apoptosis. **A,** The heatmap showing the genes in TamR-GS that are reversed by aspirin treatment, but not with other COX inhibitors (piroxicam, diclofenac) and lapatinib, a EGFR/Her2 inhibitor. The positions are normalized, and black shows the upregulated genes while white shows the downregulated genes. **B,** The correlation between TamR-GS and aspirin response score in patients from GSE26971. **C** and **D,** Tamoxifen sensitization with aspirin at different doses in MCF-7 TamR (**C**) and T-47D TamR (**D**) cells. The concentrations of tamoxifen used were 7.5 μmol/L and 5.0 μmol/L for MCF-7 TamR and T-47D TamR cells, respectively. **E,** Intracellular cAMP levels in MCF-7 TamR cells upon treatment with aspirin in combination with tamoxifen (5.0 μmol/L). **F,** Western blot analysis of p-CREB in MCF-7 TamR cells treated with aspirin in combination with tamoxifen (5.0 μmol/L). β-Actin was used as a loading control. **G,** Cell proliferation of the MCF-7 TamR cells pretreated with SQ22536, a specific cAMP inhibitor, in combination with aspirin and tamoxifen (7.5 μmol/L). **H,** Western blot analysis of stress-related kinases and AKT pathway in MCF-7 TamR treated with aspirin in the absence and presence of tamoxifen (5.0 μmol/L). **I,** Cell proliferation of the MCF-7 TamR cells treated with aspirin together with p38 inhibitor (SB203580) or JNK inhibitor (SP600125) in the presence of tamoxifen (7.5 μmol/L). **J,** Western blot analysis of ER stress–related proteins in MCF-7 TamR cells upon treatment with aspirin in combination with tamoxifen (5.0 μmol/L). **K,** Western blot analysis for apoptosis markers for combination therapies in MCF-7 TamR cells. **L,** Luminescence-based caspase-3/7 assay in MCF-7 TamR upon treatment with aspirin in combination with tamoxifen (7.5 μmol/L).

Downloaded from clincancerres.aacrjournals.org on January 20, 2022. © 2018 American Association for Cancer Research.

Published OnlineFirst January 31, 2018; DOI: 10.1158/1078-0432.CCR-17-2776

increased in aspirin and tamoxifen combination (Fig. 5J). These effects were further reflected in apoptosis where aspirin in combination with tamoxifen resulted in apoptosis as evidenced by the cleavage of caspase-7 and PARP and increase in relative apoptosis index (Fig. 5K and L).

To examine whether aspirin overcomes tamoxifen resistance *in vivo*, we generated xenografts using tamoxifen resistant MCF-7 TamR cells. The aspirin and tamoxifen combination inhibited the growth of the MCF-7 TamR tumors in nude mice as compared with the vehicle or single agents (Fig. 6A and B). Tumor weights were also significantly lower in the combination-treated group as compared with vehicle or individual treatment (Fig. 6C). We observed a reduced cell proliferation shown by Ki-67 staining and an enhanced apoptosis shown by fluorescence-based TUNEL assay in combination therapy (Fig. 6D and E). Overall, our results indicate a novel mechanism where aspirin overcomes tamoxifen resistance by modulating the PDE4D activity and increasing cAMP levels both *in vitro* and *in vivo*.

Discussion

Endocrine therapy is the most effective way to treat patients with early-stage, hormone-positive breast cancer, and tamoxifen is the preferred therapy, especially for premenopausal women. Despite its favorable efficacy, 20%–30% of patients acquire resistance during endocrine therapy, including tamoxifen (6). Multiple factors are responsible for resistance to tamoxifen, and various targeted therapies in combination with tamoxifen can be employed, depending on the pretreatment menopausal status or the change in menopausal status during the course of therapy, as well as on the risk of developing metastatic disease (29, 30). Major strategies to overcome tamoxifen resistance in breast cancer include use of an EGFR inhibitor (gefitinib), a HER2 inhibitor (trastuzumab), a dual kinase inhibitor (lapatinib), or an mTOR inhibitor (everolimus), depending upon the causal factor (31, 32). Recently, FDA has approved CDK4/6 inhibitor (palbociclib) to be used in combination with SERDs (fulvestrant) or AI (letrozole) for advanced ER-positive cancers, including those who progressed on tamoxifen (33, 34). Furthermore, fulvestrant has demonstrated clinical efficacy for patients with a second relapse after responding to tamoxifen and AIs (35). Another randomized trail demonstrated an improved median progression-free survival (PFS) in ER-positive, premenopausal metastatic patients when treated with tamoxifen plus ovarian function suppresser (36). Although early-stage disease is manageable owing to use of more potent endocrine agents, resistance inevitably develops in advance, metastatic disease (37). Therefore, identification of new targeted therapies for improving patient outcome is desirable. Here, we employed a systematic functional genomics approach to decipher the molecular mechanisms of tamoxifen resistance through combining whole-transcriptome sequencing, pathway enrichments, *in vitro* and *in vivo* assays and clinical data. This led us to identify PDE4D as a novel druggable target for overcoming tamoxifen resistance in breast cancer. PDE4D inhibition via specific siRNAs or pharmacologic inhibitors (dipyridamole and Gebr-7b) resulted in an increase in cAMP levels, induction of ER stress and increased JNK/p38 phosphorylation followed by apoptosis, overcoming resistance. Strikingly, we identified a novel mechanism by which aspirin through modulation of PDE4D and intracellular cAMP levels (similar to the effects of both PDE4D-specific inhibitor and PDE general inhibitor) overcomes tamoxifen resistance both *in vitro* and *in vivo*, highlighting the possibility of drug repositioning to expedite clinical application of our findings (Fig. 6F and G).

In the last few years, the potential role of PDEs as a target for treating inflammatory diseases, including asthma, depression, chronic obstructive pulmonary disorder (COPD) etc., has been studied. For example, roflumilast, a nonselective PDE4 inhibitor has been approved by FDA for treatment of erectile dysfunction and COPD (38). Importantly, recent studies have shown PDE4D as proliferation promoting factor in lung cancer cells (24). Inhibition of PDE4 by rolipram was shown to have antitumor effect in medulloblastoma, glioblastoma and in several hematologic malignancies making PDEs attractive targets for cancer therapy (39, 40). However, the role of PDE4D as a mediator of drug resistance has not been reported yet. We observed that blockade of PDE4D by siRNAs or specific inhibitors, for example, dipyridamole and Gebr-7b, has an antiproliferative effect on the tamoxifen-resistant breast cancer cells. Recent studies demonstrated that PDE4 inhibitors (e.g., rolipram) induce augmentation of intracellular cAMP levels leading to release of cytochrome c, reduction of antiapoptotic proteins, for example, Bcl-2 and Bcl-xL levels and activation of proapoptotic proteins, e.g., BAD, resulting in apoptosis (39). It has also been demonstrated that induction of cAMP by activation of PKA signaling induces apoptosis by activating PP2A, which dephosphorylate BAD and allowing apoptosis to commence through mitochondrial pathway. PP2A is an abundant phosphatase, which negatively regulates various signaling pathways through dephosphorylation of AKT (41). Our result also demonstrate that dephosphorylation of AKT is achieved through sustained activation of cAMP levels through cAMP analogs (cAMP-Sp) or by knockdown of PDE4D or by PDE4Is (dipyridamole and Gebr-7b) in combination with tamoxifen. Our results not only further support these findings with respect to increased apoptosis upon cAMP induction (here: upon combination of PDE4D inhibitors with tamoxifen), but also suggest that one of the mechanisms of cAMP-induced apoptosis is via inducing ER stress/p38/JNK pathways.

Under chronic ER stress, cells become incompetent to take care of unfolded protein load, and apoptosis is therefore triggered. There are three classes of ER stress–induced cell death sensors in mammals: IRE1α, PERK, and ATF6 (42). Activated IRE1α cleaves XBP1 mRNA and activates ASK1. Similarly, activated PERK phosphorylates eIF2α, which leads to the inhibition of protein synthesis and induction of ATF4, which in turn regulates genes involved in apoptosis, growth arrest, and DNA damage response (25, 26). UPR is an adaptive cellular response that evolves to regulate protein folding homeostasis, and if the UPR fails to resolve the misfolding condition, then cells undergo apoptosis (43). Hence, UPR is becoming an attractive target for cancer therapy. In response to various extracellular stimuli, G-protein coupled receptors (GPCR) are responsible for cAMP accumulation in cells. Conversion of cAMP from ATP is mediated by adenylate cyclases (AC) which, in turn, are activated via GPCRs. In response to cellular stress, both JNK and p38 MAPKs are activated by GPCRs. It has been known that cAMP and cAMP-elevating agents activate JNK and p38 MAP kinases (19, 20, 44). As evident from the literature, there is a connection between cAMP, p38/JNK signaling and apoptosis. However, it has not been known that cAMP-induced activation of p38 MAPK and JNK signaling is preceded by induction of ER stress. Our study shows that elevated levels of cAMP can potentially lead to the activation

Downloaded from clincancerres.aacrjournals.org on January 20, 2022. © 2018 American Association for Cancer Research.

Published OnlineFirst January 31, 2018; DOI: 10.1158/1078-0432.CCR-17-2776

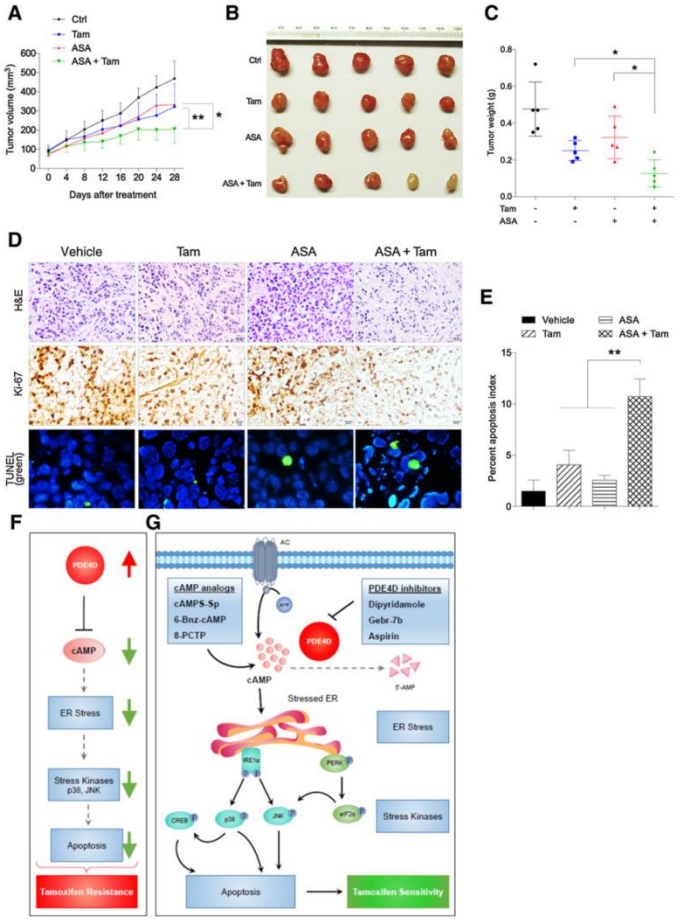


Figure 6.

Aspirin overcomes tamoxifen resistance *in vivo* and schematic summary of findings. **A,** Tumor growth in MCF-7 TamR xenografts treated with tamoxifen and aspirin individually or in combination. Treatments were started when tumor volumes reached around 100 mm^3. Mice were treated daily with tamoxifen (2 mg/kg), aspirin (100 mg/kg) or their combination for 28 days. Note that the vehicle control and Tam groups are the same as in Fig. 4. ASA; aspirin. **B,** Pictures of the tumors from mice treated with vehicle, tamoxifen, aspirin, or the combination from the treatment groups. **C,** Tumor weights of the treatment groups. Statistical significance was determined with an unpaired, two-tailed Student *t* test. **D,** H&E, Ki-67, and fluorescence-based TUNEL stainings of the tumors. Pictures of H&E and Ki-67 stainings were taken at 40× while TUNEL was taken at 100× magnification. **E,** Quantification of the apoptotic cells from TUNEL staining. **F,** Elevated PDE4D levels in TamR cells leads to a decreased cAMP level, subsequently giving rise to a decrease in ER stress, activation of stress kinases and apoptosis conferring tamoxifen resistance. **G,** Inhibition of PDE4D (with dipyridamole, Gebr-7b or aspirin) or inducing cAMP directly (with cAMPS-Sp, 6-Bnz-cAMP, or 8-PCTP) together with tamoxifen leads to elevated cAMP levels, induction of ER stress and increased JNK/p38 phosphorylation leading to activation and phosphorylation of CREB followed by apoptosis and tamoxifen sensitization.

Downloaded from clincancerres.aacrjournals.org on January 20, 2022. © 2018 American Association for Cancer Research.

Published OnlineFirst January 31, 2018; DOI: 10.1158/1078-0432.CCR-17-2776

of ER stress pathway that necessitates stress-related kinases to induce apoptosis. In the context of tamoxifen resistance, we showed, for the first time, that modulation of cAMP levels through cAMP analogues (cAMPS-Sp) or by knockdown of PDE4D or by PDE4Is (dipyridamole and Gebr-7b) in combination with tamoxifen results in stepwise induction of cAMP, activation of ER stress, elevated phosphorylation of JNK and p38 MAPK and apoptosis to overcome tamoxifen resistance in breast cancer. Thus, targeting PDE4D, or induction of cAMP in general, can be used as a sensitizer for overcoming tamoxifen resistance in breast cancer cells.

Aspirin, a more than a century old drug, has been termed as a "wonder drug" by many clinicians (45). Aspirin belongs to the group of nonsteroidal anti-inflammatory drugs (NSAID), and is one of the most widely used drugs over a century. In several meta-analyses, regular use of aspirin was associated with a reduced cancer incidence, decreased distant metastases, and improvement of overall and disease-free survival (DFS) in patients with breast cancer who had acquired chemoresistance (46, 47). However, mechanisms underlying these protective effects are still poorly known. Aspirin has been known to exert anticancer effects, most of which are attributed to its COX-2 inhibitory function (46, 47). However, here we showed, for the first time, that aspirin can be repositioned to treat tamoxifen resistance by utilizing a different mechanism other than COX-2 inhibition to cause antitumoral effects *in vitro* and *in vivo* by targeting PDE4D and elevating cAMP. While dipyridamole has been used as an anticoagulant over a half-decade, and aspirin is in use as an anti-inflammatory drug over a decade, Gebr-7b is a newly developed cell-permeable and the most specific PDE4D inhibitor of all PDE4Is available. Emesis associated with PDE4Is is an apparent translational concern; however, Gebr-7b has been shown to be 100–3,000 times less emetic than other PDE4D inhibitors in three different species (*Suncus murinus*, beagle dog, and cynomolgus monkey; ref. 48); thus showing its promising potential for clinics. Although Gebr-7b has not been tested in a clinical trial yet, dipyridamole and aspirin could be used in combination with tamoxifen for overcoming tamoxifen resistance in future.

In summary, we have uncovered a novel molecular mechanism of tamoxifen resistance by an in-depth characterization of two different tamoxifen resistant cells and identified PDE4D as a novel drug target in tamoxifen-refractory ERα-positive breast cancer. We believe that our results are the first, to the best of our knowledge, in providing cAMP induction as a novel concept for tamoxifen sensitization. As all three drugs which we showed to induce cAMP levels are readily available, and some of them are FDA approved (e.g., aspirin or dipyridamole), these drugs in combination with tamoxifen may offer new ways to overcome resistance in patients with ER-positive breast cancer.

Disclosure of Potential Conflicts of Interest

R. R. Mishra and Ö. Şahin have a pending patent (patent number: 14790/4) with Turkish Patent and Trademark Office on the use of cAMP inducers for the treatment of tamoxifen resistant breast cancer. No potential conflicts of interest were disclosed by the other authors.

Authors' Contributions

Conception and design: C. Cekic, Ö. Şahin
Development of methodology: R.R. Mishra, H. Bal, P. Jandaghi, C. Cekic
Acquisition of data (provided animals, acquired and managed patients, provided facilities, etc.): R.R. Mishra, N. Belder, S.A. Ansari, M. Kayhan, U. Raza, P.G. Ersan, S. Wiemann, Y. Riazalhosseini, Ö. Şahin
Analysis and interpretation of data (e.g., statistical analysis, biostatistics, computational analysis): R.R. Mishra, Ü.M. Tokat, Ö. Saatci, S. Wiemann, A. Üner, C. Cekic, Y. Riazalhosseini, Ö. Şahin, F. Eyüpoğlu
Writing, review, and/or revision of the manuscript: R.R. Mishra, A. Üner, C. Cekic, Ö. Şahin
Administrative, technical, or material support (i.e., reporting or organizing data, constructing databases): S. Wiemann, A. Üner, Ö. Şahin
Study supervision: Ö. Şahin

Acknowledgments

This project was supported by EMBO Installation Grant 2791 (to Ö. Şahin). Ü.M. Tokat is a scholar of TÜBİTAK BİDEB 2211/A Scholarship Program. We thank Gamze Aykut for helping us with mouse xenografts studies.

The costs of publication of this article were defrayed in part by the payment of page charges. This article must therefore be hereby marked *advertisement* in accordance with 18 U.S.C. Section 1734 solely to indicate this fact.

Received September 24, 2017; revised December 6, 2017; accepted January 25, 2018; published OnlineFirst January 31, 2018.

References

1. Davies C, Pan H, Godwin J, Gray R, Arriagada R, Raina V, et al. Long-term effects of continuing adjuvant tamoxifen to 10 years versus stopping at 5 years after diagnosis of oestrogen receptor-positive breast cancer: ATLAS, a randomised trial. Lancet 2013;381:805–16.
2. Viedma-Rodriguez R, Baiza-Gutman L, Salamanca-Gomez F, Diaz-Zaragoza M, Martinez-Hernandez G, Ruiz Esparza-Garrido R, et al. Mechanisms associated with resistance to tamoxifen in estrogen receptor-positive breast cancer (review). Oncol Rep 2014;32:3–15.
3. Fisher B, Costantino JP, Wickerham DL, Redmond CK, Kavanah M, Cronin WM, et al. Tamoxifen for prevention of breast cancer: report of the national surgical adjuvant breast and bowel project P-1 study. J Natl Cancer Inst 1998;90:1371–88.
4. Vogel VG, Costantino JP, Wickerham DL, Cronin WM, Cecchini RS, Atkins JN, et al. Update of the national surgical adjuvant breast and bowel project study of tamoxifen and raloxifene (STAR) P-2 trial: preventing breast cancer. Cancer Prev Res 2010;3:696–706.
5. Early Breast Cancer Trialists' Collaborative G, Davies C, Godwin J, Gray R, Clarke M, Cutter D, et al. Relevance of breast cancer hormone receptors and other factors to the efficacy of adjuvant tamoxifen: patient-level meta-analysis of randomised trials. Lancet 2011;378:771–84.
6. Nass N, Kalinski T. Tamoxifen resistance: from cell culture experiments towards novel biomarkers. Pathol Res Pract 2015;211:189–97.
7. Gutierrez MC, Detre S, Johnston S, Mohsin SK, Shou J, Allred DC, et al. Molecular changes in tamoxifen-resistant breast cancer: relationship between estrogen receptor, HER-2, and p38 mitogen-activated protein kinase. J Clin Oncol 2005;23:2469–76.
8. Holm C, Rayala S, Jirstrom K, Stal O, Kumar R, Landberg G. Association between Pak1 expression and subcellular localization and tamoxifen resistance in breast cancer patients. J Natl Cancer Inst 2006; 98:671–80.
9. Cannings E, Kirkegaard T, Tovey SM, Dunne B, Cooke TG, Bartlett JM. Bad expression predicts outcome in patients treated with tamoxifen. Breast Cancer Res Treat 2007;102:173–9.
10. Planas-Silva MD, Bruggeman RD, Grenko RT, Smith JS. Overexpression of c-Myc and Bcl-2 during progression and distant metastasis of hormone-treated breast cancer. Exp Mol Pathol 2007;82:85–90.

Downloaded from clincancerres.aacrjournals.org on January 20, 2022. © 2018 American Association for Cancer Research.

Published OnlineFirst January 31, 2018; DOI: 10.1158/1078-0432.CCR-17-2776

11. Rondon-Lagos M, Villegas VE, Rangel N, Sanchez MC, Zaphiropoulos PG. Tamoxifen resistance: emerging molecular targets. Int J Mol Sci 2016;17: pii: E1357.
12. Ward A, Shukla K, Balwierz A, Soons Z, Konig R, Sahin O, et al. MicroRNA-519a is a novel oncomir conferring tamoxifen resistance by targeting a network of tumour-suppressor genes in ER+ breast cancer. J Pathol 2014;233:368–79.
13. Dancik GM, Owens CR, Iczkowski KA, Theodorescu D. A cell of origin gene signature indicates human bladder cancer has distinct cellular progenitors. Stem Cells 2014;32:974–82.
14. Ward A, Balwierz A, Zhang JD, Kublbeck M, Pawitan Y, Hielscher T, et al. Re-expression of microRNA-375 reverses both tamoxifen resistance and accompanying EMT-like properties in breast cancer. Oncogene 2013; 32:1173–82.
15. Azevedo MF, Faucz FR, Bimpaki E, Horvath A, Levy I, de Alexandre RB, et al. Clinical and molecular genetics of the phosphodiesterases (PDEs). Endocr Rev 2014;35:195–233.
16. Gyorffy B, Lanczky A, Eklund AC, Denkert C, Budczies J, Li Q, et al. An online survival analysis tool to rapidly assess the effect of 22,277 genes on breast cancer prognosis using microarray data of 1,809 patients. Breast Cancer Res Treat 2010;123:725–31.
17. Bruno O, Romussi A, Spallarossa A, Brullo C, Schenone S, Bondavalli F, et al. New selective phosphodiesterase 4D inhibitors differently acting on long, short, and supershort isoforms. J Med Chem 2009;52:6546–57.
18. Delghandi MP, Johannessen M, Moens U. The cAMP signalling pathway activates CREB through PKA, p38 and MSK1 in NIH 3T3 cells. Cell Signal 2005;17:1343–51.
19. He J, Wang C, Sun Y, Lu B, Cui J, Dong N, et al. Exendin-4 protects bone marrow-derived mesenchymal stem cells against oxygen/glucose and serum deprivation-induced apoptosis through the activation of the cAMP/PKA signaling pathway and the attenuation of ER stress. Int J Mol Med 2016;37:889–900.
20. Cuadrado A, Nebreda AR. Mechanisms and functions of p38 MAPK signalling. Biochem J 2010;429:403–17.
21. Dostmann WR, Taylor SS, Genieser HG, Jastorff B, Doskeland SO, Ogreid D. Probing the cyclic nucleotide binding sites of cAMP-dependent protein kinases I and II with analogs of adenosine 3',5'-cyclic phosphorothioates. J Biol Chem 1990;265:10484–91.
22. Hochbaum D, Tanos T, Ribeiro-Neto F, Altschuler D, Coso OA. Activation of JNK by Epac is independent of its activity as a Rap guanine nucleotide exchanger. J Biol Chem 2003;278:33738–46.
23. Rovida E, Stecca B. Mitogen-activated protein kinases and Hedgehog-GLI signaling in cancer: a crosstalk providing therapeutic opportunities? Semin Cancer Biol 2015;35:154–67.
24. Pullamsetti SS, Banat GA, Schmall A, Szibor M, Pomagruk D, Hanze J, et al. Phosphodiesterase-4 promotes proliferation and angiogenesis of lung cancer by crosstalk with HIF. Oncogene 2013;32:1121–34.
25. Darling NJ, Cook SJ. The role of MAPK signalling pathways in the response to endoplasmic reticulum stress. Biochim Biophys Acta 2014;1843:2150–63.
26. Lytton J, Westlin M, Hanley MR. Thapsigargin inhibits the sarcoplasmic or endoplasmic reticulum Ca-ATPase family of calcium pumps. J Biol Chem 1991;266:17067–71.
27. Lamb J, Crawford ED, Peck D, Modell JW, Blat IC, Wrobel MJ, et al. The Connectivity Map: using gene-expression signatures to connect small molecules, genes, and disease. Science 2006;313:1929–35.
28. Guo H, Liu J, Ben Q, Qu Y, Li M, Wang Y, et al. The aspirin-induced long non-coding RNA OLA1P2 blocks phosphorylated STAT3 homodimer formation. Genome Biol 2016;17:24.
29. Klijn JG, Beex LV, Mauriac L, van Zijl JA, Veyret C, Wildiers J, et al. Combined treatment with buserelin and tamoxifen in premenopausal metastatic breast cancer: a randomized study. J Natl Cancer Inst 2000;92: 903–11.
30. Tevaarwerk AJ, Wisinski KB, O'Regan RM. Endocrine therapy in premenopausal hormone receptor-positive breast cancer. J Oncol Pract 2016;12: 1148–56.
31. Huober J, Fasching PA, Barsoum M, Petruzelka L, Wallwiener D, Thomssen C, et al. Higher efficacy of letrozole in combination with trastuzumab compared to letrozole monotherapy as first-line treatment in patients with HER2-positive, hormone-receptor-positive metastatic breast cancer - results of the eLEcTRA trial. Breast 2012;21:27–33.
32. Osborne CK, Neven P, Dirix LY, Mackey JR, Robert J, Underhill C, et al. Gefitinib or placebo in combination with tamoxifen in patients with hormone receptor-positive metastatic breast cancer: a randomized phase II study. Clin Cancer Res 2011;17:1147–59.
33. Cristofanilli M, Turner NC, Bondarenko I, Ro J, Im SA, Masuda N, et al. Fulvestrant plus palbociclib versus fulvestrant plus placebo for treatment of hormone-receptor-positive, HER2-negative metastatic breast cancer that progressed on previous endocrine therapy (PALOMA-3): final analysis of the multicentre, double-blind, phase 3 randomised controlled trial. Lancet Oncol 2016;17:425–39.
34. Finn RS, Crown JP, Ettl J, Schmidt M, Bondarenko IM, Lang I, et al. Efficacy and safety of palbociclib in combination with letrozole as first-line treatment of ER-positive, HER2-negative, advanced breast cancer: expanded analyses of subgroups from the randomized pivotal trial PALOMA-1/TRIO-18. Breast Cancer Res 2016;18:67.
35. Robertson JF, Osborne CK, Howell A, Jones SE, Mauriac L, Ellis M, et al. Fulvestrant versus anastrozole for the treatment of advanced breast carcinoma in postmenopausal women: a prospective combined analysis of two multicenter trials. Cancer 2003;98:229–38.
36. Kim HA, Ahn SH, Nam SJ, Park S, Ro J, Im SA, et al. The role of the addition of ovarian suppression to tamoxifen in young women with hormone-sensitive breast cancer who remain premenopausal or regain menstruation after chemotherapy (ASTRRA): study protocol for a randomized controlled trial and progress. BMC Cancer 2016;16:319.
37. Garcia-Becerra R, Santos N, Diaz L, Camacho J. Mechanisms of resistance to endocrine therapy in breast cancer: focus on signaling pathways, miRNAs and genetically based resistance. Int J Mol Sci 2012;14:108–45.
38. Rabe KF. Update on roflumilast, a phosphodiesterase 4 inhibitor for the treatment of chronic obstructive pulmonary disease. Br J Pharmacol 2011; 163:53–67.
39. Lerner A, Epstein PM. Cyclic nucleotide phosphodiesterases as targets for treatment of haematological malignancies. Biochem J 2006;393: 21–41.
40. Goldhoff P, Warrington NM, Limbrick DD Jr., Hope A, Woerner BM, Jackson E, et al. Targeted inhibition of cyclic AMP phosphodiesterase-4 promotes brain tumor regression. Clin Cancer Res 2008;14:7717–25.
41. Moon EY, Lerner A. PDE4 inhibitors activate a mitochondrial apoptotic pathway in chronic lymphocytic leukemia cells that is regulated by protein phosphatase 2A. Blood 2003;101:4122–30.
42. Maly DJ, Papa FR. Druggable sensors of the unfolded protein response. Nat Chem Biol 2014;10:892–901.
43. Han J, Back SH, Hur J, Lin YH, Gildersleeve R, Shan J, et al. ER-stress-induced transcriptional regulation increases protein synthesis leading to cell death. Nat Cell Biol 2013;15:481–90.
44. Li J, Dou X, Li S, Zhang X, Zeng Y, Song Z. Nicotinamide ameliorates palmitate-induced ER stress in hepatocytes via cAMP/PKA/CREB pathway-dependent Sirt1 upregulation. Biochim Biophys Acta 2015;1853: 2929–36.
45. Desborough MJ, Keeling DM. The aspirin story - from willow to wonder drug. Br J Haematol 2017;177:674–83.
46. Algra AM, Rothwell PM. Effects of regular aspirin on long-term cancer incidence and metastasis: a systematic comparison of evidence from observational studies versus randomised trials. Lancet Oncol 2012;13: 518–27.
47. Saha S, Mukherjee S, Khan P, Kajal K, Mazumdar M, Manna A, et al. Aspirin suppresses the acquisition of chemoresistance in breast cancer by disrupting an NFkappaB-IL6 signaling axis responsible for the generation of cancer stem cells. Cancer Res 2016;76:2000–12.
48. Bruno O, Fedele F, Prickaerts J, Parker LA, Canepa F, Brullo C, et al. GEBR-7b, a novel PDE4D selective inhibitor that improves memory in rodents at non-emetic doses. Br J Pharmacol 2011;164:2054–63.

Downloaded from clincancerres.aacrjournals.org on January 20, 2022. © 2018 American Association for Cancer Research.

Systems-level Analysis Reveals Multiple Modulators of Epithelial-mesenchymal Transition and Identifies DNAJB4 and CD81 as Novel Metastasis Inducers in Breast Cancer

Authors

Zeynep Cansu Uretmen Kagiali, Erdem Sanal, Özge Karayel, Ayse Nur Polat, Özge Saatci, Pelin Gülizar Ersan, Kathrin Trappe, Bernhard Y. Renard, Tamer T. Önder, Nurcan Tuncbag, Özgür Şahin, and Nurhan Ozlu

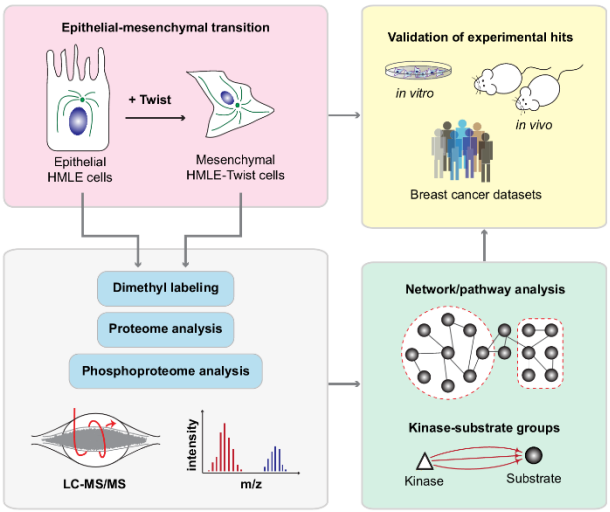
Correspondence

nozlu@ku.edu.tr

In Brief

By applying dimethyl labeling-based quantitative proteomic analysis, global alterations both at the proteome and phosphoproteome levels were determined in the Twist-induced EMT model system of HMLE cells. The epithelial and mesenchymal state specific signaling networks and the kinase-substrate interaction network of EMT were reconstructed using advanced modeling techniques. Many novel mRNA and/or protein level modulators of EMT were identified including DNAJB4 and CD81, which were validated as novel metastasis inducers in breast cancer.

Graphical Abstract



Highlights

- 314 proteins and 871 phosphopeptides were differentially regulated during EMT.
- ~65% of regulated proteins do not change at the transcriptome level during EMT.
- Epithelial and mesenchymal specific kinases and their substrates were identified.
- DNAJB4 and CD81 were identified as novel metastasis inducers in breast cancer.

Uretmen Kagiali et al., 2019, Molecular & Cellular Proteomics *18*, 1756–1771
September 2019 © 2019 Uretmen Kagiali et al. Published under exclusive license by The American Society for Biochemistry and Molecular Biology, Inc.
https://doi.org/10.1074/mcp.RA119.001446

Systems-level Analysis Reveals Multiple Modulators of Epithelial-mesenchymal Transition and Identifies DNAJB4 and CD81 as Novel Metastasis Inducers in Breast Cancer*

Zeynep Cansu Uretmen Kagiali‡‡‡, Erdem Sanal‡‡‡, Özge Karayel‡, Ayse Nur Polat‡, Özge Saatci§, Pelin Gülizar Ersan¶, Kathrin Trappe‖, Bernhard Y. Renard‖, Tamer T. Önder**‡‡, Nurcan Tuncbag§§¶¶, Özgür Şahin§¶, and Nurhan Ozlu‡**‖‖

Epithelial-mesenchymal transition (EMT) is driven by complex signaling events that induce dramatic biochemical and morphological changes whereby epithelial cells are converted into cancer cells. However, the underlying molecular mechanisms remain elusive. Here, we used mass spectrometry based quantitative proteomics approach to systematically analyze the post-translational biochemical changes that drive differentiation of human mammary epithelial (HMLE) cells into mesenchymal. We identified 314 proteins out of more than 6,000 unique proteins and 871 phosphopeptides out of more than 7,000 unique phosphopeptides as differentially regulated. We found that phosphoproteome is more unstable and prone to changes during EMT compared with the proteome and multiple alterations at proteome level are not thoroughly represented by transcriptional data highlighting the necessity of proteome level analysis. We discovered cell state specific signaling pathways, such as Hippo, sphingolipid signaling, and unfolded protein response (UPR) by modeling the networks of regulated proteins and potential kinase-substrate groups. We identified two novel factors for EMT whose expression increased on EMT induction: DnaJ heat shock protein family (Hsp40) member B4 (DNAJB4) and cluster of differentiation 81 (CD81). Suppression of DNAJB4 or CD81 in mesenchymal breast cancer cells resulted in decreased cell migration *in vitro* and led to reduced primary tumor growth, extravasation, and lung metastasis *in vivo*. Overall, we performed the global proteomic and phosphoproteomic analyses of EMT, identified and validated new mRNA and/or protein level modulators of EMT. This work also provides a unique platform and resource for future studies focusing on metastasis and drug resistance. ***Molecular & Cellular Proteomics 18: 1756–1771, 2019. DOI: 10.1074/mcp.RA119.001446.***

Carcinoma cells use epithelial-mesenchymal transition (EMT)[1], a normally latent embryonic program, to facilitate the initiation and progression of metastasis. EMT can be induced via cell intrinsic and extrinsic factors based on the communication between epithelial cells and the nearby stromal cells and plays a critical role in metastasis of cancer cells (1–4). In 1982, Greenburg and Hay first reported that epithelial cells can be converted into mesenchymal cells (5). Subsequently, numerous studies described the molecular processes during EMT and suggested alternative mechanistic models that lead to EMT (6, 7). EMT does not only trigger metastatic and invasive capabilities but can also trigger cancer stem cell properties (5, 6, 8) and drug resistance (9–12).

Throughout EMT, epithelial cells lose cell-cell contacts and cell polarity (13). Several signaling pathways that facilitate the activation of EMT have been discovered (6, 14, 15) and includes TGF-β, Wnt proteins, platelet-derived growth factors, Interleukin-6 and various receptor tyrosine kinases. All of these are involved in the activation of EMT inducing transcription factors (EMT-TF). These include Snail, Slug, Zeb1, Zeb2, and Twist (13). Ectopic expression of Twist in epithelial cells leads to the loss of adherens junction protein E-cadherin and expression of mesenchymal markers such as N-cadherin and Vimentin, suggesting the induction of EMT (3, 4, 16). Gene expression profiling of immortalized human mammary epithe-

From the ‡Department of Molecular Biology and Genetics, Koç University, 34450 Istanbul, Turkey; ‡‡School of Medicine, Koç University, 34450 Istanbul, Turkey; §Department of Drug Discovery and Biomedical Sciences, University of South Carolina, Columbia, SC 29208; ¶Department of Molecular Biology and Genetics, Faculty of Science, Bilkent University, 06800 Ankara, Turkey; ‖Bioinformatics Unit (MF1), Robert Koch Institute, 13353 Berlin, Germany; **Koç University Research Center for Translational Medicine (KUTTAM), 34450 Istanbul, Turkey; §§Graduate School of Informatics, Department of Health Informatics, ¶¶Cancer Systems Biology Laboratory (CanSyL), METU, 06800 Ankara, Turkey

Received March 15, 2019, and in revised form, May 21, 2019
Published, MCP Papers in Press, June 20, 2019, DOI 10.1074/mcp.RA119.001446

© 2019 Uretmen Kagiali et al. Published under exclusive license by The American Society for Biochemistry and Molecular Biology, Inc.

This is an Open Access article under the CC BY license.

lial (HMLE) cells that underwent EMT by expressing Goosecoid, Snail, Twist, or TGF-β, or by knocking down the expression of E-cadherin identified a "EMT core signature" that consists of 159 downregulated genes and 87 upregulated genes (4). Although transcriptomic data represents gene expression during EMT process, it may not thoroughly predict the regulation at the protein level; *i.e.* the mRNA levels may not be perfectly correlated with the translated proteins because of the post-transcriptional modifications and miRNA-mediated regulation (17–19).

As a comprehensive understanding of EMT requires combination of both transcriptomic and proteomic analyses, we systematically compared biochemical changes during EMT of human mammary epithelial cells that was induced by Twist and we performed detailed comparison of previous transcriptome profile of the same EMT model system with our proteome data. Our analysis revealed 314 differentially regulated proteins during EMT which was followed by the "omic" data integration to reconstruct EMT specific networks. In parallel, to profile the changes in signaling pathways during EMT, we systematically monitored phosphoproteome changes and reconstructed the network of the interactions between kinases and phosphoproteins. Finally, we validated several novel biochemical changes identified in this study by *in vitro* and *in vivo* experiments. Our data provide a framework for understanding the global regulation of EMT at phospho-/protein level and reveal a comprehensive data set to explore main molecular pathways that drive EMT.

EXPERIMENTAL PROCEDURES

Cell Culture—Human mammary epithelial (HMLE) cell line (20) was kindly provided by Dr. Robert A. Weinberg (Whitehead Institute for Biomedical Research, Boston, MA) and cultured in MEGM Bullet kit (CC-3151 & CC-4136, Lonza) in 5% CO_2 at 37 °C. 4-Hydroxytamoxifen (4-OHT) treatment at a final concentration of 20 nM was performed for 16 days to induce EMT in HMLE-Twist-ER cells. MCF7 and MDA-MB-231 cells were cultured in Dulbecco's Modified Eagle's Medium (DMEM, Lonza) supplemented with 10% fetal bovine serum (Sigma), 1% penicillin/streptomycin (Sigma) and 1% MEM nonessential amino acids (Gibco) in 5% CO_2 at 37 °C.

Western Blotting—Approximately 3.2 × 10^6 cells were lysed in 1× PBS buffer containing 0.1% TritonX-100, cOmplete EDTA-free protease inhibitor mixture (Roche) and PhosSTOP phosphatase inhibitor mixture (Roche). Inhibitor mixture tablets were used as 1 tablet for 10 ml of lysis buffer. Cells were disrupted by pulling the cell suspension through a thin needle. Cell debris was removed by centrifugation at 14,000 rpm for 5 min at 4 °C. Protein concentration was measured using BCA protein assay kit (23227, Pierce). Protein samples were prepared in 2X Laemmli sample buffer containing 4% (w/v) SDS, 20% glycerol, 120 mM Tris-Cl (pH 6.8), 0.02% (w/v) bromphenol blue and 100 mM dithiothreitol (DTT) as protein sample to 2× Laemmli sample buffer ratio of 1:1 (v/v). Samples were heated at 95 °C for 5 min, cooled before loading onto SDS-PAGE gel. 10–12% SDS-PAGE gels were used for the separation of proteins. After electrophoresis of samples at 120 V for 100 min, proteins were transferred to nitrocellulose membranes (BA85, Whatman Protran) by the Trans-Blot Turbo transfer system (Bio-Rad). After 45 min blocking with 4% milk in 0.1% Tween20 containing 1× TBS, the membrane was incubated with primary antibodies: 1:1000 E-cadherin (24E10) (3195, Cell Signaling), 1:1000 Vimentin (D21H3) (5741, Cell Signaling), 1:1000 Snail (C15D3) (3879, Cell Signaling), 1:1000 β-actin (AC15) (ab6276, Abcam), 1:100 DNAJB4 (R-07) (sc-100711, Santa Cruz) and 1:100 CD81 (B-11) (sc166029, Santa Cruz) overnight at 4 °C or 3 h at room temperature. The membrane was rinsed with 0.1% Tween20 containing 1× TBS Buffer for 10 min three times and incubated with secondary antibodies: 1:2000 anti-mouse IgG, HRP-linked antibody (7076S, Cell Signaling) or 1:2000 anti-rabbit IgG, HRP-linked antibody (7074S, Cell Signaling) at room temperature for 1.5 h. Finally, membranes were rinsed with 0.1% Tween20 containing 1× TBS Buffer for 10 min three times and proteins were visualized with the ECL Western blotting Substrate system (32106, Pierce).

Experimental Design and Statistical Rationale—Trypsin digested lysates of HMLE and HMLE-Twist cells were dimethyl labeled as light and heavy, respectively and mixed in equal amounts. Mixed lysates were separated into 40 fractions via SCX. Biological replicate 2 (BR2) was prepared by label swapping to remove labeling bias and separated into 40 fractions via SCX as in BR1. From each biological replicate, 2 technical replicates were prepared and analyzed in MS. Phosphoproteome quantification of the samples was designed similarly, 2 biological replicates with 2 technical replicates each, except the fractionation step. To enrich phosphopeptides, each SCX fraction was enriched using either in-house packed TiO_2 (5 μm, Sachtleben, CAS no. 13463–67-7) or Ti^{4+}-IMAC micro columns in which the beads were loaded onto GELoader tips using a C8 plug. For Ti^{4+}-IMAC columns, IMAC material was prepared and used as previously described (21). The enriched samples were combined into 10–12 fractions in both biological replicates with two technical replicates for each. Ratios of proteins and peptides quantified in the replicates were combined by taking the median.

To determine the regulated proteins between epithelial and mesenchymal states, we defined epithelial, mesenchymal specific and unchanged protein ratio distributions using known epithelial and mesenchymal markers. Epithelial and mesenchymal specific protein marker groups (supplemental Table S1) were used to determine which proteins fall into the corresponding groups. By fitting normal distributions to E/M ratios of these three groups, epithelial, mesenchymal and unchanged, the likelihood of each protein belonging to the respective groups was calculated. Using the likelihoods, the relative likelihood of each protein was calculated, $P_{relative} = P_{unchanged}/(P_{changed\text{-}epithelial}$ or $P_{changed\text{-}mesenchymal})$, for epithelial or mesenchymal group memberships. Proteins with $P_{relative} < 0.05$ were chosen as significantly changed proteins. Unmodified peptides of the unchanged proteins were chosen as unchanged peptides. Using the median normalized empirical distribution of the unchanged peptide ratio, we identified the respective lower 0.025 and 0.975 quantiles. These correspond to a lower and upper cutoff for the peptide ratios of −1.33404 and 1.555532, respectively. Aiming to identify those peptide ratios differing from the ones observed in the unchanged peptide ratios, phosphopeptide ratios below the lower cutoff value of the unchanged peptide distribution were identified as mesenchymal specific phosphorylations and phosphopeptide ratios above the upper

[1] The abbreviations used are: EMT, epithelial-mesenchymal transition; UPR, unfolded protein response; EMT-TF, EMT inducing transcription factors; HMLE, human mammary epithelial cells; IMAC, immobilized metal ion affinity chromatography; ACN, acetonitrile; HCD, Higher-energy collisional dissociation; NCE, normalized collision energy; PSM, peptide spectral match; GEO, Gene Expression Omnibus database; GSE, Genomic Spatial Event database; TCPA, The Cancer Proteome Atlas; TCGA, The Cancer Genome Atlas; RTCA, real time cell analysis; DNAJB4, DnaJ heat shock protein family (Hsp40) member B4; CD81, cluster of differentiation 81.

cutoff of the unchanged distribution were identified as epithelial specific phosphorylations.

In-solution Digestion and Stable Isotope Dimethyl Labeling—In-solution digestion was performed as described previously (22). Briefly, cell lysate was incubated for 4 h using Lys-C (enzyme:protein ratio of 1:100) in 4 M urea, followed by overnight trypsin (enzyme: protein ratio of 1:100) incubation in 1 M urea at 37 °C. The digestion was quenched by acidification and desalted using Sep-Pak C18 cartridges. On-column dimethyl labeling was performed as described in Boersema *et al.* (23). Labeling reagents consisted of 4% (v/v) of formaldehyde (CH_2O) (37% (v/v), Sigma, cat. no. 252549) and 0.6 M of sodium cyanoborohydride ($NaBH_3CN$) (Fluka, cat. no. 71435) for light and 4% (v/v) of formaldehyde ($^{13}CD_2O$) (20%, 99% ^{13}C, 98% D, Isotec, cat. no. 596388) and 0.6 M of sodium cyanoborodeuteride ($NaBD_3CN$) (96% D, Isotec, cat. no. 190020) for heavy in 50 mM NaH_2PO_4 (Fisher) and 50 mM Na_2HPO_4 (Fisher). The labeled peptides were combined in equal ratios based on their average peptide intensities. The epithelial sample was labeled with the light dimethyl label and the mesenchymal sample with the heavy label. We swapped the labels for the second biological replicate.

Strong Cation Exchange Chromatography and Phosphopeptide Enrichment—Labeled peptide mixes were fractionated using a PolySULFOETHYL A 200 × 2.1 mm (PolyLC Inc.) column using an Agilent 1100 HPLC system (Agilent Technologies, Germany) into 40 fractions. Then, pooled fractions were phospho-enriched using either Ti^{4+}-IMAC or Titanium dioxide (TiO_2) (Sachtleben, Germany) beads packaged into micro-columns as described previously (24, 25). Briefly, the samples resuspended in loading buffer (80% ACN, 6% TFA) were loaded onto micro-columns pre-equilibrated with loading buffer. Ti^{4+}-IMAC columns were sequentially washed with washing buffer 1 (50% ACN, 0.5% TFA containing 200 mM NaCl) and washing buffer 2 (50% ACN/0.1% TFA) whereas TiO_2 columns were sequentially washed with loading buffer and washing buffer 2 (50% ACN/0.1% TFA). The bound peptides were eluted into a new tube (containing 35 μl of 10% formic acid) with 20 μl of 10% ammonia by centrifugation at 100 × *g* for 20 min. The collected eluate was further acidified by the addition of 3 μl of 100% formic acid before nano-LC-MS/MS analysis. The peptides were at very low pH (<2) and ready for LC-MS/MS analysis. 20–30% of samples were loaded into system.

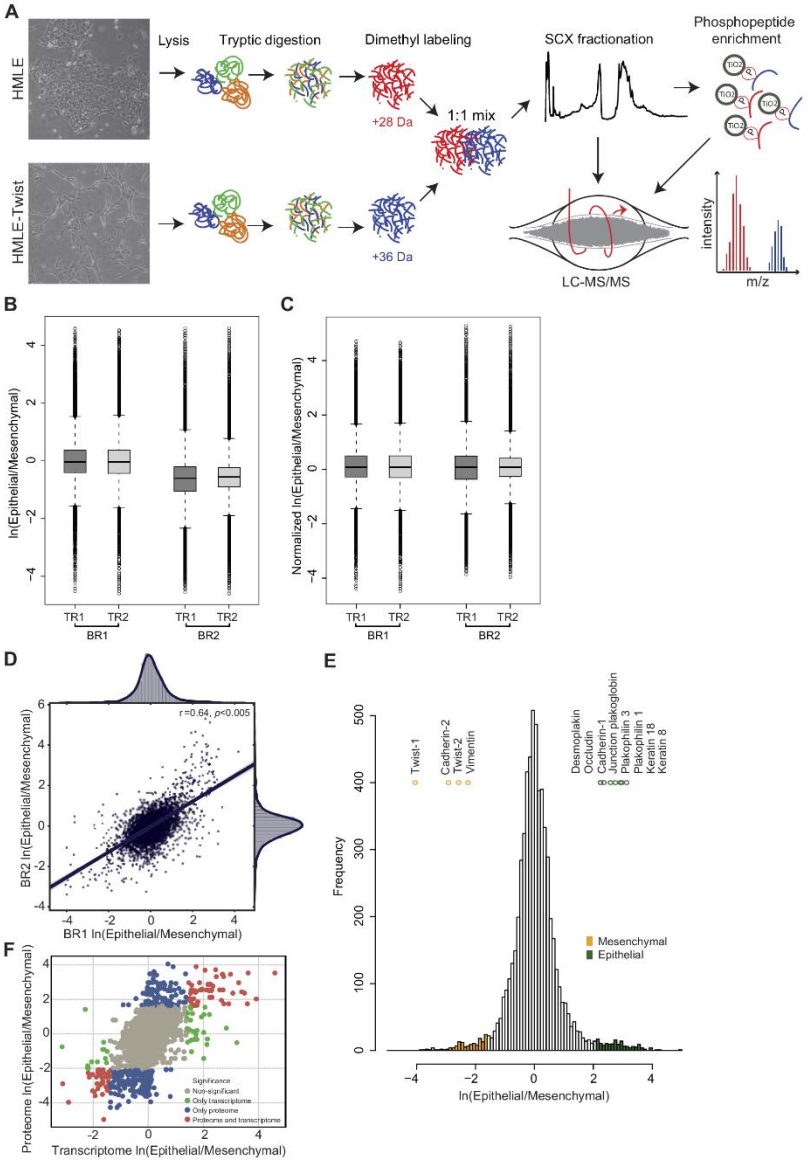
Mass Spectrometric Analysis—The peptides were subjected to a reversed phase nanoLC-MS/MS (EASY-nLC, Thermo) connected to a Q Exactive quadrupole Orbitrap mass spectrometer (Thermo Fisher Scientific, Bremen) for a 120 min analysis run. The peptides were directly loaded onto an in-house packed 100 μm i.d. × 17 cm C18 column (Reprosil-Gold C18, 5 μm, 200Å, Dr. Maisch) and separated at 300 nL/min with 120 min linear gradients, starting from 5 to 30% acetonitrile in 0.1% formic acid. Mass spectrometric analysis and spectra acquisition were performed with the following settings: Orbitrap analysis: Polarity at positive mode; resolution: 35,000; mass range: 350–1500 *m/z*; automatic gain control (AGC) target: 3e6; maximum injection time: 250 ms. Up to 10 of the most intense ions per cycle were fragmented and analyzed in the Orbitrap. MS2 analysis consisted of collision-induced dissociation (Higher-energy collisional dissociation (HCD)) (Resolution: 17,500; AGC: 5e5; maximum injection time: 120 ms; normalized collision energy (NCE): 25; charge exclusion: unassigned, 1, 7, 8, >8; dynamic exclusion: 20 s). The isolation window for MS/MS was 1.5 *m/z*.

Data Processing and Analysis—All raw data files were processed and quantified with Proteome Discoverer (version 1.4, Thermo Scientific). Peak lists containing HCD fragmentation were generated with Proteome Discoverer (PD) with a signal-to-noise threshold of 1.0. Produced data was searched against a Swissprot database version 2014_08 with taxonomy *Homo sapiens* (20,193 sequences) using the Mascot software (version 2.5.1, Matrix Science, London, UK). Settings for PD search were as following: The enzyme was specified as Trypsin and the fragment ion type was specified as electrospray ionization quadrupole time-of-flight. A mass tolerance of ±20 ppm for precursor masses and ±0.05 Da for fragment ions was used; two missed cleavages were allowed; and cysteine carbamidomethylation as a fixed modification. Light and heavy dimethylation of peptide N termini and lysine residues; methionine oxidation; phosphorylation on serine, threonine and tyrosine were set as variable modifications. Each peptide spectral match (PSM) (Mascot peptide score >25) of a phosphorylated peptide was isolated from the data in PD. The identification of the phosphopeptide site localization was performed by phosphoRS algorithm 3.0 (26), implemented in PD. A threshold of at least 0.70 probability was used for the phospho-residue localization. The 2plex dimethyl-based quantitation method was chosen in PD, with a mass precision requirement of 2 ppm for consecutive precursor mass measurements. The filter in PD was set to select only the peptides with "high confidence." We applied 0.2 min of retention time tolerance for isotope pattern multiplets and allowed spectra with a maximum of 1 missing channel to be quantified with the integrated Percolator-based filter using a false discovery rate of 1%.

Motif Analysis of Phosphopeptides—Phosphorylation sites with phosphorylation probabilities higher than 0.75 were chosen. ±7 amino acid sequence windows of the phosphorylation sites were used to extract motifs for epithelial and mesenchymal groups. Motif-x (27) implemented in rmotifx package (28) was used to identify enriched motifs in epithelial and mesenchymal specific phosphorylations. The significance threshold was set to 0.00018 (search length is 15 amino acids) in motif-x to make *p* value of each motif match to be at least 0.05 by the Bonferroni method. The motif occurrence limit is set to 5 for epithelial S phosphorylations ($n = 292$) and mesenchymal S phosphorylations ($n = 415$). The motif occurrence score is set to 2 for epithelial T phosphorylations ($n = 27$) and mesenchymal T phosphorylations ($n = 50$). The background was set to *Homo sapiens* proteins from Swissprot database version 2014_08 and the enriched motifs were converted to sequence logos via Weblogo (29). NetworKIN 3.0 (30) was used to generate kinase-substrate networks. We only used 4,060 phosphosites identified with more than 50% phosphorylation probabilities from epithelial and mesenchymal specific phosphosites and predictions scoring ≥5. Predicted kinase-substrate interaction networks were visualized using Cytoscape 3.4.0 (31). Cellular component annotations for each protein were fetched via the BioServices Python package. Kinase prediction of epithelial and mesenchymal specific phosphosites were performed via NetworKIN 3.0 (30). Predictions with scores 5 and above were selected and visualized in the network.

Network/Pathway Analysis—The forest module of the Omics Integrator (32) was used to construct epithelial and mesenchymal specific protein-protein interaction networks as explained in Karayel *et al.* (33). The iRefWeb database (34) protein-protein interaction network was used as the global proteome interactome. Significantly regulated proteins in epithelial and mesenchymal lists were used as the experimental hits (terminal proteins). Terminals are connected to each other via intermediate hidden proteins (Steiner proteins) (32) that are not identified in the experiments.

Statistical Analysis of Cell Line and Patient Data Sets—For mRNA expression analysis of genes in different breast cell lines, the GSE40059 data set (35) from NCBI GEO database was used. Epithelial and mesenchymal cell lines were assigned based on the Blick *et al.* study (36). SK-BR-3 and MDA-MB-468 cell lines were assigned as neither epithelial nor mesenchymal because of low expression of E-cadherin and the absence of mesenchymal markers, fibronectin and vimentin (36–38). Mean mRNA expression values of two groups were statistically analyzed by two-tailed Student's *t* test. TCGA mRNA data and EMT score values were downloaded from the cBio-


A
HMLE
HMLE-Twist
Lysis
Tryptic digestion
Dimethyl labeling
+28 Da
+36 Da
1:1 mix
SCX fractionation
Phosphopeptide enrichment
TiO2
LC-MS/MS
intensity
m/z
B
ln(Epithelial/Mesenchymal)
TR1
TR2
BR1
BR2
C
Normalized ln(Epithelial/Mesenchymal)
D
r=0.64, p<0.005
BR2 ln(Epithelial/Mesenchymal)
BR1 ln(Epithelial/Mesenchymal)
E
Twist-1
Cadherin-2
Twist-2
Vimentin
Desmoplakin
Occludin
Cadherin-1
Junction plakoglobin
Plakophilin 3
Plakophilin 1
Keratin 18
Keratin 8
Frequency
Mesenchymal
Epithelial
ln(Epithelial/Mesenchymal)
F
Proteome ln(Epithelial/Mesenchymal)
Transcriptome ln(Epithelial/Mesenchymal)
Significance
Non-significant
Only transcriptome
Only proteome
Proteome and transcriptome

Portal for Cancer Genomics (39, 40) and TCPA database (41), respectively. Correlation analysis of mRNA z-scores with EMT scores was performed and r values were obtained for each gene. For metastasis-free survival analysis of patients, GSE2603 microarray data (42) for primary breast cancer patients ($n = 82$) was used. Patients were separated into two groups at the median expression. Kaplan-Meier analyses were used to determine metastasis-free survival and statistical differences were determined by Log-rank (Mantel-Cox) test.

Knockdown Experiments—shRNA sequences against targets were designed using RNAi Codex database (43). pSMP-Luc plasmid (Addgene plasmid # 36394) was used for the expression of shRNAs as described previously (44). Each shRNA sequence was cloned into pSMP-Luc plasmid after the removal of Firefly luciferase targeting shRNA sequence. DNAJB4 and CD81 targeting sequences are CTGCAACTACTTGTTATGCATA and CACACGTCGCCTTCAACTGTAA, respectively. All cloning and packaging steps of viral plasmids were carried out as described previously (44). MCF-7 and MDA-MB-231 cells were used for the virus-mediated shRNA knockdown of epithelial and mesenchymal targets, respectively.

Cell Viability and In Vitro Migration Assays—To determine cell viability, MDA-MB-231 cells were incubated with Cell Titer Glo reagent and analyzed with a luminometer according to the manufacturer's protocol (Cell Titer Glo Luminescent Cell Viability Assay kit, G7571, Promega). Real-time cell migration assays were performed on xCELLigence RTCA-DP (ACEA Biosciences Inc., CA) according to manufacturer's protocol. RTCA (Real Time Cell Analyzer) is a system that quantifies the number of cells that are migrated toward a stimulus (in this case, serum). In this assay, cells were seeded in low serum (1%) media in small inserts coated with gold particles at their bottom. The inserts were placed in chambers containing high serum media (10%), and cells were expected to migrate toward the lower chamber with a pace that positively correlates with their invasiveness. As the cells move toward the high serum media, the movement causes a change in the current passing through the gold particles which is then quantified and represented as the migration cell index. For wound healing scratch assay, 0.5×10^6 cells per well were seeded in 6-well plates and grown to subconfluence. Proliferation of cells were blocked using serum-free medium and the wound area was measured at the beginning and after 24 h following scratch formation using ImageJ software (Wayne Rasband, NIH). Three independent experiments were performed for each condition. Images were taken with 4× magnification using Nikon Eclipse inverted microscope (Nikon, Japan). The statistical analysis of results was performed using two-tailed Student's *t* test.

Flow Cytometry Analysis—Cells were stained with PE-conjugated anti-CD81 antibody from BD Biosciences (JS-81) (gift of Dr. Batu Erman) as described previously (45). Samples were analyzed using SONY LE-SH800 flow cytometer. All flow data were analyzed using FlowJo_V10 software.

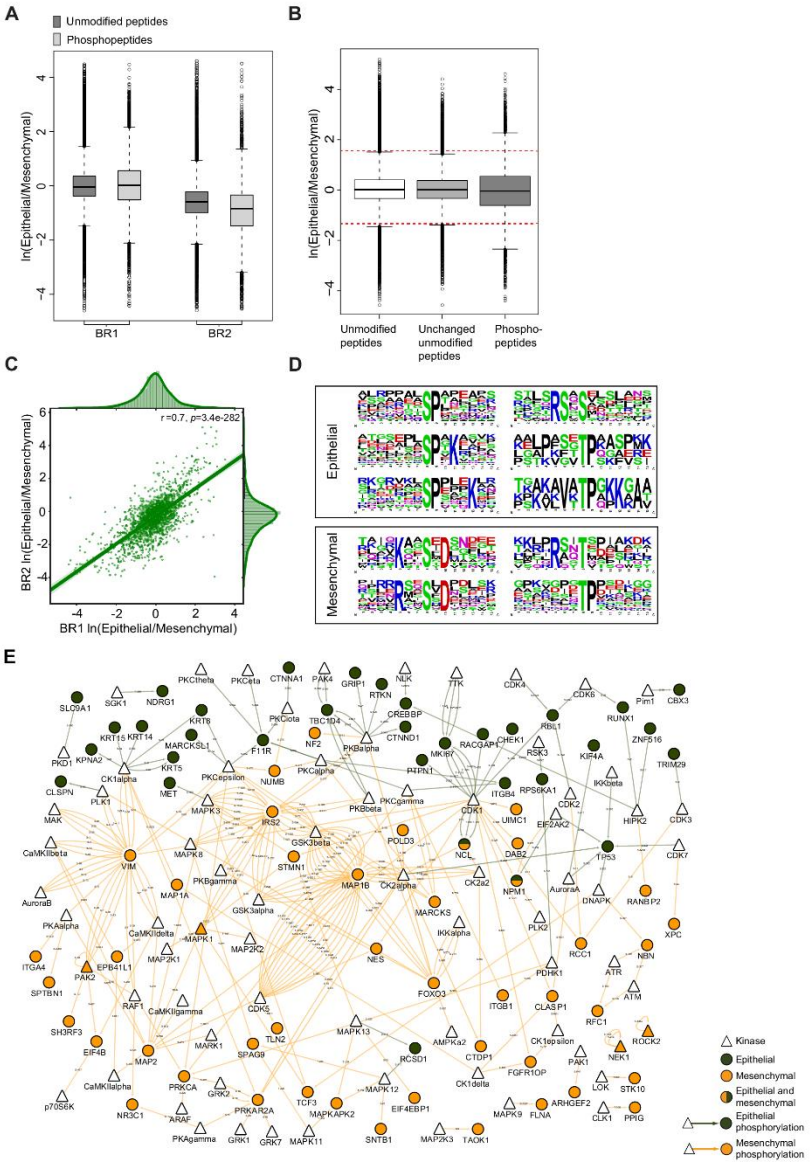
Animal Experiments—All animal experiments were approved by the animal ethics committee of Bilkent University. Six- to eight-week-old female athymic nu/nu mice were subcutaneously injected without incision, with 1×10^6 cells into mammary fat pad (MFP). Primary tumor growth was monitored by measuring the tumor volume twice a week with a caliper after tumors became palpable. Tumor volumes were calculated as length × width^2/2. Spontaneous metastasis was evaluated with a luciferase assay. Because of heterogeneous distribution of metastasis in organs, three different parts were randomly collected from each organ to make a tissue pool and weighed for normalization. Both lung and liver tissues were ground in cold PBS by tissue homogenizer and treated with cell culture lysis 5× reagent (E153A, Promega). 200 μl lysis buffer was added to 50 mg weight. After 15 min incubation, 100 μl of luciferase substrate (Promega) was added to 50 μl of the lysed sample, and luminescence was measured with a luminometer. For tail vein metastasis assay, 1.5×10^6 cells were injected into tail-vein of each 6–8-week-old female athymic nu/nu mice, with 3–5 mice per group. Lung metastasis was monitored by bioluminescence imaging (BLI). Anesthetized mice were intraperitoneally injected with 150 mg/kg D-luciferin (Perkin Elmer). Bioluminescence images were acquired with Lumina III In Vivo Imaging System (Perkin Elmer). Analysis was performed with live imaging software by measuring total photon flux. For Bouin's fixation, harvested lungs were cleaned with PBS and placed into Bouin's solution on a shaker for overnight. After fixation, they were kept in 70% alcohol.

RESULTS

Proteomic Profiling Identifies Differentially Regulated Proteins During EMT—To identify differentially expressed or phosphorylated proteins during EMT in epithelial HMLE and its mesenchymal derivative HMLE-Twist cells, we took the advantage of quantitative proteomics and phosphoproteomics approaches. Overall study design and experimental workflow is presented in supplemental Fig. S1. HMLE cells exhibiting characteristics of epithelial cells were systematically compared with HMLE cells that stably express Twist (HMLE-Twist) using dimethyl labeling (Fig. 1*A*). Twist ectopic expression has been known to induce epithelial cells to undergo EMT, thereby promoting mesenchymal cell characteristics (16). We validated these results by showing the protein level downregulation of epithelial markers, such as E-cadherin, and protein level upregulation of mesenchymal markers, such as N-cadherin, Vimentin, and Snail on Twist overexpression (supplemental Fig. S2).

To perform a systematic quantitative profiling of EMT, the equal amount of cell lysates from HMLE and HMLE-Twist cells were digested using Trypsin. The resulting peptides were differentially labeled with light and heavy isotopes using stable isotope dimethyl labeling (23) with the labeling efficiency of ~99%. The labels were swapped to eliminate any labeling bias in biological repeats. Two technical replicates were performed for each biological replicate. After combining differentially labeled peptides in equal amounts, the pooled peptides were separated by column-based SCX chromatography into

FIG. 1. **Identification of epithelial and mesenchymal specific proteins.** *A*, Experimental workflow as explained in the text. *B*, Box plots show the distribution of raw Epithelial/Mesenchymal protein ratios in the logarithmic (ln) scale for biological replicates 1 and 2 (BR1 and BR2) and corresponding technical replicates 1 and 2 (TR1 and TR2). *C*, Box plots show the normalized distribution of Epithelial/Mesenchymal protein ratios for BR1 and BR2 and corresponding TR1 and TR2 in the logarithmic (ln) scale. *D*, The correlation of the proteins between two biological replicates (Pearson correlation, $r = 0.64$). *E*, Distribution of all Epithelial/Mesenchymal protein ratios. Epithelial and mesenchymal specific proteins are labeled in green and yellow, respectively. The markers used to determine epithelial and mesenchymal groups are labeled in the histogram. *F*, Comparison of transcriptome *versus* proteome data. Epithelial/Mesenchymal ratios are compared at the mRNA (4) and protein levels (gray: no change, green: only mRNA level change, blue: only protein level change, red: both mRNA and protein levels change).


A
Unmodified peptides
Phosphopeptides
ln(Epithelial/Mesenchymal)
BR1
BR2
B
ln(Epithelial/Mesenchymal)
Unmodified peptides
Unchanged unmodified peptides
Phospho-peptides
C
r=0.7, p=3.4e-282
BR2 ln(Epithelial/Mesenchymal)
BR1 ln(Epithelial/Mesenchymal)
D
Epithelial
Mesenchymal
E
Kinase
Epithelial
Mesenchymal
Epithelial and mesenchymal
Epithelial phosphorylation
Mesenchymal phosphorylation

40 fractions, and each fraction was analyzed by LC-MS/MS in two replicates. All raw MS data were processed using the Proteome Discoverer software to identify and quantify peptides in two conditions (supplemental Fig. S1). As a result, 4,829 and 5,505 unique proteins (supplemental Table S1), as well as 29,986 and 35,591 unique peptides (supplemental Table S2*A*) were identified in biological replicate 1 (BR1) and biological replicate 2 (BR2), respectively with <1% FDR (supplemental Table S3). The logarithmic (ln) distributions of the raw and normalized Epithelial/Mesenchymal (E/M) ratios of the peptides identified in the technical replicates 1 (TR1) and 2 (TR2) for both BR1 and BR2 were plotted in Fig. 1*B*, 1*C*, respectively. The correlation of protein ratios identified in both biological replicates with an $r = 0.64$ (p value <0.005, $n = 4{,}253$) indicates the reproducibility of our workflow (Fig. 1*D*).

Based on our statistical analysis (see Experimental Procedures section), 168 proteins are significantly upregulated in epithelial cells whereas 146 proteins are significantly upregulated in mesenchymal ones (Fig. 1*E* and supplemental Table S1). As expected, many known epithelial markers, such as Desmoplakin, Occludin, and E-cadherin were significantly upregulated in epithelial cells (Fig. 1*E*, green) and many known mesenchymal markers, such as Twist1–2, Vimentin, and N-cadherin were significantly upregulated in mesenchymal cells (Fig. 1*E*, yellow). We compared our proteomics data to previously published microarray data obtained from immortalized HMLE cells underwent EMT by expressing Twist (4). Although proteomic data is significantly correlated with the transcriptomic data ($r = 0.53$, p value <0.005), alterations at proteome level are not thoroughly represented with transcriptional data in EMT (supplemental Table S1). Proteins only significantly regulated in proteome data (Fig. 1*F*, blue) comprise 67% of all regulated proteins (Fig. 1*F*, blue, green and red).

Phosphoproteome Is Unstable and Prone to Changes During EMT—To identify protein phosphorylation events of EMT, phosphopeptide enrichment was performed in all SCX fractions using TiO_2 or Ti^{4+}-IMAC columns (24, 25) (Fig. 1*A*). 7,735 and 5,685 phosphopeptides were identified with 1% FDR in BR1 and BR2, respectively (supplemental Tables S2*C* and S2*D*). Fig. 2*A* shows the distributions of all unmodified and phosphorylated peptides for BR1 and BR2 with E/M ratios displayed on the logarithmic (ln) scale. We normalized replicates by their median and plotted E/M ratios of merged (BR1+BR2) peptides for unmodified and phosphorylated peptides (Fig. 2*B*). Notably, there are more alterations in E/M ratios of phosphopeptides (std = 1.18) than the unmodified ones (std = 0.87) (Levene's test p value <0.005). Having more alterations in the phosphopeptides compared with the unmodified ones suggests a pronounced regulation at the phosphorylation status of proteins between epithelial and mesenchymal states. Combination of ratios from two replicates resulted in 4,338 phosphopeptides with at least one phosphorylated residue. Our statistical analysis (see Experimental Procedures section) revealed 357 phosphopeptides as epithelial and 514 as mesenchymal specific (supplemental Fig. S1). The correlation of phosphopeptides in both biological replicates with an $r = 0.7$ (p value <0.005, $n = 4{,}338$) indicates the high reproducibility (Fig. 2*C*). For both epithelial and mesenchymal specific phosphosites, we searched for dominant consensus motifs (supplemental Fig. S1). In epithelial cells, SP and TP motifs dominate and in mesenchymal cells, R/KxxSxD and RxxT are the enriched motifs (Fig. 2*D*). Next, we used NetworKIN 3.0 (30) in KinomeXplorer (46) to further predict potential kinase-substrate relationships of EMT based on known kinase motifs and protein-protein interactions in the STRINGv10 database (47) (supplemental Fig. S1). Accordingly, a kinase-substrate network was reconstructed that covers 73 kinase groups and their potential epithelial and mesenchymal specific substrates (Fig. 2*E*). Notably, more kinase activity and phosphorylation events take place in mesenchymal cells than in epithelial cells. ROCK, Aurora, CAMKII, and MAP kinases are among the predicted kinases for mesenchymal specific phosphorylations (Fig. 2*E*).

Reconstruction of Epithelial and Mesenchymal Specific Protein Networks Reveals Functional Subnetworks—GO enrichment analysis (48) of epithelial and mesenchymal specific proteins revealed distinct annotations in epithelial and mesenchymal cells. Based on the top 10 scoring GO biological process (BP) terms (Fig. 3*A*), cell-cell adhesion and cell junction assembly proteins are the most significant terms in epithelial state whereas regulation of fatty acid metabolism and cellular response to growth factor stimulus are uniquely significant in mesenchymal cells (Fig. 3*A*).

Next, we sought to identify signaling pathways that represent epithelial and mesenchymal states (supplemental Figs. S3 and S4). For this purpose, we took the advantage of Omics Integrator software which optimally reconstructs a network by considering the significance of the proteomic hits and the reliability of protein-protein interactions (32). Beyond the list of proteins, it searches for the either direct interactions of the given proteins or the interactions through intermediate proteins. For epithelial state, cell-cell adhesion, cell junction assembly, and epithelial cell differentiation pathways are among the significantly enriched biological proteins in the reconstructed network (Fig. 3*B*). EGFR, one of the central nodes, interacts with JUP, Col17A, and numerous Keratins. Another

FIG. 2. **Epithelial and mesenchymal specific phosphorylation analysis.** *A*, Distribution of raw ln(Epithelial/Mesenchymal) unmodified peptide and phosphopeptide ratios. Biological replicates 1 and 2 (BR1 and BR2) are shown. *B*, Distribution of normalized and combined ln(Epithelial/Mesenchymal) unmodified peptide and phosphopeptide ratios. Red dashed line illustrates the significance threshold ratio. *C*, The correlation of the phosphopeptides between two biological replicates (Pearson correlation, $r = 0.7$). *D*, The consensus motifs of epithelial and mesenchymal phosphorylation sites. Consensus was extracted using Motif-x. *E*, The predicted kinase-substrate network reveals distinct regulations of epithelial and mesenchymal states.

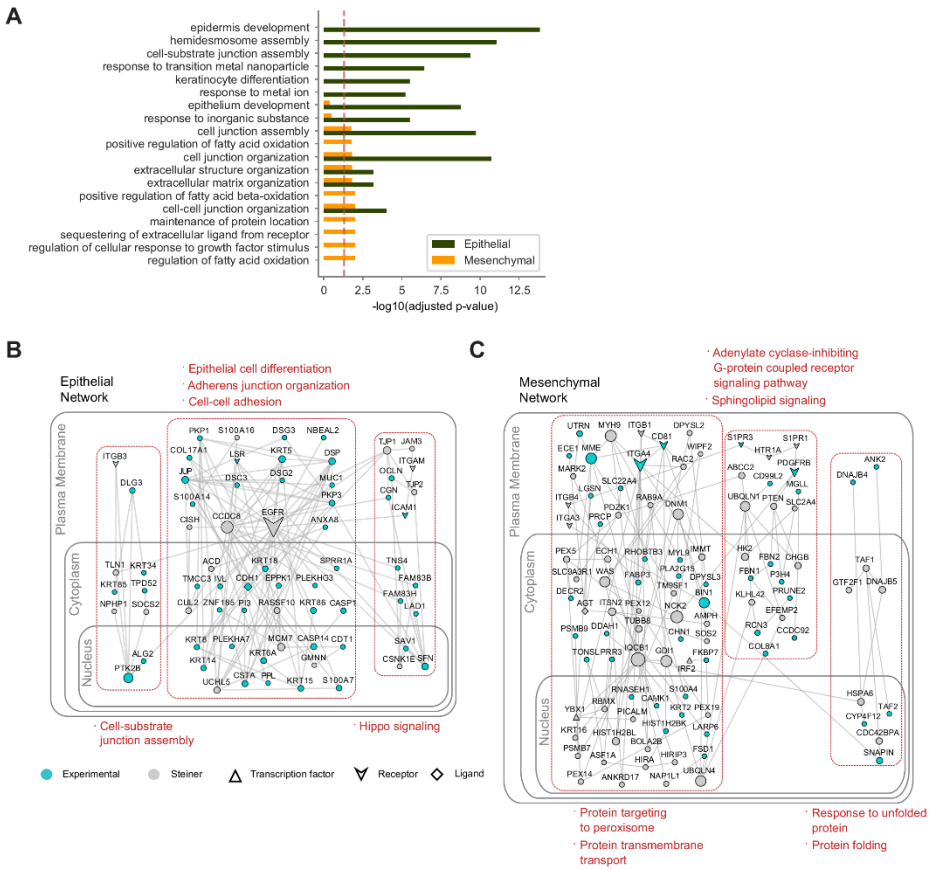
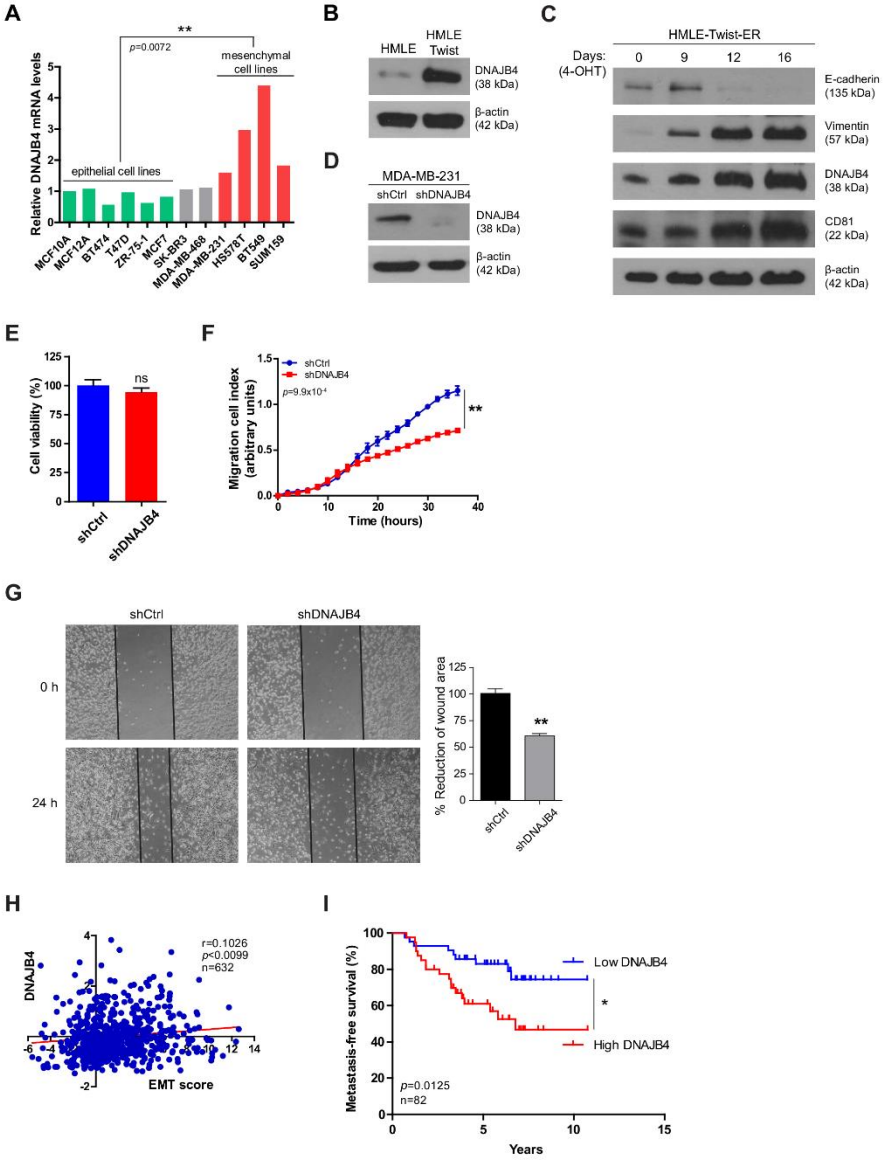


FIG. 3. **The interaction networks of epithelial and mesenchymal states reveal distinct functional subgroups.** *A*, Comparison of GO Biological Process (BP) enrichments in epithelial and mesenchymal specific states. Top 10 scoring GO BP terms for epithelial and mesenchymal specific proteins are illustrated. *B–C*, The interaction network of a subset of epithelial (*B*) and mesenchymal (*C*) specific proteins are shown with Steiner proteins added to the network. Highly interconnected subnetworks are highlighted in red rectangles and enriched GO BP terms are listed (For the networks of all identified epithelial and mesenchymal specific proteins, see supplemental Figs. S3 and S4).

significant pathway is Hippo signaling. Multiple components of Hippo signaling pathway SAV1, TJP1, TJP2, PARD6B, PARD6G, PRKCI, PRKCZ, LLGL2, and SFN (14–3-3 sigma, which is also known as epithelial cell marker protein) (49) are part of the epithelial specific network, which indicates their epithelial cell specific roles. Additionally, our network analysis revealed exocytosis, cell cycle, and regulation of proteolysis as notable cellular functions of epithelial specific proteins. Remarkably, seven members of S100 protein family, which is one of the largest calcium binding protein subfamily, are in multiple subnetworks of epithelial specific proteins including epithelial cell differentiation (Fig. 3*B*).

Multiple signaling pathways are identified in the mesenchymal specific protein network including sphingolipid signaling, regulation of antigen receptor-mediated signaling, transforming growth factor beta receptor signaling, and regulation of TOR signaling (Fig. 3*C*). Our network identified G-coupled receptors S1PR1, S1PR3, and HTR1A that are implicated in


A
**
p=0.0072
mesenchymal cell lines
epithelial cell lines
Relative DNAJB4 mRNA levels
MCF10A
MCF12A
BT474
T47D
ZR-75-1
MCF7
SK-BR3
MDA-MB-468
MDA-MB-231
HS578T
BT549
SUM159
B
HMLE
HMLE Twist
DNAJB4 (38 kDa)
β-actin (42 kDa)
D
MDA-MB-231
shCtrl
shDNAJB4
DNAJB4 (38 kDa)
β-actin (42 kDa)
C
HMLE-Twist-ER
Days: (4-OHT)
0
9
12
16
E-cadherin (135 kDa)
Vimentin (57 kDa)
DNAJB4 (38 kDa)
CD81 (22 kDa)
β-actin (42 kDa)
E
Cell viability (%)
ns
shCtrl
shDNAJB4
F
shCtrl
shDNAJB4
p=9.9x10-4
**
Migration cell index (arbitrary units)
Time (hours)
G
shCtrl
shDNAJB4
0 h
24 h
% Reduction of wound area
**
H
DNAJB4
r=0.1026
p<0.0099
n=632
EMT score
I
Low DNAJB4
High DNAJB4
*
p=0.0125
n=82
Metastasis-free survival (%)
Years

sphingolipid signaling as mesenchymal specific. Activation of those may regulate EMT. Interestingly, multiple mesenchymal specific proteins are linked to fatty acid metabolic processes such as TWIST1, DECR2, CPT1A, CYP4F12, FABP3, IRS2, LPIN3, PLA2G15, and MGLL. This suggests a link between fatty acid metabolism and induction of EMT (Fig. 3*A*, 3*C*). Another remarkable mesenchymal specific subnetwork is protein folding-response to unfolded protein (Fig. 3*C*). Within this subnetwork, two human heat shock proteins 40 family members; DNAJB4 and DNAJB5 are identified (Fig. 3*C*).

Novel Epithelial and Mesenchymal Specific Proteins Affect the Migration of Breast Cancer Cells—Next, we further studied a subclass of novel epithelial and mesenchymal specific proteins using real-time cell migration analysis (RTCA) (supplemental Fig. S5*A*). This subclass of proteins was determined compared with the transcriptome data obtained from Taube *et al.* study (4). We selected the proteins that are either regulated at proteome level or at both transcriptome and proteome levels. In addition to transcriptome data, we analyzed the mRNA expression levels of selected proteins in epithelial and mesenchymal breast cancer cell lines using the study by Luo *et al.* (35) (supplemental Fig. S5*A*). For the RTCA assay, we performed retrovirus-mediated shRNA knockdown of selected epithelial specific proteins in MCF7 cells and selected mesenchymal specific proteins in MDA-MB-231 invasive breast cancer cells. E-cadherin (CDH1) and N-cadherin (CDH2) depletions were used as positive controls (supplemental Fig. S5*B*, S5*C*). When epithelial specific proteins CASP14, PI3, TLR2, and TFAP2A were depleted, we observed that the migration of MCF7 cells increased (supplemental Fig. S5*B*). On the other hand, depletion of mesenchymal specific proteins BIN1, PDGFRB, CADM3, ANPEP, DNAJB4, and CD81 decreased the migration of MDA-MB-231 cells (supplemental Fig. S5*C*, Figs. 4*F* and 5*F*, respectively). We focused on two proteins, DNAJB4 and CD81, for the reasons explained below, to address their effects on EMT both *in vitro* and *in vivo*.

DNAJB4 Knockdown Decreases Migration of Mesenchymal Breast Cancer Cells and Its mRNA Level Predicts Metastasis-free Survival—DNAJB4 is regulated at both transcriptome and proteome level during EMT and shows increased transcription in mesenchymal breast cancer cell lines (supplemental Fig. S5*A* and Fig. 4*A*). In agreement with our quantitative proteomics data, Western blot analysis showed dramatically increased DNAJB4 protein expression in HMLE-Twist cells compared with HMLE cells (Fig. 4*B*). To analyze temporal expression of DNAJB4 during EMT, we used EMT inducible HMLE-Twist-ER cells (50). The cells were treated with 20 nM 4-OHT for 16 days to induce EMT and collected at different days to analyze their expression pattern by Western blotting. We found that DNAJB4 expression increases gradually during EMT induction (Fig. 4*C*).

To examine the roles of DNAJB4 expression on mesenchymal cells, we performed shRNA-mediated knockdown of DNAJB4 in MDA-MB-231 invasive breast cancer cells (Fig. 4*D*). After the suppression of DNAJB4, we observed no change in cell viability (Fig. 4*E*), but a significant inhibition of migration in mesenchymal cells by real-time migration assay (Fig. 4*F*). These results were further validated by a wound healing assay (Fig. 4*G*). Moreover, the correlation analysis of DNAJB4 with EMT scores revealed that DNAJB4 mRNA expression levels positively correlate with the EMT scores of breast cancer patients (Fig. 4*H*). Similarly, the metastasis-free survival analysis of patients revealed that high level of DNAJB4 mRNA expression significantly associates with worse metastasis-free survival of breast cancer patients (Fig. 4*I*). In addition to DNAJB4, the mRNA expression level of DNAJB5, which was also identified as a member of mesenchymal specific network (supplemental Fig. S4 and Fig. 3*C*), is higher in mesenchymal breast cancer cell lines (supplemental Fig. S6*A*) and positively correlates with EMT scores of breast cancer patients (supplemental Fig. S6*B*).

CD81 Knockdown Decreases Migration of Mesenchymal Breast Cancer Cells—Another prominent hit in our migration assay was a member of tetraspanins family, CD81 (supplemental Fig. S5*A*). Although most of the members of tetraspanins were present in the epithelial specific network (supplemental Fig. S3), CD81 is in the mesenchymal specific protein network (supplemental Fig. S4 and Fig. 3*C*). CD81 is regulated only at proteome level, and its transcription level does not significantly change during EMT and in breast cancer cell lines with epithelial or mesenchymal phenotype (supplemental Fig. S5*A* and Fig. 5*A*). Our Western blot analysis confirmed that CD81 protein expression dramatically increases in HMLE-Twist cells as expected from our quantitative proteomics data (Fig. 5*B*). Like DNAJB4, CD81 expression also increased

FIG. 4. **Increased DNAJB4 protein expression in mesenchymal state increases migration of breast cancer cells.** *A*, mRNA expression of DNAJB4 in GSE40059 data set based on the classification of different breast cell lines as epithelial and mesenchymal. *B*, Western blot analysis showing the increased protein expression of DNAJB4 in HMLE-Twist cells. *C*, Induction of EMT with tamoxifen-inducible Twist (Twist-ER) in HMLE cells. Cells were induced to undergo EMT for 16 days of 20 nM of 4-OHT treatment and analyzed for DNAJB4 and CD81 protein expressions. *D*, Western blot analysis of shRNA mediated knockdown of DNAJB4 protein expression in MDA-MB-231 cells. *E*, Cell viability analysis of MDA-MB-231 cells stably expressing the control and DNAJB4 shRNAs. *F*, Real time migration analysis of MDA-MB-231 cell line with DNAJB4 knockdown compared with control cells using real time cell analyzer. shDNAJB4 cells generated a lower signal suggesting that they migrate slower than shCtrl cells. *G*, Wound healing scratch assay of MDA-MB-231 cells with DNAJB4 knockdown for 24 h and the quantification of percent reduction of wound area. *H*, Correlation analysis of the mRNA expression of DNAJB4 with the EMT score in breast cancer patients from TCGA data set. *I*, Metastasis-free survival of breast cancer patients in GSE2603 data set based on mRNA expression of DNAJB4.

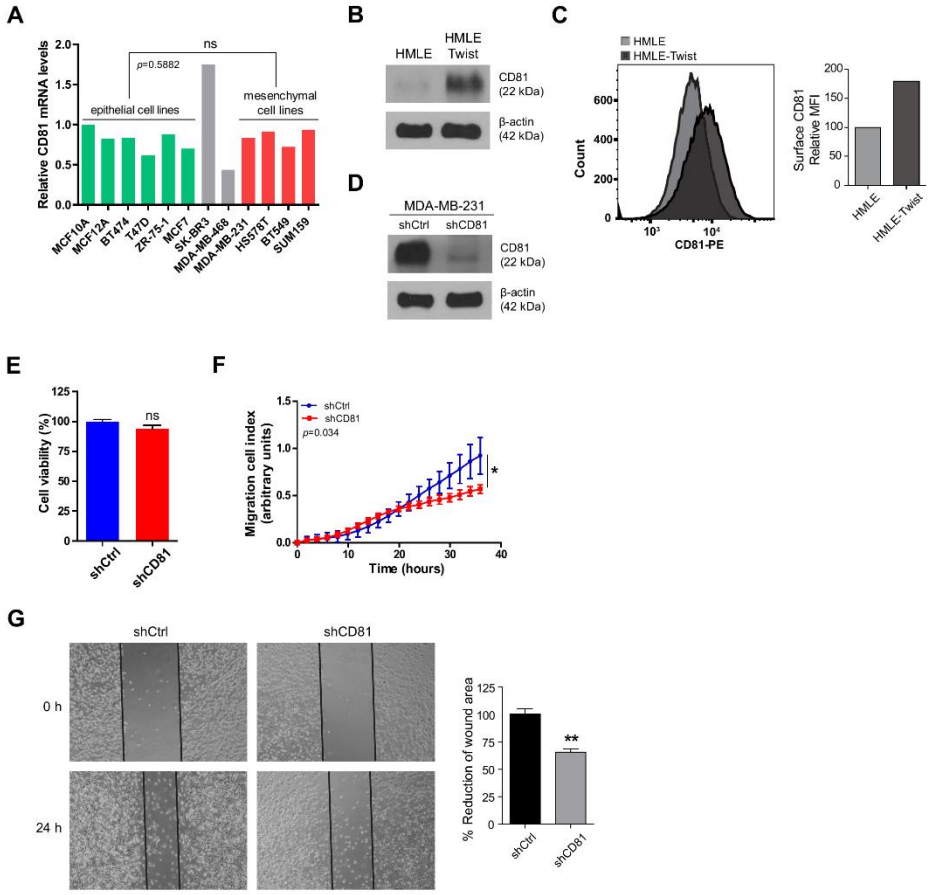


FIG. 5. **Increased CD81 protein expression in mesenchymal state increases migration of breast cancer cells.** *A*, mRNA expression of CD81 in GSE40059 data set based on the classification of different breast cell lines as epithelial and mesenchymal. *B*, Western blot analysis showing the increased protein expression of CD81 in HMLE-Twist cells. *C*, Cell surface expression analysis of CD81 on epithelial and mesenchymal cells by flow cytometry. *D*, Western blot analysis of shRNA mediated knockdown of CD81 protein expression in MDA-MB-231 cells. *E*, Cell viability analysis of MDA-MB-231 cells stably expressing the control and CD81 shRNAs. *F*, Real time migration analysis of MDA-MB-231 cell line with CD81 knockdown compared with control cells using real time cell analyzer. shCD81 cells generated a lower signal suggesting that they migrate slower than shCtrl cells. *G*, Wound healing scratch assay of MDA-MB-231 cells with CD81 knockdown for 24 h and the quantification of percent reduction of wound area.

gradually in a time dependent manner in inducible HMLE-Twist-ER cells as EMT progresses by 4-OHT treatment (Fig. 4*C*). As a potential cell surface marker, we tested whether CD81 expression increases on the mesenchymal cell surface using unpermeabilized HMLE and HMLE-Twist cells in flow cytometry. Our analyses revealed that surface CD81 expression increased 79% in HMLE-Twist cells (Fig. 5*C*).

Next, we performed shRNA-mediated knockdown of CD81 in MDA-MB-231 invasive breast cancer cells. As a result, CD81 was effectively depleted (Fig. 5*D*) and viability of cells

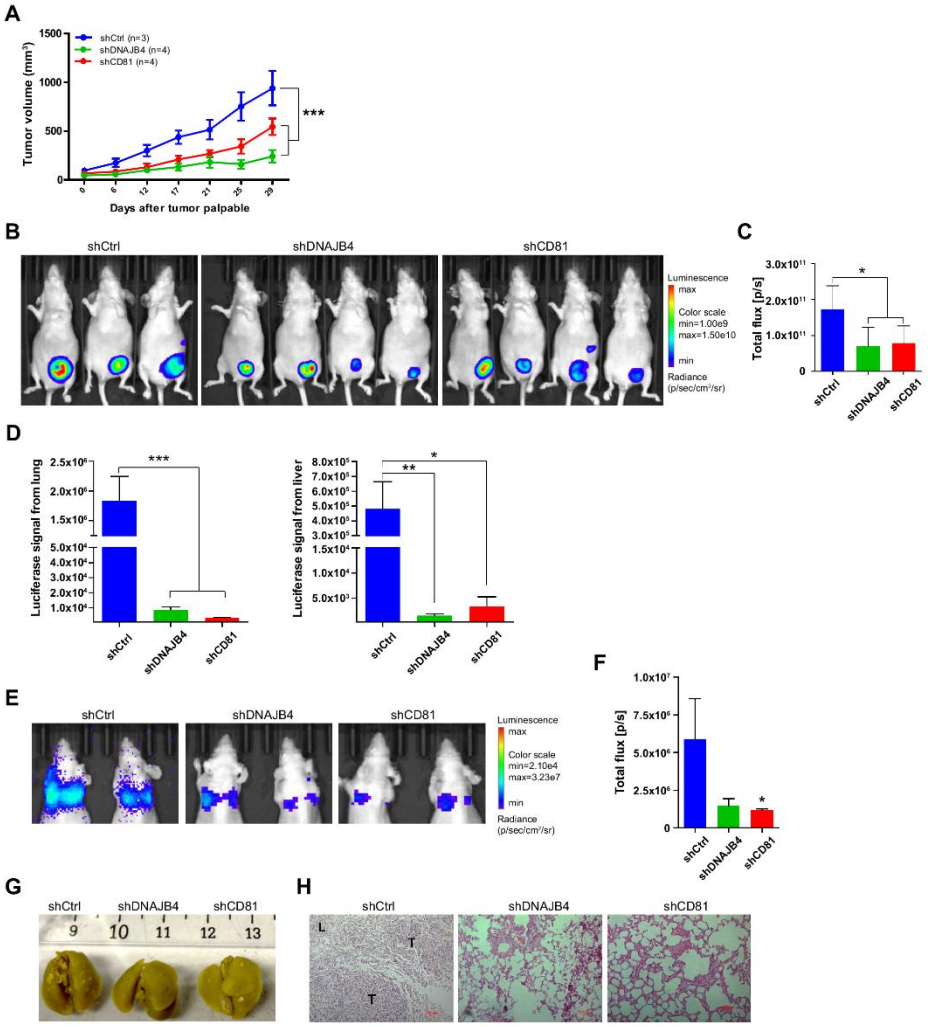


FIG. 6. **Suppression of DNAJB4 and CD81 leads to decreased primary tumor growth, spontaneous metastasis and extravasation/ colonization.** *A*, Primary tumor progression in xenografts generated by mammary fat pad injection of MDA-MB-231-Luc2-GFP control (n = 3), shCD81 (n = 4) and shDNAJB4 (n = 4) into nude mice. *B*, Bioluminescence images of nude mice from Fig. panel *A*. *C*, Quantification of the luminescence signals from mice in Fig. panel *A*, given as total flux. *D*, Luciferase signal coming from lungs and livers of mice in Fig. panel *B* as quantified by luciferase assay (shCtrl n = 3, shCD81 n = 4, and shDNAJB4 n = 3). *E*, Bioluminescence images of nude mice intravenously injected with MDA-MB-231-Luc2-GFP control, shDNAJB4 and shCD81 cells. *F*, Quantification of the luminescence signals from mice in Fig. panel *E*, given as total flux. *G*, Representative images of lungs collected from the groups given in Fig. panel *E*. Mice were sacrificed at sixth

was not affected (Fig. 5*E*). In agreement with the real-time migration assay (Fig. 5*F*), the *in vitro* wound healing assay also revealed the impairment of migration ability of MDA-MB-231 invasive breast cancer cells upon CD81 knockdown (Fig. 5*G*).

Individual Knockdown of DNAJB4 and CD81 Results in Decreased Primary Tumor Growth and Metastasis—We then examined the roles of DNAJB4 and CD81 in primary tumor growth and metastasis *in vivo*. We performed retrovirus-mediated shRNA knockdown of DNAJB4 and CD81 in MDA-MB-231-Luc2-GFP cells. To observe the effects of DNAJB4 and CD81 knockdown on the primary tumor growth, we developed primary tumor xenografts with control and knockdown cells in nude mice. Knockdown of CD81 and DNAJB4 significantly impaired the tumor growth (Fig. 6*A*, 6*B*, 6*C*). To test the effect of two candidates on the spontaneous metastasis, tumor growth has been monitored until tumors in each group reached to 1000 mm^3 (supplemental Fig. S7). One month after surgical removal of primary tumors, an *ex vivo* luciferase assay was performed. Knockdown of CD81 and DNAJB4 significantly reduced both lung and liver metastases (Fig. 6*D*).

Next, we tested whether DNAJB4 and CD81 play a role in extravasation/colonization of MDA-MB-231 invasive breast cancer cells in lungs by tail-vein metastasis assay. After 6 weeks from intravenous injection of DNAJB4 and CD81 depleted cells into nude mice, we compared their lung metastasis with control cells (Fig. 6*E*). Mouse groups injected with either CD81 or DNAJB4 knockdown cells showed a low level of lung metastasis compared with control (Fig. 6F). Similarly, we observed less nodules in lungs in the knockdown group mice compared with control mice after fixation with Bouin's solution (Fig. 6*G*). Hematoxylin and eosin (H&E) staining confirmed the differences in lung metastases in control, DNAJB4 knockdown and CD81 knockdown groups (Fig. 6*H*). These results demonstrate that both DNAJB4 and CD81 contribute to the mesenchymal characteristics of cells undergoing EMT and have roles in primary tumor growth and metastasis of breast cancer cells *in vivo*.

DISCUSSION

The transition from epithelial to mesenchymal state involves a major reorganization of multiple cellular components triggered by EMT-TF. This study used quantitative proteomics to identify biochemical changes after activation of EMT-TF. Previously, Taube *et al.* obtained the transcriptome profiles of HMLE cells in epithelial and mesenchymal states as "EMT core signature" (4). By using HMLE-Twist cells, we profiled the biochemical changes at the protein and post-translational level. Strikingly, around 65% of significantly regulated proteins did not exhibit any detectable regulation at the mRNA level (supplemental Table S1). Similarly, a previous study analyzed the cell surface protein changes during EMT using HMLE-Twist cells by performing membrane-associated protein fractionation followed by mass spectrometry analysis (14). Based on the commonly identified proteins, our whole proteome profile largely correlated with the published cell surface proteome (76% for mesenchymal and 83% for epithelial) (supplemental Tables S1 and S4). Interestingly, when significantly changed proteins were normalized to all identified ones, Lu *et al.* reported more than 2-fold significantly differentially expressed proteins compared with our whole proteome data. One likely explanation for this difference is the contribution of cellular spatial organization during EMT. Altogether, these findings suggest that besides the gene expression level regulation, EMT is regulated at multiple post-transcriptional levels including protein subcellular localization and post-translational modification.

To reveal phosphorylation-driven signaling pathways during EMT, we performed a quantitative phosphoproteomic analysis. Our analysis reveals that there are more alterations in phosphoproteome than proteome. Having more modulation at the phosphorylation level suggest the importance of phosphorylation-based signal transduction pathways during EMT. Many kinases are predicted to phosphorylate either epithelial or mesenchymal specific phosphopeptides. This may suggest that phosphorylation events in EMT are important for cells to preserve their state as epithelial or mesenchymal and transition between two states must be regulated by altered phosphorylation landscape of the cells. Overall, our data points out more global phosphorylation in mesenchymal cells (514) than epithelial cells (357) suggesting an important role of kinases during EMT. We identified 73 kinase groups and their potential epithelial and mesenchymal specific substrates. Some of these roles in EMT are previously reported: CDK5 is required for TGF-β1-induced EMT (51). CK2A2 expression levels are found to be upregulated in human colorectal cancer and downregulated through miR-1228, decreasing EMT capability (52, 53). Exosomes from transformed epithelial cells that contain PAK2 are reported to induce metastatic features in endothelial cells (54). Interestingly, GSK3β's decreased activity is found to be promoting invasive abilities of epithelial cancers via Snail and Slug activation (55–57). We also identified kinases such as PAK2, ROCK2, and NEK1 are auto-phosphorylated in a mesenchymal specific manner. These auto-phosphorylated kinases might be members of the feedback mechanisms in EMT.

Besides the kinase-substrate network, reconstructing epithelial and mesenchymal specific protein-protein interaction networks revealed key signaling pathways of cells undergoing EMT including Hippo, TGF-β, mTOR, PDGF, and cAMP. In

week and lungs were fixed in Bouin's Solution. Metastatic nodules on lung surface appear white after overnight fixation in Bouin's solution. Mice injected with shCtrl cells have more nodules on the lung surface compared with shDNAJB4 and shCD81 cells injected mice. *H*, Representative images of lungs stained with Hematoxylin-Eosin. T: for tumor, L: for lung.

addition to expected cellular machineries that are remodeled during EMT, such as cell adhesion, cell-substrate junction assembly etc., our analysis identified understudied ones, such as lipid metabolism and sphingolipid signaling (58). We found that expression of Sphingosine-1-phosphate receptors 1 and 3 increases in mesenchymal cells. In addition, the expression of fatty acid metabolic process related proteins DECR2, CPT1A, CYP4F12, FABP3, IRS2, LPIN3, PLA2G15, and MGLL were increased in mesenchymal cells. Deciphering the molecular mechanism behind the overexpression of these proteins will provide further insights into the biology of EMT.

One of the interesting signaling pathways enriched for the mesenchymal state is unfolded protein response. DNAJB4 and DNAJB5, members of the human heat shock proteins 40 family, were identified in this subnetwork. Although previous studies have shown DNAJB4 as tumor-suppressor protein (59–61), our proteomic data and patient data set analyses describe DNAJB4 as a metastasis inducer in breast cancer cells. When we compare the mRNA expression levels of DNAJB4 in epithelial and mesenchymal breast cancer cells (35), we found that DNAJB4 mRNA expression levels are significantly increased in mesenchymal cells. Our EMT induction experiment shows that DNAJB4 protein level gradually increases as EMT progresses. Importantly, knockdown of DNAJB4 in MDA-MB-231 cells leads to a decrease in migration, impairs lung metastasis of invasive breast cancer cells, and decreases primary tumor growth rate. In parallel with this, metastasis-free survival analysis of primary breast cancer patients reveals that higher levels of DNAJB4 significantly associates with a worse metastasis-free survival. Recent research demonstrated that inducing EMT causes hyper-activation of unfolded protein response (UPR) signaling pathways (62–65). It has been shown that cells in their mesenchymal state have increased synthesis and secretion of large quantities of extracellular matrix (ECM) proteins which then triggers ER stress and activation of unfolded protein response (63). It is plausible as a chaperone protein, DNAJB4 may be induced to counteract this stress induction on EMT and its expression gradually increases because of the activation of unfolded protein response during EMT. Deciphering the molecular mechanism of DNAJB4 overexpression during EMT would bring new perspectives into the relationship between EMT and unfolded protein response.

One motivation for this study was to find biomarkers for EMT. Our network analysis identified multiple cell surface proteins as epithelial and mesenchymal specific. Some of them may serve as potential biomarkers, such as TSPAN1 and FXYD3 as epithelial and CD10 (MME), CD90 (THY1) (66), Fibulin-4 (EFEMP2) and CD81 as mesenchymal markers. Interestingly, the CD81 mRNA level does not significantly alter during EMT (4) and between epithelial and mesenchymal breast cell lines. But we identified CD81 as one of the significantly upregulated proteins during the EMT process. CD81 protein levels increase gradually as cells undergo EMT. In parallel, CD81 level increased 79% on the surface of HMLE-Twist cells. Functional assays supported its potential of being a marker for EMT process. On CD81 knockdown, we observed a decrease in the migration of mesenchymal breast cancer cells as reported in Zhang *et al.* (67). Moreover, *in vivo* experiments revealed that CD81 knockdown in MDA-MB-231 cells decreased primary tumor growth rate and impaired lung metastasis. Its strong mesenchymal characteristics suggest that CD81 may also have a value as mesenchymal stem cell marker that may target a small subpopulation of cancer cells similar to CD44 (50).

In summary, our analysis combines quantitative proteomic and phosphoproteomic approaches to provide large scale biochemical changes as HMLE cells undergo EMT and reveals key signaling pathways during this process. Considering the key involvement of EMT in both metastasis and drug resistance, detailed characterization of novel EMT regulators may open new avenues for targeting metastatic tumors and overcoming drug resistance.

Acknowledgments—We gratefully acknowledge use of the services and facilities of the Koç University Research Center for Translational Medicine (KUTTAM), funded by the Republic of Turkey Ministry of Development. The content is solely the responsibility of the authors and does not necessarily represent the official views of the Ministry of Development. We thank Dr. Adema Ribic for the critical reading of the manuscript.

DATA AVAILABILITY

The data sets produced in this study are available in the following databases: Protein quantification MS data: PRIDE PXD012001 http://www.ebi.ac.uk/pride/archive/projects/PXD012001, Annotated spectra: MS-Viewer search key is 9vpxyp6xgq, http://msviewer.ucsf.edu/prospector/cgi-bin/mssearch.cgi?report_title=MS-Viewer&search_key=9vpxyp6xgq&search_name=msviewer.

* N.O. was funded by TÜBİTAK 1001 Grant (114Z267), Science Academy (Turkey) Young Scientist Award (BAGEP) and EMBO Installation Grant. Z.C.U.K. and E.S. were funded by TÜBİTAK-BİDEB 2211/E Scholarship Program. The work in T.T.Ö.'s laboratory was supported by an EMBO Installation Grant. The work in Ö.Ş.'s laboratory was, in part, supported by EMBO Installation Grant 2791 and National Institutes of Health Grant P20 GM 109091COBRE. Ö.S. was funded by Susan G. Komen Interdisciplinary Graduate Training to Eliminate Cancer Disparities (IGniTE-CD) Scholarship GTDR17500160. N.T. acknowledges Science Academy (Turkey) for Young Scientist Award (BAGEP) and UNESCO-L'Oreal National for Women in Science Fellowship.

[S] This article contains supplemental material.

‖ To whom correspondence should be addressed. E-mail: nozlu@ku.edu.tr.

‡‡‡ These authors contributed equally.

Author contributions: Z.C.U.K., Ö.K., A.N.P., P.G.E., and Ö.Ş. performed research; Z.C.U.K., E.S., and N.O. wrote the paper; E.S., Ö.S., K.T., B.Y.R., N.T., and N.O. analyzed data; T.T.Ö. and Ö.Ş. contributed new reagents/analytic tools; N.T. and N.O. designed research.

REFERENCES

1. Fidler, I. J. (2003) The pathogenesis of cancer metastasis: the 'seed and soil' hypothesis revisited. *Nat. Rev. Cancer* **3,** 453–458
2. Hanahan, D., and Weinberg, R. A. (2011) Hallmarks of cancer: the next generation. *Cell* **144,** 646–674
3. Onder, T. T., Gupta, P. B., Mani, S. A., Yang, J., Lander, E. S., and Weinberg, R. A. (2008) Loss of E-cadherin promotes metastasis via multiple downstream transcriptional pathways. *Cancer Res.* **68,** 3645–3654
4. Taube, J. H., Herschkowitz, J. I., Komurov, K., Zhou, A. Y., Gupta, S., Yang, J., Hartwell, K., Onder, T. T., Gupta, P. B., Evans, K. W., Hollier, B. G., Ram, P. T., Lander, E. S., Rosen, J. M., Weinberg, R. A., and Mani, S. A. (2010) Core epithelial-to-mesenchymal transition interactome gene-expression signature is associated with claudin-low and metaplastic breast cancer subtypes. *Proc. Natl. Acad. Sci. U.S.A.* **107,** 15449–15454
5. Greenburg, G., and Hay, E. D. (1982) Epithelia suspended in collagen gels can lose polarity and express characteristics of migrating mesenchymal cells. *J. Cell Biol.* **95,** 333–339
6. Kalluri, R., and Weinberg, R. A. (2009) The basics of epithelial-mesenchymal transition. *J. Clin. Investigation* **119,** 1420–1428
7. Lamouille, S., Xu, J., and Derynck, R. (2014) Molecular mechanisms of epithelial-mesenchymal transition. *Nat. Rev. Mol. Cell Biol.* **15,** 178–196
8. Brabletz, T., Kalluri, R., Nieto, M. A., and Weinberg, R. A. (2018) EMT in cancer. *Nat. Rev. Cancer* **18,** 128
9. Du, B., and Shim, J. S. (2016) Targeting epithelial-mesenchymal transition (EMT) to overcome drug resistance in cancer. *Molecules* **21,** pii: E965
10. Sarkar, F. H., Li, Y., Wang, Z., and Kong, D. (2009) Pancreatic cancer stem cells and EMT in drug resistance and metastasis. *Minerva Chirurgica* **64,** 489–500
11. Singh, A., and Settleman, J. (2010) EMT, cancer stem cells and drug resistance: an emerging axis of evil in the war on cancer. *Oncogene* **29,** 4741–4751
12. Wang, Z., Li, Y., Ahmad, A., Azmi, A. S., Kong, D., Banerjee, S., and Sarkar, F. H. (2010) Targeting miRNAs involved in cancer stem cell and EMT regulation: An emerging concept in overcoming drug resistance. *Drug Resistance Updates* **13,** 109–118
13. Tam, W. L., and Weinberg, R. A. (2013) The epigenetics of epithelial-mesenchymal plasticity in cancer. *Nat. Med.* **19,** 1438–1449
14. Lu, H., Clauser, K. R., Tam, W. L., Frose, J., Ye, X., Eaton, E. N., Reinhardt, F., Donnenberg, V. S., Bhargava, R., Carr, S. A., and Weinberg, R. A. (2014) A breast cancer stem cell niche supported by juxtacrine signalling from monocytes and macrophages. *Nat. Cell Biol.* **16,** 1105–1117
15. Tam, W. L., Lu, H., Buikhuisen, J., Soh, B. S., Lim, E., Reinhardt, F., Wu, Z. J., Krall, J. A., Bierie, B., Guo, W., Chen, X., Liu, X. S., Brown, M., Lim, B., and Weinberg, R. A. (2013) Protein kinase C alpha is a central signaling node and therapeutic target for breast cancer stem cells. *Cancer Cell* **24,** 347–364
16. Yang, J., Mani, S. A., Donaher, J. L., Ramaswamy, S., Itzykson, R. A., Come, C., Savagner, P., Gitelman, I., Richardson, A., and Weinberg, R. A. (2004) Twist, a master regulator of morphogenesis, plays an essential role in tumor metastasis. *Cell* **117,** 927–939
17. Filipowicz, W., Bhattacharyya, S. N., and Sonenberg, N. (2008) Mechanisms of post-transcriptional regulation by microRNAs: are the answers in sight? *Nat. Rev. Gen.* **9,** 102–114
18. Filipowicz, W., Jaskiewicz, L., Kolb, F. A., and Pillai, R. S. (2005) Post-transcriptional gene silencing by siRNAs and miRNAs. *Current Opin. Struct. Biol.* **15,** 331–341
19. Selbach, M., Schwanhäusser, B., Thierfelder, N., Fang, Z., Khanin, R., and Rajewsky, N. (2008) Widespread changes in protein synthesis induced by microRNAs. *Nature* **455,** 58
20. Elenbaas, B., Spirio, L., Koerner, F., Fleming, M. D., Zimonjic, D. B., Donaher, J. L., Popescu, N. C., Hahn, W. C., and Weinberg, R. A. (2001) Human breast cancer cells generated by oncogenic transformation of primary mammary epithelial cells. *Genes Develop.* **15,** 50–65
21. Zhou, H., Ye, M., Dong, J., Corradini, E., Cristobal, A., Heck, A. J., Zou, H., and Mohammed, S. (2013) Robust phosphoproteome enrichment using monodisperse microsphere-based immobilized titanium (IV) ion affinity chromatography. *Nat. Protocols* **8,** 461–480
22. Polat, A. N., Karayel, O., Giese, S. H., Harmanda, B., Sanal, E., Hu, C. K., Renard, B. Y., and Ozlu, N. (2015) Phosphoproteomic analysis of aurora kinase inhibition in monopolar cytokinesis. *J. Proteome Res.* **14,** 4087–4098
23. Boersema, P. J., Raijmakers, R., Lemeer, S., Mohammed, S., and Heck, A. J. (2009) Multiplex peptide stable isotope dimethyl labeling for quantitative proteomics. *Nat. Protocols* **4,** 484–494
24. de Graaf, E. L., Giansanti, P., Altelaar, A. F., and Heck, A. J. (2014) Single-step enrichment by Ti4+-IMAC and label-free quantitation enables in-depth monitoring of phosphorylation dynamics with high reproducibility and temporal resolution. *Mol. Cell. Proteomics* **13,** 2426–2434
25. Thingholm, T. E., Jorgensen, T. J., Jensen, O. N., and Larsen, M. R. (2006) Highly selective enrichment of phosphorylated peptides using titanium dioxide. *Nat. Protocols* **1,** 1929–1935
26. Taus, T., Kocher, T., Pichler, P., Paschke, C., Schmidt, A., Henrich, C., and Mechtler, K. (2011) Universal and confident phosphorylation site localization using phosphoRS. *J. Proteome Res.* **10,** 5354–5362
27. Chou, M. F., and Schwartz, D. (2011) Biological sequence motif discovery using motif-x. *Current protocols in bioinformatics* Chapter 13, Unit 13.15–24 John Wiley & Sons, Inc., Hoboken, NJ
28. Wagih, O., Sugiyama, N., Ishihama, Y., and Beltrao, P. (2016) Uncovering Phosphorylation-Based Specificities through Functional Interaction Networks. *Mol. Cell. Proteomics* **15,** 236–245
29. Crooks, G. E., Hon, G., Chandonia, J. M., and Brenner, S. E. (2004) WebLogo: a sequence logo generator. *Genome Res.* **14,** 1188–1190
30. Linding, R., Jensen, L. J., Pasculescu, A., Olhovsky, M., Colwill, K., Bork, P., Yaffe, M. B., and Pawson, T. (2008) NetworKIN: a resource for exploring cellular phosphorylation networks. *Nucleic Acids Res.* **36,** D695–D699
31. Shannon, P., Markiel, A., Ozier, O., Baliga, N. S., Wang, J. T., Ramage, D., Amin, N., Schwikowski, B., and Ideker, T. (2003) Cytoscape: a software environment for integrated models of biomolecular interaction networks. *Genome Res.* **13,** 2498–2504
32. Tuncbag, N., Gosline, S. J. C., Kedaigle, A., Soltis, A. R., Gitter, A., and Fraenkel, E. (2016) Network-based interpretation of diverse high-throughput datasets through the omics integrator software package. *PLOS Computational Biol.* **12,** e1004879
33. Karayel Ö., Şanal, E, Giese, S. H., Üretmen Kagıalı, Z. C., Polat, A. N., Hu, C.-K., Renard, B. Y., Tuncbag, N., and Özlü, N. (2018) Comparative phosphoproteomic analysis reveals signaling networks regulating monopolar and bipolar cytokinesis. *Sci. Reports* **8,** 2269
34. Turner, B., Razick, S., Turinsky, A. L., Vlasblom, J., Crowdy, E. K., Cho, E., Morrison, K., Donaldson, I. M., and Wodak, S. J. (2010) iRefWeb: interactive analysis of consolidated protein interaction data and their supporting evidence. *Database* **2010,** baq023
35. Luo, D., Wilson, J. M., Harvel, N., Liu, J., Pei, L., Huang, S., Hawthorn, L., and Shi, H. (2013) A systematic evaluation of miRNA:mRNA interactions involved in the migration and invasion of breast cancer cells. *J. Translational Med.* **11,** 57
36. Blick, T., Widodo, E., Hugo, H., Waltham, M., Lenburg, M. E., Neve, R. M., and Thompson, E. W. (2008) Epithelial mesenchymal transition traits in human breast cancer cell lines. *Clin. Exp. Metastasis* **25,** 629–642
37. Lombaerts, M., van Wezel, T., Philippo, K., Dierssen, J. W., Zimmerman, R. M., Oosting, J., van Eijk, R., Eilers, P. H., van de Water, B., Cornelisse, C. J., and Cleton-Jansen, A. M. (2006) E-cadherin transcriptional down-regulation by promoter methylation but not mutation is related to epithelial-to-mesenchymal transition in breast cancer cell lines. *Br. J. Cancer* **94,** 661–671
38. Sommers, C. L., Byers, S. W., Thompson, E. W., Torri, J. A., and Gelmann, E. P. (1994) Differentiation state and invasiveness of human breast cancer cell lines. *Breast Cancer Res. Treatment* **31,** 325–335
39. Cerami, E., Gao, J., Dogrusoz, U., Gross, B. E., Sumer, S. O., Aksoy, B. A., Jacobsen, A., Byrne, C. J., Heuer, M. L., Larsson, E., Antipin, Y., Reva, B., Goldberg, A. P., Sander, C., and Schultz, N. (2012) The cBio cancer genomics portal: an open platform for exploring multidimensional cancer genomics data. *Cancer Discovery* **2,** 401–404
40. Gao, J., Aksoy, B. A., Dogrusoz, U., Dresdner, G., Gross, B., Sumer, S. O., Sun, Y., Jacobsen, A., Sinha, R., Larsson, E., Cerami, E., Sander, C., and Schultz, N. (2013) Integrative analysis of complex cancer genomics and clinical profiles using the cBioPortal. *Sci. Signaling* **6,** pl1
41. Li, J., Lu, Y., Akbani, R., Ju, Z., Roebuck, P. L., Liu, W., Yang, J.-Y., Broom, B. M., Verhaak, R. G. W., Kane, D. W., Wakefield, C., Weinstein, J. N., Mills, G. B., and Liang, H. (2013) TCPA: a resource for cancer functional proteomics data. *Nat. Methods* **10,** 1046

42. Minn, A. J., Gupta, G. P., Siegel, P. M., Bos, P. D., Shu, W., Giri, D. D., Viale, A., Olshen, A. B., Gerald, W. L., and Massague, J. (2005) Genes that mediate breast cancer metastasis to lung. *Nature* **436,** 518–524
43. Olson, A., Sheth, N., Lee, J. S., Hannon, G., and Sachidanandam, R. (2006) RNAi Codex: a portal/database for short-hairpin RNA (shRNA) gene-silencing constructs. *Nucleic Acids Res.* **34,** D153–D157
44. Onder, T. T., Kara, N., Cherry, A., Sinha, A. U., Zhu, N., Bernt, K. M., Cahan, P., Mancarci, B. O., Unternaehrer, J., Gupta, P. B., Lander, E. S., Armstrong, S. A., and Daley, G. Q. (2012) Chromatin-modifying enzymes as modulators of reprogramming. *Nature* **483,** 598
45. Cevik, S. I., Keskin, N., Belkaya, S., Ozlu, M. I., Deniz, E., Tazebay, U. H., and Erman, B. (2012) CD81 interacts with the T cell receptor to suppress signaling. *PloS One* **7,** e50396
46. Hom, H., Schoof, E. M., Kim, J., Robin, X., Miller, M. L., Diella, F., Palma, A., Cesareni, G., Jensen, L. J., and Linding, R. (2014) KinomeXplorer: an integrated platform for kinome biology studies. *Nat. Methods* **11,** 603–604
47. Szklarczyk, D., Franceschini, A., Wyder, S., Forslund, K., Heller, D., Huerta-Cepas, J., Simonovic, M., Roth, A., Santos, A., Tsafou, K. P., Kuhn, M., Bork, P., Jensen, L. J., and von Mering, C. (2015) STRING v10: protein-protein interaction networks, integrated over the tree of life. *Nucleic Acids Res.* **43,** D447–D452
48. Ashburner, M., Ball, C. A., Blake, J. A., Botstein, D., Butler, H., Cherry, J. M., Davis, A. P., Dolinski, K., Dwight, S. S., Eppig, J. T., Harris, M. A., Hill, D. P., Issel-Tarver, L., Kasarskis, A., Lewis, S., Matese, J. C., Richardson, J. E., Ringwald, M., Rubin, G. M., and Sherlock, G. (2000) Gene ontology: tool for the unification of biology. The Gene Ontology Consortium. *Nat. Genetics* **25,** 25–29
49. Zeng, Q., and Hong, W. (2008) The emerging role of the hippo pathway in cell contact inhibition, organ size control, and cancer development in mammals. *Cancer Cell* **13,** 188–192
50. Mani, S. A., Guo, W., Liao, M. J., Eaton, E. N., Ayyanan, A., Zhou, A. Y., Brooks, M., Reinhard, F., Zhang, C. C., Shipitsin, M., Campbell, L. L., Polyak, K., Brisken, C., Yang, J., and Weinberg, R. A. (2008) The epithelial-mesenchymal transition generates cells with properties of stem cells. *Cell* **133,** 704–715
51. Liang, Q., Li, L., Zhang, J., Lei, Y., Wang, L., Liu, D. X., Feng, J., Hou, P., Yao, R., Zhang, Y., Huang, B., and Lu, J. (2013) CDK5 is essential for TGF-beta1-induced epithelial-mesenchymal transition and breast cancer progression. *Sci. Rep.* **3,** 2932
52. Jia, L., Wu, J., Zhang, L., Chen, J., Zhong, D., Xu, S., Xie, C., and Cai, J. (2013) Restoration of miR-1228* expression suppresses epithelial-mesenchymal transition in gastric cancer. *PloS One* **8,** e58637
53. Lin, K. Y., Tai, C., Hsu, J. C., Li, C. F., Fang, C. L., Lai, H. C., Hseu, Y. C., Lin, Y. F., and Uen, Y. H. (2011) Overexpression of nuclear protein kinase CK2 alpha catalytic subunit (CK2alpha) as a poor prognosticator in human colorectal cancer. *PloS One* **6,** e17193
54. Gopal, S. K., Greening, D. W., Hanssen, E. G., Zhu, H. J., Simpson, R. J., and Mathias, R. A. (2016) Oncogenic epithelial cell-derived exosomes containing Rac1 and PAK2 induce angiogenesis in recipient endothelial cells. *Oncotarget* **7,** 19709–19722
55. Kao, S. H., Wang, W. L., Chen, C. Y., Chang, Y. L., Wu, Y. Y., Wang, Y. T., Wang, S. P., Nesvizhskii, A. I., Chen, Y. J., Hong, T. M., and Yang, P. C. (2014) GSK3beta controls epithelial-mesenchymal transition and tumor metastasis by CHIP-mediated degradation of Slug. *Oncogene* **33,** 3172–3182
56. Liu, C.-W., Li, C.-H., Peng, Y.-J., Cheng, Y.-W., Chen, H.-W., Liao, P.-L., Kang, J.-J., and Yeng, M.-H. (2014) Snail regulates Nanog status during the epithelial-mesenchymal transition via the Smad1/Akt/GSK3β signaling pathway in non-small-cell lung cancer. *Oncotarget* **5,** 3880–3894
57. Wang, H., Wang, H.-S., Zhou, B.-H., Li, C.-L., Zhang, F., Wang, X.-F., Zhang, G., Bu, X.-Z., Cai, S.-H., and Du, J. (2013) Epithelial-mesenchymal transition (EMT) induced by TNF-α requires AKT/GSK-3β-mediated stabilization of snail in colorectal cancer. *PloS One* **8,** e56664–e56664
58. Levade, T., Andrieu-Abadie, N., Micheau, O., Legembre, P., and Ségui, B. (2015) Sphingolipids modulate the epithelial–mesenchymal transition in cancer. *Cell Death Discovery* **1,** 15001
59. Chen, H. W., Lee, J. Y., Huang, J. Y., Wang, C. C., Chen, W. J., Su, S. F., Huang, C. W., Ho, C. C., Chen, J. J., Tsai, M. F., Yu, S. L., and Yang, P. C. (2008) Curcumin inhibits lung cancer cell invasion and metastasis through the tumor suppressor HLJ1. *Cancer Res.* **68,** 7428–7438
60. Tsai, M. F., Wang, C. C., Chang, G. C., Chen, C. Y., Chen, H. Y., Cheng, C. L., Yang, Y. P., Wu, C. Y., Shih, F. Y., Liu, C. C., Lin, H. P., Jou, Y. S., Lin, S. C., Lin, C. W., Chen, W. J., Chan, W. K., Chen, J. J., and Yang, P. C. (2006) A new tumor suppressor DnaJ-like heat shock protein, HLJ1, and survival of patients with non-small-cell lung carcinoma. *J. Natl. Cancer Inst.* **98,** 825–838
61. Wang, C. C., Tsai, M. F., Dai, T. H., Hong, T. M., Chan, W. K., Chen, J. J., and Yang, P. C. (2007) Synergistic activation of the tumor suppressor, HLJ1, by the transcription factors YY1 and activator protein 1. *Cancer Res.* **67,** 4816–4826
62. Feng, Y., Jin, D. X., and Gupta, P. B. (2016) Abstract 2677: Unfolded protein response is required for EMT-driven metastasis by inducing CREB3L1. *Cancer Res.* **76,** 2677
63. Feng, Y. X., Sokol, E. S., Del Vecchio, C. A., Sanduja, S., Claessen, J. H., Proia, T. A., Jin, D. X., Reinhardt, F., Ploegh, H. L., Wang, Q., and Gupta, P. B. (2014) Epithelial-to-mesenchymal transition activates PERK-eIF2alpha and sensitizes cells to endoplasmic reticulum stress. *Cancer Discovery* **4,** 702–715
64. Shen, X., Xue, Y., Si, Y., Wang, Q., Wang, Z., Yuan, J., and Zhang, X. (2015) The unfolded protein response potentiates epithelial-to-mesenchymal transition (EMT) of gastric cancer cells under severe hypoxic conditions. *Med. Oncol.* **32,** 447
65. Zeindl-Eberhart, E., Brandl, L., Liebmann, S., Ormanns, S., Scheel, S. K., Brabletz, T., Kirchner, T., and Jung, A. (2014) Epithelial-mesenchymal transition induces endoplasmic-reticulum-stress response in human colorectal tumor cells. *PloS One* **9,** e87386
66. Battula, V. L., Evans, K. W., Hollier, B. G., Shi, Y., Marini, F. C., Ayyanan, A., Wang, R. Y., Brisken, C., Guerra, R., Andreeff, M., and Mani, S. A. (2010) Epithelial-mesenchymal transition-derived cells exhibit multilineage differentiation potential similar to mesenchymal stem cells. *Stem Cells* **28,** 1435–1445
67. Zhang, N., Zuo, L., Zheng, H., Li, G., and Hu, X. (2018) Increased expression of CD81 in breast cancer tissue is associated with reduced patient prognosis and increased cell migration and proliferation in MDA-MB-231 and MDA-MB-435S human breast cancer cell lines in vitro. *Med. Sci. Monitor* **24,** 5739–5747

nature COMMUNICATIONS

ARTICLE

https://doi.org/10.1038/s41467-020-16199-4 OPEN

Targeting lysyl oxidase (LOX) overcomes chemotherapy resistance in triple negative breast cancer

Ozge Saatci[1], Aysegul Kaymak[1], Umar Raza[2], Pelin G. Ersan[2], Ozge Akbulut[2], Carolyn E. Banister[1], Vitali Sikirzhytski[1], Unal Metin Tokat[2], Gamze Aykut[2], Suhail A. Ansari[2], Hayriye Tatli Dogan[3], Mehmet Dogan[4], Pouria Jandaghi[5,6], Aynur Isik[7], Fatma Gundogdu[8], Kemal Kosemehmetoglu[8], Omer Dizdar[9], Sercan Aksoy[9], Aytekin Akyol[7,8], Aysegul Uner[8,10], Phillip J. Buckhaults[1], Yasser Riazalhosseini[5,6] & Ozgur Sahin[1,2]✉

Chemoresistance is a major obstacle in triple negative breast cancer (TNBC), the most aggressive breast cancer subtype. Here we identify hypoxia-induced ECM re-modeler, lysyl oxidase (LOX) as a key inducer of chemoresistance by developing chemoresistant TNBC tumors in vivo and characterizing their transcriptomes by RNA-sequencing. Inhibiting LOX reduces collagen cross-linking and fibronectin assembly, increases drug penetration, and downregulates ITGA5/FN1 expression, resulting in inhibition of FAK/Src signaling, induction of apoptosis and re-sensitization to chemotherapy. Similarly, inhibiting FAK/Src results in chemosensitization. These effects are observed in 3D-cultured cell lines, tumor organoids, chemoresistant xenografts, syngeneic tumors and PDX models. Re-expressing the hypoxia-repressed miR-142-3p, which targets *HIF1A*, *LOX* and *ITGA5*, causes further suppression of the HIF-1α/LOX/ITGA5/FN1 axis. Notably, higher LOX, ITGA5, or FN1, or lower miR-142-3p levels are associated with shorter survival in chemotherapy-treated TNBC patients. These results provide strong pre-clinical rationale for developing and testing LOX inhibitors to overcome chemoresistance in TNBC patients.

[1] Department of Drug Discovery and Biomedical Sciences, University of South Carolina, Columbia, SC 29208, USA. [2] Faculty of Science, Department of Molecular Biology and Genetics, Bilkent University, 06800 Ankara, Turkey. [3] Department of Medical Pathology, Ankara Yildirim Beyazit University, 06800 Ankara, Turkey. [4] Department of Medical Pathology, Ankara Oncology Education and Research Hospital, 06200 Ankara, Turkey. [5] Department of Human Genetics, McGill University, Montreal, QC H3A 1B1, Canada. [6] McGill University and Genome Quebec Innovation Centre, Montreal, QC H3A 0G1, Canada. [7] Hacettepe University Transgenic Animal Technologies Research and Application Center, 06100 Ankara, Turkey. [8] Faculty of Medicine, Department of Pathology, Hacettepe University, 06100 Ankara, Turkey. [9] Department of Medical Oncology, Hacettepe University Cancer Institute, 06100 Ankara, Turkey. [10] Hacettepe University Molecular Pathology Research and Application Center, 06100 Ankara, Turkey. ✉email: sahinozgur@gmail.com

Triple negative breast cancer (TNBC) is the most aggressive subtype of breast cancer. It accounts for 10–20% of all patients, yet is responsible for 30% of all breast cancer deaths[1]. At the molecular level, TNBC is characterized by the lack of estrogen receptor alpha (ERα), progesterone receptor (PR) and epidermal growth factor receptor 2 (HER2/ErbB2)[2,3] expression. TNBC patients mostly rely on chemotherapy unlike other subtypes that can be treated with targeted therapies. Anthracyclines and taxane-based chemotherapy agents are among the most commonly used chemotherapeutics in both neo-adjuvant and adjuvant settings[4]. As compared to other subtypes, TNBC patients show low risk of recurrence if pathological complete response (pCR) is achieved[5]. However, while only 30–40% of TNBC patients show pCR towards treatment, the majority have <60% 5-year survival due to aggressive relapse[6]. Recently, the first immunotherapy for breast cancer was approved by the Food and Drug Administration (FDA) to treat locally advanced or metastatic TNBC patients. However, immunotherapy combined with chemotherapy produced only a 3 month improvement in progression-free survival, and improvement in overall survival was observed only in patients with PD-L1 positive tumors[7]. Therefore, there is still a dire need to identify novel molecular targets to improve the therapeutic benefit of chemotherapy given in first-line settings, as well as in patients with advanced, chemotherapy resistant TNBC. This will have immediate translational impact on improving the pCR rate to standard chemotherapy and will improve patient outcome for the most-aggressive breast cancer subtype.

Deregulation of distinct cell intrinsic processes, such as apoptosis[8], growth factor signaling[9], DNA repair[10] as well as alterations in the levels of drug transporter proteins[11] have previously been associated with chemoresistance. In addition, accumulating evidence suggest that the tumor extracellular matrix (ECM) may also confer resistance to therapy, either by providing a protective barrier that hinders access of anti-cancer drugs to tumors[12–14] or by activating survival signaling or blocking apoptosis upon interacting with the integrin type transmembrane receptors[15,16]. Integrins are heterodimeric cell surface receptors that control cell adhesion, cytoskeletal organization, signal transduction and cell migration via establishing focal adhesion complexes that serve as mechanical links that convey signals between ECM and the intracellular compartment of the interacting cell[17,18]. Activation of integrin signaling may lead to resistance to therapy[15,19,20] and acquisition of metastatic traits[21]. Notably, increased expression of several integrin subunits have previously been associated with poor patient outcome[19,22,23].

The ECM is a highly dynamic structure that is constantly remodeled by cells through altered synthesis, degradation, reassembly and chemical modifications[24]. While normal epithelial cells produce small amounts of ECM, fibroblasts and tumors cells produce large quantities of ECM molecules, such as collagen and fibronectin[25,26]. In addition, overexpression of ECM remodeling enzymes such as matrix metalloproteases (ECM degraders) and lysyl oxidases (ECM stiffeners) have previously been associated with tumor aggressiveness[24]. The lysyl oxidase (LOX) family proteins mediate the conversion of lysine residues in collagen and elastin precursors into highly reactive aldehydes thereby triggering cross-linking and stabilization of ECM proteins, specifically the type I collagen and elastin, and regulate cell adhesion, motility and invasion[27]. In preclinical breast cancer models, LOX secretion from breast cancer cells was shown to induce the pre-metastatic niche formation[28], and LOX inhibition suppressed lung metastasis[29]. LOX inhibition was also shown to sensitize pancreatic cancer to chemotherapy[30,31]. Furthermore, novel intracellular functions of the LOX family proteins have been reported, such as the stabilization of transcription factors and maintenance of chromosome stability[32]. Despite the relatively well-established roles of LOX in stimulating cancer metastasis, its contribution to chemoresistance in TNBCs has not yet been reported.

In this study, we combine in vivo-developed chemoresistant xenograft models with an unbiased, genome-wide transcriptomic approach, 3D cell culture systems, primary breast cancer organoids, syngeneic and patient-derived xenograft (PDX) models and patient data/tissue analyses to identify mechanisms of chemotherapy resistance in TNBCs. We show that chemoresistance is driven by the HIF-1α/miR-142-3p/LOX/ITGA5/FN1 axis and targeting either LOX or its downstream FAK/Src signaling pathway, or overexpressing miR-142-3p can overcome chemoresistance in TNBC.

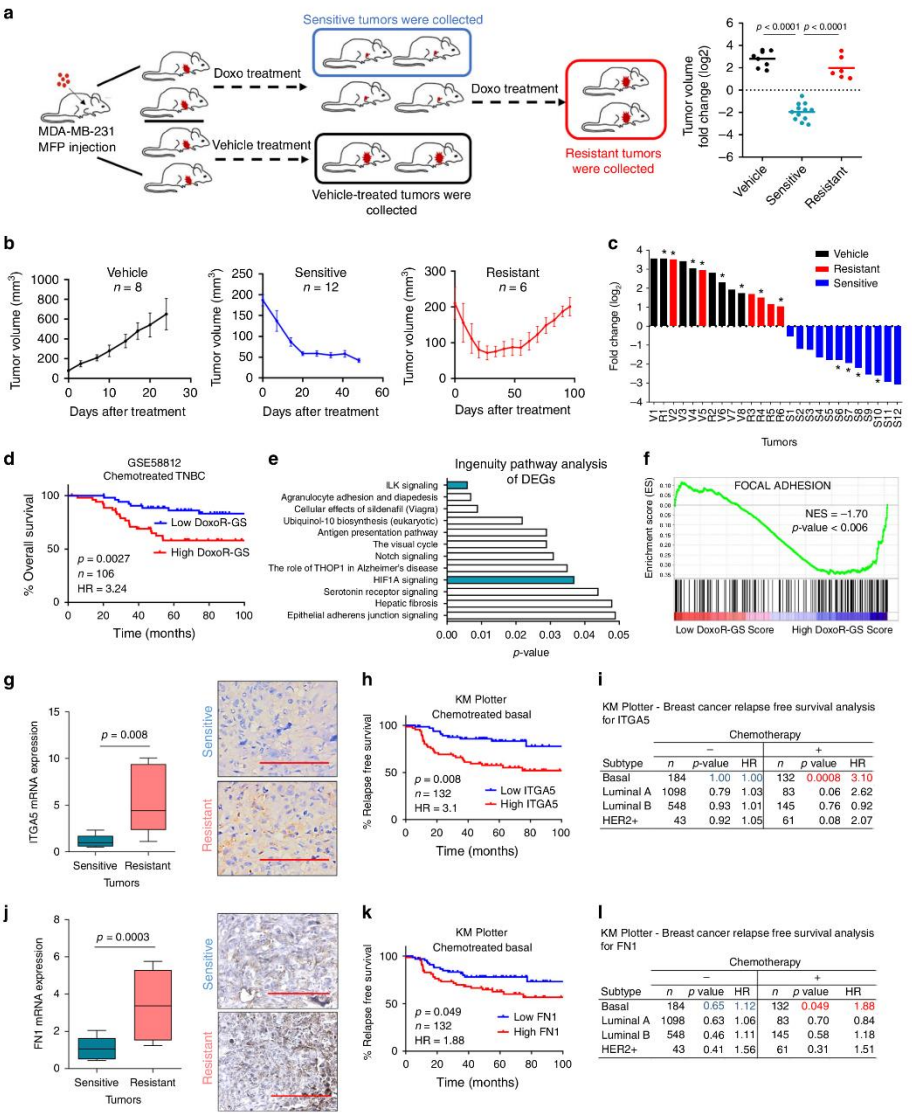
Results

Integrin signaling is a key mediator of chemoresistance in TNBCs. To elucidate the underlying mechanisms of chemoresistance in TNBCs, we modelled the clinical acquired resistance by using xenografts of the well-established TNBC cell line, MDA-MB-231[33,34]. Tumor-bearing mice were continuously treated with either vehicle or doxorubicin, and the fast-growing vehicle-treated mice were sacrificed, and tumors were denoted as vehicle. When tumors from the doxorubicin-treated group exhibited initial response to therapy and shrunk, tumors from some of the mice were collected and denoted as sensitive. The rest of the mice were kept under doxorubicin treatment until their tumors exhibited re-growth at rates comparable to vehicle-treated tumors, and those tumors were classified as resistant (Fig. 1a). The average growth curves and the Waterfall plot showing tumor volume fold change over time for vehicle-treated, doxorubicin-sensitive and -resistant tumors are depicted in Fig. 1b, c, respectively.

We performed RNA-sequencing (RNA-seq) on bulk tumors (four tumors from each group) to identify transcripts differentially expressed between doxorubicin-sensitive and -resistant tumors. We used the 441 most differentially expressed genes (fold change (FC) cut-off = 1.75, p-value < 0.05, Supplementary Data 1) to create a doxorubicin resistance gene signature (DoxoR-GS). We then tested its clinical relevance using gene expression profiling datasets of chemotherapy-treated TNBC patients (for details, see "Methods" section)[35]. Chemotherapy-treated TNBC patients from GSE58812[36] that have high DoxoR-GS scores exhibit poor overall survival (OS) as compared to those with low DoxoR-GS scores (Fig. 1d). These results were further confirmed using METABRIC dataset[37] (Supplementary Fig. 1a) and in another dataset (GSE31519) where we showed that expression of DoxoR-GS is significantly higher in patients who exhibit an event, described as either relapse- or distant metastasis (Supplementary Fig. 1b).

Having validated the clinical relevance of our in vivo-derived DoxoR-GS, we sought to identify the pathways that were most significantly represented among the differentially expressed genes. Ingenuity Pathway Analysis (IPA) revealed that integrin-linked kinase (ILK) signaling was the top deregulated pathway (Fig. 1e). Gene set enrichment analysis (GSEA) in chemotherapy-treated TNBC patients demonstrated that genes involved in focal adhesion signaling were significantly enriched in high DoxoR-GS scorers (Fig. 1f), underlining the importance of integrins and downstream focal adhesion in doxorubicin resistance.

Based on the RNA-seq analysis of our doxorubicin-resistant models, three integrin genes, *ITGA5*, *ITGA10* and *ITGB5* were significantly (FC cut-off = 1.5, p-value < 0.05) upregulated in resistant tumors (Fig. 1g and Supplementary Fig. 1c). We found that higher expression of only the integrin alpha 5 (ITGA5), but



Subtype	n	p-value	HR	n	p value	HR
	Chemotherapy					
	−			+		
Basal	184	1.00	1.00	132	0.0008	3.10
Luminal A	1098	0.79	1.03	83	0.06	2.62
Luminal B	548	0.93	1.01	145	0.76	0.92
HER2+	43	0.92	1.05	61	0.08	2.07

Subtype	n	p value	HR	n	p value	HR
	Chemotherapy					
	−			+		
Basal	184	0.65	1.12	132	0.049	1.88
Luminal A	1098	0.63	1.06	83	0.70	0.84
Luminal B	548	0.46	1.11	145	0.58	1.18
HER2+	43	0.41	1.56	61	0.31	1.51

not that of ITGA10 or ITGB5, is associated with shorter relapse-free survival (RFS) in chemotherapy-treated basal patients (Fig. 1h, i and Supplementary Fig. 1d, e). No such relationship was observed in patients with basal subtype of breast cancer who were not treated with chemotherapy or in patients with other subtypes (Fig. 1i). As around 70% of TNBCs are basal subtype, and 76% of basal subtype are TNBCs[38], we classified patients also as TNBC using ERα, PR, and HER2 expression and again observed a strong association between ITGA5 expression and RFS in chemotherapy-treated TNBC patients (Supplementary Fig. 2a). Importantly, we also detected a significant upregulation of fibronectin (FN1), the main ligand for ITGA5, in doxorubicin-

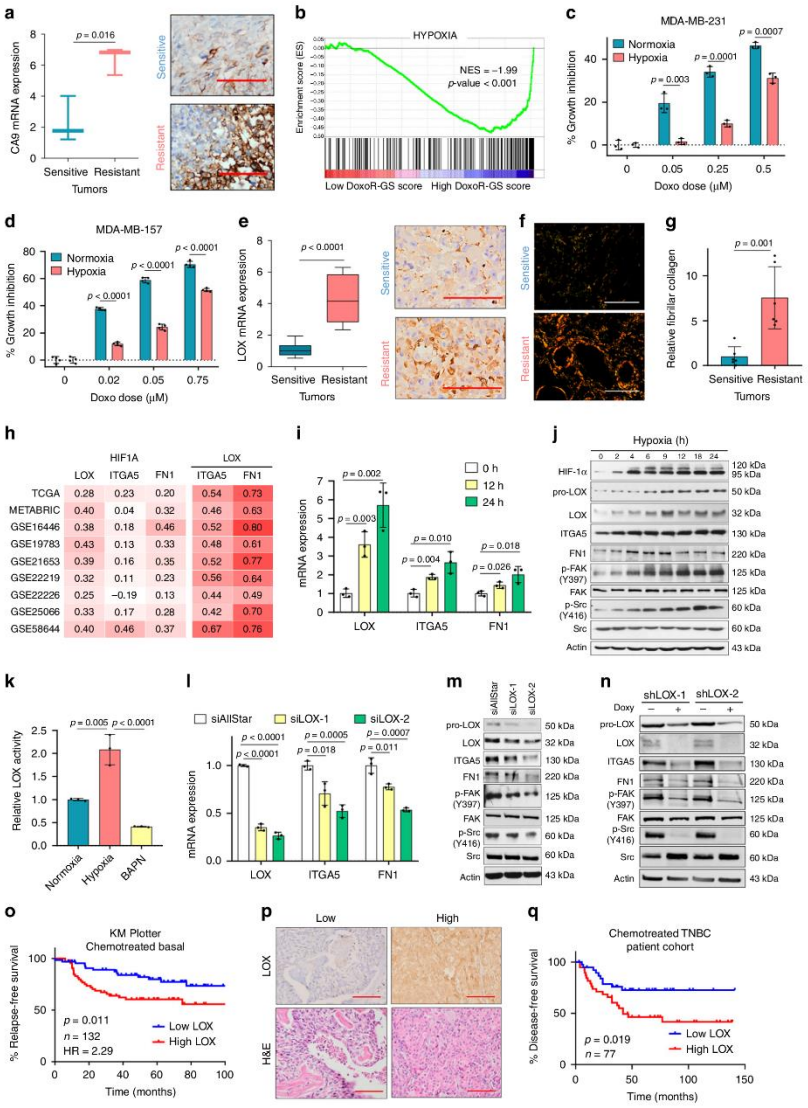
Fig. 1 Integrin signaling is a key mediator of chemoresistance in TNBCs. a Schematic representation of developing doxorubicin resistance in mice using the TNBC cell line, MDA-MB-231 (left panel). Tumor volume fold change (log2) of vehicle-treated, doxorubicin-sensitive and -resistant tumors (right panel). Clipart reprinted with permission from Springer Nature, *Nature Protocols*, FACS isolation of endothelial cells and pericytes from mouse brain microregions, Elizabeth E Crouch and Fiona Doetsch, Copyright 2018. **b** Tumor volumes of vehicle ($n = 8$), sensitive ($n = 12$) and -resistant ($n = 6$) tumors. **c** Waterfall plot of tumor volume fold change over time. Asterisk indicates tumors profiled by RNA-Seq. V vehicle; S sensitive; and R resistant. **d** Kaplan–Meier survival curve representing the percentage overall survival (OS) in chemotherapy-treated TNBC patients ($n = 106$) based on low vs. high (median) DoxoR-GS score. **e** Summary of IPA analysis showing top deregulated pathways in doxorubicin-resistant xenografts. **f** Genes associated with focal adhesion signaling are enriched in tumors of high DoxoR-GS scorers from GSE58812. **g** Expression of integrin alpha 5 (ITGA5) in doxorubicin-sensitive ($n = 8$) vs. -resistant ($n = 6$) xenografts at mRNA (left) and protein (right) levels, demonstrating membranous and cytoplasmic staining. **h** Kaplan–Meier survival curve representing the percentage relapse-free survival (RFS) in chemotherapy-treated basal patients ($n = 132$) based on low vs. high ITGA5 (median) expression. **i** Table summarizing association of ITGA5 with survival in patients of different subtypes that received or did not receive chemotherapy. **j** Expression of fibronectin (FN1) in doxorubicin-sensitive ($n = 12$) vs. resistant ($n = 12$) tumors at mRNA (left) and protein (right) levels, demonstrating mild to moderate cytoplasmic staining. **k** Kaplan–Meier survival curve representing the percentage RFS in chemotherapy-treated basal breast cancer patients ($n = 132$) based on low vs. high FN1 (median) expression. **l** Table summarizing association of FN1 with survival in patients of different subtypes that received or did not receive chemotherapy. Data on **b** represent mean ± SEM and all others represent mean ± SD. In Box plots, the box depicts median, 25th to 75th percentiles, and the whisker depicts min to max for this figure and all others. Two-sided Student's *t*-test was used to calculate statistical difference between two groups. Significance for survival analyses was calculated by log-rank (Mantel-Cox) test. NES Normalized enrichment score, HR hazard ratio. Scale bar = 100 μm for **g**, **j**. Source data are provided as a Source data file.

resistant tumors (Fig. 1j) and a significant association between high FN1 expression and poorer RFS in chemotherapy-treated basal patients (Fig. 1k, l). These results were further validated with another TNBC patient dataset (GSE58812) in which higher expression of either ITGA5 or FN1 is significantly associated with worse overall survival for the chemotherapy-treated TNBC patients (Supplementary Fig. 2b). Notably, when the patients are stratified based on ITGA5 and FN1 expressions in combination, a stronger separation of overall survival was achieved (Supplementary Fig. 2c, $p = 0.0008$; HR = 5.28). Altogether, these data suggest that deregulation of FN1-ITGA5 signaling could be a major driver of chemoresistance in TNBC.

Hypoxia-induced LOX hyperactivates ITGA5/FN1/FAK/Src axis. Hypoxia inducible factor-1 alpha (HIF-1α), encoded by the *HIF1A* gene, activates the transcription of several ECM-remodeling enzymes, including collagen prolyl and lysyl hydroxylases and lysyl oxidases thereby modulating ECM stiffness[39,40]. Importantly, our IPA analysis revealed a significant enrichment of HIF1A signaling in the doxorubicin-resistant tumors (Fig. 1e). Given the involvement of hypoxia in ECM remodeling[41,42], we hypothesized that HIF-1α could activate integrin and focal adhesion signaling. We first validated activation of the hypoxic response in chemoresistant tumors by demonstrating upregulation of the CA9 gene, which is a direct HIF-1α target gene and a well-established hypoxia marker[43]. CA9 mRNA and protein levels were significantly higher in resistant tumors (Fig. 2a). The induction of hypoxia signaling in the resistant tumors was not simply a result of an increase in tumor size, as there was no enrichment of hypoxia signaling in vehicle-treated tumors that are the largest in size vs. sensitive tumors (Supplementary Table 1). Furthermore, patients having high DoxoR-GS score also express high levels of hypoxia-related genes (Fig. 2b).

To experimentally demonstrate the acquisition of doxorubicin resistance under hypoxic conditions, we cultured MDA-MB-231 and MDA-MB-157 cells in normoxic vs. hypoxic conditions in the presence of increasing concentrations of doxorubicin. As shown in Fig. 2c, d, cells became less sensitive to growth inhibition induced by doxorubicin when grown under hypoxic conditions. Next, we performed Upstream Regulator analysis in IPA and found that 28 of 39 HIF-1α target genes had an expression direction consistent with the activation of HIF-1α (Supplementary Table 2). Among the actively transcribed genes upon HIF-1α activation during chemoresistance, we identified LOX, which is known to modulate ECM stiffness via collagen cross-linking and promote metastasis[44]. Upregulation of LOX in doxorubicin-resistant xenografts was validated by qRT-PCR and immunohistochemistry (Fig. 2e). While LOX, ITGA5, and FN1 mRNAs were upregulated between sensitive and resistant tumors under doxorubicin treatment, the fast-growing vehicle-treated tumors showed no upregulation of these genes, suggesting that their upregulation is specific to chemotherapy resistance (Supplementary Fig. 3a). Importantly, we demonstrated increased fibrillar collagen in resistant tumors compared to sensitive counterparts by picrosirius red staining (Fig. 2f, g). We then examined gene expression from 9 different breast cancer datasets and found correlation between *HIF1A* and *LOX*, *ITGA5*, and *FN1* mRNAs (Fig. 2h), supporting the upstream regulatory role of HIF1A in their transcription. Strikingly, the correlation of *LOX* with *ITGA5* and *FN1* mRNAs was the strongest among all pairs, even stronger than the correlation of these three genes with *HIF1A*. This suggested that hypoxia-induced LOX might specifically be regulating *ITGA5* and *FN1* expression, and the subsequent activation of intracellular downstream signaling could be contributing to doxorubicin resistance. Consistent with this, we detected a significant enrichment of hypoxia and focal adhesion signaling gene sets in tumors with high LOX expression (GSE58812[36], Supplementary Fig. 4a, b).

To test whether hypoxia can induce both LOX expression and integrin signaling, we cultured MDA-MB-231 cells under hypoxia for different time points and observed a prominent increase in HIF-1α protein stability that was followed by a coordinated upregulation of LOX, ITGA5 and FN1 mRNAs and protein levels (Fig. 2i, j). Hypoxia also resulted in activation of integrin signaling as shown by incases in p-FAK (Y397) and p-Src (Y416) (Fig. 2j). Moreover, LOX enzymatic activity was higher under hypoxia as compared to normoxia, potentially due to increased LOX expression (Fig. 2k). Here, BAPN, a LOX family inhibitor, was used as a negative control. The induction of LOX/ITGA5/FN1 and downstream signaling under hypoxic conditions has also been validated in another TNBC cell line, MDA-MB-157 (Supplementary Fig. 4c). Silencing LOX expression using two different siRNA sequences caused a LOX expression-dependent decrease in both ITGA5 and FN1 mRNA (Fig. 2l) and protein levels (Fig. 2m) together with attenuated downstream signaling (Fig. 2m). Moreover, stable and inducible knockdown of LOX with shRNAs also validated the inhibition of downstream signaling (Fig. 2n). These data strongly support a model in which LOX-mediated upregulation of ITGA5 and its ligand, FN1 play a role in hypoxia-mediated hyperactivation of integrin signaling.



To determine the clinical relevance of LOX expression in chemotherapy-treated TNBCs, we performed survival analyses and observed that higher *LOX* mRNA expression predicts poor RFS only in chemotherapy-treated basal breast cancer patients, but not in other breast cancer subtypes or in untreated cases (Fig. 2o and Supplementary Fig. 2d). Furthermore, in the GSE31519 dataset we observed that more than half of the patients that exhibit event, described as either a relapse or distant metastasis, express higher LOX levels (p-value = 0.012) (Supplementary Fig. 5a). Similarly, in another dataset (GSE25066), we observed that a significantly higher proportion of chemotherapy-treated TNBC patients with residual disease (RD) express higher levels of LOX (p-value = 0.011) (Supplementary Fig. 5b). Furthermore, TNBC patients with RD express significantly higher levels

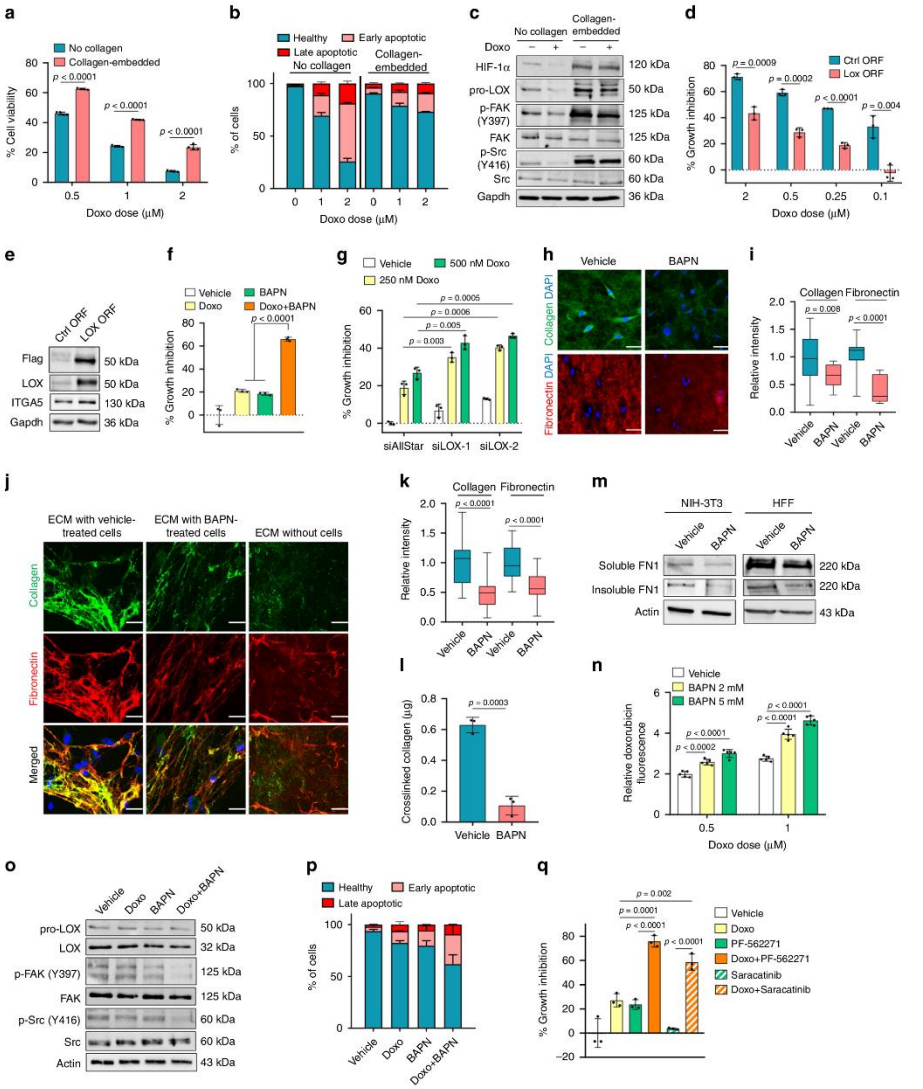
Fig. 2 Hypoxia-induced LOX hyperactivates ITGA5/FN1/FAK/Src axis in TNBCs. a Expression of a HIF-1α direct target gene, carbonic anhydrase 9 (CA9) in sensitive ($n = 3$) vs. resistant ($n = 3$) tumors at mRNA (left) and protein (right) levels, demonstrating predominantly membranous and mild cytoplasmic staining. **b** Genes upregulated upon hypoxia are enriched in patients with high DoxoR-GS score from GSE58812 ($n = 106$). **c**, **d**. % growth inhibition upon doxorubicin treatment of MDA-MB-231 (**c**) ($n = 3$) and MDA-MB-157 (**d**) ($n = 4$) cells grown under normoxic vs. hypoxic conditions. **e** Expression of LOX in sensitive ($n = 12$) vs. resistant ($n = 9$) tumors at mRNA (left) and protein (right) levels, demonstrating strong cytoplasmic and weak nuclear staining. **f**, **g** Representative images of Picrosirius red staining (**f**) and its quantification (**g**) ($n = 6$). **h** Heatmap summarizing the Pearson's correlation coefficients between *HIF1A* and *LOX*, *ITGA5* or *FN1* and between *LOX* and *ITGA5* or *FN1* in breast cancer patients. An intense red color shows a stronger positive correlation. **i** qRT-PCR analysis of *LOX*, *ITGA5*, and *FN1* under hypoxia ($n = 3$). **j** Western blot analyses of HIF-1α, LOX and integrin signaling members under hypoxia. **k** Relative LOX activity in MDA-MB-231 cells under hypoxia. BAPN was used as a negative control ($n = 3$). **l** qRT-PCR analysis of *LOX*, *ITGA5*, and *FN1* after transfection with siAllStar or siLOX ($n = 3$). **m**, **n** Western blot analyses in MDA-MB-231 cells transfected with siAllStar or siLOX (**m**) and after shLOX induction with doxycycline (**n**). **o** Kaplan–Meier survival curve representing the percentage RFS in chemotherapy-treated basal breast cancer patients ($n = 132$) separated based on low vs. high (median) LOX mRNA. **p** IHC images of TNBC patient tissues with low and high LOX protein expression. **q** Kaplan–Meier survival curve representing DFS in chemotherapy-treated TNBC patients ($n = 77$) separated from median based on LOX protein expression. Data represents mean ± SD. Two-sided Student's *t*-test was used to calculate statistical difference between two groups. Significance for survival analyses was calculated by log-rank (Mantel-Cox) test. NES Normalized enrichment score, HR hazard ratio. Scale bar = 100 μm for **a**, **e**, and **p**, and 400 μm for **f**. Source data are provided as a Source data file.

of LOX, ITGA5 and FN1 (Supplementary Fig. 5c–e). Importantly, we stained for LOX protein expression in tissues (Fig. 2p, Supplementary Table 3). In 77 TNBC patients treated with chemotherapy, we showed that higher LOX protein levels were significantly associated with worse disease-free survival (DFS) (p-value = 0.019, Fig. 2q). Although other LOX family members (LOXL1-4) have also been reported to be regulated by HIF-1α[45], none of them were significantly altered in doxorubicin-resistant xenografts (Supplementary Fig. 3b). Altogether, these data are consistent with a model in which hypoxia-induced LOX activates integrin signaling by upregulating ITGA5 and FN1, leading to poor survival and chemoresistance in TNBC patients.

LOX inhibition remodels ECM to confer chemosensitization. To test the potential role of LOX in mediating chemoresistance in TNBCs and elucidating the underlying mechanisms, we first embedded TNBC cells into a matrix of type I collagen, the major substrate of LOX, and demonstrated acquisition of resistance to doxorubicin in two different cell lines (Fig. 3a and Supplementary Fig. 4d) which was accompanied by protection against apoptosis (Fig. 3b and Supplementary Fig. 6a–c) and sustained levels of p-FAK and p-Src (Fig. 3c). Western blot analysis also demonstrated a decrease in HIF-1α expression and subsequently LOX levels upon doxorubicin treatment but only in cells cultured in the absence of collagen (Fig. 3c). Overexpressing LOX in MDA-MB-231 cells that were embedded in type I collagen conferred resistance to doxorubicin (Fig. 3d). Overexpression of LOX also caused a modest increase in ITGA5 protein levels (Fig. 3e). Analysis of LOX expression in a panel of breast cancer cell lines demonstrated that TNBC cells express relatively higher levels of LOX (Supplementary Fig. 7a). Importantly, inhibiting LOX using a LOX family inhibitor, BAPN in combination with doxorubicin in three different collagen I-embedded TNBC cell lines re-sensitized them to doxorubicin (Fig. 3f, Supplementary Fig. 7b). As BAPN is known to inhibit other LOX family members as well, we further confirmed the doxorubicin sensitization with LOX inhibition using two different siRNA sequences against LOX (Fig. 3g). Importantly, doxorubicin sensitization by LOX inhibition was specific to TNBC models. ERα+ cells express relatively low levels of LOX, and LOX inhibition did not lead to chemosensitization (Supplementary Fig. 7a, c). Finally, LOX inhibition sensitizes cells to two other DNA-damaging chemotherapy agents, epirubicin and paclitaxel (Supplementary Fig. 7d), which are common therapeutic options for TNBC patients[46].

To elucidate the mechanistic details of how LOX inhibition sensitizes TNBC cells to doxorubicin, we first examined the changes in ECM remodeling upon LOX inhibition. It has been reported that there is a molecular co-dependence between collagen cross-linking and fibronectin fibril assembly that causes reciprocal activation of both processes to ultimately increase ECM stiffness[47,48]. In addition, cell-mediated processes, such as binding of cell surface integrins to fibronectin dimers and subsequent recruitment of FAK to focal adhesion sites can trigger fibronectin fibrillogenesis[49–51]. We observed that both ITGA5 and FN1 expression, and subsequent FAK phosphorylation were dependent on LOX expression (Fig. 2). We therefore hypothesized that both collagen cross-linking (by LOX) and fibronectin deposition and assembly would be hindered by LOX inhibition. To test this hypothesis, we performed immunofluorescence staining of collagen and fibronectin in type I collagen-embedded MDA-MB-231 cells with and without LOX inhibition, and observed that TNBC cells are able to deposit large amounts of fibronectin into an ECM that is rich in collagen type I (Fig. 3h), and that LOX inhibition with BAPN decreased the extracellular deposition and assembly of fibronectin fibrils (Fig. 3h) and decreased overall extracellular fibrillar collagen content (Fig. 3i). This was validated using a cell-derived ECM system produced by human foreskin fibroblast (HFF) cells, better recapitulating the dynamics of ECM formation and stabilization. Growing cancer cells on fibroblast-derived ECM induced the formation of thick, cross-linked collagen fibers, as opposed to non-fibrillar, immature collagen in the ECM deposited in the absence of cancer cells (Fig. 3j). When LOX was inhibited with BAPN, we detected a significant decrease in the immunofluorescence staining intensities of both collagen and fibronectin, suggesting that cancer cell-derived LOX is required for the cross-linking of extracellular collagen into thick fibers and the subsequent fibronectin assembly during ECM maturation (Fig. 3k). Co-localization analysis demonstrated that almost half of the collagen fibers were in contact with fibronectin (similar to previous reports[47,48]), but co-localization was decreased by LOX inhibition (Supplementary Fig. 8a). Analysis of 3D images of vehicle and BAPN-treated cells cultured on top of HFF-derived ECM further demonstrated that cells are still in contact with the ECM even though LOX inhibition decreased the extracellular collagen and fibronectin content (Supplementary Fig. 8b, c). The decrease in collagen cross-linking and fibronectin assembly upon LOX inhibition was also validated by biochemical measurement of extracellular hydroxyproline content (Fig. 3l) and deoxycholate (DOC) lysis (Fig. 3m), respectively, which are standard methods used to assess the amount of collagen cross-linking and fibronectin deposition and assembly[52].

It has been proposed that LOX may reduce drug penetration under hypoxic conditions and lessen the cytotoxicity of chemo-agents in 3D collagen cultured cells and tumor models[53].



We showed that doxorubicin decreased the activation of FAK/Src signaling in 2D-cultured cells, but not in 3D collagen culture (Fig. 3c). Therefore, we tested if targeting LOX could increase doxorubicin penetration and decrease FAK/Src signaling, leading to apoptosis. To assess drug penetration, we quantified doxorubicin autofluorescence (ex: 495 nm, em: 595 nm[54]) and observed a significant increase in intracellular doxorubicin in combination-treated cells (Fig. 3n). This was accompanied by a decrease in FAK/Src phosphorylation (Fig. 3o) and induction of apoptosis (Fig. 3p and Supplementary Fig. 6d–g). Finally, we treated collagen-embedded cells with doxorubicin with and without inhibitors specific for FAK (PF-562271) or Src (Saracatinib) and observed a synergistic increase in growth inhibition (Fig. 3q), decreased phosphorylation of FAK and Src (Supplementary Fig. 9a), and induced apoptotic cell death (Supplementary Fig. 9b, c).

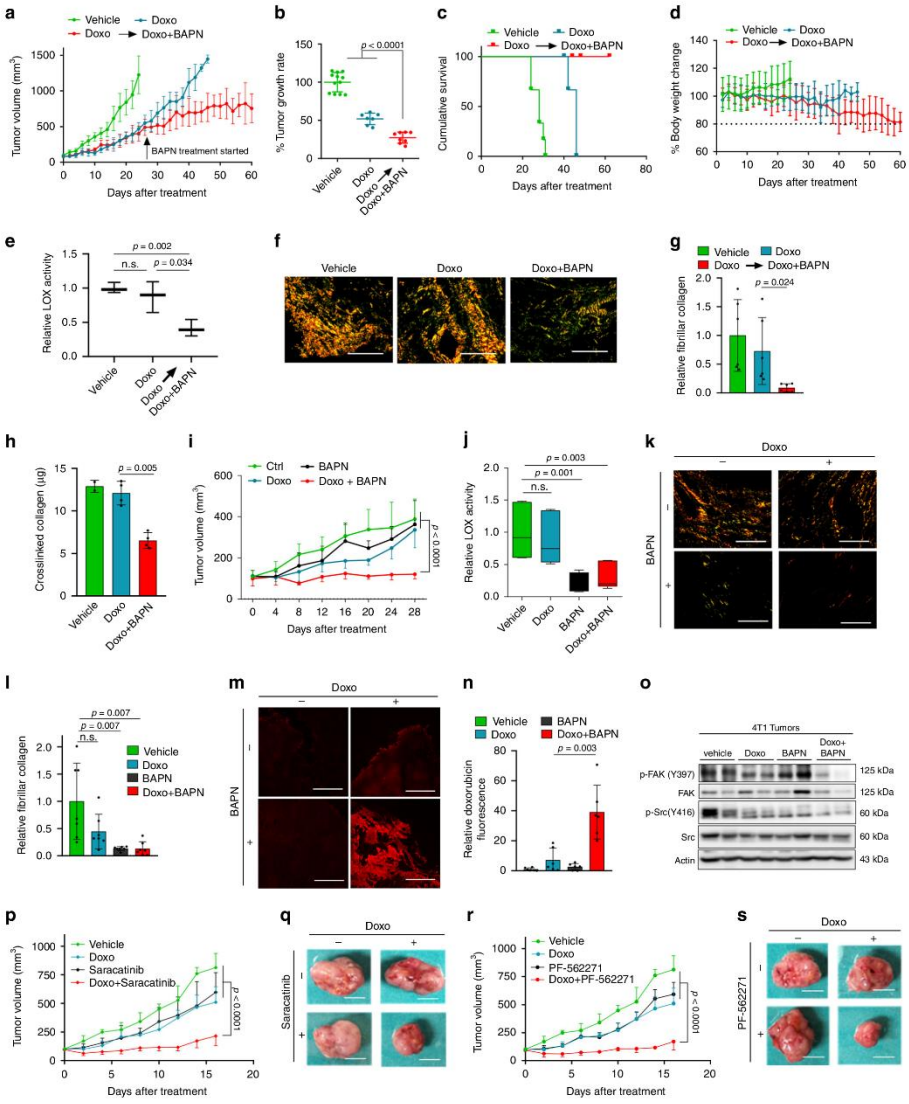
Fig. 3 LOX inhibition remodels ECM to confer chemosensitization in TNBCs. a Doxorubicin response of MDA-MB-231 cells cultured with or without type I collagen for 72 h ($n = 4$). **b** Apoptosis assay by Annexin V/DAPI staining from a ($n = 2$). **c** Western blot analysis in doxorubicin-treated cells grown with or without type I collagen. **d** Percentage growth inhibition in LOX-overexpressing cells embedded in collagen upon doxorubicin treatment ($n = 3$). **e** Western blot analyses upon LOX overexpression in MDA-MB-231 cells. **f**, **g** Percentage growth inhibition of collagen-embedded MDA-MB-231 cells treated with BAPN (**f**) or transfected with siLOX (**g**) in combination with doxorubicin ($n = 3$). **h**, **i** Immunofluorescence staining (**h**) and quantifications of the intensities (**i**) of extracellular type I collagen and fibronectin upon treatment of collagen-embedded cells with BAPN ($n = 18$ (vehicle), $n = 15$ (BAPN) for collagen, and $n = 18$ (vehicle), $n = 12$ (BAPN) for fibronectin). **j**, **k** Immunofluorescence staining (**j**) and quantifications of the intensities (**k**) of HFF-derived type I collagen and fibronectin incubated with vehicle or BAPN-treated MDA-MB-231 cells. ECM without cells represents the staining in the absence of MDA-MB-231 cells ($n = 29$ (vehicle), $n = 25$ (BAPN)). **l** Amount of cross-linked collagen in HFF-derived ECM incubated with vehicle- vs. BAPN-treated MDA-MB-231 cells ($n = 3$ different wells). **m** Western blot of soluble and insoluble FN1 obtained by deoxycholate lysis of NIH3T3- and HFF-derived ECM in contact with vehicle- vs. BAPN-treated MDA-MB-231 cells. **n** Changes in relative doxorubicin fluorescence upon BAPN-treatment in MDA-MB-231 cells embedded in type I collagen ($n = 5$). **o** Western blot analysis of LOX and FAK/Src signaling in collagen type I-embedded MDA-MB-231 cells upon doxorubicin and BAPN treatment for 24 h. **p** Annexin V/DAPI staining upon combination treatment for 72 h ($n = 2$). **q** Percentage growth inhibition induced by the combination of doxorubicin with FAK (PF-562271) or Src (Saracatinib) inhibitors in MDA-MB-231 cells embedded in type I collagen ($n = 3$). Data represents mean ± SD. Two-sided Student's *t*-test was used to calculate statistical difference between two groups. One-way ANOVA with Dunnett's test was performed to compare mean of combination-treated group with single agent treatments in **f**, **q**. Scale bar = 50 μm for **h**, **j**. Source data are provided as a Source data file.

Targeting LOX or FAK/Src overcomes chemoresistance in vivo. To test if inhibiting LOX could overcome doxorubicin resistance and enhance drug response in advanced, chemotherapy-refractory TNBCs, we re-derived doxorubicin resistance in vivo, using a protocol similar to our initial acquired resistance model (though with lower doxorubicin dose), by treating MDA-MB-231 xenografts with doxorubicin until an accelerated tumor growth was achieved despite the given therapy. At this point, some of the doxorubicin-resistant tumors were treated with the combination of doxorubicin and BAPN while the rest continued to receive doxorubicin alone. Strikingly, addition of LOX inhibitor to doxorubicin in these aggressive, fast-growing doxorubicin-resistant tumors led to a significant decrease in tumor growth rate (Fig. 4a, b) and improved survival (Fig. 4c) until experiment termination when the tumor volume cut-off was reached or due to almost a 20% decrease in body weight in BAPN-added treatment arm (Fig. 4d). We confirmed the reduction of LOX activity (Fig. 4e) and fibrillar collagen (Fig. 4f, g) upon addition of BAPN to doxorubicin. These results were further validated by performing biochemical collagen assay (Fig. 4h), suggesting that chemosensitization with LOX inhibition involves reduction in collagen cross-linking.

We also evaluated the effects of LOX inhibition on doxorubicin response in vivo in an immunocompetent setting using a syngeneic TNBC model. The 4T1 mouse mammary tumor cell line is a highly aggressive model that represents the TNBC subtype[55] and exhibits relatively low response to doxorubicin. We examined the expression of LOX in 4T1 cells grown in vitro as well as in tumors and found that they express LOX at a level similar to the high LOX-expressing MDA-MB-231 model (Supplementary Fig. 10a, b). We observed a strong inhibitory effect of the combination therapy on tumor growth in this immunocompetent tumor model (Fig. 4i and Supplementary Fig. 10c, d). The LOX activity assay and picrosirius red staining confirmed the suppression of LOX activity and collagen cross-linking, respectively in all BAPN-treated tumors (Fig. 4j–l). This was accompanied by increased penetration of doxorubicin (Fig. 4m, n) and inhibition of FAK/Src signaling in the combination-treated tumors (Fig. 4o). To test the effect of FAK or Src inhibition on doxorubicin response in vivo, we combined specific inhibitors of FAK (PF-562271) or Src (Saracatinib) with doxorubicin and observed a significant decrease in tumor growth (Fig. 4p–s) and tumor weight (Supplementary Fig. 10e, f) in combination-treated tumors, validating the key roles of FAK and Src in doxorubicin resistance.

Next, we tested combination of LOX inhibition with doxorubicin in a highly aggressive TNBC PDX model. We first analyzed the gene expression profiling and drug response data of 15 well-characterized TNBC PDX models (Jackson Lab) and observed a significant positive correlation between LOX expression and hypoxia and focal adhesion scores (Fig. 5a). Based on these analyses, we selected a TNBC PDX model (TM01278) that is resistant to doxorubicin (and several other chemotherapy agents) and expresses high levels of LOX, hypoxia and focal adhesion scores (Fig. 5a). Then, we generated organoid cultures of this doxorubicin-resistant PDX tumor and demonstrated that combination of LOX inhibitor with doxorubicin significantly decreased organoid size compared to single agent treatments after 9 days of treatment (Fig. 5b, c). In vivo testing also showed a significant decrease in tumor growth upon combination therapy in this chemoresistant PDX model expressing LOX (Fig. 5d–f). These results complement our in vitro and in vivo findings with established cell lines and increase the clinical relevance of LOX inhibition to overcome chemotherapy resistance in TNBC. Importantly, we demonstrated reduced LOX activity (Fig. 5g) and fibrillar collagen content upon LOX inhibition with BAPN (Fig. 5h, i), which was accompanied by enhanced drug penetration into tumors (Fig. 5j, k) and more effective down-regulation of downstream FAK/Src signaling in combination-treated tumors (Fig. 5l). Overall, we demonstrated that targeting LOX or its downstream FAK/Src overcomes chemotherapy resistance in highly aggressive, chemoresistant TNBC models.

Targeting LOX at the first-line potentiates chemoresponse. Having identified LOX as a determinant of chemoresistance in TNBC, we tested whether LOX is also a target in potentiating chemotherapy response in first-line settings in treatment-naïve models using our inducible shLOX expressing MDA-MB-231 derivatives (referred to 231.shLOX) (Supplementary Fig. 11a, b). Inhibiting LOX in combination with doxorubicin as a first-line therapy led to a stronger delay in tumor growth as compared to individual treatments (Fig. 6a–e). We confirmed LOX knockdown at mRNA (Fig. 6f) and protein levels (Fig. 6g, h) and the decrease in LOX activity (Supplementary Fig. 11c) together with down-regulation of its downstream ITGA5 (Supplementary Fig. 11d) after tumors were collected. We also demonstrated that other LOX family members did not decrease upon LOX knockdown (Supplementary Fig. 11e, f), further supporting our hypothesis that LOX inhibition is specifically involved in mediating chemoresponse in TNBCs. In consistent with the reduction in tumor growth, there was also a significant reduction in the proliferation marker, Ki-67 (Fig. 6i, j) and an increase in the expression of an apoptosis marker, Cleaved Caspase-3 (Fig. 6k, l) in combination-



treated group as compared to LOX inhibition or doxorubicin treatment alone. Furthermore, ITGA5 levels, phosphorylation of Src (p-Y416) and FAK (p-Y397) were reduced upon LOX knockdown in combination with doxorubicin (Fig. 6m–q).

Next, we examined the effect of combination therapy on the growth of a primary organoid model developed from a treatment-naïve TNBC patient. Combination treatment with doxorubicin and BAPN led to a significant reduction in organoid size as compared to individual treatment groups after 9 days of treatment (Fig. 6r, s). Altogether, these data demonstrate that inhibition of LOX could be a potential therapeutic strategy in combination with first-line chemotherapy in TNBCs.

Fig. 4 Targeting LOX or downstream FAK/Src overcomes TNBC chemoresistance in vivo. a Tumor growth in MDA-MB-231 xenografts treated with doxorubicin until resistance develops followed by treatment with the combination of doxorubicin (2.5 mg/kg) and the LOX inhibitor, BAPN (100 mg/kg) ($n = 12$, 7, and 8 tumors for vehicle, Doxo and Doxo+BAPN, respectively). **b** Tumor growth rates relative to vehicle from **a**. **c** Cumulative survival of mice from a. Mice were sacrificed when the tumor size cut-off was reached or when the body weight dropped to 80% of the initial body weight ($n = 6$, 4, and 4 mice for vehicle, Doxo and Doxo + BAPN, respectively). **d** Percentage change in the body weight of the mice from **c**. **e** Relative LOX activity in tumors from a ($n = 3$). **f** Representative images of Picrosirius red staining (f) and its quantification (**g**), in tumors from a ($n = 6$). **h** In vivo collagen assay in tumors from a ($n = 2$ (vehicle), $n = 4$ (Doxo, Doxo+BAPN)). **i** Tumor growth in 4T1 syngeneic model upon treatment with doxorubicin and BAPN, alone or in combination ($n = 4$ mice). **j** LOX activity in tumors from **i** ($n = 6$). **k**, **l** Representative images of Picrosirius red staining (k) and its quantification (l) in mice from i ($n = 7$). **m**, **n** Intratumoral doxorubicin levels upon treatment with the combination of doxorubicin and BAPN ($n = 6$). **o** Western blot analysis of FAK/Src signaling in combination-treated tumors from **i**. **p**, **q** Change in tumor growth (**p**) and representative images of tumors (**q**) in 4T1 model upon treatment with doxorubicin and Saracatinib, alone or in combination ($n = 4$). **r**, **s** Change in tumor growth (**r**) and representative images of tumors (**s**) in 4T1 model upon treatment with doxorubicin and PF-562271, alone or in combination ($n = 4$). Data represents mean ± SD. Two-sided Student's *t*-test was used to calculate statistical difference between two groups. Two-way ANOVA test was performed for comparing tumor growth over time among different treatment groups in **i**, **p**, and **r**. n.s. not significant. Scale bar = 400 μm for **f**, **k**; 200 μm for **m**, and 1 cm for **q**, **s**. Source data are provided as a Source data file.

miR-142-3p is a chemosensitizer regulating HIF1A/LOX/ITGA5. To elucidate the underlying molecular mechanisms of the coordinated activation of the HIF1A/LOX/ITGA5 axis under hypoxia, we sought for a common modulator. As miRNAs tend to function in a pathway-centric manner by targeting multiple genes in the same cascade[56], we searched for a potential miRNA modulator of HIF1A/LOX/ITGA5-mediated chemotherapy resistance. We examined all conserved miRNAs targeting *HIF1A*, *LOX*, and *ITGA5* and found eight common miRNAs having binding sites in the 3′-UTRs of these three genes (Fig. 7a). Out of these eight miRNAs, only two miRNAs, miR-142-3p, and miR-128-3p, showed an inverse correlation with HIF1A signature, and LOX and ITGA5 expression in basal subtype (Fig. 7b and Supplementary Fig. 12a–c). One of these two miRNAs, miR-142-3p, showed a significant association with OS specifically in chemotherapy-treated TNBC patients (Fig. 7c, d and Supplementary Fig. 12d). Furthermore, miR-142-3p was significantly downregulated in doxorubicin-resistant xenografts that we developed in vivo as compared to sensitive ones (Fig. 7e). Importantly, induction of hypoxia inhibited the expression of miR-142-3p (Fig. 7f), while silencing HIF1A upregulated miR-142-3p expression (Fig. 7g), suggesting that hypoxia-mediated downregulation of miR-142-3p potentially involves HIF1A.

We next tested to see if miR-142-3p could inhibit the expression of *HIF1A*, *LOX* or *ITGA5*. We overexpressed miR-142-3p in MDA-MB-231 cells and observed a significant downregulation of all three genes both at mRNA and protein levels, and a reduction in phosphorylation of downstream FAK/Src kinases (Fig. 7h, i). Importantly, downregulation of HIF1A, LOX and ITGA5 protein levels as well as decreased phosphorylation of FAK and Src was also seen in MDA-MB-231 xenografts stably expressing miR-142-3p (Fig. 7j and Supplementary Fig. 12e). The direct binding of miR-142-3p to the predicted binding sites in the 3′-UTRs of *HIF1A*, *LOX*, and *ITGA5* (Fig. 7k) was validated by a dual luciferase assay (Fig. 7l). Finally, ectopic expression of miR-142-3p in TNBC cells grown in type I collagen sensitized to doxorubicin-induced growth inhibition and apoptotic cell death (Fig. 7m–p). We interpret these results to indicate that HIF1A and miR-142-3p are involved in a double-negative feedback loop that further increases HIF1A, LOX and ITGA5 levels under hypoxic conditions, leading to chemoresistant tumors, and that overexpression of miR-142-3p overcomes chemoresistance by inhibiting HIF1A/LOX/ITGA5 axis.

Discussion

TNBC is the most aggressive subtype of breast cancer and is responsible for 30% of all breast cancer deaths. Chemotherapy is the mainstay treatment for TNBCs; however, resistance is common, significantly decreasing long-term survival[6]. Therefore, novel strategies are urgently needed to enhance the clinical benefit from chemotherapy. Here, we identified a mechanism of chemotherapy resistance that involves activation of the HIF1A/miR-142-3p/LOX/ITGA5/FN1 axis in TNBCs. We showed that inhibiting LOX reduces the expression of ITGA5 and FN1, decreases extracellular collagen cross-linking, fibronectin deposition/assembly and enhances drug penetration that ultimately result in inhibition of FAK/Src signaling, resulting in apoptosis and reversal of chemotherapy resistance in TNBC cells cultured in contact with ECM (Fig. 3). These results were validated in acquired resistant TNBC xenografts and de novo resistant 4T1 syngeneic TNBC model (Fig. 4) as well as in well-characterized chemoresistant TNBC PDXs (Fig. 5). We also showed that targeting LOX potentiates chemotherapy in first-line settings (Fig. 6). Importantly, targeting the signaling molecules downstream of LOX, FAK or Src, strongly sensitized cancer cells to chemotherapy when grown in collagen-embedded cultures or in vivo, showing the key role of these pro-survival signals in driving resistance (Fig. 4). Finally, we showed a double-negative feedback loop between HIF1A and miR-142-3p regulating HIF1A/LOX/ITGA5/FAK/Src axis and chemoresistance in TNBC (Fig. 7).

The ECM re-modeler, LOX is a well-known modulator of cancer metastasis[29,44]. LOX secretion from hypoxic tumors leads to collagen cross-linking at the pre-metastatic site and increases lung metastasis in TNBC models[28]. Moreover, higher LOX expression was observed in metastatic brain tumors of breast cancer patients[57]. Furthermore, Baker et al. demonstrated that LOX increases cell proliferation and invasion in colorectal cancer via Src activation[58] and enhances matrix stiffness, activates FAK, leading to invasion in vitro and metastasis in vivo in colorectal cancer[59]. In terms of the potential effects of LOX on drug response, a few studies have reported an involvement of LOX in drug resistance that primarily focused on altered distribution/penetration of chemotherapeutics, including paclitaxel and gemcitabine in tumors as a consequence of LOX-mediated ECM stiffness under hypoxic conditions[30,53]. In addition to forming a physical barrier, LOX-mediated ECM stiffness can also confer resistance via activating integrin receptors and the downstream effectors, FAK and Src kinases, leading to increased cellular survival[60]. For instance, Miller et al. demonstrated that combination of a LOX antibody with gemcitabine improved survival of a pancreatic ductal adenocarcinoma (PDAC) model via inhibiting key microenvironment-mediated pro-survival signals without any evidence of increased penetrance of gemcitabine into tumors upon LOX inhibition[31] in contrast to the studies described above[30,53]. Furthermore, it was recently shown that LOX might also be involved in transcriptional regulation of certain genes[61]. In our study, we showed that LOX

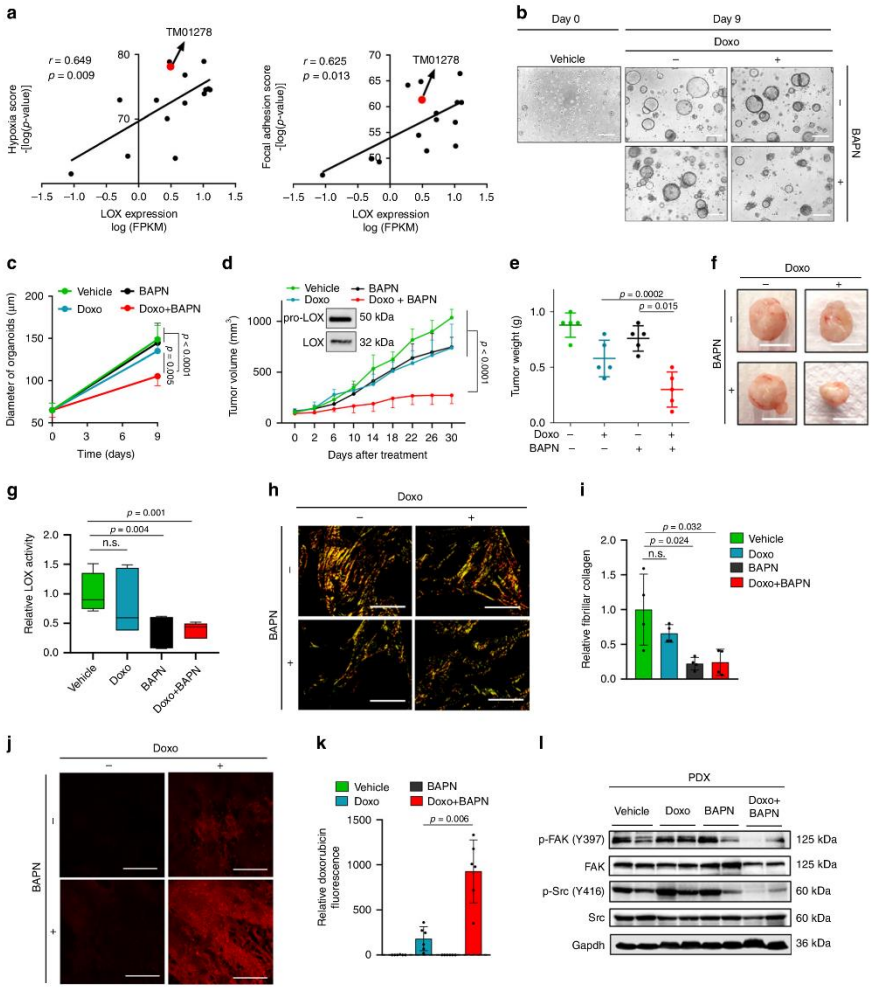
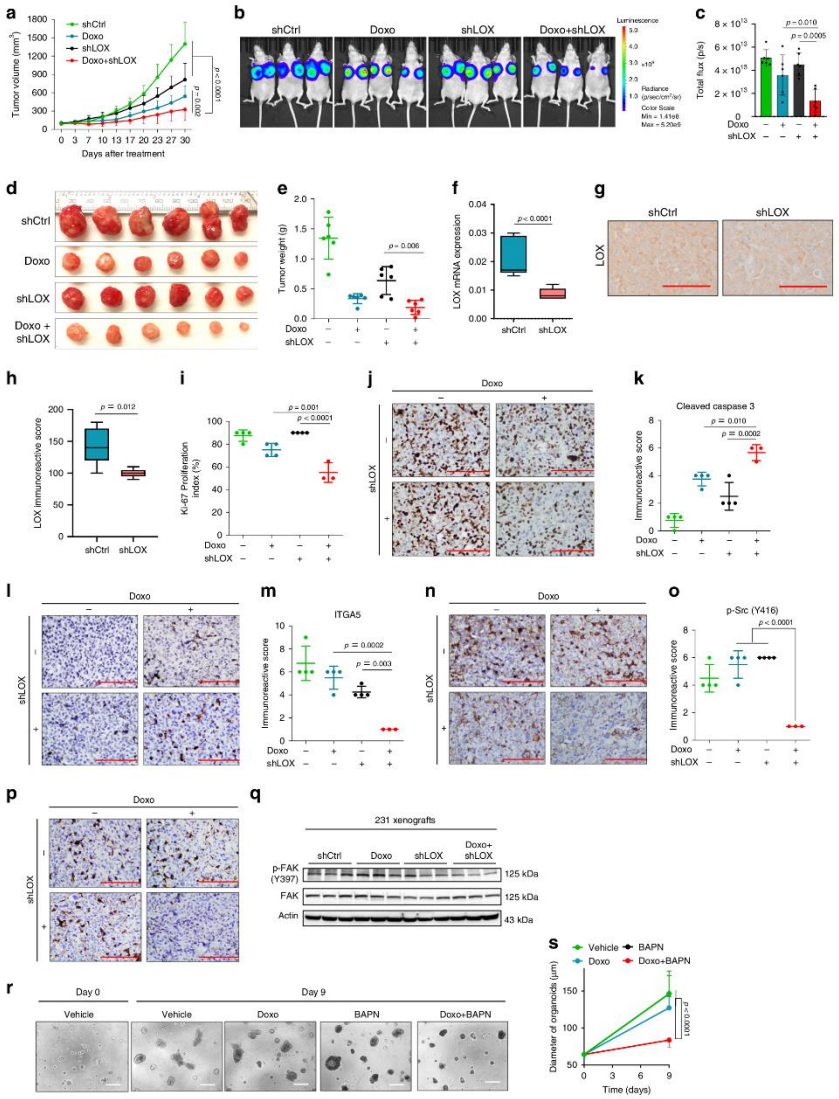


Fig. 5 Targeting LOX overcomes chemoresistance in highly aggressive TNBC PDXs. a Correlation analysis of *LOX* mRNA expression with hypoxia and focal adhesion scores in 15 different TNBC PDX models. Red dot shows the position of TM01278 PDX model selected. **b** Representative images of TM01278 PDX organoids at day 0 and day 9 after treatment with doxorubicin and BAPN treatment, alone or in combination. **c** Quantification of organoid diameter upon combination therapy for 9 days ($n = 12$ (vehicle, Doxo, BAPN), $n = 11$ (Doxo+BAPN)). **d**, **e** Tumor growth (**d**) and tumor weight (**e**) in TM01278 PDX upon treatment with doxorubicin and BAPN, alone or in combination ($n = 5$). Inset shows LOX expression in PDX tumors. **f** Representative images of tumors from **d**. **g** Relative LOX activity in tumors from **d** ($n = 8$ (vehicle), $n = 6$ (Doxo, BAPN, Doxo+BAPN)). **h**, **i** Representative images of Picrosirius red staining (**h**) and its quantification (i) in combination- and single agent-treated PDX tumors from d ($n = 4$). **j**, **k** Representative images of doxorubicin fluorescence in tumors from **d** (**j**), and its quantification (**k**) ($n = 6$). **l** Western blot analysis of FAK/Src signaling in PDXs treated with doxorubicin and BAPN, alone or in combination. Data represents mean ± SD. Two-sided Student's *t*-test was used to calculate statistical difference between two groups. One-way ANOVA with Dunnett's test was performed to compare mean of combination-treated group with single agent treatments in **e**. Two-way ANOVA test was performed for comparing tumor growth over time among different treatment groups in **d**. Scale bar = 100 µm for **b**, 1 cm for **f**, and 400 µm for **h** and 200 µm for **j**. n.s. not significant. Source data are provided as a Source data file.



overexpression upon acquisition of doxorubicin resistance, on one hand, leads to protection against doxorubicin-induced FAK/Src inhibition by increasing collagen cross-linking, fibronectin assembly and decreasing drug penetration, and on the other hand, increases ITGA5 and FN1 expression, ultimately leading to increased FAK/Src signaling and chemoresistance. Considering the known potential of inhibiting FAK/Src kinases to enhance response to different chemotherapy agents[62] and our data on the effect of LOX inhibition on FAK/Src signaling in chemosensitization, we propose that LOX inhibition reduces both the ECM stiffness to enhance drug penetration and the ITGA5/FN1 expression, thus culminating in inhibition of FAK/Src signaling, induction of apoptosis and chemosensitization. Overall, these findings suggest that LOX,

Fig. 6 Targeting LOX at the first-line settings potentiates chemoresponse in TNBCs. a Tumor volume in MDA-MB-231 xenografts upon shLOX induction in the presence or absence of doxorubicin treatment ($n = 6$). **b** IVIS images of mice from **a**. **c** Quantifications of luciferase intensity in tumors from **b** ($n = 6$). **d** Images showing isolated tumors from **a**. **e** Tumor weights in mice from **a** ($n = 6$). **f** qRT-PCR analysis of LOX in Ctrl ($n = 9$) vs. shLOX ($n = 9$) xenografts. **g**, **h** IHC staining of LOX and its quantification in Ctrl ($n = 5$) vs. shLOX ($n = 5$) tumors. **i**, **j** Ki-67 proliferation index of tumors from a ($n = 4$ (vehicle, Doxo, BAPN), $n = 3$ (Doxo+BAPN)). **k**–**p** Immunoreactive scores of Cleaved Caspase-3 (**k**, l), ITGA5 (**m**, **n**) and p-Src (Y416) (**o**, **p**) in tumors from a ($n = 4$ (vehicle, Doxo, BAPN), $n = 3$ (Doxo + BAPN)). **q** Western blot analysis of p-FAK and FAK in shLOX tumors in combination with doxorubicin. **r** Representative images of TNBC patient organoid, F149T at day 0 and day 9 after treatment with doxorubicin and BAPN, alone or in combination. **s** Quantification of organoid diameter upon combination therapy for 9 days ($n = 12$ (Day 0), $n = 9$ (vehicle, Day 9), $n = 11$ (Doxo, BAPN, Doxo+BAPN, Day 9)). Data represents mean ± SD. Two-sided Student's *t*-test was used to calculate statistical difference between two groups. One-way ANOVA with Dunnett's test was performed to compare mean of combination-treated group with single agent treatments in **c**, **e**, **i**, **k**, **m**, **o**, and **s**. Two-way ANOVA test was performed for comparing tumor growth over time among different treatment groups in **a**. Scale bar = 100 μm for **g**, **j**, **l**, **n**, **p**, **r**. Source data are provided as a Source data file.

which has primarily been studied in the context of metastasis, may also confer resistance to chemotherapy, making it a highly attractive therapeutic target.

Given the functional contribution of ECM modulation on different aspects of tumorigenesis, several inhibitors against multiple ECM modulators, such as matrix metalloproteinases, or the ECM-sensing integrin receptors have so far been developed. However, none of them achieved clinical success due to context-dependent efficacy, low specificity or severe toxicity[63]. Furthermore, inhibitors targeting the HIF pathway have so far been unable to enter clinics due to the complexity of the HIF pathway and the difficulty in targeting protein-protein interactions[64]. Therefore, identification of the well-defined modulators of ECM that are specifically overexpressed in aggressive, chemoresistant tumors, such as LOX that stands out as an attractive target with strong translational profile will be beneficial towards achieving a superior clinical outcome[44,65]. In this line, we demonstrated that more than half of the chemoresistant TNBC patients express high levels of LOX mRNA (Supplementary Fig. 5a, b) and are therefore expected to respond to LOX targeting therapies in combination with chemotherapy. In addition, we showed that high expression of LOX protein is significantly associated with survival in a cohort of chemotherapy-treated TNBC patients. Moreover, we also demonstrated a superior anti-tumorigenic effect of doxorubicin in vivo and in a TNBC organoid when combined with BAPN in the first-line settings (Fig. 6) that altogether supports the translational potential of targeting LOX with a potentially large target population in the clinic. Although BAPN is the most commonly used LOX inhibitor, it inhibits all LOX family members. In this line, there have been several recent efforts to identify novel and selective small molecule inhibitors against different family members, including LOX[66] and LOXL2[67] that can hopefully be tested in clinics to improve patient outcome in aggressive cancers, including the chemoresistant TNBCs. Moreover, our in vitro and in vivo data showing strong chemosensitization upon inhibiting FAK or Src kinases suggest that FAK/Src axis is critical for tumor cell survival in the presence of chemotherapy and targeting these proteins could also be an effective strategy to overcome chemoresistance in TNBCs in the future. Indeed, inhibitors of FAK and Src kinases are currently being tested in clinical trials and demonstrate promising results when combined with targeted therapies or chemotherapy (e.g. NCT03875820 and NCT02389309, respectively).

Signaling pathways need to be tightly regulated and are repressed in the absence of a stimulus. This ensures that target genes are activated only in the presence of a signal. miRNAs have been shown to be key regulators of this repression by inhibiting the expression of several transcripts[68]. Furthermore, others and us have previously shown that expression of genes functioning in the same cascade can be co-regulated by the same miRNA to ensure its robustness[56,68]. Therefore, we asked if miRNAs can inhibit the HIF1A/LOX/ITGA5 axis and confer chemosensitivity. We identified miR-142-3p to be significantly downregulated in chemoresistant tumors by HIF1A, and its overexpression inhibits HIF1A, LOX and ITGA5 in a robust double-negative feedback loop, thus sensitizes cells to chemotherapy. Although we have shown that miR-142-3p is significantly associated with survival specifically in chemotherapy-treated TNBC patients, future studies including miRNA profiling or in situ hybridization in large chemotherapy-treated patient cohorts are warranted to fully uncover the potential of this miRNA as a biomarker and a therapy sensitizer in TNBCs.

In summary, we uncovered a molecular mechanism of chemotherapy resistance in TNBC involving hypoxia-driven LOX expression, which on one hand, leads to increased collagen cross-linking, fibronectin assembly and decreased drug penetration, and on the other hand, increases ITGA5 and FN1 expression, collectively leading to increased FAK/Src signaling, decreased apoptosis and chemoresistance. Furthermore, hypoxia-driven repression of miR-142-3p increases HIF1A, LOX, and ITGA5 expression, leading to further activation of FAK/Src signaling (Fig. 8). Based on these results, we propose that targeting LOX or its downstream FAK or Src or restoring the hypoxia-inhibited miR-142-3p can overcome chemoresistance by effectively blocking FAK/Src signaling (Fig. 8). Overall, our results provide valuable insights into how chemoresistance can be modulated at multiple levels and a pre-clinical support for inhibiting a key ECM-remodeler, LOX in TNBCs to potentiate chemotherapy response.

Methods

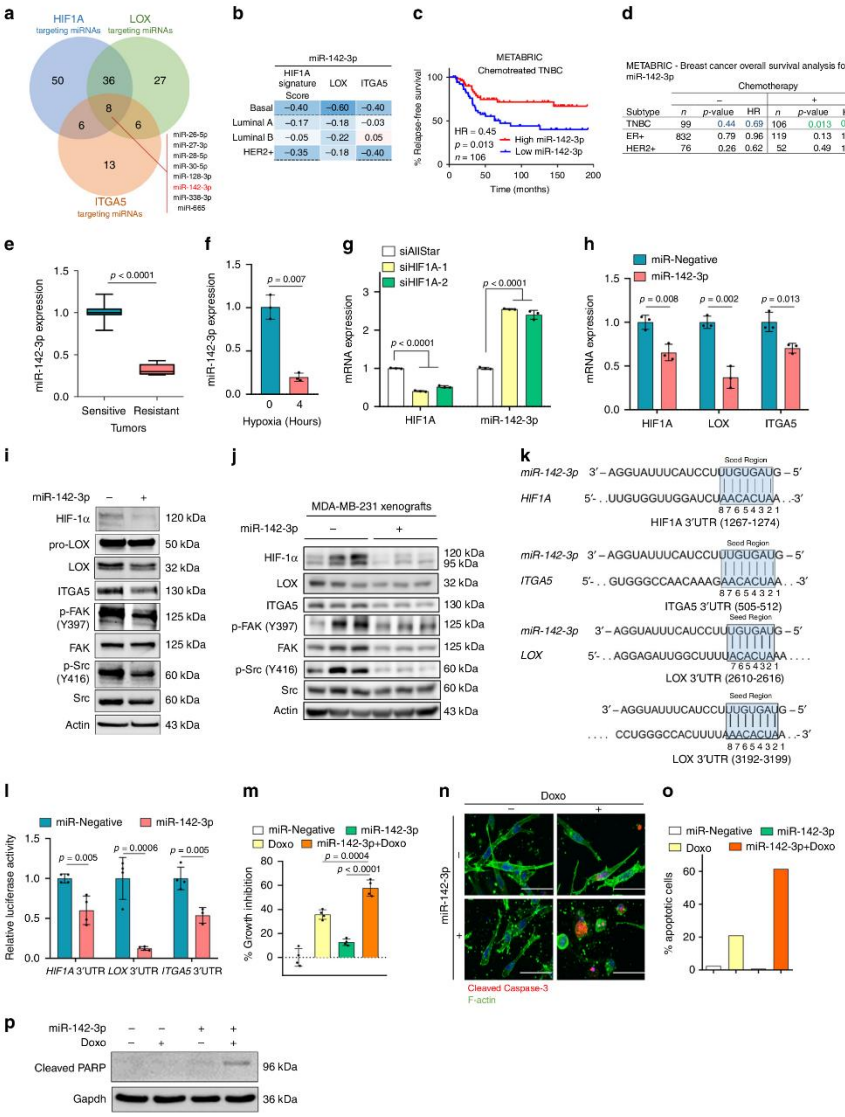
In vivo experiments. To develop doxorubicin-resistant xenografts, 6–8-weeks-old female athymic nu/nu mice were injected with 2×10^6 MDA-MB-231 cells into mammary fat pads (MFP). Mice were randomly allocated into two groups, and vehicle or doxorubicin treatments (5 mg/kg, weekly, i.v.) were started when tumors became palpable. Vehicle-treated tumors were collected and designated as vehicle. Half of the doxorubicin-treated mice were sacrificed when they were responsive to treatment, and tumors were collected and designated as sensitive. The remaining mice continued to receive doxorubicin until their tumors started regrowth. Then, these mice were also sacrificed, and tumors were collected and designated as resistant.

To test the role of LOX or FAK or Src inhibition to overcome chemotherapy resistance in immunocompetent setting, 2×10^5 4T1 cells were injected into the MFPs of 6–8 weeks-old Balb/c mice. Mice were treated with vehicle, doxorubicin (2.5 mg/kg, once a week, i.v.), BAPN (100 mg/kg, daily, ip.), PF-562271 (15 mg/kg, daily, oral), Saracatinib (25 mg/kg, daily, oral), or their combinations with doxorubicin. Once the vehicle group reached at 800 mm^3, all mice were sacrificed, and tumor weight was measured.

For shLOX induction experiments using the luciferase overexpressing MDA-MB-231.Luc2GFP cells, doxycycline was given to induce shLOX expression at 100 ug/ml in drinking water when the tumors reach at 100 mm^3. All mice were sacrificed; tumors were collected and weighed once the vehicle-treated tumors reached at 1500 mm^3. For bioluminescence imaging, mice were intraperitoneally injected with 150 mg/kg D-luciferin (Perkin Elmer, MA, USA), and images were acquired with Lumina III In Vivo Imaging System (Perkin Elmer, MA, USA). Analysis was performed with Living image software by measuring photon flux.

For PDX experiments, 2–3 mm^3 pieces of frozen PDX tumors were placed into the flank region of NSG mice. When tumors become palpable, mice were distributed into treatment groups. Doxorubicin (2 mg/kg, once a week, i.v.) and BAPN (100 mg/kg, daily, i.p.) was given individually or in combination for 30 days after which mice were sacrificed and tumors were collected for downstream analysis.

Primary tumor growth was monitored by measuring the tumor volume at least twice a week with a caliper after tumors became palpable. Tumor volumes were calculated as length × $width^2/2$. All mice used were of the same age and similar body weight. All animal experiments have been approved by the Animal Ethics Committee of Bilkent University or the Institutional Animal Care and Use



Committee of University of South Carolina. All mice were maintained under a temperature-controlled environment with a 12-h light/dark cycle and received a standard diet and water ad libitum.

Patient tumor-derived and PDX-derived organoids. For the generation of patient organoids, breast cancer surgical patients were consented under an IRB approved protocol for the USC-Palmetto Health Biorepository. TNBC organoids were established from a fresh surgical tissue by cutting the tumor into small pieces and incubating in collagenase A solution with ROCK inhibitor on a shaker at 37 °C for 30 min. The collagenase activity was inhibited by adding FBS, and pipetting was done to ensure the formation of almost a single cell solution. After several washes with PBS, the cell pellet was dissolved in matrigel. Breast organoid media containing ROCK and GSK inhibitors was added after the matrigel solidified[69]. For the PDX organoid, a small, 2–3 mm^3 piece of the PDX tumor that was freshly excised from an NSG mouse was minced and separated into single cell suspension as previously described[70]. For drug testing studies, organoids were disrupted to single

Fig. 7 miR-142-3p regulates HIF1A/LOX/ITGA5 axis to confer chemosensitization in TNBC. a Venn diagram of combinatorial target prediction analysis. Number of miRNAs targeting *HIF1A* (blue), *LOX* (green) and *ITGA5* (orange) is shown. Eight miRNAs predicted to target all three genes are shown. **b** Heatmap showing Pearson's correlation coefficients between miR-142-3p and *HIF1A* gene signature score, *LOX* and *ITGA5* mRNA expressions in patients from GSE19783. An intense blue color shows a stronger negative correlation. **c** Kaplan–Meier survival curve in chemotherapy-treated TNBC patients ($n = 106$) based on low vs. high (median) miR-142-3p expression. **d** Table summarizing the association of miR-142-3p expression with survival in different breast cancer subtypes with or without chemotherapy. **e**, **f** qRT-PCR analyses of miR-142-3p expression in doxorubicin-sensitive ($n = 11$) vs. doxorubicin-resistant ($n = 12$) xenografts (**e**) and in MDA-MB-231 cells under hypoxia for 4 h ($n = 3$) (**f**). **g**. qRT-PCR of miR-142-3p upon transfection with two different siRNAs targeting HIF1A for 48 h ($n = 3$). **h**, **i** qRT-PCR ($n = 3$) (**h**) and western blot (**i**) analyses of HIF/LOX/ITGA5 axis upon miR-142-3p transfection. **j**. Western blot analyses of the HIF1A/LOX/ITGA5 axis in MDA-MB-231 xenografts stably expressing miR-142-3p. **k** Graphical representation of miR-142-3p binding sites within the 3′-UTRs of *HIF1A*, *LOX* and *ITGA5*. **l**. Luciferase reporter assay with 3′-UTRs of *HIF1A*, *LOX* or *ITGA5* in MDA-MB-231 cells transfected with miR-Negative or miR-142-3p ($n = 4$ (*HIF1A* and *LOX*), $n = 3$–4 for (*ITGA5*)). **m** Percentage growth inhibition in collagen-embedded MDA-MB-231 cells after transfection with miR-142-3p in the presence or absence of doxorubicin ($n = 4$). **n** Immunofluorescence staining of Cleaved Caspase-3 (red) and F-actin (green) in miR-Negative or miR-142-3p transfected MDA-MB-231 cells in the presence or absence of doxorubicin. **o**. Quantification of Cleaved Caspase-3 positive cells from **n**. **p**. Western blot of cleaved PARP upon miR-142-3p transfection with or without doxorubicin treatment for 72 h. Data represents mean ± SD. Two-sided Student's *t*-test was used to calculate statistical difference between two groups. One-way ANOVA with Dunnett's test was performed to compare mean of combination-treated group with single agent treatments in **m**. Significance for survival analyses was calculated by log-rank (Mantel-Cox) test. HR hazard ratio. Scale bar = 50 μm for **n**. Source data are provided as a Source data file.

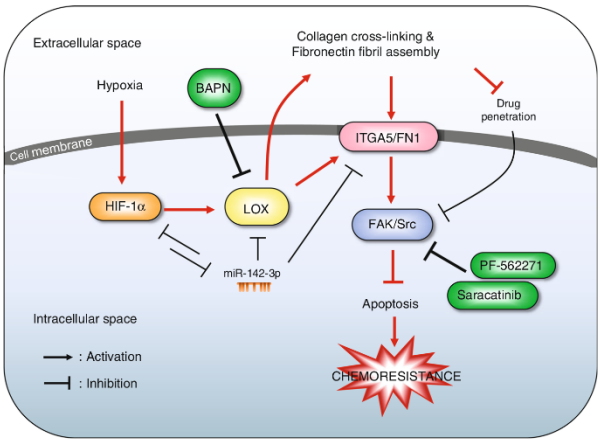


Fig. 8 Mechanistic summary and targeting approaches for overcoming chemoresistance. In the hypoxic, chemoresistant TNBC tumor microenvironment, hypoxia induces HIF-1α which then increases the transcription of LOX. LOX, on one hand, increases the expressions of ITGA5 and its ligand, fibronectin in tumor cells and on the other hand, it induces collagen cross-linking and fibronectin fibril assembly leading to reduced drug penetration into tumor cells. In meantime, hypoxia-mediated downregulation of miR-142-3p, which directly targets HIF1A, LOX and ITGA5, leads to further activation of the HIF1A/LOX/ITGA5/FN1 axis. Overall, this culminates in the activation of FAK/Src signaling, blockage of drug-induced apoptosis and chemoresistance in TNBCs. Therefore, using inhibitors targeting LOX (e.g. BAPN) or its downstream FAK (e.g. PF-562271) or Src (Saracatinib) could overcome chemoresistance in TNBCs.

cells by digesting at 37 °C for 30 min with TrypLE (A1217701, Gibco, NY, USA) in the presence of 10uM Rock inhibitor (s1049, Selleckchem, TX, USA). Organoids were plated into wells of 96-well plate (20,000 cells/well) on a collagen-coated surface with media containing 2% matrigel (356252, Corning, NY, USA). Drugs were added 72 h after plating (final concentration of doxorubicin at 40 nM and BAPN at 25 mM). Cells were grown in the presence of drug(s) or vehicle for 9 days, and the diameter of organoids were measured.

Whole-transcriptome sequencing (RNA-seq) and data analyses. rRNA-depleted stranded libraries for each condition (four biological replicates for each of vehicle, doxorubicin-sensitive tumors and doxorubicin-resistant tumors) were generated and multiplexed. Paired-end 100 bp sequencing was performed using the Illumina HiSeq 2000 platform at McGill University and Genome Quebec Innovation Centre. In all, 60–70 million sequencing reads were obtained for each sample. Raw sequence reads were aligned to the UCSC human reference genome (hg19) using TopHat. with default parameters. To count the mapped reads, HTSeq was used with the reference genome annotation (USCS, hg19). In order to determine differentially expressed genes between doxorubicin-sensitive and doxorubicin-resistant groups, Bioconductor package, edgeR, was utilized.

Patient data analyses. To analyze the effects of LOX expression on the survival of chemotherapy-treated TNBCs, we performed IHC staining of LOX in primary tumor samples from 77 TNBC patients that were diagnosed with breast cancer between 2006 and 2015 at Hacettepe University School of Medicine, Ankara, Turkey and treated with chemotherapy (35% adjuvant anthracycline-based therapy, 43% anthracyclines in combination with taxanes and 22% other chemotherapy agents). The study was approved by the Non-Interventional Clinical Research Ethics Committee of Hacettepe University (approval no: 2020/02-40). To generate DoxoR-GS scores in patients from METABRIC, GSE31519 and GSE58812, we used the top 441 differentially (up or down-regulated) expressed mRNAs between doxorubicin-sensitive vs. -resistant xenografts with a fold change cut-off of 1.75 and *p*-value cut-off of 0.05 (Supplementary Data 1). First, expression of these 441 genes in patients were converted into *z*-scores. Then, the sum of *z*-scores of the downregulated genes in the DoxoR-GS was subtracted from the sum of *z*-scores of

the upregulated genes for each patient[35] using the SPSS Statistics software. Chemotherapy-treated patient subgroup from the KM Plotter database (release version 2017) were created by selecting the adjuvant chemotherapy-treated patients and excluding the endocrine-treated ones. In GSE19783 dataset, patients are stratified based on the PAM50 subtyping (basal patients were selected) and ERα, PR and HER2 expression.

Statistics and reproducibility. The results are represented as mean ± standard deviation (SD) or mean ± standard error of the mean (SEM), as indicated in the figure legends. All statistical analyses were performed in GraphPad Prism Software using two-sided Student's t-test for comparisons between two groups, one-way ANOVA followed by Dunnett multiple comparison test for comparing combination treatment group with single agent-treated groups, and two-way ANOVA for comparing tumor volume change over time among different treatment groups. Survival curves were generated based on median separation using Kaplan–Meier method, and significance between groups was calculated by Log-rank test. For correlation analysis, Pearson correlation coefficients were calculated. Experiments were repeated two to three times independently with similar results.

Methods for cell culturing, cell-based assays, transient and stable transfections, qRT-PCR and Western blot analysis, immunofluorescence, immunohistochemical and Picrosirius red staining, Annexin V/DAPI staining, hypoxia, cloning, dual luciferase, LOX activity, collagen and deoxycholate lysis assays, other animal experiments, measuring doxorubicin penetration in vitro and in vivo, and patient data and pathway analyses were provided in Supplementary Methods. The list of primers for qRT-PCR, antibodies for Western blotting, IF and IHC as well as the primer sequences for 3′-UTR cloning are provided in Supplementary Table 4.

Reporting summary. Further information on research design is available in the Nature Research Reporting Summary linked to this article.

Data availability

The RNA-Seq data has been uploaded to the Sequence Read Archive (SRA) of NCBI with the submission ID: SUB6918779 (https://www.ncbi.nlm.nih.gov/bioproject/PRJNA607780). Data presented on Figs. 1d, f, 2b and Supplementary Figs. 2b, c, 4a, b were generated by analyzing the data available under the accession number GSE58812 from GEO depository (https://www.ncbi.nlm.nih.gov/geo/). Data presented on Figs. 1h, i, k, l, 2o and Supplementary Figs. 1d, e, 2a, d were generated by analyzing the KM Plotter database (http://kmplot.com/analysis/). Data presented on Fig. 7c, d and Supplementary Figs. 1a, 12d were generated by analyzing the METABRIC data from EMBL European Genome–Phenome Archive (http://www.ebi.ac.uk/ega/) with an accession number EGAS00000000122. GSEA gene sets were downloaded from the GSEA MSigDB Collections website: https://www.gsea-msigdb.org/gsea/msigdb/collections.jsp. Data presented on Fig. 7b and Supplementary Fig. 12a, b, c were generated by analyzing the data available under the accession number GSE19783 from NCBI. Data presented on Supplementary Figs. 1b, 5a were generated by analyzing the data available under the accession number GSE31519 from NCBI. Data presented on Supplementary Fig. 5b–e were generated by analyzing the data available under the accession number GSE25066 from NCBI. Data presented on Fig. 2h was generated by analyzing the data available under the accession numbers GSE16446, GSE19783, GSE21653, GSE22219, GSE22226, GSE25066, GSE58644 from NCBI and under METABRIC datasets and The Cancer Genome Atlas (TCGA) data. The source data underlying Figs. 1a–h, j, k; 2a–e, g–o, q; 3a–g, i, k–q; 4a–e, g–j, l, n–p, r; 5a, c–e, g, i, k–l; 6a, c, e–f, h, i, k, m, o, q, s; 7b, c, e–j, l, m, p and Supplementary Figs. 1a–c; 2a–c; 3a–b; 4c, d; 5c–e; 6b, f; 7a–d; 8a, c; 9a, c; 10a–c, e, f; 11b–f; 12e are provided as a Source Data file. All the other data supporting the findings of this study are available within the article and its Supplementary Information files and from the corresponding author upon reasonable request. A reporting summary for this article is available as a Supplementary Information file.

Received: 19 August 2019; Accepted: 20 April 2020;
Published online: 15 May 2020

References

1. Saraiva, D. P., Guadalupe Cabral, M., Jacinto, A. & Braga, S. How many diseases is triple negative breast cancer: the protagonism of the immune microenvironment. *ESMO Open* **2**, e000208 (2017).
2. Yadav, B. S., Chanana, P. & Jhamb, S. Biomarkers in triple negative breast cancer: a review. *World J. Clin. Oncol.* **6**, 252–263 (2015).
3. Foulkes, W. D., Smith, I. E. & Reis-Filho, J. S. Triple-negative breast cancer. *N. Engl. J. Med.* **363**, 1938–1948 (2010).
4. Mayer, E. L. & Burstein, H. J. Chemotherapy for triple-negative breast cancer: is more better? *J. Clin. Oncol.* **34**, 3369–3371 (2016).
5. Prowell, T. M. & Pazdur, R. Pathological complete response and accelerated drug approval in early breast cancer. *N. Engl. J. Med.* **366**, 2438–2441 (2012).
6. Liedtke, C. et al. Response to neoadjuvant therapy and long-term survival in patients with triple-negative breast cancer. *J. Clin. Oncol.* **26**, 1275–1281 (2008).
7. Schmid, P. et al. Atezolizumab and Nab-Paclitaxel in advanced triple-negative breast cancer. *N. Engl. J. Med.* **379**, 2108–2121 (2018).
8. Grassilli, E., Ballabeni, A., Maellaro, E., Del Bello, B. & Helin, K. Loss of MYC confers resistance to doxorubicin-induced apoptosis by preventing the activation of multiple serine protease- and caspase-mediated pathways. *J. Biol. Chem.* **279**, 21318–21326 (2004).
9. Dai, Z., Huang, Y. & Sadee, W. Growth factor signaling and resistance to cancer chemotherapy. *Curr. Top. Med. Chem.* **4**, 1347–1356 (2004).
10. Deffie, A. M. et al. Multifactorial resistance to adriamycin: relationship of DNA repair, glutathione transferase activity, drug efflux, and P-glycoprotein in cloned cell lines of adriamycin-sensitive and -resistant P388 leukemia. *Cancer Res.* **48**, 3595–3602 (1988).
11. Calcagno, A. M. et al. Single-step doxorubicin-selected cancer cells overexpress the ABCG2 drug transporter through epigenetic changes. *Br. J. Cancer* **98**, 1515–1524 (2008).
12. Netti, P. A., Berk, D. A., Swartz, M. A., Grodzinsky, A. J. & Jain, R. K. Role of extracellular matrix assembly in interstitial transport in solid tumors. *Cancer Res.* **60**, 2497–2503 (2000).
13. Senthebane, D. A., et al. The role of tumor microenvironment in chemoresistance: to survive, keep your enemies closer. *Int. J. Mol. Sci.* **18**, e1586 (2017).
14. Zhou, H. et al. Hyaluronidase embedded in nanocarrier PEG shell for enhanced tumor penetration and highly efficient antitumor efficacy. *Nano Lett.* **16**, 3268–3277 (2016).
15. Meads, M. B., Gatenby, R. A. & Dalton, W. S. Environment-mediated drug resistance: a major contributor to minimal residual disease. *Nat. Rev. Cancer* **9**, 665–674 (2009).
16. Sethi, T. et al. Extracellular matrix proteins protect small cell lung cancer cells against apoptosis: a mechanism for small cell lung cancer growth and drug resistance in vivo. *Nat. Med.* **5**, 662–668 (1999).
17. Humphries, J. D., Byron, A. & Humphries, M. J. Integrin ligands at a glance. *J. cell Sci.* **119**, 3901–3903 (2006).
18. Kechagia, J. Z., Ivaska, J. & Roca-Cusachs, P. Integrins as biomechanical sensors of the microenvironment. *Nat. Rev. Mol. cell Biol.* **20**, 457–473 (2019).
19. Aoudjit, F. & Vuori, K. Integrin signaling in cancer cell survival and chemoresistance. *Chemother. Res. Pract.* **2012**, 283181 (2012).
20. Seguin, L., Desgrosellier, J. S., Weis, S. M. & Cheresh, D. A. Integrins and cancer: regulators of cancer stemness, metastasis, and drug resistance. *Trends cell Biol.* **25**, 234–240 (2015).
21. Longmate, W. & DiPersio, C. M. Beyond adhesion: emerging roles for integrins in control of the tumor microenvironment. *F1000Res.* **6**, 1612 (2017).
22. Schaffner, F., Ray, A. M. & Dontenwill, M. Integrin alpha5beta1, the fibronectin receptor, as a pertinent therapeutic target in solid tumors. *Cancers* **5**, 27–47 (2013).
23. Yao, E. S. et al. Increased beta1 integrin is associated with decreased survival in invasive breast cancer. *Cancer Res.* **67**, 659–664 (2007).
24. Bonnans, C., Chou, J. & Werb, Z. Remodelling the extracellular matrix in development and disease. *Nat. Rev. Mol. Cell Biol.* **15**, 786–801 (2014).
25. Naba, A., et al. The matrisome: in silico definition and in vivo characterization by proteomics of normal and tumor extracellular matrices. *Mol. Cell. Proteomics.* **11**, M111.014647 (2012).
26. Xiong, G. X. & Xu, R. Function of cancer cell-derived extracellular matrix in tumor progression. *J. Cancer Metastasis Treat.* **2**, 357–364 (2016).
27. Kagan, H. M. & Li, W. Lysyl oxidase: properties, specificity, and biological roles inside and outside of the cell. *J. Cell. Biochem.* **88**, 660–672 (2003).
28. Erler, J. T. et al. Hypoxia-induced lysyl oxidase is a critical mediator of bone marrow cell recruitment to form the premetastatic niche. *Cancer cell* **15**, 35–44 (2009).
29. Rachman-Tzemah, C. et al. Blocking surgically induced lysyl oxidase activity reduces the risk of lung metastases. *Cell Rep.* **19**, 774–784 (2017).
30. Le Calve, B. et al. Lysyl oxidase family activity promotes resistance of pancreatic ductal adenocarcinoma to chemotherapy by limiting the intratumoral anticancer drug distribution. *Oncotarget* **7**, 32100–32112 (2016).
31. Miller, B. W. et al. Targeting the LOX/hypoxia axis reverses many of the features that make pancreatic cancer deadly: inhibition of LOX abrogates metastasis and enhances drug efficacy. *EMBO Mol. Med.* **7**, 1063–1076 (2015).
32. Barker, H. E., Cox, T. R. & Erler, J. T. The rationale for targeting the LOX family in cancer. *Nat. Rev. Cancer* **12**, 540–552 (2012).
33. Chavez, K. J., Garimella, S. V. & Lipkowitz, S. Triple negative breast cancer cell lines: one tool in the search for better treatment of triple negative breast cancer. *Breast Dis.* **32**, 35–48 (2010).
34. Holliday, D. L. & Speirs, V. Choosing the right cell line for breast cancer research. *Breast Cancer Res.* **13**, 215 (2011).
35. Dancik, G. M. & Theodorescu, D. Robust prognostic gene expression signatures in bladder cancer and lung adenocarcinoma depend on cell cycle related genes. *PloS ONE* **9**, e85249 (2014).
36. Jezequel, P. et al. Gene-expression molecular subtyping of triple-negative breast cancer tumours: importance of immune response. *Breast Cancer Res.* **17**, 43 (2015).
37. Curtis, C. et al. The genomic and transcriptomic architecture of 2,000 breast tumours reveals novel subgroups. *Nature* **486**, 346–352 (2012).

38. Bertucci, F. et al. How basal are triple-negative breast cancers? *Int. J. Cancer* **123**, 236–240 (2008).
39. Gilkes, D. M., Bajpai, S., Chaturvedi, P., Wirtz, D. & Semenza, G. L. Hypoxia-inducible factor 1 (HIF-1) promotes extracellular matrix remodeling under hypoxic conditions by inducing P4HA1, P4HA2, and PLOD2 expression in fibroblasts. *J. Biol. Chem.* **288**, 10819–10829 (2013).
40. Pez, F. et al. The HIF-1-inducible lysyl oxidase activates HIF-1 via the Akt pathway in a positive regulation loop and synergizes with HIF-1 in promoting tumor cell growth. *Cancer Res.* **71**, 1647–1657 (2011).
41. Rana, M. K., Srivastava, J., Yang, M., Chen, C. S. & Barber, D. L. Hypoxia increases the abundance but not the assembly of extracellular fibronectin during epithelial cell transdifferentiation. *J. Cell Sci.* **128**, 1083–1089 (2015).
42. Ju, J. A. et al. Hypoxia selectively enhances integrin alpha5beta1 receptor expression in breast cancer to promote metastasis. *Mol. Cancer* **15**, 723–734 (2017).
43. Olive, P. L. et al. Carbonic anhydrase 9 as an endogenous marker for hypoxic cells in cervical cancer. *Cancer Res.* **61**, 8924–8929 (2001).
44. Cox, T. R., Gartland, A. & Erler, J. T. Lysyl oxidase, a targetable secreted molecule involved in cancer metastasis. *Cancer Res.* **76**, 188–192 (2016).
45. Wong, C. C. et al. Hypoxia-inducible factor 1 is a master regulator of breast cancer metastatic niche formation. *Proc. Natl Acad. Sci. USA* **108**, 16369–16374 (2011).
46. Senkus, E. et al. Primary breast cancer: ESMO clinical practice guidelines for diagnosis, treatment and follow-up. *Ann. Oncol.* **26**(Suppl. 5), v8–v30 (2015).
47. Kubow, K. E. et al. Mechanical forces regulate the interactions of fibronectin and collagen I in extracellular matrix. *Nat. Commun.* **6**, 8026 (2015).
48. Sottile, J. & Hocking, D. C. Fibronectin polymerization regulates the composition and stability of extracellular matrix fibrils and cell-matrix adhesions. *Mol. Biol. Cell* **13**, 3546–3559 (2002).
49. Ilic, D. et al. FAK promotes organization of fibronectin matrix and fibrillar adhesions. *J. Cell Sci.* **117**, 177–187 (2004).
50. Wierzbicka-Patynowski, I. & Schwarzbauer, J. E. The ins and outs of fibronectin matrix assembly. *J. Cell Sci.* **116**, 3269–3276 (2003).
51. Wu, C., Keivens, V. M., O'Toole, T. E., McDonald, J. A. & Ginsberg, M. H. Integrin activation and cytoskeletal interaction are essential for the assembly of a fibronectin matrix. *Cell* **83**, 715–724 (1995).
52. Varadaraj, A., Magdaleno, C. & Mythreye, K. Deoxycholate fractionation of fibronectin (FN) and biotinylation assay to measure recycled FN fibrils in epithelial cells. *Bio Protoc.* **8**, e2972 (2018).
53. Schutze, F. et al. Inhibition of lysyl oxidases improves drug diffusion and increases efficacy of cytotoxic treatment in 3D tumor models. *Sci. Rep.* **5**, 17576 (2015).
54. Liang, P. C. et al. Doxorubicin-modified magnetic nanoparticles as a drug delivery system for magnetic resonance imaging-monitoring magnet-enhancing tumor chemotherapy. *Int J. Nanomed.* **11**, 2021–2037 (2016).
55. Bouchard, G. et al. Stimulation of triple negative breast cancer cell migration and metastases formation is prevented by chloroquine in a pre-irradiated mouse model. *BMC Cancer* **16**, 361 (2016).
56. Uhlmann, S. et al. Global microRNA level regulation of EGFR-driven cell-cycle protein network in breast cancer. *Mol. Syst. Biol.* **8**, 570 (2012).
57. Cha, Y. J., Jung, W. H. & Koo, J. S. Site-specific expression of amine oxidases in breast cancer metastases. *Tumour Biol.* **40**, 1010428318776822 (2018).
58. Baker, A. M. et al. The role of lysyl oxidase in SRC-dependent proliferation and metastasis of colorectal cancer. *J. Natl Cancer Inst.* **103**, 407–424 (2011).
59. Baker, A. M., Bird, D., Lang, G., Cox, T. R. & Erler, J. T. Lysyl oxidase enzymatic function increases stiffness to drive colorectal cancer progression through FAK. *Oncogene* **32**, 1863–1868 (2013).
60. Cooper, J. & Giancotti, F. G. Integrin signaling in cancer: mechanotransduction, stemness, epithelial plasticity, and therapeutic resistance. *Cancer cell* **35**, 347–367 (2019).
61. Boufraqech, M. et al. Lysyl Oxidase (LOX) transcriptionally regulates SNAI2 expression and TIMP4 secretion in human cancers. *Clin. Cancer Res.* **22**, 4491–4504 (2016).
62. Bolos, V., Gasent, J. M., Lopez-Tarruella, S. & Grande, E. The dual kinase complex FAK-Src as a promising therapeutic target in cancer. *Onco Targets Ther.* **3**, 83–97 (2010).
63. Lampi, M. C. & Reinhart-King, C. A. Targeting extracellular matrix stiffness to attenuate disease: from molecular mechanisms to clinical trials. *Sci. Transl. Med.* **10**, eaao0475 (2018).
64. Burroughs, S. K. et al. Hypoxia inducible factor pathway inhibitors as anticancer therapeutics. *Future Med. Chem.* **5**, 553–572 (2013).
65. Rodriguez, C., Rodriguez-Sinovas, A. & Martinez-Gonzalez, J. Lysyl oxidase as a potential therapeutic target. *Drug New Perspect.* **21**, 218–224 (2008).
66. Leung, L. et al. Anti-metastatic Inhibitors of Lysyl Oxidase (LOX): design and structure-activity relationships. *J. Med. Chem.* **62**, 5863–5884 (2019).
67. Hutchinson, J. H. et al. Small molecule Lysyl oxidase-like 2 (LOXL2) inhibitors: the identification of an inhibitor selective for LOXL2 over LOX. *ACS Med. Chem. Lett.* **8**, 423–427 (2017).
68. Inui, M., Martello, G. & Piccolo, S. MicroRNA control of signal transduction. *Nat. Rev. Mol. Cell Biol.* **11**, 252–263 (2010).
69. Sachs, N. et al. A living biobank of breast cancer organoids captures disease heterogeneity. *Cell* **172**, 373–386 e310 (2018).
70. Liu, C. et al. PRDM1 silences stem cell-related genes and inhibits proliferation of human colon tumor organoids. *Proc. Natl Acad. Sci. USA* **115**, E5066–E5075 (2018).

Acknowledgements

We thank Madeleine Arseneault and Ozlem Sener Sahin for technical and organizational support, and Jitao David Zhang for his help with the initial analysis of RNA-Seq data. We also thank the Center for Targeted Therapeutics (CTT) Microscopy and Flow Cytometry Core (Dr. Chang-uk Lim) of the University of South Carolina, for assistance with flow cytometry. This work was supported by National Institutes of Health Grant 2P20GM109091-06 (O.S.), and in part by European Commission FP7 Marie Curie Career Integration Grant PCIG14-GA-2013-631149 (O.S.), European Molecular Biology Organization (EMBO) Installation Grant 2791 (O.S.), the American Cancer Society Institutional Research Grant IRG-17-179-04 (O.S.), the American Cancer Society Research Scholar Grant RSG-19-194-01-CSM (O.S.), Susan G. Komen Interdisciplinary Graduate Training to Eliminate Cancer Disparities (IGniTE-CD) GTDR17500160 (Ozge S.), the scholarship from Higher Education Commission of Pakistan (U.R.), and research scholarship of the Fonds de recherche du Québec—Santé (FRQS) (Y.R.).

Author contributions

Ozge S., A.K., and U.R. designed and performed experiments, acquired and analyzed data, interpreted data, and prepared the paper; P.G.E. and O.A. contributed to in vivo experiments, IHC staining and data collection; C.E.B. generated TNBC patient organoids; V.S. contributed to confocal microscopy experiments and data analyses; S.A.A. performed cloning and luciferase reporter experiments; U.M.T. contributed to RNA-seq analyses; G.A. contributed to in vivo experiments; H.T.D., M.D., performed the IHC staining of xenografts and contributed to data interpretation; P.J. performed RNA-sequencing; A.I., F.G., K.K., A.A., and A.U. performed the IHC staining of TNBC patient tissues and contributed to data interpretation; O.D. and S.A. provided clinical information of TNBC patients and contributed to data analyses; P.J.B. contributed to TNBC tumor organoid experiments and critically read and edited the manuscript; Y.R. performed RNA-sequencing, and critically read and edited the manuscript; O.S. designed the study, oversaw experiments and data analyses, and prepared the paper. All authors reviewed and commented on the paper.

Competing interests

The authors declare no competing interests.

Additional information

Supplementary information is available for this paper at https://doi.org/10.1038/s41467-020-16199-4.

Correspondence and requests for materials should be addressed to O.S.

Peer review information *Nature Communications* thanks Matthew Ellis and the other, anonymous, reviewer(s) for their contribution to the peer review of this work. Peer reviewer reports are available.

Reprints and permission information is available at http://www.nature.com/reprints

Publisher's note Springer Nature remains neutral with regard to jurisdictional claims in published maps and institutional affiliations.

Open Access This article is licensed under a Creative Commons Attribution 4.0 International License, which permits use, sharing, adaptation, distribution and reproduction in any medium or format, as long as you give appropriate credit to the original author(s) and the source, provide a link to the Creative Commons license, and indicate if changes were made. The images or other third party material in this article are included in the article's Creative Commons license, unless indicated otherwise in a credit line to the material. If material is not included in the article's Creative Commons license and your intended use is not permitted by statutory regulation or exceeds the permitted use, you will need to obtain permission directly from the copyright holder. To view a copy of this license, visit http://creativecommons.org/licenses/by/4.0/.

© The Author(s) 2020

Cell Death & Differentiation (2019) 26:2223–2236
https://doi.org/10.1038/s41418-019-0289-6

Cell Death & Differentiation

ARTICLE

Thymidylate synthase maintains the de-differentiated state of triple negative breast cancers

Aarif Siddiqui[1] · Paradesi Naidu Gollavilli[1,2] · Annemarie Schwab[1] · Maria Eleni Vazakidou[1] · Pelin G. Ersan[3] · Mallika Ramakrishnan[4] · Dick Pluim[5] · Si'Ana Coggins[6] · Ozge Saatci[7] · Laura Annaratone[8] · Jan HM Schellens[5] · Baek Kim[6,9] · Irfan Ahmed Asangani[2] · Suhail Ahmed Kabeer Rasheed[10] · Caterina Marchiò[8,11,12] · Ozgur Sahin[3,7] · Paolo Ceppi[1]

Received: 19 June 2018 / Revised: 30 November 2018 / Accepted: 10 January 2019 / Published online: 8 February 2019
© The Author(s) 2019. This article is published with open access

Abstract

Cancer cells frequently boost nucleotide metabolism (NM) to support their increased proliferation, but the consequences of elevated NM on tumor de-differentiation are mostly unexplored. Here, we identified a role for thymidylate synthase (TS), a NM enzyme and established drug target, in cancer cell de-differentiation and investigated its clinical significance in breast cancer (BC). In vitro, TS knockdown increased the population of $CD24^{+}$ differentiated cells, and attenuated migration and sphere-formation. RNA-seq profiling indicated repression of epithelial-to-mesenchymal transition (EMT) signature genes upon TS knockdown, and TS-deficient cells showed an increased ability to invade and metastasize in vivo, consistent with the occurrence of a partial EMT phenotype. Mechanistically, TS enzymatic activity was found essential for maintenance of the EMT/stem-like state by fueling a dihydropyrimidine dehydrogenase—dependent pyrimidine catabolism. In patient tissues, TS levels were found significantly higher in poorly differentiated and in triple negative BC, and strongly correlated with worse prognosis. The present study provides the rationale to study in-depth the role of NM at the crossroads of proliferation and differentiation, and depicts new avenues for the design of novel drug combinations for the treatment of BC.

Introduction

Tumor de-differentiation contributes to the malignant phenotype of most solid tumors, including breast cancer (BC) [1, 2], and in many cases this is achieved through the epithelial-to-mesenchymal transition (EMT) and the cancer stem cell (CSC) programs [3–5]. Indeed, EMT and CSC markers are more frequently found in aggressive poorly

Edited by Y. Shi

Supplementary information The online version of this article (https://doi.org/10.1038/s41418-019-0289-6) contains supplementary material, which is available to authorized users.

✉ Paolo Ceppi
paolo.ceppi@uk-erlangen.de

[1] Junior Research Group 1, IZKF, FAU Erlangen-Nürnberg, Erlangen, Germany

[2] Department of Cancer Biology, Perelman School of Medicine, University of Pennsylvania, Philadelphia, PA, USA

[3] Department of Molecular Biology and Genetics, Bilkent University, Ankara, Turkey

[4] Georg-Speyer-Haus Institute for Tumor Biology and Experimental Therapy, Frankfurt am Main, Germany

[5] Netherland Cancer Institute, Amsterdam, The Netherlands

[6] Department of Pediatrics, Emory University School of Medicine, Atlanta, GA, USA

[7] Department of Drug Discovery and Biomedical Sciences, University of South Carolina, Columbia, SC, USA

[8] Department of Medical Sciences, University of Turin, Turin, Italy

[9] Department of Pharmacy, Kyung Hee University, Seoul, South Korea

[10] Programme in Cancer and Stem Cell Biology, Duke-NUS Medical School, Singapore, Singapore

[11] Pathology Unit, Azienda Ospedaliera Universitaria Città della Salute e della Scienza di Torino, Turin, Italy

[12] Present address: Pathology Unit, Candiolo Cancer Institute, FPO-IRCCS, Candiolo, Italy

SPRINGER NATURE
CDDpress

differentiated (high-grade) tumors in breast [2] and other cancers [6–10]. Understanding the mechanisms controlling the differentiation of BC cells can therefore lead to more effective therapeutics.

Nucleotide metabolism (NM) is classically viewed as a motor of cellular proliferation [11]. Cancer cells are, in fact, highly dependent on the de novo synthesis of nucleotides to produce sufficient DNA and RNA precursors to support their growth, and some cancer-promoting signaling pathways have been shown to regulate NM [12]. However, a few recent studies have suggested that nucleotides-generating metabolic pathways may also serve as regulators of cancer stemness [13, 14], opening the possibility that some NM enzymes are implicated in cancer cell de-differentiation.

Thymidylate synthase (TS) is the enzyme that catalyzes the conversion of deoxyuridine monophosphate (dUMP) to thymidine monophosphate (dTMP or thymidylate). Since this reaction provides the sole de novo pathway for thymidylate production, TS is essential for DNA synthesis and repair, and its absence blocks proliferation and causes cell death [15, 16]. We previously discovered that TS expression is correlated with the EMT phenotype in the NCI-60 transcriptomic database by using a pan-cancer EMT gene ratio (Vimentin/E-Cadherin, VIM/CDH1) [17], but the mechanistic involvement of the TS enzymatic activity on EMT/CSCs has never been shown. Here, we report a novel fundamental role of TS in maintaining the de-differentiated phenotype of BC cells and its differential expression in the BC subtypes, with several potential therapeutic implications.

Material and methods

Cell lines

MDA-MB-231 (ATCC), BT-549 and T-47D (NCI) were cultured in RMPI-1640 (Sigma), while Hs 578T (DSMZ) were cultured in DMEM (Sigma). Media were supplemented with 10% FBS (Sigma), 1%Pen/Strep (Sigma) and 1%L-Glutamine (Sigma). Cells were STR-profiled, used between passages 3 and 15, examined for mycoplasma and maintained in Plasmocin (Invivogen) to prevent contamination. Human umbilical vein endothelial cells (HUVEC) were cultured in Ham's F-12K Medium (Gibco) supplemented with 0.1 mg/ml heparin (Sigma) and 0.03 mg/ml endothelial cell growth supplement (Sigma) 50 µ/ml Pen/Strep (Lonza) and 10% FBS (Biowest).

Western blot analysis

Cells were lysed in RIPA buffer and quantified using the Pierce BCA kit (Thermo-Fisher). Proteins lysates (10–35 µg) were resolved on 10% SDS–PAGE gels and transferred to PVDF membrane (Thermo-Fisher). Membranes were blocked in 5% Milk (BioRad) in 1XTBS-T and incubated overnight in primary antibodies diluted in 5% milk at 4 °C. Western blot antibodies for TS (EPR4545) and DPYD (EPR8811) are from Abcam and β-Actin (8H10D10) is from Cell Signaling. After incubation with secondary antibodies (Southern Biotech), detection was performed using the ECL (Thermo-Fisher) and developed on X-Ray film (Thermo-Fisher) using a chemiluminescence imager, AGFA CP100.

Proliferation assay

For proliferation assay cells were seeded in 96-well plates in low density (5–20% initial confluency). Plates were loaded in IncuCyte ZOOM (Essen BioScience) and scanned every 2–4 h. For each scan, phase contrast image was acquired from every well and was analyzed by IncuCyte Zoom software.

Migration assay

For migration assay cells were plated in 96-well plates so that they reach 90% confluency overnight. Cells were wounded using WoundMaker (Essen BioScience) as per the instruction from the manufacturer. Plates were loaded in IncuCyte ZOOM and were automatically scanned for programmed time interval. For each scan, wound width was recorded by the software and the proliferation inside the wound was normalized to the proliferation outside the wound, giving relative wound density for each time point.

Cell surface staining and FACS

Anti-CD44-FITC and anti-CD24-PE antibodies are from Biolegend. For staining, 400,000 cells were plated in 6-well plate and allowed to grow overnight. Cells were trypsinized and collected in FACS tubes. After two washes with 1% FBS/PBS, cells were incubated with 400 ng CD24-PE and CD44-FITC (diluted in 100 µl 1% FBS/PBS) for 20 min on ice. Cells were washed twice with 1% FBS/PBS and suspended in 5 mM EDTA and 2% FBS/PBS. CD24/CD44 positivity was recorded in CytoFLEX flow-cytometer (Beckman Coulter). Gating was done using unstained cells. FACS data were analyzed using FlowJo (V10.1).

RNA sequencing

Total RNA was extracted using miRNeasy kit (Qiagen) following the manufacturer's instructions. RNA-Seq libraries were constructed using the TruSeq sample Prep Kit V2 (Illumina). Briefly, 1 µg of purified RNA was

poly-A selected and fragmented with fragmentation enzyme. After first and second strand synthesis from a template of poly-A selected/fragmented RNA, other procedures from end-repair to PCR amplification were done according to library construction steps. Libraries were purified and validated for appropriate size on a 2100 Bioanalyzer High Sensitivity DNA chip (Agilent Technologies.). The DNA library was quantified using Qubit and normalized to 4 nM before pooling. Libraries were pooled in an equimolar fashion and diluted to 10 pM. Library pools were clustered and run on Nextseq500 platform with paired-end reads of 75 bases, according to the manufacturer's recommended protocol (Illumina). Raw reads passing the Illumina RTA quality filter were pre-processed using FASTQC for sequencing base quality control. Sequence reads were mapped to UCSC human genome build using TopHat and differential gene expression determined using Cufflinks 2.1.1 and Cuffdiff2.1.1 as implemented in BaseSpace. Sequencing data has been deposited to publically available GEO dataset GSE122953.

Bioinformatic analysis

Gene set enrichment analysis (GSEA) on the differentially-expressed genes (DEGs) upon TS knockdown was performed with the Molecular Signatures Database v6.1 software. For patient data analysis, normalized gene expression data from the following patient datasets were downloaded from GEO database; GSE19783, GSE31448, GSE19536, GSE58644, GSE21653, GSE45827, and GSE58812. While GSE58812 is a dataset of triple-negative BC patients, all other datasets are of BC patients with different subtypes. For calculation of TS Knockdown (KD) score, first, z scores of the down- and up-regulated genes upon TS knockdown were calculated. Then, the sum of z scores of downregulated genes were subtracted from the sum of z scores of upregulated genes and KD scores were obtained for each patient. Patients were grouped based on either their TYMS gene expression or KD score. GSEA was performed by using patient data from GSE58644 and GSE58812. Survival graphs were generated in GraphPad and the significance was assessed by Log-rank test. Survival graphs from the KM Plotter database was generated based on TYMS expression by using the auto select best cutoff option. Statistical analyses were performed by unpaired student's t-test.

Quantitative real-time PCR

Total RNA was extracted using miRNeasy kit (Qiagen) and converted to cDNA using Tetro cDNA synthesis kit (Bioline) with random hexamers. 50 nanograms cDNA was used as template for real-time quantification. GAPDH was used as the internal control. TaqMan probes (Thermo-Fisher) were used for quantification in Applied Biosystems 7300. Fold change was calculated using the ΔΔCt method.

Mouse tail vein metastasis injection

For tail vein metastasis assay, 1.5×10^6 cells were injected into tail vein of 6–8 weeks old female athymic nu/nu mice, with three mice per group. Lung metastases were monitored by bioluminescence imaging (BLI). Anesthetized mice were intraperitoneally injected with 200 mg/kg D-luciferin (Perkin Elmer). Bioluminescence images were acquired with Lumina III in vivo Imaging System (Perkin Elmer). Analysis was performed with live imaging software by measuring photon flux. Lungs were collected and fixed in 10% buffered formalin and processed to obtain paraffin blocks. Three-micron thick sections of formalin fixed paraffin embedded samples were stained using hematoxylin and eosin. Mice experiments were approved by Animal Ethics Committee of the Bilkent University.

Real-time HUVEC invasion assay (in vitro extravasation assay)

In vitro extravasation assay was performed as previously described [18]. Briefly, 2.5×10^4 HUVEC cells in 100 µl were seeded in E-plates (ACEA xCelligence). Once HUVEC monolayer formed (19–21 h), 1×10^4 MDA-MB-231 cells were added on top of the monolayer. A decrease in cell index indicates invasion through the HUVEC monolayer by tumor cells. Penetration of HUVEC monolayer was monitored for up to 10 h by using xCelligence Real-time Cell Analyzer (Acea Biosciences).

Chick chorioallantoic membrane (CAM) assay

CAM assay for intravasation was performed as described previously [19]. Briefly, fertilized white leghorn eggs (Asby) were incubated in a rotary incubator at 37 °C with 60% humidity for 10 days. The CAM was dropped by drilling a small hole through the eggshell into the air sac and a second hole near the allantoic vein that penetrates the eggshell membrane but not the CAM. The CAM was dropped by applying a mild vacuum to the hole over the air sac. Subsequently, a cutoff wheel (Dremel) was used to cut a 1 cm^2 window, encompassing the second hole near the allantoic vein to expose the underlying CAM. The CAM was gently abraded with a sterile cotton swab to provide access to the mesenchyme and 50 µl inoculum of 2×10^6 MDA-MB-231-pLKO ($n = 10$) or MDA-MB-231-shRNA-TS#2 ($n = 10$) cells were applied. Four eggs without human cells are used as negative control. The windows were subsequently sealed and the eggs returned to incubator. The

eggs remained in the incubator for further 2 days, following which the CAM was cut into two halves and the tumor was excised from the upper CAM and the genomic DNA was extracted from the lower CAM. The lower CAM genomic DNA was then analyzed for the presence of human cells by quantitative *Alu* PCR with 500 ng cDNA. The number of intravasated human cells was then plotted in the graph as shown.

Deoxynucleotide triphosphate quantification

The cellular dNTP levels were determined by the RT-based dNTP assay [20]. Briefly, the cellular dNTPs in experimental triplicates were extracted by methanol, and the determined dNTP amounts were normalized for an equal cell number (1×10^6).

TS enzyme activity quantification

TS was quantified in MDA-MB-231 cells as previously described [21]. Briefly, cells were collected and pelleted. Cells were suspended in 300 µl ice-cold Reaction mix (RM, 20 mM $MgCl_2$, 1.5 mM NaF, 1 mM DTT in 50 mM Tris-HCl pH 7.5, after deoxygenation 0.47 (v/v%) BME was added. Next, cell lysates were prepared on ice by applying 15 pulses with a Branson 250 tip sonicator (Branson) at power input setting level 3 with a 50% duty cycle. After centrifugation at 11000 g for 20 min at 4 °C, 95 µl of supernatant was transferred to a clean 1.5 ml vial on ice for immediate determination of protein followed by TS activity analysis. Protein concentrations in PBMC cytosolic lysates were determined using the Bio-Rad protein assay (Bio-Rad). Briefly, 5 µl of PBMC cytosolic lysate was diluted with 45 µl of MilliQ water (Millipore). Five bovine serum albumin standards were prepared in concentrations ranging from 32.5 to 500 mg/ml to obtain a standard curve. In duplicate 10 µl of diluted lysate and the standard curve were transferred to a clear 96-well flat bottom plate. After the addition of 200 µl dye solution, the plate was incubated for 15 min at RT and subsequently the absorption was measured at 590 nm using an EL340 microplate reader (Bio-Tek). Immediately before the start of TS activity assay, a vial containing 2.51 mg of lyophilized MTHF was reconstituted in 500 µl of deoxygenized water and 10 µl was added to a 2.0 ml vial on ice. To this vial 85 µl of ice-cold tumor cell cytosolic lysate corresponding to 15 µg of protein was added. Next, 5 µl of 1 mM ice-cold substrate was added, and after mixing, the samples were incubated for 3 h at 37 °C in a shaking water bath. The reaction was terminated by adding 100 µl of 6.5 N HCl, and the remaining substrate was bound onto 400 µl Carbon slurry (CS, 5 g acid washed charcoal, 50 mg Dextran T500 in phosphate buffered saline) by vertical disk rotation mixing of the samples at 50 rpm at 4° C. After centrifugation at 11,000 g for 5 min at 4 °C, 300 µl of clear supernatant was transferred to a 20 ml polyethylene vial, mixed with 10 ml of Ultima Gold, and assayed for radioactivity for 5 min using a LSC2900 Tri-Carb liquid scintillation counter.

Lentiviral transduction

Plasmids for TS (TRCN000045663/66/67) and DPYD knockdown (TRCN000025799) are from Sigma. Empty vector (pLKO) was used as control. For TS reconstitution, plasmids were purchased from GeneCopoeia in which silent mutation was introduced in shTS#1 binding region (5′-G_{483}CAAAGAGTAATCGATACAAT$_{503}$–3′). Enzymatically inactive TS expression vector was generated by introducing single point mutation (5′-$C_{148}GC_{150}$–3′→5′-TGC-3′) in reconstitution vector. Empty vector (CS-T0406-LV151) was used as control. TS expression vector (Ex-T0406-LV105b) and control vector (Ex-Neg-LV105b) are from GeneCopoeia. For production of lentiviral particles, 293T cells were transfected with 8 µg knock-down/expression vectors and 2 µg of pMDL, pV_sV_g and pRevRes in complex with 24 µg PEI (Polysciences). After 48 h, supernatant was collected, centrifuged and filtered. For transduction, 100,000–150,000 cells were seeded in 6-well plate and infected presence of 8 µg/ml polybrene (Sigma). Selection was done with 3 µg/ml puromycin (Sigma) and cells were maintained in 1 µg/ml puromycin. MDA-MB–231 cells infected with TS reconstitution vectors were selected in 800 µg/ml G418 (Sigma) and cultured in 250 µg/ml G418.

Mammosphere culture

Forty thousand cells were seeded in triplicates in ultra-low attachment 6-well plates (Corning) in complete Mammocult medium (Stem Cell Technologies), prepared according to the manufacturer's instruction. After formation, spheres were counted by spinning at 300 g for 5 min and suspending in PBS (Lonza).

In vitro cell treatment

Pemetrexed was purchased from Sigma, dihydrothymine (DHT) was purchased from Selleckchem and were dissolved in DMSO to final concentration of 100 mM and 40 mM respectively. Cisplatin was purchased from Santa Cruz Biotechnology and was dissolved in PBS to the final concentration of 80 mM. For in vitro treatment cells were plated in 96-well plates (MDA-MB-231 = 3000–4000 cells/well and T-47D = 6000 cells/well) and incubated overnight. For cytotoxicity death assay, 2000X Cytotox Green Reagent (Essen BioScience) was diluted in RPMI and

working dilutions of pemetrexed and cisplatin were prepared in Cytotox Green supplemented media. Working dilutions of DHT were prepared in RPMI (without Cytotox Green). After treatment, plate was loaded in Incycuyte Zoom and images were acquired in real-time for phase to quantify growth. Activity of Cytotox reagent was simultaneously acquired at the green channel to quantify death. Incycuyte Zoom software was used for the analysis and data export.

Patients and samples

Formalin-fixed paraffin embedded samples of a series of 120 consecutive breast carcinomas collected between 2010 and 2013 at the Azienda Ospedaliera Universitaria Città della Salute e della Scienza di Torino were analyzed. All cases were reviewed and anonymized using an alpha-numerical code. The main patients' characteristics are shown in Supplementary Table 2. The use of retrospective solid tumor tissues for the immunohistochemical study was approved by the Ethic Institutional Review Board responsible for "Biobanking and use of human tissues for experimental studies" - Department of Medical Sciences, University of Turin.

Immunohistochemistry staining and scoring

Three micrometer thick sections of formalin fixed paraffin embedded samples were stained for immunohistochemistry with the EPR4545 antibody (Abcam, 1:150 dilution). Immunohistochemistry was performed using an automated slide-processing platform (Ventana BenchMarck XT Autostainer). The antibody was optimized on FFPE cell block sections of MDA-MB-231 cells and on human tonsil tissue. Positive and negative controls were included for each immunohistochemical run. Immunoreactivity was assigned based on the proportion of positive tumor cells over total tumor cells (percent positivity) ranging from 0 to 100%. Staining intensity was evaluated as negative, faint, moderate, and intense. If the staining intensity was heterogeneous, then scoring was based on the greatest degree of intensity. Data were integrated in the *H*-score, calculated as follows: $H\text{-score} = \Sigma \text{Pi } (i + 1)$, where i represents the intensity of staining (0–3+), and Pi stands for the percentage of stained tumor cells (0–100%).

Statistical analysis

Statistical tests were performed with the GraphPad software v.7 comparing groups of different conditions with replicates. In all tests, the statistical significance was set at $p = 0.05$ (in the figures * indicates $p < 0.05$, ** $p < 0.01$, *** $p < 0.001$).

Results

TS expression correlates with aggressive form of BC

In order to study the association of TS expression with EMT markers in BC, we employed a VIM/CDH1 ratio to classify the BC cell lines belonging to the CCLE dataset ($n = 52$) into epithelial, mesenchymal or intermediate phenotypes (Fig. 1a and Supplementary Table 1. Comparing epithelial (VIM/CDH1 < 2) with mesenchymal cells (>2), a significantly higher expression of TYMS mRNA was found in the latter ($p < 0.005$, Fig. 1b). Then, in order to test TS gene expression in the spectrum of BC patients, we analyzed three independent GEO datasets, and found that TS expression was significantly different among the BC subtypes. Normal-like samples or the well-differentiated tumors (like luminal A) exhibited low TS expression, whereas high TS levels were found in basal-like BC (Fig. 1c). BC with a basal-like gene signature are primarily triple-negative (TN), and are frequently enriched for and EMT markers [22].

TS is a marker of more aggressive, chemoresistant, and EMT-driven BC

In order to test the clinical significance of the TS protein and its association with the aggressive phenotype in BC, immunohistochemistry (IHC) was performed on formalin-fixed paraffin-embedded samples from 120 BC patients. Patients' characteristics are shown in the Supplementary Table 2. TS staining was quantified by an IHC score and significantly higher expression was found in the TNBC, as compared to Luminal-A (Fig. 2a) and in high grade (G3) compared to low grade tumors (Fig. 2b, c). A moderate level of correlation was found between TS and Ki67 proliferation marker ($R_s = 0.48$, Supplementary Fig 1A). Analysis of the prognostic values using large patient datasets indicated TS expression as a marker for poor overall survival in BC (all subtypes, Fig. 2d). Of note, TS prognostically stratified luminal A and luminal B patients (Fig. 2e) as well as lower grade patients (Fig. 2f), while no association was not found in more aggressive BC (Supplementary Fig 1B).

Moreover, since TS is a common anti-cancer drug target, being required for DNA repair and directly inhibited by compounds like pyrimidine or folate analogues [23], we additionally tested if change in TS expression altered BC cells' sensitivity to the anti-folate drug pemetrexed and to cisplatin, in a similar fashion as previously observed in NSCLC [19] [24]. As a result, we found that MDA-MB-231 cells were sensitized to in vitro drug treatment after TS knockdown (Fig. 2g, h), whereas TS-low T-47D cells,

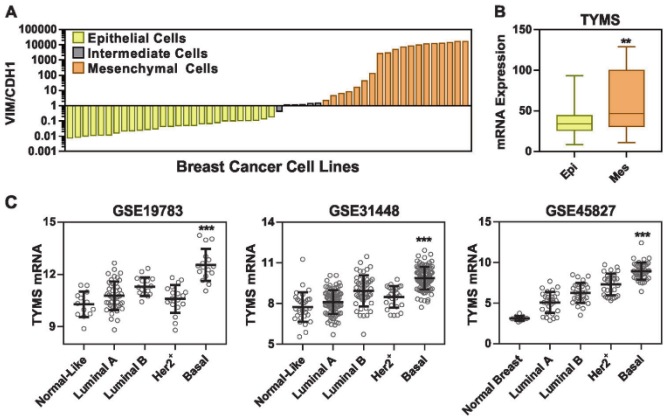


Fig. 1 TS expression correlates with aggressive form of BC. **a** Vimentin/E-cadherin (VIM/CDH1) ration in BC cell lines belonging to the CCLE database (gene expression). Cells were sorted in epithelial ($n = 27$), EMT-intermediate ($n = 6$) and mesenchymal ($n = 19$) phenotype. **b** Comparison of TS mRNA expression levels between epithelial and mesenchymal BC cell lines ($p = 0.0039$, two-tailed t-test). **c** TS mRNA levels in BC tissues divided according to molecular subtypes in indicated GEO datasets ($p < 0.0001$ in all datasets, compared between luminal A and basal subtypes, one-way ANOVA, Turkey's multiple comparison)

overexpressing ectopic TS, showed increased resistance (Fig. 2i, j).

TS is essential for the maintenance of a de-differentiated stem-like state in BC

The patient data prompted us to test whether TS plays direct role in maintaining the de-differentiated state of TNBC. Hence, we transduced the TNBC cell line MDA-MB-231 with lentiviruses containing non-overlapping shRNA sequences to knockdown TS (Fig. 3a). CD44/CD24 surface staining followed by FACS quantification indicated an increase in the population of differentiated $CD24^+$ cells, with a concomitant decrease in the $CD44^+CD24^-$ BC stem cell population (Fig. 3b). In order to carefully monitor the effects on cell growth, the confluency of infected cells was examined with real-time proliferation assays after TS depletion. The results showed a significant suppression of proliferation in cells infected with the shRNA that delivered a strong TS repression (shTS#2), while the sequence with a mild knockdown (shTS#1) did not alter the cells' growth (Fig. 3c). By contrast, a shRNA (shTS#3) sequence that induced a complete TS elimination in this cell line caused a massive growth arrest and death (Supplementary Fig. 2A, B), in line with the life-essential role of TS. To determine if the partially TS-deficient cells had reduced ability to migrate, we performed a real-time wound-healing assay where cell migration is corrected for proliferation outside the wound to account for changes in cell growth rate upon TS repression. The results showed a significant loss of migratory ability upon TS knockdown (Fig. 3d, e). Moreover, assayed for stemness-related functional phenotype, TS-deficient cells formed less mammospheres in low-adherent cultures (Fig. 3f, g). Comparable findings were obtained in other TNBC cell lines, such as Hs 578T (Fig. 3h–k) and BT-549 (Supplementary Fig. 3A–D), implying that TS could be a common EMT/CSCs regulator in TNBC.

Finally, to test the in vivo effects of TS suppression, MDA-MB-231-luc cells with TS knockdown or non-targeting control cells were injected in the tail-vein of nude mice. Interestingly, a significantly higher luciferase signal was recorded from shTS cells compared to control cells (Fig. 4a, b). Histological analysis confirmed the presence of single or multiple metastatic deposits of various size (ranging from <1 to 2 mm) and signs of lympho-vascular invasion only in mice injected with shTS cells (not shown). The increased ability of TS-deficient cells to form metastasis was independently confirmed by an in vitro real-time extravasation assay, which monitors how fast the cancer cells penetrate a monolayer of human umbilical vein endothelial cells (HUVEC) (Fig. 4c). In addition, to monitor the intravasation ability, a CAM assay on chicken embryos was performed (Fig. 4d), which confirmed an increased ability of TS-deficient cells, seeded on the upper CAM, to intravasate into the lower CAM (Fig. 4e). These observations clearly pointed at a strong impact of TS on BC differentiation and alteration of cells' behavior, which we aimed to further molecularly characterize.

TS knockdown induces loss of EMT and correlates with less aggressive BC

To further delineate the molecular pathways regulated via TS and involved in mediating the de-differentiation program in BC, we subjected shTS#1 MDA-MB-231 cells to

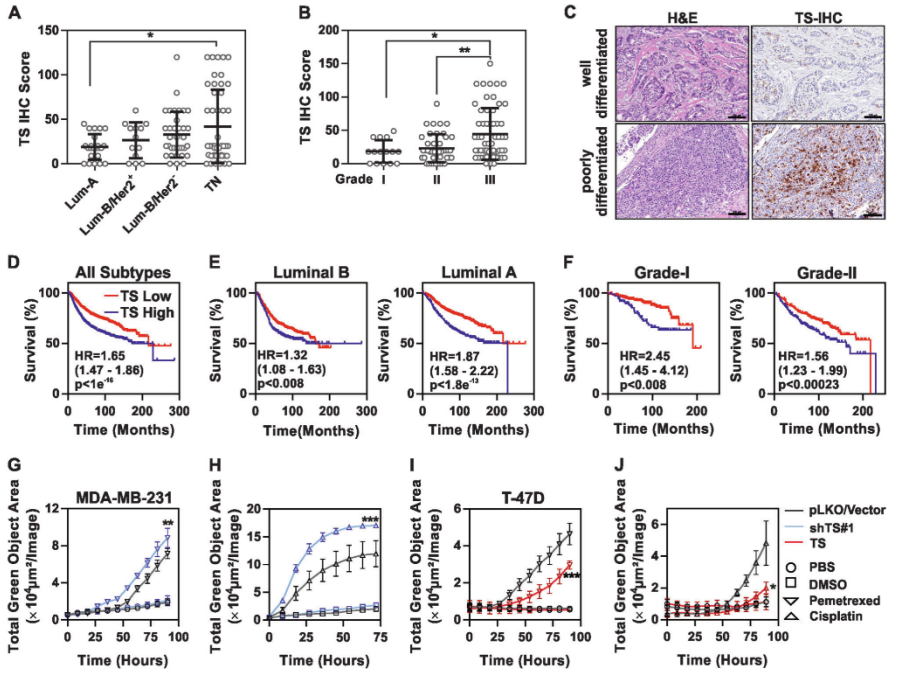


Fig. 2 TS is a marker of aggressive, chemoresistant and EMT-driven BC. **a** Immunohistochemical staining of TS in FFPE samples from BC patients ($n = 120$) segregated according to molecular subtype or **b** grade of differentiation ($p = 0.0237$ between luminal A and TNBC and 0.0119 between Grade I and III, one way ANOVA, Turkey's multiple comparison). Grade III are poorly differentiated cancers. **c** Representative images showing H&E and TS staining in well-differentiated and poorly-differentiated tumors (scale bars represent 100 µm). Kaplan–Meier curves showing the prognostic significance of TS expression in BC (all types) (**d**), in luminal (**e**), and in low grade patients (**f**). *P*-values are log-rank tests and HR is hazard ratio. MDA-MB-231 cells with shTS#1 knockdown, treated with (**g**) 1.5 mM pemetrexed and (**h**) 500 µM cisplatin ($p = 0.0019$ for pemetrexed and <0.0001 for cisplatin, between treatment of shTS#1 and pLKO, two way ANOVA, Turkey's multiple comparison). Death is recorded as green objects that represent the dying cells that incorporate Cytotoxic Green dye. T-47D cells overexpressing TS (TS, red) and empty vector (Vector, black) treated with 1.5 mM pemetrexed (**i**) and 50 µM cisplatin (**j**) in presence of Cytotoxic Green dye ($p = 0.0009$ for pemetrexed and 0.0341 for cisplatin, between treatment of empty vector and TS, two-way ANOVA, Turkey's multiple comparison). Experimental data are representative of at least two independent experiments with similar results. Points are avg ± SD

RNA-sequencing. These cells were selected because they had a discernable change in the $CD24^+$ population but no major proliferation defect, so to analyze proliferation-independent effects. By setting a stringent cutoff value of 2-fold to identify DEGs compared to non-targeting infected cells (pLKO), we found 73 and 84 genes down and up-regulated, respectively (Supplementary Table 3). Pathway analysis (GSEA) revealed that EMT was the most significantly deregulated pathway, followed by TNF-α/NFκ-β signaling (Fig. 5a), known to be functionally connected with EMT in BC [25]. RNA-seq data were validated by qPCR (Fig. 5b, Supplementary Fig. 4A) and were used to explore the prognostic significance of the gene signature associated with TS-knockdown. A system biology approach was adopted to investigate different BC gene expression datasets, dividing the patients by low or high KD score (corresponding to high or low TS, respectively). As a further confirmation of a strong association with EMT, a previously established signature of genes up-regulated during EMT [26] was found significantly enriched in patients with a low TS KD score (Fig. 5c). Moreover, a gene set predicting poor prognosis was found enriched in patients with low KD score (Fig. 5d), and similar associations with the grade of differentiation were found using both the TS KD

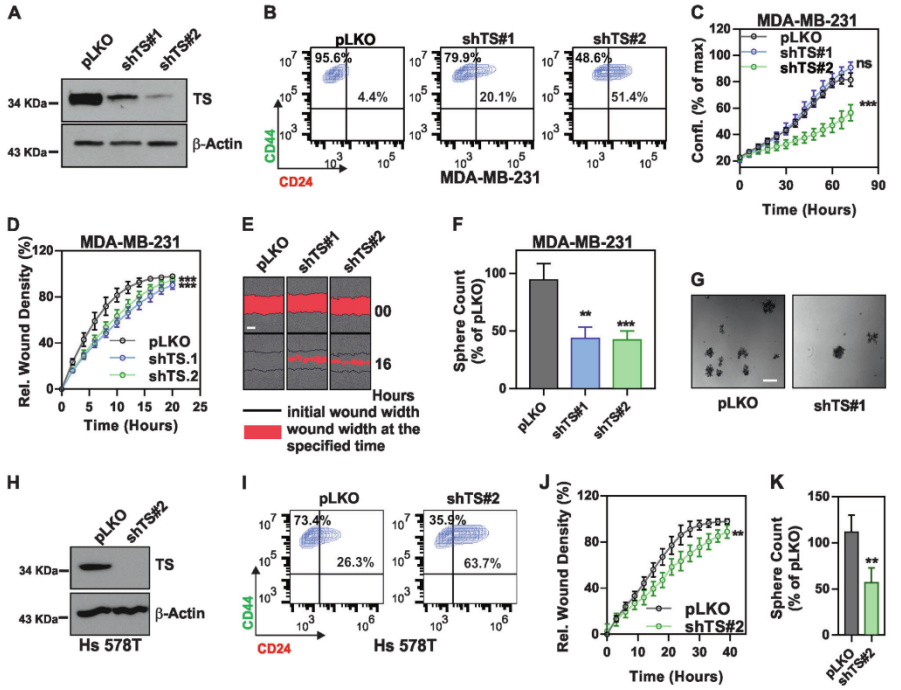


Fig. 3 TS knockdown suppresses the mesenchymal phenotype of TNBCs. **a** Efficiency of TS knockdown in MDA-MB-231 obtained with shRNA lentiviral particles. pLKO is non-targeting control. **b** FACS plots of MDA-MB-231 cells as in **a** stained with CD44-FITC and CD24-PE. Gates are based on unstained control cells. **c** Real-time measurement of growth (confluency) in MDA-MB-231 with shTS or control cell (p = ns for shTS#1 and <0.0001 for shTS#2, as compared to pLKO, two-way ANOVA, Dunett's multiple comparison). **d** Real-time migration assay in MDA-MB-231 cells with TS knockdown (p < 0.001 for shTS#1 and shTS#2, as compared to pLKO, two-way ANOVA, Dunett's multiple comparison) and **e** representative pictures showing wound width at different time points (scale bar represents 300 µm). **f** Relative counts of spheres (p = 0.0012 for shTS#1 and 0.0001 for shTS#2 as compared to pLKO, one way ANOVA, Dunett's multiple comparison) and **g** representative pictures of spheres formed by TS knockdown cells (scale bar represents 400 µm). **h** Efficiency of TS knockdown in Hs 578T obtained with shRNA lentiviral particles. **i** FACS plot of shTS and pLKO cells showing the expression of cell surface CD24/CD44. **j** Effect of TS knockdown on migration of Hs 578T cells (p = 0.0016, two-way ANOVA, Sidak's multiple comparison). **k** Relative counts of spheres in Hs 578T TS knockdown cells as compared to pLKO (p = 0.0011, unpaired Student's t-test). Experimental data are representative of at least two independent experiments with similar results. Points are avg ± SD

score and TS expression to segregate the patients (Supplementary Fig. 4B, C). Survival analysis showed a strong prognostic impact of the TS-knockdown signature, indicating a poorer prognosis for the patients with a lower score or higher TS in all subtypes (Fig. 5e), and a trend for a significant impact in TNBC (Fig. 5f). The KD score was also significantly correlated with all the major histopathological variables in BC, including histology, grade of differentiation and size of the tumors (Fig. 5g–j). All these data together indicate that TS promotes EMT-driven aggressive BCs.

TS enzymatic activity and thymidine catabolism are essential for maintaining BC de-differentiation

We then aimed at determining the impact of TS enzymatic activity on de-differentiation. TS is the only de novo source of thymidylate (dTMP), which is either further phosphorylated to maintain the dNTP pools for DNA synthesis, or directed to degradation via sequential phosphorolytic cleavages. MDA-MB-231 shTS#1 cells where subjected to dNTP quantification, but, consistently with the previously observed normal growth, no significant change in dTTP or

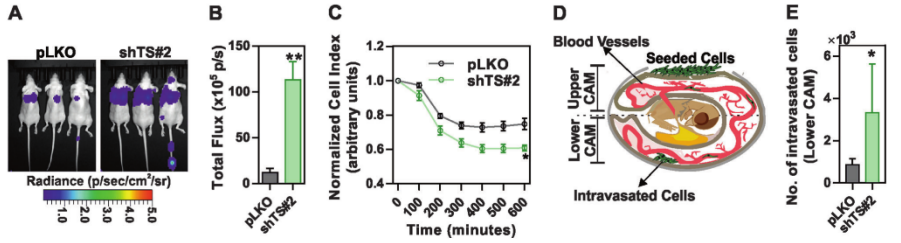


Fig. 4 Ablation of TS expression alters the invasive ability of TNBC cells. **a** Representative images of lung metastasis formation assay performed by injecting luciferase-expressing MDA-MB-231 cells in the tail-vein of nude mice ($n = 3$/group). **b** Quantification of the bioluminescence signal from the lung metastases ($p = 0.0078$, unpaired two tailed *t*-test). **c** Relative ability of TS knockdown or control cells to penetrate through a HUVEC monolayer in an in vitro extravasation assay ($p = 0.00065$ unpaired multiple *t*-test). **d** Sketch diagram representing the chorioallantoic membrane (CAM) assay and **e** quantification of control and MDA-MB-231 shTS#2 intravasation in lower CAM, 2 days after seeding in the upper CAM ($p = 0.0012$, multiple *t*-test). Experimental data are representative from at least two independent experiments with similar results. Points are avg ± SD

other dNTPs was detected (Fig. 6a). This suggested that the differentiation observed in shTS cells was not caused by dNTP imbalance, as shown in other CSC models upon knockdown of specific NM-related enzymes [13], and that while a baseline TS level is required for the cells to grow, increased TS activity could be partly involved in other cellular functions. To functionally investigate the role of TS enzymatic activity, we reconstituted shTS#1 cells with either a wild type (TS^{WT}) expressing silent mutation in shRNA binding region or an enzymatically inactive (TS^{R50C}) form of TS [27]. Western blotting confirmed the successful transduction (Fig. 6b) and TS enzymatic activity assay confirmed the loss of catalytic activity in the TS^{R50C} overexpressing cells (Fig. 6c). Strikingly, MDA-MB-231 cells overexpressing the TS^{WT} enzyme increased proliferation (Fig. 6d), reduced the population of differentiated $CD24^{-}$ cells (Fig. 6e), formed more mammospheres (Fig. 6f) and were significantly more migratory (Fig. 6g) compared to TS^{R50C} cells overexpressing the catalytically inactive TS.

These results clearly indicated that the TS enzymatic activity is essential for the maintenance of the EMT/CSCs phenotype. We therefore hypothesized that TS mediates de-differentiation via the nucleotide catabolism (Fig. 7a), rather than through the pathway leading to DNA synthesis. This was supported by the results of a recent shRNA screen on human immortalized breast cells, which revealed that pyrimidine catabolism mediated by dihydropyrimidine dehydrogenase (DPYD) was responsible for the EMT phenotype [28]. We therefore speculated existence of a TS-DPYD axis controlling EMT/CSCs in BC cells. Although DPYD mRNA expression did not show a significant prognostic role in BC patients (Supplementary Fig. 5A, B), analysis of expression data from the CCLE showed a marked increase in mesenchymal-like BC cells not only for DPYD, but also for the NT5E (CD73), which is one of the upstream 5′-nucleotidase responsible for catalyzing the first step of dTMP degradation (Fig. 7b). In order to functionally prove our hypothesis, we knocked down DPYD (Fig. 7c) and observed a significant increase in the population of $CD24^{+}$ cells (Fig. 7d) and a loss of migratory ability (Fig. 7e), in line with what we observed in TS-deficient cells. However, the $CD24^{+}$ enriching effect of DPYD knockdown could not be reverted by overexpressing TS (Fig. 7f), suggesting that TS enzymatic control of de-differentiation requires a DPYD-dependent pyrimidine catabolism. To further confirm it, we tested if the supplementation of DPYD enzymatic product DHT in medium could rescue the differentiation phenotype observed in TS knockdown cells. As a result, DHT supplementation significantly increased the counts of sphere (Fig. 7g) and reduced the $CD24^{+}$ population (Fig. 7h) in TS knockdown cells, having no effect on the cell proliferation (Supplementary Fig. 5C). In summary, our data indicate that TS enzymatic activity and pyrimidine catabolism are essential for the maintenance of the BCSC phenotype. We therefore propose a model in which dTMP produced by TS-overexpressing cancer cells is not only metabolized to support the uncontrolled proliferation, but can also partially sustain de-differentiation and EMT via DPYD-based pyrimidines degradation (Fig. 8).

Discussion

The aggressiveness and the de-differentiated phenotype of neoplastic cells have been strongly connected with alterations in specific metabolic pathways, especially those involved in the transformation of glucose [29–31], while the contribution of other pathways is still majorly unexplored.

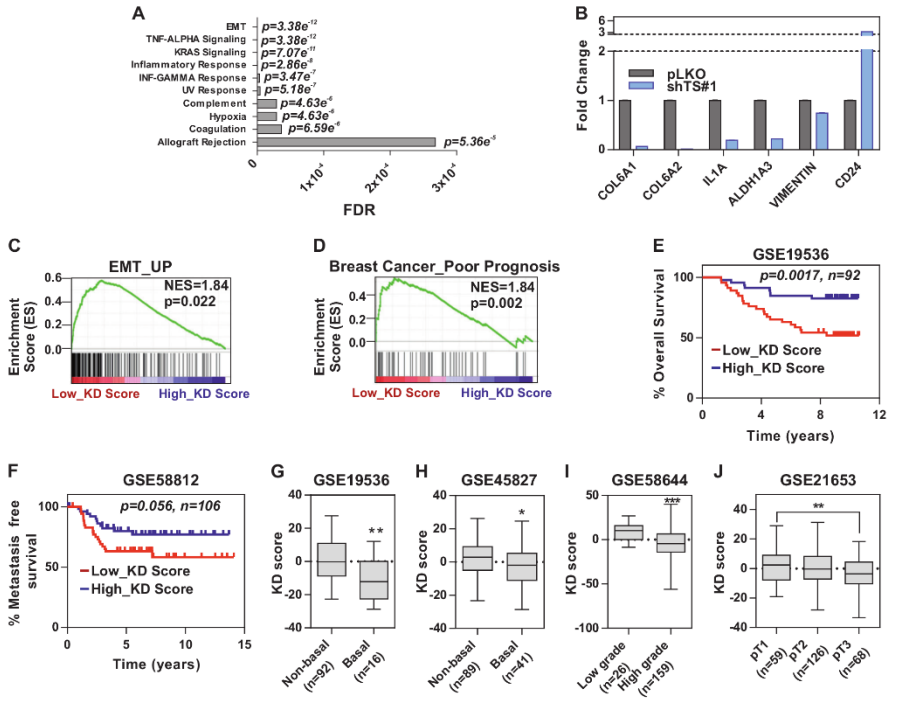


Fig. 5 TS knockdown suppresses EMT and the associated gene signature correlates with less aggressive BC. **a** Gene set enrichment (GSEA) analysis showing the most differentially regulated pathways in MDA-MB-231 with TS knockdown (RNAseq data). **b** qPCR validation of RNA-seq results in MDA-MB-231 shTS#1. Bars are avg ± SEM. GSEA of TS low and high TS KD score (derived from RNA-seq) with previously published (**c**) EMT and **d** BC poor prognosis gene signatures, representing NSE (Normalized Enrichment Score) and *p*-value. Kaplan-Meier curves of **e** overall survival and **f** metastasis-free survival in cancer patients stratified by TS KD score. *P*-values are log-rank tests. TS KD scores in BC patients divided by **g**–**h** molecular subtype ($p = 0.0022$ for GSE19536 and 0.0333 for GSE45827, unpaired two tailed *t*-test), **i** grade of differentiation ($p < 0.0001$, unpaired two tailed *t*-test), and **j** TNM tumor size ($p = 0.0091$, one-way ANOVA, Turkey's multiple comparison). Experimental data are representative from at least two independent experiments with similar results

Elevation in NM is typically associated with the tumor cells' increased demand for DNA precursors to sustain the uncontrolled proliferation [11]. However, a few studies have shown that some NM enzymes are functionally involved in de-differentiation processes, like the ecto-nucleotidase ENPP1 in the maintenance of the CSCs-like state in glioblastoma [13]. Similarly, treatment with non-toxic doses of TS-inhibiting drugs was found sufficient to induce a differentiation in multiple myeloma CSCs and sensitize the cells for radiotherapy [14]. These observations, together with the first demonstration of a connection between TS and EMT [17], prompted us to investigate the EMT-driven TNBC model [3, 22]. Functional experiments clearly indicates that loss of TS altered the de-differentiated phenotype of TNBCs, reducing $CD44^{+}CD24^{-}$ cells, and suppressing migratory and sphere-forming ability. Consistently, this was accompanied by a robust suppression of EMT-associated genes, as evaluated by RNA-seq analysis. In vivo, two independent animal models, confirmed by an in vitro extravasation assay, revealed an augmented propensity for intravasation and metastasis formation in cells with TS knockdown. These findings are in line with previous reports in which EMT-suppressing conditions enhanced the metastatic colonization capacity of

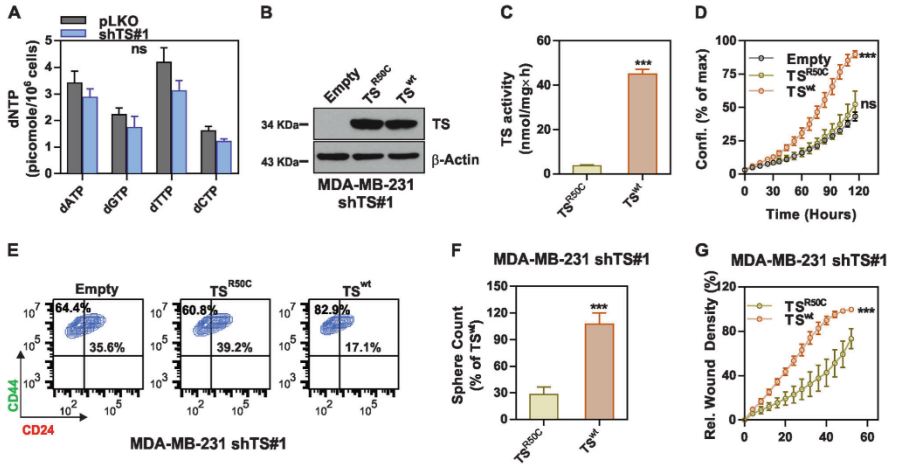


Fig. 6 TS enzymatic activity is essential for maintenance of BC de-differentiation. **a** Quantification of deoxyribonucleotide triphosphate (dNTPs) in MDA-MB-231 cells with TS knockdown and control cells. **b** Reconstitution of enzymatically inactive (TS^{R50C}) or wild-type (TS^{wt}) TS in MDA-MB-231 shTS#1 cells. **c** Measurement of TS enzymatic activity in MDA-MB-231 shTS#1 cells expressing TS^{R50C} or TS^{wt} ($p < 0.0001$, unpaired two tailed *t*-test) (**d**) Proliferation ($p = 0.0001$, two-way ANOVA, Dunnett multiple comparison), **e** CD44/CD24 FACS profile, **f** sphere-forming ability ($p < 0.0001$, unpaired two tailed *t*-test), and **g** migration capacity ($p < 0.0001$, two-way ANOVA, Turkey's multiple comparison) of cells that express either TS^{R50C} or TS^{wt}. Experimental data are representative from at least two independent experiments with similar results. Points are avg ± SD

mesenchymal-like BC cell lines [32, 33], and a plausible explanation comes from recent studies, which found that the tumor-initiating and metastatic potential is maximum when breast and other cancer cells are in an intermediate EMT (hybrid) state [34–38], leading to a partial revision of the initial model of EMT in cancer metastasis [35, 39, 40]. Our in vivo data therefore reflect the complicated nature of EMT, which may also vary in a context-dependent fashion [39, 41]. Targeting TS in other cells, in fact, exerted a clear anti-metastatic effect [42]. Nevertheless, both the immunohistochemical quantification of TS protein levels and the TS knockdown scores derived from the RNA-seq data were strongly associated with BC de-differentiation and prognosis, indicating a pivotal role of TS in the malignancy of BC. Interestingly, only a moderate co-expression between TS and the proliferation marker Ki67 was found, in line with previous data from other cancers [43, 44], supporting our model that TS activity could be implicated in other cellular functions independent of proliferation. We found, in fact, that the EMT/CSC suppression imposed by a level of TS knockdown, which did not perturb cells' proliferation and dNTP balance was rescued by overexpressing wild-type TS, but not by a catalytically inactive mutant. This was particularly important because it ruled out the possible contribution of non-enzymatic activities of TS [45], directly pointing at the enzymatic activity as the EMT/CSC driving force. Since dihydropyrimidine accumulation was previously shown to control EMT in BC [28], we tested and demonstrated the hypothesis that high TS enzymatic activity in cancer cells sustains de-differentiation and EMT via a DPYD-dependent pyrimidine catabolism. Several follow-up studies are needed, for instance, to (1) test by IHC the significance of DPYD in BC, and to identify the mechanisms by which DHT controls EMT/CSC, to understand if the underlying pathways could represent novel valuable therapeutic targets; (2) address the impact of other dTMP-transforming enzymes (like NT5E/CD73) and salvage pathways on EMT; (3) identify the regulatory pathways upstream of the TS-DPYD axis; (4) test a similar function for TS in other malignancies; (5) decipher the contribution of TS dysregulation to cancer-relevant pathways other than EMT (like inflammation). In any case, our data assert that the classical role of TS as a mere proliferation marker needs to be revisited. For instance, the previously identified oncogenic and tumor-initiating role of TS [27, 46] could be explained with the direct/indirect control of de-differentiation and stemness. The present data add the control of de-differentiation to the list of functions of TS

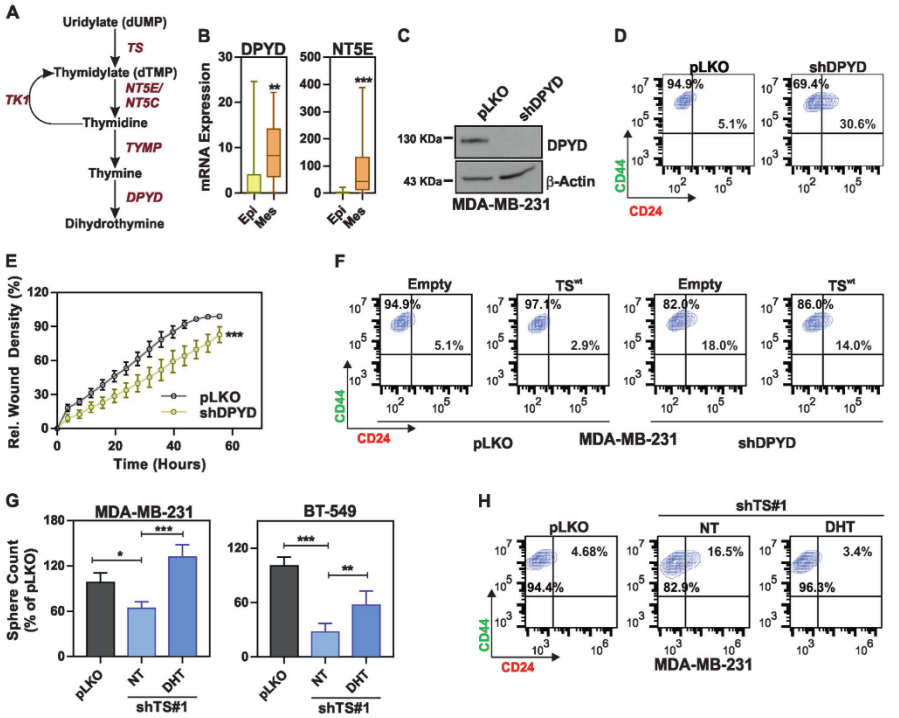


Fig. 7 TS regulates de-differentiated tumor phenotype via DPYD-mediated thymidine catabolism. **a** Scheme of the thymidylate catabolic pathway. **b** DPYD ($p = 0.0031$) and NT5E ($p = 0.0001$) mRNA expression levels in epithelial and mesenchymal BC cell lines (CCLE dataset). The statistical tests are unpaired two tailed *t*-test. **c** Western blot quantification of DPYD knockdown in MDA-MB-231, and the effects on (**d**) CD44/CD24 profile and **e** migratory ability ($p < 0.0001$, two-way ANOVA, Sidak's multiple comparison). **f** FACS plots of MDA-MB-231 cells with DPYD knockdown overexpressing TS or an empty vector and stained with CD44/CD24. **g** Sphere counts for shTS#1 cells in MDA-MB-231 ($p < 0.0394$ between pLKO and NT, $p < 0.0001$ between NT and DHT) and BT-549 ($p < 0.0001$ between pLKO and NT, $p = 0.0023$ between NT and DHT, one-way ANOVA, Turkey's multiple comparison) after treatment with 1 μM dihydrothymine (DHT). NT (DMSO) is the non-treated control. **h** CD24/44 profile showing the effect of 10 μM DHT on $CD24^+$ population in MDA-MB-231 cells with TS knock-down. Points are avg ± S

(together with proliferation and DNA repair) that can affect the prognosis of BC patients. More efforts will need to be dedicated to clarify how the cancer cells balance proliferation and differentiation, and to what exact extent other nucleotide metabolic genes are implicated in these processes.

TS is a well-established target of chemotherapy, being inhibited by drugs like 5-fluorouracil (5-FU) or by folate analogues [23], and its overexpression in tumors represents a major mechanism of chemo-resistance. From the translational point of view, our finding that TS levels can be significantly different among BC subtypes contradicts earlier works [47] and may be useful to improve the treatment strategies. In our study, TS was found higher in the aggressive BC and in high-grade tumors, in line with previous observations in other cancers [43, 44, 48], and this information could be clinically important for predicting the efficacy of anti-TS drugs. The present study, as well as other pivotal works [49], can therefore anticipate subtype-specific susceptibilities to anti-TS drugs in BC. However, these results also highlight the clinical importance of carefully assessing the potential impact of TS-inhibition on metastasis formation and, therefore, further in vivo work and retrospective studies are warranted.

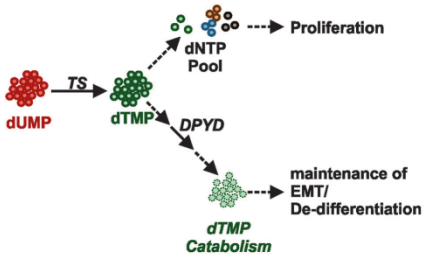


Fig. 8 Schematic representation of TS mediated BC de-differentiation. Excessive thymidylate is fluxed in the catabolic pathway for degradation mediated by DPYD. DPYD catalyzed DHT maintains the de-differentiation in BC

Acknowledgements Work supported by the Interdisciplinary Center for Clinical Research of the University of Erlangen-Nürnberg (PC), NIH GM104198 and AI136581 (BK), NMRC/BNIG/2041/2015 (SAK), Fondazione Umberto Veronesi (LA), MIUR 2015HAJH8E (CM), European Commission FP7 Marie Curie Career Integration Grant PCIG14-GA-2013–631149, National Institutes of Health Grant P20GM109091 (ÖŞ), and Susan G. Komen Interdisciplinary Graduate Training to Eliminate Cancer Disparities Scholarship GTDR17500160 (OzgeS). This work was partially presented at the 2018 European Association for Cancer Research conference. This paper is dedicated to the memory of our colleague Dr. Francesca Boella.

Compliance with ethical standards

Conflict of interest The authors declare that they have no conflict of interest.

Publisher's note: Springer Nature remains neutral with regard to jurisdictional claims in published maps and institutional affiliations.

Open Access This article is licensed under a Creative Commons Attribution 4.0 International License, which permits use, sharing, adaptation, distribution and reproduction in any medium or format, as long as you give appropriate credit to the original author(s) and the source, provide a link to the Creative Commons license, and indicate if changes were made. The images or other third party material in this article are included in the article's Creative Commons license, unless indicated otherwise in a credit line to the material. If material is not included in the article's Creative Commons license and your intended use is not permitted by statutory regulation or exceeds the permitted use, you will need to obtain permission directly from the copyright holder. To view a copy of this license, visit http://creativecommons.org/licenses/by/4.0/.

References

1. Jogi A, Vaapil M, Johansson M, Pahlman S. Cancer cell differentiation heterogeneity and aggressive behavior in solid tumors. Ups J Med Sci. 2012;117:217–24.
2. Pece S, Tosoni D, Confalonieri S, Mazzarol G, Vecchi M, Ronzoni S, et al. Biological and molecular heterogeneity of breast cancers correlates with their cancer stem cell content. Cell. 2010;140:62–73.
3. Mani SA, Guo W, Liao MJ, Eaton EN, Ayyanan A, Zhou AY, et al. The epithelial-mesenchymal transition generates cells with properties of stem cells. Cell. 2008;133:704–15.
4. Magee JA, Piskounova E, Morrison SJ. Cancer stem cells: impact, heterogeneity, and uncertainty. Cancer Cell. 2012;21:283–96.
5. Shibue T, Weinberg RA. EMT, CSCs, and drug resistance: the mechanistic link and clinical implications. Nat Rev Clin Oncol. 2017;14:611–29
6. Barbachano A, Ordonez-Moran P, Garcia JM, Sanchez A, Pereira F, Larriba MJ, et al. SPROUTY-2 and E-cadherin regulate reciprocally and dictate colon cancer cell tumourigenicity. Oncogene. 2010;29:4800–13.
7. Ceppi P, Mudduluru G, Kumarswamy R, Rapa I, Scagliotti GV, Papotti M, et al. Loss of miR-200c expression induces an aggressive, invasive, and chemoresistant phenotype in non-small cell lung cancer. Mol Cancer Res. 2010;8:1207–216.
8. Jiang F, Qiu Q, Khanna A, Todd NW, Deepak J, Xing L, et al. Aldehyde dehydrogenase 1 is a tumor stem cell-associated marker in lung cancer. Mol Cancer Res. 2009;7:330–38.
9. McKeithen D, Graham T, Chung LW, Odero-Marah V. Snail transcription factor regulates neuroendocrine differentiation in LNCaP prostate cancer cells. Prostate. 2010;70:982–92.
10. Shi Y, Wu H, Zhang M, Ding L, Meng F, Fan X. Expression of the epithelial-mesenchymal transition-related proteins and their clinical significance in lung adenocarcinoma. Diagn Pathol. 2013; 89–97
11. Lane AN, Fan TW. Regulation of mammalian nucleotide metabolism and biosynthesis. Nucleic Acids Res. 2015;43:2466–85.
12. Tong X, Zhao F, Thompson CB. The molecular determinants of de novo nucleotide biosynthesis in cancer cells. Curr Opin Genet Dev. 2009;19:32–7.
13. Bageritz J, Puccio L, Piro RM, Hovestadt V, Phillips E, Pankert T, et al. Stem cell characteristics in glioblastoma are maintained by the ecto-nucleotidase E-NPP1. Cell Death Differ. 2014;21: 929–40.
14. Morgenroth A, Vogg AT, Zlatopolskiy BD, Siluschek M, Oedekoven C, Mottaghy FM. Breaking the invulnerability of cancer stem cells: two-step strategy to kill the stem-like cell subpopulation of multiple myeloma. Mol Cancer Ther. 2014;13:144–53.
15. Costi MP, Ferrari S, Venturelli A, Calo S, Tondi D, Barlocco D. Thymidylate synthase structure, function and implication in drug discovery. Curr Med Chem. 2005;12:2241–258.
16. Wilson A, Laurenti E, Oser G, van der Wath RC, Blanco-Bose W, Jaworski M, et al. Hematopoietic stem cells reversibly switch from dormancy to self-renewal during homeostasis and repair. Cell. 2008;135:1118–29.
17. Siddiqui A, Vazakidou ME, Schwab A, Napoli F, Fernandez-Molina C, Rapa I, et al. Thymidylate synthase is functionally associated with ZEB1 and contributes to the epithelial-to-mesenchymal transition of cancer cells. J Pathol. 2017;242: 221–33.
18. Rahim S, Uren A. A real-time electrical impedance based technique to measure invasion of endothelial cell monolayer by cancer cells. J Vis Exp. 2011;50:e2792–796.
19. Rasheed SA, Efferth T, Asangani IA, Allgayer H. First evidence that the antimalarial drug artesunate inhibits invasion and in vivo metastasis in lung cancer by targeting essential extracellular proteases. Int J Cancer. 2010;127:1475–85.
20. Diamond TL, Roshal M, Jamburuthugoda VK, Reynolds HM, Merriam AR, Lee KY, et al. Macrophage tropism of HIV-1 depends on efficient cellular dNTP utilization by reverse transcriptase. J Biol Chem. 2004;279:51545–53.
21. Pluim D, Schilders KA, Jacobs BA, Vaartjes D, Beijnen JH, Schellens JH. Pharmacodynamic assay of thymidylate synthase activity in peripheral blood mononuclear cells. Anal Bioanal Chem. 2013;405:2495–503.

22. Taube JH, Herschkowitz JI, Komurov K, Zhou AY, Gupta S, Yang J, et al. Core epithelial-to-mesenchymal transition interactome gene-expression signature is associated with claudin-low and metaplastic breast cancer subtypes. Proc Natl Acad Sci USA. 2010;107:15449–54.
23. Wilson PM, Danenberg PV, Johnston PG, Lenz HJ, Ladner RD. Standing the test of time: targeting thymidylate biosynthesis in cancer therapy. Nat Rev Clin Oncol. 2014;11:282–98.
24. Takezawa K, Okamoto I, Okamoto W, Takeda M, Sakai K, Tsukioka S, et al. Thymidylate synthase as a determinant of pemetrexed sensitivity in non-small cell lung cancer. Br J Cancer. 2011;104:1594–601.
25. Li CW, Xia W, Huo L, Lim SO, Wu Y, Hsu JL, et al. Epithelial-mesenchymal transition induced by TNF-alpha requires NF-kappaB-mediated transcriptional upregulation of Twist1. Cancer Res. 2012;72:1290–300.
26. Sarrio D, Rodriguez-Pinilla SM, Hardisson D, Cano A, Moreno-Bueno G, Palacios J. Epithelial-mesenchymal transition in breast cancer relates to the basal-like phenotype. Cancer Res. 2008;68:989–97.
27. Rahman L, Voeller D, Rahman M, Lipkowitz S, Allegra C, Barrett JC, et al. Thymidylate synthase as an oncogene: a novel role for an essential DNA synthesis enzyme. Cancer Cell. 2004;5:341–51.
28. Shaul YD, Freinkman E, Comb WC, Cantor JR, Tam WL, Thiru P, et al. Dihydropyrimidine accumulation is required for the epithelial-mesenchymal transition. Cell. 2014;158:1094–109.
29. Morita M, Sato T, Nomura M, Sakamoto Y, Inoue Y, Tanaka R, et al. PKM1 confers metabolic advantages and promotes cell-autonomous tumor cell growth. Cancer Cell. 2018;33:355–67 e7.
30. Schwab A, Siddiqui A, Vazakidou ME, Napoli F, Bottcher M, Menchicchi B, et al. Polyol pathway links glucose metabolism to the aggressiveness of cancer cells. Cancer Res. 2018; 78:1604–18.
31. Sciacovelli M, Goncalves E, Johnson TI, Zecchini VR, da Costa AS, Gaude E, et al. Fumarate is an epigenetic modifier that elicits epithelial-to-mesenchymal transition. Nature. 2016;537:544–7.
32. Korpal M, Ell BJ, Buffa FM, Ibrahim T, Blanco MA, Celià-Terrassa T, et al. Direct targeting of Sec23a by miR-200s influences cancer cell secretome and promotes metastatic colonization. Nat Med. 2011;17:1101–8.
33. Le MTN, Hamar P, Guo C, Basar E, Perdigão-Henriques R, Balaj L, et al. miR-200–containing extracellular vesicles promote breast cancer cell metastasis. J Clin Invest. 2014;124:5109–28.
34. Bae YK, Choi JE, Kang SH, Lee SJ. epithelial-mesenchymal transition phenotype is associated with clinicopathological factors that indicate aggressive biological behavior and poor clinical outcomes in invasive breast cancer. J Breast Cancer. 2015;18:256–63.
35. Grosse-Wilde A, Fouquier d'Herouel A, McIntosh E, Ertaylan G, Skupin A, Kuestner RE, et al. Stemness of the hybrid epithelial/mesenchymal state in breast cancer and its association with poor survival. PLoS ONE. 2015;10:e0126522.
36. Jolly MK, Huang B, Lu M, Mani SA, Levine H, Ben-Jacob E. Towards elucidating the connection between epithelial-mesenchymal transitions and stemness. J R Soc Interface. 2014;11:20140962.
37. Pastushenko I, Brisebarre A, Sifrim A, Fioramonti M, Revenco T, Boumahdi S, et al. Identification of the tumour transition states occurring during EMT. Nature. 2018;556:463–8.
38. Yu M, Bardia A, Wittner BS, Stott SL, Smas ME, Ting DT, et al. Circulating breast tumor cells exhibit dynamic changes in epithelial and mesenchymal composition. Science. 2013;339:580–4.
39. Jolly MK, Ware KE, Gilja S, Somarelli JA, Levine H. EMT and MET: necessary or permissive for metastasis? Mol Oncol. 2017;11:755–69.
40. Lambert AW, Pattabiraman DR, Weinberg RA. Emerging biological principles of metastasis. Cell . 2017;168:670–91.
41. Celia-Terrassa T, Meca-Cortes O, Mateo F, Martinez de Paz A, Rubio N, Arnal-Estape A, et al. Epithelial-mesenchymal transition can suppress major attributes of human epithelial tumor-initiating cells. J Clin Invest. 2012;122:1849–68.
42. Kang M, Zheng W, Chen Q, Qin W, Li P, Huang S, et al. Thymidylate synthase prompts metastatic progression through the dTMP associated EMT process in pancreatic ductal adenocarcinoma. Cancer Lett. 2018;419:40–52.
43. Ceppi P, Volante M, Ferrero A, Righi L, Rapa I, Rosas R, et al. Thymidylate synthase expression in gastroenteropancreatic and pulmonary neuroendocrine tumors. Clin Cancer Res. 2008;14:1059–64.
44. Monica V, Scagliotti GV, Ceppi P, Righi L, Cambieri A, Lo Iacono M, et al. Differential thymidylate synthase expression in different variants of large-cell carcinoma of the lung. Clin Cancer Res. 2009;15:7547–52.
45. Liu J, Schmitz JC, Lin X, Tai N, Yan W, Farrell M, et al. Thymidylate synthase as a translational regulator of cellular gene expression. Biochim Biophys Acta. 2002;1587:174–82.
46. Bertino JR, Banerjee D. Thymidylate synthase as an oncogene? Cancer Cell. 2004;5:301–02.
47. Pestalozzi BC, Peterson HF, Gelber RD, Goldhirsch A, Gusterson BA, Trihia H, et al. Prognostic importance of thymidylate synthase expression in early breast cancer. J Clin Oncol. 1997;15:1923–31.
48. Ceppi P, Volante M, Saviozzi S, Rapa I, Novello S, Cambieri A, et al. Squamous cell carcinoma of the lung compared with other histotypes shows higher messenger RNA and protein levels for thymidylate synthase. Cancer . 2006;107:1589–96.
49. Lee SJ, Choi YL, Park YH, Kim ST, Cho EY, Ahn JS, et al. Thymidylate synthase and thymidine phosphorylase as predictive markers of capecitabine monotherapy in patients with anthracycline- and taxane-pretreated metastatic breast cancer. Cancer Chemother Pharmacol. 2011;68:743–51.

Research Paper

The miR-644a/CTBP1/p53 axis suppresses drug resistance by simultaneous inhibition of cell survival and epithelial-mesenchymal transition in breast cancer

Umar Raza[1], Özge Saatci[1], Stefan Uhlmann[2], Suhail A Ansari[1], Erol Eyüpoğlu[1], Emre Yurdusev[1], Merve Mutlu[1], Pelin Gülizar Ersan[1], Mustafa Kadri Altundağ[3], Jitao David Zhang[4], Hayriye Tatlı Doğan[5], Gülnur Güler[5], Özgür Şahin[1]

[1]Department of Molecular Biology and Genetics, Faculty of Science, Bilkent University, 06800 Ankara, Turkey

[2]Friedrich Miescher Institute for Biomedical Research, Maulbeerstrasse 66, 4058 Basel, Switzerland

[3]Department of Medical Oncology, Hacettepe University Cancer Institute, 06410 Ankara, Turkey

[4]Bäumlihofstrasse 429, 4125 Riehen, Switzerland

[5]Department of Pathology, Hacettepe University, 06410 Ankara, Turkey

Correspondence to: Özgür Şahin, **email:** sahinozgur@gmail.com

Keywords: *miRNAs, CTBP1, p53, EMT, therapy resistance*

Received: *January 04, 2016* ***Accepted:*** *June 26, 2016* ***Published:*** *July 08, 2016*

ABSTRACT

Tumor cells develop drug resistance which leads to recurrence and distant metastasis. MicroRNAs are key regulators of tumor pathogenesis; however, little is known whether they can sensitize cells and block metastasis simultaneously. Here, we report miR-644a as a novel inhibitor of both cell survival and EMT whereby acting as pleiotropic therapy-sensitizer in breast cancer. We showed that both miR-644a expression and its gene signature are associated with tumor progression and distant metastasis-free survival. Mechanistically, miR-644a directly targets the transcriptional co-repressor C-Terminal Binding Protein 1 (CTBP1) whose knock-outs by the CRISPR-Cas9 system inhibit tumor growth, metastasis, and drug resistance, mimicking the phenotypes induced by miR-644a. Furthermore, downregulation of CTBP1 by miR-644a upregulates wild type- or mutant-p53 which acts as a 'molecular switch' between G1-arrest and apoptosis by inducing cyclin-dependent kinase inhibitor 1 (p21, CDKN1A, CIP1) or pro-apoptotic phorbol-12-myristate-13-acetate-induced protein 1 (Noxa, PMAIP1), respectively. Interestingly, an increase in mutant-p53 by either overexpression of miR-644a or downregulation of CTBP1 was enough to shift this balance in favor of apoptosis through upregulation of Noxa. Notably, p53-mutant patients, but not p53-wild type ones, with high CTBP1 have a shorter survival suggesting that CTBP1 could be a potential prognostic factor for breast cancer patients with p53 mutations. Overall, re-activation of the miR-644a/CTBP1/p53 axis may represent a new strategy for overcoming both therapy resistance and metastasis.

INTRODUCTION

Breast cancer is the most common malignancy and the second leading cause of cancer deaths among women [1]. Depending on breast cancer subtype [2], patients are treated with chemotherapy and/or targeted agents; however, intrinsic or acquired resistance is inevitable in almost all cases. As tumor cells develop *de novo* or acquired drug resistance, residing cancer cells undergo epithelial mesenchymal transition (EMT), evade from primary tumor site and metastasize to distant organs leading to death of the patients [3]. Therefore, it is necessary to identify novel targets which do not only inhibit tumor growth, but also sensitize refractory cells to therapy and prevent metastasis.

MicroRNAs (miRNA) are 20–22 nucleotide small non-coding RNAs which regulate gene expression post-transcriptionally by preferentially binding to the seed-

matching sequence in the 3′-UTR of target mRNAs leading to either mRNA destabilization or degradation [4]. miRNAs have been classified as tumor suppressors or oncogenic ones depending on the phenotype they induce, the targets they modulate, and the tissue where they function [5, 6]. In this context, large number of oncogenic and tumor suppressor miRNAs have been shown to be associated with cancer progression, drug resistance or metastasis (reviewed in [7, 8]). However, little is known about miRNAs that can simultaneously regulate tumor proliferation and EMT whereby acting as therapy-sensitizer and metastasis blocker in breast cancer.

In this study, we identify miR-644a as a novel inhibitor of tumor cell proliferation and metastatic potential which acts as a pleotropic therapy sensitizer in breast cancer both *in vitro* and *in vivo*. These findings are further supported by the analysis of several breast cancer datasets. Mechanistically, we show that miR-644a directly targets transcriptional co-repressor CTBP1 and thereby upregulates p53 levels. We then show that this increased wild type or mutant p53 acts as a switch deciding on G1-arrest or apoptosis by inducing p21 or Noxa, respectively. Our *in silico* analyses propose CTBP1 as an important predictor for survival of breast cancer patients with p53 mutation. These results suggest that the re-activation of miR-644a/CTBP1/p53 axis may represent a new target to overcome breast cancer progression, therapy resistance, and metastasis.

RESULTS

miR-644a inhibits proliferation, promotes apoptosis, and its expression or gene signature correlates with tumor progression in breast cancer

To identify novel miRNAs regulating proliferation in breast cancer, we performed a small scale miRNA mimic cell viability screen entailing 35 miRNAs in MDA-MB-231 human breast cancer cell line (Figure 1A). As a positive control we used miR-200c, which was previously reported as a tumor suppressor miRNA by us [9] and others [10, 11]. Out of three most promising potential tumor suppressor miRNAs besides miR-200c, miR-299–3p and miR-127–5p have been reported as tumor suppressors in different cancer types [12, 13]. The other one, miR-644a, has not been characterized in the context of breast cancer. Real time cell analyzer (RTCA) assay further confirmed inhibitory role of miR-644a in viability of MDA-MB-231 cells (Figure 1B). Furthermore, miR-644a reduced viability of other cell lines representing different breast cancer subtypes and two normal breast cell lines, MCF-10A and MCF-12A, (Figure 1C).

Upon miR-644a overexpression, breast cancer cell lines with p53 mutation (p53-*mut*) only underwent apoptosis evidenced by increased cleaved caspase-3 (Figure 1D and 1E) by inducing G2/M arrest characterized by increased phosphorylation of G2/M-arrest markers Cdc2 and Cdc25C (Figure 1F and 1H). In contrast, miR-644a overexpression in p53-*wt* MCF-7 cells resulted in G1 arrest with decreased expression of G1/S transition proteins and increased expression of CDK inhibitor p21, which leads to reduced phosphorylation of Rb protein (Figure 1G and 1H).

To validate our findings *in vivo*, we engineered MDA-MB-231 cell line (referred to herein as 231.Ctrl) with lentiviral-transduced miR-644a (referred to herein as 231.miR-644a) (Supplementary Figure S1A), and observed a delayed and significantly decreased tumor growth (Figure 1I). Correspondingly, tumors collected from the 231.miR-644a group showed high levels of miR-644a expression (Figure 1L), were substantially smaller and weighed less (Figure 1J and 1K) further confirming the tumor suppressive role of miR-644a in breast cancer.

To elucidate the pathological relevance of miR-644a, we examined the expression of miR-644a in publicly available expression datasets GSE45666 and GSE58606 [14, 15], and observed significantly lower miR-644a levels in tumors as compared to normal tissues (Figure 1M and 1N). Besides breast cancer, melanoma and osteosarcoma cell lines also had lower miR-644a levels compared to their normal counterparts (Supplementary Figure S1B and S1C). In addition to gene-level analysis, we also performed gene expression profiling to derive a miR-644a signature, and used this signature to elucidate miR-644a-induced changes in a more global manner. To this end, we forced expression of miR-644a using mimics in three breast cancer cell lines representing different subtypes of breast cancer (Supplementary Figure S2A). We then collected commonly up- and down-regulated genes among these three cell lines to create a 'miR-644a signature' (Supplementary Table S1). Gene Ontology (GO) term analysis revealed association of miR-644a signature with biological processes contributing to tumor progression, such as cell cycle, apoptosis, actin cytoskeletal organization and cell adhesion (Supplementary Figure S2B). Furthermore, Gene Set Enrichment Analysis (GSEA) of GSE58644 dataset [16] showed a significant correlation between miR-644a gene signature and tumor progression in breast cancer patients. Notably a gene set containing genes downregulated in lobular carcinoma compared to normal lobular breast cells were enriched in patients with high miR-644a signature scores (Supplementary Figure S1D). Moreover, genes associated with histologic grade 1 and grade 3 in breast cancer patients were significantly enriched in high and low miR-644a signature scorers, respectively (Figure 1O and Supplementary Figure S1E). Consistent with this observation, in the same dataset, miR-644a signature score was lower in tumors with a more aggressive disease state characterized by higher tumor grade and stage (Supplementary Figure S1F and S1G). Finally, miR-644a

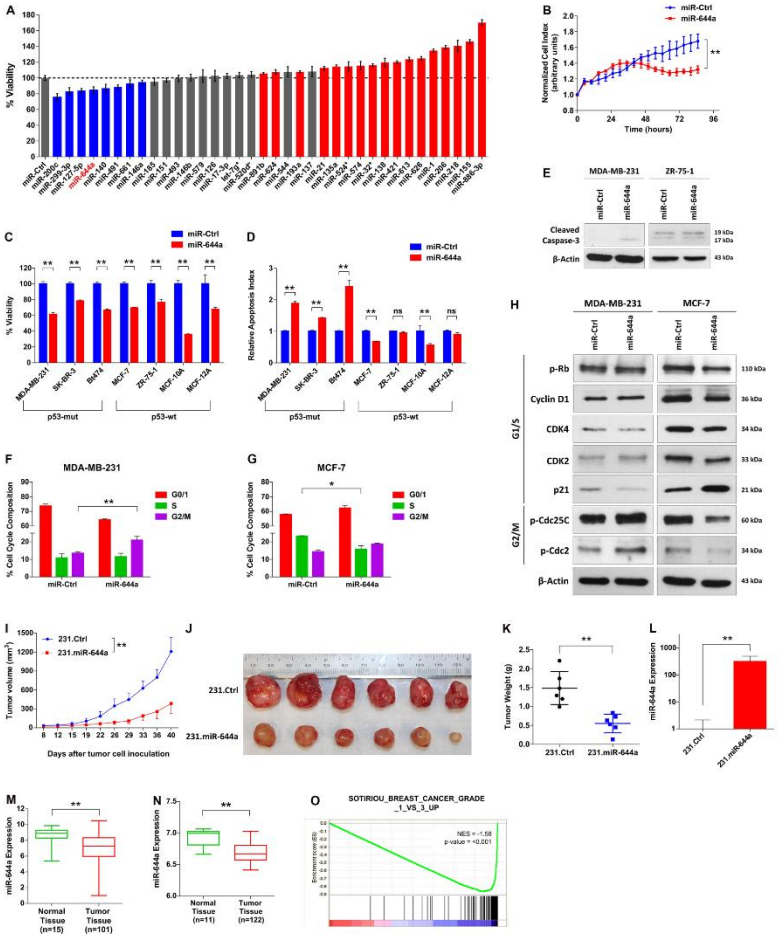


Figure 1: miR-644a reduces the viability of breast cancer cells *in vitro* and *in vivo* and miR-644a expression or its gene signature is associated with tumor progression in breast cancer. (**A**) miRNA mimic cell viability screen on MDA-MB-231 human breast cancer cell line comprising of 35 different miRNAs, with miR-200c as a positive control. The cells were transfected with 20 nM of mimics for 48 hours, and viability was measured using Cell titer Glo. Color coding of the bars depicts the effect of each miRNA on cell viability (blue: decreasing viability, red: increasing viability, gray: no effect on viability). (**B**) Real time growth of MDA-MB-231 cells transiently transfected with either a control miRNA (miR-Ctrl) or miR-644a, monitored using an RTCA (real-time cell analyzer) assay. (**C**) Effect of miR-644a overexpression on proliferation of 5 breast cancer cell lines and 2 normal breast cell lines transfected with either miR-Ctrl or miR-644a. $n = 4$. (**D**) Changes in the apoptotic index based on Caspase-3 cleavage in cells from (C). $n = 4$. (**E**) Western Blot Analysis showing the levels of cleaved Caspase-3 in p53-*mut* MDA-MB-231 (left) and p53-*wt* ZR-75-1 cells (right) after 72 hours transfection with either miR-Ctrl or miR-644a. (**F** and **G**) Flow cytometric analysis of cell cycle in cells transfected with miR-Ctrl or miR-644a showing G2/M arrest in miR-644a transfected MDA-MB-231 cells (F) and G1 arrest in miR-644a transfected MCF-7 cells (G). (**H**) Western Blot Analysis showing the levels of cell cycle proteins related to G1/S (pRb, Cyclin D1, CDK4, CDK2 and p21) and G2/M transition (p-Cdc25C and p-Cdc2) in p53-*mut* MDA-MB-231 (left) and p53-*wt* MCF7 cells (right) after 48 hours transfection with either miR-Ctrl or

miR-644a. (**I**) Tumor progression in xenografts generated by orthotropic subcutaneous injection of MDA-MB-231 cells stably expressing either a non-silencing control (231.Ctrl) or miR-644a (231.miR-644a) into nude mice. $n = 6$. (**J**) Representative images of tumors collected from xenografts of (I) on day 40. (**K**) Tumor weights in xenografts from (I) at day 40. (**L**) qRT-PCR analysis showing average miR-644a expression in 231.Ctrl and 231.miR-644a tumors collected from xenografts of (I) on day 40. $n = 3$. (**M**) miR-644a expression in 101 breast tumor tissues and 15 normal tissues from GSE45666 depicted as box-plot showing the median expression in all patients. (**N**) miR-644a expression in 122 breast tumor tissue and 11 normal tissue samples from GSE58606. (**O**) Enrichment plots of patients from GSE58644 ($n = 320$) with high or low miR-644a signature score. Genes up-regulated as breast tumors progress through histologic grade 3 were enriched in patients with low miR-644a signature score. Statistical significance was indicated ($*p < 0.05$; $**p < 0.01$; ns, not significant). Column data represent mean ± SD. Box-plots depict median number and the 25th to 75th quartiles. Upper and lower whiskers represent the minimum and maximum values in the corresponding group. This applies to all figures shown.

status was correlated with the formation and progression of not only breast cancer, but also of a variety of cancers, including melanoma, liver, lung and ovarian cancers (Supplementary Table S2), all supporting the tumor suppressive roles of miR-644a.

miR-644a inhibits metastasis and correlates with distant metastasis-free survival in patients

Since we observed enrichment of biological processes relevant to metastasis (Supplementary Table S3), we wanted to examine the effects of miR-644a on the metastatic potential of breast tumors. Transient or stable miR-644a overexpression significantly inhibited migration and invasion of MDA-MB-231 cells as assessed by wound healing, real-time migration and trans-well matrigel invasion assays (Figure 2A–2D) and reduced anchorage independent growth (Figure 2E). Furthermore, cells overexpressing miR-644a showed rearrangements of actin cytoskeletal structures from a mesenchymal to an epithelial-like state (Figure 2F) which is further confirmed by upregulated epithelial markers and downregulated mesenchymal markers both at mRNA and protein level upon miR-644a overexpression (Figure 2G–2I). Further, we tested the metastatic potential of 231.miR-644a cells in nude mice with tail-vein metastasis assay. Bouin's fixation of lungs and Hematoxylin and Eosin (H&E) staining indicated less colonization of 231.miR-644a cells to lungs as compared to 231.Ctrl cells (Figure 2J and 2K). As these cells are stably labelled with luciferase, we measured luciferase activity of lung lysates, and showed that substantially less number of cells reached metastasized to the lungs when miR-644a is expressed (Figure 2L). These data suggest that miR-644a also inhibits metastasis *in vivo*.

Then, to validate these *in vitro* and *in vivo* findings in human patient datasets, we first examined GSE38167 dataset [17], and found that expression of miR-644a is lower in primary tumors compared to normal adjacent tissues, and even further decreased in lymph node metastases (Figure 2M). This observation was further validated by GSEA which revealed an enrichment of genes whose expression in primary tumors of estrogen receptor positive (ER+) breast cancer positively correlates with developing distant metastases are enriched in patients with low miR-644a signature scores from GSE58644 (Supplementary Table S3). Moreover, miR-644a expression was found to be negatively associated with metastasis in cancers other than breast as well (Supplementary Figure S1H and S1I; Supplementary Table S3). Finally, we showed an enrichment of genes associated with poor outcome in patients having low miR-644a signature scores (Figure 2N). Consistent with this, breast cancer patients with high miR-644a signature scores have significantly longer distant-metastasis-free survival (Figure 2O). Overall, our data suggest that miR-644a is a novel tumor suppressor that is likely to be involved in progression and metastasis of multiple cancer types including breast cancer.

miR-644a is a pleiotropic therapy sensitizer in breast cancer

Since miR-644a inhibits both breast cancer cell survival and EMT, we hypothesized that it might also work as a therapy sensitizer. To test this hypothesis, we did GSEA with gene sets related to drug sensitivity and resistance. We observed that genes associated with doxorubicin (topoisomerase II inhibitor) and cisplatin (DNA cross linking agent; promising therapy for BRCA1/2 mutated/deficient tumors) resistance in gastric cancer cell lines and patients, respectively were significantly enriched in patients with low miR-644a signature scores (Supplementary Table S3). Indeed, miR-644a significantly sensitized p53-*mut* MDA-MB-231 and p53-*wt* MCF-7 cells to doxorubicin and *BRCA1*-mutated MDA-MB-436 breast cancer cells to cisplatin *in vitro* (Figure 3A, 3B and 3D). Furthermore, significantly higher miR-644a levels were observed in doxorubicin sensitive tumors developed *in vivo* as compared to resistant ones (Figure 3C), further supporting that miR-644a may play a role in chemotherapy resistance also *in vivo*.

In addition to chemotherapy agents, we found that patients with higher miR-644a signature scores have enhanced sensitivity to tamoxifen (Supplementary Table S3), which is the mainstay targeted therapy for ER+ breast cancer patients for over 40 years [18]. We demonstrated that forced miR-644a expression sensitizes cells to tamoxifen in ER+ MCF-7 cells *in vitro* (Figure 3E). Similarly, we saw that genes downregulated in gefitinib resistant non-small cell lung cancer cells undergoing prominent growth arrest and apoptosis upon

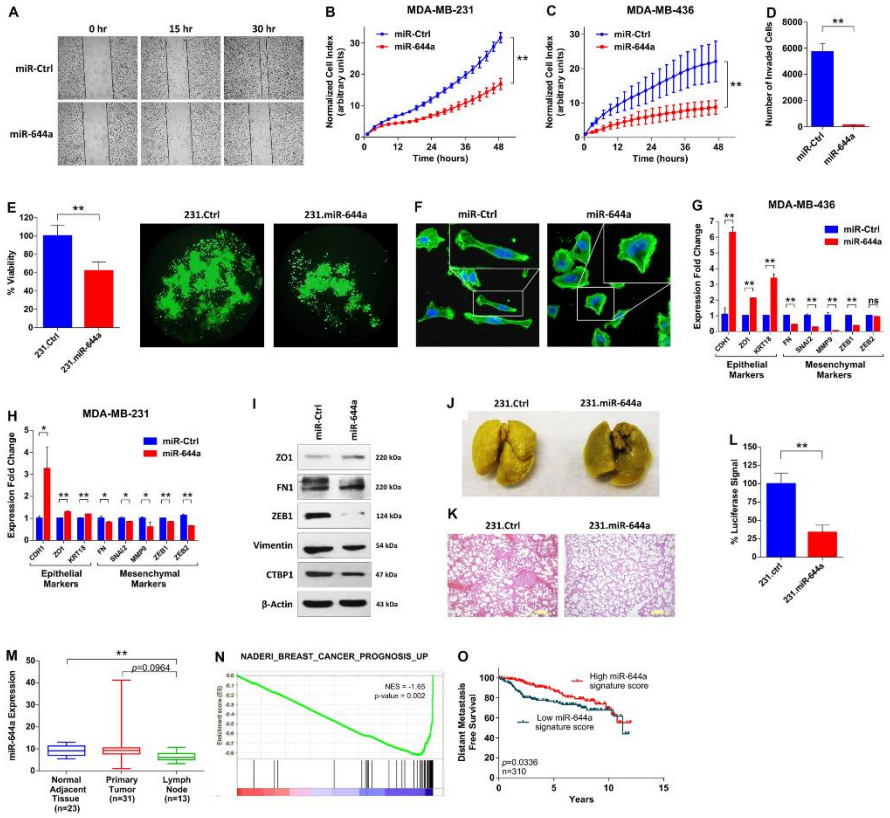


Figure 2: miR-644a inhibits metastasis, and its expression or gene signature is associated with metastasis of breast cancer patients. (**A**) Wound healing assay of MDA-MB-231 cells transfected with miR-Ctrl or miR-644a. Cells were scratched after 48 hours of transfection, and images were taken with 4× Magnification at 0, 15 and 30 hours after transfection. (**B** and **C**) Real-time migration of MDA-MB-231 (B) and MDA-MB-436 (C) cells transfected with either miR-Ctrl or miR-644a, monitored using an RTCA assay. (**D**) Number of invaded cells transfected with miR-Ctrl or miR-644a using Matrigel invasion assay. $n = 3$. (**E**) Viability of 231.Ctrl and 231.miR-644a cells grown in anchorage-independent conditions for 7 days, quantified by WST-1 assay (left) together with their fluorescence microscopy images with 10X magnification (right). (**F**) Fluorescence microscopy images of MD-MB-231 cells transfected with miR-Ctrl or miR-644a. Cell nuclei and filamentous actin were stained with 4,6-diamidino-2-phenylindole (DAPI) and Alexa Fluor 488 phalloidin, respectively. Images were taken after 72 hours of transfection with 20X magnification. Boxes at upper right corners of the images show cell morphology with higher resolution. (G and H) qRT-PCR analysis of epithelial and mesenchymal marker gene expression in MDA-MB-436 (**G**) and MDA-MB-231. (**H**) Cells transfected with miR-Ctrl or miR-644a. $n = 3$. (**I**) Western blot analysis of epithelial and mesenchymal marker expression in MDA-MB-231 cells transfected with miR-Ctrl or miR-644a. (**J**) Representative images of lungs collected from nude mice injected intravenously with 231.Ctrl or 231.miR-644a cells. Mice were sacrificed at week 7 and lungs were fixed in Bouin's Solution. (**K**) Hematoxylin and eosin staining of metastatic nodules in lungs from (J). (**L**) Luciferase signal coming from metastatic nodules in lungs of (J) as quantified by a luciferase assay. (**M**) miR-644a expression in 23 normal tissue, 31 primary tumor (IDC) and 13 lymph node metastasis tissues in GSE38167 depicted as box-plot. (**N**) Enrichment plot of patients from GSE58644 ($n = 320$) with high or low miR-644a signature score. Genes expressed higher in breast cancer patients with poor outcome as compared to those with good outcome were enriched in patients expressing low levels of miR-644a signature score. (**O**) Kaplan Meier survival curve representing the percentage distant metastasis-free survival in breast cancer patients based on miR-644a signature score median expression levels in GSE58644 ($n = 310$).

treatment with an irreversible EGFR inhibitor, CL-387,785 [19], were enriched in low miR-644a signature scorers (Supplementary Table S3). We validated this in EGFR overexpressing SK-BR-3 breast cancer cells, where miR-644a overexpression significantly sensitized cells to gefitinib (Figure 3F). Overall, multiple lines of evidence support the notion that miR-644a may be a pleiotropic sensitizer for both chemo- and targeted-therapy.

CTBP1 is a direct target of miR-644a

To identify the targets of miR-644a mediating these observed effects, we combined the list of genes downregulated upon miR-644a overexpression in our microarray analysis with targets of miR-644a predicted by three target prediction algorithms. This stringent analysis resulted in 3 genes: *CTBP1*, *CHMP7*, and *NDST1* (Figure 4A). We found CTBP1 as the most promising candidate since it is an established transcriptional co-repressor which preferentially represses the transcription of tumor suppressor genes and promotes tumor growth *via* playing pivotal roles in tumor pathogenesis [20–22].

Sequence analysis revealed that human *CTBP1* 3′-UTR has one binding site of miR-644a between nucleotides 453–460 (Figure 4B). Transient as well as stable overexpression of miR-644a significantly downregulated CTBP1 mRNA and protein levels in both MDA-MB-231 and MCF-7 cells (Figure 4C–4F). Inversely, miR-644a inhibition in MDA-MB-231 and MCF-12A cells by using hairpin inhibitors upregulated CTBP1 levels (Figure 4G and 4H). We confirmed CTBP1 as a direct target of miR-644a by measuring luciferase expression from *CTBP1* 3′-UTR constructs with or without mutation (Supplementary Figure S3A) in MDA-MB-231 and MCF-7 cells upon miR-644a transfection. In both cell lines, miR-644a overexpression significantly repressed luciferase expression when co-transfected with Wild type 3′-UTR expressing vector, but not in the case of mutated 3′-UTR expressing vector (Figure 4I and 4J). Additionally, through analyzing mRNA and miRNA expression profile dataset GSE40059 [23], we observed an inverse correlation between miR-644a and CTBP1 expression in 11 different breast cancer cell lines (Figure 4K). Overall, these data confirm that CTBP1 is a direct target of miR-644a.

Loss of CTBP1 mimics tumor- and metastasis-suppressive roles of miR-644a *in vitro* and *in vivo*

To validate that CTBP1 is a major functional target of miR-644a, we first knocked down CTBP1 with two different siRNA sequences (Supplementary Figure S4A and S4B), and examined the effect on viability, apoptosis and cell cycle. We observed a significant reduction in the viability of all tested cell lines upon CTBP1 knockdown (Figure 5A).

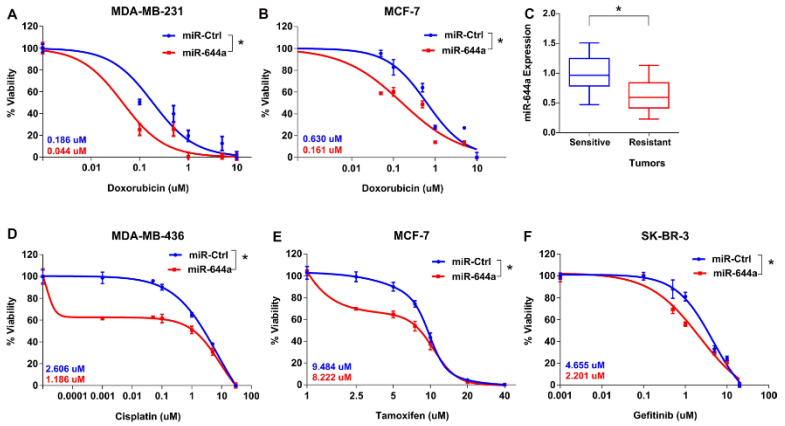


Figure 3: miR-644a overexpression acts as a therapy sensitizer in breast cancer cells and its expression correlates with doxorubicin resistance *in vivo* xenografts. (**A** and **B**) Effect of miR-644a overexpression on the response of MDA-MB-231 (A) and MCF-7 (B) cells to doxorubicin. (**C**) qRT-PCR analysis of miR-644a expression in xenografts sensitive or resistant to doxorubicin. Nude mice were subcutaneously injected with MDA-MB-231 cells and treated with doxorubicin. Among the treated mice, sensitive and resistant tumors were selected based on changes in tumor volumes upon successive drug treatments. $n = 4$. (**D**–**F**) Effect of miR-644a overexpression on the response of MDA-MB-436 cells to cisplatin (D), response of MCF-7 cells to tamoxifen (E), and response of SKBR-3 cells to gefitinib (F). IC50 values for each condition are given on the left bottom corners of each curve with a color code.

Interestingly, CTBP1 downregulation also mimicked miR-644a overexpression in increasing apoptotic cell death and inducing cleaved caspase-3 exclusively in p53-*mut* breast cancer cell lines, but not in p53-*wt* cell lines (Figure 5B and 5C). Moreover, cell cycle and western blot analysis confirmed a G2/M arrest in p53-*mut* MDA-MB-231 cells while a G1 arrest was observed in p53-*wt* MCF-7 cells upon CTBP1 knockdown similar to the effect of miR-644a (Figure 5D and 5E). For *in vivo* validation, we generated two independent CRISPR-Cas9 mediated CTBP1 knock-outs in MDA-MB-231 cells (referred to herein as 231.sgCTBP1_1 and 231. sgCTBP1_2) (Supplementary Figure S3B and S3C). Both cell lines showed efficient downregulation of CTBP1 (Figure 5F), and exhibited delayed and significantly decreased tumor growth and tumor size in nude mice (Figure 5G–5I). We could also replicate these findings using an shRNA construct against CTBP1 (Supplementary Figure S5A–S5D).

Next, we tested if the loss of CTBP1 is able to mimic the effects of miR-644a on tumor metastasis. CTBP1 knockdown significantly inhibited migration and invasion of both MDA-MB-231 and MDA-MB-436 cells (Figure 5J and 5K), and induced a more epithelial-like state (Figure 5L–5N). Inversely, CTBP1 upregulation upon miR-644a inhibitor transfection promoted mesenchymal-

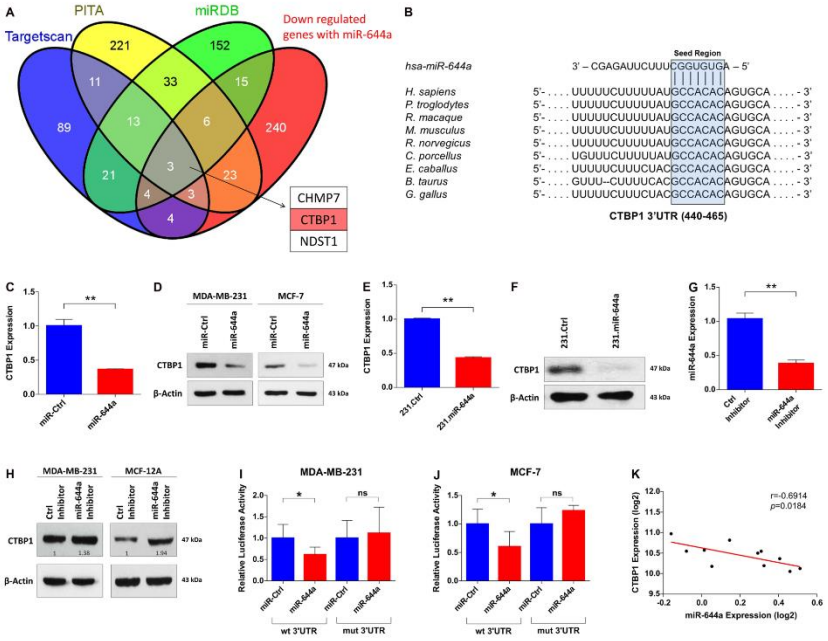


Figure 4: CTBP1 is a direct target of miR-644a. (**A**) Venn diagram for the combinatorial target prediction analysis. List of genes downregulated by miR-644a in the microarray analysis was combined with genes predicted to be miR-644a targets by three different target prediction algorithms namely TargetScan (blue), PITA (yellow) and miRDB (green). Three genes that are common in all four groups were depicted, with CTBP1 highlighted in red. (**B**) Schematic diagram showing miR-644a binding site in *CTBP1* 3′-UTR (453–460) in different species including human. (**C** and **D**) Confirmation of CTBP1 downregulation by miR-644a overexpression at transcript and protein levels with qRT-PCR analysis in MDA-MB-231 (C) and with Western Blot analysis in MDA-MB-231 (left) and MCF-7 (right) (D) cells transfected with either miR-Ctrl or miR-644a. $n = 3$ for (C). (**E** and **F**) qRT-PCR (E) and Western Blot (F) analysis of CTBP1 expression in 231.Ctrl and 231.miR-644a cells confirming downregulation of CTBP1 in transcript and protein levels in cells stably expressing miR-644a. $n = 3$ for (E). (**G**) qRT-PCR analysis of miR-644a expression in MDA-MB-231 cells transfected with either a control Inhibitor (Ctrl Inhibitor) or miR-644a Inhibitor. $n = 3$. (**H**) Western Blot Analysis showing the levels of CTBP1 in MDA-MB-231 and MCF-12A cells transfected with either Ctrl Inhibitor or miR-644a Inhibitor. (**I** and **J**) Luciferase activity of a reporter construct fused with either a *wt* or *mut CTBP1* 3′-UTR in MDA-MB-231 (I) and MCF-7 (J) cells transfected with miR-Ctrl or miR-644a. $n = 5$. (**K**) Expression of miR-644a negatively correlates with CTBP1 expression in 9 breast cancer cell lines and 2 normal breast cell lines from GSE40059.

like state (Figure 5O). Furthermore, CTBP1 knock-outs by sgRNAs or knockdown by shRNA resulted in a significant reduction in anchorage-independent growth (Figure 5P and 5Q; Supplementary Figure S5E). Re-analysis of the GSE2603 dataset [24] revealed that *in vivo* sub-lines of MDA-MB-231 with enhanced lung metastatic ability express substantially higher CTBP1 levels compared to parental cells with limited lung metastatic potential (Figure 5R). We then set to test the effect of CTBP1 in lung metastasis, and demonstrated markedly less colonization of 231.sgCTBP1_1 and 231.sgCTBP1_2 cells to lungs compared to 231.sgCtrl cells as demonstrated by Bouin's fixation and H&E staining of lungs and luciferase assay with lung lysates (Figure 5S–5U).

To elucidate the role of CTBP1 in tumor progression and metastasis in breast cancer patients, we analyzed several patient datasets. In GSE4922 [25] and GSE58644 datasets, CTBP1 levels were found to be correlated with higher tumor size and incidence of developing distant metastasis (Supplementary Figure S5F and S5G). Finally, we retrieved data form the Molecular Taxonomy of Breast Cancer International Consortium (METABRIC) project [26], and performed targeted analysis. We found that Stage 2 and 3 breast cancers where cancer starts to spread to nearby lymph nodes feature higher CTBP1 levels compared to Stage 1 breast cancer which has no or only microscopic invasion smaller than 1 mm [27]. There was also a significant increase in CTBP1 levels in Stage 4 tumors, characterized by the presence of metastases to organs other than breast (Supplementary Figure S5H). In accordance with the tumor stage, patients with 20 or more positive lymph nodes had higher CTBP1 in their primary tumors suggesting a role of CTBP1 in promoting lymph node metastasis (Supplementary Figure S5I). All of these findings suggest that CTBP1 inhibition mimics miR-644a overexpression in inhibition of breast tumor growth and metastasis.

CTBP1 is a major functional target of miR-644a mediating drug resistance and EMT

We tested if CTBP1 mediates the effect of miR-644a on drug resistance. *In silico* analysis of GSE16446 dataset [28–30] showed significantly lower levels of CTBP1 in patients with pathologic complete response (pCR) compared to patients without complete response against anthracycline treatment (Figure 6A). In the same dataset, low CTBP1 level was associated with better outcome in terms of distant metastasis-free survival (DMFS) (Figure 6B). In GSE58644, among patients treated with chemotherapy, distant metastasis incidence rate was significantly higher in patients with high CTBP1 (Figure 6C). All these suggest an important role of CTBP1 in tumor recurrence in chemotherapy treated patients.

We then tested if we can mimic the effect of miR-644a on chemotherapy response by knocking down CTBP1. We observed that knockdown of CTBP1 sensitized MDA-MB-231 cells to doxorubicin (Figure 6D). Furthermore, rescuing CTBP1 levels along with miR-644a overexpression (Figure 6E) not only increased the viability of MDA-MB-231 cells (Figure 6F), but also rendered these cells less sensitive to doxorubicin treatment compared to those cells in which only miR-644a was overexpressed (Figure 6G). Furthermore, we observed a significantly lower levels of CTBP1 in doxorubicin sensitive tumors compared to resistant tumors of the mouse models we developed (shown in Figure 3C), which is exactly the opposite of miR-644a levels in these tumors (Figure 6H). Finally, CTBP1 rescue *via* miR-644a inhibitor transfection promoted mesenchymal-like state by upregulating mesenchymal markers and downregulating epithelial markers; and this phenotype was reversed upon CTBP1 knockdown (Figure 6I). Overall, all these data confirm that CTBP1 is a major functional target of miR-644a mediating drug resistance and EMT in breast cancer.

miR-644a/CTBP1-mediated wild type or mutant p53 upregulation acts as a switch deciding on G1 arrest or apoptosis

The *in vitro* findings that overexpression of miR-644a or loss of its target CTBP1 induces apoptosis in p53-*mut,* but not in p53-*wt* cells triggered us to investigate the relationship between miR-644a, CTBP1, and p53 mutation status. First, we performed an enrichment analysis for apoptosis-related gene sets on p53-*mut* vs p53-*wt* patients that are expressing high levels of miR-644a from GSE22220 dataset [31]. We have separated the patients as p53-*wt* and p53-*mut* according to the expression levels of a gene signature associated with p53 status [32] (details are given in Material and Methods section and Supplementary Figures S8 and S9). We observed that apoptosis genes were significantly enriched in p53-*mut* patients compared to p53-*wt* patients (Figure 7A and 7B). While investigating the underlying mechanism, we found that miR-644a overexpression or CTBP1 knockdown increased the expression of p53 level in both p53-*mut* MDA-MB-231 and p53-*wt* MCF-7 cells (Figure 7C). Furthermore, in 231.miR-644a cells, p53 level was reduced upon CTBP1 ORF expression, which shows that miR-644a mediated upregulation of p53 is *via* CTBP1 downregulation (Supplementary Figure S6A). Notably, overexpression of miR-644a or knockdown of CTBP1 in MCF-7 cells did not change p53 mRNA level, which indicates a possible post-transcriptional regulation of p53 expression (Supplementary Figure S6B and S6C). Overall, these results show that miR-644a induces p53 expression/activity in a p53 status-independent manner.

It has been shown that stabilized p53 activates several genes that induce cell cycle arrest (e.g. p21) and apoptosis (e.g. Noxa, Bax and Puma) [33]. Furthermore, CTBP1 knock-out cells were shown to express high levels

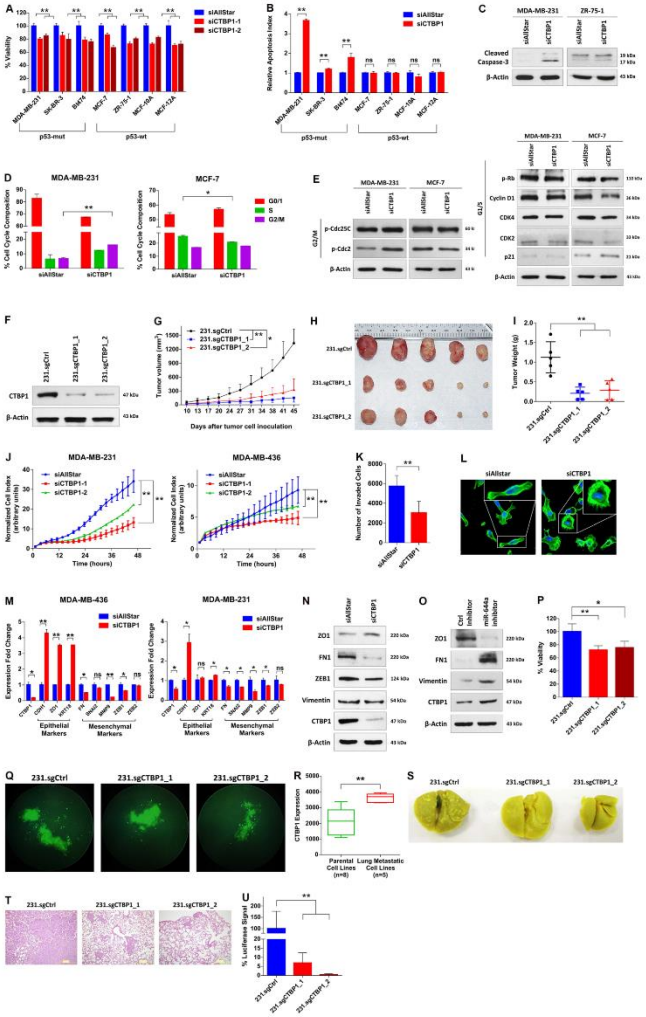


Figure 5: Loss of CTBP1 inhibits cell viability, tumor growth, migration and invasion *in vitro*, and inhibits tumor progression and metastasis *in vivo*. (**A**) Effect of CTBP1 knockdown on proliferation of cell lines previously used to test the effects of miR-644a overexpression on proliferation as in Figure 1C. Cells were transfected with either a non-targeting siRNA control (siAllStar) or different CTBP1 targeting siRNAs (siCTBP1–1, siCTBP1–2). $n = 4$. (**B**) Changes in the apoptotic index based on Caspase-3 cleavage in cells from (A) transfected with siAllStar or siCTBP1-Pool. $n = 4$. (**C**) Western Blot Analysis showing the levels of cleaved Caspase-3 in p53-*mut* MDA-MB-231 (left) and p53-*wt* MCF7 cells (right) after 72 hours transfection with siAllStar or siCTBP1-Pool. (**D**) Flow cytometric analysis of cell cycle in cells transfected with siAllStar or siCTBP1-Pool showing G2/M arrest in siCTBP1-Pool transfected MDA-MB-231 cells (left) and G1 arrest in siCTBP1-Pool transfected MCF-7 cells (right). (**E**) Western Blot analysis showing the levels of cell cycle proteins related to G2/M arrest (p-Cdc25C and p-Cdc2) (left) and G1/S (pRb, Cyclin D1, CDK4, CDK2 and p21) (right)

transition in p53-*mut* MDA-MB-231 and p53-*wt* MCF7 cells after 48 hours transfection with siAllStar or siCTBP1-Pool. (**F**) Western Blot Analysis of CTBP1 levels in MDA-MB-231.luc cells stably expressing either a non-targeting sgRNA (231.sgCtrl) or different CTBP1 targeting sgRNAs (231.sgCTBP1_1, 231.sgCTBP1_2) confirming stable knock-out of CTBP1. (**G**) Tumor progression in xenografts generated by orthotopic subcutaneous injection of 231.sgCtrl, 231.sgCTBP1_1 or 231.sgCTBP1_2. $n = 5$. (**H**) Representative images of tumors collected from xenografts of (G) on day 45. (**I**) Tumor weights in xenografts from (G) at day 45. (**J**) Real time migration of MDA-MB-231 (left) and MDA-MB-436 (right) cells transfected with siAllStar, siCTBP1–1 or siCTBP1–2, monitored using an RTCA assay. (**K**) Number of invaded cells transfected with siAllStar or siCTBP1-Pool using Matrigel invasion assay. $n = 3$. (**L**) Fluorescence microscopy images of MDA-MB-231 cells transfected with either siAllStar or siCTBP1-Pool. Cell nuclei and filamentous actin were stained with DAPI and Alexa Fluor 488 phalloidin, respectively. Images were taken after 72 hours of transfection with 20× magnification. Boxes at the upper right corners of the images show cell morphology with higher resolution. (**M**) qRT-PCR analysis of epithelial and mesenchymal marker gene expression in MDA-MB-436 (left) and MDA-MB-231 (right) cells transfected with either siAllStar or siCTBP1-Pool. $n = 3$. (**N**) Western blot analysis of epithelial and mesenchymal marker expression in MDA-MB-231 cells transfected with either siAllStar or siCTBP1-Pool. (**O**) Western blot analysis of epithelial and mesenchymal marker expression in MCF-12A cells transfected with either Ctrl inhibitor or miR-644a inhibitor. (**P** and **Q**) Viability of 231.sgCtrl, 231.sgCTBP1_1 and 231.sgCTBP1_2 cells grown in anchorage-independent conditions for 7 days, quantified by WST-1 assay (P) together with their fluorescence microscopy images with 10× magnification (Q). (**R**) CTBP1 expression in parental MDA-MB-231 cells, its single-cell-derived progenies (SCPs) and *in vivo* isolated sub-lines with different lung metastatic capabilities from GSE2603 ($n = 19$). (**S**) Representative images of lungs collected from nude mice injected intravenously with 231.sgCtrl, 231.sgCTBP1_1 or 231.sgCTBP1_2. Mice were sacrificed at week 7 and lungs were fixed in Bouin's Solution. (**T**) Hematoxylin and eosin staining of metastatic nodules in lungs from (S). (**U**) Luciferase signal coming from metastatic nodules in lungs of (S) as quantified by a luciferase assay.

of pro-apoptotic genes Noxa and Bax [34]. Therefore, we examined the expression of these in both MDA-MB-231 and MCF-7 cells upon miR-644a overexpression. While the expression of p21 was only upregulated in p53-*wt* MCF-7 cells, Noxa, but neither Bax nor Puma, was significantly upregulated in p53-*mut* MDA-MB-231 cells at mRNA and protein level upon miR-644a transfection (Figure 7D and 7E; Supplementary Figure S6D and S6E). Analysis of commonly upregulated genes by *wt*-p53 in breast cancer patients from Troester *et al.* [32] and loss of CTBP1 in MCF-7 cells from Di et *al.* [35] also identified only p21 and BTG2 (data not shown) which further supported that miR-644a mediated upregulation of *wt*-p53 and p21 is *via* CTBP1 downregulation.

We then asked whether we can induce apoptosis upon miR-644a expression or CTBP1 knockdown in p53-*wt* MCF-7 cells if *mut*-p53 was co-expressed. After confirming successful overexpression of *mut*-p53 with western blot (Figure 7F and 7I), we performed an apoptosis assay followed by qRT-PCR of Noxa. Overexpression of *mut*-p53 alone in p53-*wt* MCF-7 cells induced a certain level of apoptosis and Noxa expression, which is further enhanced either by overexpression of miR-644a or by knockdown of CTBP1 (Figure 7G–7K). This confirms that miR-644a mediates apoptosis in the presence of *mut*-p53 mainly by the pro-apoptotic gene Noxa. Furthermore, presence of *mut*-p53 did not affect downregulation of CTBP1 (Figure 7F and 7I; Supplementary Figure S6F and S6H) suggesting that there is no feedback regulation of CTBP1 by p53 in the miR-644a/CTBP1/p53 axis. Lastly, to validate that p53 serves as a switch in miR-644a/CTBP1/p53 axis in breast cancer, we checked the downstream effects of miR-644a in 6 different breast cancer cell lines (three p53-*wt* and three p53-*mut*) after forced miR-644a expression using mimics. We demonstrated that depending on the p53 status, miR-644a/CTBP1/p53 axis leads to either p21 upregulation (in case of p53-*wt* cells) or Noxa upregulation (in case of p53-*mut* cells) explaining the observed G1 arrest or apoptosis induction, respectively (Figure 7L).

p53 mutant patients with high CTBP1 level are predicted to have a worse survival

It has been known that p53-*wt* patients have better survival as compared to p53-*mut* ones [36–38]. We confirmed this by analyzing published patient data and showed that p53-*mut* patients survive less than p53-*wt* patients (Supplementary Figure S7A and 7B). Unlike the prognostic relevance of miR-644a signature, no correlation of CTBP1 mRNA levels with the survival of breast cancer patients from GSE58644 and GSE19536 [39] datasets was found (Supplementary Figure S7C and S7D). Therefore, we asked if the expression level of CTBP1 can be associated with the survival of p53-*mut* patients in these datasets. This was indeed the case for both of the datasets as well as an online survival analysis tool, Kaplan-Meier (KM) Plotter [40] (Figure 7M–7O). However, in p53-*wt* patients CTBP1 expression level did not have any significant effect on survival of the patients (Supplementary Figure S7E–S7G). We observed a similar pattern in ovarian cancer where p53-*mut* patients with high CTBP1 levels are less likely to survive compared to patients with low CTBP1 (Figure 7P; Supplementary Figure S7H). Overall, these data suggest that CTBP1 expression may be associated with survival of p53-*mut* breast and ovarian cancer patients.

DISCUSSION

Little is known about the deregulation of miR-644a in cancer. It has been shown that high expression of miR-644a (previously known as miR-644 according to

miRBase release 21 [41]) is correlated with shorter overall survival in Acute myeloid leukemia (AML) [42], and miR-644a is found to be upregulated in bladder cancer [43]. On the contrary, miR-644a overexpression was shown to downregulate an isoform of the androgen receptor, and decrease viability in prostate cancer cell lines [44]. However, there is no functional study on miR-644a, and its deregulation in breast cancer has not been reported. Here, we demonstrated that miR-644a acts as a tumor suppressor in breast cancer by regulating tumor progression, metastasis, and drug resistance affecting the patient survival (Figure 7Q). We identified the transcriptional co-repressor CTBP1 as the major functional target of miR-644a phenocopying all its effects on cell proliferation, apoptosis, EMT and drug resistance. Its loss upon miR-644a overexpression on one hand leads to G1 arrest or apoptosis by increasing p53 expression and on the other hand leads to increased E-Cadherin to inhibit EMT and metastasis.

It has been known that activated p53 can either lead to apoptosis or cell cycle arrest in a highly context dependent manner. As reviewed by Haupt *et al.* [45] and Fridman *et al.* [46], cell type, strength and nature of the stimulus as well as the presence of collateral signals can determine cell fate in the presence of a stress stimulus. Importance of the latter has been shown in case of DNA damage during which Myc shifts the balance of cell fate from cell cycle arrest to apoptosis by blocking p21 induction *via* recruiting Miz-1 to p21 promoter site, and thereby preventing p53-mediated transcription [47, 48]. Therefore, we also checked changes in Myc expression

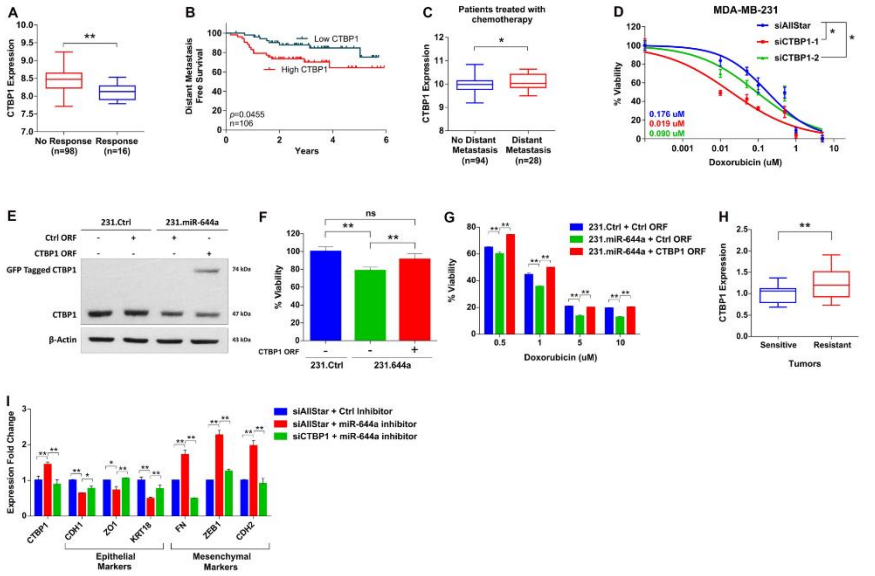


Figure 6: CTBP1 expression correlates with response to chemotherapy, and its loss sensitizes to chemotherapy and enhances epithelial-like state. (**A**) CTBP1 expression in anthracycline treated breast cancer patients from GSE16446 with no response to treatment (n = 98) or pathologic complete response (n = 16). (**B**) Kaplan Meier survival curve representing the percentage distant metastasis-free survival in breast cancer patients treated with anthracyclines based on CTBP1 median expression levels in GSE16446 dataset (n = 106). (**C**) CTBP1 expression in patients with no distant metastasis (n = 94) or with distant metastasis (n = 28) among breast cancer patients treated with chemotherapy from GSE58644. (**D**) Effect of CTBP1 knockdown on the response of MDA-MB-231 cells to doxorubicin. Cells were transfected with siAllStar, siCTBP1–1 or siCTBP1–2 and treated with increasing concentrations of doxorubicin. n = 4. (**E** and **F**) 231.Ctrl or 231.miR644a cells were transfected with Ctrl open reading frame (ORF) or CTBP1 ORF in mentioned combination to rescue the CTBP1 expression. Western Blot analysis showing rescue of CTBP1 expression in MDA-MB-231 (E). Effect of CTBP1 rescue on viability of MDA-MB-231 cells (F). (**G**) Bar graph showing the effect of CTBP1 rescue as shown in (F) on the response of MDA-MB-231 to 4 different doses of doxorubicin. n = 4. (**H**) qRT-PCR analysis of CTBP1 expression in xenografts sensitive or resistant to doxorubicin that were previously used to test the changes in miR-644a levels upon drug resistance (Figure 3C). n = 3. (**I**) qRT-PCR analysis of epithelial and mesenchymal marker gene expression in MCF-12A cells upon CTBP1 rescue by miR-644a inhibitor and further knockdown by siCTBP1.

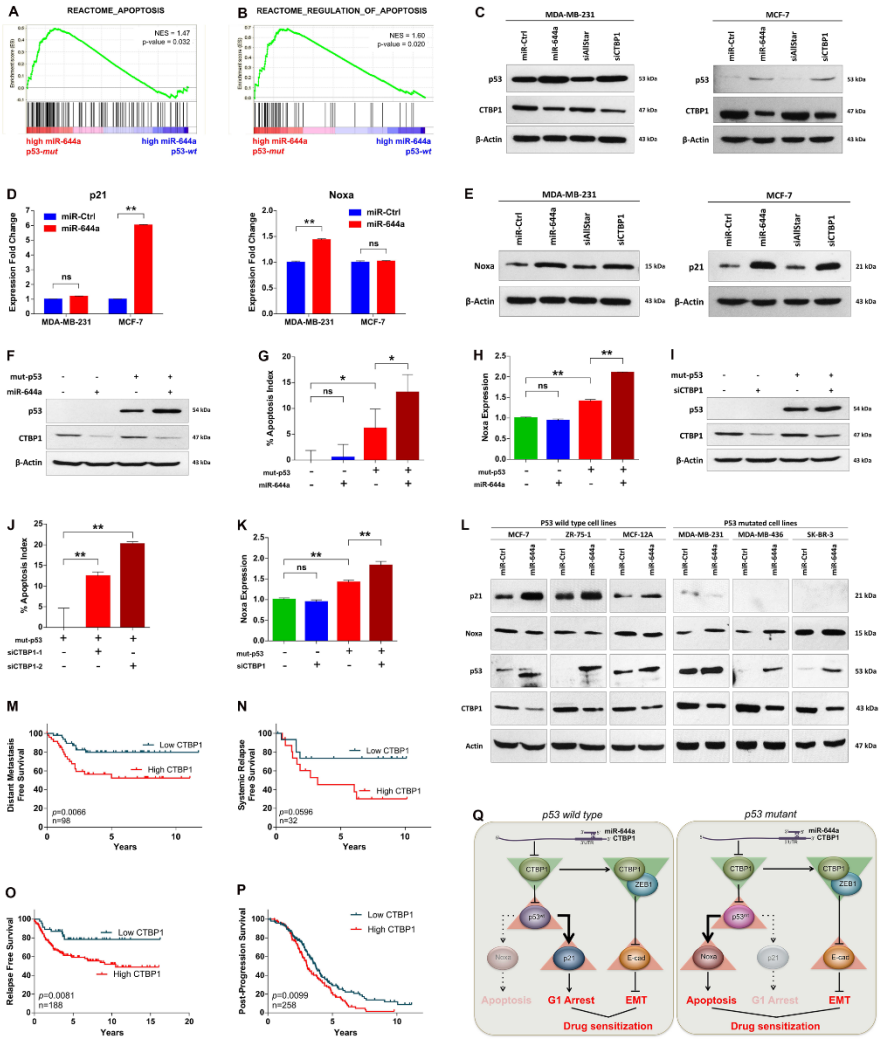


Figure 7: miR-644a/CTBP1-mediated wild type or mutant p53 upregulation acts as a switch on G1-arrest or apoptosis, and CTBP1 expression predicts survival of patients with p53 mutation. (**A** and **B**) Enrichment plots of patients from GSE22220 with high miR-644a levels (n = 105). Among patients with high miR-644a, genes annotated to Apoptosis (A) and Regulation of Apoptosis (B) pathways in Reactome were significantly enriched in p53-*mut* group as compared to p53-*wt* group. (**C**) Western Blot analysis showing the regulation of p53 in MDA-MB-231 (left) and MCF-7 cells (right) upon miR-644a overexpression or CTBP1 knockdown. (**D** and **E**) qRT-PCR (D) and western blot (E) analysis of p21 and Noxa gene expression in MDA-MB-231 and MCF-7 cells upon miR-644a overexpression or CTBP1 knockdown. (**F**–**K**) Changes in the apoptotic index based on Caspase-3 cleavage in p53-*wt* MCF-7 cells transfected with miR-644a (G) or siCTBP1–1, siCTBP1–2 (J) together with *mut*-p53 ORF. Regulation of Noxa expression upon miR-644a overexpression (H) or

CTBP1 knockdown (K) in the presence of *mut*-p53 was shown with qRT-PCR analysis. Overexpression of *mut*-p53 in p53-*wt* MCF-7 cells was confirmed with Western Blot analysis (F and I). (**L**) Western blot analysis showing CTBP1, p53, Noxa and p21 expression upon miR-644a upregulation using mimics in 6 different breast cancer cell lines. (**M** and **N**) Kaplan Meier survival curves of breast cancer patients with p53 mutation based on CTBP1 median expression levels in datasets GSE58644 (n = 98) representing percentage distant metastasis-free survival (M) and in GSE19536 (n = 32) representing percentage systemic relapse-free survival (N). (**O** and **P**) Kaplan Meier survival curve of breast (O) and ovarian (P) cancer patients with p53 mutation based on 'best cut-off' for CTBP1 expression levels in KM Plotter (n = 188 for O, n = 258 for P) representing percentage relapse-free (O) and post-progression (P) survival. (**Q**) Schematic description of miR-644a/CTBP1/p53 axis-mediated drug resistance by simultaneous modulation of cell survival and EMT in p53-*wt* (left) and p53-*mut* (right) cells.

with miR-644a overexpression, but did not observe an induction in Myc levels (data not shown), which might be due to the presence of a stimulus other than DNA damage in our system. Here, we propose that the mutation status of p53 is yet another factor that is important for the decision of undergoing either to cell cycle arrest or to apoptosis. Our results demonstrated that increase in p53 levels upon miR-644a overexpression or CTBP1 knockdown increases p21 which protects cells from p53-dependent apoptosis [17], and causes cell cycle arrest in p53-wt cells whereas it induces apoptosis *via* increasing the expression of pro-apoptotic gene Noxa in p53-*mut* cells. We saw that overexpression of *mut*-p53 in p53-*wt* MCF-7 cells was enough to shift the balance between cell cycle arrest and apoptosis in favor of apoptosis through upregulation of an established pro-apoptotic BH3-only protein, Noxa, even though p21 was still induced (Supplementary Figure S6G and S6I).

p53 is mutated in 30% of breast cancer which causes several defects in p53 functioning like altered DNA binding affinity or loss of transcriptional activity [49, 50]. However, there is substantial evidence showing that mutant p53 is still able to induce apoptosis through different mechanisms. It has been shown that a transcriptionally inactive mutant p53 can still activate the pro-apoptotic gene Bax upon DNA damage [51], and some transcription-defective mutants retain significant apoptotic activity independent of Bax induction [52, 53]. These suggest that in case of p53 mutation, a "gain of pathway" phenomenon occurs which may involve either transcription-dependent or independent activation of a different set of pro-apoptotic genes [54]. Our results support these findings with regard to induction of apoptosis by miR-644a in p53-mutant breast cancer cells by activation of Noxa. Notably, although we found no correlation of CTBP1 levels with the survival of breast cancer patients (Supplementary Figure S7C–S7H), in all datasets that we analyzed, we confirm that p53-*mut* patients with breast or ovarian cancer that show high CTBP1 level are associated with a worse survival as compared to the patients with low CTBP1 group (Figure 7M–7P). This suggests that CTBP1 could be a potential prognostic factor for breast cancer patients with p53 mutations which may be due to the fact that apoptosis induction is more effective on prolonging overall survival of patients than p53-dependent growth arrest.

As EMT and cell survival are closely related with drug resistance, we examined the effects of miR-644a and its target CTBP1 on drug sensitization, and observed that overexpression of miR-644a sensitized different breast cancer cells representing different subtypes to both chemotherapy and targeted therapy agents e.g. tamoxifen and gefitinib. In addition, low CTBP1 correlated with better response (Figure 6A) and longer distant metastasis-free survival of breast cancer patients treated with chemotherapy (Figure 6B). We have previously shown that miR-375 blocks EMT and sensitizes MCF-7 cells to tamoxifen [55]. Similarly, it has been shown that miR-147 blocks EMT and sensitizes colon cancer cells to gefinitib [56]. Although these drugs have different targets and mechanisms of action, we reveal miR-644a as a pleotropic sensitizer, which suggests that the inhibition of EMT might be a common nominator for sensitization to all drugs tested. However, as CTBP1 can increase the expression of MDR1 gene transcriptionally [57], we cannot rule out the alternative of possible downregulation of MDR1 upon miR-644a expression, which leads to inhibition of multi-drug resistance. Nevertheless, our results suggest that miR-644a or its target CTBP1 could be a potential drug candidate which can simultaneously block primary tumor growth, metastasis, and finally sensitize cancer cells to several different drugs. A recent study reported a small molecule, NSC95397, which inhibits the interaction between CTBP1 and its binding partners and blocks the CTBP1-mediated transcriptional repression [58]. Although using miRNAs as potential drugs could need longer time, small molecules targeting CTBP1 could act as potential drugs for cancer therapy in the near future. In conclusion, the miR-644a/CTBP1/p53 axis acts not only as biomarker of progression and drug response, but also could be targeted for cancer therapy.

MATERIALS AND METHODS

Cell culture and reagents

Human breast cancer cell lines MDA-MB-231, MCF-7, BT474, SK-BR-3, ZR-75–1 together with normal breast epithelial cell lines MCF-10A and MCF-12A were obtained from ATCC (Manassas, VA, USA). MDA-MB-231 and SK-BR-3 cell lines were cultured with Dulbecco Modified Eagle Medium (Lonza, NJ, USA) while MCF-7, BT474 and ZR-75–1 cell lines were cultured with DMEM supplemented with 0.1% insulin. MCF10A and MCF-12A cell line was cultured

with DMEM (Lonza, NJ, USA) supplemented with 0.1% insulin (0.01 mg/ml), 0.002% EGF (20 ng/ml) (both from Sigma-Aldrich, Saint-Louis, MO, USA). All media were supplemented with 50 U/ml penicillin/streptomycin, 1% non-essential amino acids and 10% fetal bovine serum (Lonza, NJ, USA). All cell lines were tested for mycoplasma contamination regularly using MycoAlert mycoplasma detection kit (Lonza, NJ, USA).

Transient transfection with miRNA mimics, hairpin inhibitors, siRNAs and expression constructs

Transfections were carried out as previously described [59]. Sequence of miR-644a mimic was AGUGUGGCUUUCUUAGAGC. For miRNA mimic viability screen, miRNA mimics were transfected at a concentration of 20 nM for 48 hours. For other experiments, miR-644a and all siRNA transfections were done at a concentration of 40 nM whereas hairpin inhibitors were transfected at a concentration of 100 nM for either 48 hours or 72 hours. 50 ng (for 96-well experiments) or 500 ng (for 6-well experiments) per well of GFP tagged CTBP1 (NM_001012614; Cat. No. RG208594) human ORF Clone and Myc-DDK tagged TP53 (NM_000546; Cat. No. RC200003) human mutant ORF Clone vector were purchased from Origene and used for overexpression and rescue experiments. Latter one expresses transcript variant 1 of Homo sapiens protein p53 having an R175H mutation.

Plasmid construction and site-directed mutagenesis

The construction of plasmid carrying 3′-UTR sequence of CTBP1 gene was done as previously described [9]. The 967 bp length 3′-UTR which contained last exon sequence common to two transcript variants of CTBP1 and annotated CCDS in NCBI Consensus Coding Sequence database [60] was used to design the primers. Primers used were 5′-GGCACTCGAGCTGCTGTGGAAGGTAT-3′ and 5′-ATACAAGCGGCCGCAGTCACAAACATGATTTTA AC-3′. For site-directed mutagenesis, the predicted hsa-miR-644a target site of the previously described psiCheck2/CTBP1–3′UTRwt construct were disrupted by four point mutations in the seed region (Supplementary Figure S3A).

Quantitative RT-PCR analysis of mRNAs and miRNAs

Total RNA was isolated using TRIsure (Bioline, Luckenwalde, Germany). cDNA synthesis was performed using RevertAid RT Reverse Transcription Kit (Life Technologies), following manufacturer's instructions. Each real-time PCR assay was carried out in triplicates using LightCycler 480 SYBR Green I Master kit (Roche). Sequences of the primers were provided elsewhere (Supplementary Table S5). ACTB and HPRT were used as housekeeping genes. Data were analyzed according to $\Delta\Delta C_T$ method [61]. Quantitative RT-PCR analysis for miRNAs was done as previously described [9]. RNU44 was used as the housekeeping gene.

Western blot

Whole-cell lysates were prepared using RIPA lysis buffer containing protease inhibitor Complete Mini (Roche, Basel), anti-phosphatase PhosSTOP (Roche, Basel), 10 mM NaF and 1 mM Na4VO3. Protein concentrations were determined with BCA Protein Assay Reagent Kit (Thermo Scientific, Rockford, IL). Proteins were denatured with 4× loading dye containing 10% SDS and 50% glycerol at 95°C for 5 minutes, and 20 µg proteins were loaded in each lane. Protein samples were separated by SDS-PAGE and incubated with primary antibodies (Supplementary Table S6). Horseradish peroxidase conjugated anti-mouse or anti-rabbit antibodies (Cell signaling Technology, USA) were used as secondary antibodies, and signals were detected by enhanced chemiluminescence (Thermo Scientific, Rockford, IL).

Cell cycle, viability and apoptosis assays

Cell cycle analysis was performed as previously described [62]. Transfections were done in 6-well plates (2.5×10^5 cells per well) in triplicates. For drug sensitization assays, drug treatments were done one day after miRNA mimic or siRNA transfections with doxorubicin (0.05–10 uM), cisplatin (0.001–30 uM), tamoxifen (2.5–40 uM) or gefitinib (0.1–20 uM) for 72 hours. Cell viability (including viability of miRNA mimic screen and drug sensitization assays) and apoptosis were assessed by Cell Titer Glo Luminescent Cell Viability and Caspase-Glo 3/7 assays (Promega, WI, USA), respectively according to the manufacturer's instructions. Cell viability after polyHEMA assay was assessed with WST-1 assay (Roche) according to the manufacturer's instructions.

RTCA proliferation and migration assays

Real time growth and migration of MDA-MB-231 and MDA-MB-436 cells were monitored using xCelligence Real-time Cell Analyzer system (Acea Biosciences, San Diego, CA, USA) as previously described [9, 59]. For invasion assay, cells were transfected as described above and seeded in Matrigel invasion chambers (BD Pharmingen) in 1% FBS DMEM. After 48 hours, number of invaded cells were counted by flow cytometry (FACS Calibur) and analyzed by Cell Quest Pro software (BD Bioscience). In wound healing assay, 1×10^5 cells were seeded on 24-well plates, and

pictures were taken with Axiovert 25 light microscope (Hund, Wetzlar, Germany). PolyHEMA assay was performed as previously described [55].

Dual luciferase reporter assay

Dual-luciferase reporter assay was performed as previously described [9]. Luciferase activity was measured in Synergy HT microplate reader machine (BioTek, Vermont, US) after 24 hours of transfection, and values were normalized to firefly luciferase activity.

Immunofluorescence staining and microscopy

Nuclear staining of cells were done with 4, 6-diamidino-2-phenylindole (DAPI) and filamentous actin were stained with Alexa Fluor 488 phalloidin (1:40; Invitrogen) as previously described [9]. Coverslips were mounted with Shandon Immu-Mount reagent. Images were taken using a Zeiss microscopy.

Lentiviral vector constructs and infection

SMARTchoice human lentiviral hsa-miR-644a shMIMIC hCMV-turboGFP, GIPZ human CTBP1 shRNA vectors with clone IDs V3LHS_380132, V3LHS_398420 and V3LHS_113279 encoding different shRNAs sequences and GIPZ non-silencing lentiviral shRNA control were purchased from Dharmacon (Lafayette, CO). MDA-MB-231.luc cells (a kind gift from Dr. Dihua Yu (MD Anderson, TX)) were transduced with miR-644a viral particles in 24-wells plate, and 96 hours post-transduction, selection with 1 μg/ml of puromycin was started. To produce viral particles with CTBP1 shRNAs and non-silencing shRNA control, 6 μg of each of these vectors and 4.3 μl of trans-lentiviral packaging mix (Dharmacon) were used to co-transfect HEK293FT cells in 6-wells plate with $CaCl_2$ reagent (Dharmacon). 48 hours post-transfection, first viral particles were harvested. 96 hours post-transduction, selection with 1 μg/ml of puromycin was started. LentiCRISPRv2 vector was a kind gift from Dr. Feng Zhang (MIT, Boston, MA) [63]. For sgRNA design (Supplementary Figure S3B and S3C), candidate target sequences were determined using E-CRISPR tool [64]. For the packaging of pLentiCRISPR/CTBP1 sgRNA1 and pLentiCRISPR/CTBP1 sgRNA2 vectors, 30% confluent HEK293FT cells in 100 mm plates have been co-transfected using 42 μg of these vectors, 31.5 μg of pMD2.G (Addgene) and 21 μg psPAX2 (Addgene). Transfection, transduction and selection were performed as described previously for GIPZ vectors series.

In vivo experiments

All animal experiments have been approved by the animal ethics committee of Bilkent University. For primary tumors, 6–8 week old female athymic Nu/nu mice were injected with 2×10^6 cells into both left and right mammary fat pads (MFP) subcutaneously without incision, with 5–6 mice per group. Tumor growth was monitored by measuring the tumor volume twice a week with a caliper after tumors become palpable. Tumor volumes were calculated as length × $width^2/2$. All the mice were sacrificed once one of the mice reached threshold of 1500 mm^3 volume, and tumors were collected and weighed. For doxorubicin response experiments, primary tumors were developed using above mentioned protocol, and mice were treated with a dose of 5 mg/kg body weight of mice weekly through intravenous injection when tumors became palpable. In the beginning, all tumors showed sensitivity towards treatment and showed decrease in volume. Some of these sensitive tumors were collected after 8–10 weeks of treatment. Later, remaining tumors started to increase in size, and showed resistance towards treatment, and these resistant tumors were collected after 12–15 weeks of treatment. For tail-vein metastasis assay, 1.5×10^6 cells were injected into tail vein of each 6–8 weeks old female athymic Nu/nu mice, with 3–5 mice per group. The mice were sacrificed, and lung metastasis was evaluated once one of the mice became moribund with a luciferase assay. Due to heterogeneous distribution of nodules, three different parts were randomly collected from each lung to make a tissue pool and weighed for normalization. Lung tissues were ground in cold PBS by tissue homogenizer and treated with lysis buffer (Promega). 500 ul lysis buffer was added to 140–180 mg weight. After 15 min incubation, 100 ul of luciferase substrate (Promega) was added to 20 ul of the lysed sample, and luminescence was measured with a luminometer. For Bouin's fixation, harvested lungs were cleaned with PBS and placed into Bouin's solution on a shaker for overnight. After fixation they were kept in 70% alcohol. The lung samples used for Bouin's fixation were excluded from luciferase assay and H&E staining.

miRNA target prediction

Targetscan release 6.2 (http://www.targetscan.org), PITA miRNA target recognition from Segal Lab of Computational Biology (http://genie.weizmann.ac.il) and miRDB (http://mirdb.org/miRDB/index.html) was used as target prediction algorithms for identification of miR-644a targets. Common predicted targets between all three databases and downregulated genes by miR-644a (microarray results) were represented in a Venn diagram using Venny 2.0.

Microarray analysis

Expression profiling data were normalized with quantile normalization. Quality control and differential gene expression analysis was conducted using *limma* in Bioconductor [65]. Microarray data can be retrieved from

NCBI Gene Expression Omnibus (GEO) database with the accession number GSE82058.

Patient data and statistical analysis

Cell line and patient data were retrieved from the NCBI GEO database (GSE4922, GSE2603, GSE16446, GSE19536, GSE22220, GSE38167, GSE40059, GSE45666, GSE58606 and GSE58644) and from the Molecular Taxonomy of Breast Cancer International Consortium (METABRIC) project with data deposited in EMBL European Genome–Phenome Archive (http://www.ebi.ac.uk/ega/), with an accession number EGAS00000000122. A brief summary of these datasets is provided in Supplementary Table S4. For GSE19536, patient data were retrieved from GSE3985 which is a former study done with the same patient samples and which is providing more detailed patient data. Significance scores of genes up and down-regulated by miR-644a were calculated as previously described [66]. miR-644a signature score was defined as the ratio of the significance scores of genes up and down-regulated by miR-644a. For the GSEA analysis, patients in GSE58644 dataset were grouped based on their miR-644a significance score ratios, which we defined as the miR-644a signature score. For the GSEA analysis with GSE22220 dataset, patients expressing high levels of miR-644a were separated into two groups as p53-*mut* and p53-*wt*. Survival curves were generated using Kaplan-Meier method. Patients without any available survival time or event were excluded from the corresponding patient groups. All separations were done from median. For KM Plotter curves, 'best cut-off' option was selected for the separation of patients. Significance of the differences in survival between two groups was calculated by Log-rank (Mantel-Cox) test. For the separation of patients as p53-*wt* or p53-*mut*, data provided by the publishers of the studies were utilized if available. In GSE58644 and GSE22220, the separation was done by clustering patients according to their expression levels of a gene signature associated with p53 status [32]. The accuracy of p53 status prediction with this gene signature was tested by using data from GSE19536 in which p53 status of the patients was provided. 85% and 77% of the p53-*mut* and p53-*wt* patients, respectively could be predicted from their expression levels of the p53 status signature. The generated heatmap is provided as Supplementary Figure S8. Heatmaps for the other datasets with accession numbers GSE58644 and GSE22220 are provided as Supplementary Figure S9. Gene ontology analyses were done with DAVID bioinformatics tool [67]. For the microarray datasets that contain negative expression values, a small number was added such that all values became positive [68]. Comparisons between two groups were made by two-tailed student *t*-test. Significance cut-off were taken as $P = 0.05$. For the real-time cell growth experiments, data were normalized to time of transfection and statistical significance was determined with a paired, two-tailed student *t*-test. Statistical significance between two dose response curves was also determined with a paired, two-tailed student *t*-test.

ACKNOWLEDGMENTS AND GRANT SUPPORT

This work was supported by EMBO Installation Grant 2791 (ÖŞ), FP7 Marie Curie Career Integration Grant PCIG14-GA-2013–631149 (ÖŞ), TÜBİTAK 2232 Grant 114C060 (ÖŞ), TÜBA GEBIP 2014 (ÖŞ) and the scholarship from Higher Education Commission of Pakistan (UR).

CONFLICTS OF INTEREST

The authors declare that they have no conflicts of interest.

REFERENCES

1. Siegel R, Naishadham D, Jemal A. Cancer statistics, 2013. CA Cancer J Clin. 2013; 63:11–30.
2. Perou CM, Sorlie T, Eisen MB, van de Rijn M, Jeffrey SS, Rees CA, Pollack JR, Ross DT, Johnsen H, Akslen LA, Fluge O, Pergamenschikov A, Williams C, et al. Molecular portraits of human breast tumours. Nature. 2000; 406:747–752.
3. Hanahan D, Weinberg RA. Hallmarks of cancer: the next generation. Cell. 2011; 144:646–674.
4. Lujambio A, Lowe SW. The microcosmos of cancer. Nature. 2012; 482:347–355.
5. Ambros V. microRNAs: tiny regulators with great potential. Cell. 2001; 107:823–826.
6. Zhang B, Pan X, Cobb GP, Anderson TA. microRNAs as oncogenes and tumor suppressors. Dev Biol. 2007; 302:1–12.
7. Raza U, Zhang JD, Sahin O. MicroRNAs: master regulators of drug resistance, stemness, and metastasis. J Mol Med (Berl). 2014; 92:321–336.
8. Wang L, Wang J. MicroRNA-mediated breast cancer metastasis: from primary site to distant organs. Oncogene. 2012; 31:2499–2511.
9. Jurmeister S, Baumann M, Balwierz A, Keklikoglou I, Ward A, Uhlmann S, Zhang JD, Wiemann S, Sahin O. MicroRNA-200c represses migration and invasion of breast cancer cells by targeting actin-regulatory proteins FHOD1 and PPM1F. Mol Cell Biol. 2012; 32:633–651.
10. Kopp F, Oak PS, Wagner E, Roidl A. miR-200c sensitizes breast cancer cells to doxorubicin treatment by decreasing TrkB and Bmi1 expression. Plos One. 2012; 7:e50469.
11. Liu L, Qiu M, Tan G, Liang Z, Qin Y, Chen L, Chen H, Liu J. miR-200c Inhibits invasion, migration and proliferation of bladder cancer cells through down-regulation of BMI-1 and E2F3. J Transl Med. 2014; 12:305.

12. Jong HL, Mustafa MR, Vanhoutte PM, AbuBakar S, Wong PF. MicroRNA 299–3p modulates replicative senescence in endothelial cells. Physiol Genomics. 2013; 45:256–267.

13. Willers IM, Martinez-Reyes I, Martinez-Diez M, Cuezva JM. miR-127–5p targets the 3'UTR of human beta-F1-ATPase mRNA and inhibits its translation. Biochim Biophys Acta. 2012; 1817:838–848.

14. Lee CH, Kuo WH, Lin CC, Oyang YJ, Huang HC, Juan HF. MicroRNA-regulated protein-protein interaction networks and their functions in breast cancer. Int J Mol Sci. 2013; 14:11560–11606.

15. Matamala N, Vargas MT, Gonzalez-Campora R, Minambres R, Arias JI, Menendez P, Andres-Leon E, Gomez-Lopez G, Yanowsky K, Calvete-Candenas J, Inglada-Perez L, Martinez-Delgado B, Benitez J. Tumor microRNA expression profiling identifies circulating microRNAs for early breast cancer detection. Clin Chem. 2015; 61:1098–1106.

16. Tofigh A, Suderman M, Paquet ER, Livingstone J, Bertos N, Saleh SM, Zhao H, Souleimanova M, Cory S, Lesurf R, Shahalizadeh S, Garcia Lopez N, Riazalhosseini Y, et al. The prognostic ease and difficulty of invasive breast carcinoma. Cell Rep. 2014; 9:129–142.

17. Avery-Kiejda KA, Braye SG, Mathe A, Forbes JF, Scott RJ. Decreased expression of key tumour suppressor microRNAs is associated with lymph node metastases in triple negative breast cancer. BMC cancer. 2014; 14:51.

18. Jordan VC. Tamoxifen as the first targeted long-term adjuvant therapy for breast cancer. Endocr Relat Cancer. 2014; 21:R235–246.

19. Kobayashi S, Shimamura T, Monti S, Steidl U, Hetherington CJ, Lowell AM, Golub T, Meyerson M, Tenen DG, Shapiro GI, Halmos B. Transcriptional profiling identifies cyclin D1 as a critical downstream effector of mutant epidermal growth factor receptor signaling. Cancer Res. 2006; 66:11389–11398.

20. Bergman LM, Birts CN, Darley M, Gabrielli B, Blaydes JP. CtBPs promote cell survival through the maintenance of mitotic fidelity. Mol Cell Biol. 2009; 29:4539–4551.

21. Birts CN, Harding R, Soosaipillai G, Halder T, Azim-Araghi A, Darley M, Cutress RI, Bateman AC, Blaydes JP. Expression of CtBP family protein isoforms in breast cancer and their role in chemoresistance. Biol Cell. 2010; 103:1–19.

22. Pena C, Garcia JM, Garcia V, Silva J, Dominguez G, Rodriguez R, Maximiano C, Garcia de Herreros A, Munoz A, Bonilla F. The expression levels of the transcriptional regulators p300 and CtBP modulate the correlations between SNAIL, ZEB1, E-cadherin and vitamin D receptor in human colon carcinomas. Int J Cancer. 2006; 119:2098–2104.

23. Luo D, Wilson JM, Harvel N, Liu J, Pei L, Huang S, Hawthorn L, Shi H. A systematic evaluation of miRNA:mRNA interactions involved in the migration and invasion of breast cancer cells. J Transl Med. 2013; 11:57.

24. Minn AJ, Gupta GP, Siegel PM, Bos PD, Shu WP, Giri DD, Viale A, Olshen AB, Gerald WL, Massague J. Genes that mediate breast cancer metastasis to lung. Nature. 2005; 436:518–524.

25. Ivshina AV, George J, Senko O, Mow B, Putti TC, Smeds J, Lindahl T, Pawitan Y, Hall P, Nordgren H, Wong JEL, Liu ET, Bergh J, et al. Genetic reclassification of histologic grade delineates new clinical subtypes of breast cancer. Cancer Res. 2006; 66:10292–10301.

26. Dvinge H, Git A, Graf S, Salmon-Divon M, Curtis C, Sottoriva A, Zhao YJ, Hirst M, Armisen J, Miska EA, Chin SF, Provenzano E, Turashvili G, et al. The shaping and functional consequences of the microRNA landscape in breast cancer. Nature. 2013; 497:378–382.

27. Edge SB, Byrd DR, Compton CC, Fritz AG, Greene FL, Trotti A. (2010). eds.: AJCC cancer staging manual: New York, NY; Springer).

28. Desmedt C, Di Leo A, de Azambuja E, Larsimont D, Haibe-Kains B, Selleslags J, Delaloge S, Duhem C, Kains JP, Carly B, Maerevoet M, Vindevoghel A, Rouas G, et al. Multifactorial Approach to Predicting Resistance to Anthracyclines. J Clin Oncol. 2011; 29:1578–1586.

29. Juul N, Szallasi Z, Eklund AC, Li QY, Burrell RA, Gerlinger M, Valero V, Andreopoulou E, Esteva FJ, Symmans WF, Desmedt C, Haibe-Kains B, Sotiriou C, et al. Assessment of an RNA interference screen-derived mitotic and ceramide pathway metagene as a predictor of response to neoadjuvant paclitaxel for primary triple-negative breast cancer: a retrospective analysis of five clinical trials. Lancet Oncol. 2010; 11:358–365.

30. Li Y, Zou LH, Li QY, Haibe-Kains B, Tian RY, Li Y, Desmedt C, Sotiriou C, Szallasi Z, Iglehart JD, Richardson AL, Wang ZC. Amplification of LAPTM4B and YWHAZ contributes to chemotherapy resistance and recurrence of breast cancer. Nat Med. 2010; 16:214–U121.

31. Buffa FM, Camps C, Winchester L, Snell CE, Gee HE, Sheldon H, Taylor M, Harris AL, Ragoussis J. microRNA-associated progression pathways and potential therapeutic targets identified by integrated mRNA and microRNA expression profiling in breast cancer. Cancer Res. 2011; 71:5635–5645.

32. Troester MA, Herschkowitz JI, Oh DS, He X, Hoadley KA, Barbier CS, Perou CM. Gene expression patterns associated with p53 status in breast cancer. BMC cancer. 2006; 6:276.

33. Vousden KH, Lu X. Live or let die: the cell's response to p53. Nat Rev Cancer. 2002; 2:594–604.

34. Grooteclaes M, Deveraux Q, Hildebrand J, Zhang Q, Goodman RH, Frisch SM. C-terminal-binding protein corepresses epithelial and proapoptotic gene expression programs. PNAS. 2003; 100:4568–4573.

35. Di LJ, Byun JS, Wong MM, Wakano C, Taylor T, Bilke S, Baek S, Hunter K, Yang H, Lee M, Zvosec C, Khramtsova G, Cheng F, et al. Genome-wide profiles of

CtBP link metabolism with genome stability and epithelial reprogramming in breast cancer. Nat Commun. 2013; 4:1449.

36. Kovach JS, Hartmann A, Blaszyk H, Cunningham J, Schaid D, Sommer SS. Mutation detection by highly sensitive methods indicates that p53 gene mutations in breast cancer can have important prognostic value. Proc Natl Acad Sci U S A. 1996; 93:1093–1096.
37. Murakami I, Hiyama K, Ishioka S, Yamakido M, Kasagi F, Yokosaki Y. p53 gene mutations are associated with shortened survival in patients with advanced non-small cell lung cancer: an analysis of medically managed patients. Clin Cancer Res. 2000; 6:526–530.
38. Yang P, Du CW, Kwan M, Liang SX, Zhang GJ. The impact of p53 in predicting clinical outcome of breast cancer patients with visceral metastasis. Sci Rep. 2013; 3:2246.
39. Enerly E, Steinfeld I, Kleivi K, Leivonen SK, Aure MR, Russnes HG, Ronneberg JA, Johnsen H, Navon R, Rodland E, Makela R, Naume B, Perala M, et al. miRNA-mRNA Integrated Analysis Reveals Roles for miRNAs in Primary Breast Tumors. Plos One. 2011; 6.
40. Gyorffy B, Surowiak P, Budczies J, Lanczky A. Online survival analysis software to assess the prognostic value of biomarkers using transcriptomic data in non-small-cell lung cancer. Plos One. 2013; 8:e82241.
41. Kozomara A, Griffiths-Jones S. miRBase: annotating high confidence microRNAs using deep sequencing data. Nucleic Acids Res. 2014; 42:D68–73.
42. Diaz-Beya M, Brunet S, Nomdedeu J, Tejero R, Diaz T, Pratcorona M, Tormo M, Ribera JM, Escoda L, Duarte R, Gallardo D, Heras I, Queipo de Llano MP, et al. MicroRNA expression at diagnosis adds relevant prognostic information to molecular categorization in patients with intermediate-risk cytogenetic acute myeloid leukemia. Leukemia. 2014; 28:804–812.
43. Scheffer AR, Holdenrieder S, Kristiansen G, von Ruecker A, Muller SC, Ellinger J. Circulating microRNAs in serum: novel biomarkers for patients with bladder cancer? World J Urol. 2014; 32:353–358.
44. Ostling P, Leivonen SK, Aakula A, Kohonen P, Makela R, Hagman Z, Edsjo A, Kangaspeska S, Edgren H, Nicorici D, Bjartell A, Ceder Y, Perala M, et al. Systematic analysis of microRNAs targeting the androgen receptor in prostate cancer cells. Cancer Res. 2011; 71:1956–1967.
45. Haupt S, Berger M, Goldberg Z, Haupt Y. Apoptosis - the p53 network. J Cell Sci. 2003; 116:4077–4085.
46. Fridman JS, Lowe SW. Control of apoptosis by p53. Oncogene. 2003; 22:9030–9040.
47. Herold S, Wanzel M, Beuger V, Frohme C, Beul D, Hillukkala T, Syvaoja J, Saluz HP, Haenel F, Eilers M. Negative regulation of the mammalian UV response by Myc through association with Miz-1. Mol Cell. 2002; 10:509–521.
48. Seoane J, Le HV, Massague J. Myc suppression of the p21(Cip1) Cdk inhibitor influences the outcome of the p53 response to DNA damage. Nature. 2002; 419:729–734.
49. Raycroft L, Schmidt JR, Yoas K, Hao MM, Lozano G. Analysis of p53 mutants for transcriptional activity. Mol Cell Biol. 1991; 11:6067–6074.
50. Wright JD, Lim C. Mechanism of DNA-binding loss upon single-point mutation in p53. J Biosci. 2007; 32:827–839.
51. Speidel D, Helmbold H, Deppert W. Dissection of transcriptional and non-transcriptional p53 activities in the response to genotoxic stress. Oncogene. 2006; 25:940–953.
52. Ryan KM, Vousden KH. Characterization of structural p53 mutants which show selective defects in apoptosis but not cell cycle arrest. Mol Cell Biol. 1998; 18:3692–3698.
53. Haupt Y, Rowan S, Shaulian E, Vousden KH, Oren M. Induction of apoptosis in HeLa cells by trans-activation-deficient p53. Genes Dev. 1995; 9:2170–2183.
54. He M, Rennie PS, Dragowska V, Nelson CC, Jia W. A mutant P53 can activate apoptosis through a mechanism distinct from those induced by wild type P53. FEBS letters. 2002; 517:151–154.
55. Ward A, Balwierz A, Zhang JD, Kublbeck M, Pawitan Y, Hielscher T, Wiemann S, Sahin O. Re-expression of microRNA-375 reverses both tamoxifen resistance and accompanying EMT-like properties in breast cancer. Oncogene. 2013; 32:1173–1182.
56. Lee CG, McCarthy S, Gruidl M, Timme C, Yeatman TJ. MicroRNA-147 induces a mesenchymal-to-epithelial transition (MET) and reverses EGFR inhibitor resistance. Plos One. 2014; 9:e84597.
57. Jin W, Scotto KW, Hait WN, Yang JM. Involvement of CtBP1 in the transcriptional activation of the MDR1 gene in human multidrug resistant cancer cells. Biochem Pharmacol. 2007; 74:851–859.
58. Blevins MA, Kouznetsova J, Krueger AB, King R, Griner LM, Hu X, Southall N, Marugan JJ, Zhang Q, Ferrer M, Zhao R. Small Molecule, NSC95397, Inhibits the CtBP1-Protein Partner Interaction and CtBP1-Mediated Transcriptional Repression. J Biomol Screen. 2015; 20:663–672.
59. Sahin O, Frohlich H, Lobke C, Korf U, Burmester S, Majety M, Mattern J, Schupp I, Chaouiya C, Thieffry D, Poustka A, Wiemann S, Beissbarth T, et al. Modeling ERBB receptor-regulated G1/S transition to find novel targets for de novo trastuzumab resistance. BMC Syst Biol. 2009; 3:1.
60. Pruitt KD, Harrow J, Harte RA, Wallin C, Diekhans M, Maglott DR, Searle S, Farrell CM, Loveland JE, Ruef BJ, Hart E, Suner MM, Landrum MJ, et al. The consensus coding sequence (CCDS) project: Identifying a common protein-coding gene set for the human and mouse genomes. Genome Res. 2009; 19:1316–1323.
61. Livak KJ, Schmittgen TD. Analysis of relative gene expression data using real-time quantitative PCR and the 2(-Delta Delta C(T)) Method. Methods. 2001; 25:402–408.
62. Uhlmann S, Mannsperger H, Zhang JD, Horvat EA, Schmidt C, Kublbeck M, Henjes F, Ward A, Tschulena U, Zweig K, Korf U, Wiemann S, Sahin O. Global microRNA

level regulation of EGFR-driven cell-cycle protein network in breast cancer. Mol Syst Biol. 2012; 8:570.

63. Sanjana NE, Shalem O, Zhang F. Improved vectors and genome-wide libraries for CRISPR screening. Nat Methods. 2014; 11:783–784.
64. Heigwer F, Kerr G, Boutros M. E-CRISP: fast CRISPR target site identification. Nature methods. 2014; 11:122–123.
65. Smyth GK. Linear models and empirical bayes methods for assessing differential expression in microarray experiments. Stat Appl Genet Molec Biol. 2004; 3:Article3.
66. Xu J, Acharya S, Sahin O, Zhang Q, Saito Y, Yao J, Wang H, Li P, Zhang L, Lowery FJ, Kuo WL, Xiao Y, Ensor J, et al. 14–3–3zeta turns TGF-beta's function from tumor suppressor to metastasis promoter in breast cancer by contextual changes of Smad partners from p53 to Gli2. Cancer Cell. 2015; 27:177–192.
67. Huang da W, Sherman BT, Lempicki RA. Systematic and integrative analysis of large gene lists using DAVID bioinformatics resources. Nat Protoc. 2009; 4:44–57.
68. Drăghici S. (2012). Statistics and data analysis for microarrays using R and Bioconductor. (Boca Raton, FL: CRC Press).

Immunology Letters 239 (2021) 32–41

Contents lists available at ScienceDirect

Immunology Letters

journal homepage: www.elsevier.com/locate/immlet

TLR ligand loaded exosome mediated immunotherapy of established mammary Tumor in mice

Muzaffer Yildirim [a,1], Tugce Canavar Yildirim [a,1], Nilsu Turay [a], Tugce Bildik [a], Bilgehan Ibibik [a], Irem Evcili [a], Pelin Gulizar Ersan [a,b], Unal M. Tokat [a,b], Ozgur Sahin [b], Ihsan Gursel [a,*]

[a] Thorlab, Department of Molecular Biology and Genetics, Bilkent University, Bilkent, 06800, Ankara, Turkey
[b] Drug Discovery & Biomedical Sciences (DDBS), College of Pharmacy, University of South Carolina, Columbia, SC 29208,Columbia

ARTICLE INFO

Keywords:
Cancer vaccine
TLR
Immune response
Breast tumor
Immunotherapy

ABSTRACT

Tumor-derived exosomes (TEXs) could be harnessed as an immunotherapeutic cancer vaccine. These nanovesicles are inherently possesses rich tumor antigen reservoirs. Due to their undesirable features such as poor or limited immunogenicity as well as facilitation of cancer development via mediating communication between tumor cells TEXs could be transformed into an effective immune adjuvant delivery system that initiates a strong humoral and cell-mediated tumor-specific immune response. Engineering TEXs to harbor immunostimulatory molecules still remains a challenge. Previously, we demonstrated that nucleic acid ligand encapsulated liposomes could trigger synergistic strong humoral, and cell mediated immune responses and provokes tumor regression to that of their standalone counterparts. In this study, we evaluated to immunogenicity of 4T1/Her2 cell-derived exosomes upon loading them with two potent immuno adjuvant, a TLR9 ligand, K-type CpG ODN and a TLR3 ligand, p(I:C). Engineered TEXs co-encapsulating both ligands displayed boosted immunostimulatory properties by activating antigen-specific primary and memory T cell responses. Furthermore, our exosome-based vaccine candidate elicited robust Th1-biased immunity as evidenced by elevated secretion of IgG2a and IFNγ. In a therapeutic cancer model, administration of4T1 tumor derived exosomes loaded with CpG ODN and p(I:C) to animals regress tumor growth in 4T1 tumor-bearing mice. Taken together this work implicated that an exosome-based therapeutic vaccine promoted strong cellular and humoral anti-tumor immunity that is sufficient to reverse established tumors. This approach offers a personalized tumor therapy strategy that could be implemented in the clinic.

1. Introduction

Immunotherapy has become a powerful clinical strategy to boost the activation of host immune system against tumors that evade immune surveillance and induce tolerance. These cancer therapies enhance antitumor immune responses with fewer off-target effects than traditional treatments, such as chemotherapy and radiation that lack tumor selectivity and have severe side effects [1]. Tumor antigen-based cancer immunotherapy has gained significant attention to elicit antigen-specific strong T and B cell responses, however, the purification of particular tumor antigens is challenging [2,3]. Therefore, identification of tumor-specific nanostructures that naturally harbors endogenous tumor antigens and further engineering these structures to co-deliver immune stimulating adjuvants yielding potent anti-tumor immunity is of great benefit during the management of established tumors. A depot system that permits simultaneous presentation of tumor antigen as well as initiating tumor-specific immune activation could offer effective tumor targeting while reducing undesirable toxicity could pave the way for patient specific anti-cancer immunotherapy [4,5].

Exosomes with a size between 30 and 150 nm are small extracellular vesicles secreted (any small sized EVs irrespective of their biogenesis) by all type of mammalian cells [6]. Hereafter, the term "exosomes" refers to small EVs in this work. They mediate a novel mode of intercellular communication through their bioactive cargos such as lipids, nucleic acids, metabolites, and proteins, which can be delivered to the target cells [7]. Using their natural delivery capabilities, exosomes have been successfully served as immunotherapeutic nanocarriers in cancer treatment [8]. Furthermore, they are attractive as a delivery system because

* Corresponding author.
E-mail address: ihsangursel@bilkent.edu.tr (I. Gursel).
[1] Equal Contribution

https://doi.org/10.1016/j.imlet.2021.08.004
Received 14 March 2021; Received in revised form 26 July 2021; Accepted 12 August 2021
Available online 18 August 2021
0165-2478/© 2021 European Federation of Immunological Societies. Published by Elsevier B.V. All rights reserved.

of their stability in circulation, biocompatibility, and low toxicity [9,10, 11].

Tumor derived exosomes (TEXs) are appropriate tumor specific antigen sources to induce immunity against tumor cells since they are capable of even presenting endogenous tumor-specific neoantigens [12]. They can transfer a wide spectrum of immunogenic tumor antigens expressed in parental tumor cells to DCs and elicit tumor-specific cytotoxic T lymphocytes [13, 14]. As well as their modification by different methods to enrich tumor antigens, immunostimulatory molecules and microRNAs, TEXs can be loaded with therapeutic cargo [15,16]. These engineered TEXs can increase their uptake by antigen presenting cells, upregulate the expression of cancer-specific antigenic epitopes, repress immunosuppressive targets in the tumor microenvironment, improve DC maturation and enhance tumor cell elimination [17,18,19]. Moreover, Moreover, the feasibility to isolate TEXs from patients' sera enables their use in personalized immunotherapy [20]. Taken together, TEXs as a modified carrier for immunostimulatory agents along with tumor antigens can be a novel candidate for tumor vaccine.

Among immunostimulatory agents, nucleic acid-based adjuvants are safe and effective inducer of innate immune effector functions [21,22]. CpG oligonucleotides (CpG ODNs) recognized by Toll-like receptor 9 (TLR9) is one of the most extensively used adjuvants in the clinic to stimulate immune response characterized by the production of Th1 and pro-inflammatory cytokines [23,24] K type CpG ODN activates B cells and trigger plasmacytoid dendritic cells (pDCs) to secrete tumor necrosis factor–α (TNF-α) [25]. Polyinosinic-polycytidylic acid (p(I:C)), a TLR3 agonist, is another potent adjuvant that has been widely studied as an anti-tumor drug in cancer patients [26]. p(I:C) is shown to induce type I and II interferons (IFN) and the activation of CD4+ and CD8+ *T* cell responses overcoming immunosuppressive function of regulatory T cells in the tumor microenvironment [27, 28, 29, 30].

The simultaneous delivery of tumor cell-derived exosomes and adjuvants to the same immune cells could effectively induce a potent anti-tumor immune response. Herein, we co-encapsulated CpG ODN and p(I:C) into 4T1/Her2 cell-derived exosomes. These 4T1 breast cancer cells were modified to overexpress Her2 tumor antigen that are present within TEXs. Our results revealed that dual adjuvant encapsulating exosome vaccine induced a strong Th1-biased Her2-specific immune response and increased the production of type II IFNs. We also demonstrated that dual adjuvant co-encapsulating exosome vaccine generated Her2-specific CD4+ memory T cell. Moreover, when used as a therapeutic vaccine, CpG ODN and p(I:C) loaded exosomes significantly regressed 4T1 tumor growth in mice. Taken together, we present an exosome-based therapeutic vaccine candidate that could promote strong cellular and humoral anti-tumor immune responses that offers an effective personalized tumor therapy strategy in the clinic.

2. Materials and methods

2.1. Materials

TLR9 ligand, CpG-ODN GACGTTGACGTTGACGTTGG was purchased from Alpha DNA (Canada). TLR3 ligand, p(I:C) was from Amersham (Piscataway, NJ, USA). Her2/E75 peptide was purchased from Immunostep (Spain). All cell culture media components were from Gibco (NY, USA) and Lonza (Walkersville, MD, USA). Cytokine ELISA reagents: recombinant cytokine, monoclonal unlabeled and biotinylated antibody against m-IFNγ were purchased from Mabtech (Cincinnati, OH, USA). P-nitrophenyl phosphate disodium salt substrate (PNPP) was purchased from Thermo Scientific (USA).

Immunoglobulin ELISA reagents: goat anti-mouse total IgG, IgG1, IgG2a monoclonal antibodies conjugated with alkaline phosphatase (AP) were from Southern Biotech (Birmingham, AL, USA). FACS antibodies conjugated to fluorescent chromophores were obtained from Biolegend. Rabbit monoclonal antibody against TSG101 and rabbit monoclonal antibody against Her2/ErbB2 were from Abcam (Cambridge, UK) and Cell Signaling (Massachusetts, USA) respectively. Cytofix/Cytoperm and Perm/wash buffer were purchased from BD (New Jersey, USA).

2.2. Mice and cell lines

Adult Balb/c mice (female, 6–8 weeks old) were kept in the Bilkent University animal housing facility of the Department of Molecular Biology and Genetics. Mice were housed under controlled conditions at 22 °C with 12 h light and 12 h dark cycles and provided with unlimited access of food and water. All experimental procedures were approved by the animal ethical committee of Bilkent University.

4T1-luc and 4T1/Her2 cell lines were cultured in Dulbecco's Modified Eagle Medium, (DMEM) with 10% fetal bovine serum (FBS). GFP tagged HER2 expressing mouse breast cancer cell line (4T1-HER2) was kindly provided by Prof. Michael Kershaw (Cancer Immunology Program, Peter MacCallum Cancer Center, Victoria, Australia) [41,42]. 4T1-luc cell line is originally developed by G Gary Sahagian [43].

2.3. Isolation of tumor derived exosomes from cell culture supernatant

Exosomes were isolated from 4T1/Her2 and 4T1-luc cell lines via differential ultracentrifugation method. Following supernatant collection from cultured cells, they were centrifuged at 1500 x g for 10 min at RT to discard the cell debris. Supernatants were transferred to ultracentrifugation tubes (Beckmann Coulter) and centrifuged at 10,000 x g for 10 min at +4 °C to remove any large particles, followed by a second centrifugation at 30,000 x g for 30 min. This generated a pellet consisting of medium sized EVs and an upper aqueous phase containing the exosomes. The supernatant was collected and passed through a 0.2 μm filter to ensure removal of larger particles. To sediment exosomes, filtered supernatant was centrifuged at 100,000 x g for 90 min at +4 °C. The pellet was washed once with PBS at 100,000 x g for another 90 min at +4 °C. Following washing, supernatants were aspirated, and the exosome pellet was resuspended in an appropriate volume of Ca^{2+}/Mg^{2+} free 1x PBS and used in further studies.

2.4. Exosome characterization

Forty μL of carboxyl modified latex beads (Life Technologies) were incubated with 40 μg of LEAF purified anti-mouse CD81 antibody (Biolegend) at RT for 30 min. Then, the volume was adjusted to 500 μL with 1x PBS and bead-antibody mix was incubated overnight at RT by continuous rotation. Following incubation, beads were blocked with 5% BSA containing 1x PBS for 4 h at RT by rotation. To analyze the specific molecules on exosomes, two μg of exosomes were mixed with anti-mouse CD81 conjugated beads and incubated at RT overnight. Following washing by centrifugation at 13,200 x g, bead-associated exosomes were incubated separately with 2 μg/mL anti-CD9-FITC, anti-CD81-PE antibodies in sodium azide containing FACS buffer or with their corresponding isotype controls for 30 min at RT. The exosome-bead complexes were washed and analyzed with Novocyte D3000 (Agilent, California, USA).

Total cellular and exosomal proteins were extracted using a RIPA lysis buffer and samples were vortexed and sonicated, respectively. Protein concentration was determined by BCA Protein Assay Reagent Kit (Thermo Scientific). Twenty five μg of cell lysate, medium sized EVs lysate or exosome lysate were separated on 10% SDS-polyacrylamide gel for 90 min at 120 V following 10 min run on 5% SDS-polyacrylamide resolving gel and then were transferred to PVDF membranes (Thermo Scientific) by applying 100 V for 90 min. Membranes were blocked with 5% non-fat dry milk containing 1x PBS-T for 2 h at RT. Then, blocked membranes were incubated with primary antibodies against TSG101 (Abcam) or Her2 (Cell Signaling) prepared in 5% non-fat dry milk containing 1x PBS-T at a 1:1000 dilution at +4 °C overnight. Following primary antibody incubation, membranes were washed and incubated

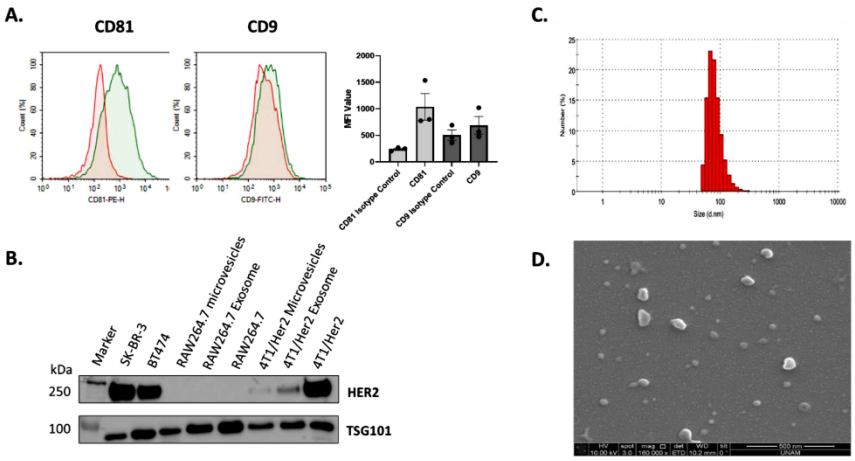


Fig. 1. Characterization of exosomes isolated from 4T1/Her2 cell line. A) Exosomes coupled to anti-CD81 conjugated beads were phenotyped using flow cytometry analysis. Bar graphs represent the average MFI values of specific antibodies to isotype control staining of 3 separate exosome batches. **B)** Western blot analysis of exosomal marker TSG101, and Her2 expression in total cell extracts and cell-derived exosomes. (SK-BR-3 and BT474 cell lines were used as positive controls and RAW264.7 cell line was used as a negative control) **C)** Dynamic Light Scattering (DLS) analysis showing average size distribution of 4T1/Her2 cell-derived exosomes (n = 3 independent batches) **D)** A representative scanning electron microscopy (SEM) image of 4T1/Her2 cell-derived exosomes. Scale bar represents 500 nm.

with 1:5000 diluted secondary antibodies, HRP conjugated horse anti-mouse IgG (Cell Signaling) for Tsg101 and Her2 in 5% non-fat dry milk supplemented 1x PBS-T at RT for 1 h Membranes were developed using the chemiluminescent detection kit, ECL+ from Amersham according to the manufacturer's protocols and visualized by Amersham Chemiluminescence Imager 600 (GE, Amersham).

To analyze the size of exosomes by dynamic light scattering (DLS) using Zetasizer Nano ZS (Malvern, UK), exosomes were diluted in PBS and triplicate readings of samples were recorded.

Purified exosomes were verified by scanning electron microscopy (SEM). Ten μL of the exosome solution were deposited on silica surfaces. After evaporation, samples were sputter-coated with 8 nm of Au/Pd alloy using a precision coating system (Gatan Inc, USA).

2.5. Loading of exosomes with CpG ODN and p(I:C)

Thirty μg of exosome were mixed with 30 μg CpG ODN and 30 μg pI:C. The mixture was snap-frozen in liquid nitrogen and lyophilized overnight in VirTis Bench Top K Freeze Dryer (SP Industries, PA, USA). The exosome-ligand powder mixture was rehydrated in a controlled fashion by addition of nuclease free ddH_2O. Then, this rehydrated mixture was vortexed for 15 s every 2 min for a period of 20 min. Next, 1 x Ca2 + /Mg2 + free PBS was added, and the mixture was incubated at RT for another 10 min. Then, the mixture was vortexed for 15 s and the controlled rehydration process was completed with the addition of 1x Ca2+/Mg2+ free PBS to adjust the desired concentration of ligand encapsulated exosome solution. As such prepared exosome formulations were maintained at +4 °C until further use.

The encapsulation efficiency was performed from three independent batches of each exosome preparations. To detect CpG ODN loading, 30 μg Cy5-labeled CpG ODN and 30 μg unlabeled pI:C were mixed with 30 μg of exosome. Following reconstitution as described above, the Cy5-signal was followed both from the exosome pellet and from the unencapsulated fraction of supernatant using fluorometer. Next, 30 μg unlabeled CpG ODN and 30 μg FITC-labelled pI:C were mixed with 30 μg of exosome, and same procedure was performed to identify the pIC loading. For each ligand the encapsulation efficiencies were found to be 88.8 ± 9.2% for the CpG ODN and 94.1 ± 7.3% for pIC.

2.6. Immunization of balb/c mice and splenocyte isolation

6–8 weeks-old female Balb/c mice (4 per group) were vaccinated 2 times in 2-week intervals intraperitoneally (I.P) with PBS, only 30 μg exosome, free form of 30 μg exosome+30 μg CpG ODN and 30 μg p(I:C) or exosome loaded with CpG ODN+p(I:C). Two weeks after the last booster dose, all mice were sacrificed and their splenocytes and blood serum were collected aseptically for the detection of cellular immune responses.

2.7. In vitro stimulation

Splenocytes (2×10^6 cell/mL in 250 μl) were stimulated with 10 μg/mL 4T1/Her2 cell-derived exosome for 72 h at 37 °C in a 5% CO_2 incubator. After stimulation, the supernatants were collected and used for IFNγ cytokine ELISA.

2.8. Enzyme-linked immunosorbent (ELISA) assay

Immulon 2 HB microtiter plates (Thermo Scientific, San Jose, CA, USA) were coated with Her2 E75 peptide (40 μg/mL), 4T1/Her2 cell lysate (10 μg/mL), 4T1/Her2 exosome lysate (10 μg/mL) and anti-mouse IFNγ (2 μg/mL) respectively, and then blocked with PBS-BSA. Serially diluted standards and culture supernatants or serially diluted mouse sera were added to plates for overnight at 4 °C. Cytokine was detected using biotinylated anti-mouse IFNγ (1 μg/mL) antibody followed by phosphatase-streptavidin whereas bound IgG subclasses were detected using alkaline phosphatase streptavidin conjugated anti-mouse IgG (1:1000), anti- mouse IgG1 (1:1000) and anti-mouse IgG2a

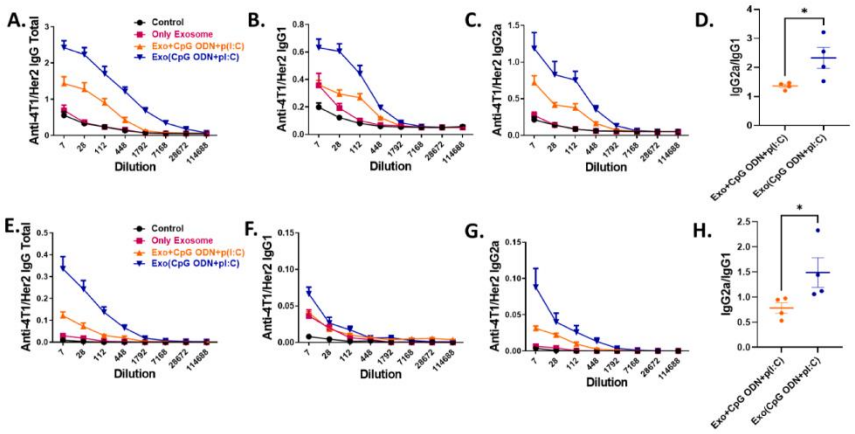


Fig. 2. 4T1/Her2 cell-derived exosomes loaded with CpG ODN and p(I:C) immunization generates sustained and magnified anti-4T1/Her2 immune responses. Mice ($n = 4$ mice/group) were injected i.p. with PBS, only 30 μg exosomes, free form of 30 μg exosomes+30 μg CpG ODN and 30 μg p(I:C) or exo(CpG ODN+p(I:C)) on days 0 and 14. Mice were sacrificed on day 28. **A-C)** Sera of immunized mice were investigated for systemic anti-4T1/Her2 antibody production against 4T1/Her2 cell lysate. End-point average titers of anti-4T1/Her2 total IgG, IgG1 and IgG2a responses of mice were shown. **D)** IgG2a/IgG1 ratio of individual mouse either immunized with free or immunized with exosomal formulation at 2 weeks after booster injection (at 1:120 dilution against 4T1/Her2 cell Lysate). Mann-Whitney test was used for statistical analysis. **E-G)** Sera of immunized mice were investigated for systemic anti-4T1/Her2 antibody production against protein extracts of 4T1/Her2 cell-derived exosomes. End-point average titers of anti-4T1/Her2 total IgG, IgG1 and IgG2a responses were shown. **H)** IgG2a/IgG1 ratio of individual mouse either immunized with free or immunized with exosomal formulation at 2 weeks after booster injection (at 1:15 dilution against protein extracts of 4T1/Her2 cell-derived exosomes). Mann-Whitney test was used for statistical analysis. The data indicate the mean ± SEM ($n = 4$). Statistically significant differences designated as follows: ns: $p > 0.05$, *:$p < 0.05$. Exo: exosome.

(1:1000) antibodies and developed by the addition of PNPP substrate.

2.9. Intracellular cytokine assay via flow cytometry

10^6 cells/mL of splenocytes in medium containing Brefeldin A (5 μg/mL, was included in the last 6 h) was stimulated with 4T1/Her2 derived exosomes (10 μg/mL) for 24 h at 37 °C. After stimulation, cells washed two times with stain buffer (2% FCS in PBS). Cells were stained with 1 μg/mL anti CD45-PE/Cy7, anti CD3-Pacific Blue, anti CD4-FITC, anti CD8-PE, anti CD44-APC/Cy7, anti CD62L-BV605 for 30 min at 4 °C. The cells were washed with stain buffer and fixed with Cytofix/Cytoperm solution. Fixed cells were washed two times with Perm/Wash buffer and then stained with 1 μg/mL anti IFNγ-FITC antibody for 30 min at 4 °C. The cells were washed with Perm/Wash buffer and suspended in 300 μL stain buffer for flow cytometric analysis with Novocyte D3000 (Agilent, California, USA).

2.10. The therapeutic model of 4T1-luc tumor mice model

6–8 week-old female Balb/c mice were injected with 2×10^5 4T1-luc tumor cells into right mammary fat pads orthotopically with 5–6 mice per group. Tumor-bearing mice were then intraperitoneally injected with a PBS and 30 μg exosome loaded with 30 μg CpG ODN and 30 μg p(I:C) at day =, 1, 4, 7, 10, 17, 24 and 31 after tumor inoculation. Tumor growth was monitored by measuring the tumor volume with a caliper after tumors become palpable. Tumor volumes were calculated as length × width^2/2.

For IVIS spectrum, Caliper Lifesciences Lumina III series was used to visualize tumor growth and each mouse received 150 mg Luciferin/kg according to the datasheet suggestion.

2.11. Statistical analysis

One-way ANOVA with Kruskal Wallis and Mann–Whitney tests were employed to assess the significance of differences among the groups. Survival analysis was performed using log-rank test (GraphPad Prism version 9, San Diego, California). $P <$ 0.05 was statistically significant.

3. Results

3.1. Characterization of exosomes

Exosomes were isolated from the 4T1/Her2 cell culture supernatants using differential ultracentrifugation method as described in Material and Methods. Isolated exosomes were subjected to analysis of i) surface marker expression by flow cytometry, ii) exosome-specific protein and Her2 expression by immunoblotting, iii) size distribution by DLS and iv) morphological analysis by SEM. Exosomes were verified by detecting the expression of positive protein markers CD81, CD9 (Fig. 1A) and TSG101 (Fig. 1B). Tumor cell-derived exosomes are a good source of cellular components that stimulate the immune response, such as tumor-associated antigens. To check whether the isolated exosome pools carry antigen, we confirmed that purified exosomes of 4T1/Her2 cells also express Her2 whereas isolated exosomes of RAW264.7 as a negative control does not (Fig. 1B). The size of exosomes abundantly ranged from 40 to 190 nm (Ave. Mean Size:70 ± 20 nm, Fig. 1C). Under scanning electron microscopy (SEM), the purified exosomes exhibited a typical round-shaped structures (Fig. 1D). Collectively, these findings support that extracellular nanovesicles derived from 4T1/Her2 cell line displays convincing exosome features.

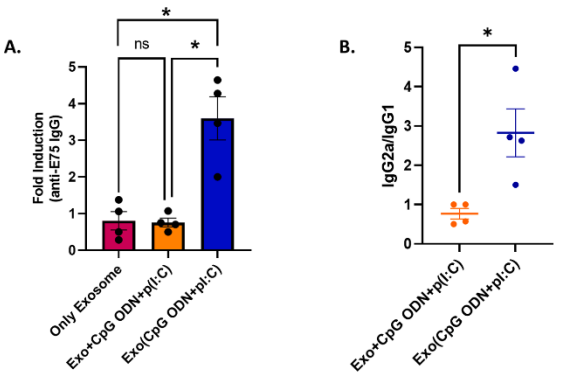


Fig. 3. 4T1/Her2 cell-derived exosome loaded with CpG ODN and p(I:C) immunization magnified anti-E75 immune responses. Mice (n = 4 mice/group) were injected i.p. with PBS, only 30 μg exosome, free form of 30 μg exosome + 30 μg CpG ODN and 30 μg p(I:C) or exo(CpG ODN+p(I:C)) on days 0 and 14. Mice were sacrificed on 14 day after the booster injection **A)** Bar graphs showing fold induction over control group of sera of immunized mice for systemic antibody production against Her2/E75 peptide. **B)** IgG2a/IgG1 ratio of individual mouse either immunized with free or immunized with EV formulation at 2 weeks after booster injection (at 1:30 dilution against Her2/E75 peptide). Mann-Whitney test was used for statistical analysis. The data indicate the mean ± SEM (n = 4). Statistically significant differences designated as follows: ns: $p > 0.05$, *: $p < 0.05$. Exo: exosome.

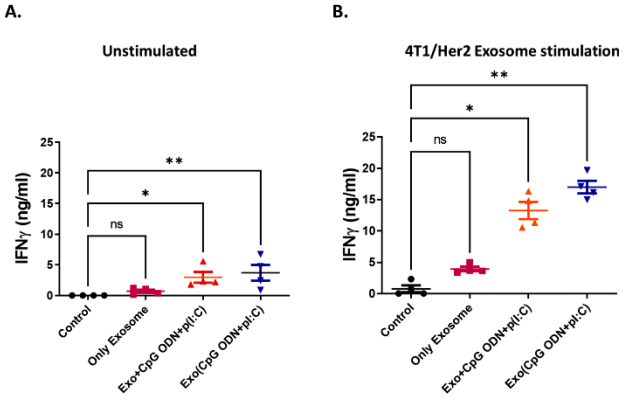


Fig. 4. IFNγ assay on ex vivo expanded splenocytes of mice immunized two times with PBS, unencapsulated 30 μg exosome, mixture of 30 μg Exosome + 30 μg CpG ODN and 30 μg p(I:C) or exosome co-loaded with (CpG ODN+p(I:C)) A) Fourteen days after the booster, the spleens of mice from each group were harvested and immune responses were evaluated using an IFNγ ELISA assay. **B)** Fourteen days after the booster, spleens of mice (n = 4) were harvested and incubated with 4T1/Her2 exosome in culture for 72 hrs and the secreted IFNγ levels were then evaluated using IFNγ ELISA kit. The data indicate the mean+SEM (n = 4). Statistical significance was analyzed by Kruskal Wallis test. Statistically significant differences designated as follows: ns: $p > 0.05$, *: $p < 0.05$, **: $p < 0.01$. Exo:exosome.

3.2. Humoral immune responses

We intended to develop an exosomal carrier system co-encapsulating two nucleic acid-based TLR ligands as immunoadjuvants naturally expressing tumor-associated antigen Her2 and analyzed its potency as a prophylactic and therapeutic vaccine. Previous studies have shown that tumor derived exosomes have a dual effect on the immune system, immunosuppressive or immunostimulatory effects. To combine and enhance the synergistic immunostimulatory activity of TLR3 (p(I:C)) and TLR9 (CpG ODN) ligands, we co-encapsulated them within 4T1/Her2 cell-derived exosomes thereby aimed to achieve simultaneous antigen and adjuvant delivery to relevant antigen presenting cell. Next, we assessed the humoral responses from sera of mice collected at day 28 following twice (@Day = 0 and 14) i.p. injection to Balb/c mice. 4T1/Her2-specific total IgG, IgG1 and IgG2a titers against 4T1/Her2 total cellular protein extract or 4T1/Her2 total exosome extract were analyzed by ELISA. As expected, there was no 4T1/Her2-specific antibody production in the control group and only exosome injected animals raised strong antibody titers. Besides, the level of 4T1/Her2 specific total IgG, IgG1 and IgG2a in sera of mice immunized with dual ligand-loaded exosomal group was significantly higher than those animals that was immunized with free combination of antigen containing exosome and TLR ligands (Fig. 2A–C and Fig 2E–G). We also detected significantly elevated IgG2a/IgG1 ratio after immunization with exosomes co-encapsulating p(I:C) and CpG ODN indicating the development of antigen specific Th1-biased immunity ($p = 0.0286$ for both antigens) (Fig. 2D and Fig 2H).

Furthermore, we analyzed whether exosome loaded with CpG ODN and p(I:C) produce Her2 specific antibodies. To assess this, we used Her2 specific E75 peptide. As shown in Fig. 3A, mice immunized with dual ligand loaded exosomes produced significantly higher Her2/E75 specific total IgG antibody compared to mice immunized with only exosome and free form of exosomal combination ($p = 0.0286$). We detected significantly elevated IgG2a/IgG1 ratio after immunization with CpG ODN plus p(I:C) loaded exosomes ($p = 0.0286$ for both antigens, Fig. 3B). Collectively these results pointed out that CpG ODN and p(I:C) loaded exosomes elicited anti-4T1/Her2 and Her2/E75 specific Th1-biased immunity.

3.3. Induction of specific IFNγ from splenocytes

To evaluate the type of immune response generated, splenocytes

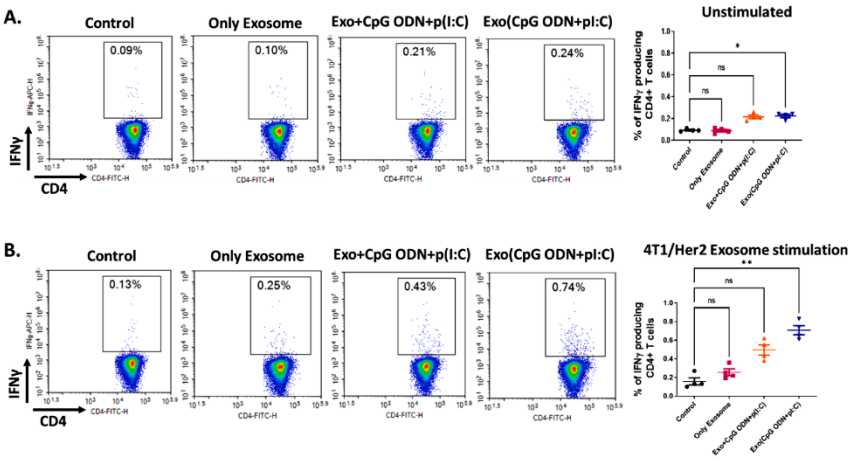


Fig. 5. Intracellular cytokine production from splenocytes of mice immunized two times with PBS, unencapsulated 30 μg exosome, mixture of 30 μg exosome plus 30 μg CpG ODN and 30 μg p(I:C) or exosome co-loaded with (CpG ODN+*p*(I:C)). A) Fourteen days after the booster, isolated splenocytes of different groups of vaccinated mice (4 mice from each group) were stained with CD45-PE/Cy7, CD3-Pacific Blue, CD4-FITC surface markers and then with anti-IFNγ-APC antibodies. **B)** Fourteen days later the booster, isolated splenocytes of different groups of vaccinated mice were stimulated with 4T1/Her2 exosome for 24 hrs in culture and stained with CD45-PE/Cy7, CD3-Pacific Blue, CD4-FITC surface markers and then with anti-IFNγ-APC antibodies. The frequency of IFN-γ producing cells within CD4+ population were determined by Novocyte 3000 Cell analyzer. The data indicate the mean±SEM ($n = 4$). Statistical significance was analyzed by Kruskal Wallis test. Statistically significant differences designated as follows: ns: $p > 0.05$, *:$p < 0.05$, **: $p < 0.01$. Exo:exosome.

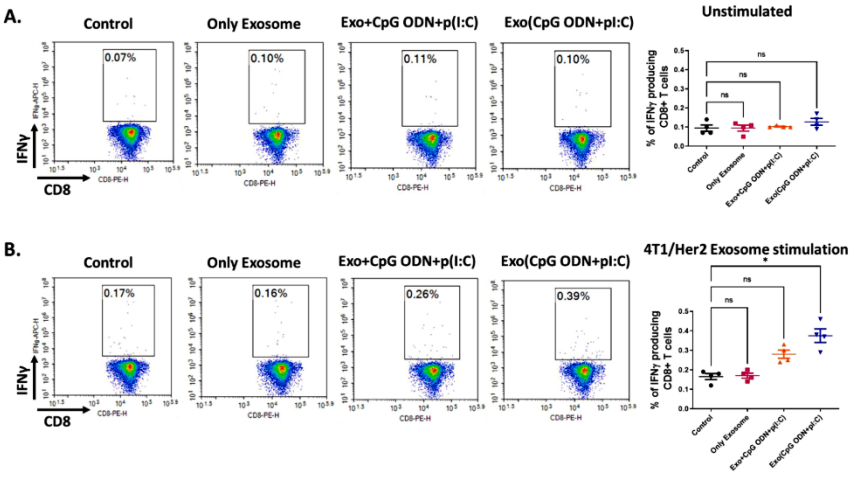


Fig. 6. Intracellular cytokine production assay on splenocytes of mice immunized two times with PBS, unencapsulated 30 μg exosome, mixture of 30 μg exosome + 30 μg CpG ODN and 30 μg p(I:C) or exosome co-loaded with (CpG ODN+p(I:C)). A) Fourteen days later after the booster, isolated splenocytes of different groups of vaccinated mice (4 mice from each group) were stained with CD45-PE/Cy7, CD3-Pacific Blue, CD8-PE surface markers and then with anti-IFNγ-APC antibodies. **B)** Fourteen days later after the booster, isolated splenocytes of different groups of vaccinated mice were incubated with 4T1/Her2 exosome for 24 hrs and stained with CD45-PE/Cy7, CD3-Pacific Blue, CD8-PE surface markers and then with anti-IFNγ-APC antibodies. The frequency of IFN-γ producing cells within CD8+ population were determined by Novocyte 3000 Cell analyzer. The data indicate the mean ± SEM ($n = 4$). Statistical significance was analyzed by Kruskal Wallis test. Statistically significant differences designated as follows: ns: $p > 0.05$, *:$p < 0.05$. Exo:exosome.

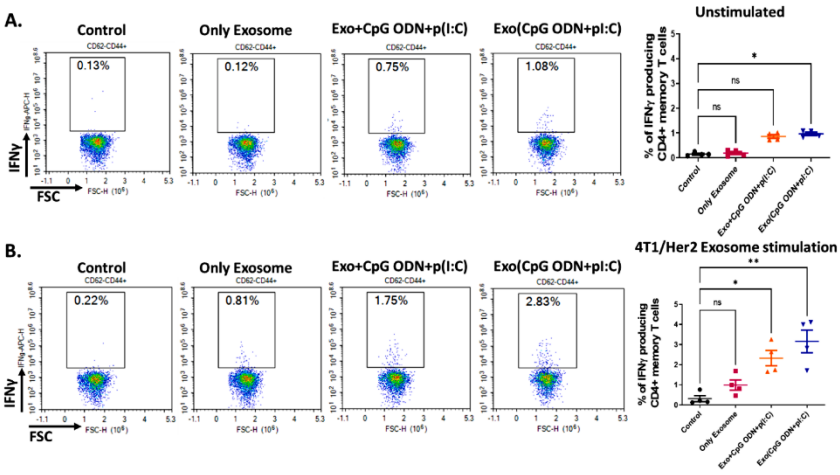


Fig. 7. IFN-γ producing CD4+ memory T cell assay on splenocytes of mice immunized two times with PBS, unencapsulated 30 μg exosome, mixture of 30 μg exosome+30 μg CpG ODN and 30 μg p(I:C) or co-loaded with (CpG ODN+*p*(I:C)). A) Fourteen days later after the booster, isolated splenocytes of different groups of vaccinated mice (4 mice from each group) were stained with CD45-PE/Cy7, CD3-Pacific Blue, CD4-FITC, CD44-APC/Cy7, CD62L-BV605 surface markers and then with anti-IFNγ-APC antibodies. **B)** Fourteen days later after the booster, isolated splenocytes of different groups of vaccinated mice were stimulated with 4T1/Her2 exosome in culture for 24 h and stained with CD45-PE/Cy7, CD3-Pacific Blue, CD4-FITC, CD44-APC/Cy7, CD62L-BV605 surface markers and then with anti-IFNγ-APC antibodies. CD4+ memory T cell was identified as CD45+CD3+CD4+CD8-CD44^{high}CD62L^{low}. The frequency of IFN-γ producing memory T cells within CD4+ population were determined by Novocyte 3000 Cell analyzer. The data indicate the mean ± SEM (n = 4). Statistical significance was analyzed by Kruskal Wallis test. Statistically significant differences designated as follows: ns: $p > 0.05$, *:$p < 0.05$, **: $p < 0.01$. Exo:exosome.

were isolated two weeks after the last booster injection and IFNγ production was analyzed by ELISA assay. As shown in Fig. 4A, we detected that both non-encapsulated combination and dual ligand co-encapsulated exosome group generated more IFNγ compared to control group ($p = 0.0143$, $p = 0.0089$, respectively). Furthermore, Fig. 4B shows that when the splenocytes of immunized mice were activated with 4T1/Her2 exosomes, specific IFNγ productions of non-encapsulated combination and co-encapsulated exosome group were boosted significantly compared to control groups ($p = 0.0347$, $p = 0.0019$, respectively).

3.4. CD4+ and CD8+ T cell responses

To further differentiate the contribution of TLR ligand co-encapsulation within exosomes on cellular immunity that was raised against 4T1 tumors, we performed IFNγ specific intracellular cytokine staining on splenocytes. To this end, the IFNγ + *T*-cell subsets following staining of CD4 and CD8 positive T cells were analyzed by flow cytometry. The data showed that before and after 4T1/Her2 exosome stimulation in culture the induction of IFNγ producing +CD4 *T* cells were significantly higher in mice immunized with exosomes loaded with TLR ligands compared to the control groups. ($P = 0.046$, $P = 0.0032$ respectively) (Fig. 5A, B).

As seen in Fig 6, similarly intracellular cytokine staining assay revealed that when splenocytes were stimulated overnight with 4T1/Her2 exosome in culture, only Exo(CpG ODN+p(I:C)) group had significantly augmented IFNγ production from CD8+ *T*-cells compared to the control group ($P = 0.0127$).

4T1/Her2 specific memory T-cell is one of the major contributing cell populations to eliminate Her2 expressing tumor cells, therefore, we analyzed the immunized mice splenocytes to assess the antigen-specific CD4+ memory T cell percentage. We determined that mice immunized with Exo(CpG ODN+p(I:C)) generated significantly higher IFNγ producing CD4+ memory T cell compared to the control group ($p = 0.016$) (Fig. 7A). When immunized mice cells were incubated with 4T1/Her2 expressing exosome, IFNγ producing CD4+ memory T cells expanded significantly in Exo(CpG ODN+ *p*(I:C)) treated group compared to the control group ($p = 0.0042$) (Fig. 7B).

3.5. Therapeutic effects of exosome vaccination in 4T1-luc bearing BALB/c mice

Considering the strong cellular and humoral immune responses in vaccinated mice (Figs. 2–7), it was expected that the immune responses would lead to antitumor activity in an established 4T1-luc tumor model. To evaluate if the cellular and humoral immune responses induced by the Exo(CpG ODN+p(I:C)) vaccination were potent enough to induce an in vivo antitumor effect, the mice were injected with 4T1-luc tumor cells orthotopically into the right mammary fat pads. Following after tumor inoculation, animals were intraperitoneally injected with Exo(CpG ODN+*p*(I:C)) and were observed for tumor regression during 36 days post tumor formation. As shown in Fig. 8A, during the days 10–36, the group of mice that received Exo(CpG ODN+p(I:C)) regressed tumor development significantly in comparison with untreated control group ($P = 0.0045$ for day 32 and $P = 0.0024$ for day 36). Also, the survival time was significantly prolonged in Exo(CpG ODN+p(I:C)) treated groups in comparison with the control group receiving PBS ($P = 0.0229$). All mice belonging to control group were dead by day 49 whereas 3 out of 5 mice treated with Exo(CpG ODN+p(I:C)) were alive by day 60. Furthermore, We analyzed the IFNγ secretion, helper T cell and cytotoxic T cell population from splenocytes of animals that treated with the PBS and CpG ODN+p(I:C) loaded exosomes at day= 1, 4, 7, 10, 17, 24 and 31 after tumor inoculation. As shown in Fig. 8B, Splenocytes from animals that treated with TLR ligands loaded formulation secretes

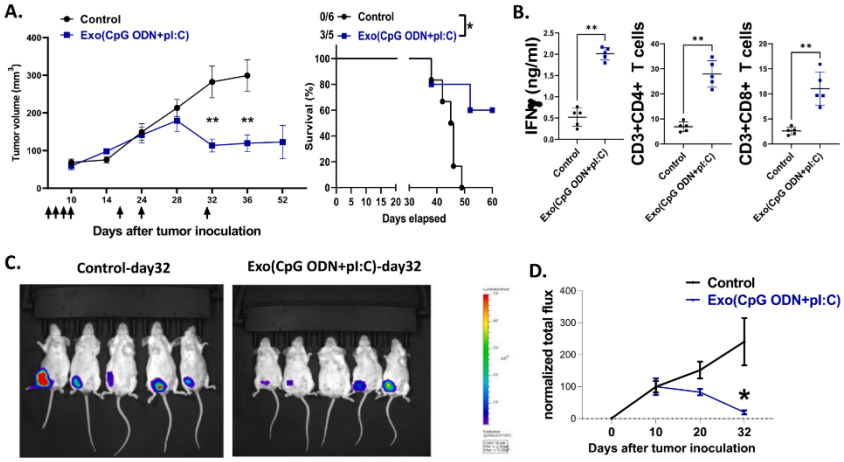


Fig. 8. Therapeutic effect of vaccination with PBS and exo(CpG ODN+*p*(I:C)) in BALB/c mice against a 4T1-luc in vivo established tumor mice model A) 4T1-luc tumor development is suppressed by immunization with exosome co-loaded with CpG ODN+*p*(I:C) (30ug each, arrows indicates i.p. injections of exosome vaccine formulation) and the effect of vaccination on the survival time of mice (6 for control group and 5 for vaccinated group) was observed during a 60-day period post tumor inoculation. **B)** IFNγ assay, Helper T cell and Cytotoxic T cell staining on ex vivo expanded splenocytes of mice treated with PBS, and exosome loaded formulation **C)** In vivo luciferase images of 4T1-luc tumors in control and vaccinated group at day 32. (IVIS Spectrum). **D)** Luciferin signal activity normalized to the signal obtained at day 1 following ortholog tumor injection. Tumor volume plot is collected from 2 independent experiments ($n = 5$ in each group). Mann-Whitney test was used for statistical analysis. Statistical significance for tumor volume and survival time was analyzed by Šídák's multiple comparisons test and Log-rank (Mantel-Cox) test, respectively. Normalized total flux was analyzed by Bonferroni's multiple comparisons test. Statistically significant differences designated as follows: ns: $p > 0.05$, *:$p < 0.05$, **: $p <$ 0.01.Exo:exosome.

significantly higher level of IFNγ. Also, we found that the percentage of CD4+ and CD8+ T cells in splenocytes are significantly higher than mice treated with TLR ligands loaded exosomes compared to control group($P = 0.0079$).The anti-tumor effect of Exo(CpG ODN+*p*(I:C)) group was evaluated by measurement using an IVIS imaging system. We measured bioluminescence activity every 10 days (day 0, day 10, day 20 and day 32 after tumor inoculation).As shown in the bioluminescence imaging results at day32, 1 out of 5 mice treated with Exo(CpG ODN+p(I:C)) had no luciferase signal (Fig. 8C) and exosome treated group had significantly lower luciferin activity over time (Fig. 8D)

Collectively, our findings implied that a combination of p(I:C) and CpG ODN ligands within exosomal formulations induced stronger and persistent humoral and cellular anti-4T1/Her2 specific immune response sufficient to regress tumor growth.

4. Discussion

Tumor-derived exosomes (TEXs) are promising candidates as the next generation immuno-therapeutic vaccines against cancers. Besides being a good reservoir of various tumor antigens, TEXs take an active role in the communication of tumor cells in all steps of cancer development and regulate immune responses through both immunosuppressive and immunostimulatory functions [31]. It is of great significance to consider the safety profile of ligand loaded exosomes as less detrimental cancer antigen carriers as they initiate inflammatory responses due to its immunostimulatory nature of its cargo. We anticipate that the safety concerns could be alleviated due to its inflammatory character when harnessed as a therapeutic vaccine carrier. Due to this differential role of TEXs, and their limited immunogenicity, their modifications into an effective immuno-adjuvant delivery system that can stimulate a strong humoral and cell-mediated immune responses remains a challenge. In this study, we modified 4T1/Her2-cell-derived exosomes by loading with two potent adjuvants, CpG ODN and p(I:C). Modified exosomes co-encapsulating both CpG ODN and p(I:C) have shown immunostimulatory properties by activating antigen-specific primary and memory T cell responses. Furthermore, our exosome-based adjuvant vaccine stimulated robust Th1 type immune responses via the elevated secretion of IgG2a antibody and IFNγ, resulting in tumor regression in 4T1 tumor-bearing mice.

Combination of TLR adjuvants like CpG ODN and p(I:C) triggers synergistic immune response more apparently than their standalone counterparts when given within a carrier system [32]. Therefore, we evaluated to immunogenicity of modified TEXs co-encapsulated with the combination of both adjuvants. As expected, administration of only tumor derived exosomes to the mice did not generate statistically significant responses while exosomes loaded with CpG ODN and p(I:C) significantly increased CD4+ and CD8+ *T* cell responses and the production of antigen-specific antibodies (Fig. 2-7). It is important to note that while mixing exosomes with CpG ODN and p(I:C) improves CD4+ and CD8+ *T* cell specific IFNγ this response is neither significant from untreated control nor exosome alone treated animals. In this respect, only encapsulation of ligands within exosomes triggered significantly higher IFNγ from the these animals, although comparison of mixture treated group vs ligand loaded exosome group animals did not yield significantly different responses. Since co-encapsulating CpG ODN and p(I:C) was the most active than other treatment groups, we investigated its potential therapeutic effect against the established 4T1 tumor model in mice. Our exosome-based adjuvant formulation significantly regressed tumor growth (Fig. 8). Furthermore, the simple co-administration of adjuvant with TEXs in clinical trials resulted in insufficient anti-tumor immunity due to inefficient simultaneous delivery of tumor antigen and adjuvant to the same antigen presenting cells (APCs) [33]. In the present study, we successfully encapsulated two adjuvants into TEXs carrying endogenous antigens and have shown that

compared to co-administration mixture of (Exo+CpGODN+p(I:C)), co-encapsulation Exo(CpG ODN+p(I:C)) strategy yielded i) stronger antigen-specific Th1-biased humoral immunity, ii) higher levels of IFNγ secretion and iii) more IFNγ producing CD4+ and CD8+ T cells (Fig. 2-6).

Induction of tumor antigen-specific cytotoxic T lymphocytes and humoral immune responses generated by efficient delivery of tumor antigens to APCs are essential requirements for effective cancer immunotherapy [34]. For this reason, vaccines against cancers focus on the identification of immunogenic antigen epitopes that selectively stimulates the induction of robust T helper cells, B cells and cytotoxic T cells [35]. However, only a few tumor-associated antigens have been identified for many cancer types and they can be poorly immunogenic or may not be found in a significant percentage of patients [36]. Moreover, the identification and purification of new epitopes that can be able to activate T and B cells are incredibly challenging. Using experimental approaches to screen immunodominant epitopes is quite expensive and its complexity is required the support of bioinformatic based predictions. Therefore, we proposed to harness tumor-derived exosomes isolated from the tumor biopsy or a tumor cell that are capable of expressing all biologically relevant antigens (including the neoantigens) as an efficient cancer vaccine carrier, thereby excludes the need to identify these epitopes. Her2 is considered as an ideal target for cancer vaccine development regarding its 100-fold higher overexpression in patients with breast cancer and correlates with poor clinical outcomes [37]. E75 is a 9-amino acid human leukocyte antigen– (HLA-) restricted peptide located in the Her2 extracellular domain, which is currently under clinical trials [38]. Studies have shown that E75 peptide vaccine improve CTL and CD4+ Th1 responses [39,40], however, this vaccine can be used in limited patient population due to HLA class I restriction. Using TEXs from HER2-overexpressing cell lines as an adjuvant delivery system overcomes this restriction and activate more broad immune responses, since these exosomes express a full length Her2 molecule (Fig. 1) as well as the whole panel of tumor related antigens. Therefore, TEXs are potent delivery systems that can stimulate a breadth of T cell clones by presenting multiple antigenic epitopes. Besides stimulating strong Th1 type immune responses via the elevated production of IgG2a antibody against 4T1/Her2-derived exosomes (Fig. 2), our 4T1/Her2--derived exosome-adjuvant formulation efficiently activated humoral immune responses against E75 peptide as well (Fig.3). Based on these findings, using tumor-derived exosomes as a delivery system for cancer immunotherapy is more convenient and suitable approach, as it is applicable to all cancer types, where biopsies are available from the patient.

In conclusion, we demonstrated that modified TEXs with CpG ODN and p(I:C) co-encapsulation generated humoral and cell-mediated immune responses and regress tumor growth in 4T1 tumor-bearing mice. as a well as extended survival (Fig. 8). The combination of adjuvants with tumor antigens inherently expressed by tumor-derived exosomes (without inserting additional antigen epitope) exerted stronger anti-tumor immune responses. These findings propose a useful TEX-based adjuvant delivery system as a promising cell-free vaccine and are of great interest for future vaccine design experiments in the clinical practice.

5. Funding

This work was supported by Ministry of Development (Grant name: UMRAM-ASI, Project #: 2015BSV302 to I.G.).

Declaration of competing interest

The authors confirm that there are no known conflicts of interest associated with this publication.

Acknowledgments

We thank Dr. Gamze Aykut for breeding and daily caring of our animals. We extend our appreciation to Prof. Dr. Mayda Gursel and Dr. Tamer Kahraman for their insightful comments and critical reading of the manuscript.

References

[1] A.D. Waldman, J.M. Fritz, M.J. Lenardo, A guide to cancer immunotherapy: from T cell basic science to clinical practice, Nat. Rev. Immunol. (2020) 20, https://doi.org/10.1038/s41577-020-0306-5.
[2] S. Stevanovic, Identification of tumour-associated T-cell epitopes for vaccine development, Nat. Rev. Cancer. 2 (2002), https://doi.org/10.1038/nrc841.
[3] T. Cancer, G. Atlas, Integrated genomic analyses of ovarian carcinoma the cancer genome atlas research network, Nature (2011) 474, https://doi.org/10.1038/nature10166.Integrated.
[4] R.S. Riley, C.H. June, R. Langer, M.J. Mitchell, Delivery technologies for cancer immunotherapy, Nat. Rev. Drug Discov. 18 (2019), https://doi.org/10.1038/s41573-018-0006-z.
[5] L. Zhou, P. Zhang, H. Wang, D. Wang, Y. Li, Smart nanosized drug delivery systems inducing immunogenic cell death for combination with cancer immunotherapy, Acc. Chem. Res. (2020) 53, https://doi.org/10.1021/acs.accounts.0c00254.
[6] M. Tkach, C. Théry, Communication by Extracellular Vesicles: where we are and where we need to go, Cell 164 (2016), https://doi.org/10.1186/s12951-020-00711-5, 10.1016/j.cell.2016.01.043.
[7] M. Colombo, G. Raposo, C. Théry, Biogenesis, secretion, and intercellular interactions of exosomes and other extracellular vesicles, Annu. Rev. Cell Dev. Biol. (2014) 30, https://doi.org/10.1146/annurev-cellbio-101512-122326.
[8] D. Ha, N. Yang, V. Nadithe, Exosomes as therapeutic drug carriers and delivery vehicles across biological membranes: current perspectives and future challenges, Acta Pharm. Sin. B. (2016) 6, https://doi.org/10.1016/j.apsb.2016.02.001.
[9] E.V. B.atrakova, M.S. Kim, Using exosomes, naturally-equipped nanocarriers, for drug delivery, J. Control. Release. (2015) 219, https://doi.org/10.1016/j.jconrel.2015.07.030.
[10] J.G. Van den Boorn, J. Daßler, C. Coch, M. Schlee, G. Hartmann, Exosomes as nucleic acid nanocarriers, Adv. Drug Deliv. Rev. (2013) 65, https://doi.org/10.1016/j.addr.2012.06.011.
[11] P. Vader, E.A. Mol, G. Pasterkamp, R.M. Schiffelers, Extracellular vesicles for drug delivery, Adv. Drug Deliv. Rev. (2016) 106, https://doi.org/10.1016/j.addr.2016.02.006.
[12] Y. Huang, K. Liu, Q. Li, Y. Yao, Y. Wang, Exosomes function in tumor immune microenvironment, Adv. Exp. Med. Biol. (2018), https://doi.org/10.1007/978-3-319-74470-4_7.
[13] J. Wolfers, A. Lozier, G. Raposo, A. Regnault, C. Théry, C. Masurier, C. Flament, S. Pouzieux, F. Faure, T. Tursz, E. Angevin, S. Amigorena, L. Zitvogel, Tumor-derived exosomes are a source of shared tumor rejection antigens for CTL cross-priming, Nat. Med. 7 (2001), https://doi.org/10.1038/85438.
[14] M. Jiang, W. Zhang, R. Zhang, P. Liu, Y. Ye, W. Yu, X. Guo, J. Yu, Cancer exosome-derived miR-9 and miR-181a promote the development of early-stage MDSCs via interfering with SOCS3 and PIAS3 respectively in breast cancer, Oncogene (2020) 39, https://doi.org/10.1038/s41388-020-1322-4.
[15] L. Alvarez-Erviti, Y. Seow, H. Yin, C. Betts, S. Lakhal, M.J.A. Wood, Delivery of siRNA to the mouse brain by systemic injection of targeted exosomes, Nat. Biotechnol. (2011) 29, https://doi.org/10.1038/nbt.1807.
[16] J.M. Cooper, P.B.O. Wiklander, J.Z. Nordin, R. Al-Shawi, M.J. Wood, M. Vithlani, A.H.V. Schapira, J.P. Simons, S. El-Andaloussi, L. Alvarez-Erviti, Systemic exosomal siRNA delivery reduced alpha-synuclein aggregates in brains of transgenic mice, Mov. Disord. (2014) 29, https://doi.org/10.1002/mds.25978.
[17] S.I. Ohno, M. Takanashi, K. Sudo, S. Ueda, A. Ishikawa, N. Matsuyama, K. Fujita, T. Mizutani, T. Ohgi, T. Ochiya, N. Gotoh, M. Kuroda, Systemically injected exosomes targeted to EGFR deliver antitumor microrna to breast cancer cells, Mol. Ther. (2013) 21, https://doi.org/10.1038/mt.2012.180.
[18] A. Taghikhani, Z.M. Hassan, M. Ebrahimi, S.M. Moazzeni, microRNA modified tumor-derived exosomes as novel tools for maturation of dendritic cells, J. Cell. Physiol. (2019) 234, https://doi.org/10.1002/jcp.27626.
[19] L. Wang, X. Zhou, W. Zou, Y. Wu, J. Zhao, X. Chen, G.G. Zhou, Exosomes containing miRNAs targeting HER2 synthesis and engineered to adhere to HER2 on tumor cells surface exhibit enhanced antitumor activity, J. Nanobiotechnology. 18 (2020).
[20] Z. Xu, S. Zeng, Z. Gong, Y. Yan, Exosome-based immunotherapy: a promising approach for cancer treatment, Mol. Cancer. 19 (2020), https://doi.org/10.1186/s12943-020-01278-3.
[21] C.J. Desmet, K.J. Ishii, Nucleic acid sensing at the interface between innate and adaptive immunity in vaccination, Nat. Rev. Immunol. (2012) 12, https://doi.org/10.1038/nri3247.
[22] S. Pandey, T. Kawai, S. Akira, Microbial sensing by toll-like receptors and intracellular nucleic acid sensors, Cold Spring Harb. Perspect. Biol. 7 (2015), https://doi.org/10.1101/cshperspect.a016246.
[23] D.M. Klinman, Immunotherapeutic uses of CpG oligodeoxynucleotides, Nat. Rev. Immunol. (2004) 4, https://doi.org/10.1038/nri1329.
[24] A.M. Krieg, CpG still rocks! Update on an accidental drug, Nucleic Acid Ther (2012) 22, https://doi.org/10.1089/nat.2012.0340.

[25] D.M. Klinman, D. Currie, I. Gursel, D. Verthelyi, Use of CpG oligodeoxynucleotides as immune adjuvants, Immunol. Rev. (2004) 199, https://doi.org/10.1111/j.0105-2896.2004.00148.x.
[26] C.H. Ewel, W.J. Urba, W.C. Kopp, J.W. Smith, R.G. Steis, J.L. Rossio, D.L. Longo, M. Jane Jones, W. Gregory Alvord, C.M. Pinsky, J.M. Beveridge, K.L. McNitt, S. P. Creekmore, Polyinosinic-Polycytidylic Acid Complexed with Poly-L-lysine and Carboxymethylcellulose in Combination with Interleukin 2 in Patients with Cancer: clinical and Immunological Effects, Cancer Res 52 (1992).
[27] J.L. Lepe-Zuniga, J. Rotbein, J.U. Gutterman, Production of interferon-α induced by dsRNA in human peripheral blood mononuclear cell cultures: role of priming by dsRNA-induced interferons-γ and -β, J. Interferon Res. 9 (1989) https://doi.org/10.1089/jir.1989.9.445.
[28] A.E. Gelman, J. Zhang, Y. Choi, L.A. Turka, Toll-like receptor ligands directly promote activated CD4 + T cell survival, J. Immunol. (2004) 172, https://doi.org/10.4049/jimmunol.172.10.6065.
[29] M.L. Salem, A.N. Kadima, D.J. Cole, W.E. Gillanders, Defining the antigen-specific T-cell response to vaccination and poly(I:C)/TLR3 signaling: evidence of enhanced primary and memory CD8 T-cell responses and antitumor immunity, J. Immunother. 28 (2005), https://doi.org/10.1097/01.cji.0000156828.75196.0d.
[30] R. Perret, S.R. Sierro, N.K. Botelho, S. Corgnac, A. Donda, P. Romero, Adjuvants that improve the ratio of antigen-specific effector to regulatory T cells enhance tumor immunity, Cancer Res 73 (2013), https://doi.org/10.1158/0008-5472.CAN-13-0875.
[31] W. Olejarz, A. Dominiak, A. Zołnierzak, G. Kubiak-Tomaszewska, T. Lorenc, Tumor-derived exosomes in immunosuppression and immunotherapy, J. Immunol. Res. (2020), https://doi.org/10.1155/2020/6272498.
[32] M. Krummen, S. Balkow, L. Shen, S. Heinz, C. Loquai, H.-C. Probst, S. Grabbe, Release of IL-12 by dendritic cells activated by TLR ligation is dependent on MyD88 signaling, whereas TRIF signaling is indispensable for TLR synergy, J. Leukoc. Biol. (2010) 88, https://doi.org/10.1189/jlb.0408228.
[33] Y. Sun, J. Liu, Potential of cancer cell-derived exosomes in clinical application: a review of recent research advances, Clin. Ther. (2014) 36, https://doi.org/10.1016/j.clinthera.2014.04.018.
[34] A.W. P., J. M., J. R., More than one reason to rethink the use of peptides in vaccine design, Nat. Rev. Drug Discov. 6 (2007).
[35] J.S. Testa, R. Philip, Role of T-cell epitope-based vaccine in prophylactic and therapeutic applications, Future Virol 7 (2012), https://doi.org/10.2217/fvl.12.108.
[36] A. Arora, S.A. Ahmad, C.E. Binkley, W.M. Burke, A.E. Chang, V.M. Cimmino, K. M. Diehl, G.M. Doherty, D.A. DuBay, E.M. Gartner, P.G. Gauger, J.D. Geiger, S. D. Gitlin, K. Graziano, P.J. Hodul, E.H. Huang, M.D. Iannettoni, K.M. Woods Ignatoski, C. Johnston, J. Kim, J. Lin, Q.P. Ly, E.A. Newman, J.M. Pow-Sang, M. E. Ray, A. Rodriguez, D.E. Rollison, M.S. Sabel, E.A. Shaughnessy, D.M. Simeone, V.K. Sondak, S.L. Sugg, J.J. Sussman, S. Tsai, C.Y. Williams-Covington, K. Wilson, M.J. Wolfe, D.T. Woodrum, Contributors, Essentials Surg. Oncol. (2007), https://doi.org/10.1016/b978-0-8151-4385-7.50004-7.
[37] Y. Yarden, Biology of HER2 and its importance in breast cancer, Oncology (2001), https://doi.org/10.1159/000055396.
[38] R.L.B. Costa, B.J. Czerniecki, Clinical development of immunotherapies for HER2+ breast cancer: a review of HER2-directed monoclonal antibodies and beyond, Npj Breast Cancer 6 (2020), https://doi.org/10.1038/s41523-020-0153-3.
[39] E.A. Mittendorf, J.P. Holmes, S. Ponniah, G.E. Peoples, The E75 HER2/neu peptide vaccine, Cancer Immunol. Immunother (2008), https://doi.org/10.1007/s00262-008-0540-3.
[40] M.T. Hueman, A. Stojadinovic, C.E. Storrer, Z.A. Dehqanzada, J.M. Gurney, C. D. Shriver, S. Ponniah, G.E. Peoples, Analysis of naive and memory CD4 and CD8 T cell populations in breast cancer patients receiving a HER2/neu peptide (E75) and GM-CSF vaccine, Cancer Immunol. Immunother. (2007) 56, https://doi.org/10.1007/s00262-006-0188-9.
[41] M.H. Kershaw, J.T. Jackson, N.M. Haynes, et al., Gene-engineered T cells as a superior adjuvant therapy for metastatic cancer, J. Immunol. 173 (3) (2004) 2143–2150.
[42] C.S. Özverel, Y. Uyanikgil, İ. Karaboz, A. Nalbantsoy, Investigation of the combination of anti-PDL1 mAb with HER2/neu-loaded dendritic cells and QS-21 saponin adjuvant: effect against HER2 positive breast cancer in mice, Immunopharmacol Immunotoxicol 42 (4) (2020) 346–357, https://doi.org/10.1080/08923973.2020.1775644.
[43] M.Fang K.Tao, G.G.Sahagian J.Alroy, Imagable 4T1 model for the study of late stage breast cancer, BMC Cancer 8 (2008) 228, https://doi.org/10.1186/1471-2407-8-228.

Clinical & Experimental Metastasis (2017) 34:449–456
https://doi.org/10.1007/s10585-018-9886-x

MEETING REPORT

EACR-MRS conference on Seed and Soil: In Vivo Models of Metastasis

I. Teles Alves[1] · N. Cohen[2] · P. G. Ersan[3] · R. Eyre[4] · I. Godet[5,6] · D. Holovanchuk[7] · R. Jackstadt[8] · L. Kyjacova[9] · K. Mahal[7] · A. Noguera-Castells[10] · L. Recalde-Percaz[11,12] · J. P. Sleeman[8,13,14]

Received: 9 February 2018 / Accepted: 10 March 2018 / Published online: 27 March 2018
© Springer Science+Business Media B.V., part of Springer Nature 2018

Abstract
New experimental tools are urgently required to better understand the metastatic process. The importance of such tools is underscored by the fact that many anti-cancer therapies are generally ineffective against established metastases. This makes a major contribution to the fact that metastatic spread is responsible for over 90% of cancer patient deaths. It was therefore timely that the recent "Seed and Soil: In Vivo Models of Metastasis" conference held in Berlin, Germany (27–29 of November 2017) aimed to give an in-depth overview of the latest research models and tools for studying metastasis, and to showcase recent findings from world-leading metastasis researchers. This Meeting Report summarises the major themes of this ground-breaking conference.

Keywords Metastasis · Mouse models · Signaling

Introduction

The "Seed and Soil: In Vivo Models of Metastasis" conference was held in Berlin, Germany from the 27–29 of November 2017, and was the first ever joint conference held by the European Association for Cancer Research (EACR) and the Metastasis Research Society (MRS). Spear-headed by the conference chair Janine Erler with support from the scientific programme committee (Jonathan Sleeman, Ulrike Stein and Christof von Kalle), the conference focused on the latest exciting developments in modelling metastasis, including new animal models and advances in imaging techniques. Harnack House, the historic meeting place of the Max Planck Society that has hosted discussions between numerous Nobel Prize winners and other leading scientists over more than a century, provided an inspiring and atmospheric location for the conference. The intimate setting with a limited number of participants and innovative features such as the "conference debate", "round table discussions" and "meet-the-expert" sessions all helped to foster collaborations

✉ I. Teles Alves
ines.alves@springernature.com

1 Department of Cell Biology and Biochemistry, Springer Science + Business Media B.V., Dordrecht, The Netherlands

2 Department of Pathology, Sackler School of Medicine, Tel Aviv University, Tel Aviv, Israel

3 Departments of Molecular Biology and Genetics, Faculty of Science, Bilkent University, Ankara, Turkey

4 Breast Biology Group, Breast Cancer Now Research Unit, Division of Cancer Sciences, Faculty of Biology, Medicine and Health, Manchester Cancer Research Centre, University of Manchester, Wilmslow Road, Manchester, UK

5 Department of Oncology, The Sidney Kimmel Comprehensive Cancer Center, The Johns Hopkins University School of Medicine, Baltimore, MD, USA

6 Department of Chemical and Biomolecular Engineering, The Johns Hopkins University, Baltimore, MD, USA

7 Molecular Oncology group, Cancer Research UK, Manchester Institute, The University of Manchester, Manchester, UK

8 Cancer Research UK, Beatson Institute, Glasgow, UK

9 Medical Faculty Mannheim, Centre for Biomedicine and Medical Technology Mannheim (CBTM), University of Heidelberg, Mannheim, Germany

10 Department of Medicine, University of Barcelona, Barcelona, Spain

11 Institut d'Investigacions Biomédiques August Pi i Sunyer, Barcelona, Spain

12 Department of Medicine, University of Barcelona, Barcelona, Spain

13 Medical Faculty Mannheim, University of Heidelberg, Mannheim, Germany

14 Institute of Toxicology and Genetics, Karlsruhe Institute for Technology (KIT), Karlsruhe, Germany

amongst the attendees. With 13 invited speakers, 6 proffered papers and 103 posters, the 168 participants were treated to a rich and varied scientific menu of excellent quality. Keynote addresses were given by Robert Kerbel, Andreas Trumpp and Erik Sahai, the latter being kindly supported by a grant from the European Molecular Biology Organisation. Additionally, seven EACR-Worldwide Cancer Research Meeting Bursaries and five MRS Meeting Bursaries were awarded. The majority of the recipients of these awards have also co-authored the summary below that outlines the contents of this exciting conference.

Opening keynote lecture and conference debate

The joint congress began with keynote speaker, Robert S. Kerbel (University of Toronto, Toronto, Canada), focusing on the use of metastatic models for experimental therapeutics and introducing a new era of anti-vascular therapy. He reported that preclinical models of metastatic disease including genetically engineered mouse models (GEMMs) and patient derived xenografts (PDXs) are highly effective for testing treatments for primary tumors, but fail to predict treatment of advanced metastatic disease in phase III clinical trials [1]. His studies testing antiangiogenic tyrosine kinase inhibitor (TKI) drugs, i.e. sunitinib, alone or with chemotherapy recapitulated the negative phase III clinical results [2]. However, an antibody targeting the VEGF pathway (DC101) combined with paclitaxel chemotherapy has impact on treating advanced metastatic breast cancer [2].

It is known that the lack of efficacy of some anti-angiogenic drugs is due to acquired resistance [3]. One major explanation for resistance to anti-angiogenic drugs is "vessel co-option", the ability of tumors to hijack the existing vasculature in organs, which results in the absence of sprouting angiogenesis [4]. To this end, Dr. Kerbel concluded with a discussion of the potential anti-angiogenic therapy targeting vessel co-option in tumors as a means to suppress or prevent metastasis.

The opening keynote lecture was followed by the "Conference Debate", in which Dr. Helmut Augustin and Dr. Yibin Kang discussed the hurdles and difficulties that need to be overcome if preclinical data is to be translated into successful clinical trials.

Dr. Augustin described the process of metastasis as one of the last mysteries in cancer research, which is partially due to the fact that broadly used preclinical mouse models lack relevance to the clinics. He highlighted results from his recently published review describing an overview of the currently used mouse models in cancer [5]. In conclusion, most studies employ xenograft mouse models generated by cancer cell line injection, which fail to model crucial steps of the metastatic cascade. The use of cell lines that have been selected in culture for many years and which have lost the primary tumor characteristics represents a major reason why preclinical studies are difficult to translate into the clinics. To overcome these problems, Dr. Augustin suggested analyses and approaches which are more clinically relevant, e.g. to investigate metastatic spread after surgical removal of the primary tumor, and the use of autochthonous mouse models. Another improvement could be data standardization, meaning a uniform way to analyze and describe data, eventually helping to interpret results across different institutes and countries.

Dr. Kang explained the importance of preclinical mouse models in efforts to understand metastasis, particularly because these mouse models help to understand the biological relevance of targets, stromal interactions, drug effects and to define/find therapeutic windows. He described the evolution of mouse models and the differences between immunocompetent and immunodeficient models. Furthermore, he highlighted recent developments in the field, such as humanized mouse models and CRISPR/Cas9 technology, which already improved current mouse models and will continue to do so. In a study where he investigated Metadherin (MTDH), he explained the need of multiple mouse models to fully describe the function of this and other molecules in cancer metastasis [6–8].

The points that Dr. Augustin and Dr. Kang discussed concordantly emphasize that one single mouse model is not sufficient to understand and challenge the process of metastasis to such a level that the results can be directly translated into the clinic. The researcher should always use several of the best-suited model systems available and combine those to overcome the potential limitations of each model and obtain more relevant and applicable data.

New models of metastasis

The biological complexity underlying metastasis requires complex and clinically relevant animal models for its study. The need for better models, and discussion as to what are the most relevant models available today were topics of intense debate during the first conference session.

Yibin Kang (Princeton University, New Jersey, USA) identified miR-199a as a common regulator of stem cell activity both in normal mammary stem cells (MaSCs) and tumor-initiating cells (TICs)/cancer stem cells (CSCs) isolated from various breast cancer mouse models [9]. He showed that by suppressing a nuclear receptor corepressor LCOR, miR-199a protects normal MaSCs from interferon-alpha (IFN-α)-mediated senescence and differentiation allowing the cells to retain self-renewal capacity. Importantly, Dr. Kang demonstrated that miR-199a-LCOR-IFN axis is active also in TIC/CSCs-rich ER- breast tumors, promotes tumor initiation and metastasis and predicts poor

clinical outcome in ER- breast cancer patients. Altogether, Dr. Kang concluded that in mammary gland and immune cell-rich tumors, miR-199a-LCOR axis decreases the sensitivity of normal and malignant stem cells to autocrine/paracrine interferon-mediated suppressive effects.

Neta Erez (Tel Aviv University, Tel Aviv, Israel) presented a new model of spontaneous melanoma brain metastasis, which provides a platform to study the changes that occur in the brain metastatic niche and enables molecular detection of micrometastases [10]. Dr. Erez demonstrated that initiation of astrogliosis and neuroinflammation occur at early stages of metastases formation. Moreover, Dr. Erez showed that astrocytes play a major role in facilitating the growth of disseminated melanoma cells in the brain, presumably through the induction of a wound healing and astrogliosis response. This novel model can serve as a platform to study questions in the emergent field of the metastatic microenvironment, and to test new therapeutic combinations.

Alberto Hernandez-Barranco (Spanish National Cancer Research Centre, Madrid, Spain) moved the focus to the role of exosomes in promoting lymph node (LN) metastases. He showed that exosomes derived from highly metastatic or lymphotropic melanoma tumor cells spread through the lymphatic system better than exosomes derived from low or non-metastatic tumor cells. Moreover, Hernandez-Barranco indicated that in the LN, most exosomes are incorporated into lymphatic endothelial cells (LECs) and macrophages. To elucidate the changes that follow exosome uptake, LECs were incubated with melanoma-derived exosomes. This resulted in an increase in the expression of lymphangiogenesis-related genes. With this, Hernandez-Barranco described a mechanism by which melanoma-secreted exosomes promote LN metastases formation via activation of the LN microenvironment.

The focus of Jonathan P. Sleeman's talk (University of Heidelberg, Mannheim, Germany) was the novel, lymphangiogenesis-independent role of the vascular endothelial growth factor-C (VEGF-C). Dr. Sleeman showed that VEGF-C is systemically increased in breast cancer patients compared to healthy controls. To mimic increased VEGF-C levels in circulation, he used adeno-associated viruses to stably elevate VEGF-C blood levels in various breast cancer animal models. He observed that systemic VEGF-C promotes metastasis formation by pre-metastatic conditioning of lungs via recruitment of CD11b + Gr1 + Ly6G + granulocytic MDSCs/neutrophils to the terminal bronchioles. Mechanistically, he showed that this process is dependent on VEGF-C receptor VEGFR-3 but not VEGFR-2. Collectively, Dr. Sleeman demonstrated that VEGF-C can foster metastasis independently of its effect on peritumoral lymphangiogenesis, changing our understanding of how VEGF-C contributes to metastasis.

Imaging metastasis

Dr. Peter Friedl opened the "imaging metastasis" session by presenting important insights into cancer cell migration in vivo through the use of intravital multiphoton microscopy. By applying this advanced imaging technique to subcutaneous tumors of HT1080 (sarcoma) and MV3 (melanoma) cells in nude mice in a modified dorsal skin-fold chamber model, Dr. Friedl observed that the tumor invades 100–500 µm a day, and that in confined areas, the invading cancer cells undergo a jamming transition and move as individual cells or multicellular clusters [11]. Furthermore, during tumor progression, microniches existent in the tissue act as tracks that facilitate collective migration of cancer cells. Importantly, finger-like protrusions are also observed in human histology, matching these channel-like structures. By injecting dextran-FITC, he demonstrated that these channels are present in both healthy and cancerous tissues. In their experimental models, tumors were resected 3 weeks after tumor cells implantation, then spontaneous distant metastases were assessed on week 8.

The three-step model of invasive cell migration states that tumor cells attach to the ECM, proteolytic degradation of the extracellular matrix (ECM) occurs, then tumor cells migrate through the remodelled ECM [12]. Contrary to this model, Friedl and co-workers found different types of invasion. They found that cancer cells expand against the tissue in a non-destructive way, suggesting that tissue geometry dictates the invasion pattern without a need for proteolytic degradation. They identified two types of collective invasion patterns in response to the connective tissue: linear collective invasion where the organ cells stay intact and confined; and broad or diffuse collective invasion, which is also confined but with higher perfusion. By using CLEM, an intravital fluorescence with 3D reconstruction, Dr. Friedl tracked expansion by leader cells that started invading out and spreading, while the tissue structure remained fully preserved. Dr. Friedl and his team applied pressure to the tumor to induce a passive position change, which resulted in the tumor invading into the surrounding tissue in the range of 500–600 µm, suggesting that the pre-formed tracks in the tissue act as highways that collective and single cell migration can follow in a process of guided migration. The in vivo imaging of PDX models would be the next step, but the fluorescent labeling is still a challenge.

In addition to the environmental drive of cancer invasion and metastasis, Dr. Friedl also recognized the importance of cell adhesion. Although there is plenty of evidence about how integrins influence metastasis, there are cases where cells can move in an integrin-independent manner, such as leukocyte migration [13]. Dr. Friedl

questioned whether integrins are required for attachment to the basement membrane. Since knock out of integrins in vitro is often lethal, they used a multi-targeted interference approach by combining RNAi and β1 and β3 integrins antibodies. Dr. Friedl and his team observed a reduction in adhesion force to collagen type I through atomic force spectroscopy. In vivo, tumor growth was critically affected. However, invasion was still possible. Thus, integrins are indispensable for tumor growth but dispensable for migration. Dr. Friedl highlighted that the speed of different migration modes remained mainly unperturbed.

Absence of integrins has been widely related to a strong reduction in metastasis [14, 15], yet Dr. Friedl imaged cell dissemination and observed the same rate of metastatic events during lung colonization. Actually, when normalized by tumor mass, there is an enhanced probability of lung colonization after integrin targeting. Thus, reducing integrin availability potentially contributes to cell motility, metastasis and decreased tumor growth. These microenvironmental factors are important to improve anti-cancer therapies. For instance, MMP inhibitors may not efficiently prevent invasion, since the migratory channels are already shaped in the tissues. Combined anti-migration and cytotoxic therapies to combat metastatic transitions may be a better target.

By definition, the extracellular matrix (ECM) is a collection of extracellular molecules that are secreted by cells, and its structure as well as its mechanical and physical properties influence cell fate and behaviour. Extensive changes in the cellular microenvironment can promote cancer development and contribute to metastatic dissemination. As Dr. Chris Madsen (Lund University, Sweden) highlighted, it is crucial to study and understand changes in tissue-specific ECM composition as this represent important an important regulatory component in cancer development and progression. He introduced a fast and efficient method to improve the analysis of native versus tumor ECM architecture, the so called 'in situ decellularization of tissue' (ISDoT) approach, which allows removal of all cells in a tissue, only leaving an extracellular matrix scaffold for further analysis. This technique is based on the delivery of decellularization reagents through the cardiovascular system of the mouse to any organ or anatomical area [16]. These 3D decellularized tissues maintain their original tissue-specific structure and typical composition, and can be used for high-resolution fluorescence imaging and for comparative quantitative proteomic analyses. This approach allows the comparison of the structure and composition of native, healthy ECM of a specific organ with the destructive, dramatically changed ECM found in macro-/micrometastatic tissue of the same organ. It also shows the vast structural differences between intratumoral fibers and the decellular ECM fibers in the adjacent stroma of macrometastatic lung tissue observed through fluorescence imaging. In summary, the ISDoT technique allows the preservation of typical ECM and basement membrane (BM) integrity of any organ of interest and can be used to quantify its biochemical ECM and BM composition. In addition, ISDoT can be used to map the 3D topology of the ECM at different time points of metastatic dissemination and organ colonisation, which will fundamentally improve the study and the understanding of ECM remodelling during the metastatic process.

Proffered Paper 2 was presented by Adam Marcus and was entitled "using an image-guided genomics platform to probe the phenotypic heterogeneity of collective cancer invasion". With the aim of investigating the fascinating phenotypic heterogeneity of cancer cell populations, Dr. Adam Marcus and his team created an image-guided genomics technique named spatiotemporal genomic and cellular analysis (SaGA). This advanced technique consists of a precise selection through the optical highlighting of cells of interest, followed by their analysis.

Collective invasion (Ecad, SP-C) was observed in lung tissue from the Gilbert-Ross mouse model Kras, which is a Kkb1 metastatic lung adenocarcinoma GEMM using LV-Cre that promotes lung adenocarcinoma in 90% of the mice. The same collective invasion phenomenon was also observed in 3D spheroids [17]. In a video of an invading spheroid, Dr. Marcus showed that some cells initiate invasion by breaking through the matrix and seem to be followed by the other cells, forming cellular streams. When these starting cells move too far and lose contact with the spheroid body, the adjacent cells instantly stop following in 84% of the cases [17]. Therefore, invasion seems to be regulated by a specific class of cells that Dr. Marcus termed "leaders". These leader cells can move back to the spheroid, allowing the follower cells to re-attach and follow them again [17]. To further investigate this hypothesis, Dr. Marcus and his team applied SaGA and after dissociating leader and follower cells by FACS, they observed that both populations retain their morphology and properties. While spheroids made of leader cells are highly invasive, follower cells remain packed and hardly invaded. When mixing both cell populations, leader cells remain leaders and rescue follower cells promoting their migration again [17]. Leader cells also appear to be more drug resistant. Interestingly, the two cell populations also behave differently in vivo. Leader cells are unable to establish a tumor at the injection site but appear to promote metastatic disease, whereas follower cells establish tumors and show significantly less metastasis. Subsequent RNASeq on these cell populations suggested an atypical VEGF-based vasculogenesis signaling that promotes the recruitment of follower cells, and a focal adhesion kinase-fibronectin signaling that facilitates the leader cell motility. The model proposed by Dr. Marcus is a symbiotic ecosystem model, where leader cells provide an escape mechanism to follower cells and in return, follower cells provide leader cells with

increased growth and survival. Moreover, the phenotype of leader cells seems to be maintained through epigenetic reprogramming of the follower cells. Dr. Marcus is currently working towards applying this methodology and hypothesis to patient-derived organoids, with the aim of pursuing new therapies targeting this cooperation.

Veronika te Boekhorst presented Proffered Paper 3, which had the title "Calpain-2 induced shutdown of β1 integrin function controls amoeboid reprogramming and dissemination under hypoxic challenge". During metastatic dissemination, cancer cells can use a variety of single cell or collective migration strategies [18]. Plasticity of tumor cell migration can be affected by changes in cell adhesion, mechano-signalling adaptations, proteolysis and other microenvironment challenges [19]. The team of Dr. Peter Friedl has recently identified tumor hypoxia as a promoter of the dissemination of amoeboid-moving single cells from otherwise collectively invasive epithelial cells, the so called collective-to-amoeboid transition [19]. Dr. Veronika te Boekhorst (MD Anderson Cancer Center, Houston, USA) described how hypoxic stress and elevated levels of HIFs (hypoxia-inducible factors) in a 3D spheroid model of epithelial breast and squamous carcinoma cells induced a switch from collective invasion to an amoeboid-type of single cell movement. These cells are characterized by blebby or actin-rich pseudopodal protrusions that can initiate invasion. β1 integrins at the leading edge confer adhesion and contractility and reduced β1 integrin therefore is rate limiting for the switch from an elongated to an amoeboid migration phenotype. It was also observed that the cysteine protease calpain-2 controls β1 integrin shutdown as a consequence of hypoxia and HIF stabilization and mediates the blebby amoeboid migration switch. In vitro as well as in human squamous carcinoma xenografts, calpain-2 levels are high in reprogrammed and disseminated amoeboid-rounded cells upon HIF stabilization. The inhibition of calpain-2 expression or function can reverse the amoeboid to a mesenchymal migration type. Dr. te Boekhorst concluded that the HIF-induced and calpain-2-mediated integrin shutdown may represent a physiologically important escape mechanism of cells upon metabolic changes in the surrounding tissue areas. Overall, these results improve our understanding of this clinically relevant mechanism that is conserved in epithelial cancer cells and allows plasticity reprogramming by the microenvironment, eventually driving and promoting metastatic dissemination.

Transgenic models of metastasis

Mouse models to study cancer biology and metastatic dissemination have evolved significantly since the first transplantable tumor model in nude mice 50 years ago [20]. Currently, genetically engineered mouse models (GEMMs) are gaining favor over transplantable and cell inoculation models. Indeed, as opposed to models involving immunodeficient mice, GEMMs recapitulate all the steps in the metastatic process, including the interactions with the microenvironment and the immune system, which makes them appealing to use in preclinical studies.

Dr. Karin de Visser (The Netherlands Cancer Institute, Amsterdam, Netherlands), in collaboration with Prof. Jos Jonkers' group is using a conditional knockout breast cancer mouse model (K14::cre; Cdh1loxP/loxP; p53loxP/loxP) [21] to study tumor-induced systemic inflammation and metastasis. One of the limitations of GEMMs is the appearance of multiple tumors and tumor regrowth after excision of the primary, which hampers the study of metastasis. In order to uncouple tumor initiation from metastasis, primary tumors can be excised and implanted into new immunocompetent mice without losing their metastatic ability. This is known as a GEMM-derived syngraft. Using both GEMMs and GEMM-derived syngrafts, Dr Visser's group has observed increased levels of circulating neutrophils in both models, which correlated with the metastatic tumor burden [22]. More importantly, clinical data show that breast cancer patients with elevated levels of neutrophils have worse prognosis. Conversely, neutrophil depletion with anti-Ly6G antibody significantly reduced lung metastases formation in mice. Hence, in an effort to discover the cancer cell genetic background responsible for neutrophil activation, they profiled a panel of 16 GEMMs with different tumor-initiating genetic modifications and observed elevated levels of neutrophils in *Tp53* deficient mice. Further in vitro studies led to the discovery of interplay between *Tp53* deficient tumor cells and macrophages, which trigger macrophages to release pro-inflammatory cytokines.

The biggest challenge the metastasis research field currently faces is translating pre-clinical findings successfully into the clinic, as exemplified by the failure of several clinical trials with anti-angiogenic drugs. This was emphasized by Prof. Augustin, Prof. Kerbel and others. Prof. Augustin (German Cancer Research Center, Heidelberg, Germany) advocates the use of GEMMs with fully functioning immune systems, and studying the mechanisms that drive metastasis in a spatio-temporal manner, rather than focusing on endpoints. Through this approach, and in collaboration with Prof. Clare Isacke's group, Prof. Augustin described how endosialin-positive pericytes facilitate breast cancer cells' intravasation and consequent metastatic dissemintation [23].

With a series of examples of new GEMM-derived models, Prof. Augustin explained how our understanding of metastasis and the efficacy of clinical trials can be improved. The first strategy presented used a GEMM-derived syngraft model (derived from the MT/ret mouse model of melanoma), which was employed to study anti-angiogenic treatment with anti-angiopoietin2 antibody

(anti-Ang2) in a neoadjuvant setting, as compared to adjuvant treatment [24]. Approximately 60% of mice treated in a neoadjuvant setting were completely free of metastases, while the remaining 40% did not show signs of lymph node dissemination. This suggests that anti-Ang2 prevents cancer cells from colonizing lymph nodes during tumor growth. This observation can be recapitulated by removal of draining lymph nodes upon primary tumor removal.

The second strategy for focal tumor formation was local electroporation, which can be used to induce tumorigenesis. This was demonstrated using the BrafV600E; PtenloxP/loxP mouse melanoma model [25] and the local delivery of plasmids expressing Tyr:Cre. The tyrosinase promoter on these plasmids can be activated with UV light or depilation. The tumors can be removed and these mice will develop metastases several weeks after surgery. This approach can be extended to other models, such as hepatocellular carcinoma to study intra-hepatic metastases.

It is worth mentioning that the two aforementioned strategies are not mutually exclusive but can rather be used in parallel. The advantage of the syngraft model is the capacity for scaling up the tumor material and allowing for biobanking, while the electroporation model can be employed to study the metastatic process from tumor initiation onward.

In addition, understanding the mechanisms of how disseminated tumor cells grow in a specific secondary organ is another hurdle that GEMMs are managing to overcome. Metastases need a reciprocal adaptation between tumor and stromal cells at the metastatic niche that will allow the initial metastatic colonization and the progression of the disease. Dr. Shani, an MD PhD student in Dr. Neta Erez' group (Tel Aviv University, Tel Aviv, Israel) has focused her research on cancer associated fibroblasts from the metastatic microenvironment that are the most abundant stromal cells in the lung [26]. She demonstrated that lung fibroblasts are essential for permissive metastatic-niche formation using an innovative transgenic mice model. Combining the MMTV-PyMT model of mammary carcinogenesis and the YFP-Collagen-1α (Col1α) expressing mouse model they generated the PyMT-Col1α-YFP model that develops an autochthonous mammary tumor with spontaneous lung metastases. Using these mice, they isolated lung fibroblasts at different stages of metastasis and found different gene expression patterns using RNA-sequencing. HIF1α, c-myc and EGF, among others, changed their expression in the early stage fibroblasts, whereas metastasis-associated fibroblasts presented changes in genes associated with inflammation, extracellular matrix remodeling and stress responses. Throughout this study, Dr. Shani and colleagues showed a dynamic co-evolution of lung fibroblasts in the metastatic microenvironment during breast cancer metastasis, emphasizing the importance of studying the gene-expression modifications in fibroblasts and the contribution these pathways may have in breast cancer lung metastasis development.

Finally, reinforcing the importance of the metastatic stroma in metastasis evolution, Dr. Gelman (Roswell Park Cancer Institute, Buffalo, NY, USA) and his group studied the metastasis-regulating gene SSeCKS/AKAP12 which is down-regulated in many metastases compared to the primary tumor. To study the role of the kinase scaffolding protein SSeCKS/AKAP12 [27] in melanoma Dr. Gelman used a knock-out (KO) mouse model for SSeCKS where B16F10 melanoma cells (Brafwt) or their metastatic variant SM1WT1-LM3 (bearing Braf human melanoma mutation, BrafT1799A) were inoculated. They showed that the KO-mice had increased peritoneal metastasis, which could be due to the increased levels of chemo-attractants in the peritoneal-fluid (PF). Two of the most abundant chemokines in the PF were CXCL9 and CXCL10, both CXCR3 ligands, and loss of the receptor inhibited both the chemotaxis and the metastatic ability in KO-mice. These results suggested that KO-mice peritonea secrete high levels of CXCR3 ligands, thereby facilitating melanoma cells chemoattraction and thus metastasis. Besides, they determined that these chemoattractants were secreted by KO peritoneal membrane fibroblasts (PMF) that showed a senescence-associated secretory phenotype (SASP). Finally, using SSeCKS scaffolding-site mutants and different kinase inhibitors, Dr. Gelman defined PKC, PKA and PI3K/AKT signalling pathways as CXCL10 expression regulators in KO PMF. With this work, Dr. Gelman and his group described the role of stromal SSeCKS protein as a metastasis-suppressor [28]. Loss of SSECKS/AKAP12 increased secretion of chemokines and senescence factors by PMF that form the pre-metastatic niche and promoted the peritoneal metastatic chemotaxis of B16F10 melanoma cells.

In summary, this session presented different mouse models that allow a more appropriate study of metastatic tumours due to their similarity with human disease, and reinforced the importance of using such models in cancer research.

Modeling metastasis

The final session of the meeting was dedicated to metastatic models and their relevance in answering specific research questions. First, Bin-Zhi Qian (University of Edinburgh, UK) discussed the mononuclear phagocyte system and its role in breast cancer metastasis, where they have previously shown the importance of host macrophages for lung metastasis [29, 30]. Dr Qian focused on breast cancer bone metastasis, where they found that the CCL2/CCR2 axis was critical in recruiting macrophages derived from circulating inflammatory monocytes. This event promoted the ability of breast cancer cells to metastasize to the bone. Furthermore, they

found two sub-locations of macrophages in the bone marrow: the perivascular niche with resident macrophages, and the endosteal niche with osteal tissue macrophages that are important in metastatic seeding. These extravasating macrophages secrete VEGF, which increases vascular permeability, enabling tumor cells to extravasate and metastasize to the bone. The gene expression profile of inflammatory monocytes and macrophages showed that there are several macrophages subpopulations with different profiles.

As it is well established that tumor cells do not work alone but need to interact with surrounding stromal cells such as fibroblasts. Erik Sahai (The Francis Crick Institute, London) focused on the interactions between fibroblasts and cancer cells in the primary tumor niche. Fibroblasts and cancer cells are mechanically coupled (through heterotypic interactions by E-cadherin and N-cadherin) enabling fibroblasts to pull cancer cells [31]. Dr Sahai also focused on the interaction between disseminated tumor cells and the stroma in the lung metastatic niche. Using the D2.0R and D2.A1 dormancy models they performed several co-cultures with different stromal populations of the lung. They focused on alveolar cells type I and II cells to try and identify growth arrest genes or survival repressors, and proliferation genes or survival inducers. They continue to investigate the critical role of the cross talk with epithelial cells in the lung parenchyma in lung metastasis.

There is evidence that breast cancer metastases are seeded by cancer stem cells (CSCs), as Rachel Eyre (University of Manchester, UK) discussed in the final proffered paper of the meeting. Dr Eyre presented data from in vitro and in vivo models that demonstrated that IL1β-Wnt signalling promotes bone colonization by breast CSC. The inhibition of IL1β-Wnt signalling prevented bone metastases in vivo. This observation suggests that clinically available drugs that target this pathway should be considered as adjuvant therapy in breast cancer patients.

Identifying biomarkers that predict the ability of tumors to metastasize is key goal in cancer research. Ulrike Stein (MDC, Germany) summarized extensive research carried out in her lab on MACC1, a novel gene identified as a potential target for metastasis therapy [32]. Since its discovery, it has been shown that MACC1 expression can be used as a prognostic marker for progression, metastasis and survival in several solid tumors [33], and MACC1 has been considered an anti-metastasis target. As Lovastatin (a member of the statin family) has been identified as an inhibitor of MACC1, it might be appropriate to use this drug for the treatment of patients with MACC1-induced metastasis who are at high risk for shorter survival.

The closing keynote lecture was given by Andreas Trumpp (DKFZ, Germany), and was dedicated to new metastasis models and their uses in key areas of cancer research. Professor Trumpp focused initially in pancreatic adenocardinoma (PDAC), a poor prognosis cancer, and his use of PDX models to develop a stratification system for molecular subclassification [34]. Using these models, clinical outcome can be predicted, and CYP3A5 was identified as a key factor mediating drug resistance in PDAC. Next, Professor Trumpp described leukapheresis as a technique that can be used to isolate large numbers of circulating tumors cells (CTCs) from metastatic breast cancer patients. CTCs can be isolated for single cell RNAseq, and both cellular heterogeneity and response to therapy can be observed at the single cell level. He concluded that new technologies will prove powerful tools for preventing and treating cancer metastasis.

Conclusions and perspectives

The Seed and Soil conference 2017 was clearly an outstanding success, and exceeded the expectations of the organisers. In many conferences, the auditorium is full for the first couple of sessions then starts to empty out. This was not the case for the Seed and Soil conference, and the auditorium was packed throughout the meeting right up to the last talk. The quality of the questions and discussion during the sessions was highly informative and of excellent quality. The amount of interest in poster sessions is always a good measure of the success and relevance of the conference, and it is therefore also notable that the poster sessions were uniformly crammed full of attendees eager to talk to poster presenters, with discussions going well over the allotted time frame and into the night. The interest and enthusiasm engendered by the conference clearly illustrates the importance of the topic for the cancer research community. With this in mind, the conference organisers are already making plans for another Seed and Soil conference in 2 years time.

References

1. Francia G et al (2011) Mouse models of advanced spontaneous metastasis for experimental therapeutics. Nat Rev Cancer 11(2):135–141
2. Guerin E et al (2013) A model of postsurgical advanced metastatic breast cancer more accurately replicates the clinical efficacy of antiangiogenic drugs. Cancer Res 73(9):2743–2748
3. Kuczynski EA et al. (2016) Co-option of liver vessels and not sprouting angiogenesis drives acquired sorafenib resistance in hepatocellular carcinoma. J Natl Cancer Inst. https://doi.org/10.1093/jnci/djw030
4. Donnem T et al (2013) Vessel co-option in primary human tumors and metastases: an obstacle to effective anti-angiogenic treatment? Cancer Med 2(4):427–436
5. Gengenbacher N, Singhal M, Augustin HG (2017) Preclinical mouse solid tumour models: status quo, challenges and perspectives. Nat Rev Cancer 17(12):751–765

6. Hu G et al (2009) MTDH activation by 8q22 genomic gain promotes chemoresistance and metastasis of poor-prognosis breast cancer. Cancer Cell 15(1):9–20
7. Hu G, Wei Y, Kang Y (2009) The multifaceted role of MTDH/AEG-1 in cancer progression. Clin Cancer Res 15(18):5615–5620
8. Wan L et al (2014) MTDH-SND1 interaction is crucial for expansion and activity of tumor-initiating cells in diverse oncogene- and carcinogen-induced mammary tumors. Cancer Cell 26(1):92–105
9. Celià-Terrassa T, Liu DD, Choudhury A, Hang X, Wei Y, Zamalloa J, Alfaro-Aco R, Chakrabarti R, Jiang YZ, Koh BI, Smith HA, DeCoste C, Li JJ, Shao ZM, Kang Y (2017) Normal and cancerous mammary stem cells evade interferon-induced constraint through the miR-199a-LCOR axis. Nat Cell Biol 19(6):711–723
10. Schwartz H, Blacher E, Amer M, Livneh N, Abramovitz L, Klein A, Ben-Shushan D, Soffer S, Blazquez R, Barrantes-Freer A, Müller M, Müller-Decker K, Stein R, Tsarfaty G, Satchi-Fainaro R, Umansky V, Pukrop T, Erez N (2016) Incipient melanoma brain metastases instigate astrogliosis and neuroinflammation. Cancer Res 1 76(15):4359–4371
11. Haeger A, Krause M, Wolf K, Friedl P (2014) Cell jamming: collective invasion of mesenchymal tumor cells imposed by tissue confinement. Biochim Biophys Acta Gen Subj 1840(8):2386–2395. https://doi.org/10.1016/j.bbagen.2014.03.020
12. Liotta LA (2016) Adhere, degrade, and move: the three-step model of invasion. Cancer Res. https://doi.org/10.1158/0008-5472.CAN-16-1297
13. Lämmermann T, Bader BL, Monkley SJ, Worbs T, Wedlich-Söldner R, Hirsch K, Sixt M (2008) Rapid leukocyte migration by integrin-independent flowing and squeezing. Nature 453(7191):51–55. https://doi.org/10.1038/nature06887
14. Grzesiak JJ, Cao HST, Burton DW, Kaushal S, Vargas F, Clopton P, Bouvet M (2011) Knockdown of the β1 integrin subunit reduces primary tumor growth and inhibits pancreatic cancer metastasis. Int J Cancer 129(12):2905–2915. https://doi.org/10.1002/ijc.25942
15. Ju JA, Godet I, Ye IC, Byun J, Jayatilaka H, Lee SJ, Gilkes DM (2017) Hypoxia selectively enhances integrin α 5 β 1 receptor expression in breast cancer to promote metastasis. Mol Cancer Res 15(6):723–734. https://doi.org/10.1158/1541-7786.MCR-16-0338
16. Mayorca-Guiliani AE, Madsen CD, Cox TR, Horton ER, Venning FA, Erler JT (2017) ISDoT: in situ decellularization of tissues for high-resolution imaging and proteomic analysis of native extracellular matrix. Nat Med 23:890–898
17. Konen J, Summerbell E, Dwivedi B, Galior K, Hou Y, Rusnak L, Marcus AI (2017). Image-guided genomics of phenotypically heterogeneous populations reveals vascular signalling during symbiotic collective cancer invasion. Nat Commun. https://doi.org/10.1038/ncomms15078
18. Friedl P, Locker J, Sahai E, Segall JE (2012) Classifying collective cancer cell invasion. Nat Cell Biol 14:777–783
19. Lehmann S, te Boekhorst V, Odenthal J, Bianchi R, van Helvert S, Ikenberg K, Ilina O, Stoma S, Xandry J, Jiang L, Grenman R, Rudin M, Friedl P (2017) Hypoxia induces a HIF-1-dependent transition from collective-to-amoeboid dissemination in epithelial cancer cells. Curr Biol 27:392–400
20. Kersten K, de Visser KE, van Miltenburg MH, Jonkers J (2017) Genetically engineered mouse models in oncology research and cancer medicine. EMBO Mol Med 9:137–153
21. Derksen PWB et al (2006) Somatic inactivation of E-cadherin and p53 in mice leads to metastatic lobular mammary carcinoma through induction of anoikis resistance and angiogenesis. Cancer Cell 10:437–449
22. Coffelt SB et al (2015) IL-17-producing γδ T cells and neutrophils conspire to promote breast cancer metastasis. Nature 522:345–348
23. Viski C et al (2016) Endosialin-expressing pericytes promote metastatic dissemination. Cancer Res 76:5313–5325
24. Srivastava K et al (2014) Postsurgical adjuvant tumor therapy by combining anti-angiopoietin-2 and metronomic chemotherapy limits metastatic growth. Cancer Cell 26:880–895
25. Dankort D et al (2009) BrafV600E cooperates with Pten loss to induce metastatic melanoma. Nat Genet 41:544–552
26. Cohen N, Shani O, Raz Y, Sharon Y, Hoffman D, Abramovitz L et al (2017) Fibroblasts drive an immunosuppressive and growth-promoting microenvironment in breast cancer via secretion of Chitinase 3-like 1. Oncogene 36(31):4457–4468
27. Su B, Gao L, Meng F, Guo L, Rothschild J, Gelman IH. Adhesion-mediated cytoskeletal remodeling is controlled by the direct scaffolding of Src from FAK complexes to lipid rafts by SSeCKS/AKAP12. Oncogene 32(16):2016–2026
28. Muramatsu M, Gao L, Peresie J, Balderman B, Akakura S, Gelman IH (2017) SSeCKS/AKAP12 scaffolding functions suppress B16F10-induced peritoneal metastasis by attenuating CXCL9/10 secretion by resident fibroblasts. Oncotarget 8(41):70281–70298
29. Qian BZ et al (2011) CCL2 recruits inflammatory monocytes to facilitate breast-tumour metastasis. Nature 475(7355):222–225
30. Qian BZ et al (2015) FLT1 signaling in metastasis-associated macrophages activates an inflammatory signature that promotes breast cancer metastasis. J Exp Med 212(9):1433–1448
31. Labernadie A et al. (2017) A mechanically active heterotypic E-cadherin/N-cadherin adhesion enables fibroblasts to drive cancer cell invasion. Nat Cell Biol 19(3):224–37
32. Stein U et al (2009) MACC1, a newly identified key regulator of HGF-MET signaling, predicts colon cancer metastasis. Nat Med 15(1):59–67
33. Rohr UP et al (2017) Prognostic value of MACC1 and proficient mismatch repair status for recurrence risk prediction in stage II colon cancer patients: the BIOGRID studies. Ann Oncol 28(8):1869–1875
34. Noll EM et al. (2016) CYP3A5 mediates basal and acquired therapy resistance in different subtypes of pancreatic ductal adenocarcinoma. Nat Med 22(3):278–287

Published OnlineFirst April 16, 2021; DOI: 10.1158/0008-5472.CAN-21-0340

Targeting Adenosine with Adenosine Deaminase 2 to Inhibit Growth of Solid Tumors

Lin Wang[1], Luz M. Londono[1], Jessica Cowell[1], Ozge Saatci[2], Mertkaya Aras[2], Pelin G. Ersan[2], Sara Serra[3], Hong Pei[4], Renee Clift[1], Qiping Zhao[1], Kim B. Phan[1], Lei Huang[1], Michael J. LaBarre[5], Xiaoming Li[1], H. Michael Shepard[1], Silvia Deaglio[3], Joel Linden[4], Christopher D. Thanos[1], Ozgur Sahin[2], and Caglar Cekic[1]

ABSTRACT

Extracellular adenosine in tumors can suppress immune responses and promote tumor growth. Adenosine deaminase 2 (ADA2) converts adenosine into inosine. The role of ADA2 in cancer and whether it can target adenosine for cancer therapy has not been investigated. Here we show that increased ADA2 expression is associated with increased patient survival and enrichment of adaptive immune response pathways in several solid tumor types. Several ADA2 variants were created to improve catalytic efficiency, and PEGylation was used to prolong systemic exposure. In mice, PEGylated ADA2 (PEGADA2) inhibited tumor growth by targeting adenosine in an enzyme activity–dependent manner and thereby modulating immune responses. These findings introduce endogenous ADA2 expression as a prognostic factor and PEGADA2 as a novel immunotherapy for cancer.

Significance: This study identifies ADA2 as a prognostic factor associated with prolonged cancer patient survival and introduces the potential of enzymatic removal of adenosine with engineered ADA2 for cancer immunotherapy.

Introduction

The tumor microenvironment (TME) has several mechanisms that can suppress immune cell activity and cause resistance to therapy in solid cancers (1, 2); the accumulation of extracellular adenosine is potentially one such mechanism. Accumulation of extracellular adenosine may result from events associated with tumor growth, such as increased metabolic activity, hypoxia, inflammation, and cell death, and is a characteristic of the microenvironment of many human solid tumors (3, 4). Adenosine triphosphate released in the TME by apoptotic cells, or by cells undergoing high metabolic activity or stress, may be converted to adenosine by ectonucleotidases, resulting in the accumulation of extracellular adenosine (3, 4).

Extracellular adenosine can bind and activate four G-protein-coupled receptors: A_{1R}, A_{2AR}, A_{2BR}, and A_{3R} (5). Nonclinical and clinical evidence suggest that adenosine signaling in immune and tumor cells promotes tumor growth and metastasis (4). Deletion of A_{2AR} in natural killer (NK) cells, T cells, and antigen-presenting cells (APC), as well as systemic or local treatment with A_{2AR} antagonists, reduces growth and metastasis of syngeneic melanoma, lung, bladder, and breast tumors in *in vivo* murine models (6–10). A_{2BR} on APCs and tumor cells has been associated with the growth and metastasis of bladder and breast tumors (7, 9). In fact, A_{2BR} signaling in APCs intrinsically regulates tumor antigen-specific $CD8^+$ T-cell responses and promotes growth of solid tumors (11). It has also been suggested that adenosine signaling via A_{1R}, A_{3R}, or intracellular metabolic pathways involving adenosine kinase and 5′ AMP-activated protein kinase (AMPK) activation may delay the growth of colon carcinoma, mesothelioma, and breast tumors (12–15). Also, recent evidence suggests the requirement of A2AR signaling in endogenous $CD8^+$ T cells for their maintenance and responsiveness to immune-checkpoint blockade (6, 16–18). Therefore, the overall impact of adenosine accumulation on tumor growth, rather than on particular receptors, is poorly understood.

Adenosine deaminase (ADA) exists mainly as two isoforms in humans: ADA1, encoded by the *ADA* gene, a predominantly intracellular monomeric enzyme that catalyzes the deamination of both adenosine and deoxyadenosine; and ADA2, encoded by the *CECR1* gene, a serum dimeric enzyme expressed by multiple cell types (19), which mainly catalyzes adenosine deamination (20). ADA2 has optimal activity at pH 6.5 (19), which is a pH level commonly found in many solid tumors. In addition to an active site, ADA2 has a heparin-binding region and a putative growth factor-like domain (19). The K_m value of ADA2 is higher than ADA1 (21), suggesting the affinity of ADA2 to adenosine is lower than that of ADA1. Notably, both serum and tumor levels of ADA2 are elevated in patients with breast cancer (22, 23). Overall, these qualities suggest a role for ADA2 in the pathologic conditions associated with elevated extracellular adenosine rather than steady-state conditions. However, it is not known whether ADA2 expression is prognostic in patients with cancer or whether treatment with ADA2 can influence tumor growth or metastasis.

Here, we show that ADA2 gene (*CECR1*) expression is associated with favorable outcomes in several solid tumor indications as well as changes in immune responses, suggesting that ADA2 may be a promising anticancer immunotherapy candidate. To develop ADA2 as an anticancer immunotherapy, we engineered ADA2 in two respects. First, we increased ADA2's circulating half-life through PEGylation and, second, we increased ADA2's catalytic activity by introducing two key mutations in the catalytic site. We performed reverse translational experiments in vitro using mouse and human

[1]Formerly of Halozyme Therapeutics, Inc., San Diego, California. [2]Department of Drug Discovery and Biomedical Sciences, University of South Carolina, Columbia, South Carolina. [3]Department of Medical Sciences, University of Torino, Turin, Italy. [4]La Jolla Institute for Immunology, La Jolla, California. [5]Halozyme Therapeutics, Inc., San Diego, California.

Note: Supplementary data for this article are available at Cancer Research Online (http://cancerres.aacrjournals.org/).

L. Wang and L.M. Londono contributed equally to this work.

Corresponding Author: Caglar Cekic, Halozyme Therapeutics, Inc., San Diego, CA 92121. Phone: 858-201-8874; Fax: 858-704-8311; Email: caglarcekic@gmail.com

Cancer Res 2021;81:3319–32

doi: 10.1158/0008-5472.CAN-21-0340

©2021 American Association for Cancer Research.

Downloaded from cancerres.aacrjournals.org on January 20, 2022. © 2021 American Association for Cancer Research.

Published OnlineFirst April 16, 2021; DOI: 10.1158/0008-5472.CAN-21-0340

cells and *in vivo* using syngeneic mouse models in preclinical settings. We show that treatment with engineered ADA2 inhibits tumor growth and metastasis by modulating adaptive immune system responses, and that combining ADA2 with immune checkpoint inhibitors more effectively blocks tumor growth in different tumor models.

Materials and Methods

Cell lines

An A375 melanoma cell line ($CD73^{high}/CD26^{-}$) was obtained through the ATCC. Cell lines were sourced as follows: MB49 bladder carcinoma cell line from Dr. Timothy Ratliff of Purdue University, West Lafayette, Indiana. Metastatic breast adenocarcinoma cell line 4T1, expressing luciferase enzyme were from Tufts University (Medford, Massachusetts), EMT6 murine breast cancer and CT26 murine colon cancer cell lines [ATCC; authenticated by short tandem repeat (STR) DNA profiling], and MC38-ev murine colon cancer cell line (Mark J. Smyth Lab; QIMR Berghofer Medical Research Institute, Brisbane, Australia).

All cell lines were maintained in complete RPMI medium or DMEM, supplemented with 10% FBS, and were routinely tested using MycoAlert Mycoplasma Detection Kit (Lonza) and polymerase chain reaction (IDEXX). Only low-passage (<3) cell lines were used for the study.

Mouse tumor models

C57BL6 and BALB/c female mice, 5 to 6 weeks of age, were purchased from Taconic and Charles River Laboratories, and handled in accordance with approved Institutional Animal Care and Use Committee protocols. Mice were subcutaneously inoculated with MB49, CT26, or MC38-ev cells into the right flanks, or orthotopically inoculated with EMT6 cells into the ninth mammary fat pad. When tumors reached 100 to 200 mm^3, mice were staged to receive the intravenous vehicle control and PEGADA2 variants at multiple doses twice weekly for 2 to 3 weeks. For $CD8^+$ T-cell depletion, mice bearing EMT6 tumors were treated by intraperitoneal injection with 200 μg anti-mouse CD8α antibodies (Clone L3; Bio X Cell) or Rat IgG2b isotype controls. $PEGADA2^{HCA}$ treatment (3 mg/kg) was performed by intraperitoneal injection biweekly in the first week and three times a week in subsequent weeks. 4T1-Luc cells (10^6) were injected intravenously via tail vein into Balb/c mice. $PEGADA2^{HCA}$ treatment was performed twice weekly for the first week, then every other day until mice were analyzed for lung metastases. Intraperitoneal injection of 150 mg/kg D-luciferin was performed to measure luciferase activity by IVIS imaging (PerkinElmer) as a measure of lung dissemination.

Tumor growth was tracked using an electronic caliper (Vernier Software & Technology, Beaverton). Tumor volume in mm^3 was calculated using the formula: tumor volume $= {}^1/_2$ [length × $(\text{width})^2$]. Body weight (BW) was measured as percent change as compared with baseline was calculated for each individual mouse by BW/Baseline BW (BW before the first dose) × 100. Terminal bleeding was performed to assess plasma levels of the alanine aminotransferase (ALT), creatinine, blood urea nitrogen (BUN), and glucose from plasma using LIASYS clinical chemistry analyzer. To assess the effects of PEGADA2 and anti-PD-L1 on tumor growth, mice with ∼100 mm^3 MB49 or MC38-ev tumors were randomized into treatment groups: in the MB49 model, 3 μg/kg i.v. $PEGADA2^{HCA}$, and 0.3 mg/kg i.p. anti-PD-L1 mouse immunoglobulin G2b (Rat IgG2b, κ isotype; clone 10F.9G2; Bio X Cell) were administered alone or in combination; in the MC38-ev model, 3 μg/kg i.v. $PEGADA2^{HCA}$ and 1 mg/kg i.p. anti-PD-L1 mouse IgG2b were administered alone or in combination (from one experiment, $n = 8$/group). Anti-mouse PD-L1 (clone 10F.9G2) and anti-mouse PD-1 (RMP1–14) were purchased from Bio X Cell and were diluted in phosphate-buffered saline (PBS) before administration.

ADA2 variant design, screening, and PEGylation

ADA2 variants were designed on the basis of its structure–function relationship [Protein Data Bank (PDB) code: 3LGD; ref. 19]. Surface residue K374, residues R222, L224, E133, D416, S265, H267, and those in proximity to ADA2 active site were selected to introduce single or multiple mutations to either improve catalytic efficiency or to deactivate ADA2 enzymatic activity for mechanism of action studies. The Phyre 2 server was used to model the structures of ADA2 variants. Modeled structures were superimposed on the structure of ADA2 WT complexed with the adenosine transition state analog coformycin (PDB 3LGG) using the PyMOL Molecular Graphics System (https://www.pymol.org/sites/default/files/pymol_0.xml), Version 2.0 (Schrödinger, LLC).

Variants were generated using the QuickChange Lightning Multi Site-Directed Mutagenesis Kit (catalog no. 210518; Agilent Technologies) and were expressed in Chinese hamster ovary-suspension cells. FLAG-tagged ADA2 variants were purified using an anti-FLAG M2 affinity resin (catalog no. L00432; GenScript). The untagged ADA2 variants, NME8058 and NME8062, were purified by cation-exchange chromatography (CM-650M; Tosoh Bioscience LLC), followed by hydrophobic interaction chromatography (Butyl-650S; Tosoh Bioscience LLC). The butyl elution pool containing the ADA2 enzymes were exchanged into 1× PBS buffer (10 mmol/L PO_4^{3-}, 137 mmol/L NaCl, and 2.7 mmol/L KCl, pH 7.4). Once purified enzymes were tested for enzymatic activity, purity by reversed-phase high-performance liquid chromatography (HPLC) and endotoxin level by Limulus amebocyte lysate (LAL) test cartridges (catalog no. PTS20F; Charles River Laboratories).

ADA2 was PEGylated using 20 kDa PEG (JenKem Technology USA, Inc.) in a 15:1 molar ratio of PEG to ADA2 at 4°C for 18 hours, and the reaction was terminated by 25 mmol/L glycine. PEGADA2 was purified using hydrophobic interaction chromatography (GE Phenyl Sepharose HP; GE Healthcare). After purification, the endotoxin level was retested for PEGADA2 as described. The elution pool containing PEGADA2 was buffer-exchanged into 1× PBS, and retested for enzymatic activity, protein concentration, and endotoxin level before the material was released for *in vitro* and *in vivo* studies. Completion of the PEGylation reaction was verified by SDS-PAGE analysis.

Enzymatic activities of 5 μg/mL PEGADA2 variants were tested using the ADA Assay Kit (Cat. BQ014EALD; GenWay Biotech). **Table 1** lists the ADA2 variants used in this study and their key properties. Variants with similar enzymatic activity (Supplementary Figs. S1 and S2) were used interchangeably for some studies, due to the limitations of material availability.

In vitro and *in vivo* measurements for extracellular adenosine

A375 melanoma cells (5×10^4/0.5 mL) were incubated (60 minutes, 37°C) in AIM V serum-free medium in the presence of 200 μmol/L AMP (Sigma-Aldrich), with or without ADA2 variants (1.0, 2.5, 5.0, and 10.0 μg/mL). After incubation, supernatants were immediately stored at −80°C or processed for HPLC analysis using a Waters Alliance 2965 Separation Module (Waters Corporation). Supernatants (100 μL) were precipitated with 400 μL of cold methanol (VWR Chemicals) and filtered with Phree phospholipid removal tubes (Phenomenex). Samples were dried overnight in a vacuum desiccator and reconstituted in 100 μL of ultrapure Milli-Q water (Merck Millipore) before injection (50 μL) into the HPLC system. Separation of AMP,

Downloaded from cancerres.aacrjournals.org on January 20, 2022. © 2021 American Association for Cancer Research.

Published OnlineFirst April 16, 2021; DOI: 10.1158/0008-5472.CAN-21-0340

Table 1. Kinetic parameters of FLAG-tagged ADA2 variants.

Variant	V_{max} (μmol/L/minute)	K_m (mmol/L)	k_{cat} (second^{-1})	k_{cat}/K_m (millisecond^{-1})
Wild-type	23.13	4.398	45.35	10.312
R222Q	52.49	1.681	102.92	61.226
S265N	73.32	2.701	143.76	53.226
R222Q/S265N	86.3	1.023	169.22	165.411

Note: Kinetic parameters of ADA2 variants R222Q, S265N, and R222Q/S265N (NME62;ADA2HCA) were improved compared with wild-type ADA2. Double-mutant R222Q/S265N exhibited 16-fold greater Kcat/Km compared with ADA2. pH = 7.6, [*E*] = 8.5 nmol/L.
Abbreviations: K_{cat}, turnover number; K_m, Michaelis–Menten constant; V_{max}, maximum initial velocity.

adenosine, and inosine was performed using a method based on a binary mobile phase, which consists of 7 mmol/L ammonium acetate (Buffer A; Sigma-Aldrich), pH 3, and acetonitrile (Buffer B; VWR Chemicals) at a flow rate of 1 mL/minute and UV detection set at 260 nm. Peak identities were confirmed by using reference standard compounds, and μmol/L concentrations of adenosine were inferred by comparing the peak area of samples with the calibration curve for the peak areas of adenosine standard. Levels of AMP, inosine, and adenosine were analyzed using HPLC to assess whether PEGADA2 effectively depleted adenosine in a tumor-like environment *in vitro*.

In vivo adenosine measurement studies were performed by Charles River Laboratories. Briefly, in mice, a microdialysis tumor probe with a 4 mm polyacrylonitril membrane (NO-PAN; Charles River Laboratories) was positioned in CT26 tumors when tumor size reached 250 mm^3; 1 day after surgery, baseline samples were collected. After the treatment of 3 mg/kg PEGADA2^{HCA}, samples were collected in 30-minute intervals for 5 hours and also collected after 24 hours. HPLC with MS-MS detection using 13C5-adenosine as internal standard (IS) to assess adenosine concentrations.

Human T-cell isolation and activation

Human CD8$^+$ T cells were isolated from fresh peripheral blood mononuclear cells (PBMC; from the San Diego Blood Bank) using the Human CD8$^+$ T Cell Enrichment Kit (StemCell Technologies) and resuspended in 10 ml PBS containing 2 μmol/L CellTrace Violet proliferation dye (Thermo Fisher Scientific). They were then incubated for 15 minutes at 37°C and 5% CO_2 in the dark, quenched for 5 minutes with 5 mL FBS, and washed and seeded at 3×10^5 cells/well in RPMI medium with 10% FBS supplemented with nonessential amino acids, 4-(2-hydroxyethyl)-1-piperazineethanesulfonic acid, and sodium pyruvate. After addition of PEGADA2, cells were treated with 500 μmol/L adenosine and with Human T-Activator Dynabeads (Life Technologies) coated with anti-CD3/anti-CD28 (1:2 bead:cell ratio) for 72 hours. Adenosine (500 μmol/L final) was added every 24 hours. At the end of the incubation proliferation was analyzed using the Novocyte Flow Cytometer (ACEA Biosciences).

Tumor dissociation and flow cytometry

Tumors and spleens were kept in PBS on ice during processing. Tumors were minced, placed in 2.5 mL RPMI medium containing 0.2 Wünsch units/mL Liberase DH and 100 Units/mL DNaseI (Roche), and dissociated using the GentleMACs Octo Dissociator (Miltenyi Biotec). Samples were dissociated using the pre-installed program 37C_m_TDK_1, then filtered through a 70 μmol/L cell strainer to remove any remaining large tissue fragments and washed with 10 mL RPMI medium. Cell suspension was then centrifuged at 300 × *g* for 7 minutes and the cell pellet was resuspended in 2 mL of staining buffer (2% FBS in PBS with 0.05% sodium azide). Spleens were dissociated with a syringe plunger, filtered through a 70 μmol/L cell strainer with 2% FBS in PBS, washed, and resuspended in 5 ml of staining buffer.

For each staining panel, tumor (200 μL) and spleen (50 μL) samples were transferred to 96-well round bottom plates, centrifuged at 500 × *g* for 3 minutes, and resuspended in 50 μL of antibody cocktail (see Supplementary Table S1) in staining buffer containing 0.5 μL/sample purified mouse Fc-blocking antibody (eBioscience) and 3 μL/ml Near InfraRed Fixable viability dye (Thermo Fisher Scientific). Plates were incubated on ice in the dark for 20 minutes, then centrifuged. Cell pellets were resuspended in 100 μL of fixation/permeabilization buffer (eBioscience) and incubated at room temperature for 10 minutes. Samples were then resuspended in staining buffer [1× permeabilization buffer for the lymphoid panel (eBioscience)] and intracellular staining was performed.

Flow cytometry was conducted using a Novocyte 3-laser flow cytometer and analyzed using NovoExpress software (ACEA Biosciences). The gating strategy used for the flow cytometry analysis is shown in Supplementary Fig. S3.

Macrophage stimulation

C57BL/6 mice were injected with 4% thioglycolate medium, and peritoneal exudates containing macrophages were collected 3 days later. Adherent macrophages cultured for 3 hours in tissue culture plates with RPMI with 10% FBS were detached and seeded at a density of 10^5 cells/well in 96-well flat-bottom plates. Cells were stimulated with 0.1 μg/mL ultra-purified LPS-EB (InvivoGen) with or without 50 μmol/L adenosine, in the presence or absence of varying concentrations of PEGADA2 variants for 24 hours. LPS alone and no-add groups were used as positive and negative controls, respectively. In some experiments, CPI-444 (Chemgood LLC), an adenosine A2 receptor antagonist was used. After LPS stimulation, cell culture supernatants were collected, and concentrations of IL12p70 and IL10 were determined using the U-PLEX platform (MesoScale Discovery).

Adenosine-dependent intracellular accumulation of cAMP in human T cells and the MDA-MB-231 breast cancer cell line

MDA-MB-231 breast cancer cell line (ATCC) was maintained in tissue culture as an adherent monolayer in RPMI with L-glutamine and 10% FBS at 37°C and 5% CO_2. On the day prior to the experimental procedure, cells were detached with trypsin and ethylenediaminetetraacetic acid, counted using a Nexcelom Cellometer Auto2000 (Nexcelom Bioscience), diluted to 1×10^6 cells/mL, and seeded at 1×10^5 cells/well in flat-bottom 96-well plates. Total human T cells were isolated from frozen PBMCs (from San Diego Blood Bank) using T cell enrichment kits (StemCell), counted, seeded at 5×10^5 cells/well in flat-bottom 96-well plates in the presence of 2.5×10^5 Dynabeads Human T-Activator CD3/CD28, and incubated for 24 hours at 37°C and 5% CO_2. For both cell types, culture medium and activation beads were removed from the wells. Cells were rinsed with PBS and resuspended in 50 μmol/L rolipram or PBS (test and control, respectively). Samples were incubated for 30 minutes (37°C, 5% CO_2), then PEGADA2 100 to 0.001 μg/mL was added followed by 50 μmol/L adenosine in PBS. Cells were incubated again, washed with PBS, and resuspended in lysis buffer provided with the Cyclic AMP XP Assay Kit (Cell Signaling Technology), and assayed for cAMP content with an ELISA. For MDA-MB-231, 1 μmol/L of adenosine receptor agonists 2′MeCCPA (A_{1R}), CGS21680 (A_{2AR}), BAY 60–6583 (A_{2BR}), and 2-Cl-

Downloaded from cancerres.aacrjournals.org on January 20, 2022. © 2021 American Association for Cancer Research.

Published OnlineFirst April 16, 2021; DOI: 10.1158/0008-5472.CAN-21-0340

IB-MECA (A_{3R}), and adenosine analog *N*-ethylcarboxamidoadenosine (control) were added to respective wells and incubated for 15 minutes at 37°C and 5% CO_2, followed by cAMP ELISA as described. Adenosine receptor antagonists (1 μmol/L), PSB36 (A_{1R}), SCH58621 (A_{2AR}), PSB603 (A_{2BR}), MRS1523 (A_{3R}), and XAC (nonspecific adenosine receptor antagonist control) were added to respective wells in the presence of 50 μmol/L adenosine and incubated for 15 minutes at 37°C and 5% CO_2, followed by cAMP ELISA. Rolipram (50 μmol/L) was added to the cells before adenosine receptor activation to allow cAMP accumulation.

Bioinformatics analyses

Survival analysis of high versus low ADA2 expressors for different solid tumor indications was performed using OncoLnc tool (from http://www.oncolnc.org; ref. 24) and bioinformatics analysis for differential gene expression in lung and breast cancer was performed by Rancho BioSciences using The Cancer Genome Atlas (TCGA) database. Briefly, TCGA RNA-sequencing (RNA-seq) data for breast cancer and lung adenocarcinoma were downloaded from the Genomic Data Commons Data Portal (https://portal.gdc.cancer.gov/repository) using the 'gdc-client' (RNAseq measurements) and 'gdc-tsv-tool.py' (clinical data) command-line tools. Datasets were assembled by simplifying clinical sample annotation and labeling samples (e.g., BRCA_F_WH_IIA_C50.9_1, cancer_gender_race_cancer stage_tissue code_number for individual samples), filtering samples not fully annotated for these attributes, removing normal samples and genes with low expression, and keeping genes with count >5 in ≥260 (lung) or 550 (breast) samples. The assembled datasets were used in subsequent analyses.

To identify differential gene expression patterns for patients with $ADA2^{high}$ versus $ADA2^{low}$, RNA-seq data from the tumors of patients with breast and lung cancer were downloaded from TCGA database. The top and bottom 30% *CECR1* gene (the gene coding for ADA2) expressers, based on RNA counts ($ADA2^{high}$ vs. $ADA2^{low}$, respectively), were compared using Morpheus software (Morpheus, http://software.broadinstitute.org/morpheus). Gene expression patterns for each individual patient were adjusted using *z*-score (minimum value of −2, maximum value of 2) and grouped as $CECR1^{high}$ versus $CECR1^{low}$ patient groups. Differential gene expression analysis was performed between these two groups. Pathway analysis was performed on the lists of genes showing significant difference [$P < 0.05$ and Log2FC>1 (i.e., an average change of two-fold or more)] between the two conditions, using the hypergeometric test in R's clusterProfiler-package and the Gene Ontology-Biological Pathway (GO-BP; refs. 25, 26).

The correlation of ADA2 expression with T-cell infiltration into tumors and with T-cell activation was analyzed using GEO dataset GSE58644 (27, 28). T-cell infiltration and costimulation scores for each patient were calculated using published gene signatures (29, 30), as the sum of *z* scores of all the genes in the signature.

Survival analyses for lung and breast cancer, including CD73/CD39 stratification, and breast and colon cancer subtypes based on the expression of ADA2 were performed using the KMPlotter database (27, 31) and the GEO dataset, GSE39582 (32), respectively. Significance was calculated using Log-rank test.

Results

Increased expression of the ADA2 gene *CECR1* is associated with increased survival in patients with different solid tumors

We analyzed the association of survival with *CECR1* expression in patients with breast cancer, lung adenocarcinoma, sarcoma, melanoma, pancreatic cancer, or kidney cancer, using data from TCGA database, and observed that those with high *CECR1* mRNA counts (designated $ADA2^{high}$; i.e., the top 30%) had significantly longer survival than patients whose tumors exhibited low *ADA2* mRNA counts ($ADA2^{low}$; i.e., the bottom 30%; **Fig. 1A**). In an analysis of the Gene Expression Omnibus (GEO; ref. 33) dataset GSE39582, which has gene expression-profiling data for five different subtypes (32), higher ADA2 expression was found to predict better survival in the C2 and C5 molecular subtypes. Although the C5 tumors were characterized by high chromosomal instability, frequent mutations in *KRAS* and *TP53*, and activated Wnt signaling, the C2 subtype was characterized by high microsatellite instability and increased immune system activation (**Fig. 1A**). We also observed increased survival in patients with breast and lung cancer based on higher ADA2 expression, as assessed using microarray-based datasets (Supplementary Fig. S4; ref. 31). Association between elevated ADA2 expression and increased survival was particularly substantial among patients with triple-negative (basal) and HER2+ breast cancer subtypes (Supplementary Fig. S4), two of the most aggressive subtypes of breast cancer.

Engineered ADA2 double mutant showed 16× catalytic efficiency compared with wild-type ADA2

The K_m value and catalytic activity of ADA2 is low (21). Therefore, we introduced single-point mutations in the ADA2 catalytic site to increase its catalytic activity. Engineered ADA2 variants with FLAG tags were expressed in CHO-S cells, purified by anti-FLAG resin, screened by activity assay, and ranked on the basis of their activity. Among tested mutants, the single mutants, R222Q and S265N, showed significant improvement in kinetic parameters compared with the wild-type enzyme (ADA2 WT; **Fig. 1B**). After combining these mutations (R222Q/S265N), the catalytic efficiency increased 16-fold in comparison with ADA2 WT (**Table 1**). Therefore, the double mutant (NME62) was selected for further biological characterization. The triple mutant, R222Q/S265N/K374D (NME58), with an additional mutation in its heparin binding site had similar activity to NME62 and was used in some experiments. A variant with double mutation, E333A/D416V (NME133), had no detectable activity in a screening assay and was used as a negative control in biological mechanism-of-action studies (Supplementary Table S2).

A structural analysis approach was used to help determine the cause of the significant improvement in the catalytic efficiency of NME62 and NME58. We observed two major differences when a structural model of NME62, predicted by the modelling server Phyre 2 (34), was compared with the structure of ADA2 WT complexed with the substrate, the adenosine transition state analog coformycin. The first difference observed was in the secondary structure changes in the active site region containing residues 81 to 89. D89 is a key residue that contributes to ADA2 catalysis, and H86 and H88 are the zinc-coordinating residues of ADA2. This region forms a β strand in the ADA2 WT-coformycin complex structure, whereas the same region was predicted to be a loop by Phyre 2 in NME62 (**Fig. 1C**). This indicates a possible increase in flexibility of the NME62 active site with a subsequent impact on substrate binding and turnover rate. The second difference was that two newly formed H-bonds were observed between the Q222 residue and the substrate coformycin in the structure model of NME62; in comparison, H-bonds were not observed between the R222 residue and the coformycin in the ADA2 WT. This may also contribute to changes in substrate binding (**Fig. 1C**).

Downloaded from cancerres.aacrjournals.org on January 20, 2022. © 2021 American Association for Cancer Research.

Published OnlineFirst April 16, 2021; DOI: 10.1158/0008-5472.CAN-21-0340

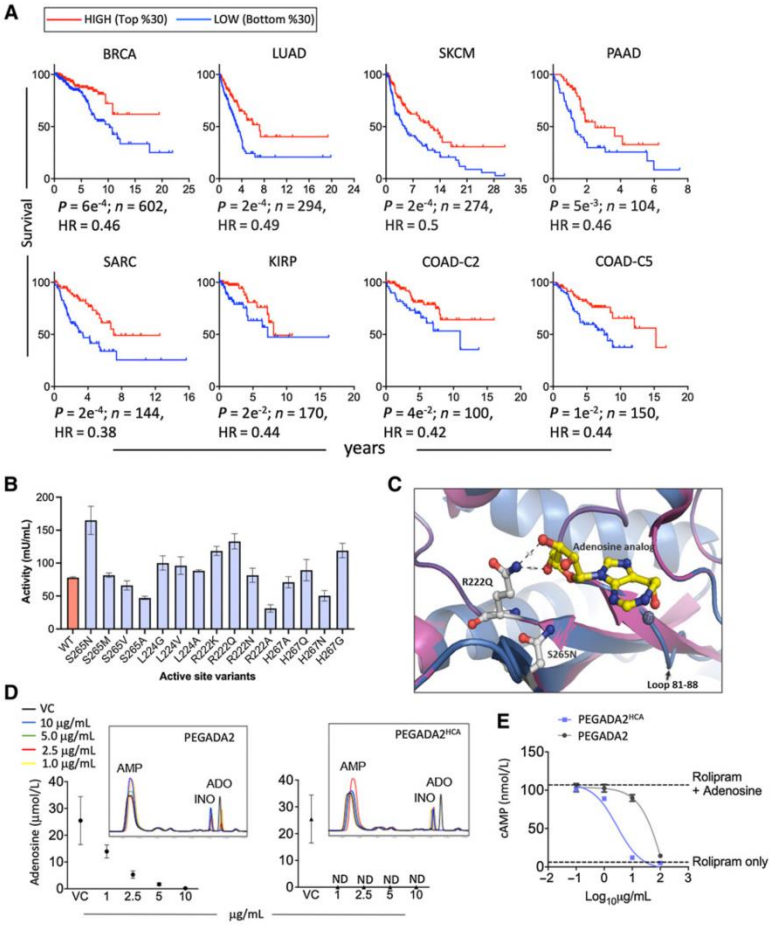


Figure 1.

Clinical association between ADA2 and patient survival and identification of ADA2 mutants for increased catalytic activity for drug development. **A,** Survival analysis of cancer subtypes other than colon cancer was performed using TCGA database and the OncoLnc tool (from ref. 24). Cancer types with higher ADA2 expression were associated with significantly longer survival. Survival analysis of patients with colon cancer from different subtypes based on the expression of ADA2 was performed using the GEO dataset, GSE39582 (32). **B,** ADA2 active site variant screening and ranking. Error bars, ±SD. **C,** Comparison of ADA2 structure and ADA2 double mutant R222Q/S265N modeled structure. In the modeled structure (blue), the region containing residues 81 to 88 at the active site formed a more flexible loop, whereas in ADA2 they form a β strand (magenta). **D,** Adenosine levels measured by HPLC using supernatants from CD73^{-} A375 melanoma cells treated with AMP in the absence or presence of PEGADA2^{HCA} (1.0, 2.5, 5.0, and 10.0 µg/mL). **E,** Accumulation of cAMP in MDA-MB-231 human TNBC cell line was tested after stimulation with 50 µmol/L adenosine for 15 minutes in the presence or absence of PEGADA2^{HCA} versus PEGADA2. Rolipram (50 µmol/L) was added to the culture to allow the accumulation of cAMP before the addition of adenosine. Error bars for **B**, **D**, and **E**, ±SD.

Downloaded from cancerres.aacrjournals.org on January 20, 2022. © 2021 American Association for Cancer Research.

Published OnlineFirst April 16, 2021; DOI: 10.1158/0008-5472.CAN-21-0340

Because all ADA2 variants R222Q/S265N and R222Q/S265N/K374D, with and without FLAG tags, had comparable enzymatic activity, we named them collectively "high catalytic activity" variants to simplify nomenclature. High catalytic activity variants are abbreviated as ADA2^{HCA} or PEGADA2^{HCA} for the PEGylated version (Supplementary Table S2).

PEGylation significantly improved pharmacokinetics of ADA2^{HCA}

The results of the pharmacokinetic study showed that both half-life and AUC of PEGADA2^{HCA} were significantly increased compared with non-PEGylated ADA2 WT (Supplementary Fig. S5), indicating successful pharmacokinetic (PK) improvement with PEGylation.

PEGADA2^{HCA} inhibits tumor-associated adenosine accumulation and adenosine signaling *in vitro*

CD73 is expressed in the TME on the cell surface and converts adenosine monophosphate (AMP) to adenosine (35). We treated a CD73^{+} A375 melanoma cell line with AMP to simulate an adenosine-generating TME, and compared PEGADA2 and PEGADA2^{HCA} with respect to the depletion of tumor generated adenosine. PEGADA2 and PEGADA2^{HCA} each prevented extracellular adenosine accumulation in supernatants of CD73^{+} A375 melanoma cells treated with AMP. Notably, at least 10-fold less PEGADA2^{HCA} than PEGADA2 was required to prevent adenosine accumulation (**Fig. 1D**).

Previous studies have indicated that adenosine plays a role in the aggressiveness of breast tumors by directly stimulating adenosine receptors (9). In a test of PEGADA2's effect in human breast tumors, we confirmed that MDA-MB-231 human triple-negative breast cancer cell line (TNBC) accumulated cyclic AMP (cAMP) in response to adenosine signaling (Supplementary Fig. S6), and established that PEGADA2^{HCA} more effectively reversed cAMP accumulation than PEGADA2 in MDA-MB-231 cells stimulated with adenosine (**Fig. 1E**). These results suggest that engineered PEGADA2^{HCA} effectively reduces tumor-generated adenosine, which can translate into a decrease in intracellular adenosine signaling.

PEGADA2^{HCA} effectively reverses adenosine-mediated polarization of macrophages to an anti-inflammatory phenotype

We evaluated whether PEGADA2 variants prevent the adenosine-mediated polarization of macrophages into an anti-inflammatory phenotype by incubating peritoneal macrophages from C57BL/6 mice with PEGADA2 or PEGADA2^{HCA} in the presence of lipopolysaccharide (LPS) and adenosine. Adenosine strongly suppressed the release of proinflammatory and immuno-stimulatory cytokine IL12, while increasing anti-inflammatory IL10 production by peritoneal macrophages from C57BL/6 mice in the presence of LPS (**Fig. 2A**). These adenosine-mediated polarization effects were reversed by both PEGADA2 and PEGADA2^{HCA}, with PEGADA2^{HCA} having greater potency (**Fig. 2A**). PEGADA2 variants demonstrated similar functional activity to the non-PEGylated variants for reversing the effect of adenosine on IL12 and IL10 release from macrophages (**Fig. 2B**), suggesting that the engineered ADA2 variants retained functional activity after PEGylation. PEGADA2^{INACT}, an engineered inactive variant with intact growth factor and heparin-binding domains, but no ability to convert adenosine to inosine based on enzymatic activity (Supplementary Table S2), was used as a control for possible nonenzymatic effects. This variant failed to reverse the effect of adenosine on macrophage polarization into an anti-inflammatory phenotype (**Fig. 2C**). **Figure 2D** shows that, at the same concentrations, PEGADA2^{HCA} but not the small molecule adenosine receptor blockade CPI-444, completely reversed adenosine inhibition of IL12 release. Collectively, these results suggest that PEGADA2 effectively reverses adenosine suppression of macrophages in an enzyme-activity dependent manner and this effect is not influenced by PEGylation.

PEGADA2^{HCA} decreases growth and lung colonization of tumor cells

Previous studies have shown that the MC38 and CT26 murine colon cancer models are responsive to checkpoint inhibitors (36). These tumors have very low levels of adenosine converting enzyme CD73; however, they have been shown to be sensitive to CD73-generated adenosine from nontumor resources such as regulatory T cells and stromal cells (37, 38). Nonmetastatic EMT6 and highly metastatic 4T1 orthotopic breast tumor models represents CD73^{+} TNBC subtypes (39–41) and found to be responsive to adenosine receptor/CD73 blockade (42). Therefore, we have tested the effect of PEGADA2^{HCA} on tumor growth on MC38, CT26, and EMT6 models, and tested lung dissemination using 4T1 model. Treatment of MC38 tumor-bearing mice with PEGADA2^{HCA} significantly reduced tumor growth in a dose-dependent manner. An antibody against programmed cell death ligand-1 (PD-L1) was used as a positive control (**Fig. 3A**). PEGADA2^{HCA} also reduced the growth of EMT6 breast adenocarcinoma (**Fig. 3B**) and CT26 colon carcinoma tumors (**Fig. 3C**). PEGADA2^{HCA} significantly reduced adenosine accumulation in the tumor (**Fig. 3D**). Inhibition of tumor growth was absent in the group receiving the enzyme-inactive variant (**Fig. 3E**). PEGADA2^{HCA} treatment significantly reduced the lung colonization of 4T1 tumors (**Fig. 3F** and **G**) versus vehicle. These data suggest that PEGADA2^{HCA} treatment effectively decreases tumor growth by targeting adenosine and reducing metastatic colonization.

Increased expression of the ADA2 gene *CECR1* is associated with enrichment of immune-related pathways in humans

We performed differential gene expression analysis between ADA2^{high} and ADA2^{low} breast cancer and lung adenocarcinoma using data from the TCGA database. We identified more than 1,000 genes differentially expressed in ADA2^{high} versus ADA2^{low} tumors using the criteria of $P < 0.05$ and $\log_2 FC > 1$ (**Fig. 4A**). More than 50% of the genes and pathways that are significantly higher in the ADA2^{high} group are common to both lung adenocarcinoma and breast cancer (**Fig. 4B–E**). Pathway analysis indicated that high ADA2 expression is associated with enrichment of immune-related pathways (**Fig. 4C** and **D**). The most significantly enriched pathway is the adaptive immune response pathway for both cancer types in ADA2^{high} tumors (**Fig. 4E**). ADA2^{high} tumors also show high expression of IFNγ gene signatures (**Fig. 4B**), which predict increased response to checkpoint blockade (43) and low expression of genes associated with tumor progression and metastasis such as *TGFBR3 L* (44) and *STC2* (Supplementary Fig. S7; ref. 45). All the differentially expressed genes and pathways including the common genes and pathways between ADA2high expressors of patients with lung and breast cancer were indicated in Supplementary Table S3.

PEGADA2^{HCA} increases tumor infiltration of immune cells *in vivo*

We tested the effect of PEGADA2^{HCA} on tumor infiltration of immune cells using syngeneic MC38 and CT26 tumor models 1 day after the third dose, when the sizes of tumors treated with PEGADA2HCA tends to diverge as compared with the vehicle control groups (Supplementary Fig. S8). PEGADA2^{HCA} significantly increased the density of the CD8^{+} tumor-infiltrating

Downloaded from cancerres.aacrjournals.org on January 20, 2022. © 2021 American Association for Cancer Research.

Published OnlineFirst April 16, 2021; DOI: 10.1158/0008-5472.CAN-21-0340

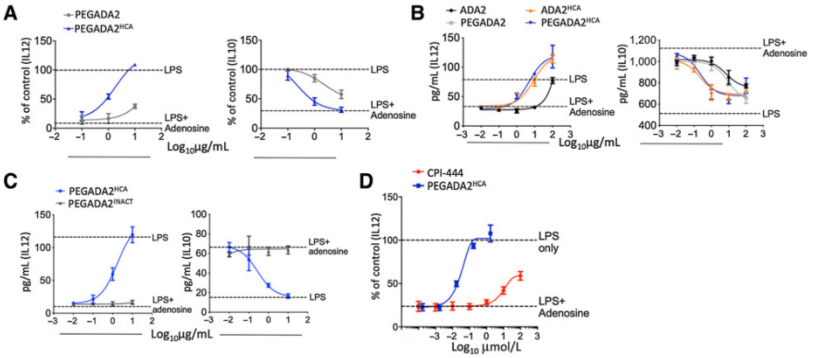


Figure 2.

PEGADA2 reverses adenosine-mediated polarization of peritoneal macrophages into suppressive phenotype in an enzyme activity–dependent manner. Peritoneal macrophages elicited after thioglycolate treatment were stimulated with 1 µg/mL LPS ± 50 µmol/L adenosine. **A–C,** Effect of different concentrations of PEGADA2 versus PEGADA2^{HCA} (**A**), PEGADA2 versus non-PEGylated ADA2 and PEGADA2 versus PEGADA2^{HCA} (**B**), PEGADA2^{HCA} versus PEGADA2^{INACT} (**C**) on immunostimulatory IL12 and anti-inflammatory IL10 secretion was tested using multiplex cytokine enzyme-linked immunosorbent assay. **D,** PEGADA2^{HCA} versus the small-molecule adenosine A2 receptor blocker, CPI-444, was tested by enzyme-linked immunosorbent assay. **B** and **D** are from one experiment with three replicates. **A** and **D** are normalized from three independent experiments with three replicates. **B** and **C** are representative of one of two experiments with similar results (n = 3/group). Error bars, ±SEM for **A** and **D**, and ±SD for **B** and **C**.

lymphocyte (TIL) population, CD4$^+$ TIL, NK cells, and CD103$^+$MHCII$^+$CD11b^{dim} type I dendritic cells (cDC1) within MC38-ev tumors, but not in the spleen (**Fig. 4F**; Supplementary Fig. S9). PEGADA2^{HCA} did not change the density of tumor- or spleen-associated CD103$^-$MHCII$^+$CD11b$^+$CD11c$^+$ myeloid dendritic cell populations (MyDC; cDC2), macrophages, or Ly6G$^+$ granulocytic myeloid-derived suppressor cell populations (GrMDSC; **Fig. 4F**; Supplementary Fig. S9). PEGADA2^{HCA} also significantly increased both the density and proportion of CD8$^+$ TIL, cDC2, and cDC1 populations in a CT26 model (**Fig. 4G**).

PEGADA2^{HCA} modulates adaptive immune responses to suppress tumor growth

Clinically, high tumor expression of ADA2 in patients with breast cancer was positively associated with the density of TIL and T-cell costimulation scores (**Fig. 5A** and **B**, respectively). In a test of the effect of PEGADA2 on direct adenosine signaling in primary human T cells, incubation of prestimulated T cells with PEGADA2^{HCA} prevented cAMP accumulation after adenosine administration (**Fig. 5C**). PEGADA2^{HCA} completely reversed adenosine suppression of T-cell proliferation in a dose-dependent manner (**Fig. 5D**). Depletion of CD8$^+$ T cells from tumor-bearing animals completely reversed tumor growth inhibition (TGI) by PEGADA2^{HCA} (**Fig. 5E**). Collectively, these results suggest that tumor enrichment of ADA2 or PEGADA2 treatment can promote adaptive immune responses to inhibit tumor growth.

In both preclinical and clinical setting targeting both adenosine A2 receptors and PD-1 causes combinatorial effect in control of tumor growth (46). Our bioinformatics analysis also indicates that increased ADA2 expression was associated with increased expression of the immunotherapy response genes/signatures (**Fig. 4B**). Therefore, we tested the effect of PEGADA2HCA alone or in combination with anti-PD-L1 antibody on growth of MC38 and MB49 tumors. Although monotherapy with PEGADA2^{HCA} or anti-PD-L1 resulted in 39% and 35% TGI, respectively, combining these two agents resulted in 62% TGI (**Fig. 5F**). Likewise, we evaluated combining PD-L1 blockade with PEGADA2^{HCA} in MB49 tumors, which are known to be sensitive to adenosine receptor blockade (7). Combining PD-L1 blockade with PEGADA2^{HCA} resulted in significantly greater TGI, compared with the control group or treatment with single agents alone (**Fig. 5G**). Overall, these results suggest that enzymatic targeting of adenosine in the TME shows promise as a novel cancer immunotherapy, and this approach can potentially be further improved by increasing the catalytical activity and/or half-life of the enzyme.

High ADA2 expression is associated with better survival for TNBC and NSCLC patients with high CD73 and CD39 expression

When gene expression profiles of microdissected tumor epithelium and stroma from 38 TNBC tumors were analyzed, both ADA1 and ADA2 expression was found to be higher in stroma as compared with tumor cells (**Fig. 6A**). However, ADA2 expression was higher than ADA1 expression in both stroma and tumor (**Fig. 6B**). Overall survival of chemotherapy-treated patients with TNBC, based on ADA2 expression levels, was evaluated after stratifying patients as expressing high versus low levels of CD73 and CD39. Higher expression of ADA2 was significantly associated with better survival in only those patients with high levels of CD73 and CD39, but not those with low levels of CD73 and CD39 (**Fig. 6C**). Similarly, when the chemotherapy-treated patients with non–small cell lung cancer (NSCLC) were stratified on the basis of CD73 and CD39 expression, higher ADA2 levels were significantly associated with better disease-specific survival only in

Downloaded from cancerres.aacrjournals.org on January 20, 2022. © 2021 American Association for Cancer Research.

Published OnlineFirst April 16, 2021; DOI: 10.1158/0008-5472.CAN-21-0340

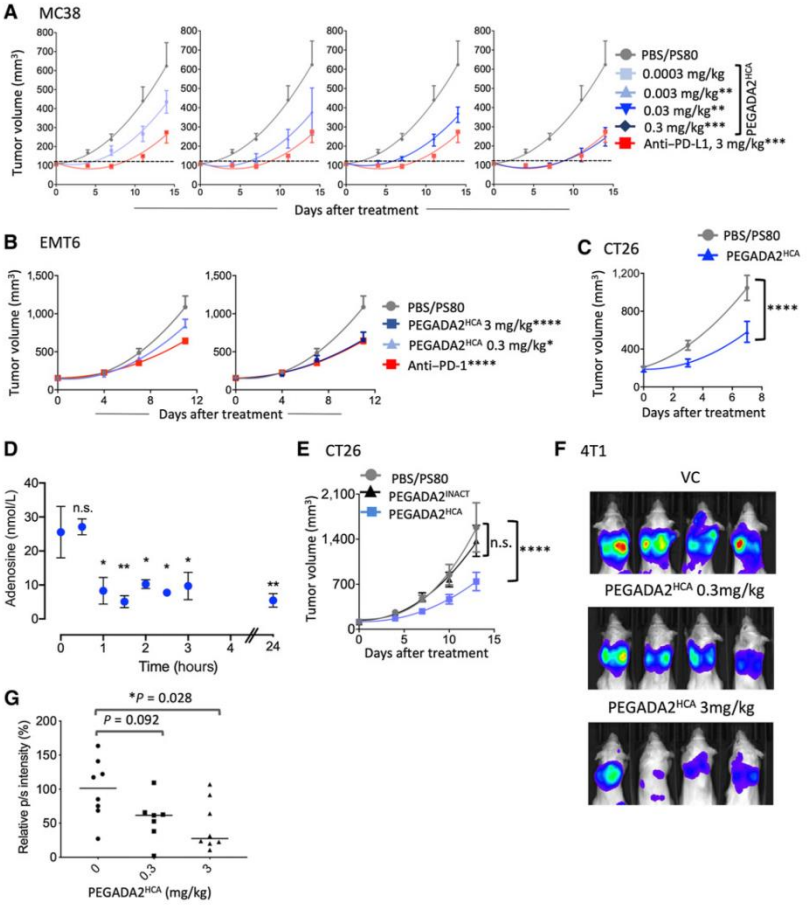


Figure 3.

PEGADA2^{HCA} inhibits tumor growth and lung dissemination. **A,** Mice with ~100 mm^3 MC38-ev tumors were randomized and administered with intraperitoneal anti-mouse PD-L1 (clone 10F.9G2) and intravenous PEGADA2^{HCA}, or its vehicle (PBS), twice weekly (results from two experiments with similar results, $n = 8$/group). **B,** EMT6 breast tumor cells were inoculated orthotopically in BALB/c mice. When tumors reached ~150 mm^3, mice were treated intravenously with 0.3 or 3.0 mg/kg PEGADA2^{HCA} twice weekly using anti-PD-1 5 mg/kg as a positive control (results from one of two experiments with similar results, $n = 10$). **C,** CT26 tumor-bearing mice were treated biweekly with PEGADA2^{HCA} 0.3 mg/kg when tumors reached ~200 mm^3. **D,** Microdialysate from CT26 tumor-bearing animals were tested for adenosine concentrations before and after PEGADA2^{HCA} treatment by HPLC with MS-MS detection. **E,** CT26 tumor-bearing mice were treated with PEGADA2^{HCA} and PEGADA2^{INACT} (0.3 μg/kg; results from one experiment, $n = 8$/group). Results were analyzed by two-way ANOVA and *post hoc* Dunnett or Tukey tests. **F,** Balb/c mice injected intravenously with 4T1-Luc tumor cells (10^6) were treated with indicated concentrations of PEGADA2^{HCA}. Lung dissemination was measured by IVIS imaging of luciferase activity 3 weeks after tumor cell inoculation. **G,** Analysis of normalized values of luciferase activity in photons/second (p/s; results from pooled data from two cohorts, $n \geq 7$/group). Results were analyzed by one-way ANOVA and *post hoc* Tukey tests. *, $P < 0.05$; **, $P < 0.01$; ***, $P < 0.001$; ****, $P < 0.0001$. Error bars, ±SEM for **A–E**.

Downloaded from cancerres.aacrjournals.org on January 20, 2022. © 2021 American Association for Cancer Research.

Published OnlineFirst April 16, 2021; DOI: 10.1158/0008-5472.CAN-21-0340

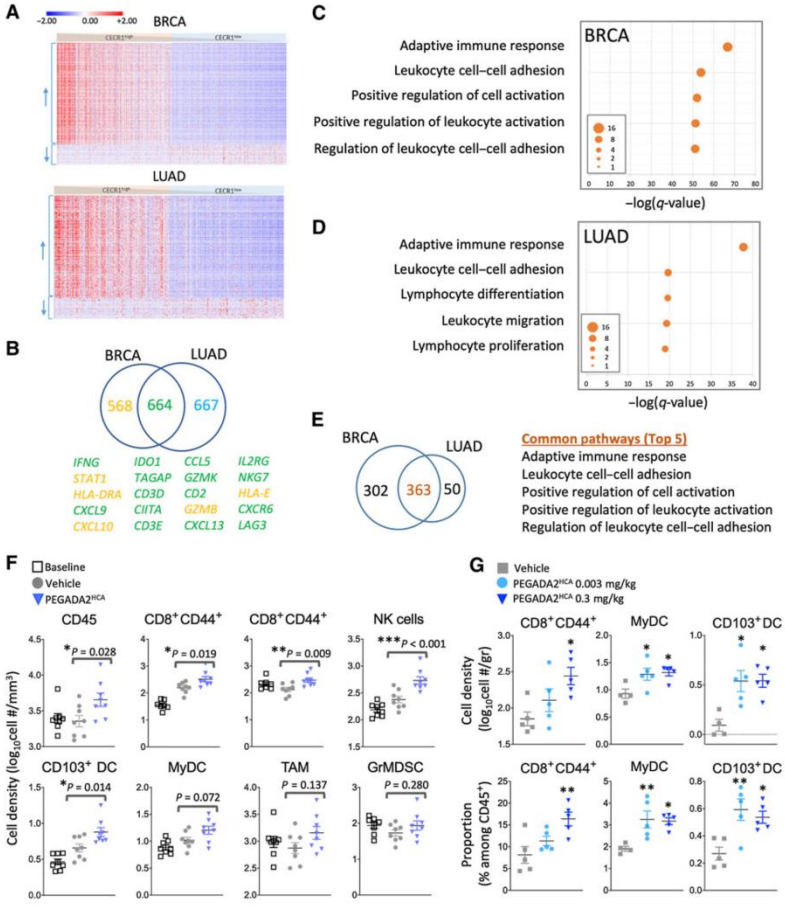


Figure 4.

Endogenous ADA2 expression and exogenous PEGADA2^{HCA} both promote adaptive immune responses. RNA-seq data from the tumors of patients with breast and lung cancer were downloaded from TCGA database. The top and bottom 30% *CECR1* gene (gene coding for ADA2) expressers, based on RNA counts (ADA2^{high} vs. ADA2^{low}, respectively), were compared for differential gene expression patterns. **A,** Gene expression patterns for each individual patient were normalized using *z*-score (minimum value of −2, maximum value of 2) and grouped as *CECR1*^{high} versus *CECR1*^{low} patient groups to generate the heatmap for differential gene expressors. **B,** Number of genes differentially expressed by patients with *CECR1*^{high} BRCA, LUAD, and BRCA plus LUAD. **C** and **D,** Pathway enrichment analysis was performed for the genes significantly upregulated among patients with *CECR1*^{high} using the GO-BP database (25, 26) for patients with breast cancer (**C**) and lung cancer (**D**). **E,** Numbers of GO-BP pathways enriched in patients with *CECR1*^{high} BRCA, LUAD, and BRCA plus LUAD and the top five common pathways between the two indications. **F** and **G,** Tumor infiltration of indicated immune cell populations in MC38-ev (**F**) and CT26 (**G**) tumors was tested by flow cytometry 24 hours after the third dose of PEGADA2^{HCA}. For MC38-ev tumors, baseline represents samples stained for flow cytometry during stratification of animals for dosing (9 days after tumor inoculation). **F** and **G** are from one experiment ($n \geq 7$ mice/group). Results were analyzed by one-way ANOVA and *post hoc* Tukey test. Error bars, ±SEM for **F** and **G**.

Downloaded from cancerres.aacrjournals.org on January 20, 2022. © 2021 American Association for Cancer Research.

Published OnlineFirst April 16, 2021; DOI: 10.1158/0008-5472.CAN-21-0340

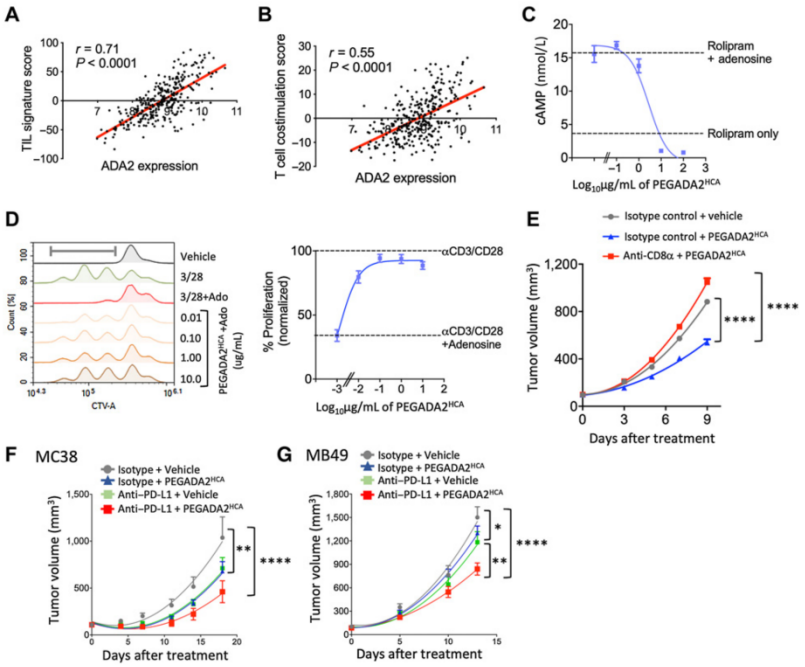


Figure 5.

ADA2 expression correlates with TIL phenotype. PEGADA2 modulates adaptive immune responses to inhibit tumor growth and causes combinatorial effects with PD-1 blockade. **A** and **B,** TIL score (**A**) and T-cell costimulation score (**B**) in association with ADA2 expression in patients with breast cancer (GEO dataset, GSE58644). **C,** Human T cells enriched from PBMCs were stimulated with anti-CD3/anti-CD28–coated Dynabeads and incubated with 50 μmol/L adenosine and PEGADA2^{HCA}. cAMP accumulation was measured after 15 minutes of adenosine exposure. Rolipram (50 μmol/L) was added before addition of adenosine to block the phosphodiesterase activity to permit cAMP accumulation. **D,** Human CD8$^+$ T cells were stimulated with anti-CD3/anti-CD28–coated Dynabeads for 72 hours, with 500 μmol/L adenosine added daily. Proliferation was measured by dilution of CTV label. **E,** EMT6 tumor-bearing mice received anti-CD8α–depleting antibody (200 μg/mouse) or IgG control on study days −1, 3, and 7, with intraperitoneal injection of 3.0 mg/kg PEGADA2^{HCA} twice weekly. PBS + IgG isotype control was vehicle control. **F,** Expression of PD-1$^-$ tumor-infiltrating CD8$^+$ cells from MC38-ev tumors were tested by flow cytometry at second or third dose of PEGADA2^{HCA}. **G,** MC38-ev tumor-bearing mice received 1 mg/kg anti-mouse PD-L1 or 3 μg/kg PEGADA2^{HCA} alone or in combination (one experiment, $n = 8$/group). **H**, MB49 tumor-bearing mice received 3 μg/kg PEGADA2^{HCA} intravenously and antimouse PD-L1 0.3 μg/kg i.p., alone or in combination (pooled data from two independent experiments, $n \geq 10$/group). Results were analyzed by two-way ANOVA and *post hoc* Dunnett or Tukey tests. *, $P < 0.05$; **, $P < 0.01$; ****, $P < 0.0001$. Error bars, ±SD for **C** and ±SEM for **D–H**.

those expressing high levels of CD73 and CD39 (**Fig. 6D**). Increased ADA1 expression is not correlated with survival in CD73/CD39high or CD73/CD39low subgroups among patients with TNBC or NSCLC (**Fig. 6E** and **F**). These results underlie an important role for adenosine and expression of ADA2 in TME.

Chronic treatment of PEGADA2^{HCA} does not cause overt toxicity in mice

To test if PEGADA2^{HCA} treatment can potentially be well tolerated as a potential new therapy we have tested changes in weights and several clinical chemistry parameters in mice, indicative of renal or hepatotoxicity. Treatment of mice with different doses of PEGADA^{HCA} caused no weight reduction and lead to weight changes similar to that of vehicle group both in MC38-bearing C57BL/6 mice and CT26-bearing Balb/c mice (Supplementary Fig. S10). When terminal bleeding samples from the same mice were analyzed for basic markers of hepatotoxicity or renal toxicity from plasma, we did not observe any significant and/or dose-dependent changes after PEGADA2^{HCA} treatment as compared with vehicle group (Supplementary Fig. S11).

Downloaded from cancerres.aacrjournals.org on January 20, 2022. © 2021 American Association for Cancer Research.

Published OnlineFirst April 16, 2021; DOI: 10.1158/0008-5472.CAN-21-0340

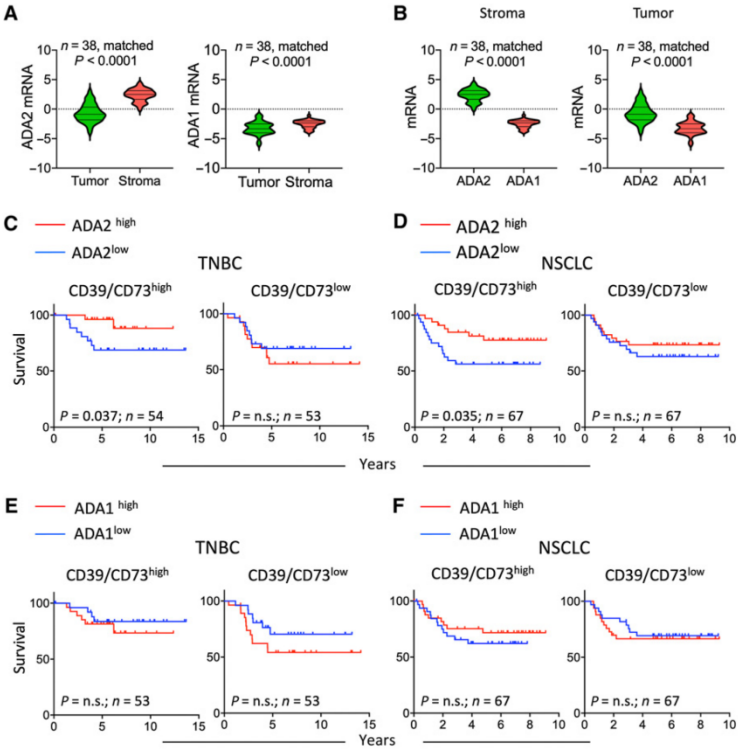


Figure 6.
High ADA2 expression predicts better survival for patients with TNBC and NSCLC with high CD73 and CD39 expression. **A,** Gene expression profiles of ADA1 and ADA2 in microdissected tumor epithelium versus stroma from 38 patients with TNBC were analyzed using GEO dataset GSE88715. **B,** Graphs in **A** were used to compare ADA1 versus ADA2 expression in stroma or tumor. **C,** Survival analysis of patients with breast cancer with different molecular subtypes based on the expression of ADA2 and CD73/CD39 was performed using the KMPlotter database and the GEO dataset, GSE58812. **D,** The survival analysis of patients with NSCLC based on ADA2 and CD73/CD39 was performed using the GEO dataset, GSE14814. n.s., nonsignificant.

Discussion

Adenosine has been associated with both protumoral (35) and antitumoral effects (13–15). Much of the *in vivo* evidence for protumoral effects of adenosine relies heavily on targeting one or two receptor subtypes, adenosine generation mechanisms, and on evaluating the effects of particular adenosine receptors in knockout animals. Our study provides direct evidence that the extracellular adenosine molecule acts as a tumor promoter. We also introduce engineered ADA2 as a novel cancer immunotherapy, which can inhibit tumor growth by reducing adenosine in an enzyme activity-dependent manner and by modulating immune responses. Reducing adenosine through enzymatic degradation may offer advantages over other single-agent therapies that target the adenosine pathway, such as small molecule blockade of individual adenosine receptors or CD39/CD73 blockade. These potential advantages may arise for three reasons. First, more than one receptor promotes tumor growth through adenosine. Second, blockade of adenosine receptors promotes generation of more adenosine, and finally, there are other pathways that promote adenosine generation along with the CD39/CD73 pathway in the TME (35, 41).

ADA2 catalyzes deamination of adenosine into inosine, a more stable nucleoside than adenosine. Recent studies have indicated that

Downloaded from cancerres.aacrjournals.org on January 20, 2022. © 2021 American Association for Cancer Research.

Published OnlineFirst April 16, 2021; DOI: 10.1158/0008-5472.CAN-21-0340

inosine can be an additional carbon source for CD8 T cells in TME (47). Also, inosine generated by microbiome can weakly stimulate adenosine A2A receptors (17), which can provide basal level A2AR signaling required for T-cell maintenance and growth factor responsiveness of $CD8^+$ T cells (6, 16, 17). Therefore, ADA2 may have a dual mechanism of action: inhibiting immunosuppressive adenosine signaling by reducing adenosine and increasing CD8+ T cell fitness by generating inosine. These observations provide a rationale to test $PEGADA2^{HCA}$ in subset of patients with low levels of inosine-generating microbiomes and increased expression of recently discovered adenosine gene signature (46), which indicates activation of immunosuppressive myeloid cells through adenosine signaling.

ADA2 expression among patients with breast, lung, pancreas, melanoma, and sarcoma tumor types; and increased ADA2 expression in a subgroup of patients with colon and kidney carcinoma is associated with improved prognosis. A hallmark of some of these tumors is elevated adenosine levels. Some are known as inflamed tumors, which are associated with increased tumor mutational burden and immune cell infiltration (i.e., lung cancer and melanoma), and some are known to be tumors with limited immune cell infiltration (48, 49). We observed an association between ADA2 expression and survival in all these tumor types. Immune cells, tumor cells and cells adjacent to tumor cells can be sources of adenosine through high expression of CD39 and/or CD73 (50–52). In immunologically active tumors, adenosine generation can be achieved by infiltrating immune cells, causing autocrine/paracrine signaling for suppression, whereas in immune-excluded tumors, adenosine can be generated by tumor cells to suppress the immune responses even at early phases of tumor growth, causing these tumors to stay immunologically dormant. In addition, it is important to note that high ADA2 expression was not associated with prolonged survival in all cancer indications, suggesting that adenosine could couple with other suppressive mechanisms in these indications or play a minor role for tumor growth. Further research is required to contextualize how ADA2 and other sources of adenosine generation, such as nucleoside transporters, may fit in this picture.

Higher expression of CD73 (which converts AMP to adenosine, contributing to adenosine accumulation) has been associated with poor prognosis (51) or decreased survival (53) in patients with some cancers such as TNBC. Our data indicate that increased expression of the adenosine-lowering ADA2 enzyme is associated with a favorable prognosis, providing further evidence that activation of pathways leading to adenosine accumulation (low ADA2, high CD73) is immunosuppressive. Importantly, our analyses further showed that higher expression of ADA2 is significantly associated with better survival in both patients with TNBC and NSCLC with only high CD39/CD73 levels, suggesting a critical role for ADA2 in controlling adenosine levels in the tumor microenvironment. Current approaches targeting adenosine signaling utilize CD39 and CD73 blocking antibodies, and/or small-molecule inhibitors of adenosine receptors (54). Deletion of A_{2AR} significantly increases CD73 expression, suggesting a potential auto-regulatory loop exploited by tumors for generation of more adenosine (41). There are also overlapping and nonoverlapping tumor-promoting effects of A_{2AR} and A_{2BR} (7, 8, 10, 11, 55, 56). Therefore, evidence to date indicates that targeting multiple receptors, or targeting adenosine receptors with CD73 blockade, may result in a stronger effect on tumor growth than targeting single receptors or ectonucleotidases (41). Enzymatic depletion of tumor-associated adenosine with $PEGADA2^{HCA}$ can be an alternative and more direct approach compared with targeting multiple components of adenosine signaling separately. Importantly, we found that suppression of macrophage activation by adenosine was completely reversed by $PEGADA2^{HCA}$ but not by small molecule adenosine receptor blockade, and that $PEGADA2^{HCA}$ alone caused monotherapy effects in a wide dose range and in models refractory to adenosine receptor blockade as a monotherapy, such as CT26 (57). These observations support the potential benefits of targeting the adenosine pathway by PEGADA2 as compared with other therapies. Co-blockade of A2AR and CD73 causes a strong combinatorial effect in control of tumor growth (41). It remains tested whether combinatorial targeting of purinergic signaling with adenosine receptor blockade and/or CD39/CD73 blockade and PEGADA2 will cause a stronger TGI as compared with single approaches alone.

Our analysis of public data suggested ADA2 expression is associated with the enrichment of pathways leading to adaptive immune system activation, increased T-cell costimulation and tumor infiltration by T cells. We observed $PEGADA2^{HCA}$-mediated infiltration of $CD8^+$ T cells and cDC1 in two different syngeneic tumor models with different genetic backgrounds and showed that $CD8^+$ T-cell depletion reversed TGI caused by $PEGADA2^{HCA}$. These suggest that the association between ADA2 expression and the enrichment of adaptive immune response pathways in humans can be caused by functional effects of ADA2 expressed in the TME. Patients with ADA2 deficiency syndrome (DADA2) commonly have mutations in the regions coding for the catalytic site (58). Therefore, further epidemiologic evaluation of patients with ADA2 deficiency with respect to cancer incidence and progression, or testing $PEGADA2^{HCA}$ in the clinic, may shed further light on this association.

PEGylated monomeric isoform of adenosine deaminase (PEGADA1) is used in clinic as an enzyme replacement therapy (ERT) for the rare genetic disease called adenosine deaminase deficiency, which causes severe combined immunodeficiency (ADA-SCID). Both ADA1 and ADA2 have advantages over one another as a potential novel cancer therapy. ADA1 has higher affinity towards adenosine and higher catalytic activity as compared with ADA2. Also, there is more clinical experience with ADA1 as it has been used for decades for ERT. Being an intracellular protein ADA1 lacks a secretion signal sequence and has more potential to have immunogenicity among immunocompetent patient population (unlike patients with ADA-SCID) especially if high doses are required and if combined with other immunotherapies. Unlike ADA2, ADA1 can equally target both adenosine and deoxyadenosine whereas ADA1 has more selective towards adenosine. However, whether dual targeting of adenosine and deoxyadenosine in cancer setting is an advantage or disadvantage should be further investigated. ADA2 has a lower catalytic activity but has several features that position this enzyme well as a novel therapy for cancer such as acidic pH optimum often seen in the tumor microenvironment, being a secreted protein (which promotes its developability as a new molecular entity and reduces risk of immunogenicity), and potential to reduce not steady state but pathological levels of adenosine.

To further develop $PEGADA2^{HCA}$ as an anticancer immunotherapy, more research is needed to explore dosing regimens and potential therapeutic response to $PEGADA2^{HCA}$ in human clinical trials. Because high expression of ADA2 itself is potentially prognostic for better survival, and indicative of increased expression of IFNγ-gene signatures in some indications, ADA2 expression could serve as a possible biomarker for patient selection for immunotherapies or therapies targeting adenosine signaling.

Downloaded from cancerres.aacrjournals.org on January 20, 2022. © 2021 American Association for Cancer Research.

Published OnlineFirst April 16, 2021; DOI: 10.1158/0008-5472.CAN-21-0340

Authors' Disclosures

L. Wang reports a patent for US 9,969,998 B2 issued. M.J. LaBarre reports other support from Halozyme outside the submitted work. H. Shepard reports employment with Halozyme Therapeutics, Inc. C.D. Thanos reports a patent 9,969,998 issued. O. Sahin reports grants from Halozyme Therapeutics, Inc. during the conduct of the study, personal fees from OncoCube Therapeutics LLC outside the submitted work, and is a co-founder of OncoCube Therapeutics LLC. C. Cekic reports employment and ownership of shares with Halozyme Therapeutics, Inc. No disclosures were reported by the other authors.

Data Sharing Statement

Halozyme Therapeutics, Inc. follows policies established by the International Committee of Medical Journal Editors. The studies were conducted by Halozyme Therapeutics, Inc., and the data are held by the company. The availability of the biological material, PEGylated adenosine deaminase 2, will require Material Transfer Agreements through Halozyme Therapeutics, Inc. Additional information about the studies and/or datasets can be obtained by contacting Halozyme Therapeutics, Inc., 11388 Sorrento Valley Road, San Diego, CA 92121. Phone: 1-858-794-8889; Email: publications@halozyme.com.

Authors' Contributions

L. Wang: Conceptualization, resources, investigation, project administration, writing–review and editing. **L.M. Londono:** Formal analysis, investigation, methodology, project administration, writing–review and editing. **J. Cowell:** Investigation, methodology, writing–review and editing. **O. Saatci:** Data curation, formal analysis, investigation, writing–review and editing. **M. Aras:** Investigation, methodology, writing–review and editing. **P.G. Ersan:** Investigation, methodology, writing–review and editing. **S. Serra:** Investigation, methodology, writing–review and editing. **H. Pei:** Investigation, methodology, writing–review and editing. **R. Clift:** Investigation, methodology, writing–review and editing. **Q. Zhao:** Resources, methodology. **K.B. Phan:** Investigation, methodology, writing–review and editing. **L. Huang:** Resources, investigation, methodology. **M.J. LaBarre:** Project administration, writing–review and editing. **X. Li:** Investigation, methodology, writing–review and editing. **H.M. Shepard:** Investigation, project administration, writing–review and editing. **S. Deaglio:** Resources, investigation, project administration, writing–review and editing. **J. Linden:** Resources, investigation, project administration, writing–review and editing. **C.D. Thanos:** Conceptualization, investigation, project administration, writing–review and editing. **O. Sahin:** Resources, investigation, methodology, project administration, writing–review and editing. **C. Cekic:** Conceptualization, data curation, supervision, investigation, methodology, writing–original draft, project administration, writing–review and editing.

Acknowledgments

Development of this manuscript was supported by Halozyme Therapeutics, Inc. The authors would like to thank Sanna Rosengren, Robert Connor, Curt Thompson, Daniel C. Maneval, Keri Cannon, Charvi Nanavati, Michael Ouellette, Celine Derunes, Raju Koduri, Darin Taverna, Barbara Blouw, and Benjamin Thompson for their support with this program and for valuable scientific discussions. They thank Özlem S. Sahin for helping with *in vivo* experiments. The results published here are, in part, based upon data generated by the TCGA Research Network: https://www.cancer.gov/tcga. Minor editorial and medical writing support, under the direction of the authors, was provided by Rachel O'Meara, PhD, Cristina Tomás, PhD, Natalie Morton, MSc, and Michelle Seddon, Dip Psych, all of Paragon Medica, and was funded by Halozyme Therapeutics, Inc.

The costs of publication of this article were defrayed in part by the payment of page charges. This article must therefore be hereby marked *advertisement* in accordance with 18 U.S.C. Section 1734 solely to indicate this fact.

Received January 31, 2021; revised March 22, 2021; accepted April 13, 2021; published first April 16, 2021.

References

1. Joyce JA, Fearon DT. T cell exclusion, immune privilege, and the tumor microenvironment. Science 2015;348:74–80.
2. Hanahan D, Weinberg RA. Hallmarks of cancer: the next generation. Cell 2011; 144:646–74.
3. Eltzschig HK. Extracellular adenosine signaling in molecular medicine. J Mol Med (Berl) 2013;91:141–6.
4. Cekic C, Linden J. Purinergic regulation of the immune system. Nat Rev Immunol 2016;16:177–92.
5. Hasko G, Linden J, Cronstein B, Pacher P. Adenosine receptors: therapeutic aspects for inflammatory and immune diseases. Nat Rev Drug Discov 2008;7: 759–70.
6. Cekic C, Linden J. Adenosine A2A receptors intrinsically regulate CD8+ T cells in the tumor microenvironment. Cancer Res 2014;74:7239–49.
7. Cekic C, Sag D, Li Y, Theodorescu D, Strieter RM, Linden J. Adenosine A2B receptor blockade slows growth of bladder and breast tumors. J Immunol 2012; 188:198–205.
8. Kjaergaard J, Hatfield S, Jones G, Ohta A, Sitkovsky M. A2A adenosine receptor gene deletion or synthetic A2A antagonist liberate tumor-reactive CD8(+) T cells from tumor-induced immunosuppression. J Immunol 2018; 201:782–91.
9. Mittal D, Sinha D, Barkauskas D, Young A, Kalimutho M, Stannard K, et al. Adenosine 2B receptor expression on cancer cells promotes metastasis. Cancer Res 2016;76:4372–82.
10. Young A, Ngiow SF, Gao Y, Patch AM, Barkauskas DS, Messaoudene M, et al. A2AR adenosine signaling suppresses natural killer cell maturation in the tumor microenvironment. Cancer Res 2018;78:1003–16.
11. Chen S, Akdemir I, Fan J, Linden J, Zhang B, Cekic C. The expression of adenosine A2B receptor on antigen-presenting cells suppresses CD8(+) T-cell responses and promotes tumor growth. Cancer Immunol Res 2020;8:1064–74.
12. Antonioli L, Blandizzi C, Pacher P, Hasko G. Immunity, inflammation and cancer: a leading role for adenosine. Nat Rev Cancer 2013;13:842–57.
13. Saito M, Yaguchi T, Yasuda Y, Nakano T, Nishizaki T. Adenosine suppresses CW2 human colonic cancer growth by inducing apoptosis via A(1) adenosine receptors. Cancer Lett 2010;290:211–5.
14. Nakajima Y, Kanno T, Nagaya T, Kuribayashi K, Nakano T, Gotoh A, et al. Adenosine deaminase inhibitor EHNA exhibits a potent anticancer effect against malignant pleural mesothelioma. Cell Physiol Biochem 2015;35:51–60.
15. Hashemi M, Karami-Tehrani F, Ghavami S, Maddika S, Los M. Adenosine and deoxyadenosine induces apoptosis in oestrogen receptor-positive and -negative human breast cancer cells via the intrinsic pathway. Cell Prolif 2005;38:269–85.
16. Cekic C, Sag D, Day YJ, Linden J. Extracellular adenosine regulates naive T cell development and peripheral maintenance. J Exp Med 2013;210:2693–706.
17. Mager LF, Burkhard R, Pett N, Cooke NCA, Brown K, Ramay H, et al. Microbiome-derived inosine modulates response to checkpoint inhibitor immunotherapy. Science 2020.
18. Koyas A, Tucer S, Kayhan M, Savas AC, Akdemir I, Cekic C. Interleukin-7 protects CD8(+) T cells from adenosine-mediated immunosuppression. Sci Signal 2021;14.
19. Zavialov AV, Yu X, Spillmann D, Lauvau G, Zavialov AV. Structural basis for the growth factor activity of human adenosine deaminase ADA2. J Biol Chem 2010; 285:12367–77.
20. Gakis C. Adenosine deaminase (ADA) isoenzymes ADA1 and ADA2: diagnostic and biological role. Eur Respir J 1996;9:632–3.
21. Zavialov AV, Engstrom A. Human ADA2 belongs to a new family of growth factors with adenosine deaminase activity. Biochem J 2005;391:51–7.
22. Aghaei M, Karami-Tehrani F, Salami S, Atri M. Adenosine deaminase activity in the serum and malignant tumors of breast cancer: the assessment of isoenzyme ADA1 and ADA2 activities. Clin Biochem 2005;38:887–91.
23. Aghaei M, Karami-Tehrani F, Salami S, Atri M. Diagnostic value of adenosine deaminase activity in benign and malignant breast tumors. Arch Med Res 2010; 41:14–8.
24. Anaya J. OncoLnc: linking TCGA survival data to mRNAs, miRNAs, and lncRNAs. PeerJ Computer Science 2016;2:e67.
25. Ashburner M, Ball CA, Blake JA, Botstein D, Butler H, Cherry JM, et al. Gene ontology: tool for the unification of biology. the gene ontology consortium. Nat Genet 2000;25:25–9.
26. The Gene Ontology Consortium. The gene ontology resource: 20 years and still GOing strong. Nucleic Acids Res 2018;47:D330–D8.

Downloaded from cancerres.aacrjournals.org on January 20, 2022. © 2021 American Association for Cancer Research.

Published OnlineFirst April 16, 2021; DOI: 10.1158/0008-5472.CAN-21-0340

27. Gyorffy B, Lanczky A, Eklund AC, Denkert C, Budczies J, Li Q, et al. An online survival analysis tool to rapidly assess the effect of 22,277 genes on breast cancer prognosis using microarray data of 1,809 patients. Breast Cancer Res Treat 2010; 123:725–31.
28. Tofigh A, Suderman M, Paquet ER, Livingstone J, Bertos N, Saleh SM, et al. The prognostic ease and difficulty of invasive breast carcinoma. Cell Rep 2014;9: 129–42.
29. Rooney MS, Shukla SA, Wu CJ, Getz G, Hacohen N. Molecular and genetic properties of tumors associated with local immune cytolytic activity. Cell 2015; 160:48–61.
30. Rody A, Holtrich U, Pusztai L, Liedtke C, Gaetje R, Ruckhaeberle E, et al. T-cell metagene predicts a favorable prognosis in estrogen receptor-negative and HER2-positive breast cancers. Breast Cancer Res 2009;11:R15.
31. Nagy A, Lanczky A, Menyhart O, Gyorffy B. Validation of miRNA prognostic power in hepatocellular carcinoma using expression data of independent datasets. Sci Rep 2018;8:9227.
32. Marisa L, de Reynies A, Duval A, Selves J, Gaub MP, Vescovo L, et al. Gene expression classification of colon cancer into molecular subtypes: characterization, validation, and prognostic value. PLoS Med 2013;10:e1001453.
33. Barrett T, Wilhite SE, Ledoux P, Evangelista C, Kim IF, Tomashevsky M, et al. NCBI GEO: archive for functional genomics data sets—update. Nucleic Acids Res 2012;41:D991–D5.
34. Kelley LA, Mezulis S, Yates CM, Wass MN, Sternberg MJ. The Phyre2 web portal for protein modeling, prediction and analysis. Nat Protoc 2015;10:845–58.
35. Vijayan D, Young A, Teng MWL, Smyth MJ. Targeting immunosuppressive adenosine in cancer. Nat Rev Cancer 2017;17:709–24.
36. Selby MJ, Engelhardt JJ, Johnston RJ, Lu LS, Han M, Thudium K, et al. Preclinical development of ipilimumab and nivolumab combination immunotherapy: mouse tumor models, in vitro functional studies, and cynomolgus macaque toxicology. PLoS One 2016;11:e0161779.
37. Hay CM, Sult E, Huang Q, Mulgrew K, Fuhrmann SR, McGlinchey KA, et al. Targeting CD73 in the tumor microenvironment with MEDI9447. Oncoimmunology 2016;5:e1208875.
38. Stagg J, Divisekera U, Duret H, Sparwasser T, Teng MW, Darcy PK, et al. CD73-deficient mice have increased antitumor immunity and are resistant to experimental metastasis. Cancer Res 2011;71:2892–900.
39. Yu JW, Bhattacharya S, Yanamandra N, Kilian D, Shi H, Yadavilli S, et al. Tumor-immune profiling of murine syngeneic tumor models as a framework to guide mechanistic studies and predict therapy response in distinct tumor microenvironments. PLoS One 2018;13:e0206223.
40. Ouzounova M, Lee E, Piranlioglu R, El Andaloussi A, Kolhe R, Demirci MF, et al. Monocytic and granulocytic myeloid derived suppressor cells differentially regulate spatiotemporal tumour plasticity during metastatic cascade. Nat Commun 2017;8:14979.
41. Young A, Ngiow SF, Barkauskas DS, Sult E, Hay C, Blake SJ, et al. Co-inhibition of CD73 and A2AR adenosine signaling improves anti-tumor immune responses. Cancer Cell 2016;30:391–403.
42. Stagg J, Beavis PA, Divisekera U, Liu MC, Moller A, Darcy PK, et al. CD73-deficient mice are resistant to carcinogenesis. Cancer Res 2012;72:2190–6.
43. Ayers M, Lunceford J, Nebozhyn M, Murphy E, Loboda A, Kaufman DR, et al. IFN-gamma-related mRNA profile predicts clinical response to PD-1 blockade. J Clin Invest 2017;127:2930–40.
44. Jovanović B, Beeler JS, Pickup MW, Chytil A, Gorska AE, Ashby WJ, et al. Transforming growth factor beta receptor type III is a tumor promoter in mesenchymal-stem like triple negative breast cancer. Breast Cancer Res 2014;16: R69.
45. Chen B, Zeng X, He Y, Wang X, Liang Z, Liu J, et al. STC2 promotes the epithelial-mesenchymal transition of colorectal cancer cells through AKT-ERK signaling pathways. Oncotarget 2016;7:71400–16.
46. Fong L, Hotson A, Powderly JD, Sznol M, Heist RS, Choueiri TK, et al. Adenosine 2A receptor blockade as an immunotherapy for treatment-refractory renal cell cancer. Cancer Discov 2020;10:40–53.
47. Wang T, Gnanaprakasam JNR, Chen X, Kang S, Xu X, Sun H, et al. Inosine is an alternative carbon source for CD8(+)-T-cell function under glucose restriction. Nat Metab 2020;2:635–47.
48. Alexandrov LB, Nik-Zainal S, Wedge DC, Aparicio SA, Behjati S, Biankin AV, et al. Signatures of mutational processes in human cancer. Nature 2013; 500:415–21.
49. Galon J, Bruni D. Approaches to treat immune hot, altered and cold tumours with combination immunotherapies. Nat Rev Drug Discov 2019; 18:197–218.
50. Bastid J, Regairaz A, Bonnefoy N, Dejou C, Giustiniani J, Laheurte C, et al. Inhibition of CD39 enzymatic function at the surface of tumor cells alleviates their immunosuppressive activity. Cancer Immunol Res 2015;3:254–65.
51. Buisseret L, Pommey S, Allard B, Garaud S, Bergeron M, Cousineau I, et al. Clinical significance of CD73 in triple-negative breast cancer: multiplex analysis of a phase III clinical trial. Ann Oncol 2018;29:1056–62.
52. Deaglio S, Dwyer KM, Gao W, Friedman D, Usheva A, Erat A, et al. Adenosine generation catalyzed by CD39 and CD73 expressed on regulatory T cells mediates immune suppression. J Exp Med 2007;204:1257–65.
53. Jiang T, Xu X, Qiao M, Li X, Zhao C, Zhou F, et al. Comprehensive evaluation of NT5E/CD73 expression and its prognostic significance in distinct types of cancers. BMC Cancer 2018;18:267.
54. Leone RD, Emens LA. Targeting adenosine for cancer immunotherapy. J Immunother Cancer 2018;6:57.
55. Beavis PA, Divisekera U, Paget C, Chow MT, John LB, Devaud C, et al. Blockade of A2A receptors potently suppresses the metastasis of CD73+ tumors. Proc Natl Acad Sci U S A 2013;110:14711–6.
56. Cekic C, Day YJ, Sag D, Linden J. Myeloid expression of adenosine A2A receptor suppresses T and NK cell responses in the solid tumor microenvironment. Cancer Res 2014;74:7250–9.
57. Willingham SB, Ho PY, Hotson A, Hill C, Piccione EC, Hsieh J, et al. A2AR Antagonism with CPI-444 induces antitumor responses and augments efficacy to anti-PD-(L)1 and anti-CTLA-4 in preclinical models. Cancer Immunol Res 2018;6:1136–49.
58. Meyts I, Aksentijevich I. Deficiency of adenosine deaminase 2 (DADA2): updates on the phenotype, genetics, pathogenesis, and treatment. J Clin Immunol 2018; 38:569–78.

Downloaded from cancerres.aacrjournals.org on January 20, 2022. © 2021 American Association for Cancer Research.

Published OnlineFirst April 16, 2021; DOI: 10.1158/0008-5472.CAN-21-0340

Cancer Research
The Journal of Cancer Research (1916–1930) | The American Journal of Cancer (1931–1940)

AACR American Association for Cancer Research

Targeting Adenosine with Adenosine Deaminase 2 to Inhibit Growth of Solid Tumors

Lin Wang, Luz M. Londono, Jessica Cowell, et al.

Cancer Res 2021;81:3319-3332. Published OnlineFirst April 16, 2021.

Updated version	Access the most recent version of this article at: doi:10.1158/0008-5472.CAN-21-0340
Supplementary Material	Access the most recent supplemental material at: http://cancerres.aacrjournals.org/content/suppl/2021/04/15/0008-5472.CAN-21-0340.DC1

Cited articles	This article cites 56 articles, 19 of which you can access for free at: http://cancerres.aacrjournals.org/content/81/12/3319.full#ref-list-1
Citing articles	This article has been cited by 1 HighWire-hosted articles. Access the articles at: http://cancerres.aacrjournals.org/content/81/12/3319.full#related-urls

E-mail alerts	Sign up to receive free email-alerts related to this article or journal.
Reprints and Subscriptions	To order reprints of this article or to subscribe to the journal, contact the AACR Publications Department at pubs@aacr.org.
Permissions	To request permission to re-use all or part of this article, use this link http://cancerres.aacrjournals.org/content/81/12/3319. Click on "Request Permissions" which will take you to the Copyright Clearance Center's (CCC) Rightslink site.

Downloaded from cancerres.aacrjournals.org on January 20, 2022. © 2021 American Association for Cancer Research.